Delineating how PI3K/PTEN oncogenic signalling contributes to Prostate Cancer

---

Manisha Mullen

European Cancer Stem Cell Research Institute
School of Biosciences
Cardiff University

Thesis submitted to Cardiff University for the degree of
Doctor of Philosophy
2021

Ysgoloriaethau Sgiliau Economi Gwybodaeth
Knowledge Economy Skills Scholarships

Llywodraeth Cymru
Welsh Government
Ewrop & Chymru: Buddsoddi yn eich dyfodol
Cronfa Gymdeithasol Ewrop
Europe & Wales: Investing in your future
European Social Fund

Acknowledgements

I would like to express my sincere gratitude to my supervisors Helen Pearson, Richard Clarkson and Matt Smalley, alongside my funding bodies KESS 2 and Tenovus Cancer Care, for providing me with the opportunity to carry out a PhD at Cardiff University.

It has been a remarkable experience made even better with the people I have met at ECSCRI, especially past and current members of the HBP lab group (including Nick and Dan), who kept up morale both pre- and post-COVID. I'd also like to thank Sarah, Giusy, Valerie and Jolene for never failing to lend me a helping hand.

I wish to thank the Transgenic 2-unit staff and other technical staff for their contributions and support towards my project. *In vivo* work can at times be very challenging, however it was made much easier with assistance from these kind people.

Finally, I would like to thank my close family and friends for their continued support throughout my academic career, especially my husband who has been there with me each step of the way, therefore Stephen I dedicate this thesis to you.

Abstract

In 2020, an estimated 19.3 million new cancer cases were diagnosed, 7.3 % of which were cancer of the prostate. It is evident that the development of prostate tumours is highly dependent on the acquisition of genomic alterations and recent work has identified the potential to stratify patients for therapies based on their mutational status.

The phosphatidylinositol-3-kinase (PI3K) signalling cascade is frequently activated in prostate cancer, promoting tumour growth and survival. Additionally, the PI3K pathway has been shown to mediate resistance to androgen-deprivation therapy (ADT), leading to lethal and currently untreatable castrate-resistant prostate cancer (CRPC), thus a key clinical challenge faced in the clinic is how to effectively target the PI3K pathway.

Previous work in the lab has identified that *Pten* loss and *Pik3ca* activation, that frequently drive PI3K signalling in patients with prostate cancer, cause distinct prostate cancer pathologies and can cooperate to accelerate tumorigenesis and CRPC transition *in vivo*, suggesting that different genetic drivers within the PI3K pathway can mediate distinct signalling events.

To delineate the mechanisms in which oncogenic *Pik3ca* (*Pik3ca*$^{+/H1047R}$) and *Pten* loss (*Pten*$^{fl/fl}$) in the prostate drive tumorigenic processes, this project utilised RNA-Sequencing (RNA-Seq) and ensemble gene set enrichment pathway analysis (eGSEA). In the intact (uncastrated) setting, we identified significant upregulation of NF-κB transcription factors, pathway mediators and transcriptional targets in *Pten*-deficient prostate cancer relative to *Pik3ca*-activated prostate tumours. Our bioinformatic based findings were further validated in *Pten*-deficient *in vitro* and *ex vivo* models of prostate cancer, highlighting the NF-κB pathway as a PI3K-independent avenue for therapeutic intervention in patients with PTEN-null prostate cancer.

Furthermore, to determine whether *Pten* loss in fibroblasts could additionally drive tumorigenic processes in the prostate, this project examined the phenotype of *Col1a2CreER(T2) wild-type, Pten*$^{+/fl}$ *and Pten*$^{fl/fl}$ transgenic mouse prostates. We observed focal prostate hyperplasia within all prostate lobes following heterozygous and homozygous loss of fibroblast cell PTEN, indicating that PTEN loss in either epithelial or stromal cells of the prostate can disrupt normal tissue homeostasis. These findings highlight the need to further understand how PI3K/PTEN signalling coordinates tumour-stroma interactions during prostate tumorigenesis, which may uncover new therapeutic targets and/or predictive biomarkers.

Abbreviations

ACT	A-1-antichymotrypsin
ADT	Androgen deprivation therapy
ALDH1A1	Aldehyde dehydrogenase 1 family member A1
ALDH1A3	Aldehyde dehydrogenase 1 family member A3
ALL	Acute lymphoblastic leukaemia
AMP	Amplification
AP-1	Activation protein 1
APC	Anaphase-promoting complex
apCAF	Antigen-presenting cancer-associated fibroblasts
AR	Androgen receptor
ARE	Androgen responsive element
ATM	Ataxia-telangiectasia mutant kinase
ATR	ATM Rad3 related kinase
AWERB	Animal welfare ethical review body
B	B lymphocytes
BCL10	B-cell lymphoma 10
BCL3	B-cell leukaemia/lymphoma 3
BCR	B-cell receptor
BPH	Benign prostate hyperplasia
BSA	Bovine serum albumin
CAA	Cancer-associated adipocytes
CAF	Cancer-associated fibroblasts
CARD11	Caspase recruitment domain-containing protein 11
CC3	Cleaved caspase 3
CDH1	Chromodomain helicase DNA-binding protein 1
CDHR1	Cadherin related family member 1
cfDNA	Cell-free DNA
CID	Chemical inducers of dimerization
CK14	Cytokeratin 14
CK18	Cytokeratin 18
CK5	Cytokeratin5
CK8	Cytokeratin 8
COL10A1	Collagen type X alpha 1 chain
COL11A2	Collagen type XI alpha 2 chain
COL25A1	Collagen type XXVII alpha 1 chain
CRISPR	Clustered regularly interspaced short palindromic repeat
CREB	cAMP response element binding protein
CRPC	Castration resistant prostate cancer
CSC	Cancer stem cells
CXCR1/2	C-X-C chemokine receptor 1 / 2
DC	Dendritic cells
DEFB50	Beta-defensin 50 precursor
DEG	Differentially expressed gene
DEL	Deep deletion

DEPTOR	DEP domain containing MTOR interacting protein
DHT	Dihydrotestosterone
DMSO	Dimethyl sulphoxide
DNA-PK	DNA-dependent protein kinase
DRE	Digital rectal examination
DSB	Double strand break
E	Epithelial cells
ECM	Extracellular matrix
EGF	Epidermal growth factor
EGFR	Epidermal growth factor receptor
eGSEA	Ensemble Gene Set Enrichment Analysis
EMC	Epithelial to mesenchymal communication
EMT	Epithelial to mesenchymal transition
EndMT	Endothelial to mesenchymal transition
ER	Estrogen receptor
F	Fibroblasts
FAK	Focal adhesion kinase
FBS	Foetal bovine serum
FFPE	Formalin-fixed paraffin-embedded
FGF	Fibroblast growth factor
FGFR1	Fibroblast growth factor receptor 1
FISH	Fluorescent in situ hybridization
FMO	Fluorescence minus one
FMS	Fibromuscular sheath
FMT	Fibroblast-to-myofibroblast transition
FOXA1	Forkhead box protein A1
FSP1	Fibroblast marker fibroblast specific protein 1
GAP	GTPase activating protein
GAPDH	Glyceraldehyde-3-phosphate dehydrogenase
GBM	Glioblastoma multiform
GEMM	Genetically engineered mouse models
GR	Glucocorticoid receptors
GSK3β	Glycogen synthase kinase 3 beta
GU	Genitourinary
H&E	Haematoxylin and eosin
HDAC	Histone deacetylase
HGPIN	High-grade prostatic intraepithelial neoplasia
HSP70	Heat shock protein 70
HRP	Horseradish peroxidase
HSA	Highest single agent
HTA	Human Tissue Act
HOXB13	Homeobox protein 13
HUVEC	Human umbilical vein endothelial cells
iCAF	Inflammatory cancer-associated fibroblasts
IF	Immunofluorescence
IGF	Insulin-like growth factor

IHC	Immunohistochemistry
IL-8	Interleukin 8
JOCK	Juxtaposition of CID and kinase1
KC	Keratinocyte-derived protein chemokine
KGF	Keratinocyte growth factor
KLK1B2	Kallikrein 1-related peptidase b26
L	Lymphatic endothelial cells
LBD	Ligand binding domain
LIX	Lipopolysaccharide-induced CXC chemokine
LMAN1L	Lectin mannose binding 1 protein
LN_2	Liquid nitrogen
Log2CPM	Log_2 counts per million read
LoxP	Locus of x-over, P1
LPB	Large PB
M	Macrophages
MALT1	Mucosa-associated lymphoid tissue lymphoma translocation protein 1
mCRPC	Metastatic CRPC
MCTP	Michigan Center for Translational Pathology
MDS	Multidimensional scaling
MDSC	Myeloid-derived suppressor cells
MIP-2	Macrophage inflammatory protein-2
miRNAs	MicroRNAs
MMPs	Matrix metalloproteinases
MMTV	Mouse mammary tumour virus
MRI	Magnetic resonance imaging
MSC	Mesenchymal stem cells
MSKCC	Memorial Sloan-Kettering Cancer Centre
mTORC1	Mechanistic target of rapamycin complex 1
mTORC2	Mechanistic target of rapamycin complex 2
MUT	Mutation
myCAF	Myofibroblastic cancer-associated fibroblasts
N	Neutrophils
NER	Nucleotide excision repair
NEPC	Neuroendocrine prostate cancer
NF-κB	Nuclear Factor kappa Beta
NFKBIE	NF-κB inhibitor epsilon
NHS	Normal horse serum
NIK	NF-κB inducing kinase
NK	Natural killer cells
NLS	Nuclear localisation sequence
NO	Nitric oxide
NOD	Nonobese diabetic
NSE	Neuron specific enolase
NSG	NOD scid gamma
p-4EBP1	Phosphorylated eukaryotic translation initiation factor 4E-binding protein 1
p70S6K	Ribosomal protein S6 kinase beta-1

PAMPs/DAMPs	Pathogen- / damage- associated molecular patterns
PAR-4	Prostate apoptosis response 4 protein
PBSN	Probasin
PCA3	Prostate cancer antigen 3
PCNA	Proliferating clear nuclear antigen
PDAC	Pancreatic ductal adenocarcinoma
PDE	Patient derived explant
PDGF	Platelet-derived growth factor
PDGFRα	Platelet-derived growth factor receptor alpha
PDK1	Phosphoinositide-dependent kinase 1
PDX	Patient derived xenograft
PEL	Primary effusion lymphoma
PI3K	Phosphatidylinositol 3-kinase
PIKK	Phosphatidylinositol-3-kinase-related kinase
PIN	Prostatic intraepithelial neoplasia
PIP2	Phosphatidylinositol-4,5-bisphosphate
PIP3	Phosphatidylinositol-3,4,5-triphosphate
PLL	Poly-L-lysine
PKCγ	Protein kinase C gamma
PRCAD	Protocadherin 21
PRRs	Pattern-recognition receptors
PSA	Specific antigen
PtdIns	Phosphatidylinositides
PX	Phox
PTEN	Phosphatase and tensin homologue
qRT-PCR	Quantitative real-time PCR
RAC1	Rac family small GTPase 1
Rb	Retinoblastoma protein
RB1	Retinoblastoma
RBC	Red blood cell
RFP	Red fluorescent protein
RHD	Rel homology domain
RICTOR	RPTOR independent companion of MTOR
Rheb	Ras homolog expressed in brain
RIN Value	RNA integrity number
RNA-Seq	RNA-Sequencing
RPPA	Reverse phase protein array
S6K1	Ribosomal protein S6 kinase beta-1
SAHF	Senescence-associated heterochromatin foci
SASP	Senescence associated secretory phenotype
SBP	Spermine-binding protein
SCID	Severely compromised immune deficient
SCNA	Somatic copy number aberration
sgRNAs	Single-guide RNAs
SPINK3	Serine protease inhibitor kazal-type 3
STAT	Signal transducer and activator of transcription

STC2	Stanniocalcin 2
STR	Short tandem repeat
SU2C/PCF	Stand Up 2 Cancer / Prostate Cancer Foundation
SV40	Simian virus 40
T	T lymphocytes
TA	Transactivation domain
TAM	Tumour-associated macrophages
TAN	Tumour-associated neutrophil
TBS	Tris buffered saline
TCGA	The Cancer Genome Atlas
TCR	T cell receptor
TDE	Tumour derived extracellular vesicles
TEC	Tumour endothelial cells
TEL2	Telomere length regulation protein
TGF-β	Transforming growth factor beta
TIR	Toll/IL-1 receptor resistance
TMA	Tissue microarray
TNBC	Triple negative breast cancer
TLR2	Toll-like receptor 2
TLR2-Myd88	Toll-like receptor 2 - myeloid differentiation primary response gene 88
TME	Tumour microenvironment
TMPRSS-ERG	Transmembrane protease serine 2:v-ets erythroblastosis virus E26 oncogene homolog
TNF	Tumour necrosis factor
TNF-α	Tumour necrosis factor alpha
TNM	Tumour, node, metastasis
TP53	Tumour promoting P53
TRAMP	The TRansgenic Adenocarcinoma Mouse Prostate
Treg	Regulatory T lymphocytes
TTI	TEL2 interacting protein 1
TURP	Transurethral resection of the prostate
VCFG	Victorian Centre for Functional Genomics
VPS34	Vacuolar sorting protein sorting 34
WB	Western blotting
WCB	Wales Cancer Bank
ZIP	Zero interaction potency
ΔΔCt	Delta delta Ct

Contents

Table of figures

Table of tables

Chapter 1

1. Introduction

1.1. The prostate

1.1.1. Prostate development and function

As a reproductive accessory organ, the prostate functions to produce a third of the overall seminal fluid required to nourish sperm and maintain a high semen pH (Leslie and Siref 2018). Regulated by the nervous and endocrine systems, the male reproductive system produces sperm from the seminiferous tubules of the testis that subsequently mature within the epididymis (Figure 1.1). During ejaculation, seminal fluid produced by the prostate and seminal vesicles, travel through the urethra to combine with sperm expelled through the vas deferens (also called ductus deferens), thus generating semen (Mawhinney and Mariotti 2013).

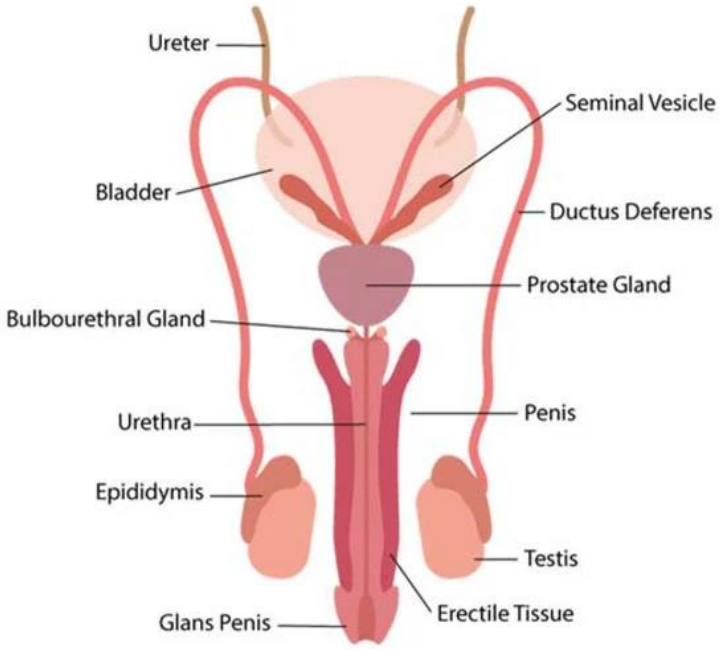

Figure 1.1: The male reproductive tract. Schematic depicts anatomical structures of the primary and accessory sex organs involved within the male reproductive system. (Image source: (Da Silva 2018))

Through the processes of epithelial budding, branching morphogenesis and epithelial differentiation, prostate organogenesis begins at ten weeks of gestation from the urogenital sinus and ends once maximal organ size has been reached during puberty (Toivanen and Shen 2017). Prostatic epithelial cell specification and cellular differentiation is dependent on key transcription factors and regulators such as the homeobox protein 13 gene (*HOXB13*) and NK homeobox 1 gene (*NKX3.1*) (Toivanen and Shen 2017), but most importantly androgen signalling via the androgen receptor (AR) (Cunha et al. 2018). Binding proteins such as Forkhead box protein A1 (FOXA1), recruit AR to androgen response

elements (ARE) within promoter regions of open and accessible chromatin, to enable transcription of prostate and AR specific genes (Toivanen and Shen 2017).

During cell fate specification (Figure 1.2A), urogenital epithelial progenitor cells are generally considered to give rise to basal and luminal progenitors, which further progress into (a) basal cells that express cytokeratin 5 and 14 (CK5/CK14) and the transcription factor p63, (b) luminal cells that express cytokeratin 8 and 18 (CK8/CK18) and secretory proteins including prostate specific antigen (PSA, encoded by *KLK3*), NKX3.1, and AR, or c) a putative intermediate cell type that co-expresses both basal and luminal markers (Henry et al. 2018).

Urogenital mesenchyme progenitor cells give rise to smooth muscle cells, infiltrating mesenchymal stem cells that can produce stromal fibroblasts, and a rare type of prostate epithelial cell termed neuroendocrine cells, which are hypothesised to originate from neural crest progenitors; expressing synaptophysin, chromogranin A and neuron specific enolase (NSE) (Toivanen and Shen 2017). Collectively, the basal, luminal and neuroendocrine cells establish the prostatic epithelial layer which is surrounded by a layer of smooth muscle cells and the stroma containing fibroblasts, endothelial cells (blood vessels), dendritic cells (neurons), infiltrating immune cells, alongside various structural and matricellular proteins and factors (Levesque and Nelson 2017).

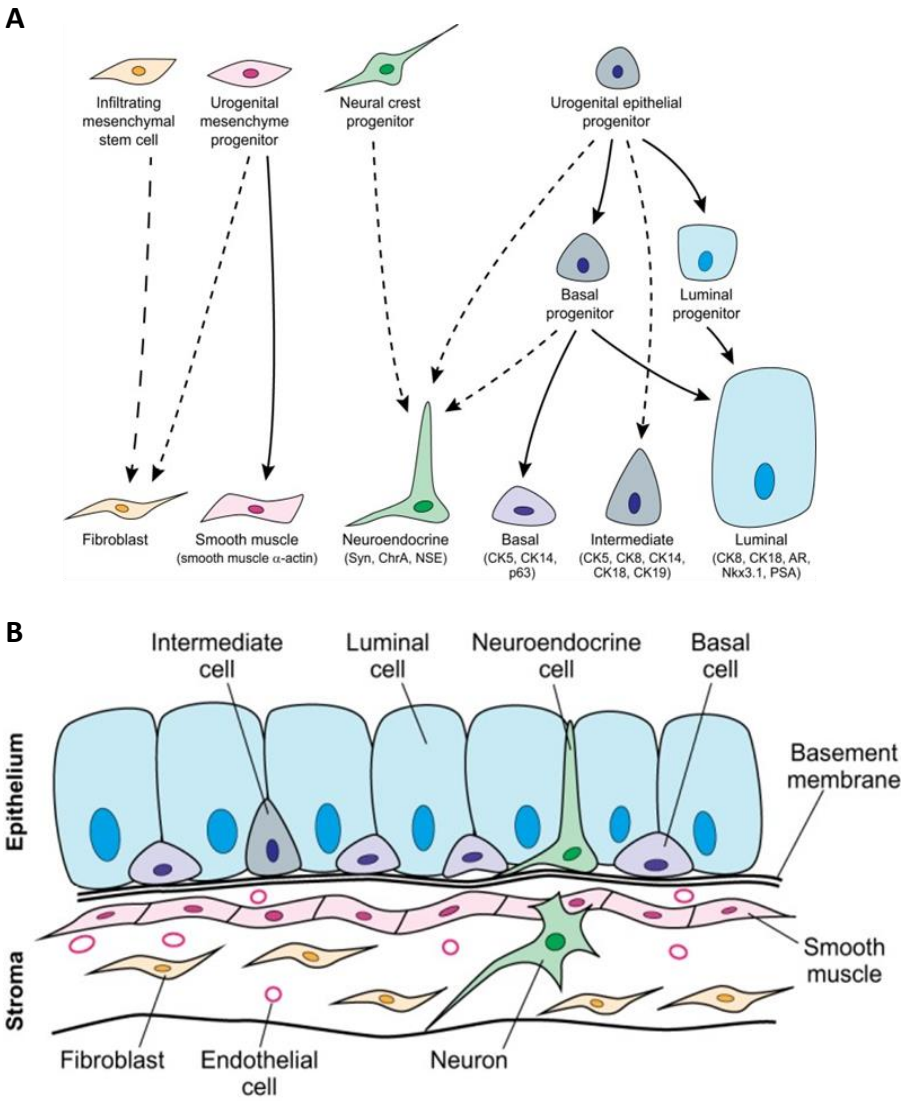

Figure 1.2: Lineages and cell arrangement within the prostate. Diagram depicts A) the progenitor cells that give rise to the differentiated cell populations that enable prostate functionality and B) positioning of these cells within the prostate epithelium and stroma. (Images taken and adapted from Toivanen and Shen 2017).

AR expression is observed both in the prostate epithelium and stroma, such that prostate gland development is reliant on reciprocal paracrine signalling between them (Crumbaker et al. 2017). AR signalling is vital for conferring differentiation between the epithelium cell types and the stroma, as each have independent roles in prostate homeostasis (Zarif and Miranti 2016). Foetal androgen signalling mediated through stromal AR, is responsible for prostate ductal morphogenesis, epithelial differentiation and regulation of proliferation and apoptosis, whereas within adulthood, epithelial AR signalling governs cellular homeostasis and regulation of the prostate secretory function (Chauhan et al. 2020).

Following induction of AR by extracellular androgens, the stroma can also produce andromedins (growth factors mediated by androgens), which further regulate epithelial cell differentiation, growth and survival (Hägglöf and Bergh 2012). Andromedins include members of the Wnt, epidermal growth factor (EGF), insulin-like growth factor (IGF) and fibroblast growth factor (FGF) families (Hägglöf and Bergh 2012).

1.1.2. Human and mouse prostate anatomy

1.1.2.1. The human prostate

The human prostate is situated beneath the bladder, encircling the urethra, and is partitioned into three zones categorised based on their anatomical location, histological and embryological features (Figure 1.3A) (Vargas et al. 2012). The peripheral zone dominates prostatic volume at 70%, with the central zone making up 20%, and the remaining 10% formed of the transition zone. Together they compose a lobular structure consisting of epithelial ducts surrounded by a thick continuous fibromuscular stroma (Toivanen and Shen 2017).

Within these prostatic ducts, basement membranes are lined with non-secretory basal cells and positioned above these, luminal cells that secrete components of seminal fluid including proteins such as zinc, citric acid and PSA (Figure 1.2B) (Mawhinney and Mariotti 2013). A large structural network of growth factor and nerve signalling, immune cells, blood and lymphatic vessels, support the contractile activity of the smooth muscle within the mesenchyme that is required for the expulsion of seminal fluid from within the ducts (Toivanen and Shen 2017).

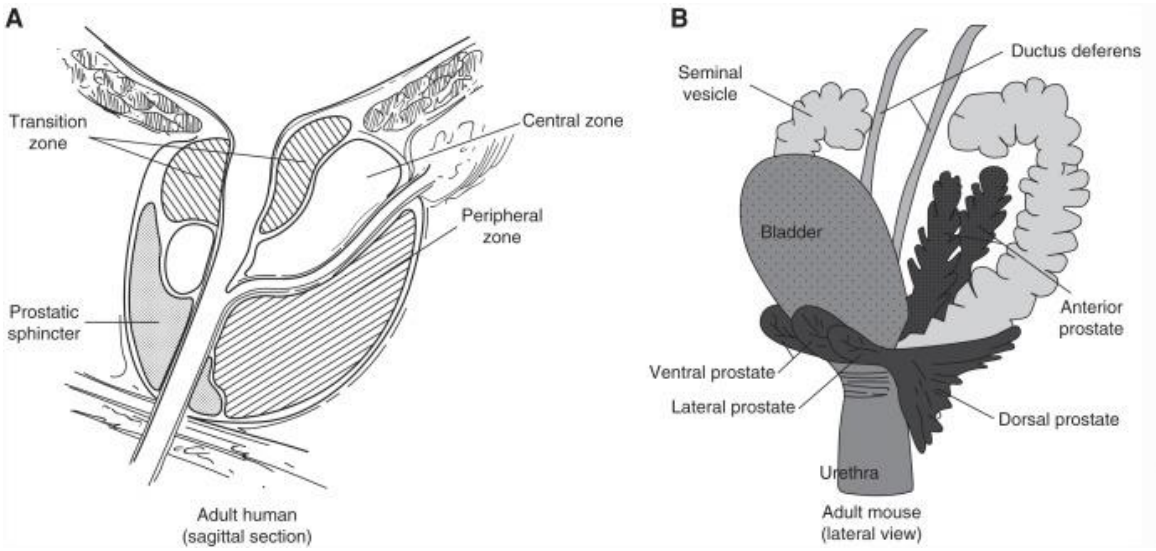

Figure 1.3: Human and mouse prostate anatomical structures. Schematics depict A) the human prostate as one singular anatomical structure containing the central, transition and peripheral zones and B) the mouse prostate, comprised of 4 bi-lobular prostate glands, known as the ventral, lateral, dorsal and anterior lobes. (Image source: Ittman 2018).

1.1.2.2. The mouse prostate

The overall anatomical structure of the mouse prostate largely differs from the compact human prostate (Figure 1.3B). Instead, the mouse prostate is composed of lobes distinguished via their spatial orientation: anterior, dorsal, lateral, and ventral, where the dorsal and lateral lobes are often referred to together as the dorsolateral lobe (Ittmann 2018). With regards to similarities, the dorsolateral lobes of the mouse are most homologous to the human peripheral zone and the mouse anterior lobes most similar to the human central zone, however there is no human equivalent for the ventral lobe (Oliveira et al. 2016). Glands of the mouse prostate also show similarities with human prostate basal cell, luminal cell and neuroendocrine cell populations; although the mouse prostate can additionally display discontinuous basal cell layers around each gland (Shappell et al. 2004).

Interestingly, each of the mouse prostatic lobes display a unique morphology (Figure 1.4), such that long-term studies of murine prostate tissue stained with haematoxylin and eosin, have enabled researchers to better identify each of the varying structures within their own investigations (Ittmann 2018).

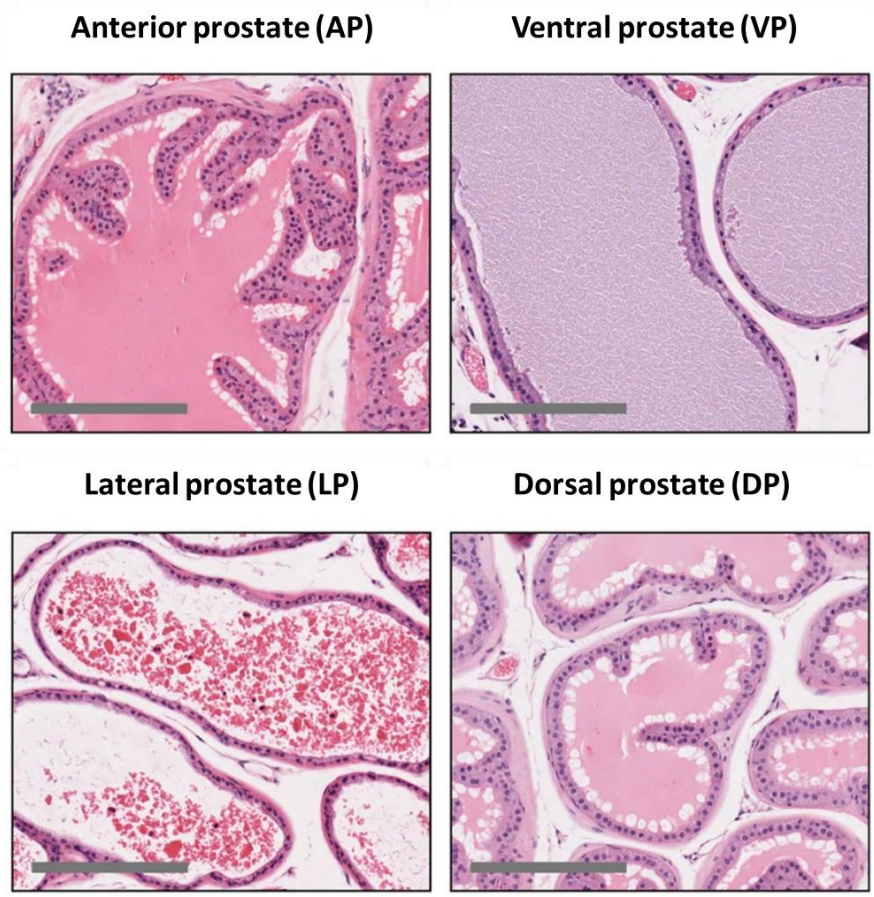

Figure 1.4: Mouse prostate lobe histology. Images display H&E staining of wildtype mouse prostate, with each scale bar shown representing 200 µm. Image source: (Jurmeister et al. 2018).

1.1.3. Oncogenic transformation

Once the human prostate has reached a state of maturity post-puberty, epithelial cell regeneration becomes slow and the organ quiescent. Nevertheless, the adult prostate is reported to succumb to oncogenic transformation far more significantly than any other male sex organ (Toivanen and Shen 2017), which can be associated with a range of physiological issues including decreased sexual function, urinary and faecal incontinence, haematuria, dysuria, leg pain and paralysis (Leslie and Siref 2018). Some prostate cancer patients however remain asymptomatic (Donnelly et al. 2019).

Prostate adenocarcinoma most commonly develops within the peripheral zone (Leslie and Siref 2018), which can arise from both transformed basal or luminal cell types, typically due to an accumulation of mutations (Park et al. 2016). These mutations that occur ordinarily result in activation of oncogenes which promote tumour progression or inactivation of tumour suppressors, which inhibit their protective role against cancer. Activation of oncogenes often transpires through point mutations,

amplification and structural rearrangements, whereas gene inactivation usually develops from a loss of genomic DNA, which can be a result of large or focal structural rearrangement (Rubin and Demichelis 2018).

Although heterogeneous in nature, frequent mutations within prostate cancer have been identified through genomic studies. These include loss of the tumour suppressor gene retinoblastoma (*RB1)*, loss of chromosome 8p, loss of heterozygosity or mutation of the tumour suppressor tumour promoting P53 (*TP53)*, deletion at 10q24, *MYC* amplification, AR mutation/amplification and *PTEN* deletion/mutation (Rubin & Demichelis, 2018). Several single nucleotide polymorphisms have also been shown to frequently contribute to the development of prostate cancer (Gandhi et al. 2017).

Preneoplastic lesions are considered precursors for the development of prostate cancer. Within the prostate, hyperplasia (an increase in cell number) can occur through both glandular and stromal proliferation, but in most cases, this is a benign form of lesion (Ng and Baradhi 2021). This is often followed by the development of prostatic intraepithelial neoplasia (PIN), which can be defined as proliferation and dysplasia exhibited within prostate ducts (Wang et al. 2018a) (Figure 1.5). Furthermore, PIN can present itself as low and high-grade forms (LG-PIN and HG-PIN respectively). PIN can exhibit a range of different architectural types including, cribriform, flat, micropapillary and tufting patterns (Abate-Shen and Shen 2000).

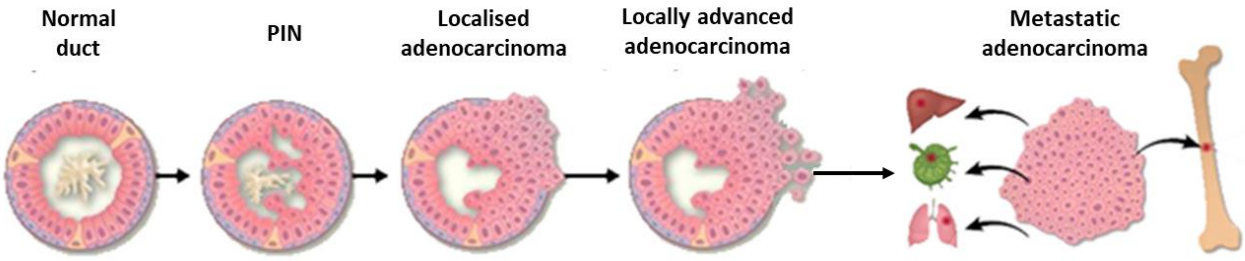

Figure 1.5: Morphological changes involved with prostate cancer progression. Schematic depicts the main stages of prostate cancer development, increasing both in complexity and aggressiveness**.** Prostate tumour cells most commonly metastasise to bone; however, metastases also occur to the liver, lymph nodes and lung**.** Figure adapted from (Wang et al. 2018a).

Subsequently, as the prostate undergoes further oncogenic transformation, PIN progresses into localised prostate carcinoma that can develop microinvasion or local invasion as the tumour progresses, where degradation of the basal lamina can enable tumour cells to invade the TME, disseminate to nearby lymph nodes and GU tissues, and distally metastasise to visceral tissues; most predominantly the bone (Wang et al. 2018a).

1.2. Prostate cancer

1.2.1. Epidemiology and aetiology

Prostate cancer is the second most frequently diagnosed cancer within men and the fifth leading cause of male cancer-related deaths worldwide (Rawla 2019). Despite mortality being the highest within middle and southern Africa, incidence of the disease is highest within the Oceanic, North American and European regions, possibly reflecting huge discrepancies in screening and diagnoses world-wide. It is estimated that by 2040, world-wide prostate cancer incidence will increase by almost 80% due to increased life expectancy and the expansion of a larger ageing population (Rawla 2019), as the strongest risk factor for prostate cancer is age. Currently the median age of diagnosis is 66 years old and although incidence has been shown to increase with age, the overall aggressiveness of prostate cancer is reported to decrease with age (Gandhi et al. 2017; Leslie and Siref 2018).

Prostate cancer incidence is also dependent on racial and geographical variation. For instance, men from African descent have both the highest incidence rate and mortality rate compared to those with European ancestry (Cuzick et al. 2014; Gandhi et al. 2017). A western-influenced diet and lifestyle have also been shown to play an important role in the development of prostate cancer risk such that immigrant populations of men from developing countries display a substantially increased risk whilst living within a westernised country (Rawla 2019). Specific dietary factors including red meat, obesity, smoking and a sedentary lifestyle pose as additional risk factors (Cuzick et al. 2014; Leslie and Siref 2018). Furthermore, urinary tract infections as well as ultraviolet and ionizing radiation, have also been linked to prostate cancer risk (Cuzick et al. 2014).

An individual's familial history also implicates their risk of developing prostate cancer. For example, a male with two affected first-degree relatives (either brother or father) will have a five-fold risk of developing prostate cancer in comparison to those with unaffected relatives (Leslie and Siref 2018). Some individuals will also have a hereditary predisposition to developing prostate cancer if possessing multiple single polymorphisms in genes such as *BRCA1, BRCA2, HOXB13, CHEK2* and *ATM* (Zhen et al. 2018).

1.2.2. Detection and biomarkers

Digital rectal examination (DRE) to assess enlargement or abnormal growth of the prostate is a common clinical practice used in making a prostate cancer diagnosis prior to obtaining a biopsy (Leslie and Siref 2018). Furthermore, non-invasive procedures such as screening for urinary markers including prostate cancer antigen 3 (PCA3) or transmembrane protease serine 2:v-ets erythroblastosis virus E26 oncogene homolog (TMPRSS-ERG) fusions have also been reported to show high specificity and sensitivity (Cuzick et al. 2014).

The 4Kscore prostate cancer test may also be carried out to measure levels of total PSA (PSA complexed with a-1-antichymotrypsin (ACT)), free PSA (unbound protein), intact PSA (a form of unbound PSA) and human kallikrein 2 protein within the blood, which has been shown in many cases to eliminate the need for biopsy due to its high predictability index (Olleik et al. 2018).

As prostate cancer can be very heterogenous in nature, identification of novel biomarkers and subsequent tests are essential for both accurate diagnoses as well as clinical management of the patient; research into new and improved serum, urine and tissue-based biomarkers are enabling this to happen (Porzycki and Ciszkowicz 2020).

For assessment of metastatic disease, magnetic resonance imaging (MRI) scans can additionally be used to identify enlargement of regional lymph nodes (Leslie and Siref 2018). Furthermore, bioactive molecules present within tumour derived extracellular vesicles (TDE) are being explored as biomarkers of metastases (Tai et al. 2020).

1.2.3. Histopathology and staging

Prior to the development of adenocarcinoma, a patient may present with pre-malignant prostate conditions, such as benign prostate hyperplasia (BPH) or prostate intraepithelial neoplasia (PIN). The transition zone of the prostate is associated with a high prevalence of benign prostatic hyperplasia; a disease caused by aberrant proliferation of normal prostate epithelial cells (Foo 2017). Although benign, BPH can cause lower urinary tract problems due to enlargement of the prostate glands restricting the urethra (Bachmann and de la Rosette 2011). Like prostate cancer, BPH has been widely linked to ageing, genetic traits (e.g. an autosomal dominant pattern of inheritance) and lifestyle/diet; but has been more recently associated with obesity, erectile dysfunction and inflammation of the prostate (Lim 2017). High-grade prostatic intraepithelial neoplasia (HGPIN, a form of PIN as detailed in Section 1.1.3) is most commonly found within the peripheral zone of the human prostate, whereby

acini, small secretory cavities, along with prostatic ducts, present significant atypia and proliferation of epithelial cells. High-grade PIN has been acknowledged as the primary precursor to prostate carcinoma (Zhou 2018).

During histopathological analysis of patient prostate biopsies, a pathologist will assign a Gleason score (Figure 1.6), consisting of a primary and secondary grade that are added together to account for potential tumour heterogeneity (Chen and Zhou 2016). Healthy tissue is scored zero and abnormal tissue given a numerical score between 1 – 5 for each sample assessed. For instance, a Gleason score of 6 (e.g., 3+3) or less is suggestive of a pre-malignant phenotype with slow tumorigenic growth, whereas a Gleason score of 7 (e.g. 3+4 or 4+3) is indicative of an intermediate risk for the cancer to become aggressive, and scores ≥8 identify tumours that are or would be metastatic, very aggressive and with a poor prognosis (Chen and Zhou 2016).

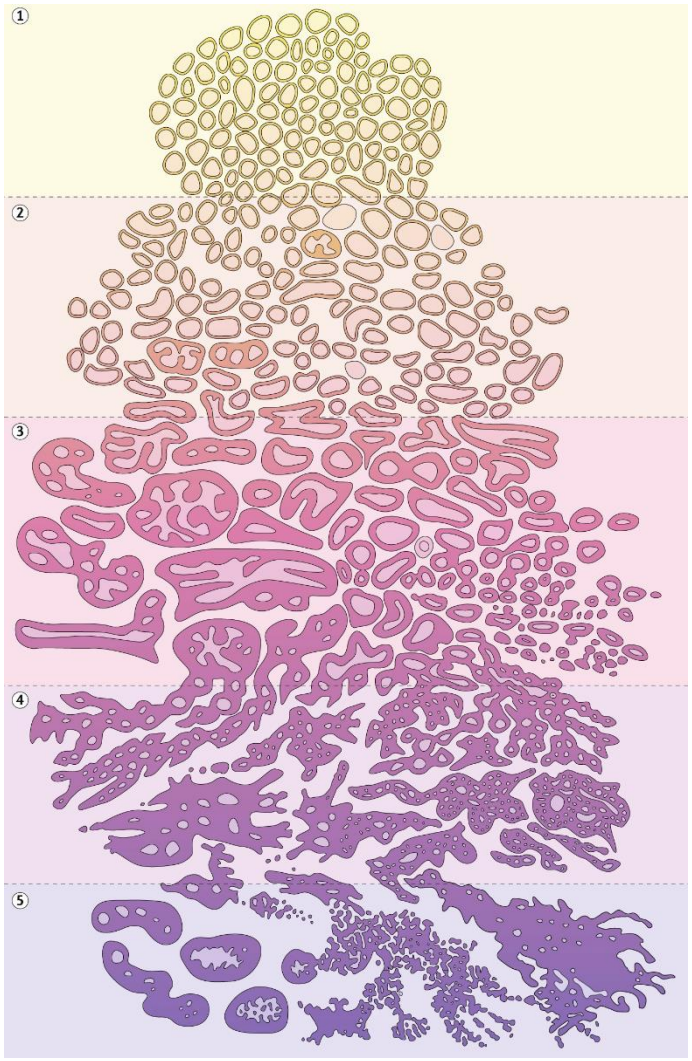

Figure 1.6: Representation of Gleason scores. Schematic depicting the Gleason score system. A score of 1 is given to uniform, closely compacted glands and a score of 2 given when increased stroma between glands of variable sizes is detected. 3 is given when irregular gland patterning starts to occur and a score of 4, given to cribriform, poorly formed glands. A score of 5 is allocated when solid nests and sheets of cells can be seen, alongside the build-up of necrotic cells within a tumour (Chen and Zhou 2016). Figure source: (Sathianathen et al. 2018).

Cancerous biopsies are also routinely staged using the TNM (tumour, node, metastasis) staging system that assesses disease development and/or spread, to aid prognosis prediction and treatment selection. Subsequent to the retrieval of cancerous tissue, the letters and numbers T0 – T4, N0 – N2 and M0 – M1 are assigned according to the amount of transformed prostatic tissue present; including its invasiveness (T) and the presence of lesions within regional lymph nodes and distant metastases (N and M respectively) (Table 1.1). Depending on the TNM combination, the patient is consequentially categorised as having stage I – IV cancer (Cheng et al. 2012).

Table 1.1: TNM staging system. Data source: (Turner and Drudge-Coates 2010).

TNM classification	Definition
T1	Incidental (impalpable and not detectable by ultrasonography)
T2	Locally confined to prostate
T3	Locally extensive
T4	Fixation onto, or invasion of, neighbouring organs
N0	No regional lymph node metastasis
N1	Metastasis in single regional lymph node <2cm in largest dimension
N2	Metastasis in single regional lymph node >2cm but <5cm in largest dimension
N3	Metastasis in regional lymph node >5cm in largest dimension
M0	No distant metastasis
M1	Distant metastasis
M1a	Metastasis in non-regional lymph nodes
M1b	Metastasis in bone
M1c	Metastasis in other sites

1.2.4. Current treatments and therapies

Patients diagnosed with localised prostate cancer generally have a very good outcome (5-year survival >99%), and treatment options include surgery, radiotherapy and/or 'active surveillance' (Duchesne 2011). If tumours progress, patients are typically offered hormone therapy, to deplete androgens such as testosterone that are utilised by the tumour for growth (Crawford et al. 2019). The survival rate of patients with prostate cancer is highly dependent on factors such as disease status, age and other genetic conditions that may impact efficacy of treatment (Gillessen et al. 2018).

1.2.4.1. Hormone therapy

The androgen receptor is a member of the steroid and nuclear receptor superfamily, that is activated upon ligand binding of androgens, testosterone or dihydrotestosterone (DHT) (Zarif and Miranti 2016). The Leydig cells of the testes and the adrenal glands can produce the androgenic steroid hormone testosterone, that is subject to conversion into DHT by cytochrome P450 enzyme 5α-reductase through the gamma-5 metabolic pathway (Lonergan and Tindall 2011; Drobkova et al. 2017). Both have AR binding capabilities, however there is a 10x greater affinity for DHT binding in comparison to testosterone (Gandhi et al. 2017). Additionally, 17α-hydroxylase present within adrenal, testicular and

prostatic tumour tissue can mediate pregnenolone conversion to testosterone (Zarif and Miranti 2016).

In the absence of androgenic steroids, AR is retained within the cytoplasm by heat shock proteins HSP90/70/56, and cytoskeletal proteins such as Filamin A, that also mediate regulation of AR nuclear translocation and thus transcriptional activity through AR hinge region interactions (Figure 1.7) (Lonergan and Tindall 2011).

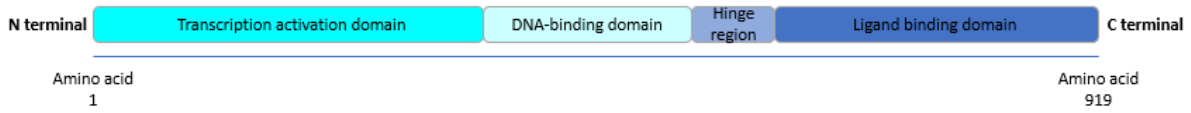

Figure 1.7: Androgen receptor subunit structure. The N terminal transcription activation domain is responsible for mediating AR functional activity, whilst the DNA-binding domain enables contact with DNA. The hinge region plays a role within AR nuclear transport and the ligand binding domain facilitates DHT and testosterone binding. Figure adapted from (Lonergan and Tindall 2011).

Sex hormone binding globulins mediate delivery of circulating testosterone to AR positive cells, where AR is then subjected to intracellular reduction (Zarif and Miranti 2016). Upon DHT binding, AR undergoes a conformational change releasing itself from HSP90. Once AR is within the nucleus, its DNA binding domain can associate with androgen responsive elements (AREs) to dimerise; recruiting transcriptional co-activators or repressors that aid with mediating transcription of AR responsive genes that instruct prostate cells to proliferate, differentiate and migrate (Bennett et al. 2010; Crumbaker et al. 2017).

AR regulates increased transcription of AR target genes including *PSA*, keratinocyte growth factor (*KGF*), *NKX3.1* and *Pbsn* (Probasin), as well as downregulation of the epidermal growth factor receptor (*EGFR*) (McEwan 2004; Traish and Morgentaler 2009; Bennett et al. 2010; Carver et al. 2011). The presence and requirement of AREs within the promoter region of an AR target gene however may not always be necessary, as AR has also been shown to bind upstream of promoters/enhancers of genes that do not possess putative AREs through interactions with other transcription factors (Zarif and Miranti 2016).

In prostate cancer, AR-mediated downregulation of *EGFR* is often lost, driving increased expression of *EGFR* mRNA and consequential downstream activation of EGFR signalling cascades such as RAS, PI3K/AKT and STAT (signal transducer and activator of transcription), resulting in increased cell

proliferation, survival, and migration to promote tumour growth (Traish and Morgentaler 2009). Additionally, it has been identified that AR within a tumorigenic setting, uncharacteristically has the potential to bind to off-target genes via interactions with additional transcription factors (Zarif and Miranti 2016).

In the absence of androgens, AR is also subject to phosphorylation at sites Ser80/95/641; conferring protection against proteolytic degradation. This phosphorylation can be mediated through ERK, MAPK, JNK or AKT signalling, which can additionally increase the response of AR during limited androgen availability (Bennett et al. 2010).

Due to the important role of androgens within prostate cancer, androgen deprivation therapy is a widely used treatment aimed at reducing the amount of circulating testosterone within the body to serum levels (i.e. below 50 ng/dL), by suppressing androgen production (Table 1.2) (Ritch and Cookson 2016; Zarif and Miranti 2016). Although a large proportion of patients experience tumour shrinkage due to the anti-proliferative and pro-apoptotic effects mediated by ADT, many individuals acquire therapeutic resistance, resulting in regression to advanced disease and consequential development of castrate resistant prostatic cancer (CRPC) (Bosso et al. 2017) (Figure 1.8).

Upon the emergence of resistant growth following treatment with first generation ADT agents (e.g., bicalutamide), second generation androgen/AR pathway inhibitors are typically administered, which are more potent inhibitors of the AR pathway (e.g., abiraterone acetate, enzalutamide and apalutamide). Depending on the aggressiveness of the tumour, androgen/AR pathway inhibitors may be given in combination with chemotherapy (e.g., docetaxel or cabazitaxel). Alternatively, patients may receive targeted therapies such as recently approved PARP inhibitors if a DNA damage repair mutation is present or are able to join an eligible clinical trial. Currently, survival outcome is poor for this patient cohort (1 - 2 years survival), owing to the limited efficacy of current treatment options against advanced, metastatic CRPC.

Table 1.2: Current clinically available treatments for prostate cancer. (Adapted from (Board 2002)).

Treatment type	Treatment approach	Treatment outcome
Hormone therapy	Abiraterone acetate	Prevents prostate cancer from producing androgens.
	Orchiectomy – surgical castration of one or both testicles	Decreases testosterone production.
	Estrogens	Aids decreased testosterone production however harmful.
	Luteinizing hormone-releasing hormone agonists	Blocks testosterone production e.g., buserelin, goserelin & leuprolide.
	Anti-androgens	Inhibits androgen action (via androgen binding or AR binding) e.g., bicalutamide, enzalutamide, flutamide & nilutamide.
	Adrenal gland inhibitors	Prevents androgen production from the adrenal glands e.g., aminoglutethimide and ketoconazole.
Surgery	Radical prostatectomy	Removal of the prostate gland, seminal vesicles, and other surrounding tissues as treatment for localised disease.
	Pelvic lymphadenectomy – removal of the pelvic lymph nodes	When a patient presents invasive/metastatic disease; the prostate is not always removed but other treatments can be provided.
	Transurethral resection of the prostate (TURP) – prostatic tissue removal	Via resectoscope through the urethra. Can aid with alleviating symptoms.
Radiation Therapy *Patient will be at increased risk of bladder/gastrointestinal cancer following radiation therapy for PC	External radiation – radiation administered via a machine outside of the body	Includes conformal radiotherapy which generates a 3D picture for optimal targeting and lessened damage to healthy tissue.
	Hypofractionated radiation – treatment of large doses that reduces number of treatment days	Potential to induce severe side effects.
	Internal radiation – direct/nearby placement of radioactive substances into the prostate	A more direct treatment preventing off-target effects.
	Radiopharmaceutical therapy – such as alpha emitter radiation therapy	Radium-223 is injected into the bloodstream, where it collects in cancerous bone mass to kill the cells.
Chemotherapy	Systemic chemotherapy – administration via mouth or bloodstream	Allows drugs such as docetaxel and cablitaxel to travel within the body.

	Regional chemotherapy – administration into organ/body cavity/ cerebrospinal fluid	Allows direct treatment to a specific area.
Biological therapy	Utilisation of the immune system - natural or lab produced substances enhance/restore aspects of the system to fight cancer	E.g., Sipuleucel-T treatment for PC that has spread; cells are collected from a patient & treated with a protein combination of growth factor & a PC protein – injected back into the patient to stimulate T cells.
Bisphosphonate therapy	Drugs e.g., clodronate & zeledronate reduce bone disease/lessen risk of bone fractures	Ideal for those treated with orchiectomy/anti-androgen therapy as they pose increased risk of bone loss.
Alternative bone pain relief	Analgesic, corticosteroids, radioisotopes e.g., strontium-89 (form of strontium which is up taken by growing bones), monoclonal antibodies e.g., denosumab (can treat giant cell bone tumours & osteoporosis)	Ideal for those treated with orchiectomy/anti-androgen therapy as they pose increased risk of bone loss.
Presently at clinical trial	Cryosurgery	Freezing and destruction of cancerous cells.
	High intensity focused ultrasound	Use of an endorectal probe to generate ultrasound to destroy cells.
	Proton beam radiation therapy	Specific targeting of tumours with streams or protons to reduce off-target effects.

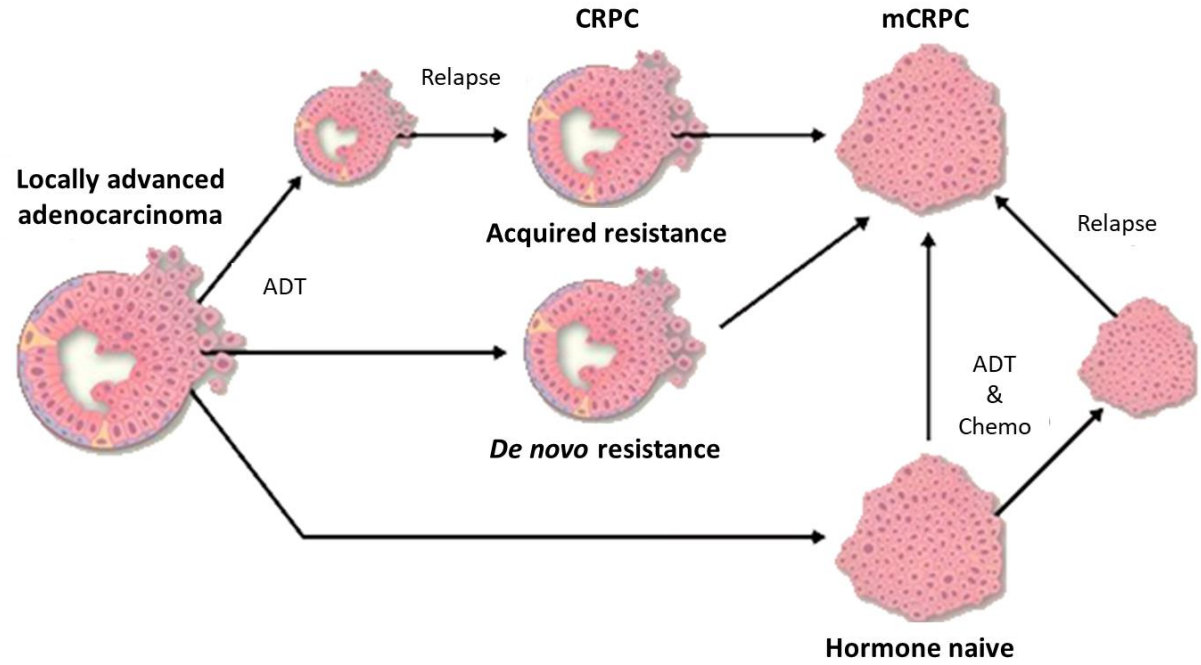

Figure 1.8: Development of CRPC and mCRPC. During treatment of androgen deprivation therapy (ADT) and/or chemotherapy, tumour cells may become insensitive thus acquiring therapeutic resistance. *De novo* resistance to ADT may also occur where the tumour simply does not respond to treatment. AR dependent tumours may also initially response to treatment but then develop resistance. In all cases, this resistance to therapy can lead to mCRPC. Figure source: (Wang et al. 2018a).

Clinically, CRPC is diagnosed when serum testosterone levels are below 1.7nmol / L yet cancer progression is still evident through increasing PSA levels and development of new soft tissue or bone lesions (Huang et al. 2018). 20 - 30% of CRPC patients display *AR* overexpression or amplification (Zarif and Miranti 2016). It is estimated that 10 - 20% of prostate cancers develop castration resistance within 5 years of diagnosis, and that 84% of newly diagnosed CRPC patients have already undergone metastases (Wade and Kyprianou 2018).

Resistance to ADT occurs via multiple, poorly understood mechanisms. These include *AR* genetic alterations or splicing events, that despite decreased testosterone availability with androgen/AR pathway inhibitors, AR remains functionally active (Isikbay et al. 2014). For example, mutations within the ligand binding domain (LBD) that result in structural alterations can allow other hormones such as progesterone and hydrocortisone to bind and activate AR in the absence of androgens (Ritch and Cookson 2016). Furthermore, previous work has identified androgen independent signalling via MAPK,

PI3K and IL-6 pathways that have been shown to trigger AR signalling in the absence of androgens (Traish and Morgentaler 2009).

Additionally, androgen-independent AR signalling has also been linked to clonal selection from a heterogeneous population of androgen independent cells, stem cell adaptation or prostate cancer cell differentiation stimulated by androgen deprivation and adrenal androgens triggering AR activation within prostate cells (Traish and Morgentaler 2009; Zong and Goldstein 2013). A luminal cell population expressing NKX3.1, termed CARNs, have also shown self-renewable abilities in the absence of androgens to promote prostate tumorigenesis in mice (Wang et al. 2009).

If given sufficient time, CRPC will inevitably progress to form metastatic disease, where prostate cancer cells disseminate into the tumour microenvironment, intravasate into the blood/lymphatic vessels, travel via the blood and or lymphatic system, and extravasate and colonise at a distant site to form a secondary tumour (Leslie and Siref 2018). mCRPC treatment options such as the AR antagonist enzalutamide, chemotherapy (such as docetaxel), and the PARP inhibitor olaparib, have been reported to reduce disease progression in a select fragment of patients, however, mCRPC is currently incurable (Huang et al. 2018). For example, the survival rate for mCRPC patients treated with docetaxel alone only increases by a mere 4 months (Carver et al. 2011). Further scientific investigation to identify CRPC/mCRPC prevention strategies and drug resistance mechanisms is urgently required.

1.3. Prostate cancer models

A range of comprehensive prostate cancer models have been developed and well-studied to enable further investigation of prostate cancer initiation and growth, whilst additionally providing platforms for pre-clinically testing therapeutics.

1.3.1. Human prostate cancer models

1.3.1.1. Immortalized prostate cancer cell lines

In vitro assays using 2D cultures are one of the most common approaches for rapidly studying the functional consequence of genetic events and to screen novel therapeutic strategies, where several immortalised prostate epithelial cell lines have been developed from normal (e.g., RWPE-1 and PNT-2A), benign (e.g., BPH1) and cancer (e.g., DU145, LNCAP and PC3) tissues from patients (Saranyutanon et al. 2020). Established prostate cancer cells are often well characterised, easy to manipulate, and provide an inexpensive method for obtaining high throughput data for drug related studies, where treatment-resistant lines such as those resistant to chemotherapy or anti-androgens can also be

generated to provide an accessible model for studying resistance mechanisms (Namekawa et al. 2019).

There are numerous established lines that are routinely used in prostate cancer research that model pre-cancerous, hormone-naïve and castrate resistant disease states; DU145 (AR positive, CRPC), LNCAP (AR positive, androgen-sensitive) and PC3 (AR negative, CRPC) cells (Figure 1.9) have often been referred to as the gold standard of prostate cancer cell culture lines (Cunningham and You 2015).

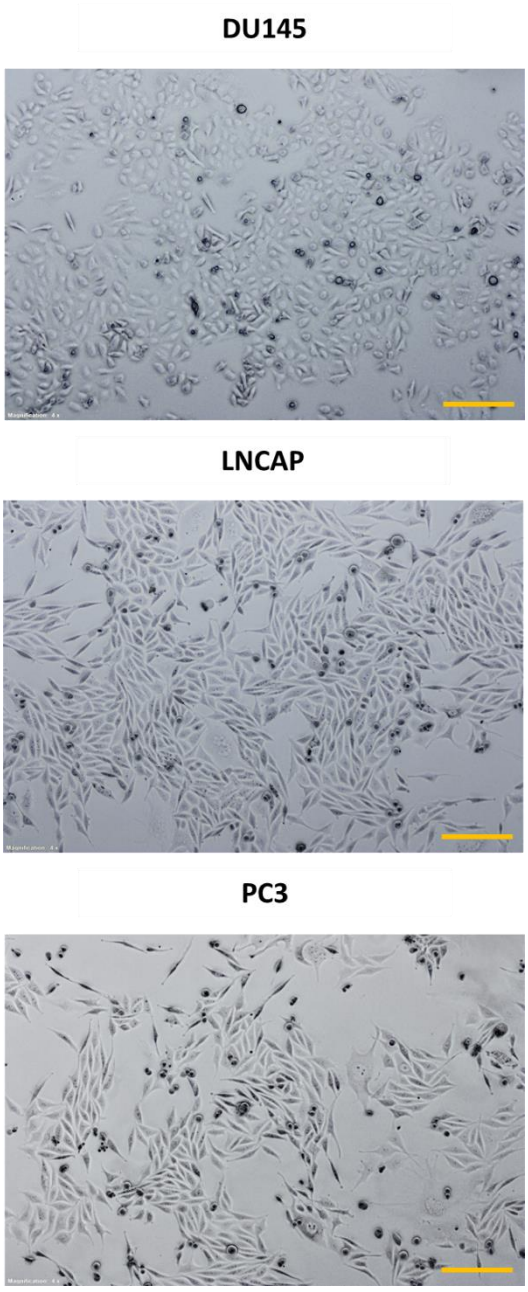

Figure 1.9: DU145, LNCAP and PC3 cell morphology. Images were obtained on a basic light microscope with use of a 4x lens. Each scale bar shown represents 200 µm.

Furthermore, established prostate cancer cell lines can be cultured to produce spheroids via methods such as the hanging drop technique and suspension cell culture, enabling creation of a 3D model from 2D cells (Fontana et al. 2020).

1.3.1.2. Primary prostate cancer cell lines

Through years of research within the Peehl and Maitland labs, methods have been optimised to fractionate human and mouse prostate tissues into their many constituent cell types for culturing *in vitro,* thus enabling study of both normal and cancerous primary prostate lines (Peehl et al. 1991; Maitland 2017).

Although more difficult to generate, they can provide more heterogeneity than established lines; however in either model, both lack a tumour-microenvironment as well as endocrine and immune systems, and therefore do not provide a true representation of an *in situ* prostate tumour (Namekawa et al. 2019).

1.3.1.3. Patient derived xenografts (PDX)

A PDX model comprises of a human tissue specimen, directly engrafted into an immunodeficient mouse such as an athymic nude, severely compromised immune deficient (SCID) mouse or NOD–SCID gamma (NSG) mouse (Figure 1.10A), generating surplus tissue that retains the architecture and cell-cell interactions present within the original tissue used (Jung et al. 2018).

PDXs developed from tumours are largely used for evaluating anti-cancer drug efficacy and toxicity prior to administration of treatment *in vivo*, due to the presence of a tumour microenvironment and immune response. In addition, biobanks of human samples can be generated through serial transplantation and propagation of PDXs, enabling multiple researchers access to a specific tumour or model, however this process can be both lengthy and costly, with risk of a poor success rate (Namekawa et al. 2019).

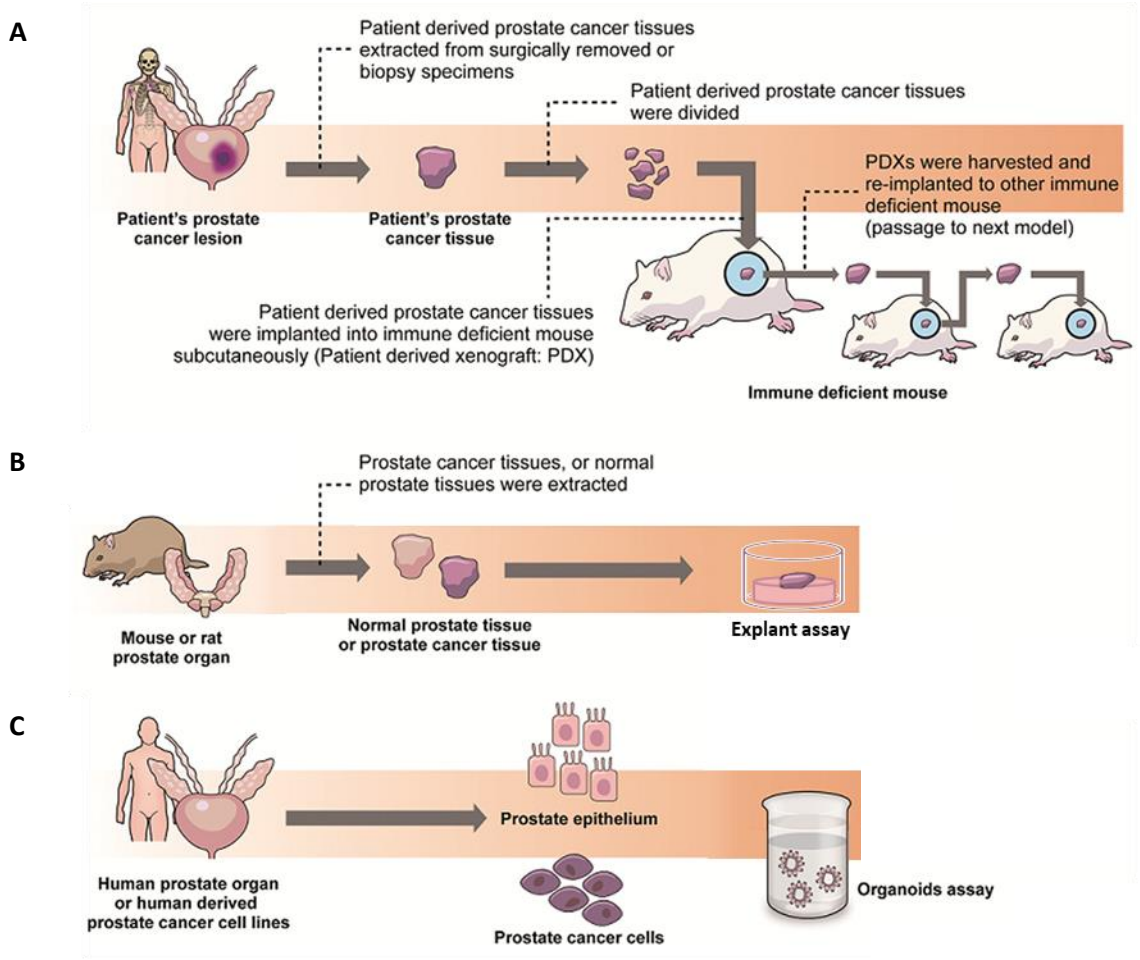

Figure 1.10: Alternatively used 3D prostate cancer models. Schematic depicts the basic processes involved in development of A) patient derived xenograft (PDX) models, B) explant culture and C) organoid culture. Figure taken and adapted from (Kato et al. 2021).

1.3.2. Murine prostate cancer models

To study pathological changes within the human prostate, the mouse is an invaluable tool due to an approximate 95% shared identity with the human genome, similar prostate histopathology and simplicity in maintenance as a laboratory animal (Oliveira et al. 2016).

1.3.2.1. Genetically engineered mouse models (GEMM)

Basic cancer research and translational oncology are heavily reliant on the use of genetically engineered mouse models due to their extensive applications within cancer gene discovery and validation, cell-of-origin studies, genotype to phenotype correlation studies, drug target validation and pre-clinical studies (Kersten et al. 2017).

The TRansgenic Adenocarcinoma Mouse Prostate (TRAMP) model was the first reported GEMM of prostate cancer, that under the prostate steroid binding protein (C3-1) promoter increased expression of the simian virus 40 (SV40) early region to promote prostatic and mammary gland adenocarcinoma, in addition to lymph node and pulmonary metastasis (Grabowska et al. 2014). Similar to this model, the LADY GEMM utilises the large PB promoter (LPB) to drive expression of SV40 Large T-antigen (Tag), that develops local invasive adenocarcinoma very rapidly but doesn't metastasise; making it ideal for studying drivers of metastatic prostate cancer (Grabowska et al. 2014).

Germline and non-germline (somatic cell) GEMMs can both utilise the clustered regularly interspaced short palindromic repeat (CRISPR) / Cas9 editing system, where the nuclease is directed to a predefined genomic locus using single-guide RNAs (sgRNAs) to mediate DNA double strand breaks (DSBs). These breaks are then repaired either via non-homologous end-joining or homologous recombination, resulting in gene knockout or modification respectively (Kersten et al. 2017).

The most conventionally used GEMMs often harbour transgenic expression of an oncogene of interest under the control of a tissue-specific promoter (Kersten et al. 2017); these promoters can additionally be used in conjunction with Cre-*loxP* technology for the excision of genetic material within a specific-tissue type.

Cre recombinase (Cre) is a 38kDa tyrosine site-specific DNA recombinase that recognises DNA sequences called *loxP* (locus of x-over, P1) sites, consisting of a 34 base pair sequence that contains two 13 base pair inverted, palindromic repeats, as well as an 8 base pair core sequence that provides directionality (Kim et al. 2018). *LoxP* sites are inserted either side of a locus and upon detection of these sites, Cre can excise the *loxP* flanked DNA and cause gene inactivation in a process termed floxing (Figure 1.11), or additionally induce genetic inversion or translocation of the flanked DNA depending on *loxP* site orientation and location (Kim et al. 2018). Furthermore, some GEMMs employ inducible Cre systems that provide better control over Cre activation. Induction of tamoxifen (Figure 1.11B) or tetracycline within the *CreloxP* technology can enable both time and cell specific recombination events (Kim et al. 2018).

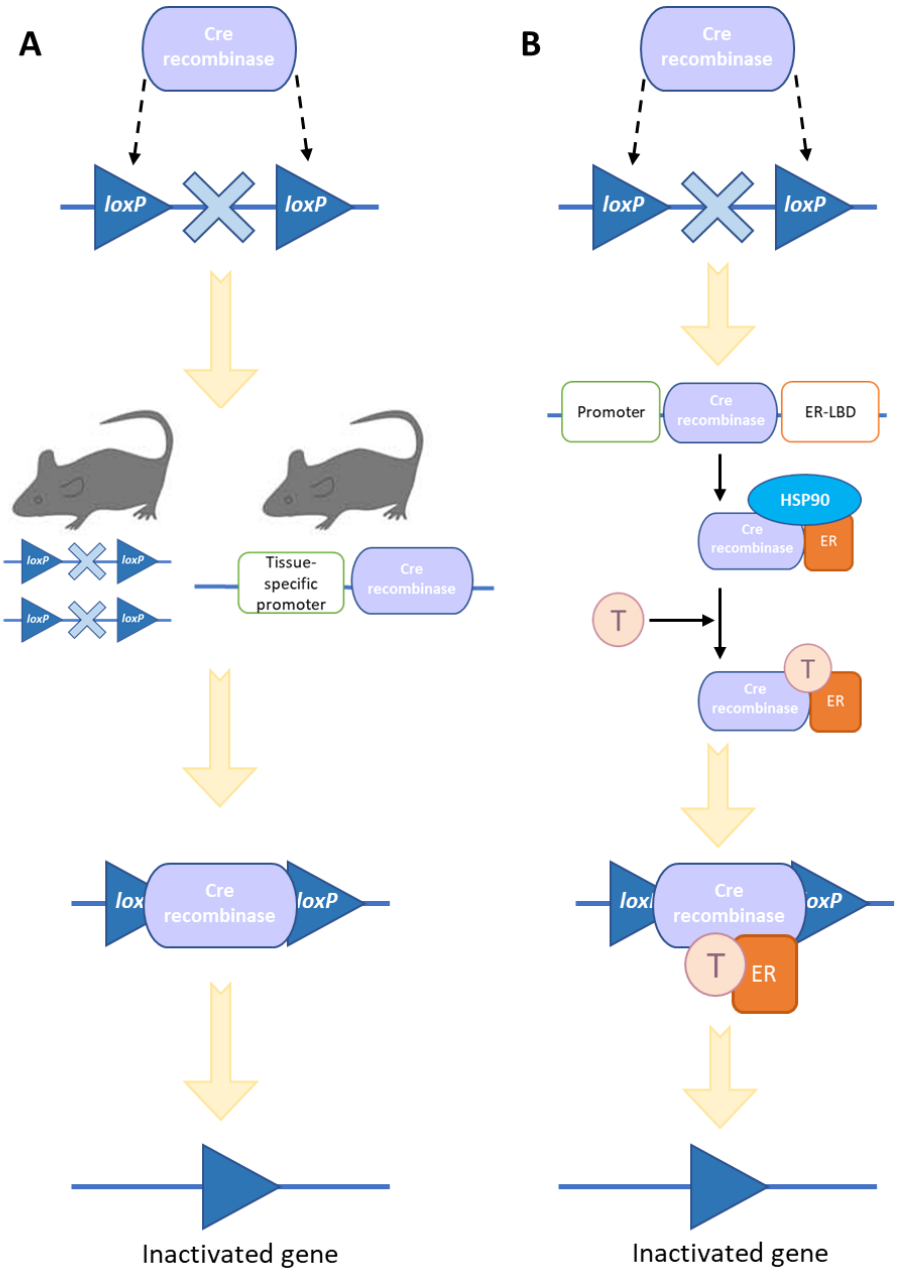

Figure 1.11: Modes of Cre-loxP targeted gene inactivation. Schematic depicts A) tissue specific gene deletion, which for prostate cancer can be instigated through use of a promoter such as Probasin, and B) Tamoxifen inducible gene deletion, where the estrogen receptor (ER) is fused to Cre recombinase, producing CreER. Upon the addition of tamoxifen, the interaction of HSP90 with CreER is eliminated, subsequently enabling nuclear translocation of Cre. Figure adapted from (Kim et al. 2018).

1.3.2.2. PTEN mouse models

GEMMs encompassing several types of *Pten* alteration have been specifically generated to study the various stages of prostate cancer. *In utero*, homozygous knockout of mouse *Pten* causes embryonic lethality (Grabowska et al. 2014), though can be rescued with heterozygous ($Pten^{+/-}$) or hypomorphic alleles ($Pten^{+/hyp}$ or $Pten^{hyp/-}$; which express half the level of *Pten* relative to wild-type alleles) (Trotman et al. 2003).

Instead, controlled conditional deletion of *Pten* can be used to drive tumour development within the prostate and has been successfully demonstrated by models such as the *MMTVCre* (mouse mammary tumour virus) $Pten^{fl/fl}$ GEMM that exhibits HG-PIN by 2 weeks old and invasive adenocarcinoma by 3 weeks old, in addition to the *PbCre4* $Pten^{fl/fl}$ GEMM that develops invasive disease from 9 weeks old, that can later progress into metastatic disease (as reviewed by (Knobbe et al. 2008)).

To address interactions between PTEN and other key mediators known to contribute to prostate cancer, numerous models utilising *Pten* loss as the main driver have additionally been generated. These include the highly penetrant *PbCre4* $Pten^{loxp/loxp}$; $TP53^{loxp/loxp}$ mouse model that benefits from loss of p53-mediated senescence (Chen et al. 2005), and the $PbCre4^{+}$ $K\text{-}Ras^{+/V12}$; $Pten^{fl/fl}$ model, that employs activated KRAS to augment tumour rate of growth and potentiate metastatic spread (Jefferies et al. 2017).

Moreover, GEMMs with germline *Pten* mutations have been developed to study underlying mechanisms contributing to alternative conditions such as Cowden and Bannayan-Riley-Ruvalcaba syndromes. The Eng group were the first to successfully generate a model with four missense mutations in exon 7 of the mouse *Pten* locus, whereby homozygosity of these mice led to reduced PTEN protein levels, a higher proportion of cytoplasmic PTEN and increased AKT activation (Lee and Pandolfi 2020).

Pten-deficient and *Pten*-mutant models thus complement the range of GEMMs that are being used to study the PI3K signalling pathway in cancer and disease (Klarenbeek et al. 2013; Carnero and Paramio 2014).

1.3.3. *Ex vivo* primary culture

1.3.3.1. Explant culture

Another approach utilised for studying drug efficacy and responses within tumours involves culture and treatment of explants (Figure 1.10B). Tissue from GEMMS or humans (also known as patient-derived explants, or PDEs, are sectioned between the range of 200 – 300 µm using an appropriate method, then cultured on sponge scaffolds (Fontana et al. 2020; Powley et al. 2020).

As the tissue is sectioned horizontally, intra-/inter-tumoural heterogeneity is often represented, in addition to the presence of any normal tissue surrounding the cancerous tissue, therefore making the model advantageous for studying on-target specificity. Tumour–stroma interactions are also maintained, thus also enabling experiments that co-target both components (Powley et al. 2020).

Although these models can be predictive of *in vivo* drug responses, especially within PDEs, there are many limitations surrounding use of the models; including how tissue architecture can begin to disintegrate following 72 hours plus of culturing, along with the difficulty to perform high-throughput assays as experimental set-up is very labour-intensive (Powley et al. 2020).

1.3.3.2. Organoid culture

Organoid culture (Figure 1.10C), refers to the culture of stem cells within a reconstituted *in vitro* extracellular matrix that enables the cells to differentiate and propagate into 'self-organised, mini-organs' that can simulate the 3D tissue architecture and biological functions of the organ of origin (Drost et al. 2016; Ma et al. 2017).

Using organoid culture media supplemented with growth factors, single dissociated tumour cells can form organoid structures from both basal and luminal cells, typically within 2 – 5 days. They are very robust, allowing for multiple high-throughput assays. If derived from humans, organoids represent human physiology with high accuracy and can also be subjected to genetic manipulation. Although organoids are grown within an extracellular matrix, they lack an extensive microenvironment, and supplements required for optimal growth can be costly (Kim et al. 2020).

1.4. Phosphatidylinositol 3-kinase (PI3K) pathway

1.4.1. PI3K and PI3K signalling

Through phosphorylation of phosphatidylinositides (PtdIns), the PI3K family of lipid kinases mediate numerous signalling pathways that regulate cell growth and proliferation, motility, metabolism and survival (Faes and Dormond 2015). Consisting of multiple isoforms, the PI3K family is categorised into three classes based on isoform structure and substrate specificity (Figure 1.12) (Thorpe et al. 2015).

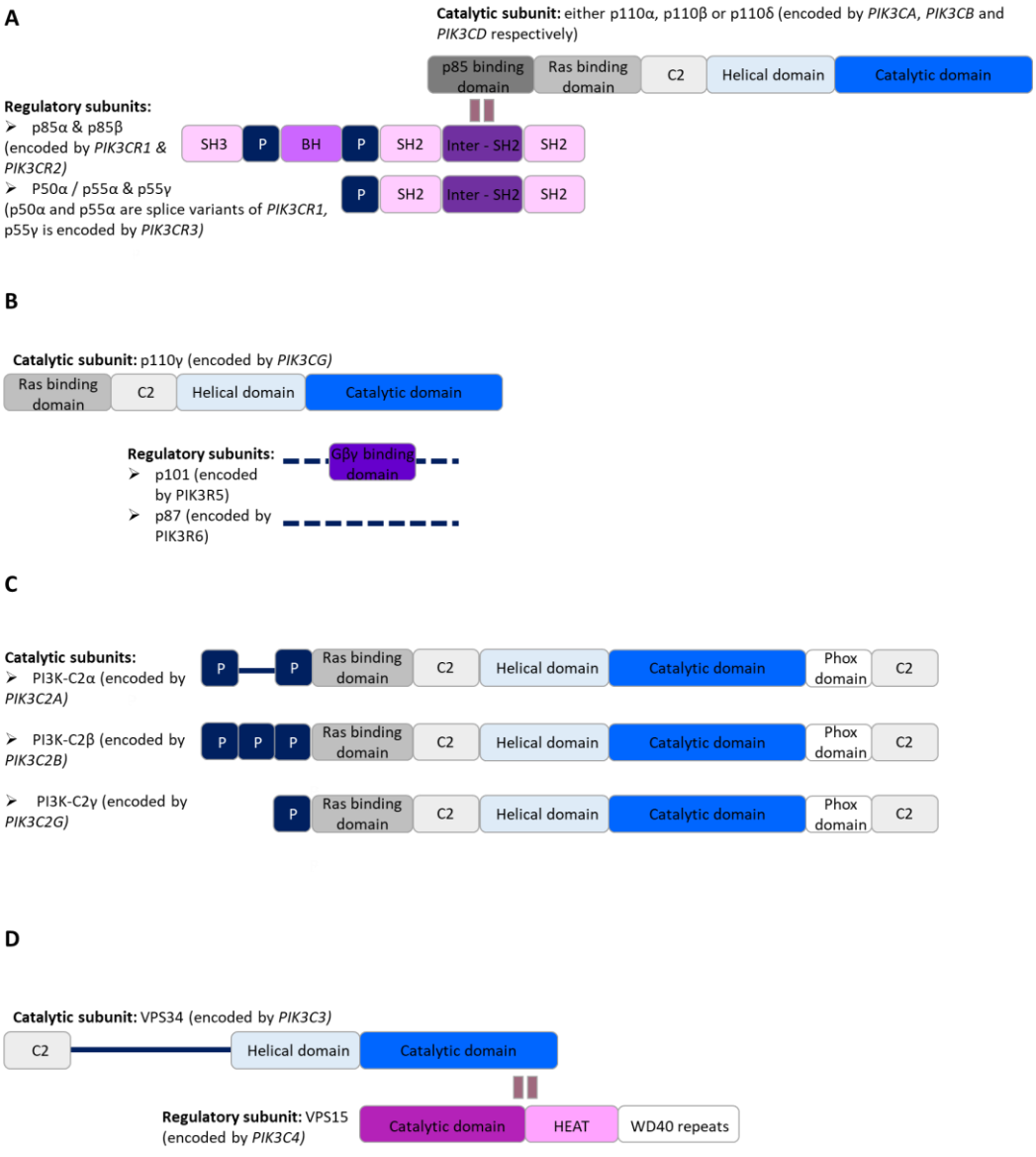

Figure 1.12: PI3K isoform structures. Graphical representation of A) Class IA isoforms, B) Class IB isoform, C) Class II isoforms and D) the Class III isoform. Adapted from (Thorpe et al. 2015). BH; breakpoint homology domains, C2; membrane interacting domain, Gβγ; G beta-gamma complex, HEAT; (Huntington, EF3A, ATM, TOR repeats), P; proline-rich domain, SH; Src homology domain.

During canonical signalling, class I PI3K heterodimers containing a catalytic and a regulatory subunit are recruited to the plasma membrane upon tyrosine kinase receptor or G-protein coupled receptor activation (Thorpe et al. 2015). In the absence of an activating signal, the p85 regulatory subunit of PI3K class IA isoforms self-inhibit the catalytic domain of the p110 subunit via binding domain interactions (Figure 1.12A) (Thorpe et al. 2015; Shorning et al. 2020).

However, when a signal is mediated through growth factor binding, the p85 induced inhibition is terminated leading to tyrosine phosphorylated peptides binding to p85 and stimulation of a p110 subunit conformational change (Jimenez et al. 2002). As a result, subunit p110 can now catalyse the phosphorylation of its substrates, converting phosphatidylinositol-4,5-bisphosphate (PIP_2) into phosphatidylinositol-3,4,5-triphosphate (PIP_3) (Thorpe et al. 2015). p110 α/δ and the Class IB p110γ isoforms have also been shown to be alternatively activated through associations with RAS, and p110β is also uniquely regulated by GPCRs (Jimenez et al. 2002; Thorpe et al. 2015; Shorning et al. 2020).

Class IB isoforms also have a p110 catalytic subunit, but these do not possess a p85 binding domain (Figure 1.12B). Instead p110 can adhere to either the p101 or p87 regulatory subunits, the binding of which is not yet established, as further investigation into p101 and p85 subunit domain structures is still required (Thorpe et al. 2015). Expression of this subclass is predominant within the haemopoietic system, as are the class IA heterodimers containing a p110δ catalytic subunit; the additional class IA isoforms are ubiquitously expressed (Thorpe et al. 2015).

The protein structures of the class II PI3K isoforms (PI3K-C2α, PI3K-C2β and PI3K-C2γ) differ widely from class I isoforms, all of which are monomeric with no regulatory subunit (Figure 1.12C). Instead they possess a C terminal extension unique to this class; a PX (Phox) and C2 (membrane binding) domain which allow for preferential PIP_2 binding (Jean and Kiger 2014). The physiological roles of these isoforms are not fully implicit, however PI3K-C2β is strongly believed to be associated within angiogenesis and cilium function (Thorpe et al. 2015).

Class III PI3Ks consist of a single catalytic isoform, Vps34 (vacuolar sorting protein sorting 34) which forms heterodimers with the Vps15 adaptor protein, that can regulate both Vps34 activity and Vps34 intracellular membrane localisation (Figure 1.12D). As a result, this class of kinase can regulate a variety of different functions including cytokinesis, autophagy, endosome and lysosome maturation, but mainly functions to control intracellular membrane trafficking (Jean and Kiger 2014).

During class I PI3K signalling, the conversion of PIP_2 into PIP_3 causes signalling proteins phosphoinositide-dependent kinase 1 (PDK1) and protein kinase B (also known as AKT) to dock at the cell membrane (Figure 1.13). The interaction between PI3K and the pleckstrin homology domain of AKT induces a conformational structure change within AKT, allowing activation loop access. PDK1 can then phosphorylate AKT at site Thr308, causing a 100-fold increase in AKT activity. However, for complete AKT activation, site Ser473 must also be phosphorylated, which is performed by mTOR complex 2 (mTORC2) (Hers et al. 2011). Additionally, protein kinases ataxia-telangiectasia mutant and Rad3 related (ATM and ATR), along with DNA-dependent protein kinase (DNA-PK) have also been shown to activate AKT via phosphorylation at site Ser473, highlighting the diverse role AKT plays within other pathways (Rinne et al. 2021).

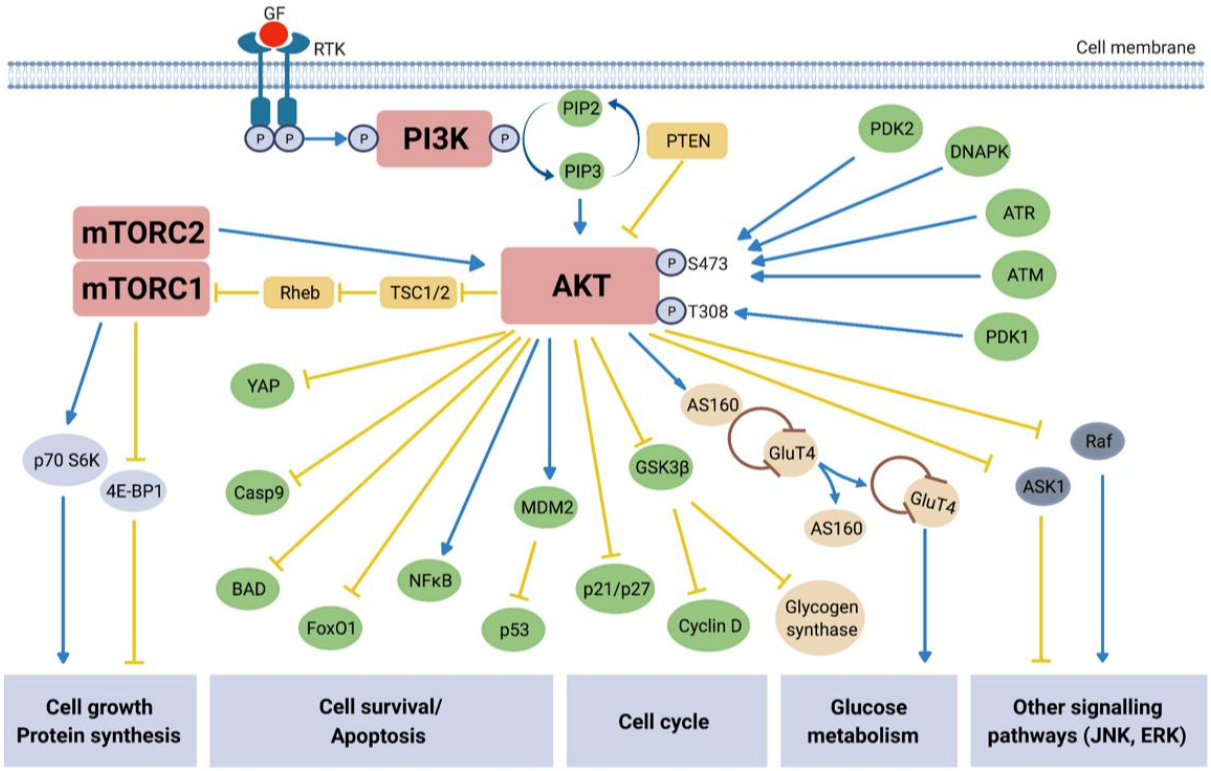

Figure 1.13: Overview of the PI3K signalling pathway. Graphical representation of canonical class I signalling that drives multiple cellular process including cell growth and survival, protein synthesis, metabolism, the cell cycle, in addition to activation of other signalling pathways. Image source: (Rinne et al. 2021).

The mechanistic target of rapamycin complex 2 (mTORC2) is one of two mTOR protein kinase complexes within the phosphatidylinositol-3-kinase-related kinase (PIKK) family, acting as regulatory signalling components within cellular growth and metabolism pathways (Oh and Jacinto 2011).

Core scaffold subunits RPTOR independent companion of MTOR (RICTOR) and SIN1 are vital for maintaining mTORC2 stability and integrity, with subunit LST8 acting as the constitutive binding partner (Ebner et al. 2017). Protein PRR5 also known as PROTOR1, alongside proteins such as heat shock protein 70 (HSP70), telomere length regulation protein (TEL2)/ TEL2 interacting protein 1 (TTI), and Rac family small GTPase 1 (RAC1), positively regulate the complex, whereas the protein DEP domain containing MTOR interacting protein (DEPTOR) can negatively regulate the complex.

DEPTOR has been shown to be highly overexpressed in various cancers including prostate cancer, which can both alleviate mTORC2 suppression and sustain AKT activation (Oh and Jacinto 2011; Wang et al. 2012). HSP70 has been shown to regulate RICTOR levels and is involved within the mTOR and RICTOR interaction, whereas TEL2 and TTI assist with the overall assembly and maturation of the complex (Oh and Jacinto 2011).

Within mTORC2, mTOR itself can be auto phosphorylated at site Ser2481 to self-regulate its own intrinsic catalytic activity (Soliman et al. 2010). Furthermore, this phospho-site is often used as a surrogate marker for structurally complete mTORC2 (Oh & Jacinto, 2010). RICTOR is subject to phosphorylation at numerous sites, most importantly at Thr1135 by S6K1 (ribosomal protein S6 kinase beta-1), which inhibits the RICTOR-mTOR association (Bhattacharya et al. 2016). Additionally, RICTOR phosphorylation at Ser1235 by glycogen synthase kinase 3 beta (GSK3β) occurs during endoplasmic reticulum stress, causing interference of mTORC2 and AKT binding (Oh & Jacinto, 2010).

Once phosphorylated, AKT dissociates from the cell membrane, where it targets multiple substrates both in the cytoplasm and nucleus through phosphorylation, enabling activation and repression of numerous downstream signal transduction pathways (Hers et al. 2011).

One key target is the TSC1-TSC2 tuberous sclerosis complex, a protein assembly of hamartin and tuberin. Bound together with a third subunit TBC1D7, the TSC1-TSC2 complex negatively regulates the mechanistic target of rapamycin complex 1 (mTORC1) (Armstrong et al. 2017). The N-terminal region of TSC2 allows for its stable association to TSC1. TSC2 also provides the TSC1-TSC2 complex with its GTPase activating protein (GAP) domain; which is imperative for binding to Ras homolog expressed in

brain (Rheb), a ubiquitously expressed G protein with intrinsic GTPase activity (Hoogeveen-Westerveld et al. 2012). Upon TSC1-TSC2 phosphorylation by AKT and subsequent Rheb binding, Rheb-GTP is converted into Rheb-GDP, preventing TSC1-TSC2 complex inhibition of mTORC1 (Huang and Manning 2008).

Activated mTORC1 can regulate multiple processes such as nucleotide, lipid and protein synthesis via further phosphorylation of activators and repressors, including S6K1 and 4E-BP1 (Hua et al. 2019). In addition to the mTOR catalytic subunit, the mTORC1 complex contains the inhibitory subunits of DEPTOR and PRAS40, scaffolding protein RAPTOR and stabilising subunit mLST8 (Rabanal-Ruiz et al. 2017).

A crucial regulator of the entire PI3K pathway is phosphatase and tensin homologue (PTEN), that with its lipid phosphatase activity can dephosphorylate PIP_3 upstream (Figure 1.13), causing pathway inactivation (Thorpe et al. 2015). Furthermore, the p85α regulatory subunit of class I PI3K is reported to bind to PTEN to enhance PTEN activity (Chagpar et al. 2010), and p85 binding to phosphatidylinositol 3-phosphate (PtdIns3P) or SHP-1 phosphatases can downregulate PI3K signalling (Jimenez et al. 2002). In addition to its PI3K dependent functions, PTEN also regulates double stranded DNA break repairs, cell motility, SRC and JNK pathway activation and mitochondrial metabolism (Milella et al. 2015).

1.4.2. PI3K signalling crosstalk

Components of the PI3K cascade interact with a plethora of other cell signalling pathways (Figure 1.14), which enable essential intra- and extracellular signalling responses to be regulated at multiple levels, including a series of complex positive and negative feedback loops (Shorning et al. 2020; Ghomlaghi et al. 2021).

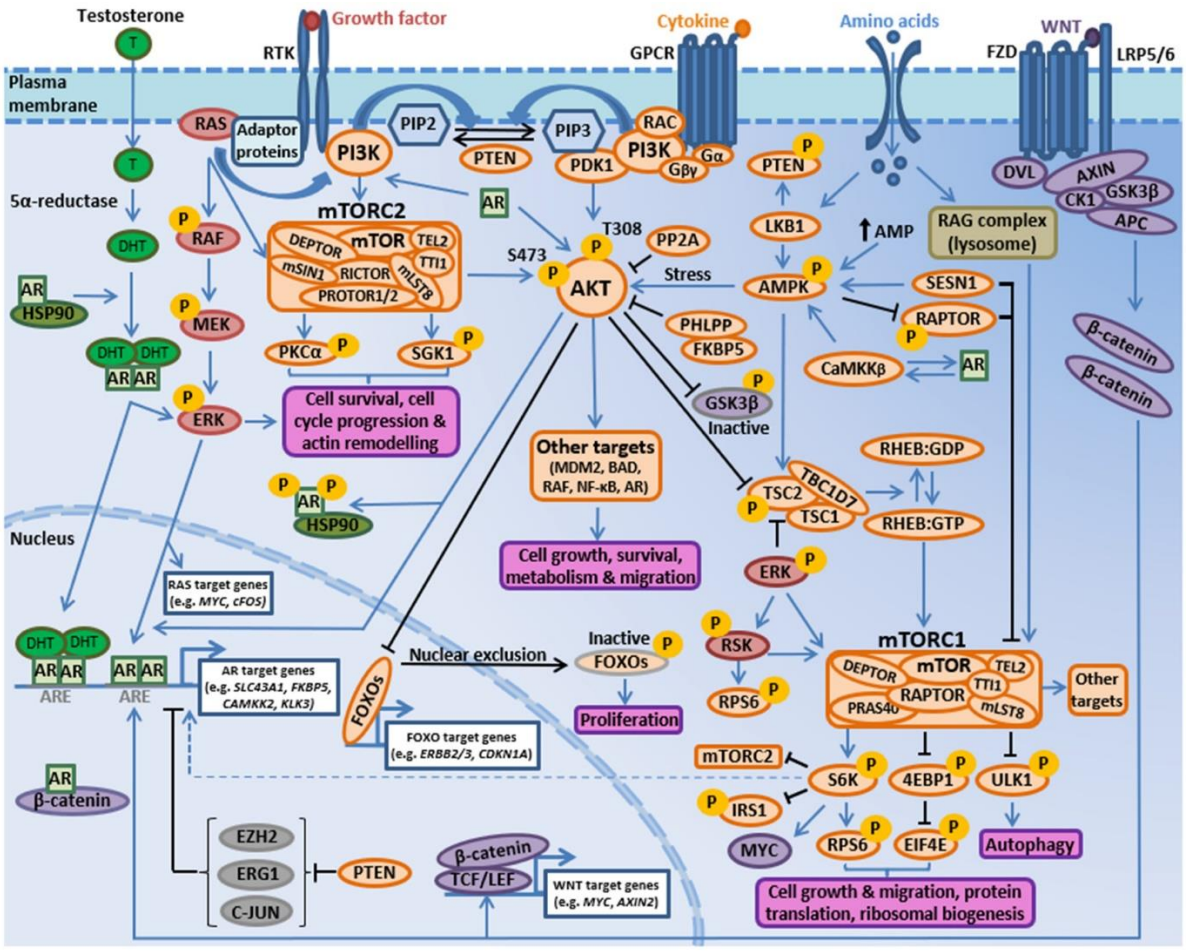

Figure 1.14: PI3K signalling at the centre of cellular processes. Schematic depicts the interactions of the PI3K pathway with AR, MAPK/ERK and WNT signalling pathways to regulate shared cellular process. Figure source: (Shorning et al. 2020).

Crosstalk between the PI3K signalling cascade and AR pathway occurs through an abundance of interactions, including AR-mediated amino acid transport to regulate mTORC1 activity, PTEN-mediated histone modifications that regulate AR, and direct mTOR-AR interactions within the nucleus to initiate metabolic rewiring, as reviewed in (Shorning et al. 2020).

Owing to its complexity, PI3K-AR crosstalk in prostate cancer has also been shown to drive therapeutic resistance. In response to AR inhibition, AKT/mTOR signalling has been demonstrated to increase (Carver et al. 2011). Mechanistically, AR blockade reduces transcription of key AR target genes, such as FK506-binding protein-5 (encoded by gene FKBP5), that is essential for mediating PHLPP-dependent AKT dephosphorylation to inactivate AKT (Carver et al. 2011). Conversely, inhibition of the PI3K signalling pathway can upregulate AR signalling via several mechanisms. For example, inhibition of AKT prevents AKT-mediated FOXO nuclear exclusion, thus enabling increased transcription of target

genes such as ERBB2/3 (that encodes HER2/3) that subsequently stimulate AR in addition to preventing AR targeted proteasomal degradation (Shorning et al. 2020).

Due to the presence of shared upstream receptors such as GPCRs and RTKs, as well as shared downstream targets, the PI3K and MAPK signalling pathway are also highly interconnected. The pathways possess the ability to cross-regulate one another through various cytosolic signalling events, including the stimulation of mTORC1 via ERK, suppression of RAF via AKT, stimulation of mTORC2 through RAF and overall regulation of RTK signalling mediated through mTORC1, as reviewed in (Shorning et al. 2020). Furthermore, MAPK signalling can promote resistance to PI3K/AKT pathway inhibition, therefore combination therapies targeting both these pathways are currently being explored (Shorning et al. 2020).

Moreover, the PI3K pathway including its key mediators AKT and mTORC1/2, have also been shown to interact with the Hippo/MST, Rb signalling and nutrient signalling pathways (Ghomlaghi et al. 2021). For example, tumour suppressor, Retinoblastoma protein (Rb) that mediates G1 phase arrest, when phosphorylated has also been shown to supress mTORC2 activity, thus preventing AKT activation, whereas cyclin A2 that is abundant within the S phase of the cell cycle, together with CDK2 can instead promote AKT activity through phosphorylation of sites that stabilise phosphorylation of AKT at site Ser473 (Ghomlaghi et al. 2021).

1.4.3. PI3K pathway genetic alterations in prostate cancer

Approximately 17 - 40% of primary cases and 40 - 70% of metastatic prostate cancer cases possess forms of genetic alterations within the PI3K pathway (Carver et al. 2011; Armenia et al. 2018). Taylor et al, also report that 42% of primary prostate cancer cases and 100% of metastatic prostate cancer cases have PI3K pathway alterations (Taylor et al. 2010). Genetic aberrations occur within a large variety of PI3K signalling cascade components, with the most common summarised in Table 1.3. In general, genetic aberrations are more frequent in metastatic/CRPC disease compared to primary tumours (Shorning et al. 2020).

Table 1.3: Common PI3K-AKT-mTOR pathway genetic alterations in prostate cancer. Table source: (Shorning et al. 2020).

Common genetic alterations in PI3K-AKT-mTOR pathway genes	Frequency in prostate cancer
PTEN deletion/mutation	16.4 – 32.0%
DEPTOR amplification	5.1 – 21.4%
SGK mutation/amplification	5.6 – 20.5% (*SGK3*)
	0.2 – 2.7% (*SGK1*)
FOXO deletion	0.0 – 15.2% (*FOXO1*)
	4.5 – 13.4% (*FOXO3*)
MAP3K7 deletion	5.9 – 14.8%
RRAGD deletion	6.5 – 14.4%
SESN1 mutation/deletion	5.4 – 13.6%
PIK3CA mutation/amplification	5.5 – 11.5%
PIK3C2B mutation/amplification	1.4 – 11.5%
PDPK1 amplification	0 – 8.1%

1.4.3.1. *PIK3CA*

PIK3CA mutations and gene amplification occur in up to 11.5% of prostate cancers (Table 1.3). The most common hotspot mutations that occur in prostate cancer within the *PIK3CA* gene occur at residue H1047 in the kinase domain and sites E542 and E545 in the helical domain. The histidine residue at 1047 is most frequently substituted for arginine (H1047R), and glutamic acids at 542 and 545 are commonly substituted for a lysine residue (E542K/E545K) (Ligresti et al. 2009; Pearson et al. 2018). These mutations confer an increase in the kinase activity of p110α, potentially at different levels of activation, as H1047R mutations have been shown to accelerate tumour development *in vitro* (Nisa et al. 2017). Furthermore, our lab has shown that conditional heterozygous expression of the *Pik3ca* H1047R mutation in mouse prostate epithelium can cause prostate tumorigenesis *in vivo* (Pearson et al. 2018).

A recent study investigating cell-free DNA (cfDNA) also identified that 6% of their metastatic prostate cancer patient cohort possessed an activation mutation within *PIK3CA* (Herberts et al. 2020), further highlighting how mutations within this gene can contribute to more aggressive and lethal forms of the disease.

1.4.3.2. *PTEN*

Tumour suppressor *PTEN* is one of the most common genes in prostate cancer to be inactivated or deleted (Milella et al. 2015), which facilitates PI3K signalling through elevated PIP_3 levels and enhanced mTORC2 formation (Bhattacharya et al. 2016).

PTEN inactivation through truncation mutations, homozygous deletion, and less commonly epigenetic silencing has been observed in approximately 20% of primary prostate tumours and up to 50% of CRPC tumours (Jamaspishvili et al. 2018), although several other mechanisms such as post-translational modifications (including ubiquitylation and phosphorylation) and suppression of PTEN-targeting microRNAs (miRNAs) have also been shown to mediate loss of PTEN function (Turnham et al. 2020).

In prostate cancer patients, PTEN inactivating mutation correlates with a higher Gleason score and poor prognosis (Pearson et al. 2018; Sun et al. 2019). In addition, PTEN loss in prostate cancer has been linked to faster progression to castration-resistant disease, increased angiogenesis, as well as increased risk of relapse (Switlyk et al. 2019).

PTEN deletion is frequently observed in highly heterogenous prostate tumours, however heterogeneity of *PTEN* loss within a primary prostate tumour can also impact clinical outcomes (Turnham et al. 2020). Due to the high prevalence of genetic *PTEN* alterations in prostate cancer, *PTEN* status is being explored as a prognostic biomarker, including to help distinguish between Grade 1 and 2 prostate tumours, thus enabling improved decision making for treatment options and informing patient selection for active surveillance (Jamaspishvili et al. 2018; Turnham et al. 2020).

1.4.3.3. *AKT*

Genetic aberrations in *AKT* within prostate cancer are uncommon, especially mutations that drive elevated activation; conversely, *AKT1/2/3* gene amplification that augment AKT activity is observed in up to 4.5%, 2%, and 4.7% prostate cancer cases respectively (Shorning et al. 2020). Like PIK3CA activation, AKT activation within prostate cancer has also been linked with a high Gleason score and more invasive properties (Shorning et al. 2020).

Interestingly, a requirement for AKT in PTEN deleted prostate cancer has been established, where *Akt1* haplodeficiency was shown to limit HG-PIN development in mice with one functional *PTEN* allele (Chen et al. 2006). Additionally, through further studies, constitutive activation of AKT has also been

linked to mTOR and ribosomal protein S6 kinase beta-1 (p70S6K) activation, as well as regulation of FOXO proteins (Majumder and Sellers 2005).

Although not from prostate cancer studies, AKT isoforms are also reported to possess distinct, non-overlapping functions in solid tumours (Khan et al. 2013). In breast cancer, increased activation of AKT1 has been linked to tumour initiation and growth, proliferation, and the suppression of apoptosis, whereas AKT2 has been shown to regulate cytoskeletal dynamics and therefore involved in invasion and metastasis (Martorana et al. 2021). The functional consequence of AKT3 hyperactivation is yet to be fully determined, although it is hypothesised AKT3 activation can increase cell proliferation due to knockdown experiments indicating loss of AKT3 impairs HER2-positive breast cancer cell proliferation (Hinz and Jücker 2019). Therefore, it is generally considered that pan-AKT inhibition is likely to be more effective in supressing tumour growth and progression, in comparison to isoform selective AKT inhibitors.

1.4.4. PI3K inhibitors for the treatment of prostate cancer

1.4.4.1. Mode of action of PI3K pathway inhibitors currently in the clinic

A range of PI3K pathway inhibitors have been developed for the treatment of solid tumours that target PI3K, AKT or the mTORC1/2 complexes, in addition to dual inhibitors that co-target PI3K and mTORC1 or mTORC2 (Table 1.4).

Table 1.4: PI3K pathway inhibitors currently in clinical trials. Examples of PI3K pathway inhibitors tested within short term clinical trials. Data obtained from (Roudsari et al. 2021).

Treatment	Study design	Duration	Clinical trial ID
Temsirolimus (mTORC1i) + bevacizumab (VEGFi)	Phase I/II trial, men with mCRPC	3 weeks	NCT01083368
Sapanisertib (dual mTORCi)	Phase II clinical trial, mCRPC patients pre-treated with abiraterone acetate and/or enzalutamide	3-30 weeks	NCT02091531
Everolimus (mTORC1i) + radiation therapy	Phase I clinical trial, men with adenocarcinoma of the prostate following prostatectomy	17.8 months	NCT01548807
Bicalutamide + Everolimus	Phase II clinical trial, mCRPC, progressive and Bicalutamide-naïve CRPC, pre-treated with androgen deprivation	28 months	NCT00814788
Ipatasertib (pan-AKTi) + abiraterone + prednisone	Phase 1b/II clinical trial, mCRPC patients pre-treated within docetaxel	24 months	NCT01485861

Clinical trials testing pan-PI3K inhibitors have often showed adverse effects within patients and limited responses (Turnham et al. 2020). Improvements in efficacy were seen when using isoform selective inhibitors, targeting PI3Ks different catalytic subunits with greater drug specificity and therefore minimized toxicity (Hashemzadeh et al. 2019), however their use in patients will be highly dependent on which isoforms are promoting tumour progression. Research has already established resistance mechanisms associated with PI3K isoform specific inhibitors, suggesting that inhibiting the PI3K cascade at multiple levels might be more efficacious (Turnham et al. 2020). Conversely, isoform specific inhibitors of AKT 1, 2 and 3 have shown limited efficacy in comparison to pan AKT inhibitors; the same holding true for drugs targeting the mTOR complexes (Sarker et al. 2009; Edlind and Hsieh 2014).

1.4.4.2. PI3K/AKT-independent mechanisms leading to therapeutic resistance

Due to the extensive PI3K signalling network, several regulatory mechanisms and feedback loops within the PI3K pathway and cross-talk with interacting pathways have been shown to mediate resistance mechanisms to PI3K/AKT inhibitors, as well as resistance to other standard therapeutics such as radiotherapy and immunotherapy (Park et al. 2018).

For example, when PI3K is inhibited, AKT-mediated phosphorylation of FOXO is reduced, causing an accumulation of nuclear FOXO. As a result, FOXO-mediated transcription of various RTKs including EGFR, HER2, c-KIT and IGF1R is activated, which can partially restore PIP3 activity. Furthermore, FOXO can upregulate RICTOR, an essential component of mTORC2, thus resulting in increased phosphorylation of AKT at Ser473, and activation of AKT substrates to facilitate cancer growth (Wright et al. 2021).

Pharmacological inhibition of PI3K or mTORC1 and mTORC2 has also been shown to increase AR signalling through elevated HER2 and HER3 signalling. Conversely, when AR is lost or inhibited, AKT phosphorylation and subsequent activation increase, owing to the downregulation of AR target genes that negatively regulate AKT, such as FKBP5 and PHLPP (Carver et al. 2011).

Insulin signalling is a potent mediator of the PI3K pathway and is reported to also play a role during therapeutic resistance to PI3K pathway inhibition. Hyperglycaemia and hyperinsulinemia are two commonly observed adverse effects within patients treated with PI3K inhibitors at clinical trial; where liver glycogenolysis is promoted but AKT2 regulation of GLUT transport is downregulated, initiating hyperglycaemia as less glucose is absorbed by cells and hyperinsulinemia triggered as the body

increases insulin production to overcome high blood glucose levels. This surge of insulin in response to PI3K/AKT pathway inhibition can stimulate insulin receptor signalling, thus promoting therapeutic resistant tumour growth (Wright et al. 2021).

Although the resistance mechanisms to PI3K/AKT pathway inhibitors are yet to be fully established, it is apparent that combination therapies targeting the pathway at multiple points, or simultaneously inhibiting different signalling axes that crosstalk with the PI3K/AKT cascade (e.g., AR and AKT co-inhibition) are beginning to show promise in the clinic (Shorning et al. 2020).

Furthermore, some patients possess genetic predispositions that limit their sensitivity to therapy or increase their risk for developing drug resistance; these include KRAS mutation, altered expression of c-MYC, PDK-1, FOXM1, NOTCH, SGK1 and SGK3 proteins, but most notably loss of *PTEN* (Wright et al. 2021), thus it is important that future work addresses which patients are likely to respond to treatment based on their mutational status.

1.5. Nuclear Factor kappa Beta (NF-κB) pathway

1.5.1. NF-κB subunit structures

The inducible NF-κB transcription factor family are responsible for the tight regulation of numerous genes involved in essential processes that regulate cell growth and differentiation during development, along with the immune and inflammatory responses (Hayden and Ghosh 2012; Napetschnig and Wu 2013).

In eukaryotic cells, the NF-κB family consists of five members (p50, p52, p65, RelB and c-Rel) with shared structural features (Figure 1.15). All five members possess a conserved Rel Homology Domain (RHD) required for protein dimerization and DNA binding. In addition, p65, RelB and c-Rel also possess a transactivation domain (TA) that is essential for subunit transcriptional activity (Christian et al. 2016).

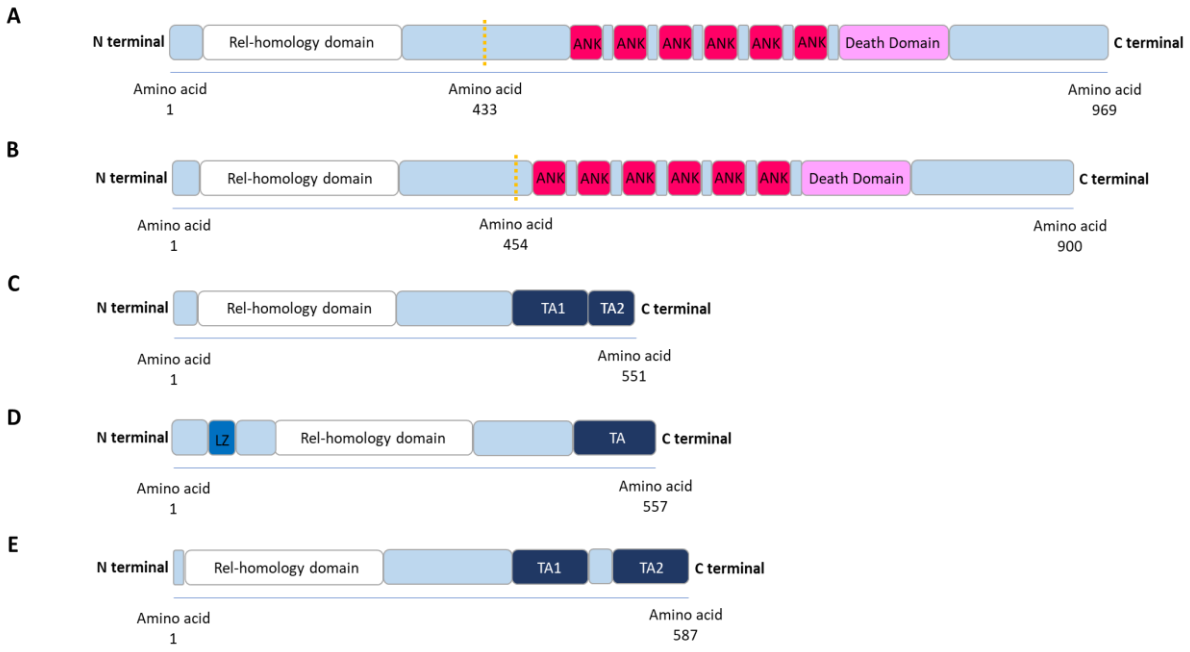

Figure 1.15: Protein depiction of the NF-κB transcription factor family members. A) p105, B) p100, C) p65, D) RelB and E) c-Rel are encoded by genes *NFKB1, NFKB2, RELA, RELB* and *REL*, respectively. Rel-homology domains are essential for protein dimerization and DNA binding whereas transactivation domains (TA) are required for transcriptional activity. Yellow dashed lines indicate where processing of p105 and p100 occurs during cleavage of inhibitory ankyrin (ANK) repeats to generate active proteins p50 and p52, respectively. LZ = Leucin zipper like motif. Adapted from (Hoesel and Schmid 2013).

When the signalling pathway is inactive, NF-κB proteins are sequestered within the cytoplasm by inhibitory proteins of the IkB family (α/β/ε), where they bind and inhibit the DNA binding domains of NF-κB family (Hoesel and Schmid 2013). With regards to p50 and p52 subunits, precursors p105 and p100 respectively prevent any transcriptional activity, which require protein cleavage to generate the functional p50 and p52 structures that can be activated (Hoesel and Schmid 2013). As neither p50 or p52 possess transactivation domains, they serve as transcriptional repressors unless bound to RelB, p65 or BCL3, an IkB family member with a transactivation domain (Hoesel and Schmid 2013). Upon stimulation, NF-κB proteins form active homodimers or heterodimers whereby protein dimerization can occur in up to 15 different combinations, which are influenced by cell type and tissue environment (Dorrington and Fraser 2019).

1.5.2. NF-κB signalling

1.5.2.1. Canonical and non-canonical NF-κB signalling

The principal function of the NF-κB pathway is to respond to various types of stimuli and stress including bacteria, viruses, physiological stress (e.g., acidic pH, hyperglycaemia, and oxidative stress) as well as physical stress (e.g., ionising radiation and UV light) (Mussbacher et al. 2019). The pathway also coordinates a series of cellular processes including upregulation of pro-inflammatory downstream target genes to activate defence and escape mechanisms, as well as maintenance of tissue homeostasis (Mussbacher et al. 2019). To achieve this, NF-κB transcription factors function via two distinct signalling mechanisms, termed the canonical and non-canonical (or alternative) NF-κB pathways.

The canonical NF-κB pathway is activated by ligands such as pathogen- / damage- associated molecular patterns (PAMPs/DAMPs) and pro-inflammatory cytokines binding to the extracellular domain of pattern-recognition receptors (PRRs), T and B cell receptors, TNF receptors and various cytokine receptors (Liu et al. 2017; Taniguchi and Karin 2018). In contrast, the non-canonical NF-κB pathway is stimulated by the binding of ligands (e.g., CD40 ligand, TNFSF13B, lymphotoxin and TNFSF11) to a niche subset of TNF receptors that include CD40, BAFFR, LTβR and RANK respectively (Taniguchi and Karin 2018). Consequently, the non-canonical NF-κB pathway possesses specific regulatory functions within the adaptive immune response that supplements the role of the canonical NF-κB pathway that is involved in both the innate and adaptive immune responses (Liu et al. 2017).

For induction of the canonical axis, stimuli activate phosphorylation of the IKK complex, consisting of catalytic subunits IKKα and IKKβ along with the regulatory modulator subunit NEMO (Liu et al. 2017). The IKK complex is then able to phosphorylate NF-κB bound IkB, causing its polyubiquitination; priming IkB for proteasomal degradation as shown in Figure 1.16. Once destroyed, the negative regulation of IkB is abolished, thus allowing the NF-κB proteins to translocate into the nucleus and consequently initiate transcription of target genes encoding proteins such as IL-6, CCL2, MMP9, MYC, NOS2, VEGF and VCAM1 (Taniguchi and Karin 2018; Dorrington and Fraser 2019); mediating processes such as cell survival and proliferation.

For induction of the non-canonical axis, cytokine activation of upstream receptors leads to activation of the NF-κB inducing kinase (NIK), which is essential for phosphorylating p100 and initiating its proteasomal processing into p52 (Park and Hong 2016). Non-canonical NF-κB pathway activation does not rely upon IKKβ or NEMO, and often results in the dimerization of p52 with RelB (Hoesel & Schmid,

2013), whereas canonical signalling mainly comprises of dimers formed of the p65, p50 and c-Rel subunits (Liu et al. 2017). Key non-canonical pathway target genes include *CCL19*, *CXCL12* and *CXCL13* (Taniguchi and Karin 2018), that mediate processes such as B cell survival and maturation, alongside differentiation of osteoclasts (Sun 2017).

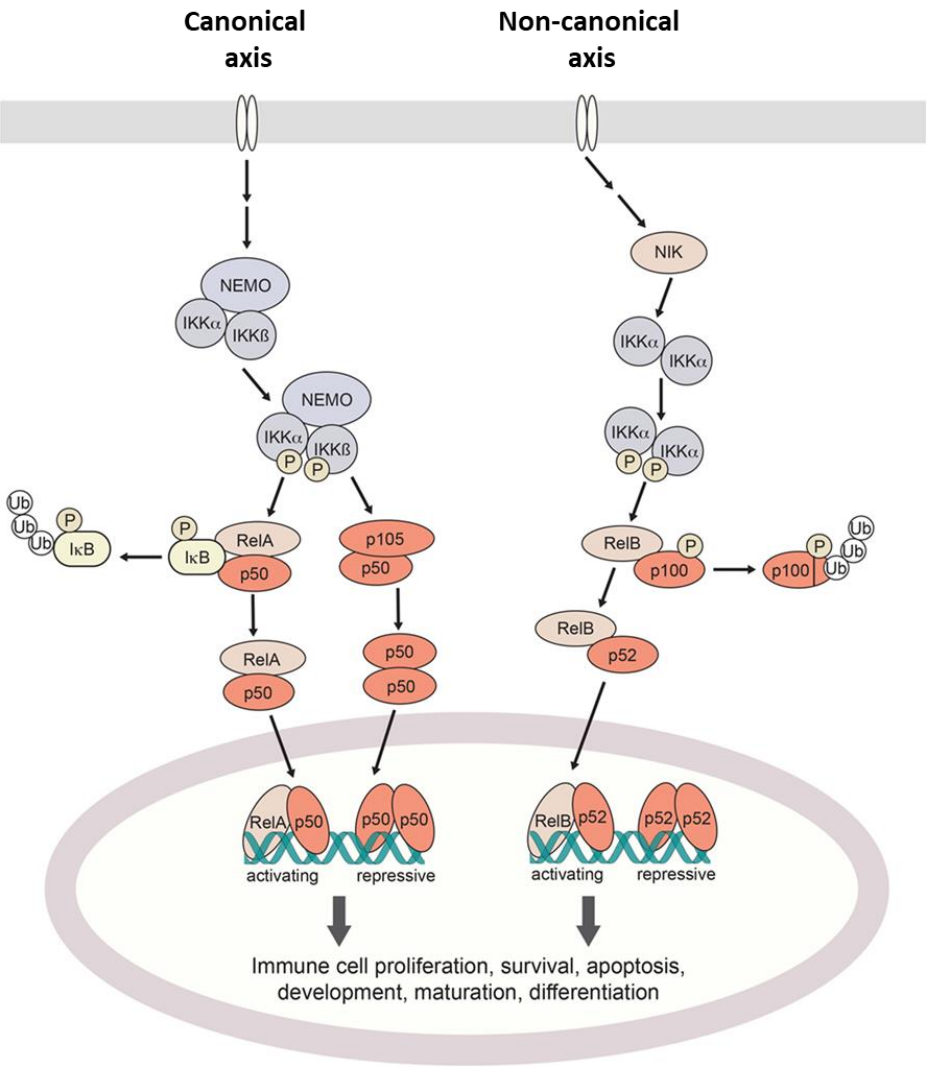

Figure 1.16: Mechanisms of canonical and non-canonical NF-κB signalling. Diagram shows processing of the NF-κB subunit dimers to allow for nuclear translocation and regulation of target genes. The assembly of hetero-dimer or homo-dimer conformations determine whether NF-κB will exert gene activating or repressive functions. Image source: (Hoeger et al. 2017).

1.5.2.2. The atypical NF-κB signalling pathway

There are also additional pathways that trigger NF-κB activation known as atypical NF-κB signalling (Hoesel and Schmid 2013). One such route involves genotoxic stress mediated translocation of NEMO to the nucleus and its ubiquitination, driven by the checkpoint kinase ATM. Both NEMO and ATM

return to the cytoplasm, stimulating IKKβ catalytic activity to enable NF-κB release from IkB (Hoesel and Schmid 2013). Another route involves the cell cycle control and DNA damage protein kinase CK2, that upon stimulation by UV light activates Calpain, a cysteine protease, that primes IkB for proteasomal degradation, thus enabling NF-κB release and nuclear translocation (Godwin et al. 2013).

1.5.3. NF-κB pathway interactions with additional cell signalling pathways

Directly and indirectly, the NF-κB pathway has been shown to interact with a variety of cell signalling pathways (Dorrington and Fraser 2019), including the PI3K-AKT-mTOR and RAS-RAF-MEK signalling cascades, which in turn results in the constitutive activation of NF-κB and subsequent regulation of pathway responsive genes (Chaturvedi et al. 2011).

Interestingly, IKKα is an AKT substrate which can be directly phosphorylated at site Thr23, whereby IKKα can also mediate activation of mTORC1 through phosphorylation at site Ser1415. IKKα is also believed to interact with mTORC2, however the regulatory mechanism involved is yet to be fully established (Ghomlaghi et al. 2021).

Further crosstalk between the NF-κB and the PI3K pathway has been identified in a study exploring primary effusion lymphoma, where inactivation of p65 via inhibitor and siRNA knockdown experiments resulted in the inactivation of AKT and its downstream targets FOXO1, GSK3 and BAD (Hussain et al. 2012). Conversely, AKT pharmacological or siRNA inhibition resulted in IKBα inhibition within these cells (Hussain et al. 2012).

Overexpression of MAPK-ERK pathway regulators, including NAK, TAK1, MEKK1 and MEKK3, and kinases such as PKC-θ, PKC-ζ and PKC-λ, have also been shown to phosphorylate and activate IKKs (Oeckinghaus et al. 2011), although the mechanisms remain unclear. Interestingly JNK signalling has also been identified as a critical downstream target of NF-κB, thus NF-κB-mediated phosphorylation of JNK can also contribute to tumour migration and invasion (Koul et al. 2013; Jin et al. 2014).

Moreover, Notch receptor ligand Notch-1, can activate NF-κB via a direct interaction with IKKα and has also been shown to interact with p50. Additionally, expression of NF-κB subunits can be regulated in a Notch-dependent manner, where transcriptional regulation of Notch pathway components also can occur in a NF-κB dependent manner (Oeckinghaus et al. 2011).

Furthermore NF-κB has also been evidenced to interact with transcription factors. NF-κB and STAT3 have been shown to facilitate promoter recruitment to increase self-transcription, in addition to directly interacting with one another to synergistically regulate cytokine and chemokine target genes, as well as those involved in cell cycle control and inhibition of apoptosis (Hoesel and Schmid 2013). Interactions between canonical NF-κB subunits with tumour suppressors such as p53 have also been documented, where p53 has been shown to repress the transcriptional activity of NF-κB and subunit p65 to conversely prevent p53 transactivation (Hoesel and Schmid 2013).

1.5.4. NF-κB signalling in prostate cancer

Despite its prominent role in innate immunity, NF-κB signalling has been shown to contribute to cancer initiation and progression, in addition to facilitating evasion of tumour cells from immune-surveillance (Hoesel and Schmid 2013). Genetic alterations in NF-κB pathway components that cause elevated NF-κB signalling are common in lymphoid type cancers, whereas aberrant NF-κB signalling in solid tumours is associated with high level cytokine secretion within the tumour microenvironment (Hoesel and Schmid 2013).

NF-κB transcription factors have been shown to upregulate the expression of anti-apoptotic genes such as c-FLIP, C-IAPs and TRAF1/2 to prevent apoptosis (Luo et al. 2005), upregulate growth factors such as VEGF to facilitate angiogenesis, induce the expression of matrix metalloproteinases (MMPs) that breakdown the extracellular matrix (ECM) to promote metastatic spread, and further potentiate inflammation; generating cytokine storms that are able to continue augmenting NF-κB activity (Hoesel and Schmid 2013).

Aberrant activation of NF-κB signalling is associated with a poor prognosis in prostate cancer patients and CRPC progression (Zhang et al. 2016a). Genetic alterations in genes encoding the various NF-κB family members have been evidenced both in primary prostate cancer and metastatic CRPC as shown in Table 1.5. The most common genetic alteration in primary prostate cancer is *RELA* amplification (1.2%), which is further amplified in mCRPC (3.38%), whilst mutations in NF-κB genes are rare (>0.9%). These data indicate that NF-κB activation is not driven by genetic aberrations in NF-κB genes, but instead a consequence of augmented ligands that drive upregulation of NF-κB signalling.

Table 1.5: Prevalence of NF-κB subunit genetic alterations in human prostate cancer. Clinical data obtained from the TCGA Firehose Legacy Prostate Adenocarcinoma dataset (2015) and the Stand Up 2 Cancer / Prostate Cancer Foundation (SU2C/PCF) Dream Team Metastatic Prostate Adenocarcinoma dataset (Abida et al. 2019), via the cBioPortal (Cerami et al. 2012; Gao et al. 2013). Abbreviations used; Mutation (Mut), Deep Deletion (Del), and Amplification (Amp).

Gene	Alterations present in TCGA (primary prostate cancer) dataset n = 499*	Alterations present in SU2C 2019 (metastatic CRPC) dataset n = 444*
NFKB1	Mut 0.2% & Del 0.8%	Mut 0.9%, Amp 1.35% & Del 0.9%
NFKB2	Amp 0.2% & Del 2.61%	Mut 0.66%, Amp 1.8% & Del 2.48%
RELA	Mut 0.6%, Amp 1.2% & Del 0.4%	Mut 0.45%, Amp 3.38% & Del 0.23%
RELB	Mut 0.2%, Amp 0.2% & Del 0.8%	Mut 0.45%, Amp 1.58% & Del 0.9%
REL	Amp 0.2% & Del 0.4%	Mut 0.23%, Amp 2.03% & Del 0.23%

Inflammation has been widely linked to prostate tumorigenesis (Karan and Dubey 2016), and castration in the prostate linked to an induction of the inflammatory response (Staal and Beyaert 2018). Loss of AR signalling has been shown to activate oncogenic PKC family members; where isoforms such as PKCλ and PKCι, can promote NF-κB mediated, androgen-independent growth of prostate cancer cells via the induction of IL-6, subsequently activating BCL3 mediated tumour cell survival. Additionally, PKCε has been shown to synergise with PTEN loss, activating NF-κB to drive further transcription of pro-inflammatory genes (Staal and Beyaert 2018).

Previous studies investigating the PTEN-null PC3 cell line identified that the NF-κB pathway can be induced in an AKT-dependent manner through the direct association of activated mTORC1 with IKKα and IKKβ, as established by co-immunoprecipitation experiments (Dan et al. 2008). Additionally, siRNA-mediated knockdown of *RELA* (encoding p65) or *IKBKB* (encoding IKKβ) in PC3 cells, is reported to increase apoptosis and reduce cell proliferation, migration and stemness properties (Zhang et al. 2016a) highlighting possible tumour suppressive roles of these proteins in prostate cancer. As NF-κB signalling has also been shown to mediate the transcription of self-renewal genes including *SOX2*, *NANOG* and *OCT4* in PC3 cells (Zhang et al. 2016a), a possible link may exist between elevated NF-κB activity, tumour progression and the ability to develop resistance when excessive AKT signalling occurs.

Crosstalk between the AR and NF-κB signalling pathways has been observed in prostate cancer, as the NF-κB subunit p52 can directly bind with AR to form a heterodimer to trans-activate the transcription of a subset of AR target genes (Staal and Beyaert 2018). Thus, NF-κB regulation of AR-mediated genes

can contribute to CRPC growth in the absence of androgens. AR signalling has also been shown to inhibit canonical NF-κB dependent transcription and conversely activate non-canonical NF-κB signalling (Staal and Beyaert 2018). Within prostate cancer cells, p52 can also activate metabolic reprogramming providing an additional mechanism whereby NF-κB signalling can promote tumour progression (Staal and Beyaert 2018).

Interestingly, *in vitro* work has shown that AR-negative prostate cancer cell lines, such as PC3 or DU145 cells, display constitutive NF-κB activation in 2D culture, whereas NF-κB activation is generally lower in AR-positive prostate cancer cells such as androgen-sensitive LNCAP cells (Verzella et al. 2016). These findings suggest that NF-κB activity is required for AR-negative cancer cell growth and survival in environments of low-level AR signalling (Verzella et al. 2016).

1.5.5. NF-κB and PI3K/PTEN signalling in prostate cancer

Growth factor mediated PI3K signalling has been shown to activate NF-κB; both in an AKT-dependent manner via mTORC1 mediated translation of NF-κB target genes and regulated mRNAs, as well as in an AKT-independent manner through activated mTORC2, that can drive decreased IkBα expression and increased IkBα phosphorylation via RICTOR (Tanaka et al. 2011; Godwin et al. 2013). Conversely, PTEN has been shown to inhibit NF-κB activation, as PTEN loss within leukaemia cell lines has been reported to drive IKK activation via the PI3K-AKT pathway, leading to constitutive NF-κB activation (Gu et al. 2004; Verzella et al. 2016).

Despite its regulatory role, PTEN itself can be down regulated by the NF-κB subunit p65. Vasudevan et al, showed within a range of studies that elevated levels of p65 could supress *PTEN* expression in both human thyroid and lung cancer cells (Vasudevan et al. 2004). Two sites within the PTEN promoter were hypothesised as potential NF-κB binding sites, however work has now identified that *PTEN* repression is not mediated by p65 binding at these sites, but instead competitive interactions with the p300 and CBP transcriptional co-activators. In addition, PTEN expression could be rescued via use of p65 targeting siRNA, as well as by overexpressing IkB (Vasudevan et al. 2004). Furthermore, the restoration of PTEN was found to impede NF-κB activity, as PTEN can inhibit the transactivation potential of p65 and consequently sensitise cells to TNF-induced apoptosis (Mayo et al. 2002; Vasudevan et al. 2004).

Recent studies have also highlighted a link between the cellular protein Profilin and PTEN in regulating NF-κB signalling, such that Profilin interactions prevent PTEN ubiquitination and consequent

degradation, enabling PTEN to attenuate IKK phosphorylation and therefore limit NF-κB signalling (Zaidi and Manna 2016). Downregulation of Profilin correlates with low PTEN expression and high NF-κB expression patterns within human breast tumours (Zaidi and Manna 2016), thus modulating Profilin expression to protect and enhance PTEN tumour suppressive activity warrant further investigation.

Independently of the conventional PI3K signalling pathway, the predicted tumour suppressor, prostate apoptosis response 4 protein (PAR-4), can also negatively regulate AKT. Interestingly, microarray data from human prostate cancer samples revealed that *PTEN*-positive tumours positively correlate with *PAR-4* positivity, and those with no or low-levels of *PTEN* mRNA had little to none *PAR-4* mRNA (Fernandez-Marcos et al. 2009). Together this data indicates that these two tumour suppressors may cooperate to prevent tumour growth *in vivo.*

Together, these findings suggest a clear co-regulatory loop between PTEN and NF-κB, and that loss of PTEN, a common characteristic of prostate cancer, can activate canonical NF-κB signalling to promote tumorigenic growth. PI3K/PTEN/AKT- mediated activation of the non-canonical NF-κB axis is not well characterised, although Garg et al have shown that following PTEN loss, overexpression of PKCε within the mouse prostate promotes a migratory and invasive phenotype; driven by upregulation of CXCL13-CXCR5 signalling mediated through transcriptional activity of the non-canonical NF-κB proteins (Garg et al. 2017). Thus, non-canonical and canonical NF-κB signalling pathways are likely to contribute to PTEN-deficient prostate cancer growth, however the molecular mechanisms behind this possible involvement remain yet to be fully determined.

1.6. The role of the tumour microenvironment in prostate cancer

1.6.1. The tumour microenvironment (TME)

A key contributor to tumour formation and progression is the TME, that is comprised of a variety of stromal cells, immune cells and additional non-cellular components within the extracellular matrix (ECM) (Figure 1.17). Together, the TME components engage complex signalling networks and communication processes to respond to the demands of the epithelial tumour as it evolves and progresses, assisting in its growth and mediation of drug-resistance (Baghban et al. 2020).

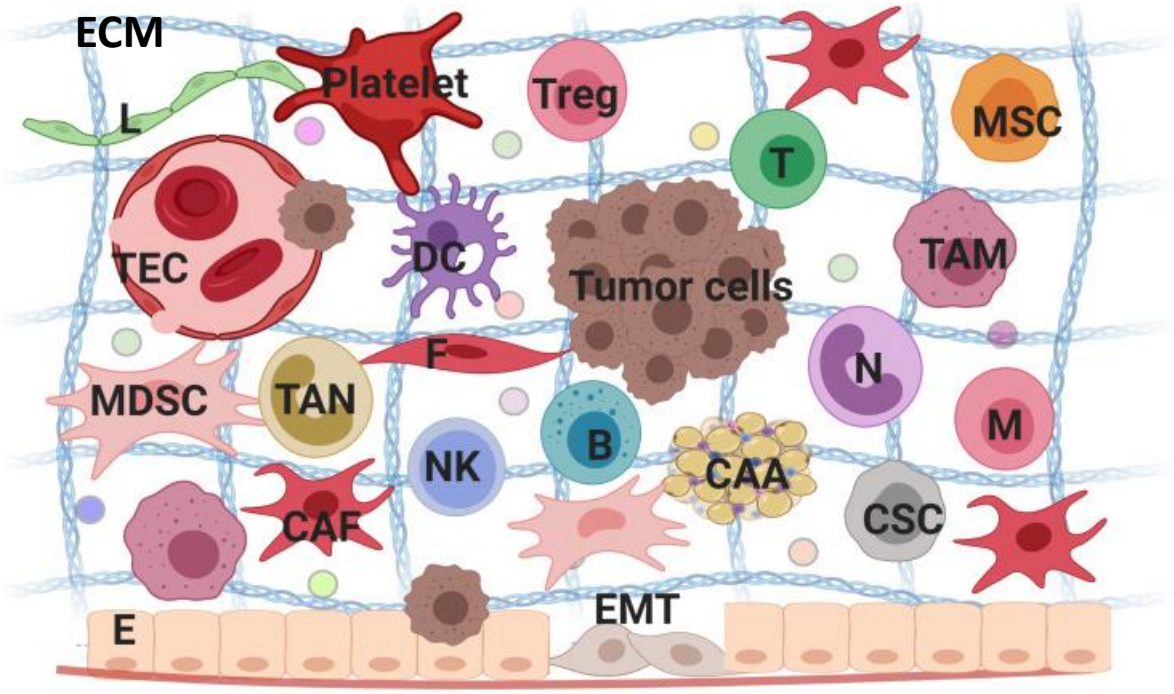

Figure 1.17: Components of the tumour microenvironment. Schematic depicts components of the TME. Abbreviations used include: B, B lymphocytes; CAA, cancer-associated adipocytes; CAF, cancer-associated fibroblasts; CSC, cancer stem cells; DC, dendritic cells; E, epithelial cells; ECM, Extracellular matrix, EMT, epithelial-mesenchymal transition; F, fibroblasts; L, lymphatic endothelial cells; M, macrophages; MDSC, myeloid-derived suppressor cells; MSC, mesenchymal stem cells; N, neutrophils; NK, natural killer cells; T, T lymphocytes; TAM, tumour-associated macrophages; TAN, tumour-associated neutrophil; TEC, tumour endothelial cells; Treg, regulatory T lymphocytes. Figure source: (Ni et al. 2021).

It is important to note, that alongside the tumour cells within the TME, non-malignant cells also play a significant role in contributing to pro-tumorigenic conditions. Stromal cells such endothelial cells, aid in protecting the tumour from the immune system, as well as assisting in the development and branching of angiogenic vessels for nutritional support. Moreover, fibroblasts, another key stromal component, can assist these endothelial cells undergoing angiogenesis and provide means of passage, as fibroblasts aid migration of the primary tumour into the bloodstream, initiating metastasis (Arneth 2019).

The ECM constitutes a dense network of collagens, enzymes and glycoproteins that support varied biomechanical activities and functions, and due to its ability to influence cell adhesion, proliferation, and communication, the ECM is also known to play an extensive role in cancer progression. By altering

its physical properties and composition, the ECM can promote tumour cell migration and regulate the speed at which tumour cells can migrate from one area to another (Arneth 2019). Additionally, growth factors such as integrins that are present within the ECM and near cell membranes, have been also shown to facilitate communication of cells within the TME (Arneth 2019).

One of the most important pro-tumorigenic contributions comes from the immune cells present within the TME. For example, macrophages have been shown to promote circulation and extravasation of cancer cells; furthermore, tumour associated macrophages (TAMs), have been shown to both facilitate and diminish the activity of various anti-tumour therapies including irradiation and checkpoint inhibitors (Arneth 2019). In addition, tumours have been shown to attract and expand populations of myeloid-derived suppressor cells (MDSCs) and Foxp3-positive regulatory T cells (Tregs) as a method of controlling effector lymphocytes and reducing the activation of tumour-reactive lymphocytes, resulting in immunosuppression (Labani-Motlagh et al. 2020).

There are two main phases involved in cancer immunosuppressive functions, the first being the equilibrium phase where despite being recognised, the tumour continues to grow, and the second, the escape phase, where the tumour evades and bypasses immune surveillance and elimination (Labani-Motlagh et al. 2020). This tumour mediated evasion can occur through multiple processes including the release of immunosuppressive extracellular vesicles such as exosomes, the shedding of soluble major histocompatibility complex 1, loss or downregulation of adhesion molecules and tumour antigens, as well as upregulating proteins such as BCL-2 to drive resistance to apoptosis (Labani-Motlagh et al. 2020).

1.6.2. Stromal – epithelial crosstalk during normal prostate development and tissue homeostasis

During prostate development, mesenchymal cells differentiate and form smooth muscle that is abundant in AR, especially in cells adjacent to the epithelium. These androgen receptors play a vital role in prostate development where stimulation from circulating androgens results in stage-specific regulation of the epithelial cells (Singh et al. 2014).

Androgens in the stroma can also directly act upon epithelial AR to mediate differentiation, however most of the androgenic activity is believed to occur through the release of paracrine factors and their mediators such as epithelial growth factor (EGF), fibroblast growth factor (FGF), nerve and insulin growth factor family members that are independent of epithelial AR and androgens (Singh et al. 2014).

In addition to AR signalling, crosstalk between the prostate epithelium and stroma is also heavily reliant of TGF-β signalling (Lee et al. 2014). The integrity of the various ductal regions of the adult prostate is determined and maintained by highly regulated TGF-β signalling. For instance, in regions where TGF-β is highly expressed, proliferation of adjacent epithelial cells is suppressed, and apoptosis increased. Variations in stromal-epithelial cross talk and discrepancies within regional TGF-β signalling can consequently result in the abnormal growth of the prostate, as well as the development of BPH and prostate cancer (Lee et al. 2014).

1.6.3. Stromal – tumour crosstalk during prostate cancer

Communication between prostate tumour cells and its microenvironment occurs via multiple bidirectional and dynamic processes (Baghban et al. 2020). This has been evidenced as direct cell-cell contact, as well as cell-free contact mediated through the ECM, with secreted mediators including soluble factors and molecules also shown to play a part in both cellular and non-cellular communication (Baghban et al. 2020).

Intercellular communication has been frequently acknowledged to occur through a complex network of inflammatory mediators, cytokines, chemokines and matrix remodelling enzymes, however more recently, novel routes of interaction have been identified that include exosomes, circulating tumour cells, cell-free DNA and apoptotic bodies, which can all deliver critical information from the main tumour to surrounding non-tumorigenic cells as well as distal secondary tumour cells (Baghban et al. 2020), highlighting the complexity of interactions that can facilitate tumorigenic growth.

Whilst the stimuli required to initiate and sustain prostate inflammation are not fully understood, it is evident that inflammation within the adult prostate is highly prevalent and thus has been implicated as a driver of prostate cancer (Cai et al. 2019). Repetitive genomic damage and cellular stress instigated by inflammation and inflammatory injury can render tumour suppressor genes more susceptible to mutagenesis, silence stress response genes and degrade proteins that protect against oxidative damage. Moreover, DNA damage brought on by inflammation can induce both cellular senescence and its associated secretory phenotype, SASP; that in turn further augment inflammation whilst promoting the loss of tumour suppressor genes such as *PTEN* (Cai et al. 2019; de Bono et al. 2020).

1.6.3.1. Role of the tumour microenvironment during tumour initiation and progression

Animal studies have identified that following interactions with cancerous prostate epithelial cells, normal or benign stromal cells experience a decrease in proliferation while the epithelial cancer cells show reduced malignant properties, indicating non-malignant stroma can protect against tumour development (Singh et al. 2014).

Both in a normal and cancerous prostate setting; surrounding stromal cells, specifically cancer associated fibroblasts (CAFs), can produce various secretory growth factors, cytokines and anti-apoptotic factors that mediate paracrine functions that contribute to epithelial cancer cell growth and survival (Chauhan et al. 2020). CAFs can additionally stimulate remodelling of the basement membrane, which facilitates openings that tumour cells can migrate through and disseminate to distal sites (Glentis et al. 2017).

High-grade PIN has been shown to secrete cytokines and chemokines that recruit myeloid-derived suppressor cells (MDSCs), which in turn secrete IL-23 and other paracrine factors that enhance oncogenic signalling; whereas in malignant prostate tissue, inflammation produces infiltrate primarily consisting of macrophages, T lymphocytes and an expanded population of leukocytes, which contribute to the release of cytokines and free radicals that induce DNA damage, atrophy and cell proliferation (Cai et al. 2019; de Bono et al. 2020).

Moreover, the efferent pathway, a concept proposed by De Wever and Mareel, is also thought to be an early event in prostate cancer progression. It has been hypothesised that oncogenic epithelial cells can induce neoplastic transformation of surrounding stromal cells, in addition to triggering a release of soluble factors including TGF-β and platelet-derived growth factor (PDGF) into the stroma, that can both induce the differentiation of fibroblasts into myofibroblasts, as well as epithelial to mesenchymal transition (EMT) (Niu and Xia 2009).

The reactive stroma of a prostate tumour is mainly characterised by an increase of myofibroblasts and decrease of smooth muscle cells. These significant changes to the microenvironment both promote evasion of immunosurveillance and androgen independence, resulting in further cancer progression (Singh et al. 2014). Through analysis of tumour and adjacent stromal tissue of prostate cancer specimens obtained via TURP and radical prostatectomy, stromal AR expression was shown to decrease when HG-PIN was present. Loss of stromal AR expression also correlated with higher histological grades, with 94% loss observed in Gleason grades 8 – 10 (Singh et al. 2014), illustrating

the importance of stromal AR and AR signalling not only in prostate organogenesis but also within the development of prostate cancer, which has been summarised in Table 1.6.

Table 1.6: Effects of epithelial and stromal AR on prostate cell growth. Table highlights the main outcomes of AR presence and signalling during different prostatic phases. Data adapted from (Singh et al. 2014).

	Epithelial AR	Stromal AR
Foetal prostate	Promoter of epithelial cell growth	Promoter of epithelial cell growth
Benign adult prostate	Promoter of epithelial cell growth	Inhibitor of epithelial cell growth
Prostate adenocarcinoma	Promoter of cancer growth	Inhibitor of cancer growth

1.6.3.2. Role of the tumour microenvironment during therapeutic resistance

The TME generates both innate and acquired resistance to therapies via cellular interactions and host adaptive responses respectively (Sun 2016). Analysis of published literature have indicated CAFs as a significant contributor to resistance mechanisms, although the ECM, immune cells and exosomes present within the microenvironment, have also been shown to influence drug and treatment responses (Sun 2016).

CAFs have been evidenced to augment ECM deposition and increase both synthesis and secretion of cytokines such as IL-6, PDGF and VEGF, all of which have been shown to contribute to a chemoresistance-triggering secretome mediated through the PI3K-AKT pathway. Mediated via pro-inflammatory signals, CAFs also facilitate leukocyte infiltration, drive NF-κB dependent tumour progression, and promote vascular permeability (Sun 2016). In addition to tumour vasculature providing vital oxygen and nutrient supplies, vessel-tumour spatial distance and micro-vessel density have also recently been implicated as factors that can influence drug delivery and distribution within tumours (Sun 2016).

Furthermore, CAFs have been shown to mediate hyperactivation of the Wnt pathway through the reduction of secreted frizzled-related protein 2 and the increase of Wnt10B and Wnt16B ligands (Son et al. 2017). Hyperactivation of this pathway in cancer drives a surge of p-glycoprotein and ATP-binding cassette G2 expression, which together can also lead to chemoresistance (Son et al. 2017). In prostate cancer, docetaxel resistance has been linked to the induction of EMT, which can additionally be mediated through CAFs (Nakazawa et al. 2017).

The ECM can contribute to cancer treatment resistance in various ways, including adhesion-mediated drug resistance driven by integrin binding to collagen, fibronectin, and laminin (Sun 2016). The ECM has also been shown to change polarity of tumour cells that are directly attached, conferring resistance to chemotherapy-induced apoptosis (Sun 2016). Moreover, when a reactive stroma displays elevated collagen fibre crosslinking and increased ECM biosynthesis, integrin signalling is promoted, which can further contribute to radiation and chemotherapy resistance by enhancing RTK and EGFR signalling (Sun 2016).

Exosomes secreted from fibroblasts have additionally been evidenced as key drivers of resistance. These lipid-membrane encompassed vesicles that contain numerous proteins and nucleic acids secreted from a host cell, can be recognised by a recipient cell via the presence of membrane bound signal receptors, and thus stimulate new activity and function (Son et al. 2017)These fibroblast-derived exosomes have been shown to activate the NOTCH signalling pathway inducing chemoresistance within recipient tumour cells as well as stimulating exocytic drug efflux within cancer cells (Son et al. 2017).

Growth factor signalling such as FGF activation of PI3K and MAPK pathways, have also been shown to suppress expression of critical pro-apoptotic factors and proteins such as BCL-xL, which consequentially limits apoptotic responses to chemo- and/or radiotherapy (Son et al. 2017). Together, these findings indicate a clear function of the tumour microenvironment in yielding tumour cell therapeutic resistance.

In summary, the TME plays multiple critical functions in regulating tumour growth and therapeutic response, however the molecular mechanisms behind this remain to be yet fully understood and warrant further investigation.

Chapter 2

2. Materials and Methods

2.1 Experimental mice

2.1.1 Transgenic mouse models

Genetically engineered mouse model (GEMM) studies were performed under a UK Home Office project license and approved by the Cardiff University Animal Welfare Ethical Review Body (AWERB) committee. Animal models utilised included mice on a pure Fvb/n background harbouring *Pik3ca*$^{+/H1047R}$ and *Pten*$^{fl/fl}$ transgenes targeted by the constitutive, prostate specific *Probasin Cre (PBiCre)* (provided by the Peter MacCallum Cancer Centre (Lesche et al. 2002; Jin et al. 2003; Kinross et al. 2012; Pearson et al. 2018), in addition to the tamoxifen inducible *Col1a2CreER(T2)* (*Tg(Col1a2-cre/ERT,-ALPP)7Cpd/J*) strain on a C57BL/6J and DBA/2J mixed background, that generates endogenous *Pten* deletion within fibroblast-type cells (provided by Dr Valerie Meniel, Cardiff University (Zheng et al. 2002).

The *Col1a2CreER(T2) Pten* transgenic line was also crossed with the *Gt(ROSA)26Sor<tm1Hjf (RFP)* strain on a mixed background that had been backcrossed to C57BL/6J at least 8 times (provided by Dr Catherine Hogan, Cardiff University (Luche et al. 2007)), to generate a reporter model that expresses red fluorescence protein in *Col1a2CreER(T2)*-driven recombined cells.

Staff within the Transgenic-2 animal facility at Cardiff University executed the set-up of breeding pairs, weaning and ear notching of pups, in addition to the feeding and cage cleaning of GEMM cohorts.

2.1.2 Induction of CreER(T2) recombination

2.1.2.1 Preparation of Tamoxifen

Aseptically, tamoxifen (Sigma, #T5648-1G) was weighed within a 1.5 ml Eppendorf tube or 15 ml falcon tube, then dissolved in 2 µl of 100% ethanol (Fisher Scientific, #BP2818-S00) per mg of tamoxifen. Corn oil (Sigma, #C8267-500ML) in the required ml per mg of tamoxifen was then added, before tubes were wrapped in foil, vortexed and left to shake in an incubator for 3 – 4 hours at 50°C.

2.1.2.2 Administration of Tamoxifen

Prior to injection, sealed tamoxifen solution was heated within a water bath at 70°C. Using one 26-gauge needle (BD, #300600) and one 1 ml syringe (Terumo, #SS+01T1) per animal, tamoxifen solution was administered via intraperitoneal injection in the lower left quadrant of the abdomen.

For induction of the *Col1a2CreER(T2)* and RFP reporter mouse models, 8 mg/ml tamoxifen solutions were freshly prepared in the morning of the initial injection day. Once weighed, animals were

administered 80 mg/kg doses once a day, for 4 consecutive days. Control injections were also administered consisting of corn oil only.

2.2 Patient-derived xenografts (PDXs)

PDX generation, implantation, passaging and maintenance was performed by members of the Pearson Lab alongside the PDX platform team. I assisted through media and testosterone pellet production.

2.2.1 Record keeping

In line with Human Tissue Act (HTA) regulations, all details of human tissue obtained for scientific investigation were thoroughly recorded on databases, including locations and usage of cryopreserved samples and tissue blocks; with samples securely stored behind two lockable doors at all times.

2.2.2 Generation of CRPC PDX models

CRPC 201.2 lung and 27.2 lymph node CRPC PDX models were provided by Prof. Gail Risbridger, Monash University, Melbourne, Australia (Lawrence et al. 2018). Cryopreserved tumour specimens were shipped on dry ice and stored in liquid nitrogen (LN_2) dewars until implantation into NSG mice with a 5 mm Testosterone pellet (refer to section 2.2.3), as previously described (Lawrence et al. 2013). Experiments were approved by the School of Biosciences Research Ethics Committee (approval number: SREC 1810-01).

In collaboration with the Cardiff University PDX platform led by Prof. Richard Clarkson, Prof. Howard Kynaston, Prof. John Staffurth and the Wales Cancer Bank (WCB), Dr Helen Pearson received 2 mm biopsy core specimen from an image guided, lymph node biopsy donated by a consenting patient with mCRPC via the WBC (Ethical approval #17-014, HTA project: #520). The specimen was immediately placed into 20 ml of sterile transport media (Table 2.1) on ice by WCB nurses at the University Hospital of Wales, Heath Park, Cardiff and de-identified. Samples were transported on ice to the animal unit for immediate processing by Dr Pearson and Dr Gillian Seaton. 3 mm tissue fragments were implanted into an adult male NSG mouse bilaterally into the flank subcutaneously, together with a 5 mm testosterone pellet, as previously described (Lawrence et al. 2013) (Pearson Lab, unpublished data). Tumour volume was measured biweekly with calipers.

Table 2.1: Patient biopsy transport media.

Reagent	Volume
1x RPMI 1640 culture media (Thermofisher, #21875059)	17.719 ml
1x Heat inactivated FBS (Thermofisher, #10270106)	2 ml
10,00 U/ml Penicillin/Streptomycin (Thermofisher, #15140-122)	200 µl
250 µg/ml Amphotericin B (Gibco, #15290-026)	40 µl
50 mg/ml Gentamycin (Lonza, #17-518Z)	40 µl
100mM Rock inhibitor Y-27637 (HelloBio, #HB2297)	1 µl
TOTAL	20 ml

2.2.3 Testosterone pellet production and implantation

For optimal PDX growth within recipient mice, in addition to preventing the tumours from experiencing near castrate conditions, 5 mm testosterone pellets were produced in-house for dorsal subcutaneous implantation. Aseptically within a laminar flow cabinet, silastic laboratory tubing (Dow Corning, #508-009) was cut into 8 mm sized lengths, then one end sealed with 1 mm of adhesive silicone (Bond It, #BDMT).

After 24 hours, 5 mm of each pellet was filled with tightly compacted testosterone powder (Sigma, #T1500) using a glass pipette and vortex, before being fully sealed with another 1 mm of adhesive silicone. Pellets were left to air-dry for 24 hours within the laminar flow cabinet, UV treated for 1 hour, wrapped in foil, then stored within a locked, controlled substance cabinet at room temperature. Testosterone usage and pellet allocation was recorded as per controlled substance regulations. Testosterone pellets were sterilised in 70% EtOH, air dried and implanted subcutaneously into the upper dorsal midline of an NSG mouse under anaesthetic at the time of tissue implantation for a period of up to 3 months.

2.2.3.1 Cryopreservation of propagated PDX tissue

To enable continual use of the PDX tumour tissue within subsequent experiments, 2 to 6, 1 - 3 mm^3 sized tumour pieces were frozen in cryovials (Nunc, #10577391) containing 1 ml cryopreservation media (as prepared in Table 2.2), through use of a Corning CoolCell freezing container (Corning #432003) to obtain a standardized controlled-rate of freezing of 1°C/minute within a -80°C freezer.

Table 2.2: PDX cryopreservation media.

Reagent	Volume
1x Dimethyl Sulphoxide (DMSO) (Sigma, # D2650)	500 µl
1x Heat inactivated FBS	4499.75 µl
100mM Rock inhibitor Y-27637	0.25 µl
Total	5 ml

Tissue was stored at -80°C for 24 hours before being transferred into LN_2 dewars for long term storage.

2.2.3.2 Passaging of PDX tissue

Fresh tumour fragments (1 - 3 mm^3) or cryopreserved tumour fragments thawed on ice, were transferred into dissection media (Table 2.3) at 4°C. Immunodeficient NOD scid gamma (NSG) mice were anaesthetised using isoflurane, and an incision within the left flank of mouse made for insertion of one 3 mm tumour fragment. Tissue was aseptically flash dipped in ice cold 70 % ethanol prior to implantation and the wound closed with tissue adhesive (3M, #1469SB). This process was repeated in the right flank, and a 5 mm testosterone pellet implanted subcutaneously (dorsal, near to the right shoulder blade). The incision was closed with tissue adhesive and the mice were given time to successfully recover (1 – 2 minutes).

Table 2.3: PDX dissection media.

Reagent	Volume
1x DMEM/F12 culture media (Gibco, #12634-010)	17.75 ml
1x Heat inactivated FBS	2 ml
10,00 U/ml Penicillin/Streptomycin	200 µl
250 µg/ml Amphotericin B	40 µl
100mM Rock inhibitor Y-27637	1 µl
Total	20 ml

Tumour formation was measured twice a week using calipers and mice were sacrificed once prostate tumours had reached a volume of 1 - 1.5 cm^3, approximately 4 - 8 weeks post-engraftment.

2.3 Genotyping of transgenic mice

2.3.1 DNA isolation

To genotype transgenic mice, ear biopsies were taken from each animal by the Transgenic-2 facility staff at Cardiff University. A master mix of (n + 1) x 250 µl of cell lysis solution (Qiagen, #1045696) and 5 µl of Proteinase K (20mg/ml) (Roche, #03115828001) was produced. To each ear notch biopsy, a final volume of 255 µl reaction mix was added and left to incubate with gentle agitation, overnight at 37°C. The following day, 100 µl of protein precipitation solution (Qiagen, #1045697) was added to each sample and centrifuged at 13,000 rpm for 10 minutes at 13°C to pellet unwanted cell debris and protein.

Sample supernatant was then transferred into 250 µl of isopropanol (VWR, #20842.312) and centrifuged at 13,000 rpm for 15 minutes at 13°C. Supernatant was discarded as waste and DNA pellets airdried for up to 5 minutes. Pellets were then resuspended in 200 µl of DNase free/ MilliQ H_2O and stored at 4°C until use or at -20°C for long-term storage of re-clips.

2.3.2 gDNA PCR

On ice, 9.5 µl of PCR master mix (Tables 2.4 and 2.5) was pipetted into individual 0.2 ml PCR tubes (Greiner Bio One, # 608281) or wells of a 96 well plate (Greiner Bio One, #655180), followed by the addition of a 0.5 µl gDNA sample. A negative control containing 0.5 µl of DNAse free, autoclaved MilliQ H_2O and where necessary, positive controls were included within each experiment. Thermocycling was performed using the outlined conditions (Table 2.6) using BioRad PCR machines.

Table 2.4: Forward and reverse primer base sequences used for genomic DNA PCR.

Oligonucleotide for gene detection	Sequence 5' – 3'	Reference
Cre F (*Probasin/Col1a2*)	GGGATTGCTTATAACACCTGTT	(Ireland et al. 2004)
Cre R (*Probasin/Col1a2*)	TATTCGGATCATCAGCTACACCA	
Pten F	CTCCTCTACTCCATTCTTCCC	(Suzuki et al. 2001)
Pten R	ACTCCCACCAATGAACAAAC	
Pik3ca F1	TTGGTTCCAGCCTGAATAAAGC	(Kinross et al. 2012)
Pik3ca F2	TCCACACCATCAAGCAGCA	
Pik3ca R1	GTCCAAGGCTAGAGTCTTTCGG	
Rfp F1	AAGGGAGCTGCAGTGGAGTA	(Luche et al. 2007)
Rfp F2	TAAGCCTGCCCAGAAGACTCC	
Rfp R1	AAGACCGCGAAGAGTTTGTCC	

Table 2.5: Reagent mastermix compositions for GEMM genotyping protocols.

For all Cre and Pten protocols			For Pik3ca and Rfp protocols	
Reagent	**Volume (µl)**		**Volume (µl)**	**Volume (µl)**
5x Green Buffer (Promega, #M7805)	2		5x Green Buffer (Promega, #M7805)	2
25 mM $MgCl_2$ (Promega, #M7805)	1		25 mM $MgCl_2$ (Promega, #M7805)	1
100 mM DNTPs (PCRBiosystems, #PB10.72.05)	0.08		100 mM DNTPs (PCRBiosystems, #PB10.72.05)	0.08
100 µM F Oligo	0.02		100 µM F1 Oligo	0.02
100 µM R Oligo	0.02		100 µM F2 Oligo	0.02
GoTaq Enzyme (Promega, #M7805)	0.04		100 µM R1 Oligo	0.02
Autoclaved H_2O	6.34		GoTaq Enzyme (Promega, #M7805)	0.04
Total: 9.5µl			Autoclaved H_2O	6.32
			Total: 9.5µl	

Table 2.6: Thermocycling conditions for GEMM genotyping protocols.

Thermocycling protocol	Temperature (°C)	Time	No. of cycles
Probasin Cre	95	15 min	1
	94	1 min	35
	55	2 min	
	72	1 min	
	72	5 min	1
	12	∞	
Col1a2 Cre	95	2.5 min	1
	94	1 min	35
	58	1 min	
	72	1 min	
	72	10 min	1
	12	∞	

Lesche *Pten*	94	3 min	1
	94	30 sec	30
	60	30 sec	
	72	40 sec	
	72	10	1
	4	5	1
	12	∞	
Suzuki *Pten*	95	2.5 min	1
	94	1 min	35
	58	1 min	
	72	1 min	
	72	10 min	1
	12	∞	
Rfp	95	3 min	1
	94	10 sec	35
	62	30 sec	
	72	30 sec	
	72	5 min	1
	12	∞	
Pik3ca H1407R	95	10 min	1
	95	30 sec	35
	55	30 sec	
	72	40 sec	
	72	5 min	1
	12	∞	

2.3.3 Gel electrophoresis for gDNA PCR

For genomic DNA band visualisation, a 100 ml 2% Agarose (SLS, #BIO41026) / TBE gel (TRIS (Fisher Scientific, #BP152-1), boric acid (Sigma, #B7660-1KG), EDTA (Invitrogen, #15575-038) and autoclaved MilliQ H_2O) was produced in a 250 ml conical flask within a microwave. 4 µl SafeView Nucleic Acid stain (NBS Biologicals, #NBS-SV1) was added to the gel, then poured into a mould containing deep wells and left to set for 30 minutes at room temperature before use.

10 µl of each sample to be genotyped and 5 µl of 100 – 1000 base pair DNA ladder (Promega, #G2101) were electrophoresed at 100 V for 45 minutes. Using the Bio-Rad ChemiDoc Imaging machine, nucleic acid detection parameters were applied to identify the PCR products (Table 2.7).

Table 2.7: Sizes of PCR products used in establishing GEMM genotypes.

Target	PCR products (base pair sizes)
Probasin Cre	286 bp (single band presence indicates positivity)
Col1a2 Cre	240 bp (single band presence indicates positivity)
Lesche *Pten*	Wildtype approx. 190bp, Heterozygous approx. 190bp + 210bp, Homozygous approx. 210 bp
Suzuki *Pten*	Wildtype 228bp, Heterozygous 228bp + 335bp + 390bp, Homozygous 335bp
Rfp	Wildtype 200bp, Heterozygous 200bp + 300bp, Homozygous 300bp
Pik3ca H1407R	Wildtype 372bp, Heterozygous 372bp + 553bp + 601bp, Homozygous 601bp

2.4 Tissue preparation

2.4.1 Harvesting procedures

At allocated experimental time points, animals were subject to Schedule 1 termination, with complete neck dislocation and permanent cessation of the circulatory system confirmed before initiating tissue harvest. Each animal was weighed for its total body weight before dissection of the prostate. Fat, seminal vesicles and the urinary bladder were removed as quickly as possible from the prostate and the total prostate weighed, before being placed into 10% formalin (Sigma Aldrich, #HT501128-4L) on ice for fixation (16-24 hours max.).

If snap frozen tissue was required, a single anterior, dorsolateral, and ventral prostate lobe was dissected (Figure 2.1), weighed individually in a lockable 1.5 ml labelled tube then immediately placed into liquid nitrogen. The remaining prostate lobes were weighed and fixed in 10% formalin on ice (16-24 hours max.).

The remainder of the genitourinary tract (urethra, seminal vesicles, bladder, testes, epididymis and vas deferens) and major organs (liver, pancreas, kidneys, heart and lung alongside salivary glands,

salivary lymph nodes and lumbar lymph nodes) were also dissected, then placed into 10% formalin on ice (16 - 24 hours max.).

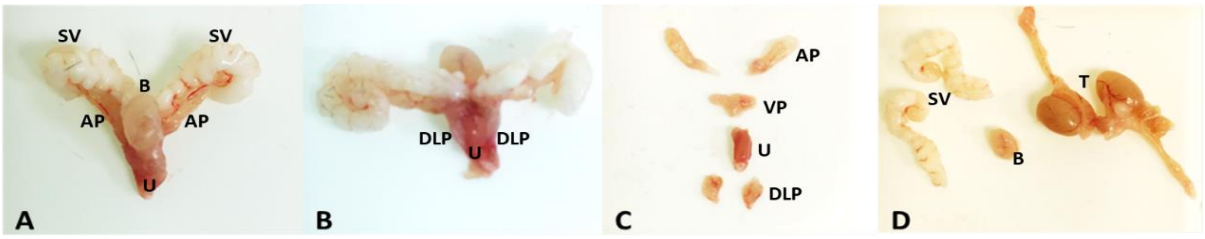

Figure 2.1: Images of dissected prostate and genitourinary (GU) tissues. Orientations shown in **(A)** anterior view, **(B)** posterior view, **(C)** as separated lobes and **(D)** main GU tissues attached to the prostate. AP; anterior prostate, B; bladder, DLP; dorsolateral prostate, SV; seminal vesicle, T; testes, U; urethra, VP; ventral prostate. Scale bar not shown.

Any abnormal growths or anomalies found during the harvests were recorded and a second ear notch biopsy taken to confirm the genotype via gDNA PCR.

2.4.2 Storage

Snap frozen tissue was transferred from liquid nitrogen (LN_2) to dry ice for transportation, then immediately stored at -80°C until requirement for RNA or protein extraction.

Following overnight fixation of samples in formalin at 4°C, tissues were transferred into 70% reagent grade ethanol (VWR, #20821.330) and stored at 4°C for further processing.

2.4.3 Paraffin wax embedding of tissues

After removal of excess fat from the GU tract and major organs, fixed tissue was taken to the Cardiff University Histology Laboratory for processing (cassetting, tissue dehydration, embedding) and embedded into paraffin to generate formalin-fixed paraffin-embedded (FFPE) tissue blocks. Mouse IDs were de-identified for non-biased analysis.

2.4.4 FFPE Tissue Sectioning and H&E staining

FFPE tissue blocks were sectioned by the Cardiff University Histology team via microtome, generating 3 µm slices that were transferred onto baked Poly-L-lysine (PLL) coated slides.

Haematoxylin and eosin (H&E) staining was also performed upon request.

2.5 Cell Culture

2.5.1 Prostate cancer immortalised cell lines

A panel of human prostate cancer epithelial cell lines, as detailed in Table 2.8 were used for *in vitro* studies.

Table 2.8: Details and characteristics of human prostate cancer cell lines used *in vitro*.

Cell line	Derivation	Cancer Subtype	Sourced from	AR status	PTEN status	Mycoplasma test
DU145	Brain metastatic lesion	CRPC	ATTC (via Peter MacCallum Cancer Centre)	Negative	Positive (although possesses a coding SNP in *PTEN*) (Lotan et al. 2011)	Negative
LNCAP	Lymph node metastatic lesion	HSPC	The ATTC	Positive	Negative (one deleted allele, one mutated allele; codon 6 AAA to A frameshift mutation)	Negative
PC3	Grade IV bone metastatic lesion	CRPC	The ATTC	Negative	Negative (homozygous deletion)	Negative
22RV1	Carcinoma xenograft	CRPC	Laboratory of Prof. N. J Maitland, University of York	Positive	Positive (wild type)	Negative

2.5.1.1 Cell line authentication

Formal cell authentication was coordinated by Dr Daniel Turnham. Genomic DNA from cell lines detailed in Table 2.8 was extracted using a DNeasy kit (Qiagen, #69504) as per manufacturer's instructions and sent to Eurofins Scientific for validation. The short tandem repeat (STR) cell authentication profile is shown in Appendix 1.

2.5.2 Maintenance of human prostate cancer cell lines

2.5.2.1 Thawing of cells

Cells preserved in cyrovials were taken from storage in LN_2 dewars and immediately placed onto dry ice. Cells were thawed gently within a 37°C thermal bead bath and aseptically transferred into a laminar flow cabinet for seeding.

2.5.2.2 Seeding and tissue culture conditions

To seed, cells within cryopreservation media were pipetted into 4 ml of pre-prepared and pre-warmed culture media tailored for optimal growth of the cell line (Table 2.9), then centrifuged at 1200 rpm, at 13 °C for 5 minutes to pellet cells and remove traces of DMSO.

The cell pellet was resuspended in 5 ml fresh culture media and pipetted into a TC25 flask (Thermofisher Scientific, #156367). The flask was left within a 37°C incubator possessing atmospheric O_2 and 5% CO_2 levels to allow cells to attach and grow. Culture media was changed every 48 - 72 hours until cells reached 75 - 85% confluency and required passaging.

Table 2.9: Culture media components for human prostate cancer cell lines used.

Cell line	Culture Media	1x Foetal Bovine Serum (FBS) Concentration	100x Penicillin-Streptomycin (10,000 U/mL) concentration
DU145 / LNCAP/ PC3 / 22RV1	RPMI 1640 + L-Glutamine (Thermofisher, #21875059)	10 % of total media volume (Thermofisher, #10270106)	1 % of total media volume (Thermofisher, #15140122)

2.5.2.3 Passaging

For passaging/splitting highly confluent cell populations, cells were washed in 5 ml pre-warmed PBS, followed by the addition of 1 ml trypsin-EDTA (0.25%) (Thermofisher scientific, #25200056) for cell dissociation. After incubation of cells in trypsin at 37°C for 5 minutes, 5 ml of culture media was then added to the cells for trypsin inactivation.

6 ml of the cell solution was transferred into a sterile 15 ml falcon tube and centrifuged at 1200 rpm, for 5 minutes at 13 °C to pellet the cells. The media was removed, and cells resuspended in 5 ml fresh culture media before being pipetted into a TC75 flask (Thermofisher Scientific, #156449) containing another 5 ml culture media. Flasks were left in the incubator, with media changed every 48 hours until cells required further passaging.

2.5.2.4 Cryopreservation

Following cell detachment, trypsin inactivation, cell pelleting and resuspension, cells were quantified using the Luna Automated Cell Counter. The number of cells required to achieve 1 - 2 million cells per 1 ml of media was calculated, added to culture media supplemented with 10% DMSO (Sigma, # D2650), then pipetted into labelled 2 ml cryovials (Nunc, #10577391).

Cryovials were then placed into Corning CoolCell LX cell freezing containers (Corning #432003) and stored at -80°C to freeze cells at a rate of -1°C/minute for at least 48 hours, before transferring cells into LN_2 for long-term storage.

2.5.2.5 Mycoplasma testing

Using a PCR testing kit (PromoCell, #PK-CA91-1096), media taken from highly confluent cell cultures was screened for mycoplasma populations regularly, in order to detect any contamination that could compromise cell growth and reproducibility of subsequent assays.

100 µl of media taken directly from cell culture, was transferred into sterile 0.2 ml PCR tubes, then heated at 95°C for 10 minutes to create templates that were stable for up to 5 days at 4°C.

23 µl of rehydration buffer was added to n + 1 pre-prepared reaction tubes within the kit, followed by 2 µl of each sample media in addition to 2 µl fresh, non-cell media into the spare tube as a negative control. Tubes were sealed using caps provided. 23 µl rehydration buffer and 2 µl sterile DNA-free H_2O was also added to one pre-prepared reaction tube and sealed to generate a positive control.

Each tube was gently flicked and left to incubate for 5 minutes at room temperature. Tubes were briefly spun before being placed into a thermocycler and ran using the conditions outlined in Table 2.10.

Table 2.10: Thermocycling conditions for the detection of mycoplasma.

Thermocycling protocol	Temperature (°C)	Time	No. of cycles
Mycoplasma	95	2 min	1
	94	30 sec	40
	55	30 sec	
	72	40 sec	
	4	∞	

Once the PCR was complete, tubes were vortexed before adding 8 µl PCR reaction into wells of a 1.5% agarose/TBE gel, along with 5 µl 100 – 1000 base pair DNA ladder. Electrophoresis was performed at 100 V for 25 minutes, and the gel imaged using the Bio-Rad ChemiDoc machine.

Each lane showed the presence of an internal control band at 479 bp, indicating a successful PCR, and if mycoplasma were present a 270 bp band could be seen, parallel to the band within the positive control. Mycoplasma test results of cell lines used within this project are shown in Appendix 2.

2.5.3. *In vitro* assays

2.5.3.1. Dose response assay to determine drug synergy

Within a sterile laminar flow cabinet, cells were seeded 24 hours prior to treatment within a 96-well plate (Greiner Bio One, #655180) in triplicate, per dose to be tested. For DU145, LNCAP and PC3 studies, 1000 cells per well were plated, and 5000 cells per well for 22RV1 studies due to differences in cell-doubling times.

Aseptically, drugs were diluted to the desired µM doses in culture media using pre-prepared 10-, 25-, 50- and 100 mM drug stock solutions formulated in DMSO. Care was taken to ensure the volume of DMSO solution added did not go over 0.1% of the total volume of culture media to prevent DMSO associated toxicity. If required, further DMSO was added to warrant equal solvent consistency between the treatments.

At the time of dosing, culture media was removed from the seeded cells by pipette and 100 µl of drug media added to each well in triplicate. 100 µl of normal culture media was also added to 3 separate wells to act as no-cell, background controls. Cells were placed into a 37°C incubator possessing atmospheric O_2 and 5% CO_2 levels for 48 hours.

2.5.3.2. Cell viability assay (PrestoBlue)

15 minutes prior to the experimental end point, 10 µl culture media was removed from the wells of plated cells and replaced with 10 µl 10x PrestoBlue reagent (Invitrogen, #A13262). 10 µl of reagent was also pipetted into the culture media only control wells. Plates were returned to the 37°C incubator for 15 minutes before taking fluorescence measurements.

To assess viability of 2D cell culture, each 96 well plate was individually inserted into the ClarioStar plate reader, and a fluorescence intensity protocol applied. Using bottom optics, a gain of 2057, excitation at 552-10 nm and emission at 592-10 nm; measurements from each cell containing well, plus controls, were taken.

Results from each signal read were transferred into the ClarioStar MARS software for the conversion and exportation of the data as a Microsoft excel file.

2.5.3.3. Calculation of synergistic doses

Blank corrected cell viability outputs were inputted in matrix format onto the online SynergyFinder platform (https://synergyfinder.fimm.fi (Ianevski et al. 2020). Dose-response matrices containing standard error of the mean values were generated, in addition to 2D and 3D plots displaying synergy distribution with a synergy score based on a chosen drug interaction model and respective 95% confidence interval values.

A synergistic score of less than 0 suggested an antagonistic response between two different drugs, a score between 0 – 10 implied an additive effect, and a score greater than 10 indicated a synergistic drug interaction.

2.5.3.4. IncuCyte real time analysis

For real time cell growth analysis, the Essen Bioscience IncuCyte live cell imaging and analysis system was utilised. For a no-reagent/dye assessment, standard settings were applied with scanning of the phase only channel selected. Once the system was made aware of the culture plate specifications, as well as plate positioning within the machine, scan patterns were established including allocation of the wells to be scanned, the number of images per well to be taken and setting of a timetable of scans for the duration of the experiment.

Using the IncuCyte basic analyser, scan patterns were established such that within each cell containing well, 4 images were taken every 6-hours to assess proliferative changes. After completion of the 96-hour experiment, representative images from random wells were selected to refine and optimise a confluency mask, then applied to correctly detect cell morphology of each line at each scan timepoint. Phase contrast was then used a readout of cell proliferation and plotted against each scan timepoint using IncuCyte 2020B software.

2.6. RNA isolation, quantitation, and qRT-PCR analysis

Prior to initiation of any RNA experimental procedure, to prevent RNase contamination, all surfaces and pipettes were cleaned with RNaseZap solution (Sigma Aldrich, #R2020-250ML), with only new, sterile filter pipette tips used.

2.6.1. RNA extraction from cell culture

After removal of culture media from highly confluent cells within a 6-well plate, cells were washed with 1 ml of ice-cold PBS. Following the removal of PBS, 500 µl of pre-chilled Trizol reagent (Invitrogen,

#AM9738) was added to each well to lyse the cells. Cells were scraped off the plastic surface, transferred into sterile 1.5 ml RNase free tubes, then placed on ice.

100 µl ice-cold chloroform (Honeywell, #C2432-1L) was pipetted into the cell and Trizol solution, mixed thoroughly and left to incubate for 10 minutes on ice. Tubes were centrifuged at 10000 rpm, for 10 minutes at 4°C to generate three distinct RNA (clear), DNA (white) and protein (pink) layers. The colourless upper layer of RNA was carefully pipetted into new sterile 1.5 ml RNase free tubes on ice, ensuring no collection of DNA or protein. 250 µl of room temperature isopropanol (VWR, #20842.312) was pipetted and gently mixed into the tubes, then left to incubate for 10 minutes at room temperature.

Samples were centrifuged at 14000 rpm, for 15 minutes at 4°C, then immediately placed on ice. Supernatant was carefully removed and discarded by pipette without disturbing the RNA pellets. 500 µl cold 70% ethanol diluted in RNase free H_2O was then added to the tubes to wash the pellets before centrifuging at 9500 rpm for 5 minutes at 4°C.

Samples were placed back on ice and once again the supernatant removed. Tube lids were then left open for 2 minutes to allow the pellets to air dry. The pellets were finally resuspended in 20 µl cold, sterile RNAse free H_2O, and heated for 5 minutes at 55°C. Total RNA was either DNase treated (see section 2.7.3) or stored at -80°C until required.

2.6.2. RNA extraction from mouse tissue

Snap frozen prostate tissue was removed from storage at -80°C and placed onto dry ice. 350 µl complete RLT buffer provided within the RNeasy Mini Kit (Qiagen, #74104) per tissue sample was pipetted into sterile 2 ml RNase lysing matrix D tubes (Fisher Scientific, # 11422420) containing 2 - 5mm ceramic beads on ice. Sterile forceps cleaned in 70% ethanol diluted in DEPC H_2O (Invitrogen, #46-2224), were then used to transfer the snap frozen tissue into the RLT buffer.

Using the FastPrep24 Homogeniser, prostate samples in RLT buffer were processed at 60 ms for 60 seconds to achieve complete tissue disintegration, then placed immediately on ice. 350 µl 70% ethanol was added to the lysate and thoroughly mixed by pipetting.

700 µl of sample was then transferred into a Qiagen spin column placed inside a 2 ml collection tube and RNA extraction performed as per the manufacturer's instructions. 30 µl of sterile RNase free H_2O

was used to elute the total RNA from the spin column, with RNA either directly DNase treated or stored at -80°C until required.

2.6.3. DNase treatment

A Turbo Kit (Invitrogen, #AM1907) master mix consisting of (n+1) 2 µl 10x TURBO buffer and 1 µl DNase enzyme was produced on ice. 3 µl master mix was pipetted into 20 µl RNA sample and left to incubate for 20 minutes at 37 °C. 2 µl Turbo Stop solution was mixed into the samples and after a 5 minute incubation at room temperature, samples were centrifuged at 9000 rpm, for 1.5 minutes at 4°C. 20 µl clear supernatant was carefully extracted from the samples and pipetted into sterile 1.5 ml tubes. Total DNase treated RNA was kept at -80°C for long-term storage and thawed thoroughly on ice before further use.

2.6.4. RNA Quantitation

After blanking the NanoDrop instrument with 1.5 µl sterile RNase free H_2O, 1 µl of each RNA sample resting on ice, was loaded onto the NanoDrop sensor to determine RNA concentration and quality. RNA samples with a 260/280 ratio of 1.8 – 2 and a 230/260 ratio of 2 – 2.2 were deemed acceptable for use. Between each sample run, the sensor was wiped using Whatman lens cleaning tissue (GE Healthcare Life Sciences, #2105-841).

2.6.5. cDNA synthesis (Reverse Transcription)

2 µg RNA in 11 µl sterile RNAse free H_2O was prepared on ice in 200 µl PCR strip tubes (Eppendorf, # 12341359). 2 µl random hexamers from the Transcriptor 1st strand cDNA kit (Roche, #04379012001) were pipetted into the RNA. Following a quick 5 second bench top centrifuge, samples were heated for 10 minutes at 65°C, then immediately placed on ice. Samples were spun again for 5 seconds before the addition of 7 µl pre-prepared reverse transcription mastermix (Table 2.11). After a thorough mixing and 5 second bench top centrifuge, samples were placed into a BioRad thermocycler and reverse transcription performed using the cDNA synthesis programme (outlined in Table 2.12).

Table 2.11: Reverse transcription mastermix components.

Reagent	Volume per RNA sample
5x Transcriptor reverse transcriptase buffer	4 µl
Protector RNase inhibitor	0.5 µl
2 mm deoxynucleotide mix	2 µl
Transcriptor reverse transcriptase	0.5 µl
Total per well	7 µl

Table 2.12: Thermocycling conditions required for cDNA synthesis.

Temperature	Time
25°C	10 minutes
55C	30 minutes
85°C	5 minutes
4	∞

To the 20 µl of cDNA, 180 µl sterile DNase/RNase free H_2O was added to produce a working concentration of 10 ng/µl. cDNA was then put into long-term storage at -20°C, avoiding repeat freeze-thaw cycles to prevent structural damage.

2.6.6. Quantitative real-time PCR (qRT-PCR)

qRT-PCR mastermixes were prepared on ice (Table 2.13). In 384-well qRT-PCR plates (Applied Biosystems, #4309849) resting on ice or a cooling block, 1 µl (10 ng) cDNA was carefully pipetted into the bottom of wells (n = 3 technical repeats, n = 3 biological repeats). No template controls (cDNA negative) and negative reverse transcriptase controls (samples where reverse transcriptase was excluded from the cDNA synthesis reaction) were also included. 9 µl of each primer mastermix was pipetted into the wells at an angle to prevent tip contamination and the plate thoroughly sealed with plastic sealing film (Applied Biosystems, #4311971).

Table 2.13: qRT-PCR mastermix.

Reagent	Final Concentration	Volume
2x qPCRBIO Sy Green Blue Mix (PCRBiosystems, #PB20.16)	1x	5 µl
10 µM Forward Primer	400 nM	0.4 µl
10 µM Reverse Primer	400 nM	0.4 µl
Template cDNA	10 ng	1 µl
ddH_2O (Promega, #P119C)	1x	3.2 µl
Total		10 ul

Plates were briefly centrifuged to remove bubbles, before being placed into the QuantStudio 7 qRT-PCR machine and subject to a fast, comparative Ct thermocycling protocol with Tm melt curve step (conditions outlined in Table 2.14).

Table 2.14: Thermocycling conditions required for qRT-PCR.

Temperature	Time	No. of cycles
95°C	2 minutes	1
95°C 65°C	5 seconds 30 seconds	40

2.6.7. Designing primers

Where primer sequences were not readily available, primers were designed for qRT-PCR use via emsembl.org (Yates et al. 2019), Primer3 (Kõressaar et al. 2018) and BLAST (Ye et al. 2012). Transcript IDs were established in ensemble following selection of the species and gene of interest. An exon of the gene was then transferred into Primer3 software ensuring no introns were copied over. Once primers were generated, they were cross referenced within BLAST to confirm 100% alignment to the specific gene of interest. If a lack of specificity was shown, a different exon was selected, and the process re-started.

Table 2.15: Primers used in qRT-PCR.

Designed primers				
Target	**Primer sequence**	**Amplicon size**	**Tm (°C)**	
RelB	F: FCTTTGCCTATGATCCTTCTGC R: GAGTCCAGTGATAGGGGCTCT	150	57.8 62.6	
Cxcl1	F: TGAGCTGCGCTGTCAGTGCCT R: AGAAGCCAGCGTTCACCAGA	260	67 60.5	
Primers identified in publications				
Target	**Primer sequence**	**Amplicon size**	**Tm (°C)**	**Reference**
Gapdh	F: ATGTGTCCGTCGTGGATCTGAC R: AGACAACCTGGTCCTCAGTGTAG	132	63.8 62.6	(Yamamoto et al. 2009)
Nkx3.1	F: TCCGTCTTTTGGCTCTGAGT R: GTGAAAGTGCACGCTGAAAA	82	58.2 56.2	(Pearson et al. 2018)
Plekhs1	F: GAATGACCTGAAACCCCAAAG R: ACTGGTGTCTTAAGGAGCATG	149	61.2 61.9	Provided by Dr Tamara Chessa (Babraham Institute)

Once suitable primers were found, sequences were inputted into the Sigma oligonucleotide manufacturing website for production using the following specifications: scale - 0.05 Mole, purification – desalt, format – dry.

Primers were resuspended at 100 mM in RNase and nuclease free, sterile H_2O, then aliquoted into smaller volumes to prevent repeated freeze-thaw cycles during use and stored at -20°C.

2.6.8. Primer validation

To ensure the primers would correctly amplify only one PCR product of interest, primers were initially tested on surplus wild type, ventral mouse prostate cDNA obtained through procedures (2.7.2 – 2.7.6).

qRT-PCR was performed on non-dilute, 1:10, 1:100 and 1:1000 serially diluted cDNA, and C_T values plotted against the logarithm of the cDNA concentrations. Primers were deemed valid for further use when all three of the following criteria were met:

i. The R^2 value of the linear regression trendline of the plotted C_T data was ≥ 0.9
ii. A single peak was seen within the primer melt curve data obtained

iii. A single band was seen when the qRT-PCR products were visualised by gel electrophoresis (similar to Section 2.3.3)

Authentication results of new primers used within this project are shown in Appendix 3.

2.6.9. Quantification of gene expression

The relative gene expression fold change for each sample was calculated through use of the delta delta Ct method (ΔΔCt) (Pearson et al., 2018). For each gene of interest, all technical repeat Ct values were averaged and then subtracted from the average of the housekeeping gene technical repeat Ct values to obtain a ΔCt value per sample and per gene probed.

For the control group, the average of its three-biological repeat ΔCt values was taken, with each individual sample ΔCt value then subtracted from this control group average to generate ΔΔCt values. Relative gene expression was calculated by performing equation $2^{-\Delta\Delta Ct}$, and the biological average taken to generate fold change values normalised to expression of the housekeeping gene *Gapdh*. An example of this methodology is shown in Appendix 4.

2.7. Protein isolation, quantitation and western blot analysis

2.7.1. Protein extraction from cell lines

After a set experimental end point, culture media was removed from cells within a 6-well plate on ice. Cells were washed with 1 ml of ice-cold PBS and 250 µl freshly prepared ice-cold RIPA buffer (Sigma Aldrich, #R0278) containing 1x phosphatase inhibitor tablet (Sigma Aldrich, #4906845001) and 1x mini protease inhibitor cocktail tablet (Sigma Aldrich, #4693124001) per 10 ml of RIPA buffer) added to each well. Cells were scraped off the plastic surface before being transferred into sterile 1.5 ml tubes and placed on ice.

After a 30-minute incubation, cells were centrifuged at 14000 rpm, for 15 minutes at 4°C. Supernatant was transferred into new sterile 1.5 ml tubes and kept on ice for protein quantification or put into -80°C for long term storage.

2.7.2. Protein quantitation (Bradford assay)

On ice, 3 µl of each protein sample was added into a new tube containing 12 µl RIPA buffer and mixed thoroughly (samples taken out of -80°C were thawed on ice for 30 minutes before use).

Within a 96-well plate, 5 µl of 0.125, 0.25, 0.5, 0.75, 1, 1.5 and 2 µg bovine serum albumin (BSA) standards (BioRad, #500-0207) were pipetted into wells alongside 5 µl of each diluted protein sample and 5 µl H_2O controls in duplicate. 250 µl of 1x room temperature Bradford reagent (BioRad, #5000205) was added to each well and the plate left for 10 minutes to incubate at room temperature in the dark.

Using the ClarioStar plate reader, absorbance of the plate was read at 595 nm and a standard curve of the BSA standards generated using Mars Wizard software. The linear equation of the standard curve was then used to calculate sample protein concentrations (µg/ml).

2.7.3. Western Blot

For every 20 µl of sample to be processed; in 1.5 ml tubes on ice, 10 µl 2x Laemlli buffer (Sigma Aldrich, #S3401-1VL), protein sample and H_2O solutions were prepared, ensuring all solutions contained an identical protein concentration. Samples were heated for 5 minutes at 95°C to denature, before immediately being placed back on ice ready for loading of 10-20 µl of protein into a gel, depending on the number of wells present.

Mini-PROTEAN TGX precast 10% or 4 – 20% gradient gels in plastic cassettes (BioRad, #4561026/#4561096) were placed within a Bio-Rad Mini-PROTEAN Tetra vertical electrophoresis cell, and its inner chamber filled with 700 – 1000 ml 1x TRIS-Acetate SDS buffer (Thermofisher Scientific, #LA0041). 6 µl 10 – 250 kDa protein ladder (BioRad, #1610374) was carefully pipetted into the first well of the gel, followed by 20 µl of sample. Blank wells were filled with 5 µl Laemlli buffer to act as loading controls. After being electrophoresed at 150 V for 40 – 50 minutes, gels were removed.

Per gel to be transferred, 2 Mini Trans-Blot Turbo RTA transfer PVDF stacks (BioRad, #10026931) were fully immersed in transfer buffer (made as per manufacturers instructions (BioRad, #10026938)) and 1 membrane (BioRad, #10026933) fully submerged in 100 % ethanol. After 1 minute, the membrane was then transferred into fresh transfer buffer for 2 minutes, to become fully saturated.

Following the removal of excess buffer, one transfer stack was placed flat onto the base of a Trans-Blot chamber. The membrane was placed on top of this transfer stack, followed by a gel with its plastic cassette removed. Excess buffer was squeezed out of the final transfer stack and placed on top of the gel. Each sandwich was compacted using a western blot roller (Thermofisher Scientific, # LC2100) to fully flatten and remove bubbles.

After attachment of its lid, the Trans-Blot chamber was placed into the Bio-Rad Trans-Blot Turbo Transfer System machine and ran using the 1.5 mm gel setting for 10 minutes.

Once the membrane transfer had finished, the membrane was placed into a pre-prepared 5% BSA (Sigma Aldrich, #A9647-50G) or skimmed milk in 1x 0.1% TBS/T (TBS; Fisher Scientific, #BP2471-1, Tween20; Fisher Scientific, #BP337-500) blocking solution for 1 hour at 4°C to prevent nonspecific antibody binding.

Where required, membranes were cut using a scalpel then placed into a minimum of 2 ml of pre-prepared primary antibody solution (Table 2.15) within a 50 ml tube and left to incubate overnight at 4°C on a high-speed roller to maintain constant coverage of the membrane.

The following day, membranes were washed in a plastic tray containing in 1x TBS/Tween 20 (0.1%) (3 x 5-minute washes) using a rocker at room temperature to remove excess primary antibody, then placed into pre-prepared horseradish peroxidase (HRP) secondary antibody solutions (Table 2.16) and left to incubate for 1 hour at room temperature on top of a roller. Membranes were washed once more in trays containing in 1x TBS/Tween 20 (0.1%) (3 x 5-minute washes) using a rocker at room temperature.

Table 2.16: Primary and secondary antibodies used for western blot analysis.

Target	Primary antibody dilution & diluent	Secondary antibody dilution & diluent
GAPDH	1:5000 in 5% BSA 0.1%TBS/T (Millipore, #MAB374)	1:2500 mouse HRP in 5% BSA 0.1%TBS/T
p-AKT (T308)	1:1000 in 5% BSA 0.1%TBS/T (CST, #13038S)	1:2500 rabbit HRP in 5% BSA 0.1%TBS/T
Total-AKT	1:1000 in 5% BSA 0.1%TBS/T (CST, #4691X)	1:2500 rabbit HRP in 5% BSA 0.1%TBS/T
p-4EBP1	1:1000 in 5% BSA 0.1%TBS/T (CST, #2855S)	1:2500 rabbit HRP in 5% BSA 0.1%TBS/T
p-ERK	1:1000 in 5% BSA 0.1%TBS/T (CST, #91015)	1:2500 rabbit HRP in 5% BSA 0.1%TBS/T
Total-ERK	1:1000 in 5% BSA 0.1%TBS/T (CST, #16955)	1:2500 rabbit HRP in 5% BSA 0.1%TBS/T
RELB	1:200 in 5% milk 0.1%TBS/T (Santa Cruz, #SC-48366)	1:2500 mouse HRP in 5% milk 0.1%TBS/T

To visualise the probed proteins of interest, an ECL substrate solution was produce by mixing 1 ml Clarity western peroxide reagent with 1 ml Clarity western luminol/enhancer reagent (BioRad, # 1705060) within a foil wrapped 15 ml falcon tube.

The entire membrane was then covered with ECL substrate, before being scanned using the Bio-Rad ChemiDoc Imaging machine for band visualisation. To calculate the optimal exposure time for each individual protein target, high sensitivity chemiluminescent settings were initially applied, programming the ChemiDoc to take images every 1 or 2 seconds until 4 minutes had passed. Once bands were clearly detected, high resolution settings were applied to obtain the best image for densitometry analysis. Protein ladder was visualised using the colorimetric setting.

2.7.4. Densitometry analysis of Western Blots

To quantify differences in protein expression between samples, TIFF images of scanned membranes were opened within the ImageJ software platform for analysis. Using the rectangle selection tool, a box was drawn around each individual band in sequential order. To associate the first band to the first lane, command CTRL + 1 was pressed on the keypad, with all other bands following in numerical order labelled using CTRL + 2. Once all bands were selected, command CTRL + 3 was used to generate a histogram for each sample.

Using the line selection tool, a straight line was drawn under each peak that connected both sides of the histogram. Via the wand tool, each histogram was selected by clicking into the area under the curve, then a report generated using the label peaks processor found under gel analysis options.

The area and percentage data for each sample was transferred into a Microsoft excel spreadsheet and the relative density for each sample calculated by dividing each individual percentage value by the value of the first sample. After the same procedures had been performed on protein bands representative of a loading control, relative density values for the protein targets of interest were then divided by their respective sample loading control density values for expression normalisation.

2.8. RNA-Sequencing Analysis

2.8.1. RNA-Sequencing

A single batch RNA-Sequencing experiment was performed on RNA isolated from snap frozen prostate tissue using the RNeasy Mini kit ((Qiagen, #74134) as per Section 2.7.2) by Dr Helen Pearson (Pearson et al., 2018). Total RNA was DNase treated using the TURBO kit ((Invitrogen, #AM1907) as per Section

2.7.3)) and was submitted for quality inspection using the BioAnalyser at the Victorian Cancer Centre for Genomics at the Peter MacCallum Cancer Centre, Melbourne, Australia.

To ensure analysis of high-quality RNA, only samples with an RNA integrity number (RIN value) exclusively between 7 – 10 were used for 50 bp paired-end RNA-Sequencing within the Illumina NextSeq500 system at the Victorian Centre for Functional Genomics (VCFG) based at the Peter MacCallum Cancer Centre (Melbourne, Australia), using the Illumina TruSeq RNA kit (PolyA bead capture). FASTQ raw data was normalised, aligned and gene expression fold changes quantitated using in-house protocols developed by the bioinformatics team at the Peter MacCallum Cancer Centre (Dr Jason Li) (Hunter et al. 2015).

Through use of an Ensembl automated pipeline, the team also annotated coding regions identified within the RNA-Seq using the Mus_musculus.GRCm38.73.gtf annotation file and computational predictions. Ensembl BioMart was then used to convert associated gene IDs into human orthologues for downstream analysis.

Differentially expressed gene (DEG) Log_2 fold change data, normalised Log_2 counts per million read (Log2CPM) matrix data, and raw count data in HTSeq_Expression_Matrix.txt format for all samples sequenced was subsequently generated, then made available for use within this PhD project at Cardiff University.

2.8.2. Ensemble Gene Set Enrichment Analysis (eGSEA)

eGSEA was performed using R software through adaptation of a published script (Appendix 5) (Alhamdoosh et al. 2017), on HTSeq expression matrix data obtained through RNA sequencing of total, DNase treated RNA isolated from ventral prostate lobes from *PBiCre$^{+/-}$; Pik3ca$^{+/H1407R}$*, *PBiCre$^{+/-}$; Pten$^{fl/fl}$* and *PBiCre$^{+/-}$; Pik3ca$^{+/H1407R}$; Pten$^{fl/fl}$* mice when carcinoma was prevalent (age 370d, 270 d and 100 d respectively), either intact or 2 weeks post-castration (n = 5 per genotype/cohort). DEG data files were then filtered (criteria: Log_2 Fold change ± 1.5 or 2, adjusted p-value < 0.05) and top hits within eGSEA enriched pathways further investigated as per the workflow outlined in Figure 2.2). Heatmaps to visualise the transcriptional differences between the phenotypic datasets were generated using Log2CPM matrix data and online visualisation and analysis software, Morpheus (https://software.broadinstitute.org/morpheus).

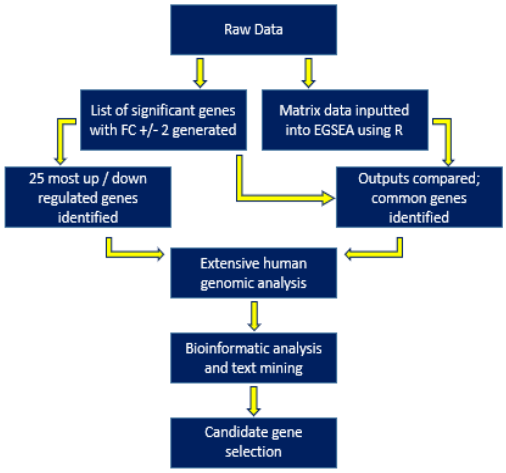

Figure 2.2: Workflow process used to select candidate genes from RNA-Sequencing data.

2.8.3. Analysis of prostate cancer patient genomic datasets

Genes that had been identified as enriched (i.e., significant genes that have human homologues with Log 2-Fold change ± 1.5 or 2 and adjusted p. value < 0.05, present in the top 20 eGSEA associated pathways), were scrutinized against four clinical prostate cancer patient datasets present within the cBioPortal database for human mutational information (Primary adenocarcinoma datasets: (Taylor et al. 2010; 2015) ; Metastatic CRPC datasets; (Grasso et al. 2012; Abida et al. 2019). Correlation patterns between these individual genes, *PIK3CA* H1047R mutation and *PTEN* homozygous deletion in human disease were also analysed using cBioPortal (Cerami et al. 2012; Gao et al. 2013).

2.8.4. Promoter analysis

The online GeneCards human gene database was used to obtain information on transcription factor binding sites within promoter regions of the enriched genes (Stelzer et al. 2016).

2.9. Immunohistochemistry (IHC)

2.9.1. Slide rehydration and antigen retrieval

Slides were stored at room temperature in slide boxes or racks. IHC analysis of phospho-proteins was performed on tissue within 1 week of sectioning, or on slides that had been immediately re-dipped in paraffin wax post-sectioning.

PLL slides were dewaxed in xylene (Fisher Scientific, #X/0220/17) (2 x 5-minute soaks) and rehydrated to ddH_2O via a series of decreasing concentrations of ethanol (100%, 95%, 70% - 3-minute soaks in

each). For slides double dipped in paraffin to protect protein phosphorylation sites, an initial overnight dewaxing step was performed in Histoclear solution (SLS, # NAT1334) at room temperature.

Working stocks of antigen retrieval solution were prepared by diluting 100 ml 10X citrate buffer (Thermofisher Scientific, # AP9003500) and 10X high pH buffer (Dako, # S237584) in 900 ml ddH_2O. Proteinase K antigen retrieval solution was prepared by adding 250 µl 20 mg/ml Proteinase K stock to 250 ml 1x TBS/Tween20 (0.1%) (TBS; Fisher Scientific, #BP2471-1) Tween20; Fisher Scientific, #BP337-500) to achieve a final concentration of 20 µg/ml.

Slides were placed into a IHC staining rack within a plastic container filled with antigen retrieval solution (Table 2.17), then sealed inside a microwave pressure cooker (Nordic Ward, #62104) containing 500 ml ddH_2O. The pressure cooker was heated within a microwave at full power for 15 minutes.

Following removal from the microwave, steam was carefully released prior to fully opening the pressure cooker. The plastic container holding the slides was removed and set to cool at room temperature for at least 30 minutes.

For RFP staining, slides were instead placed into a coplin jar filled with Proteinase K solution, heated at 37°C for 16 minutes in a water bath, before immediately continuing onto blocking steps.

Table 2.17: Reagents required for antigen retrieval, blocking and primary antibody staining for IHC.

Target	Antigen retrieval solution	Initial block - H_2O_2 conc.	Secondary block – BSA concentration	Primary antibody diluent (and catalogue code)
CC3	1x High pH buffer (pH9)	3%	2%	1:300 in 2% BSA TBS/T (0.1%) (CST, #9664)
CD45	1x EDTA (pH8)	3%	2%	1:200 in 2% BSA TBS/T (0.1%) (Abcam, #10558)
Human mitochondria	1x Citrate buffer (pH6)	1.5 %	1 %	1:200 in 2% BSA TBS/T (0.1%) (Sigma Aldrich, #MAB1273)
p-4EBP1	1x Citrate buffer (pH6)	3%	3%	1:500 in 3% BSA TBS/T (0.1%) (CST, #2855S)
PCNA	1x EDTA (pH8)	3%	2%	1:400 in 2% BSA TBS/T (0.1%) (BD Labs, #610665)

PTEN	1x High pH buffer (pH9)	1.5%	2%	1:300 in 2% BSA TBS/T (0.1%) (CST, #9559)
p65	1x Citrate buffer (pH6)	3%	Mouse IgG block	1:300 in 2.5% NHS (Santa Cruz, #SC-8008)
RELB	1x Citrate buffer (pH6)	3%	Mouse IgG block	1:100 in 2.5% NHS (Santa Cruz, #SC-48366)
RFP	1x Proteinase K solution	3%	5%	1:200 in 5% BSA TBS/T (0.1%) (Rockland, # 600-401-379S)
TENASCIN C	1x EDTA (pH8)	3%	1%	1:2500 in 1% BSA TBS/T (0.1%) (Abcam, #108930)

2.9.2. Blocking and Primary antibody

Once cool, slides were removed from the antigen retrieval solution and washed in ddH_2O for 5 minutes. Using a PAP pen (Dako, #S2002) to ensure blocking reagent and antibody coverage, wax rings were drawn carefully around the tissue on the slide. Hydrogen peroxide solution (Sigma Aldrich, #H1009-500ML) was then pipetted onto the tissue for 10 minutes (concentrations as per Table 2.17, 20 minutes for RFP staining), before being washed twice in ddH_2O for 5 minutes and once in 1x TBS/Tween20 (0.1%) within a glass coplin jar, using a rocker. A secondary block of BSA 1x TBS/Tween20 was then pipetted onto the tissue (concentrations as per Table 2.17), with slides left to incubate at room temperature for 30 – 60 minutes.

For RelB and p65 staining, the secondary block consisted of a mouse IgG blocking reagent (Vector Labs, #MP-2400) that was prepared by mixing 2 drops into 2.5 ml of 1x TBS/Tween20. After a 1-hour incubation at room temperature, an additional 2.5% normal horse serum (NHS) block (Vector Labs, #MP-2400) was required for 5 minutes following 2x 2-minute slide washes in 1x TBS/Tween20.

Primary antibodies were prepared as per Table 2.17 and 30 - 100 µl of each depending on sample size pipetted onto the tissue, ensuring no bubbles were present on the tissue sample. Slides were left to incubate overnight at 4°C.

2.9.3. Secondary antibody and signal amplification

The following day, slides were washed in 1x TBS/Tween 20 (0.1%) (3 x 5-minute washes within a glass coplin jar, using a rocker), before the addition of secondary antibodies (as per Table 2.18). Following a 30-minute incubation at room temperature, slides were washed again in 1x TBS/Tween20 (0.1%) (3

x 5-minute washes within a glass coplin jar, using a rocker). For Biotin-conjugated secondary antibodies, Avadin-Biotin complex solution (ABC kit; Vector Laboratories, # PK-4000), containing equal amounts of reagent A and reagent B (8 µl A + 8 µl B per 1 ml 1x TBS/Tween20 (0.1%) was prepared 30 minutes before use. The solution was added onto the tissue, left to incubate for 30-minutes at room temperature then washed in fresh 1x TBS/Tween20 (0.1%) (3 x 5-minute washes within a glass coplin jar, using a rocker).

Table 2.18: Reagents required for secondary antibody staining for IHC.

Target	Secondary antibody	ABC kit	DAB development time
CC3	1:300 biotinylated goat-anti-rabbit (Dako #E0432) in 2% BSA TBS/T (0.1%)	+	90 seconds
CD45	1:300 biotinylated goat-anti-rabbit (Dako #E0432) in 2% BSA TBS/T (0.1%)	+	30 seconds
Human mitochondria	1:500 biotinylated rabbit-anti-mouse (Sigma Aldrich, #MAB1273) in 1% BSA TBS/T (0.1%)	+	60 seconds
p-4EBP1	Rabbit impress reagent (Vector Labs, #MP-7401-50)	-	3 minutes
PTEN	Rabbit impress reagent (Vector Labs, #MP-7401-50)	-	50 seconds
p50	1:300 biotinylated goat-anti-rabbit (Dako #E0432) in 2% BSA TBS/T (0.1%)	+	60 seconds
p65	Mouse on mouse impress reagent (Vector Labs, #MP-2400)	-	30 seconds
RELB	Mouse on mouse impress reagent (Vector Labs, #MP-2400)	-	20 seconds
RFP	1:200 biotinylated goat-anti-rabbit (Dako #E0432) in 5% BSA TBS/T (0.1%)	+	5 minutes
TENASCIN C	1:300 biotinylated goat-anti-rabbit (Dako #E0432) in 1% BSA TBS/T (0.1%)	+	3 minutes

2.9.4. Visualisation and counterstaining

Prior to use, fresh Dako DAB chromogen solution (Dako, #K3468) containing 1 drop of chromogen per 1 ml substrate buffer was prepared according to manufacturer instructions. 50 – 100 µl DAB was pipetted onto each tissue section and developed for a specific length of time that allowed emergence of brown coloured staining (as per Table 2.18). Slides were washed in fresh 1x TBS/Tween 20 (0.1%) and ddH_2O (1 x 5-minute washes in each using a rocker), then placed into 1% Mayer's haematoxylin

counterstain (Merck, #109249) for 8-10 seconds, before being gently rinsed in flowing tap H_2O for 5 minutes.

Dehydration of the tissue was performed by soaking the slides in increasing concentrations (70%, 95%, 100%) of ethanol (1 x 3-minute soaks in 70% and 95%, 2 x 3-minute soaks in 100%). Slides were submerged in xylene (2 sets of 5-minute soaks), before coverslip (Fisher Scientific, #12373128) mounting using DPX solution (Merck, #1.00579.0500). Slides were left to air-dry overnight in a fume hood then placed into long-term storage at room temperature within storage racks.

2.9.5. Slide scanning

To obtain clear detailed images for staining quantitation; IHC slides were scanned using the Olympus VS200 slide scanner with brightfield settings applied at 20x magnification. Files were saved in VSI format and immediately backed up onto the Cardiff University shared drive for secure access.

2.9.6. Image preparation and use of QuPath 0.2.3 software

VSI image files were opened using Olympus OlyVia viewing software to assess clarity of images in addition to enhancing stain intensities on slides with poor colour contrast, before being transferred into a QuPath project (Bankhead et al. 2017).

After using the drawing tool to select a single prostate duct or region of interest, colour deconvolution thresholds were adjusted to define a strong contrast between the DAB and haematoxylin staining and these colours saved for automatic detection along with background values.

Using the positive cell detection analysis feature, parameters were set and adjusted to ensure all cells and relevantly stained nuclei, cytoplasm or cell membranes within the selected region were correctly detected; including detection type (set to optical density sum), pixel size (set to 0.2743 μm) and cell expansion (set to 0). Area of nuclei, intensity thresholds, and positivity values were set accordingly to the tissue and stain type.

A final script that could be used on other ducts or regions within the same image or a new image within the project file was generated from the workflow used for optimisation; when executed, positive and negative values were then provided for each area being scored.

2.9.7. IHC Quantitation

To determine the percentage of staining obtained from performing immunohistochemical analyses on whole tissue samples, 7 - 10 prostate lobes or regions of interest were assessed (n = 3/genotype), averaging upon 2000 – 3000 cells being analysed per animal. For explant cultures, 800 – 1000 cells were analysed per technical/biological repeat.

The total number of nuclei and the total number of positively stained nuclei, cytoplasm or cell membranes per section were counted via QuPath software (Section 2.10.6), with a percentage of positivity per lobe or region generated. With this data, the average percentage of positive cells per genotype was calculated and the standard error of the mean determined using GraphPad Prism 9 software.

2.10. Immunofluorescence (IF)

2.10.1. Antigen retrieval

For PLL slides with 3 µm tissue slices attached, rehydration and antigen retrieval processes were performed as outlined for IHC (section 2.9.1).

2.10.2. Permeabilization

For slides with adherent single cells, a permeabilization step was performed instead to obtain intracellular and cytoplasmic epitopes. 0.3% Triton-X solution (Triton X-100 (Sigma Aldrich, #X-100) in 1x PBS) was pipetted onto the cells with pre-drawn PAP wax rings and left to incubate for precisely 5 minutes at room temperature.

2.10.3. Blocking and primary antibody

Slides were washed in ddH_2O (1 x 5-minute) then washed in 1x PBS/Tween 20 (0.1%) (2 x 5-minute washes). Where needed, PAP wax rings were drawn carefully around tissue sections.

Slides were left to incubate in 3% BSA 1xPBS/ Tween 20 (0.1%) blocking solution for 1 hour at room temperature. Primary antibodies were prepared as per Table 2.19, pipetted onto the tissue and left to incubate overnight at 4°C.

Table 2.19: Antibodies used for immunofluorescent detection of proteins.

Target	Primary antibody	Secondary antibody
RFP	1:200 in 3% BSA 1x PBS/ Tween 20 (0.1%) (Rockland, # 600-401-379S)	1:500 AF647 in 3% BSA 1x PBS/ Tween 20 (0.1%) (Thermofisher, #A21245)
FSP1	1:100 in 3% BSA 1x PBS/ Tween 20 (0.1%) (CST, #13018S)	1:500 AF488 in 3% BSA 1xPBS/ Tween 20 (0.1%) (Thermofisher, #A21206)

2.10.4. Secondary antibody and signal amplification

Slides were washed in 1x PBS/Tween 20 (0.1%) (3 x 5-minute washes) before incubation with secondary antibodies (as prepared in Table 2.19) for 1-hour at room temperature in the dark. Slides were re-washed in 1x PBS/Tween 20 (0.1%) (3 x 5-minute washes) and coverslips mounted using Prolong Gold + DAPI (Invitrogen, #15395816; pre-warmed for 30 minutes at room temperature prior to use) for counterstaining, with coverslips secured in place with small amounts of nail varnish. Slides were kept covered in foil at 4°C and imaged within 24 - 48 hours. Slides were stored at 4°C in the dark for long-term storage.

2.10.5. Visualisation and quantification

To obtain clear detailed images for staining quantitation, slides with large tissue sections were visualised through use of the Olympus VS200 slide scanner (similar to Section 2.10.5) with standard immunofluorescence detection settings applied. For slides with single cells, a confocal microscope was used for better optical resolution at 10 - 20x magnification.

IF quantitation was performed on stained tissue sections using QuPath 0.2.3 software as outlined in Section 2.10.6-7), except fluorescence parameters were applied using RBG channels instead of DAB.

2.11. Additional biological staining procedures

2.11.1. Toluidine blue staining

For staining of mast cells, a 10 % working toluidine blue stain solution was formulated using pre-prepared 1% toluidine blue stock solution (1 g (Fisher Scientific, #30611518) in 100 ml 70% ethanol) and freshly prepared 1% sodium chloride solution at pH 2.3 (0.5 g (Fisher Scientific, #S/3160/60) in 50 ml distilled water).

PLL slides were dewaxed in xylene (2 x 5-minute soaks) and rehydrated to ddH_2O via a series of decreasing concentrations of ethanol (100%, 95%, 70% - 3-minute soaks in each).

Slides were placed into the working toluidine blue stain for 3 minutes, then washed in distilled water (3 x 5-minute washes using a rocker). Slides were quickly dehydrated in 95% and 100% ethanol (10x dips in 1x 95% soak and 2x 100% soak) then submerged in xylene (2 sets of 3-minute soaks), before the addition of coverslips as per Section 2.10.4.

2.11.2. Masson's trichome staining

For staining of connective tissues and collagen, Masson's trichome staining was performed using a complete Light Green Masson 1929 stain kit (Atom Scientific, #RRSK21-100).

PLL slides were dewaxed in xylene (2 x 3-minute soaks) and rehydrated to ddH_2O via a series of decreasing concentrations of ethanol (100%, 95%, 70% - 2-minute soaks in each). Equal volumes of Weigerts Haematoxylin A and B solutions were mixed (Atom Scientific, #RRSK21-100), then pipetted onto the PLL slides ensuring each tissue section was fully covered. After a 15-minute incubation at room temperature, slides were rinsed in gently flowing tap water for 10 minutes.

Ponceau fuchsin Masson solution was added onto the tissue sections, then removed after 5 minutes. Following a quick rinse in ddH_2O, 1% phosphotungstic acid solution (Atom Scientific, #RRSK21-100) was added onto the slides and left for 30 minutes. Carefully, the acid was tipped off and immediately replaced with 2% light green Masson stain in 2.5% acetic acid, for 5 minutes. Slides were briefly rinsed again in tap water before dehydration in 70%, 95% and 100% ethanol (2-minute soaks in each) and saturation in xylene (2 sets of 3-minute soaks), before the addition of coverslips as per Section 2.10.4.

2.12. Flow cytometry

2.12.1. Dissociation of tissue into single cells

Following whole prostate dissection from experimental mice, tissues were placed into ice cold transportation media as prepared in Table 2.23, then immediately transported on ice from the animal unit into the laboratory for processing.

Aseptically within an allocated primary mouse tissue laminar flow cabinet, prostates were dipped 3x in 70% ethanol, then transferred into fresh 5 ml transportation media. Using a new petri dish and scalpel per sample, prostate tissue was thoroughly chopped and minced before being placed into 5ml

pre-warmed dissociation media (Table 2.23) within 15 ml tubes (containing 7.5 mg Trypsin (Sigma Aldrich, #T4799) and 15 mg Collagenase A (Roche, #10103586001)). Samples were placed horizontally into shaking incubators for 1 hour at 37°C.

Tubes were centrifuged at 1500 rpm, for 5 minutes at 4°C, then the media removed. The pellet was resuspended in 5 ml Red Blood Cell (RBC) lysis buffer (Sigma Aldrich, #R7757), and left to incubate for 5 minutes at room temperature. Samples were centrifuged at 1500 rpm, for 5 minutes at 4°C, the supernatant then discarded and replaced with 2 ml sorting media (Table 2.20), pipetting multiple times to break up clumps before being placed on ice.

The cell suspension was passed through a 2 µM cell strainer (Corning, #431751) and collected into new flow cytometry tubes on ice. 10 µl of the strained cell suspension was also pipetted into a FastRead counting slides (Immune Systems, #BVS100) with cells counted to estimate the total number of cells present per ml of media. The sample with the least number of cells was then used as a reference value to which all other samples would need to match, as allocating a set number of cells to stain facilitates removal of bias in order to achieve a fair comparison between each biological sample.

Table 2.20: Flow cytometry media.

Reagent	Volume used in Transportation Media	Volume used in Dissociation Media	Volume used in Sorting Media
1x RPMI 1640 culture media	43.5 ml	48.5 ml	47.5 ml
1x FBS	5 ml	-	1 ml
100x Penicillin-Streptomycin (10,000 U/mL)	0.5 ml	0.5 ml	0.5 ml
1 M HEPES (Fisher Scientific, #15630056)	1 ml	1 ml	1 ml
Total volume	50 ml	50 ml	50 ml

2.12.2. Antibody staining

Within individual 1.5ml Eppendorf tubes; single stain and fluorescence minus one (FMO) controls were prepared on ice in 100 µl sorting media as per Table 2.21. A mastermix with all antibodies combined in 100 ul sorting media was prepared for each experimental sample.

Table 2.21: Antibodies and their required dilution for flow cytometry.

Target	Antibody product code	Fluorophore	Volume required for staining 1 million cells
PDPN	BioLegend, #127409	APC	1.25 µl
CD45	BD, #552848	PE-Cy7	5 µl
CD24	BD, #553261	FITC	1.25 µl
LY6C	BioLegend, #128037	BV711	2.5 µl
MHCII	Miltenyi Biotec, #130-119-122	VioGreen	2 µl
Nuclei	*DAPI/PBS solution	*Excitation at 405 nm - Violet	*2 µl per 100 µl media

100,000 cells allocated for controls / fluorescent compensation and the pre-determined maximum number of cells from each experimental sample were transferred into 5 ml flow cytometry suitable Falcon tubes, then centrifuged at 1500 rpm at 4°C for 5 minutes. The supernatant was discarded, the cell pellet resuspended in its relevant antibody media solution and left to incubate in the dark, on ice for 30 minutes.

1 ml fresh sorting media was added to each tube to inactivate the antibodies, and tubes were centrifuged once again at 1800 rpm at 4°C for 5 minutes. Once the supernatant was removed, cell pellets for the single stain and FMO controls were resuspended in 100 µl fresh sorting media, with experimental cell pellets resuspended in 500 µl fresh sorting media. Tubes were placed back on ice and immediately sorted.

2.12.3. Cell sorting

Machine cleaning/calibration, fluorochrome detection, compensation, exclusion of dead cells/debris and sorting of experimental samples was performed on the BD FACSAria Fusion by Mr Mark Bishop (Lab manager, European Cancer Stem Cell Research Institute).

2.12.4. Processing of sorted cells

100 cells at a time, were directly sorted onto poly-L-lysine coated glass microscope slides (Fisher Scientific, #10219280) and a PAP wax circle immediately drawn around the droplet for identification. Cells were left for a couple of seconds to adhere before 50 µl 10% formalin was gently pipetted onto them. After 5 minutes of fixation, formalin was tipped off and the slide placed into a slide container filled with 1x PBS. Slides were kept submerged in PBS at 4°C until IF staining (Section 2.11).

Additionally, cell populations were also sorted into 1.5ml Eppendorf tubes filled with 500 µl sorting media. Cells were centrifuged at 1800 rpm, 5 mins at 4°C, the pellet resuspended in 350 µl complete RLT buffer, then placed into -80°C for long term storage for future work.

2.13. *Ex-vivo* tissue culture

2.13.1. Collection of tumour tissue for explant culture

Prostate tumours were harvested and placed into sterile pre-prepared transportation media (Table 2.1) (Centenera et al. 2013; Majumder et al. 2015; Risbridger et al. 2018; Zhang et al. 2019), put immediately on ice and processed within 0.5 – 2 hours post-dissection.

2.13.2. *Ex-vivo* explant culture preparation

Prior to attainment of tumour tissue, within a primary culture laminar flow cabinet, culture media was produced as per Table 2.22. Where needed, working drug stocks were also pre-prepared within this media for dosing experiments and stored at 4 °C until use.

Table 2.22: Explant culture media.

Reagent	Final Concentration	Volume
1x RMPI 1640 cell culture media	-	43.583 ml
1x FBS	10 %	5 ml
10,00 U/ml Penicillin/Streptomycin	1 %	500 µl
10 mg/ml Gentamicin (Sigma Aldrich, #G1272)	0.1 mg/ml	500 µl
250 µg/ml Amphotericin B (Fisher Scientific, #15290-026)	0.5 ug/ml	100 µl
3.44 mM DHT (Sigma Aldrich, D-073)	1 nM	14.52 µl
2 mg/ml Hydrocortisone (Sigma Aldrich, #H6909)	0.01 mg/ml	250 µl
10 mg/ml Insulin (Sigma Aldrich, #I0516)	0.01 mg/ml	50 µl
10 0mM Rock inhibitor (HelloBio, #HB2297)	5 µM	2.5 µl
Total		50 ml

Aseptically, 1 cm^3 squares of Surgispon haemostat gelatin based sponge (Vet Direct, #SGSP001) were cut with a scalpel and placed into wells of a 24-well plate (Greiner BioOne, # 662160) using sterile forceps. 500 µl vehicle or drug media was added to each corresponding sponge and placed into a 37°C incubator 30 minutes prior to tumour sectioning.

2.13.3. Explant sectioning

Within a 25 ml conical flask, a 4% low melt agarose gel (Promega, # V2111) was prepared using sterile 1x PBS. Once fully dissolved, the agarose solution was poured into the lid of a sterile 15 ml tube lined with foil and immediately placed into a 37°C water bath to cool. When the agarose reached a tacky, almost set consistency, a chunk of pre-cut tumour was carefully placed into the middle of the mould using sterile forceps, before being placed onto ice to allow the gel to fully set.

Super glue (Bostik, #30611518) was used to attach the agarose embedded tumour to the sectioning plate of the Leica V1200S vibratome, which was then placed into a buffer bath of ice cold sterile 1x PBS surrounded in ice, to ensure the temperature was kept at a constant.

Using the following parameters (sectioning speed: 1.40 mm/s and amplitude: 1.80 mm), 250 µm slices were sectioned from the tumour. Each slice was carefully collected and placed back into fresh explant culture media within a sterile petri dish. Once all slices were cut and collected, at random, slices were deposited in triplicate onto the drug treated gelatin based sponges before being placed back into the incubator (37°C with atmospheric O_2 and 5% CO_2 levels) for 48 hours.

After 48 hours, tumour slices were removed from their respective sponges and placed into 1.5 ml tubes filled with 10% formalin at 4°C for fixation (16-24 hours max.). Tissue was then transferred into 70% ethanol and delivered to the Cardiff University Histology department for further processing as detailed in Sections 2.4.3 and 2.4.4 in Histogel (Fisher Scientific, # 12006679).

2.13.4. Generation of organoids from mouse tissue

Propagation and maintenance of GEMM tumour derived organoids used within this project, was performed by Dr Daniel Turnham (as per protocols described in (Gao et al. 2014; Drost et al. 2016)).

Prostate tumour tissue was dissected using sterile tools, placed directly into ADMEM/F12+/+/+ culture media (Thermofisher Scientific, #12634-010) on ice, then transported back to the lab for immediate processing. Within a primary tissue culture laminar flow cabinet, tissue was minced on ice within a petri dish containing 5 ml ADMEM/F12+/+/+ culture media using a scalpel. The tissue was then transferred into a 15 ml tube and briefly centrifuged at 200 g for 1 minute to pellet the sample.

After the supernatant was removed and each pellet carefully resuspended in 1 ml pre-prepared, warm digestion buffer per 50 mg prostate tissue (Table 2.23), samples were left to incubate for 60 – 90 minutes at 37°C on a rocking incubator. During this period, basic organoid culture media (Table 2.24) and cell culture plates were pre-heated to 37°C, Matrigel (VWR, #734-1101) left to thaw on ice, and TrypLE dissociation solution (Gibco, #12605028) containing 10 µM Y-27632 dihydrochloride (Sigma Aldrich, #Y0503) and 0.1 mg/ml DNAse (Sigma Aldrich, #90083) prepared.

Table 2.23: Digestion buffer for mouse prostate organoid propagation.

Reagent	Final Concentration	Volume
1x ADMEM/F12+/+/+ culture media	-	663 µl
1x Heat inactivated FBS	7.5 %	75 µl
10 mg/ml Collagenase type II (Sigma Aldrich, #C5138)	2.5 mg/ml	250 µl
10 mg/ml DNase I	0.1 mg/ml	10 µl
10 mM Y-27632 dihydrochloride	10 µM	1 µl
1 µM DHT	1 nM	1 µl
Total		50 ml

Table 2.24: Primary mouse prostate organoid basic culture media.

Reagent	Final Concentration	Volume
1x ADMEM/F12+/+/+ culture media	-	44 ml
100x Glutamax (Sigma Aldrich, #35050-061)	1 %	0.5 ml
10,00 U/ml Penicillin/Streptomycin	1 %	0.5 ml
1 M HEPES (Fisher Scientific, #15630056)	10 mM	5 ml

Once the digestion incubation was complete, cells were washed in warm 5 ml ADMEM/F12+/+/+ culture media, then centrifuged at 200 g for 5 minutes at 4°C. Following removal of the supernatant, 1 ml pre-warmed TrypLE dissociation solution was added to each tube, then placed into a 37°C bead bath for 10 minutes.

To the tubes, 4.5 ml ADMEM/F12+/+/+ culture media plus 500 µl FBS was added to wash and neutralise the dissociation solution before being passed through a cell strainer (SLS, # 431751) into a

50 ml tube. To ensure maximum collection of cells, the membrane was additionally rinsed with 1 ml ADMEM/F12+/+/+ culture media using a 5 ml syringe (Fisher Scientific, #10345844). Tubes were centrifuged at 200 g for 5 minutes at 4°C, supernatant then removed, and cells resuspended in 1 ml ADMEM/F12+/+/+ culture media.

After utilising Trypan Blue (Lonza, # LZ17-942E) to estimate cell count (5 µl trypan blue solution per 20 µl cell solution), the desired number of cells were centrifuged at 200 g for 5 minutes at 4°C, and once again supernatant removed. One ice, cells were resuspended in Matrigel to achieve a final concentration of 500 cells/µl.

40 µl Matrigel/cell mix was carefully pipetted into the centre of wells within the pre-warmed culture plate, taking care to ensure bubbles were not created in the process. After allowing the gel to solidify for a few minutes, culture plates were placed upside down within an 5% O_2 incubator at 37°C for 15 minutes to prevent adherence of cells to the bottom of the plate.

To each well, 500 µl complete prostate organoid media (Table 2.25) was added, and plates returned to the incubator. Culture media was removed and replaced with fresh medium after 3 days, with media freshly prepared every 7 days.

Table 2.25: Mouse prostate complete organoid media.

Reagent	Final Concentration	Volume
1x ADMEM/F12+/+/+ culture media	-	44 ml
100x Glutamax	1 %	0.5 ml
10,00 U/ml Penicillin/Streptomycin	1 %	0.5 ml
1 M HEPES	10 mM	5 ml
20 µg/ml EGF (PeproTech, #AF-100-15-500)	20 ng/ml	5 µl
50x B27 (Life Technologies, #17504-044)	0.2 %	100 µl
1 µM DHT	1 nM	5 µl
10 mM Y-27632 dihydrochloride	10 µM	5 µl
Total		50 ml

2.13.5. Treatment of organoid culture

After 5 days of organoid propagation, culture media was removed and replaced with fresh culture media supplemented with drug inhibitors of interest. Plates were left to incubate, and images taken 40 minutes prior to the experimental timepoint using a light microscope for visual phenotypic analysis.

2.13.6. Cell viability assay (Cell Titre Glo)

30 minutes prior to the experimental end point, pre-thawed, 100 µl Cell Titre Glo reagent (Promega, #G7572) was added to each well of the organoid culture plate, and immediately covered to limit light exposure. Plates were placed into a shaking incubator for 5 minutes at room temperature, then left stationary for another 20 minutes before taking luminescence measurements.

To assess viability of 3D organoid culture, each 96 well plate was individually inserted into the ClarioStar plate reader, and a luminescence intensity protocol applied. Using bottom optics, a gain of 3600 and with the number of multichromatics set to 1; measurements from each well were taken.

Similar to section 2.6.3, results were transferred into the ClarioStar MARS software for the conversion and exportation of the data as a Microsoft excel file.

2.14. Statistics

Statistical analyses were performed using the functions available within GraphPad Prism 9.0.0. All error bars plotted on graphs represent standard error of the mean. * indicates a p value of ≤0.05, ** indicates a p value of ≤0.01 and *** indicates a p value of ≤0.001.

One way ANOVA with Tukey's multiple correction tests were performed on qRT-PCR data, IHC stain quantitation data, western blot data and cell viability data. If more than 3 groups were not being compared, an unpaired 2-tailed T test was performed.

A Mantel Cox test was performed on mouse survival data. For analysis of transcriptomic data (RNA-Seq vs qRT-PCR), linear regression was performed and R^2 coefficients calculated. For synergy calculations, 95% confidence intervals were generated.

Chapter 3

3. Identification of PI3K-independent actionable targets for the treatment of PTEN-deficient prostate cancer

3.1 Introduction

A diverse range of PI3K pathway genetic alterations have been identified within prostate cancer patients (Shorning et al. 2020), and various PI3K-AKT-mTOR pathway inhibitors are being assessed for their therapeutic potential in both hormone sensitive and castration-resistant prostate cancer (Turnham et al. 2020). Whilst some PI3K-AKT-mTOR-directed therapies are beginning to show promise in the clinic, such as pan-AKT inhibition, resistance to PI3K pathway inhibitors has also been observed due to pathway redundancy, feedback loops and PI3K pathway crosstalk with other oncogenic signalling pathways (Shorning et al. 2020).

To better understand the impact of two frequently observed PI3K pathway genetic alterations, *PTEN* loss and *PIK3CA* hyperactivation, Dr Helen Pearson and colleagues developed a novel GEMM harbouring a heterozygous activating mutation in *Pik3ca* (H1047R) in epithelial cells of the prostate (Pearson et al. 2018), and compared the prostate phenotype directly with the well-established prostate tumour model harbouring bi-allelic loss of epithelial cell *Pten* (Lesche et al. 2002; Jin et al. 2003). In addition to the dependency of signalling complexes detailed in Table 3.1, these models showed clear differences in histopathology, invasive potential and the number of proliferating or apoptotic cells, indicating that *Pik3ca*-mutant prostate cancer and *Pten*-deficient prostate cancer do not phenocopy (Pearson et al. 2018). Furthermore, upon combining both alterations within a compound mutant model, the PI3K pathway alterations showed synergy, co-operating to accelerate tumorigenic growth relative to the single mutant models (Pearson et al. 2018).

Table 3.1: Summary of key differences between *PBiCre*$^{+/-}$ *Pik3ca*$^{+/HR}$, *PBiCre*$^{+/-}$ *Pten*$^{fl/fl}$ and *PBiCre*$^{+/-}$ *Pik3ca*$^{+/HR}$; *Pten*$^{fl/fl}$ prostate tumours established by Pearson et al. 2018 (as summarised by (Triscott and Rubin 2018)).

	***Pik3ca*-mutant tumours**	***Pten*-null tumours**	**Compound mutant tumours**
PI3K catalytic isoform dependency	p110α	p110α/β	p110α/β
mTOR complex dependency	mTORC1	mTORC1/2	High mTORC1/2
Tumour burden	Low	Moderate	High
Onset of castration resistance	Acquired	Acquired	*De novo*

Whilst reverse phase protein array (RPPA) analysis was performed on lysates extracted from intact and castrated *Pik3ca*$^{+/HR}$, *Pten*$^{fl/fl}$, and *Pik3ca*$^{+/HR}$;*Pten*$^{fl/fl}$ prostates to determine potential mechanisms driving the differences seen between the models and possible contributions of each genetic alteration to the synergistic relationship observed in the compound mutant, only 94 proteins were investigated, and a lack of antibody sensitivity was observed (Pearson et al. 2018).

To better comprehend the signalling events or pathways that may have been deregulated following *Pik3ca*-hyperactivation and/or *Pten* loss, Dr Pearson additionally isolated RNA from each prostate tumour type for subsequent analysis of the cellular transcriptome via RNA-Sequencing, with the intention of identifying novel therapeutically targetable arms for *PTEN*-deficient prostate cancer.

Given that PTEN also possesses numerous protein phosphatase functions in addition to its PI3K dependent lipid phosphatase role, it was anticipated that these supplementary PTEN functions may also contribute to the phenotype observed in the *PBiCre*$^{+/-}$ *Pten*$^{fl/fl}$ model.

Most PTEN protein phosphatase activity has been evidenced within the cell nucleus, with involvement in multiple DNA damage repair pathways including distinct roles in DSB repair and nucleotide excision repair (NER) (Turnham et al. 2020). Moreover, nuclear PTEN has been shown to interact with the anaphase-promoting complex (APC), driving APC–cadherin 1-mediated protein degradation to regulate cellular senescence (Vidotto et al. 2020).

In prostate cancer cells, loss of PTEN can thus trigger senescence activated cytokine secretion, as well as drive upregulation of inflammatory-associated genes, contributing to an immunosuppressive TME (Turnham et al. 2020; Vidotto et al. 2020). Similarly, PTEN has been shown to bind and promote the degradation of DNA-binding factor chromodomain helicase DNA-binding protein 1 (CHD1); whereby loss of PTEN leading to CHD1 stabilisation and subsequent downstream epigenetic interactions, can facilitate increased transcription of genes such as those involved in the TNFα and NF-κB signalling cascades (Vidotto et al. 2020). Thus, involvement of these additional signalling pathways in PTEN-deficient prostate cancer may also be attractive candidates for therapeutic targeting.

3.2 Aims

Whilst it was identified that the two genetic drivers of the PI3K cascade, *PIK3CA* and *PTEN*, mediate distinct signalling pathways, the full scope of the diverse molecular mechanisms remain to be determined. It is important that studies continue to search for PI3K-independent targets to enable development of new therapeutic strategies that overcome bypass or resistance mechanisms to PI3K pathway inhibition, such as in the case of PTEN-deficient prostate cancer where AKT inhibition is not efficacious.

We hypothesised that deepening our understanding of each genetic driver using the unbiased approach of RNA-Sequencing, would identify new avenues for therapeutic intervention for patients harbouring these genetic alterations.

Given the access to RNA-Seq data from each model (i.e., wildtype, uncastrated and castrated *Pik3ca* mutant, *Pten*-null and compound mutant GEMMs), two pairs of datasets were prioritized for further evaluation. Based on the phenotypes previously observed by Pearson et al., the *PBiCre$^{+/-}$; Pik3ca$^{+/HR}$* vs *PBiCre$^{+/-}$; Pten$^{fl/fl}$* uncastrated model comparison was chosen to explicitly identify PI3K-independent roles of PTEN in prostate cancer, whilst the *PBiCre$^{+/-}$; Pik3ca$^{+/HR}$; Pten$^{fl/fl}$* vs *PBiCre$^{+/-}$; Pten$^{fl/fl}$* castrated model comparison was chosen to establish *de novo* drivers of CRPC.

To this end, this chapter aimed to:

1. Determine significantly deregulated genes and signalling pathways specific to *Pten*-deficient prostate cancer by comparing *Pten*-deficient and *Pik3ca*-mutant RNA-Seq profiles
2. Identify putative PI3K-independent actionable targets for *Pten*-deficient prostate cancer
3. Validate key pathway alterations in *Pten*-deleted and *Pik3ca*-mutant mouse prostate carcinoma tissue

3.3 Results

3.3.1 *Pten*-deficient and *Pik3ca*-hyperactivated GEMM prostate carcinomas display distinct transcriptomic profiles

To identify the diverse molecular mechanisms that underpin *Pik3ca*-hyperactivated and *Pten*-deficient prostate cancer, the unbiased approach of bulk RNA-Sequencing (RNA-Seq) was employed. RNA-Seq provides a comprehensive insight into the transcriptomic changes within tissue or cell specific populations (Kukurba and Montgomery 2015). This high throughput technology is an effective way to analyse transcriptional deviations caused by oncogenic events, thus enabling quantification of mRNA expression levels to further establish functional changes between cohorts, determine deregulation of signalling pathways and consequently assist in the identification of novel anti-cancer therapeutic strategies.

DNase treated, ventral prostate RNA isolated from *PBiCre$^{+/-}$; Pik3ca$^{+/H1047R}$* and n = 5 *PBiCre$^{+/-}$; Pten $^{fl/fl}$* invasive prostate carcinoma lesions (isolated at 270 and 370 d of age respectively, n = 5 / cohort), was prepared by Dr Helen Pearson (as detailed in Section 2.7.2 – 3) for RNA-Seq analysis at the Victorian Centre for Functional Genomics, Peter MacCallum Centre, Melbourne, Australia. 50 bp paired-end

sequencing was performed using the Illumina TruSeq Poly-A kit on quality checked RNA (RIN value >7.4), as detailed in Section 2.9.1 (results shown in Appendix 6).

Subsequently, alignment methods, gene symbol annotations, calculation of gene expression fold change and statistical analyses was performed by Dr Li (Peter MacCallum Centre, Melbourne, Australia) using in-house protocols established by the Peter MacCallum Bioinformatics Department (Waldeck et al. 2016).

To assess the quality and variation of the data, multidimensional scaling (MDS) plots were created by Dr Li using the Limma package on R. Principal component analysis indicated the *Pik3ca*$^{+/H1047R}$ and *Pten* $^{fl/fl}$ prostate tumour samples were genetically dissimilar, while the biological repeats for each genotype were genetically similar; confirming suitability for use in further scientific analyses (Figure 3.1). Of note, a sample outlier was detected through the absence of clustering within the *PBiCre*$^{+/-}$*; Pten*$^{fl/fl}$ cohort group and subsequently removed (data point not shown). Although the RNA quality of this sample was high, some transcriptomic alterations may have occurred during the lengthy processing of the tissue that rendered this sample non-representative of its genotype.

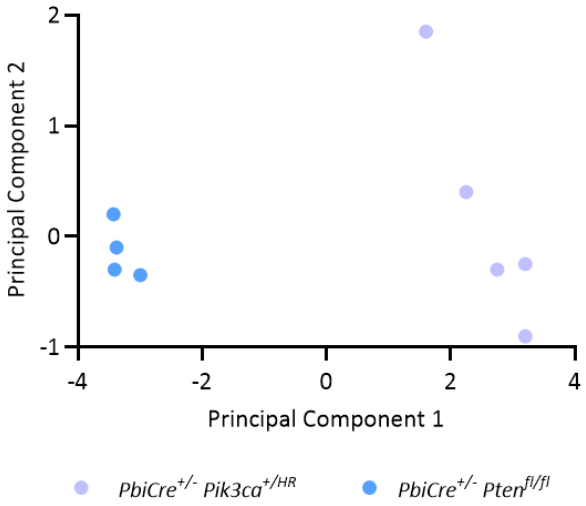

Figure 3.1: *Pten*-deleted prostate cancer and *Pik3ca*-mutant prostate cancer are transcriptionally different. MDS plot representing total RNA samples isolated from *PBiCre*$^{+/-}$*; Pik3ca*$^{+/H1047R}$ (n = 5, 300 d old) and *PBiCre*$^{+/-}$*; Pten*$^{fl/fl}$ (n = 4, 200 d old) invasive ventral lobe prostate carcinoma.

To determine differential gene expression between *Pten*-deficient and *Pik3ca*-hyperactived prostate carcinomas, RNA-Seq data was analysed using Morpheus matrix visualisation and analysis software

(Broad Institute - https://software.broadinstitute.org/morpheus). Expression data values for all genes mapped, were entered into the software to generate a heatmap for data visualisation (Figure 3.2).

Hierarchical clustering utilising one minus spearman rank correlation analysis revealed distinct groupings of genes within the *PBiCre$^{+/-}$; Pten $^{fl/fl}$* prostate tumours, that were either over-expressed or depleted when compared to the *PBiCre$^{+/-}$; Pik3ca$^{+/H1047R}$* prostate tumours. Biological repeats for each genotype also clustered together, indicating the *Pik3ca$^{+/H1047R}$* and *Pten $^{fl/fl}$* prostate tumour samples are transcriptionally different and further supporting the Limma MDS plot results (Figure 3.1).

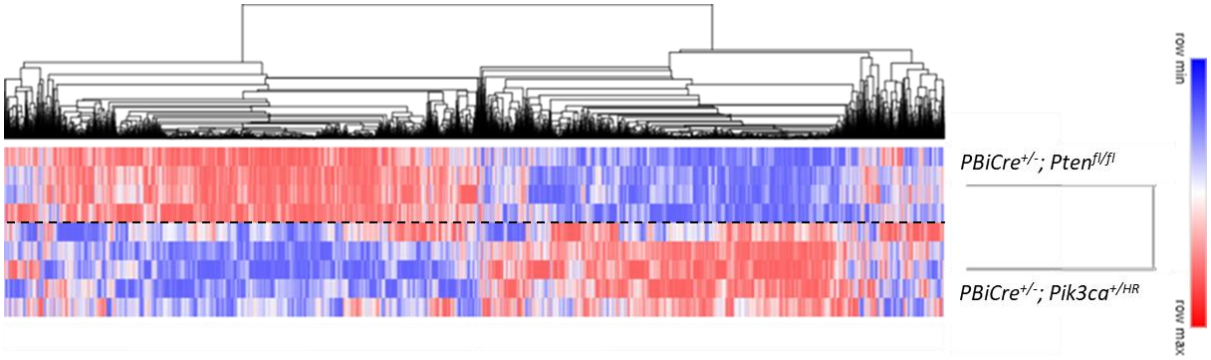

Figure 3.2: *Pten*-deleted prostate cancer and *Pik3ca*-mutant prostate cancer display distinct transcriptomic profiles. Clustered heatmap indicates differential gene expression of 14,094 genes within *PBiCre$^{+/-}$; Pik3ca$^{+/H1047R}$* (n = 5, 300 d old) and *PBiCre$^{+/-}$; Pten$^{fl/fl}$* (n = 4, 200 d old) invasive ventral lobe prostate carcinoma as probed for within RNA-Seq. Red bars denote upregulation and blue bars denote downregulation.

To better visualise the overall distribution and differential gene expression status within the *Pten$^{fl/fl}$* tumour model relative to the *Pik3ca$^{+/H1047R}$* model, a volcano plot was created in GraphPad Prism 9.0.0 using the Log_2FC and adjusted P value data (Figure 3.3). To refine the gene list, and reduce false positives, filters were applied to obtain a list of deregulated genes within the *Pten $^{fl/fl}$* prostate tumour model relative *to Pik3ca$^{+/H1047R}$* tumour model, with Log_2 fold change values of ± 2 and an adjusted P value of ≤0.05.

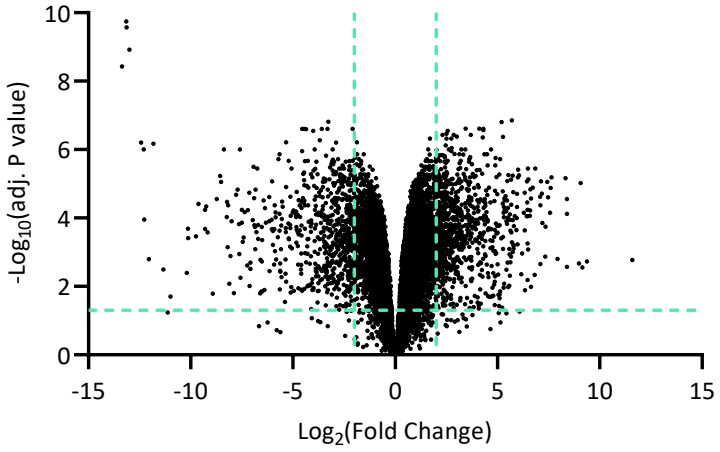

Figure 3.3: RNA-Seq data identified significantly deregulated clusters of genes in *Pten*-deficient prostate cancer vs. *Pik3ca*-mutant prostate cancer. Volcano plot indicates the differential expression of genes within the *PBiCre$^{+/-}$; Pten$^{fl/fl}$* prostate tumour model relative to the *PBiCre$^{+/-}$; Pik3ca$^{+/H1047R}$* tumour model**.** Adjusted P values were Log_{10} transformed to allow plotting of each data point. The horizontal dashed line represents the adjusted P value cut off value of ≤0.05, and vertical dashed lines represent Log_2 fold change cut off values of ± 2. Out of the 14,094 genes identified by RNA-Seq, 1599 genes had a significant adjusted P value of ≤0.05; where 897 these genes were upregulated (Log_2 fold change ≥ 2) and 702 genes were downregulated (Log_2 fold change ≤ -2).

Visually, the volcano plot appeared to show very similar levels of significantly deregulated genes, although there were almost 200 more upregulated genes in comparison to those that were downregulated, that were identified within the *Pten*-deficient prostate tumours relative to the *Pik3ca*-mutant prostate tumours.

The volcano plot also indicated some of the most highly significant genes to be downregulated, which included *Mus musculus* specific genes such as prostatic spermine-binding protein (*Sbp*), beta-defensin 50 precursor (*Defb50*), kallikrein 1-related peptidase b26 (*Klk1b2*), as well as genes with unknown function such as *9530002B09Rik*. To overcome this, all genes meeting set fold change and statistical significance criteria (Log_2 fold change ≤ -2 or ≥ 2, adjusted P-value ≤ 0.05) were reassessed for the presence of human homologues to ensure biological relevancy to human prostate cancer. The top 25 most upregulated and downregulated genes within the *Pten$^{fl/fl}$* prostate tumour model relative to the *Pik3ca$^{+/H1047R}$* tumour model were then plotted in heatmap format using the matrix expression data within Morpheus for a more detailed comparison (Figure 3.4).

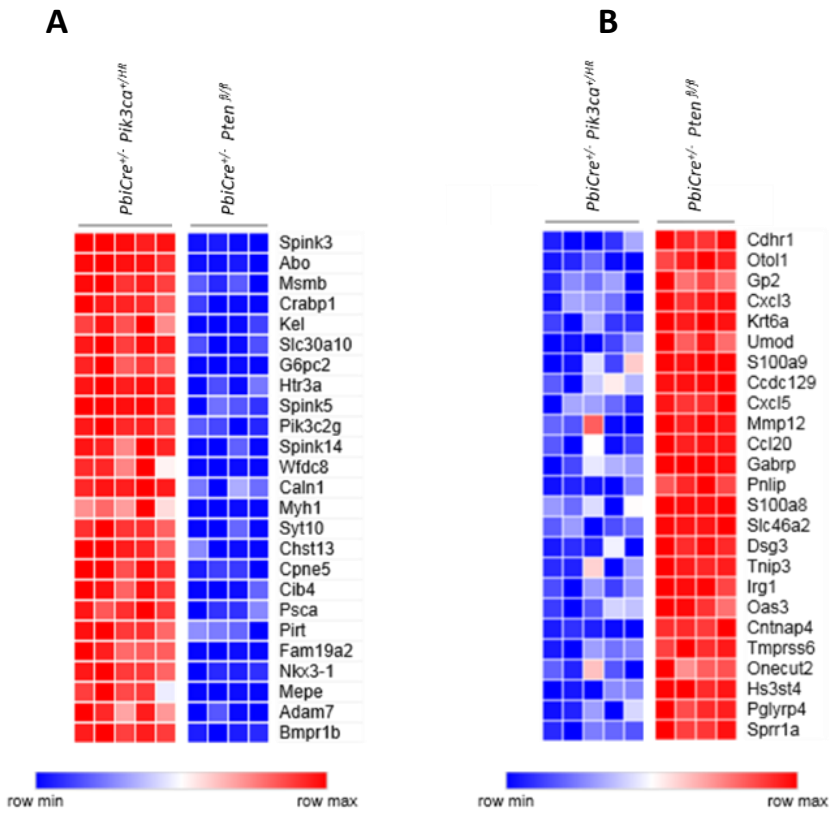

Gene	Log_2 Fold Change	Adjusted P Value
Spink3	-13.1489	1.81E-10
Abo	-12.2979	9.97E-07
Msmb	-12.2666	0.000112
Crabp1	-12.0543	0.001595
Kel	-10.9881	0.019754
Slc30a10	-9.29483	5.79E-05
G6pc2	-9.16822	0.000266
Htr3a	-8.55832	5.88E-06
Spink5	-8.38327	9.99E-07
Pik3c2g	-8.24511	9.41E-05
Spink14	-8.19468	0.000717
Wfdc8	-8.12031	0.008323
Caln1	-7.71333	1.48E-05
Myh1	-7.5628	0.005566
Syt10	-7.50525	5.82E-05
Chst13	-7.49729	0.000137
Cpne5	-7.42307	0.000372
Cib4	-7.35909	6.74E-05
Psca	-7.3261	6.87E-05
Pirt	-7.23898	0.002437
Fam19a2	-7.20262	5.93E-05
Nkx3-1	-7.13271	1.84E-05
Mepe	-7.11659	0.009696
Adam7	-7.08297	0.002001
Bmpr1b	-6.93157	3.19E-06

Gene	Log_2 Fold Change	Adjusted P Value
Cdhr1	9.056855	9.46E-06
Otol1	8.392269	2.80E-05
Gp2	8.391944	0.002664
Cxcl3	8.386721	7.54E-05
Krt6a	8.325539	6.91E-06
Umod	7.926517	0.001559
S100a9	7.571205	7.01E-05
Ccdc129	7.468068	2.50E-05
Cxcl5	7.431454	8.86E-06
Mmp12	7.346855	0.000178
Ccl20	7.16773	1.94E-05
Gabrp	7.123941	8.51E-06
Pnlip	7.089385	4.30E-05
S100a8	7.087066	2.41E-05
Slc46a2	6.83824	3.60E-06
Dsg3	6.632704	2.67E-05
Tnip3	6.5915	6.04E-05
Irg1	6.584449	8.65E-05
Oas3	6.499978	0.000836
Cntnap4	6.481113	3.59E-06
Tmprss6	6.473497	8.81E-05
Onecut2	6.470101	0.006507
Hs3st4	6.441737	8.51E-06
Pglyrp4	6.422372	8.87E-05
Sprr1a	6.328345	1.84E-05

Figure 3.4: The top 50 most deregulated genes within the *PBiCre$^{+/-}$; Pten $^{fl/fl}$* prostate tumours relative to *PBiCre$^{+/-}$; Pik3ca$^{+/H1047R}$* prostate tumours. Comparative heatmaps display A) 25 of the most downregulated genes and B) 25 of the most upregulated genes within *PBiCre$^{+/-}$; Pten$^{fl/fl}$* (n = 4, 200 d old) vs. of *PBiCre$^{+/-}$; Pik3ca$^{+/H1047R}$* (n = 5, 300 d old) invasive ventral lobe prostate tumours. Tables underneath indicate the Log_2 fold change and significance values for each gene.

The most significantly downregulated gene identified in the *PBiCre$^{+/-}$; Pten $^{fl/fl}$* prostate tumour model when compared with the *PBiCre$^{+/-}$; Pik3ca$^{+/H1047R}$* tumour model was identified as *Spink3* (serine protease inhibitor kazal-type 3, also known as *SPINK1* in humans). SPINK1 is generally considered to function as an endogenous protein inhibitor of trypsin within the pancreas, although SPINK3 was initially characterised in the mouse ventral prostate and was often referred to as P12 protein (Romac et al. 2010). Previous studies have indicated that SPINK1 overexpression in prostate cancer can be associated with a poor prognosis and higher risk of disease recurrence (Shen et al. 2014), where androgen deprivation can lead to this overexpression (Tiwari et al. 2020).

Additional studies have shown that deletion of *Spink3* within the pancreas can drive high levels of autophagy (Ohmuraya et al. 2012). Autophagy is an essential cellular process required for the degradation of damaged or abnormal proteins to maintain energy and metabolic homeostasis, although within a tumour setting, autophagy has also been shown to assist in overcoming hypoxic and nutrient deprived conditions to promote tumour cell growth and survival (Yun and Lee 2018).

A Log_2 fold change value of -13.2 indicated huge downregulation of *Spink3* within the *Pten*-null tumours, suggesting increased autophagy may play an important role in promoting tumorigenesis in *Pten*-deleted prostate cells only. As activation of the AKT and mTOR pathway has been identified to suppress autophagy (Gabriele et al. 2018), this also suggests that *Spink3* regulation may be a PTEN specific function.

Interestingly, *Pik3c2g* also was identified as a significantly downregulated gene within the *Pten*-deleted tumours. *Pik3c2g encodes* a Class II PI3K catalytic subunit isoform that plays an important role in insulin-dependent phosphorylation of AKT2 and regulation of cellular metabolism, in addition to being predominantly expressed in the liver, stomach, prostate and testis (Margaria et al. 2019). In human prostate cancer, *PIK3C2G* genetic alterations are uncommon (Shorning et al. 2020), where low *PIK3C2G* copy number has been linked to an increased probability of recurrence and risk of death in stage III colorectal cancer patients (Margaria et al. 2019). The significance and contribution of reduced *Pik3c2g* expression in respect to *Pten* deletion within prostate cancer is yet to be determined and may provide further insight in the insulin-mediated metabolic changes that contribute to the phenotype observed.

Conversely, *Cdhr1* (cadherin related family member 1) was the most significantly upregulated gene within the *Pten*-deficient tumour model when compared with the *Pik3ca*-hyperactivated model.

Cdhr1, also known as *Prcad* (protocadherin 21), encodes for a calcium-dependent cell adhesion protein that is specific to photoreceptor cells (Fu et al. 2018a). It is interesting to observe elevated expression of this gene within the prostate considering there is a tissue expression bias, therefore this could be a consequence of RNA-Seq library contamination or a reference gene mapping error, however it has been widely noted that altered calcium signalling is a common event within cancer (Stewart et al. 2015).

In prostate cancer signalling through calcium channels and calcium-dependent proteins have been linked to increased angiogenesis and metastasis, where mechanisms of calcium-dependent inhibition of apoptosis driven by the loss of PTEN have also been proposed (Ardura et al. 2020). It has been shown in prostate cancer cells that mitochondrial apoptosis can be prevented through a reduction of intercellular and mitochondrial calcium levels following inactivation or loss of PTEN, thus enabling enhanced cell survival and proliferation (Ardura et al. 2020).

It could therefore be speculated that *Cdhr1* does in fact play some sort of calcium-dependent role within the *Pten*-deleted tumours, possibly providing the tumours with heightened invasive potential, especially given how at the various experimental end points previously investigated, the $Pten^{fl/fl}$ model tumours displayed locally invasive carcinoma at a proportion far greater than the tumours derived from the $Pik3ca^{+/H1047R}$ model (Pearson et al. 2018).

3.3.2 Identification of key pathway alterations in *Pten*-deficient prostate cancer vs. *Pik3ca*-mutant prostate cancer

To identify the key pathway alterations in *Pten*-deleted prostate cancer compared to *Pik3ca*-mutant prostate cancer, we utilised the bioinformatic tool of Ensemble Gene Set Enrichment Analysis (eGSEA) to perform wide-scale differential gene expression pathway analysis. By facilitating access to large publicly available transcriptomic datasets and performing comparative associations, this software program streamlines use of previously published research to help better understand which cellular processes become deregulated in models of interest (Alhamdoosh et al. 2017).

Using a pre-prepared script written by Dr Li and his team, expression matrix data files were analysed using R and the EGSEAdata package, to associate $PBiCre^{+/-}; Pik3ca^{+/HR1047R}$ and $PBiCre^{+/-}; Pten^{fl/fl}$ prostate tumour gene expression data with the mouse C2 MSigDB gene collection. Ordered by median ranking (differential expression based on median expression values for each phenotype), eGSEA ranked and revealed the top 20 deregulated pathways within *Pten*-deficient invasive prostate carcinoma

specimens isolated from stage-matched *PBiCre*$^{+/-}$*; Pten*$^{fl/fl}$ mice relative to *Pik3ca*-mutant invasive prostate carcinoma from *PBiCre*$^{+/-}$*; Pik3ca*$^{+/H1047R}$ mice (200 d and 300 d old respectively) (Figure 3.5). The eGSEA data indicated significant upregulation of genes involved within tumour cell of origin, evasion of cell death and inflammatory pathways, suggesting increased signalling within these subsets of pathways occurred in the tumours following *Pten* loss, relative to Pik3ca-hyperactivation.

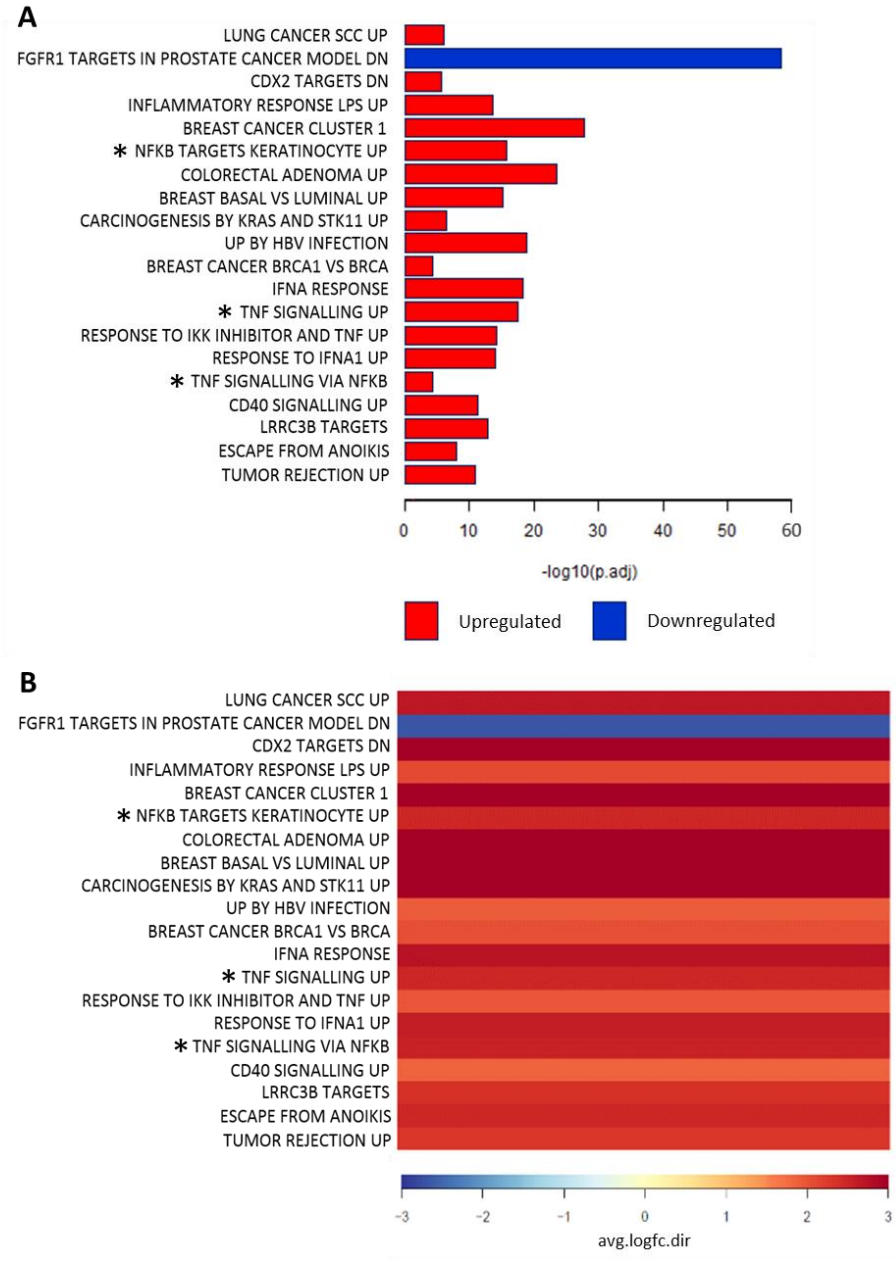

Figure 3.5: eGSEA identified distinct pathway alterations in *Pten*-deficient prostate cancer vs. *Pik3ca*-mutant prostate cancer. Graphs depict the 20 most significantly deregulated pathways within invasive prostate tumours isolated from *PBiCre*$^{+/-}$*; Pten*$^{fl/fl}$ (n = 4, 200 d old) compared with stage-matched *PBiCre*$^{+/-}$*; Pik3ca*$^{+/H1047R}$ (n = 5, 300 d old) prostate tumours. Ordered by median ranking, eGSEA generated figures displaying A) statistical significance in adjusted P values, B) average log fold change direction.

When comparing *Pten*-deficient and *Pik3ca*-mutant prostate carcinomas, multiple TNF-NF-κB related gene signatures (as indicated by an asterisk in Figure 3.5A) and basal cell signatures (including Breast Basal vs Luminal Up) were significantly increased in the context of *Pten* loss (Figure 3.5A). These findings were strongly supported by the literature, for instance, the loss of PTEN has been previously linked to activation of the NF-κB signalling pathway within multiple cancer types including leukaemia, bladder cancer and glioblastoma, whereby activation of NF-κB was understood to be driven through increased AKT activation (Jiang et al. 2004; Cahill et al. 2016; Man et al. 2019). Furthermore, Wang and colleagues have showed that *Pten* deletion within the mouse prostate epithelium results in the expansion of the basal cell population during tumorigenesis, which can be associated with alterations in both morphology and localisation (Wang et al. 2006).

Taken together, these findings suggest that the accelerated growth observed within the *Pten*-null tumours relative to the *Pik3ca*-mutant tumours, is driven through elevated activation of the NF-κB pathway and expansion of the basal cell population, and thus both events may represent PI3K-independent mechanisms of tumour progression associated with the loss of PTEN.

3.3.3 Identification of the most deregulated genes in *Pten*-deficient prostate cancer vs. *Pik3ca*-mutant prostate cancer

To identify putative, PI3K-independent actionable targets for PTEN-deficient prostate cancer and establish the most commonly deregulated genes across the top 20 deregulated pathways determined by eGSEA, a clustered heatmap of all pre-filtered differentially expressed genes was generated using Morpheus software (filter criteria: human homologues, Log_2 fold change ≤ -2 or ≥ 2, adjusted P-value ≤ 0.05) (Figure 3.6) alongside a summary table (Table 3.2).

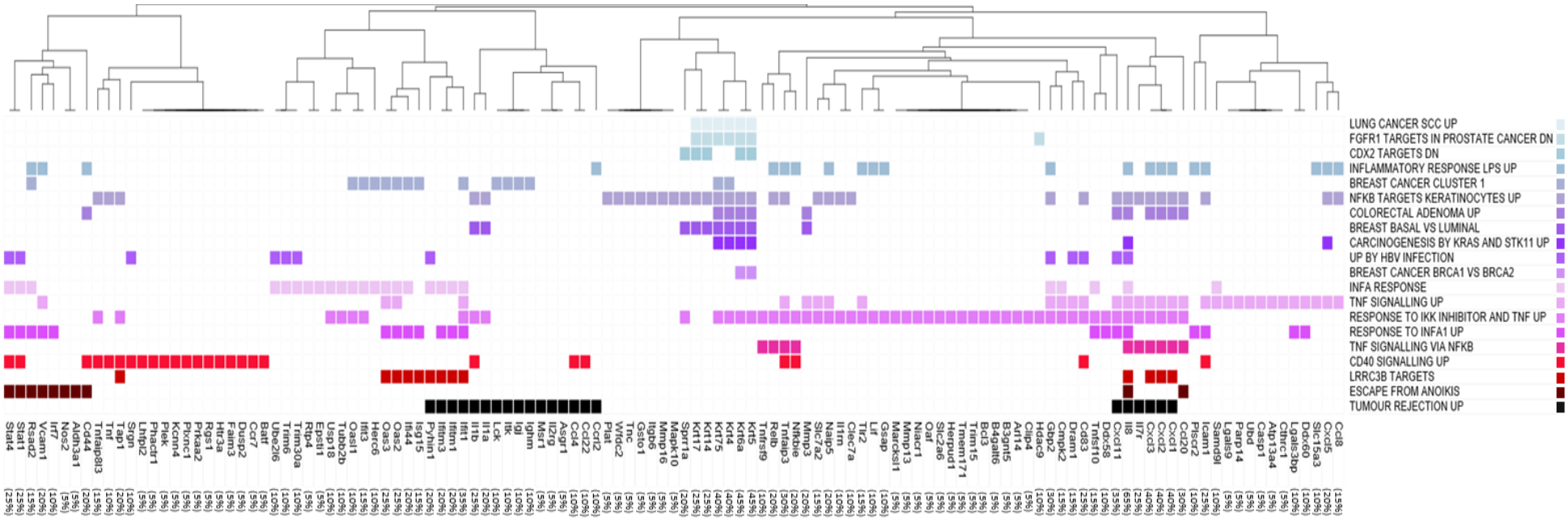
LUNG CANCER SCC UP
FGFR1 TARGETS IN PROSTATE CANCER DN
CDX2 TARGETS DN
INFLAMMATORY RESPONSE LPS UP
BREAST CANCER CLUSTER 1
NFKB TARGETS KERATINOCYTES UP
COLORECTAL ADENOMA UP
BREAST BASAL VS LUMINAL
CARCINOGENESIS BY KRAS AND STK11 UP
UP BY HBV INFECTION
BREAST CANCER BRCA1 VS BRCA2
INFA RESPONSE
TNF SIGNALLING UP
RESPONSE TO IKK INHIBITOR AND TNF UP
RESPONSE TO INFA1 UP
TNF SIGNALLING VIA NFKB
CD40 SIGNALLING UP
LRRC3B TARGETS
ESCAPE FROM ANOIKIS
TUMOUR REJECTION UP

Figure 3.6: Identification of the most frequently deregulated genes enriched in *Pten*-deleted prostate cancer in comparison to *Pik3ca*-mutant prostate cancer. Comparative heatmap displaying all significantly deregulated mouse genes possessing human homologues, sequenced within the *PBiCre$^{+/-}$; Pten$^{fl/fl}$* prostate tumour model enriched within pathways identified by eGSEA, relative to the *PBiCre$^{+/-}$; Pik3ca$^{+/H1047R}$* prostate tumour model. Percentages indicate gene incidence within the top 20 pathways.

Table 3.2: Top 10 most enriched genes deregulated in *Pten*-deleted prostate cancer relative to *Pik3ca*-mutant prostate cancer. Table indicates the most frequently enriched genes as established in Figure 3.6.

Gene	Percentage of association to the top 20 enriched pathways
Il8	65%
Ktr5	45%
Krt6a	45%
Cxcl1	40%
Cxcl2	40%
Cxcl3	40%
Krt4	40%
Krt17	40%
Cxcl11	35%
Ifit1	35%

3.3.3.1. *Il8* is significantly upregulated in *Pten*-deficient prostate cancer

Noticeably, interleukin 8 (*Il8* or *Cxcl8*), a gene significantly upregulated within the *Pten*-deficient tumours (Log_2 fold change = 4.122081027, adjusted P value = 3.97E-06), was present in 13 of the top 20 deregulated pathways as identified by eGSEA. Although mice do not express IL-8, they possess functional murine homologues such as keratinocyte-derived protein chemokine (KC), macrophage inflammatory protein-2 (MIP-2), and lipopolysaccharide-induced CXC chemokine (LIX) (Hol et al. 2010), and thus could be identified as being significantly deregulated following Ensembl BioMart association (Subramanian et al. 2005).

IL-8 is a pro-inflammatory chemokine that plays an important functional role in maintaining inflammatory homeostasis by activating and recruiting neutrophils to sites that require pathogen clearance (Benakanakere et al. 2016). Elevated *IL8* transcription and more specifically increased protein expression, has been associated with development of chronic inflammatory diseases as well as ovarian, lung, bladder and prostate cancers (Waugh and Wilson 2008; Benakanakere et al. 2016). Interestingly within a recent evaluation of human primary and metastatic prostate tumours, IL-8

protein expression was shown to be significantly increased in comparison to other interleukin members, especially within higher grade samples (Maynard et al. 2020).

Work by the de Bono Lab, exploring inflammatory storms and their contribution to prostate tumorigenesis, also highlights a strong correlation between loss of PTEN and increased IL-8 protein expression in human prostate cancer (de Bono et al. 2020), whereby IL-8 was additionally described to initiate widespread tumour promoting, chemokine-based, tumour-stroma crosstalk through increasing expression of other chemokine–receptor pairs in PTEN-deficient prostate cancer cell lines (Maxwell et al. 2014). Notably, PI3K signalling driven by PTEN loss may contribute to the phenotype observed in the *PBiCre$^{+/-}$; Pten$^{fl/fl}$* model, however our data suggests that increased *Il8* transcription could be meditated through events driven explicitly by *Pten* deletion rather being a PI3K cascade related phenomenon, due the significant difference in expression between the *PBiCre$^{+/-}$; Pik3ca$^{+/H1047R}$* model and the *PBiCre$^{+/-}$; Pten$^{fl/fl}$* model.

3.3.3.2. *AR* target gene transcription is reduced in the context of *Pten*-loss

Additionally, it is understood that androgen levels can impact the transcription of *IL8* and consequently in advanced prostate cancer where androgen independence is gained, IL-8 levels have been shown to increase; promoting growth, angiogenesis and metastasis (Araki et al. 2007; Maynard et al. 2020). For an initial look into whether genes that could be controlled by AR signalling were also deregulated within the GEMM prostate tumours, a heatmap was generated in Morpheus by cross referencing the *Pten*-deficient and *Pik3ca*-mutant prostate cancer RNA-Seq data with a list of AR responsive murine transcriptional targets (n = 132) previously identified by the Carver group (Carver et al. 2011).

Following implementation of statistical significance criteria (Log_2 fold change ≤-2 or ≥2, adjusted P-value ≤0.05), findings indicated clear differences in the transcriptomic profiles of AR target genes (n = 42) following *Pten*-deletion relative to *Pik3ca*-hyperactivation (Figure 3.7). Analysis of the heatmap revealed 31 genes were significantly downregulated in *Pten*-deficient prostate cancer compared to *Pik3ca*-mutant prostate cancer, including *Abo*, *Crabp1* and *Nkx3.1*, which were also identified as some of the mostly highly downregulated genes in the *PBiCre$^{+/-}$; Pten$^{fl/fl}$* tumour model relative to the *PBiCre$^{+/-}$; Pik3ca$^{+/H1047R}$* tumour model (Figure 3.4).

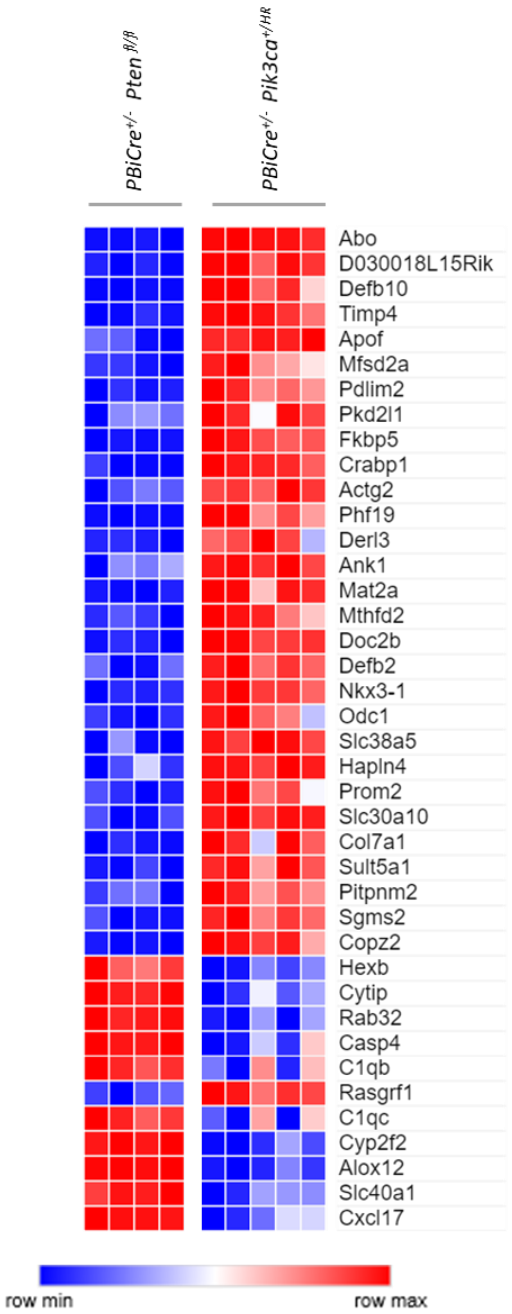

Gene	Log$_2$ Fold Change	Adjusted P Value
Abo	-12.2979	9.97E-07
D030018L15Rik	-11.3358	0.003222
Defb10	-5.98275	0.000614
Timp4	-5.71809	1.92E-06
Apof	-3.38897	1.51E-06
Mfsd2a	-2.36832	0.000955
Pdlim2	-2.62741	1.03E-05
Pkd2l1	-2.91341	0.002065
Fkbp5	-4.55232	2.48E-07
Crabp1	-12.0543	0.001595
Actg2	-4.12665	5.25E-06
Phf19	-4.22798	0.00013
Derl3	-3.36122	0.002649
Ank1	-3.88513	4.42E-05
Mat2a	-4.45887	4.67E-06
Mthfd2	-2.15904	0.000134
Doc2b	-6.02609	8.51E-06
Defb2	-5.84884	9.54E-05
Nkx3-1	-7.13271	1.84E-05
Odc1	-2.22732	0.000293
Slc38a5	-6.43725	3.10E-05
Hapln4	-4.44635	3.11E-05
Prom2	-2.22939	8.59E-05
Slc30a10	-9.29483	5.79E-05
Col7a1	-3.43176	0.000517
Sult5a1	-2.56071	2.80E-05
Pitpnm2	-2.04852	4.92E-05
Sgms2	-2.17857	5.36E-06
Copz2	-2.62408	3.60E-06
Hexb	2.164098	2.08E-05
Cytip	3.592857	1.48E-05
Rab32	2.198772	8.29E-06
Casp4	2.342308	0.000122
C1qb	2.217231	0.004294
Rasgrf1	-5.35318	0.000261
C1qc	2.15515	0.003234
Cyp2f2	3.114964	7.19E-06
Alox12	4.307854	2.68E-07
Slc40a1	3.261591	1.27E-05
Cxcl17	3.230934	6.39E-05

Figure 3.7: *Pten*-deficient prostate cancer displays reduced transcription of AR-target genes relative to *Pik3ca*-mutant prostate cancer. Heatmap of AR target gene expression comparing *PBiCre$^{+/-}$; Pten$^{fl/fl}$* (n = 4, 200 d old) *with PBiCre$^{+/-}$; Pik3ca$^{+/H1047R}$* (n = 5, 300 d old) invasive ventral lobe prostate carcinoma. Data shows only those that were significantly deregulated (Log$_2$ fold change ≤ -2 or ≥ 2 and an adjusted P value of ≤0.05), therefore displaying only 42 out of the 132 genes cross-referenced. Table indicates the Log$_2$ fold change and significance values for each gene.

AR target genes including *Nkx3.1* are frequently downregulated in a castrated setting, which can be attributed to the reduction of androgen signalling (Prescott et al. 1998). Together with our findings, this supports the regulatory function of PTEN on AR mediated activity (Lin et al. 2004; Carver et al. 2011; Nguyen et al. 2018), and suggests that in comparison to *Pik3ca*-mutant prostate cancer, PTEN loss drives a reduction in AR signalling.

3.3.3.3. *Pten*-deficient prostate cancer is associated with elevated CXCR1/2 signalling relative to *Pik3ca*-mutant prostate cancer

Clustered closely to *Il8*, *Cxcl1*, *Cxcl2* and *Cxcl3* (C-X-C motif chemokine ligands 1/2/3) were also present in 40% of the top 20 deregulated pathways identified by eGSEA (Figure 3.6). Secretion of these four chemokine ligands from stromal cells has been linked to promotion of inflammation and initiation of prostatic tumorigenesis (Kogan-Sakin et al. 2009), with high levels of CXCL1 identified to increase the invasive and metastatic potential of breast cancer cells through NF-κB/SOX4 signalling, and high levels of CXCL3 also shown to increase aggression and migratory capacity of DU145, LNCAP and PC3 prostate cancer cells via signalling through its receptor CXCR2 (Gui et al. 2016; Wang et al. 2018b).

Furthermore, *Cxcr2* gene expression was shown to be significantly upregulated within the *Pten*-deficient vs. *Pik3ca*-mutant prostate tumour RNA-Seq data (Log_2 fold change= 5.933, adjusted P value = 0.0001), indicating a possible biological relevancy of increased CXCR2 in PTEN-null prostate cancer. Importantly, early onset/accelerated prostate cancer progression was observed previously by our lab in *PBiCre*$^{+/-}$*; Pten*$^{fl/fl}$ transgenic mice relative to *Pik3ca*-mutant mice (Pearson et al., 2018), thus it is possible that increased CXCL1/2/3 signalling may contribute to rapid tumour formation and/or progression. Taken together, these findings indicate targeting the CXCR1/2 signalling axis could be an effective therapy for patients with PTEN-deficient prostate cancer.

3.3.3.4. *Pten*-deficient prostate cancer is associated with elevated NF-κB signalling relative to *Pik3ca*-mutant prostate cancer

NF-κB signalling has been widely implicated within prostate cancer, such that elevated NF-κB signalling in patients with hormone sensitive disease has been linked to worsened prognoses, and in patients with hormone insensitive disease, increased NF-κB signalling has been correlated with disease progression (Zhang et al. 2016a). Previous work by Zhang et al has linked PTEN loss within PC3 prostate cancer cells to upregulation of NF-κB and mTORC1, where IKK complex association to mTORC1 enhances its activity, whilst mTORC1 promotes IKKα and IKKβ activity, thus upregulating NF-κB function in a positive feedback loop (Zhang et al. 2016a).

A large proportion of enriched genes were detected within three eGSEA established NF-κB related pathways, with 30.8 % of the significantly deregulated genes identified in the *Pten*-null model associated with 'NF-κB targets keratinocytes up' pathway, 27.5 % to 'TNF signalling up' pathway and 44.2 % 'Response to IKK inhibitor and TNF up' pathway. Respectively, these gene lists were established from three independent studies investigating p65/p50 mediated regulation of proinflammatory and antiapoptotic genes in normal epidermal and dermal skin cells (Hinata et al. 2003), tumour necrosis factor alpha (TNFα) induced gene expression changes in primary endothelial cells (Sana et al. 2005), and inhibition of TNFα-mediated activation of the IKK/NF-κB pathway in pancreatic tumour cells (Zhang et al. 2008); suggesting that canonical NF-κB signalling may be augmented within the *Pten*-deficient prostate tumour model.

For a more stringent comparison of genes that are directly and indirectly involved with NF-κB signalling, a list of known NF-κB signalling mediators both involved in the canonical and non-canonical pathways, was generated through use of the Boston University NF-κB target gene resource (http://www.bu.edu/NF-κB/gene-resources/target-genes/) (n = 29 genes selected at random), that facilitate a range of cellular processes driven by antigen presentation, cell adhesion, chemokines/cytokines, immune receptors, NF-κB enzymes, stress responses and transcription factors. A heatmap was generated using Morpheus software to display the comparative gene expression data for *Pik3ca*-mutant and *Pten*-deficient prostate carcinoma (Figure 3.8).

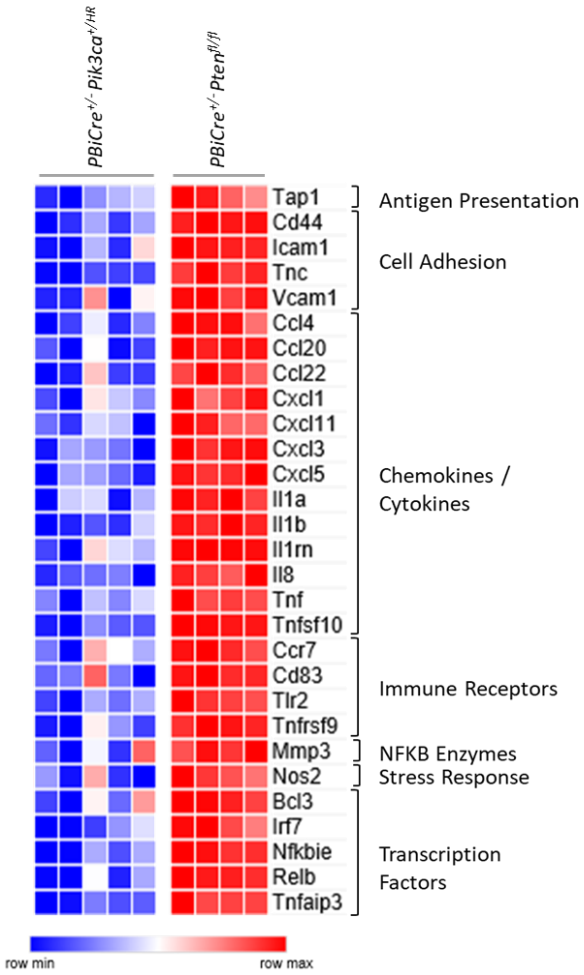

Gene	Log_2 Fold Change	Adjusted P Value
Tap1	2.045993	0.000177
Cd44	3.646391	6.44E-06
Tnc	2.747804	1.11E-06
Vcam1	2.280255	0.00074
Ccl4	3.496394	0.000171
Ccl20	7.16773	1.94E-05
Ccl22	4.149326	0.000278
Cxcl1	2.598631	0.000305
Cxcl11	4.647973	0.000751
Cxcl3	8.386721	7.54E-05
Cxcl5	7.431454	8.86E-06
Il1a	3.112681	0.000147
Il1b	4.019532	1.36E-05
Il1rn	4.649214	3.53E-05
Il8	4.122081	3.97E-06
Tnf	3.71885	0.000126
Tnfsf10	5.265216	4.28E-07
Ccr7	3.772454	0.00053
Cd83	2.312625	0.00038
Tlr2	2.241682	1.84E-05
Tnfrsf9	3.063574	7.51E-05
Mmp3	6.164928	0.004455
Nos2	3.627904	0.000707
Bcl3	2.818061	0.000551
Irf7	4.017188	0.000126
Nfkbie	2.466745	1.26E-05
Relb	2.273801	4.42E-05
Tnfaip3	2.119104	5.12E-06

Figure 3.8: NF-κB pathway genes are upregulated in *Pten*-deficient prostate cancer. Comparative heatmap of NF-κB pathway mediator gene expression within *PBiCre$^{+/-}$; Pik3ca$^{+/H1047R}$* and *PBiCre$^{+/-}$; Pten$^{fl/fl}$* GEMM prostate tumours (n = 4/5, 200 and 300 d old, ventral prostate carcinoma respectively). All genes are statistically significant (adj. p.value <0.05) and are grouped by function. Table indicates the Log_2 fold change and significance values for each gene.

The heatmap showed high expression of all 29 NF-κB associated genes within the *PBiCre$^{+/-}$; Pten$^{fl/fl}$* cohort relative to the *PBiCre$^{+/-}$; Pik3ca$^{+/H1047R}$* cohort. Whilst many of the *Pik3ca*-mutant tumours showed lessened expression, there were some discrepancies within this cohort where expression showed to be much higher for genes such as *Vcam1* and *Mmp3*. This could be attributed to heterogeneity of the tumours, whereby varied levels of tumour and stromal content may have had an impact. Despite this, these NF-κB genes were all deemed to be significantly upregulated in the *Pten*-deficient tumours relative to the *Pik3ca*-mutant tumours.

Noticeably, the NF-κB transcription factor family member RelB which plays an essential role during non-canonical NF-κB signalling, a pathway requisite for immune homeostasis and responses, is significantly upregulated upon *Pten* deletion compared to *Pik3ca* mutation. Furthermore, *Bcl3* (B-cell leukaemia/lymphoma 3) and *Nfkbie* (NF-κB inhibitor epsilon), both of which are known to inhibit canonical NF-κB signalling, were also significantly upregulated following *Pten* loss. Together, these data suggest that *Pten* loss leads to activated non-canonical signalling and inhibition of the canonical NF-κB pathway.

Moreover, NF-κB family member p65 is reported to mediate transcription of IκB inhibitory proteins such as IκBα, to create regulatory feedback loops within the NF-κB pathway (Hoesel & Schmid, 2013), thus, potentially underpinning the significant increase in *Bcl3* and *Nfkbie* transcription observed within the *PBiCre$^{+/-}$; Pten$^{fl/fl}$* model and is in keeping with the significant upregulation of pro-inflammatory cytokines and chemokines also observed (Figure 3.8). Additionally, previous work has shown that p100 can regulate PTEN expression via interactions with ERK to stabilise *PTEN* mRNA, independently of its inhibitory role in within the NF-κB signalling pathway (Wang et al. 2016). Whilst this doesn't link increased activation of non-canonical NF-κB signalling to a PTEN-null setting, it does support direct interactions between non-canonical NF-κB subunits and PTEN.

For further investigation into whether non-canonical NF-κB signalling provides a pro-tumorigenic advantage in the *Pten*-deleted tumours relative to the Pik3ca-hyperactivated tumours, RNA-Seq expression data of several canonical and non-canonical NF-κB transcriptional target genes was

assessed (Table 3.3); however, analysis of these genes revealed that both non-canonical and canonical transcriptional target genes are upregulated, where large fold changes were observed in canonical target genes *Ccl3* and *Il1b* (Log_2 fold change = 4.94 and 4.02 respectively) and non-canonical target genes *Glycam1* and *Cxcl13* (Log_2 fold change = 5.78 and 2.54 respectively). These findings indicate that both canonical and non-canonical NF-κB cascades are active in *Pten*-deficient prostate cancer, and that both these pathways promote tumorigenic growth following deletion of *Pten*, however further work is required to fully elucidate their distinct roles.

Table 3.3: Non-canonical and canonical NF-κB transcriptional target genes are deregulated in *Pten*-depleted prostate cancer in comparison to *Pik3ca*-mutant prostate cancer. Table shows transcriptomic data of non-criteria filtered, canonical and non-canonical NF-κB pathway target genes expressed in *PBiCre$^{+/-}$; Pten$^{fl/fl}$* tumours compared to *PBiCre$^{+/-}$; Pik3ca$^{+/H1047R}$* GEMM prostate tumours, as determined by RNA-Seq (n = 4/5, 200 and 300 d old, ventral prostate carcinoma respectively). Gene lists were obtained from (https://www.creative-diagnostics.com/The-NF-κB-Signaling-Pathway.htm).

Pathway/Process	Gene	Log_2FC (*PBiCre Pten$^{fl/fl}$* GEMM relative to *PBiCre Pik3ca$^{+/H1047R}$* GEMM)	Adjusted P value
Canonical NF-κB target genes	*Ccl3*	4.94	0.001
	Ccl5	1.24	0.004
	Icam1	3.05	0.0001
	Il1b	4.02	1.36E-05
	Nos2	3.63	0.0007
	Vcam1	2.28	0.0007
Non-canonical NF-κB target genes	*Ccl12*	1.17	0.0058
	Ccl21	1.01	0.1539
	Cxcl13	2.54	0.0043
	Glycam1	5.78	0.0006
	Irf3	-0.49	0.0025
	Tnfsf13b	1.41	0.0041

Universally, it is accepted that the non-canonical pathway drives developmental processes alongside mediating immune homeostasis, whilst the canonical pathway is predominantly associated with regulation of proinflammatory gene expression and is a critical mediator of the inflammatory response (Yu et al. 2020).

Both signalling axes can also interact, where induction of *Nfkb2* and *RelB* expression can also occur via canonical NF-κB stimulation (Mitchell et al. 2016). Furthermore, unprocessed p100 which can form an inhibitor of NF-κB (IκBδ), has been shown to trap canonical NF-κB dimers and prevent their association with canonical IκB proteins (Mitchell et al., 2016). Additionally, RelA has also been reported to associate with the C-terminal portion of p100, such that if mice express mutant p100 that cannot be processed into p52, the defective activation of these p100-RelA dimers result in the impaired development of osteoclasts and secondary lymphoid organs (Shih et al. 2011).

It is also therefore possible that crosstalk mechanisms could be occurring between the two signalling axes within *Pten*-deficient prostate cancer to facilitate accelerated growth and tumour cell survival, however further investigation would be required to underpin the exact regulatory mechanisms they may be exerting on one another.

To further establish the impact of NF-κB activation and signalling, transcription factor binding sites were investigated for genes enriched within the RNA-Seq data that met significance and fold change criteria and possessing human homologues within the intact *PBiCre$^{+/-}$; Pten $^{fl/fl}$* prostate tumours (as indicated in Figure 3.6). Through use of the publicly available gene database GeneCards, (Weizmann Institute of Science and LifeMap Sciences; www.genecards.weizmann.ac.il/v3/cgi-bin/carddisp.pl), transcription factor information was obtained (Data in Appendix 7). This data highlighted many genes under the transcriptional control of the NF-κB family, further supporting its extensive role within this tumour model that would not have been detected through analysis of RNA-Seq data alone.

3.3.3.5. Validation of RNA-Sequencing data

To verify the accuracy of the RNA-Sequencing data, qRT-PCR was performed on cDNA reversed transcribed from DNase treated, total RNA isolated from the ventral prostate lobe of age matched *PBiCre$^{+/-}$* wildtype mice, and stage-matched intact and castrated *PBiCre$^{+/-}$; Pik3ca$^{+/H1047R}$*, *PBiCre$^{+/-}$; Pten $^{fl/fl}$* and *PBiCre$^{+/-}$; Pik3ca$^{+/H1047R-}$; Pten $^{fl/fl}$* invasive prostate carcinoma (as per Section 2.7, n = 3/cohort). Genes were chosen to encompass a range of significantly and insignificantly deregulated genes.

Using glyceraldehyde-3-phosphate dehydrogenase (*Gapdh)* as a housekeeping gene to normalise target gene expression, relative mRNA expression of *RelB*, *Cxcl1*, *Plekhs1* and *Nkx3.1* within the various models was determined (Figure 3.9), using the ΔΔCt method as detailed in Section 2.7.9.

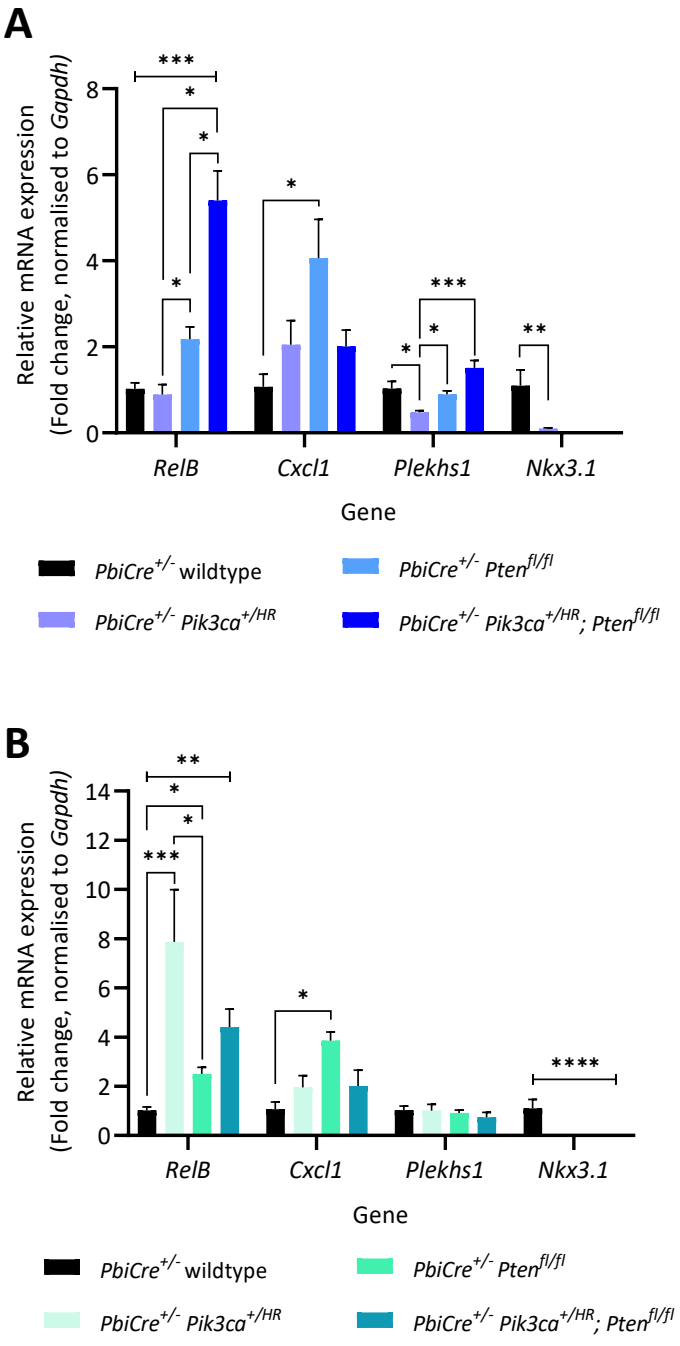

Figure 3.9: qRT-PCR validation of differentially expressed genes identified by RNA-Sequencing.

Graphs depict the log fold change of mRNA expression within A) *PBiCre$^{+/-}$; Pik3ca$^{+/H1047R}$* wildtype, *PBiCre$^{+/-}$; Pik3ca$^{+/H1047R}$*, *PBiCre$^{+/-}$; Pten $^{fl/fl}$* and *PBiCre$^{+/-}$; Pik3ca$^{+/H1047R}$; Pten $^{fl/fl}$* GEMM ventral prostate carcinoma (n = 3/cohort) and B) *PBiCre$^{+/-}$; Pik3ca$^{+/H1047R}$* wildtype, castrated *PBiCre$^{+/-}$; Pik3ca$^{+/H1047R}$*, castrated *PBiCre$^{+/-}$; Pten $^{fl/fl}$*

and castrated *PBiCre*$^{+/-}$*; Pik3ca*$^{+/H1047R}$*; Pten* $^{fl/fl}$ GEMM ventral prostate carcinoma (n = 3 /cohort). Data was normalised to *Gapdh* mRNA expression. Data shown is a representation of mean values. Error bars = SEM. Statistical analysis was performed via a one-way ANOVA with a Tukey's multiple comparison test. * = P value of ≤ 0.05, ** = P value of P ≤ 0.01, *** = P value of P ≤ 0.001 and **** = P value of P ≤ 0.0001.

Analogous to the results obtained via RNA-Seq, higher expression of *RelB*, *Cxcl1* and *Plekhs1* was observed in intact *Pten*$^{f/fl}$ tumours compared to the intact *Pik3ca*$^{+/H1047R}$ model by qRT-PCR (Figure 3.9A). In support, concordant RNA-Seq and qRT-PCR data was also observed when comparing *RelB, Cxcl1,* and *Plekhs1* mRNA expression in a castrated setting, where comparable levels of expression for all genes were deemed non-significant within castrated Pik*3ca*$^{+/H1047R}$*; Pten* $^{fl/fl}$ prostate tumours relative to the castrated *Pten*$^{f/fl}$ model (Figure 3.9B). These findings indicate that the RNA-Sequencing established accurate transcriptional readouts within the intact and castrated tumour models, as determined by the high reproducibility of results via qRT-PCR.

To directly compare fold change obtained via RNA-Seq with fold change determined by qRT-PCR data, simple linear regression plots were generated for intact *Pik3ca*$^{+/H1047R}$ and *Pten*$^{fl/fl}$ prostate tumours, and the R^2 co-efficient calculated (Figure 3.10). High R^2 values of > 0.9 were observed for both datasets, suggesting a strong correlation exists between the RNA-Seq and qRT-PCR fold change values, further indicating the RNA-Seq results can be regarded as reliable. Owing to several samples with negligible or absent levels of *Nkx3.1* mRNA, this data was excluded from the linear regression assessment.

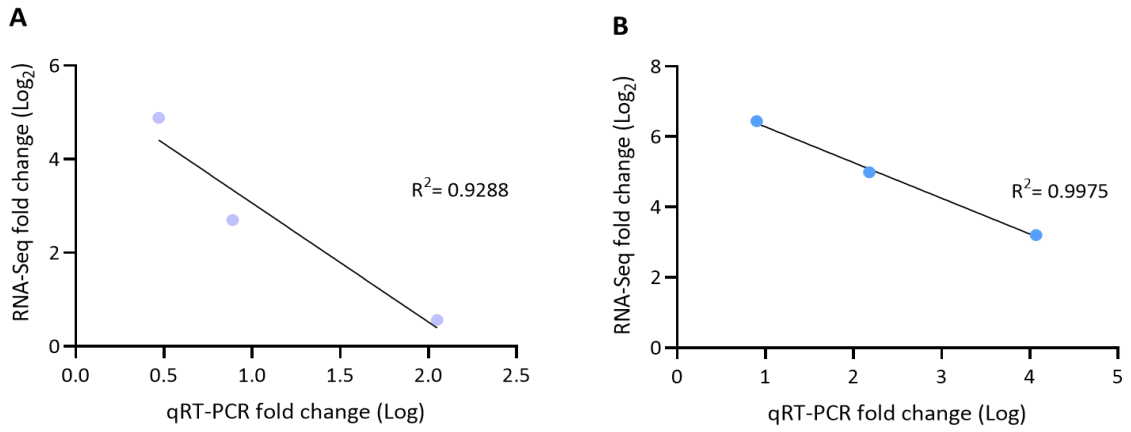

Figure 3.10: Technical validation of RNA-Seq fold change and qRT-PCR fold change. Linear regression plots comparing qRT-PCR log fold change (x axis) and RNA-Seq Log_2 fold change (y axis) for *RelB*, *Cxcl1* and *Plekhs1* mRNA expression data within stage-matched A) *PBiCre*$^{+/-}$*; Pten* $^{fl/fl}$ and B) *PBiCre*$^{+/-}$*; Pik3ca*$^{+/H1047R}$ ventral prostate carcinoma (n = 3/cohort). Simple linear regression was performed to obtain coefficient of determination (R^2) values.

3.3.3.6. *Pten*-deficient prostate cancer displays an increased basal cell gene signature relative to *Pik3ca*-mutant prostate cancer

Within the top 20 deregulated pathways identified by eGSEA (Figure 3.5), downregulation of the 'fibroblast growth factor receptor 1 (FGFR1) targets in prostate cancer model down' gene set was identified as the second most significant deregulated pathway (Figure 3.5). This dataset was generated from an *in vivo* study investigating *Fgfr1* within the juxtaposition of CID and kinase1 (JOCK1) GEMM that enables activation of inducible FGFR1 through use of chemical inducers of dimerization (CID) (Acevedo et al. 2007).

In comparison to wild-type untreated JOCK1 mice, experimental mice given prolonged treatment developed invasive adenocarcinoma from 42 weeks onwards, that further led to epithelial to mesenchymal transition (EMT) and metastasis (Acevedo et al. 2007). However, closer inspection of the significantly deregulated genes within this gene signature revealed a handful of cytokeratin encoding genes were upregulated in the *Pten*-deficient setting when compared to Pik3ca-mutant prostate cancer, while *Hdac9* was downregulated (Figure 3.11).

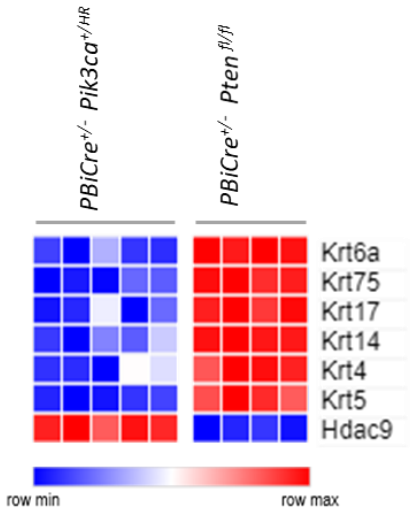

Gene	Log_2 Fold Change	Adjusted P Value
Krt6a	8.325539	6.91E-06
Krt75	5.743986	5.74E-06
Krt17	4.989902	2.01E-05
Krt4	2.221695	0.000336
Krt5	2.015134	1.04E-06
Hdac9	-5.20858	2.13E-06

Figure 3.11: Basal cell genes are upregulated in *Pten*-deficient prostate cancer. Comparative heatmap of genes with human homologues identified within *PBiCre$^{+/-}$; Pik3ca$^{+/H1047R}$* and *PBiCre$^{+/-}$; Pten$^{fl/fl}$* GEMM prostate tumours (n = 4 / 5, 200 and 300 d old, ventral prostate carcinoma respectively), enriched within the FGFR1 pathway identified by eGSEA**.** Genes shown met the significance and Log2 fold change criteria set (Log_2 fold change ≤- 2 or ≥ 2, adjusted P-value ≤0.05). Table indicates the Log_2 fold change and significance values for each gene.

Notably, these cytokeratin genes were also present in the 'Breast basal vs luminal' pathway identified by eGSEA, with this dataset obtained from study investigating the effect of ionizing radiation on mammary cells; showing that subsequent to DNA damage, luminal cells undergo a longer cell cycle arrest whereas basal cells undergo a more rapid and unstable cell cycle arrest, which may contribute to increased predisposition of the basal cell population to oncogenic transformation (Huper and Marks 2007).

Encouragingly, this identification of epithelial cell differences by eGSEA through the transcriptional data of the two tumour types, highlighted an increase in genes upregulated in basal cells. Importantly, these findings support previous work published by the lab showing *PBiCre$^{+/-}$; Pten$^{fl/fl}$* prostate tumours are comprised of cytokeratin-8 (CK8)-positive luminal cells interspersed within an expanded cytokeratin-5 (CK5)-positive basal cell population, whilst the *PBiCre$^{+/-}$; Pik3ca$^{+/H1047R}$* model derived tumours are predominantly CK8-positive luminal cells, and CK5-positive basal cells scarce (Pearson et al., 2018). Together these findings imply that the FGFR1 pathway is not deregulated in *Pten*-null prostate tumours relative to *Pik3ca*-mutant prostate cancer, but instead emphasise key differences in the cell type of origin.

Together these results indicate a strong basal cell signature within the *Pten*-null tumours that is absent within the *Pik3ca*-mutant tumours and suggest a possible functional role or advantage of basal cells in promoting tumorigenic growth when PTEN is lost.

3.3.4. Identification of putative drivers of *de novo* castration resistance

3.3.4.1. *De novo* CRPC in *Pik3ca*-mutant and *Pten*-deficient tumours display a distinct transcriptional profile relative to acquired CRPC in *Pten*-deleted prostate carcinomas in mice

With limited therapeutic options available for patients with castration resistant prostate cancer (Turnham et al., 2020), a deeper understanding of the molecular mechanisms involved in CRPC transition and progression is required, alongside methods of identifying the genetic changes that facilitate innate and acquired resistance, needed to aid patient care.

Given how PTEN loss has been shown to correlate with ADT resistance; *Pik3ca*-mutant, *Pten*-null and compound mutant prostate tumours were also assessed for their ability to develop castration-resistant disease (Pearson et al., 2018). Histopathological and IHC analyses indicated that the single mutant models acquired resistance to androgen deprivation following castration at invasive disease stages, whilst the castrated *Pik3ca*$^{+/HR}$*; Pten*$^{fl/fl}$ model phenocopied intact (non-castrated) controls and showed no reduction in tumour burden, indicating *Pik3ca*-oncogenic mutation and *Pten*-homozygous deletion cooperate to promote *de novo* CRPC (Pearson et al., 2018).

Thus, Pearson and colleagues showed that use of the castrated *PBiCre*$^{+/-}$ *Pik3ca*$^{+/H1047R}$*; Pten* $^{fl/fl}$ and *PBiCre*$^{+/-}$*Pten* $^{fl/fl}$ models can provide a unique advantage to identify drivers of *de novo* CRPC, where further characterisation of these models may also present novel therapeutic targets or biomarkers for use in the clinic.

To establish the key molecular mechanisms that contribute to *de novo* CRPC, RNA isolated from the ventral lobe of *PBiCre* $^{+/-}$ *Pik3ca* $^{+/H1407R}$*; Pten* $^{fl/fl}$ compound mutant mice 2-weeks post-castration (when *de novo* CPRC was prevalent) and from *PBiCre* $^{+/-}$ *Pten* $^{fl/fl}$ tumours harvested 10-weeks post-castration (i.e., when acquired CRPC was prevalent), with surgical castration performed once invasive carcinoma had developed at 100 and 200 d respectively. RNA-Sequencing was then performed on DNase treated total RNA (RIN > 7.4) (as detailed above in Section 3.3.1) (n = 5/cohort).

MDS plots were generated by Dr Li (Peter MacCallum Cancer Centre), to assess the quality and variation of the data (Figure 3.10). Principal component analysis indicated that the castrated *PBiCre*$^{+/-}$*; Pten* and the castrated *PBiCre*$^{+/-}$*; Pik3ca*$^{+/H1047R}$*; Pten* $^{fl/fl}$ biological repeat samples were relatively similar and clustered together, whilst the two different genotypes did not cluster together, indicating they have distinct transcriptional profiles (Figure 3.12).

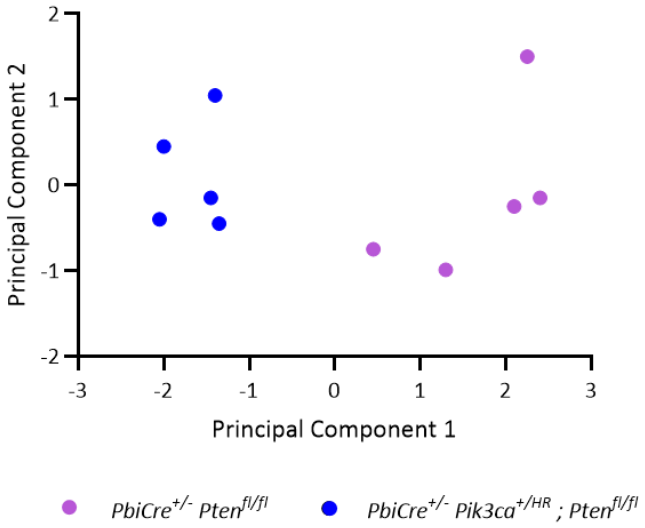

Figure 3.12: Castrated compound mutant prostate cancer and castrated *Pten*-deficient prostate cancer are transcriptionally different. MDS plot representing total RNA samples isolated from *PBiCre* $^{+/-}$ *Pik3ca* $^{+/H1407R}$*; Pten* $^{fl/fl}$ (n = 5, 114 d) and *PBiCre*$^{+/-}$*; Pten*$^{fl/fl}$ (n = 5, 270 d) castrated invasive ventral lobe prostate carcinoma**.**

To better visualise the overall distribution and direction of differential gene expression within the castrated *PBiCre*$^{+/-}$*; Pik3ca*$^{+/H1047R}$*; Pten* $^{fl/fl}$ tumour model relative to the castrated *PBiCre*$^{+/-}$*; Pten* model, a volcano plot was created with Log_2 fold change ≤-1.5 or ≥1.5 and adjusted P-value ≤0.05 filters applied (Figure 3.13). A smaller Log_2 fold change of ± 1.5 was selected, as the initial ± Log_2 fold change criteria utilised yielded very few genes (n = 670) for further investigation.

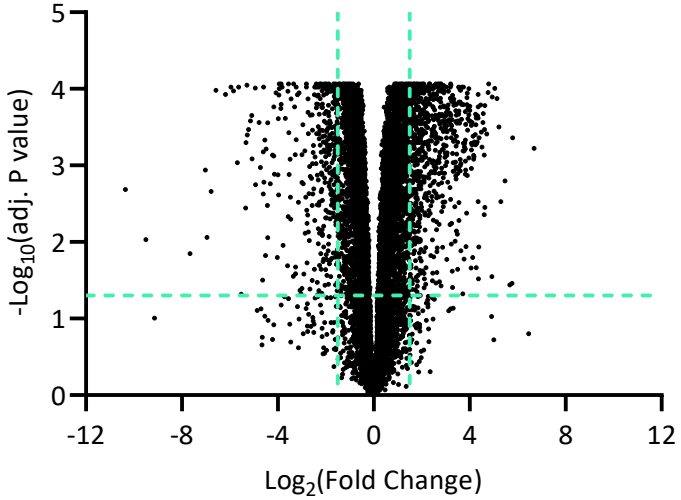

Figure 3.13: RNA-Seq data identified significantly deregulated clusters of genes in castrated *Pik3ca*-mutant and *Pten*-deficient prostate cancer vs. castrated *Pten*-deleted prostate cancer. Volcano plot indicates the differential expression of genes within the castrated *PBiCre*$^{+/-}$*; Pik3ca*$^{+/H1047R}$*; Pten* $^{fl/fl}$ prostate tumour model

relative to the castrated *PBiCre$^{+/-}$; Pten* tumour model. Adjusted P values were Log_{10} transformed to allow plotting of each data point. The horizontal dashed line represents the adjusted P value cut off value of ≤0.05, and vertical dashed lines represent Log_2 fold change cut off values of ± 1.5. Out of the 14898 genes identified by RNA-Seq, 1195 genes had a significant adjusted P value of ≤0.05; where 823 of these genes were upregulated (Log_2 fold change ≥ 1.5) and 372 genes were downregulated (Log_2 fold change ≤ -1.5).

When comparing castrated compound mutant tumours (*PBiCre$^{+/-}$ Pik3ca$^{+/H1047R}$; Pten$^{fl/fl}$)* with castrated *Pten*-deleted tumours (*PBiCre$^{+/-}$; Pten* tumours), the proportion of genes that were identified as being significantly altered was relatively low (1195 out of 14898 genes) (Figure 3.13). Interestingly, there were more deregulated genes that were upregulated (n = 823) than downregulated (n = 372), where these deregulated genes were anticipated to include genes that play a key role in promoting innate CRPC.

The most significantly downregulated gene identified through the comparison of the castrated compound mutant relative to the castrated *Pten*-deficient mutant was *Lman1l,* that encodes lectin mannose binding 1 protein (LMAN1L) (Figure 3.14). LMAN1 mainly functions as a carrier of glycoproteins within ER/Golgi transport and mutational inactivation of LMAN1 has been frequently observed in sporadic microsatellite unstable (MSI-H) colorectal tumours (Roeckel et al. 2009). Previous work has shown that LMAN1 deficiency in these tumours can decrease secretion of Alpha-1 antitrypsin A1AT, an inhibitor of several serine proteases that can exert both anti-proteolytic and angio-inhibitory functions (Roeckel et al. 2009). This suggests that decreased expression of *Lman1l* in the castrated compound mutant model may facilitate deregulation of proteasome signalling and contribute to angiogenesis.

Conversely the most significantly upregulated gene within the *de novo* CRPC model in comparison to the acquired CRPC model was identified as *Kera*, a gene encoding the keratan sulfate proteoglycan protein, keratocan (Figure 3.14). Glycans are more recently being explored as potential diagnostic and prognostic biomarkers for prostate cancer, given how they can also contribute to tumour cell proliferation and survival (Scott and Munkley 2019). Various proteoglycans that constitute part of the extracellular matrix have been studied in prostate cancer, where versican has been shown to increase motility of prostate tumour cells, whilst perlecan can upregulate hedgehog signalling (Scott and Munkley 2019). Despite this, very little published literature could be found implicating keratocan in prostate disease as this protein is mainly expressed within the cornea (Carlson et al. 2005), thus further work exploring this link to our model of *de novo* CRPC is required.

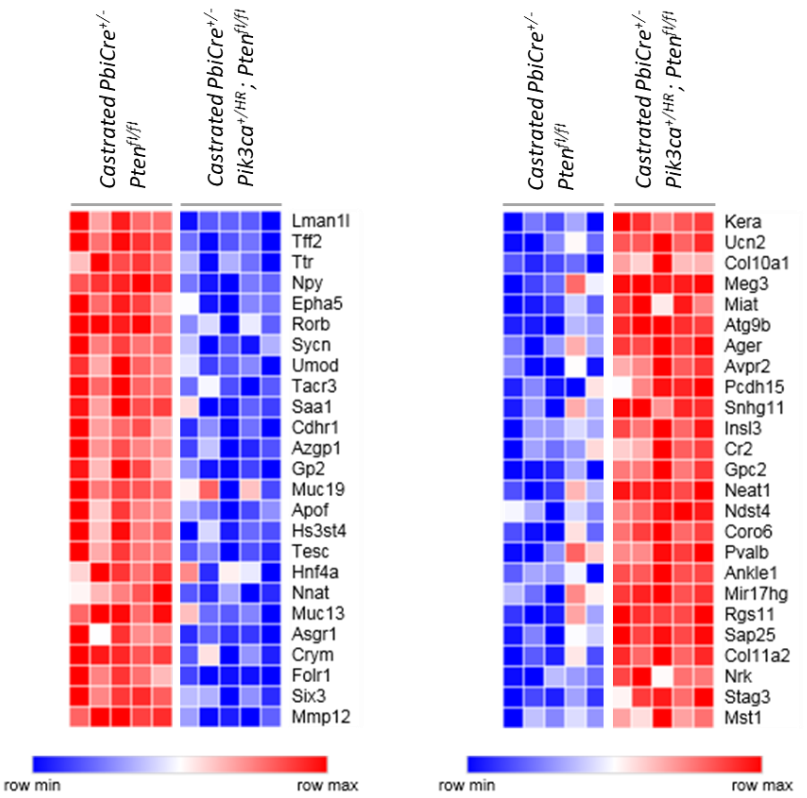

Gene	Log2 Fold Change	Adjusted P Value
Lman1l	-7.66434	0.014227
Tff2	-6.58363	0.000104
Ttr	-5.68657	0.000917
Npy	-5.28684	8.92E-05
Epha5	-5.21926	0.000341
Rorb	-5.13874	0.000262
Sycn	-5.08859	0.000222
Umod	-4.92572	0.001795
Tacr3	-4.77653	0.000276
Saa1	-4.60886	0.000663
Cdhr1	-4.59942	9.46E-05
Azgp1	-4.49134	0.000608
Gp2	-4.41766	0.000277
Muc19	-4.41667	0.008816
Apof	-4.30957	0.001739
Hs3st4	-4.13942	0.001304
Tesc	-4.07904	0.000113
Hnf4a	-4.01868	0.015928
Nnat	-3.99267	0.001333
Muc13	-3.98248	0.000245
Asgr1	-3.96406	0.002421
Crym	-3.94039	9.96E-05
Folr1	-3.87868	0.000181
Six3	-3.85728	0.00016
Mmp12	-3.85336	8.64E-05

Gene	Log2 Fold Change	Adjusted P Value
Kera	6.682037	0.000599
Ucn2	5.790245	0.000434
Col10a1	5.302998	0.002967
Meg3	5.217117	0.000315
Miat	4.925234	0.028425
Atg9b	4.790763	8.64E-05
Ager	4.715303	0.00039
Avpr2	4.606795	0.000734
Pcdh15	4.60107	0.004414
Snhg11	4.353769	0.002976
Insl3	4.314724	0.000496
Cr2	4.275982	0.021679
Gpc2	4.244569	0.000215
Neat1	4.184951	0.000767
Ndst4	4.167858	0.000832
Coro6	4.134388	0.000414
Pvalb	4.12957	0.015861
Ankle1	4.095782	0.000276
Mir17hg	4.074508	0.001098
Rgs11	3.985063	0.000262
Sap25	3.930573	0.000182
Col11a2	3.910495	0.000345
Nrk	3.892189	0.01178
Stag3	3.877092	0.004208
Mst1	3.841886	0.011479

Figure 3.14: The top 50 most deregulated genes within castrated *PBiCre$^{+/-}$; Pik3ca$^{+/H1047R}$; Pten $^{fl/fl}$* prostate tumours relative to castrated *PBiCre$^{+/-}$; Pten* prostate tumours. Comparative heatmaps display A) 25 of the most downregulated genes and B) 25 of the most upregulated genes within *PBiCre$^{+/-}$ Pik3ca $^{+/H1407R}$; Pten $^{fl/fl}$* (n = 5, 114 d) vs *PBiCre$^{+/-}$; Pten$^{fl/fl}$* (n = 5, 270 d) castrated invasive ventral lobe prostate carcinoma. Tables underneath indicate the Log_2 fold change and significance values for each gene.

3.3.4.2. Identification of key pathway alterations in *Pik3ca*-mutant and *Pten*-deficient *de novo* CRPC vs. *Pten*-deleted acquired CRPC

To assess which genes may contribute to innate castration resistance RNA-Seq data from castrated *PBiCre*$^{+/-}$ *Pik3ca*$^{+/H1047R}$; *Pten*$^{fl/fl}$ and castrated *PBiCre*$^{+/-}$; *Pten*$^{fl/fl}$ prostate tumours was inputted into eGSEA for pathway analysis. Ordered by median ranking, Figure 3.15 displays the top 20 deregulated pathways identified and the associated average fold change.

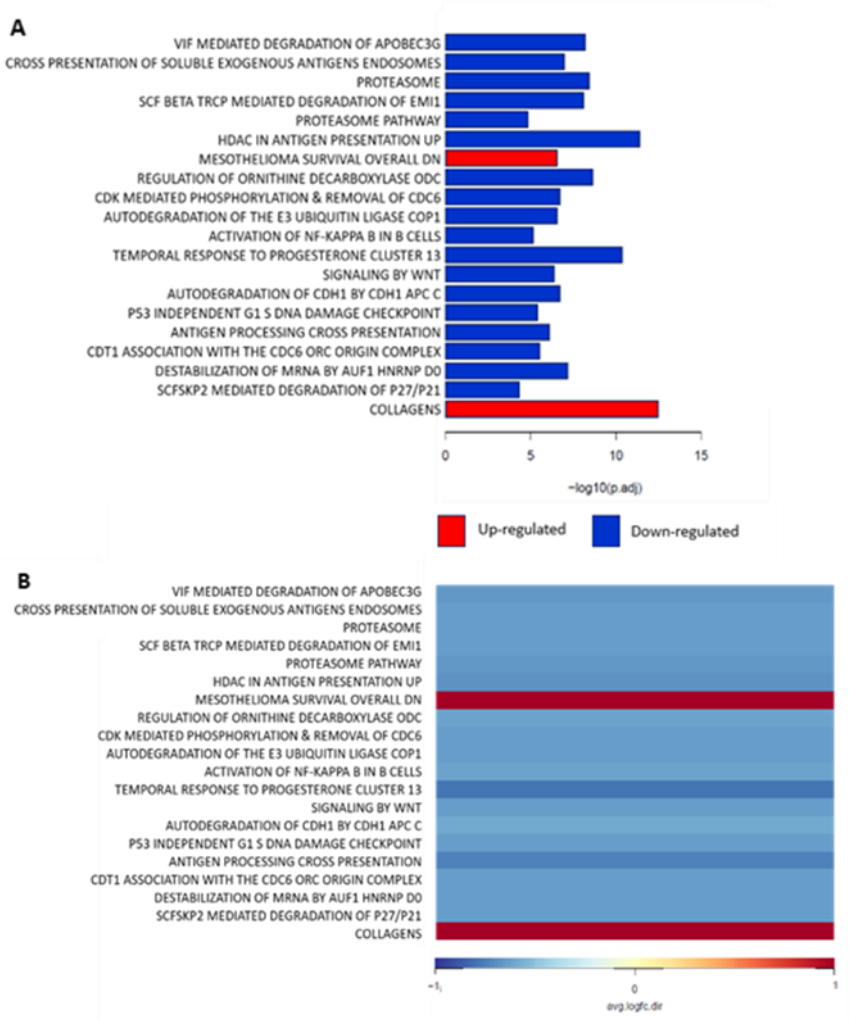

Figure 3.15: eGSEA identified distinct pathway alterations in castrated *Pik3ca*-mutant and *Pten*-deficient prostate cancer vs. castrated *Pten*-deleted prostate cancer. Graphs depict the 20 most significantly deregulated pathways within *PBiCre* $^{+/-}$ *Pik3ca* $^{+/H1407R}$; *Pten* $^{fl/fl}$ (n = 5, 114 d) and *PBiCre*$^{+/-}$; *Pten*$^{fl/fl}$ (n = 5, 270 d) castrated invasive ventral lobe prostate carcinoma**.** Ordered by median ranking, eGSEA generated figures displaying A) statistical significance in adjusted P values and B) average log fold change direction.

It is interesting that the x - axis of the heatmap generated by R representing average log fold change direction, appears restricted to ± 1 (Figure 3.13B), suggesting that although these events are significant (adjusted p-value <0.05), they are not as substantial as those identified within the intact *PBiCre*$^{+/-}$ *Pten*$^{fl/fl}$ and *PBiCre*$^{+/-}$ *Pik3ca*$^{+/H1047R}$ GEMMs (Figure 3.5), however it is important to note that both of these models harbour genetic loss of *Pten.*

90% of the top 20 pathways associated through eGSEA indicated downregulation of pathways within innate CRPC tumours relative to acquired CRPC (Figure 3.15). The most significant pathway that was identified as downregulated was termed 'HDAC in antigen presentation up', where this molecular signature was derived from a study investigating the effects of histone deacetylase (HDAC) inhibition in human B-lymphoblastoid cancer cells (Pellicciotta et al. 2008).

This study showed that inhibition of HDAC *in vitro* could mediate downregulation of genes involved in endogenous antigen presentation, leading to increased evasion of immune surveillance (Pellicciotta et al. 2008). Whilst the study data associated to our RNA-Seq output constitutes a list of genes that were upregulated in response to HDAC treatment, eGSEA identified these genes to be downregulated in the *PBiCre*$^{+/}$ *Pik3ca*$^{+/H1047R}$*; Pten*$^{fl/fl}$ tumour model, further implying that the model may mediate downregulation of antigen presentation to avoid detection of tumour-killing cells, possibly in an epigenetic manner. This concept of immune surveillance evasion is strongly supported by the association of numerous pathways indicating downregulation of antigen presentation related pathways in the castrated compound mutant model relative to castrated *Pten*-deficient prostate cancer.

3.3.4.3. *Pik3ca*-mutant and *Pten*-deficient *de novo* CRPC is associated with upregulated collagen formation relative to *Pten*-deleted acquired CRPC

To identify mediators of *de novo* castration resistance relative to acquired resistance, the differential gene expression data generated by Dr Li, was filtered for human homologues, and analysed for presence in eGSEA associated pathways following the application of significance criteria (Log_2 fold change ≤-1.5 or ≥1.5, adjusted P-value ≤0.05) (Table 3.3). A heatmap was also generated using Morpheus for visual analysis (Figure 3.14). These criteria identified a subset of 31 differentially expressed genes; where collagen type X alpha 1 chain (*Col10a1*) and collagen type XI alpha 2 chain (*Col11a2*) were identified as the most upregulated enriched genes within the castrated compound mutants relative to *Pten*-deficient acquired CRPC tumours, whereas Collagen type XXV alpha 1 chain (*Col25a1*) and Stanniocalcin 2 (*Stc2*) to be the most downregulated (Table 3.4).

Table 3.4: Genes are significantly deregulated in castrated *Pik3ca*-mutant and *Pten*-deficient prostate cancer vs. castrated *Pten*-deleted prostate cancer. Profiles of differentially expressed genes within castrated *PBiCre*$^{+/-}$ *Pik3ca*$^{+/H1047R}$; *Pten*$^{fl/fl}$ prostate cancer relative to castrated *PBiCre*$^{+/-}$; *Pten*$^{fl/fl}$ prostate cancer as determined by RNA-Seq (n = 5 / cohort, 114 and 270 d old, castrated ventral prostate carcinoma respectively). Genes listed have been filtered for human homologues and have reached the significance criteria set (Log_2 fold change ≤-1.5 or ≥1.5, adjusted P-value ≤0.05).

Gene	Log_2 Fold Change	Adjusted P Value	Identified In Pathway
ATP binding cassette subfamily C member 5 (Abcc5)	2.070304	0.000104	Temporal Response To Progesterone Cluster 13
ATP binding cassette subfamily C member 8 (Abcc8)	2.486382	0.005164	Temporal Response To Progesterone Cluster 13
Caspase recruitment domain-containing protein 11 (Card11)	1.855737	0.007285	Activation of NFKB in B Cells
Collagen type I alpha 1 chain (Col1a1)	2.44975	0.000122	Collagens / Mesothelioma Survival Overall DN
Collagen type I alpha 2 chain (Col1a2)	2.001422	0.00011	Collagens / Mesothelioma Survival Overall DN
Collagen type III alpha 1 chain (Col3a1)	2.27605	0.000562	Collagens / Mesothelioma Survival Overall DN
Collagen type IIII alpha 5 chain (Col4a5)	1.880477	8.64E-05	Collagens / Mesothelioma Survival Overall DN
Collagen type IIII alpha 6 chain (Col4a6)	1.695015	0.00019	Collagens / Mesothelioma Survival Overall DN
Collagen type V alpha 1 chain (Col5a1)	1.853724	0.000227	Collagens / Mesothelioma Survival Overall DN
Collagen type V alpha 2 chain (Col5a2)	2.072661	0.000647	Collagens / Mesothelioma Survival Overall DN
Collagen type V alpha 3 chain (Col5a3)	1.988841	0.003501	Collagens / Mesothelioma Survival Overall DN
Collagen type VI alpha 1 chain (Col6a1)	1.698746	0.000408	Collagens
Collagen type VI alpha 2 chain (Col6a2)	1.893306	0.000501	Collagens
Collagen type VI alpha 3 chain (Col6a3)	1.693208	0.00044	Collagens
Collagen type VII alpha 1 chain (Col7a1)	3.544511	9.45E-05	Collagens / Mesothelioma Survival Overall DN
Collagen type VIII alpha 1 chain (Col8a1)	2.052917	8.64E-05	Collagens
Collagen type IX alpha 3 chain (Col9a3)	2.02258	0.000399	Collagens
Collagen type X alpha 1 chain (Col10a1)	5.302998	0.002967	Collagens
Collagen type XI alpha 2 chain (Col11a2)	3.910495	0.000345	Collagens
Collagen type XV alpha 1 chain (Col15a1)	1.523770	0.005482	Collagens
Collagen type XX alpha 1 chain (Col20a1)	1.733177	0.000253	Collagens
Collagen type XXV alpha 1 chain (Col25a1)	-2.66968	0.001029	Collagens
Collagen type XXVII alpha 1 chain (Col27a1)	2.532088	0.000308	Collagens / Mesothelioma Survival Overall DN
Eukaryotic translation initiation factor 4E-binding protein 1 (Eif4ebp1)	-1.51599	0.00144	Temporal Response To Progesterone Cluster 13
Homeobox B6 (Hoxb6)	1.893095	9.46E-05	Mesothelioma Survival Overall DN
Integrin subunit alpha 8 (Itga8)	-1.61674	0.000701	Antigen Processing Cross Presentation
Plexin B1 (Plxnb1)	1.525905	9.46E-05	Mesothelioma Survival Overall DN
Protein kinase C gamma (Prkcg)	2.169277	0.002344	Activation of NFKB in B Cells
Proline and serine rich coiled-coil 1 (Psrc1)	2.522964	9.05E-05	Mesothelioma Survival Overall DN
SEC61 translocon alpha 2 subunit (Sec61a2)	1.867843	0.000148	Antigen Processing Cross Presentation
Stanniocalcin 2 (Stc2)	-2.04915	8.64E-05	Mesothelioma Survival Overall DN

3 out of these four most highly deregulated genes were linked to the most significant pathway as identified by eGSEA, 'Collagens' (Figure 3.15A), with *Col25a1* identified as the only significant gene encoding a collagen to be downregulated within the castrated *PBiCre*$^{+/-}$ *Pik3ca*$^{+/H1047R}$; *Pten*$^{fl/fl}$ model in contrast to all other collagen encoding genes that instead displayed upregulation (Figure 3.16).

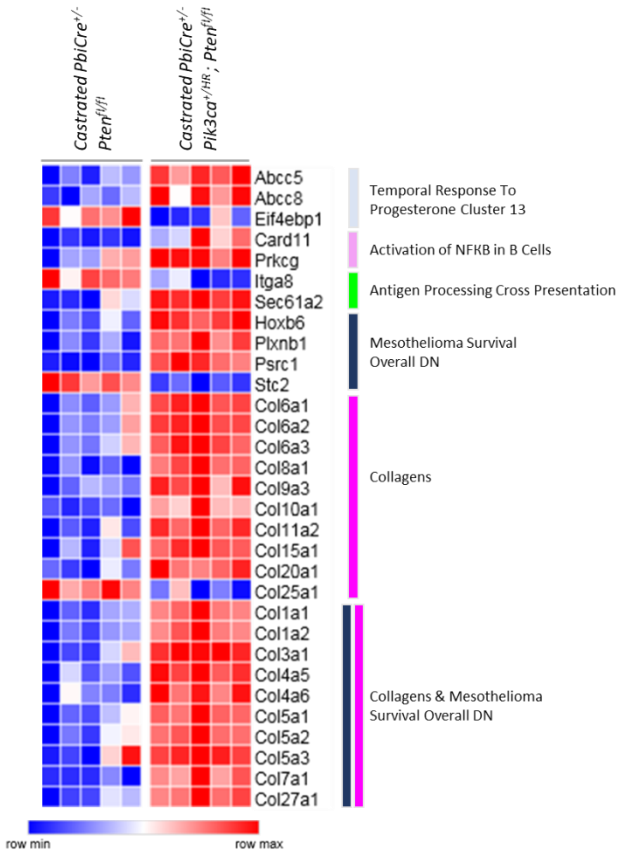

Figure 3.16: Collagen genes are upregulated in castrated *Pik3ca*-mutant and *Pten*-deficient prostate cancer. Comparative heatmap of genes with human homologues identified within castrated *PBiCre*$^{+/-}$; *Pik3ca*$^{+/H1047R}$; *Pten*$^{fl/fl}$ and *PBiCre*$^{+/-}$; *Pten*$^{fl/fl}$ GEMM prostate tumours (n = 5 / cohort, 114 and 270 d old, castrated ventral prostate carcinoma respectively), and their incidence within the enriched pathways identified by eGSEA**.** Genes shown met the significance and Log_2 fold change criteria set (Log_2 fold change ≤- 1.5 or ≥ 1.5, adjusted P-value ≤0.05).

The role of collagens in cancer has been widely studied due to their presence within the extracellular matrix (ECM), which assist in creating an extensive network that can also be exploited during tumorigenesis (Nissen et al. 2019). Collagens have been linked to promoting cancer progressive traits; with type I collagen shown to increase proliferation and reduce sensitivity to apoptosis, type III shown to mediate increased invasion and migration, and type XI connected with cancer associated fibroblasts (CAFs), that have been evidenced to instigate malignant transformation in healthy cells and drive ECM remodelling to aid metastasis (Nissen et al. 2019). The castrated compound tumour model harbouring *Pik3ca*-hyperactivation and *Pten*-loss displayed a higher proportion of proliferating cells and fewer apoptotic cells in comparison to the castrated *Pten*-deficient tumours alone (Pearson et al. 2018), although these characteristics can be controlled by numerous other pathways, the contribution of type I collagens warrant further investigation.

Interestingly, *Col6a1* that was significantly upregulated within the castrated *PBiCre*$^{+/-}$*; Pik3ca*$^{+/H1047R}$*; Pten*$^{fl/fl}$ prostate tumours, has also been shown to be elevated in human CRPC (Zhu et al. 2015), and through cell line studies of androgen sensitive and insensitive prostate cancer, COL6A1 is speculated to drive transformation of androgen-dependent prostate cancer to a state of androgen independence (Zhu et al. 2015).

Immunohistochemistry (IHC) analysis to detect AR revealed nuclear AR localisation in castrated compound *Pik3ca*-hyperactivated and *Pten*-deficient prostate tumours, indicating androgen-independent AR signalling activation which was absent in castrated *Pten*-deficient tumours (Pearson et al. 2018). Consequently, increased expression of *Col6a1* and *Col6a1*-mediated biological processes may facilitate innate CRPC transition in compound *Pten*-deficient and *Pik3ca*-mutant tumours, potentially providing them with an inherent resistance to ADT, relative to *Pten* loss alone. Taken together these findings indicate that *Col6a1* may be mechanistically important for driving *de novo* castration resistance, however further work will be required to better understand its contribution.

The downregulation of *Col25a1* requires further investigation to understand its functional relevance within the castrated compound mutant tumour model. *COL25A1* encodes a transmembrane-type collagen that has been associated with cell adhesion and intramuscular innervation (Munezane et al. 2019). With axonogenesis and neurogenesis identified within higher grade and more aggressive prostate cancers (March et al. 2020), it could therefore be hypothesised there would be increased expression of a gene such as *Col25a1* within the castrated *PBiCre*$^{+/-}$*; Pik3ca*$^{+/H1047R}$*; Pten*$^{fl/fl}$ prostate

tumours, however this was not observed. The functional role of COL25A1, or more specifically type XXV collagen, remains yet to be determined in the setting of cancer.

3.3.4.4. Proteasome signalling is downregulated in *Pik3ca*-mutant and *Pten*-deficient de novo CRPC relative to *Pten*-deleted acquired CRPC alone

Remarkably, analysis of the eGSEA data comparing innate CRPC compound mutant tumours with acquired CRPC in *Pten*-deleted prostate cancer revealed 13 of the top 20 deregulated pathways were associated with downregulation of the proteasome/degradation pathways (Figure 3.12A), including "proteasome pathway", "auto-degradation of CDH1" and "auto-degradation of E3 ubiquitin ligase COP1". These findings suggest that a significant downregulation of the proteasome and related mechanisms in compound mutant CRPC tumours may facilitate *de novo* CRPC. The proteasome plays an essential role in intracellular protein regulation; selectively cleaving and degrading peptide bonds within short-lived or aberrant proteins to destroy unwanted proteins, generate truncated proteins and release inhibitory proteins, such as those bound to NF-κB (Jang 2018).

Through visiting the dedicated REACTOME pages of the eGSEA associated proteasome pathways that were enriched to the RNA-Seq data, involvement of the 26S proteasome was identified. 26S is a ubiquitin and ATP dependent proteasome that degrades polyubiquitinated, damaged or abnormally folded proteins, in addition to targeting proteins undergoing oxidative stress, by self-dissociating 19S regulatory particles bound to the 20S proteasome subunit that collectively make up the 26S proteasome (Jang 2018).

It is interesting that an aggressive, advanced tumour mediated by *Pik3ca* mutation and *Pten*-loss would drive downregulation in proteasome associated pathways when inhibition of the proteasome has been shown to increase apoptosis, decrease cell migration and adhesion, generate cell cycle and growth arrest, as well as limiting inflammatory and DNA damage responses; features that advocate the use of proteasome inhibitors as cancer therapeutics (Frankland-Searby and Bhaumik 2012). However, recent studies have demonstrated that cancer stem cells within human mammary epithelial cell lines selectively downregulate the proteasome to induce EMT, with further investigation showing cells treated with selective proteasome inhibitors developing an innate ability to self-renew alongside increasing TGF-β1 signalling to drive EMT (Banno et al. 2016), therefore it could be speculated the cancer stem cell population within the compound mutant tumours could be responsible for driving downregulation of protein degradation pathways to augment their migratory capacity, however further investigation to determine this theory is needed.

Despite the strong signature, none of the enriched genes following implementation of the <0.05 adj. P value and ±1.5 Log_2 fold change threshold, were identified within any of the proteasome associated pathways (Figure 3.16), except for genes *Itga8* and *Sec61a2* that were enriched to 'Antigen processing cross presentation', a pathway related specifically to the adaptive immune response through MHC class I signalling (Table 3.3). MHC I peptide presentation enables CD8+ T cells to identify viral antigens or neoantigens for cell elimination (Dhatchinamoorthy et al. 2021). Many cancers, including prostate adenocarcinoma, have displayed loss of MHC I expression to assist with immune evasion (Dhatchinamoorthy et al. 2021), therefore this association via eGSEA suggests that the *PBiCre$^{+/-}$; Pik3ca $^{+/H1047R}$; Pten$^{fl/fl}$* CRPC model may utilise this type of mechanism for tumour survival.

It is also important to note, that due to the more aggressive phenotypes generated within the castrated *PBiCre$^{+/-}$; Pik3ca $^{+/H1047R}$; Pten$^{fl/fl}$*, it is possible that these tumours contained a disproportionate stroma:tumour ratio relative to the *PBiCre$^{+/-}$; Pten$^{fl/fl}$* CRPC model. To date, methods for normalisation of stromal content within bulk RNA-Seq have been relatively unsuccessful, however have been shown to be more effective within single cell RNA-Seq data (Gong et al. 2021). Notably, high stromal content has been linked to invasive potential and therapeutic resistance (Valkenburg et al. 2018), thus indicating that if compound mutants CRPC tumours do comprise a higher stromal content than *Pten*-deficient CRPC tumours, they are likely to possess higher metastatic potential.

3.3.4.5. NF-κB, Wnt and p53 signalling is also associated with castrated *Pten*-deleted and *Pik3ca* mutant prostate cancer relative to castrated *Pten*-deficient prostate cancer alone

3.3.4.5.1. NF-κB signalling is deregulated in compound mutant *de novo* CRPC relative to *Pten*-deficient acquired CRPC

eGSEA associated genes protein kinase C gamma (*Prkcg*) and caspase recruitment domain-containing protein 11 (*Card11*) to the enriched pathway "Activated NF-κB signalling in B cells" (Figure 3.16); where both genes were significantly upregulated in the castrated compound mutant tumours relative to the *Pten*-deficient tumours. Interestingly, the RPPA analysis initially performed on castrated *PBiCre$^{+/-}$ Pik3ca$^{+/HR}$; Pten$^{fl/fl}$* tumours and castrated *PBiCre$^{+/-}$ Pten$^{fl/fl}$* tumours identified expression of phosphorylated PKCγ protein to be lower in the compound mutant tumours relative to the *Pten*-null model alone (Pearson et al., 2018), thus suggesting less activation. PKCγ function within cancer is not well established, however recent studies in colon cancer have suggested a key role in colony forming and migratory capacity (Dowling et al. 2017).

In contrast, the second enriched gene *Card11* (also known as *Carma1*), has well known associations within the NF-κB pathway; with CARD11 playing key roles in both B-cell receptor (BCR)- and T-cell receptor (TCR)- induced NF-κB activation through recruitment and binding of B-cell lymphoma 10 (BCL10) and mucosa-associated lymphoid tissue lymphoma translocation protein 1 (MALT1), leading to recruitment of the IKK complex for consequent NF-κB activation (Jiang & Lin, 2012). Interestingly, CARD11 also has a transcription factor binding site for the p50 NF-κB subunit (Appendix 8).

Of interest, *RelB* mRNA expression was identified to be significantly higher within the castrated *PBiCre$^{+/-}$ Pik3ca$^{+/H1047R}$; Pten$^{fl/fl}$* model tumours relative to the castrated *PBiCre$^{+/-}$; Pten$^{fl/fl}$* tumours (Figure 3.14), suggesting depleted androgen signalling may be a contributing factor in driving upregulation of *RelB*. *RelB* however is not directly activated or repressed by AR but instead possesses a regulatory transcriptional binding site for glucocorticoid receptors (GR) (Appendix 7). GR signalling has been identified as a compensatory mechanism utilised by tumour cells in castrate environments due to shared transcriptional targets with AR (Isikbay et al., 2014), and may therefore also play an important role in mediating transcription of *RelB*.

Taken together, these findings indicate that NF-κB signalling in the castrated compound mutant may not be downregulated as suggested by the eGSEA association, given the upregulation of *Card11* as identified by RNA-Seq and upregulation of *RelB* as identified by qRT-PCR. Therefore further work will be required to determine whether NF-κB signalling is up or downregulated in the castrated *PBiCre$^{+/-}$ Pik3ca$^{+/H1047R}$; Pten$^{fl/fl}$* tumour model relative to the castrated *PBiCre$^{+/-}$ Pten$^{fl/fl}$* model and the impact this has on developing resistance to ADT.

3.3.4.5.2. Wnt and p53 signalling is downregulated in compound mutant *de novo* CRPC relative to *Pten*-deficient acquired

Additionally, pathways associated to Wnt and p53 signalling were identified by eGSEA, indicting downregulation of these pathway in the castrated double mutant model relative to the castrated *Pten*-null model (Figure 3.15). Interestingly, no significantly deregulated genes based on our criteria, were identified within these pathways and thus were not further explored in detail. In depth investigation is therefore needed to determine the true extent of the deregulation within these pathways and to establish their role during CRPC transition.

3.3.5. NF-κB transcription factor protein expression corresponds with transcriptional differences seen within the GEMM prostate tumour models

To evaluate whether the changes seen within the NF-κB pathway at a transcriptional level occurred and/or were maintained at a translational level, IHC to detect the status and localisation of several NF-κB pathway components was performed on FFPE tissue sections of *PBiCre*$^{+/-}$ wildtype, *Pik3ca*$^{+/H1047R}$, *Pten*$^{f/fl}$ and *Pik3ca*$^{+/H1047R}$; *Pten*$^{f/fl}$ prostate (n = 3 / genotype); more specifically for assessment of non-canonical subunits RelB and p52, and canonical subunits p50 and RelA (p65). As NF-κB can either be present within the cell nucleus (active) or sequestered within the cytoplasm by inhibitory proteins (inactive) (Albensi 2019), visual detection of these proteins by IHC enables a better understanding of how they are mechanistically contributing to the phenotypes generated within the various models.

IHC to detect RelB, revealed nuclear localisation of RelB was present in all prostate lobes and genotypes analysed, indicating activation of the non-canonical NF-κB pathway (Figure 3.17).

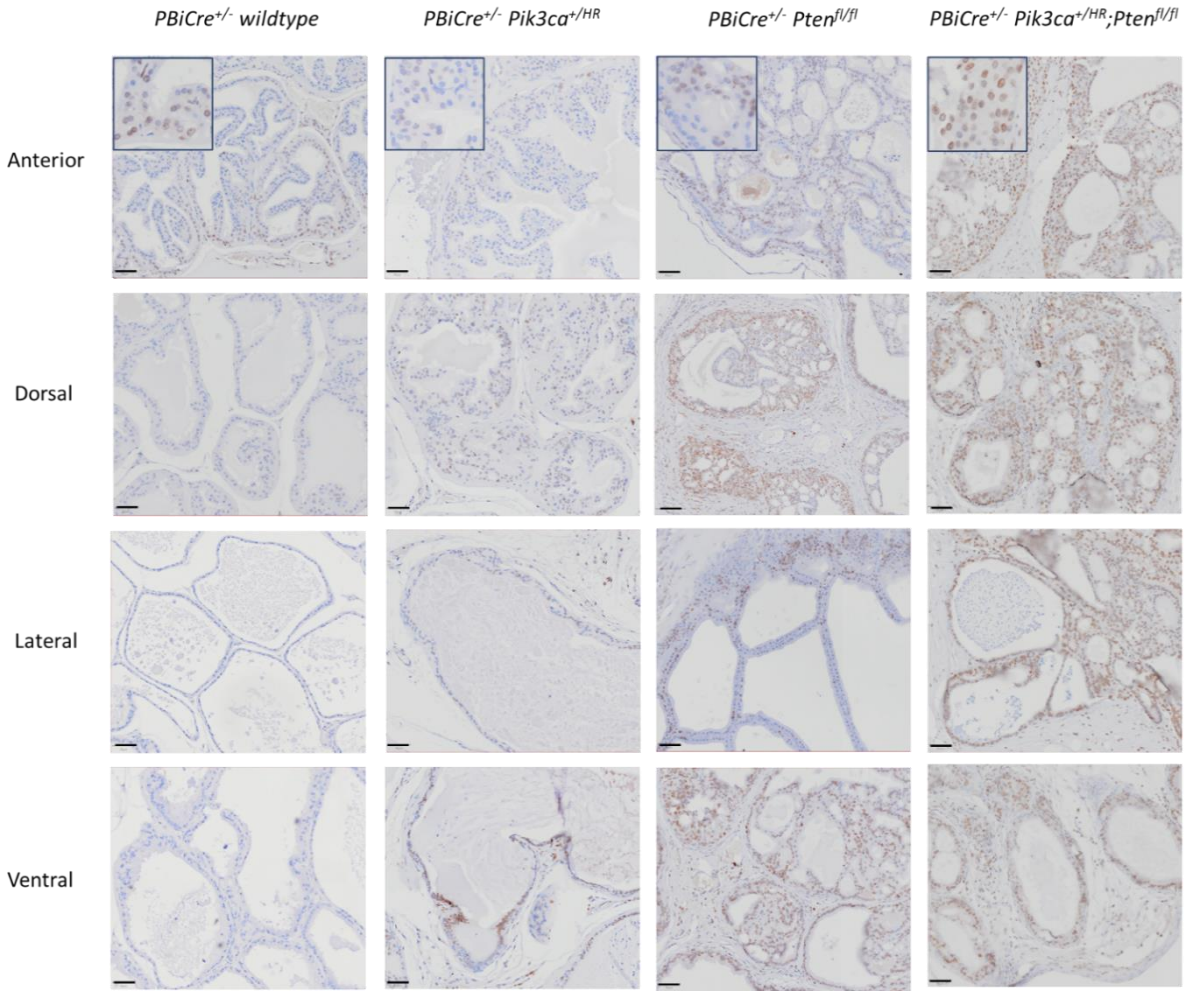

Figure 3.17: Active, nuclear RELB is augmented in *Pten*-deficient prostate cancer relative to *Pik3ca*-mutant prostate cancer. Representative images of RelB IHC in all mouse prostate lobes from *PBiCre*$^{+/-}$ wildtype prostate tissue and stage-matched *Pik3c*a-hyperactivated, *Pten*-null and double mutant tumours (10x magnification, scale bar = 50 µm).

Quantitation revealed a statistically significant increase in the number of RelB-positive prostate epithelial cells in *Pten*-deficient and *Pik3ca*$^{+/HR}$; *Pten*$^{fl/fl}$ compound mutant tumours relative to *Pik3ca*-mutant and wildtype controls. Moreover, there was a further significant 1.75-fold increase in compound mutants relative to PTEN loss alone (Figure 3.18). These findings indicate that RelB activation facilitates *Pten*-deficient prostate cancer, and not *Pik3ca*-mutant prostate cancer, presenting a putative PI3K-independent target for prostate cancer patients with PTEN loss. Importantly, these finding correlate with the *RelB* mRNA expression data (discussed in Section 3.3.3.5, Figure 3.9).

Furthermore, these data provide new insight into how these two genetic drivers might cooperate to accelerate tumour growth. In addition to the previously reported hyperactivation of AKT and elevated mTORC1 signalling identified within the compound mutant model (Pearson et al., 2018), *Pik3ca* and *Pten* genetic alterations may also cooperate to accelerate tumour progression via augmented RelB-mediated non-canonical NF-κB signalling.

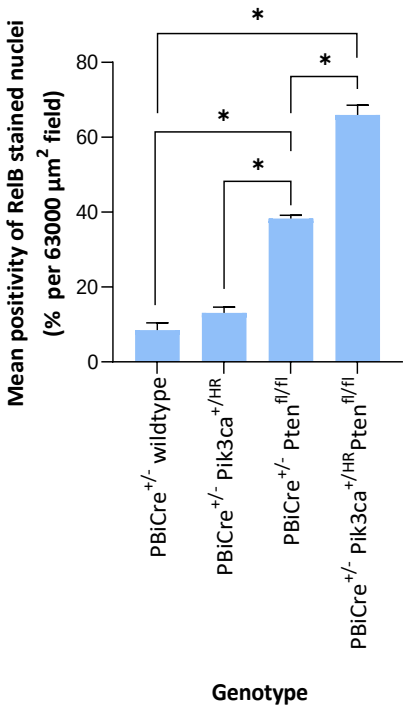

Figure 3.18: RELB activity is augmented in *Pten*-deficient prostate cancer relative to *Pik3ca*-mutant prostate cancer. Quantitation of RelB positive cells detected by IHC nuclear staining of whole prostate tissues from *PBiCre*$^{+/-}$ wildtype and stage matched locally invasive *Pten*-deficient, *Pik3ca*-hyperactivated and double mutant prostate carcinomas (n = 3/genotype). Data shown is the quantitation of all prostate lobes combined. Statistical analysis was performed via a One-way ANOVA with a Tukey's multiple comparison test.

Unfortunately, optimisation of IHC to detect p52, the second key transcription factor involved in non-canonical NF-κB signalling, was attempted but unsuccessful. Nevertheless, RNA-Seq data revealed a small, yet significant 0.5-fold change in *Nfkb2* expression within *PBiCre*$^{+/-}$ *Pten*$^{f/fl}$ tumours relative to *PBiCre*$^{+/-}$ *Pik3ca*$^{+/H1047R}$ stage-matched tumours, supporting the concept that non-canonical NF-κB signalling is augmented in PTEN-deficient prostate tumours, however further work will be required to confirm contributions from p52.

IHC to detect RelA (p65) and p50 was subsequently performed, to determine the activation status of the main transcription factor duo essential for canonical NF-κB signalling. Negligible levels of p65 were observed in *Pik3ca*-mutant prostate tumours and weak cytoplasmic staining was present within the *Pten*-deficient tumours. Staining was also observed in the compound mutant tumours (Figure 3.19). IHC Staining for p50 also mirrored these cytoplasmic findings, with staining detected in all genotypes assessed (Figure 3.20).

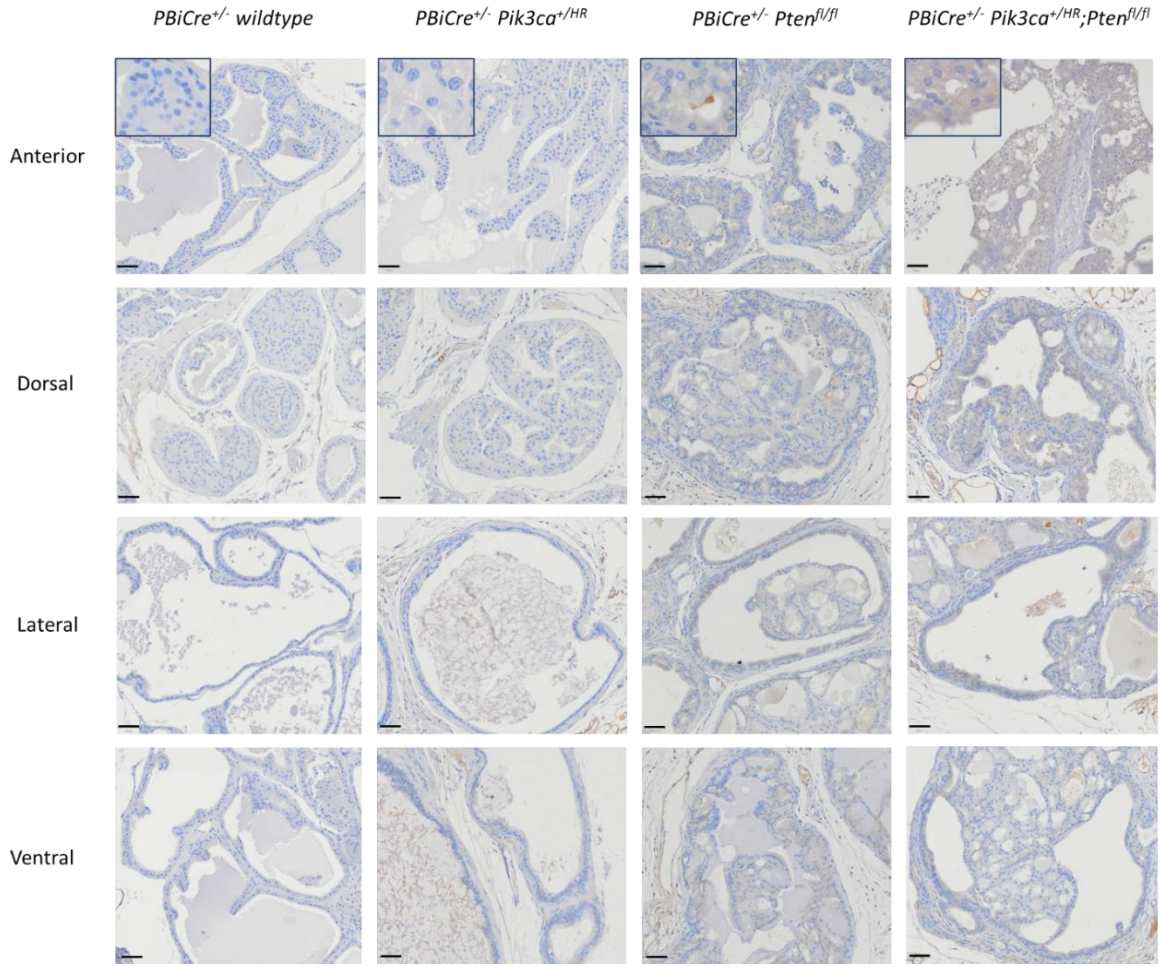

Figure 3.19: Increased cytoplasmic p65 is detected in *Pten*-deficient prostate cancer relative to *Pik3ca*-mutant prostate cancer. Representative images of p65 IHC in all mouse prostate lobes from *PBiCre*$^{+/-}$ wildtype prostate tissue and stage-matched *Pik3c*a-hyperactivated, *Pten*-null and double mutant tumours (10x magnification, scale bar = 50 µm).

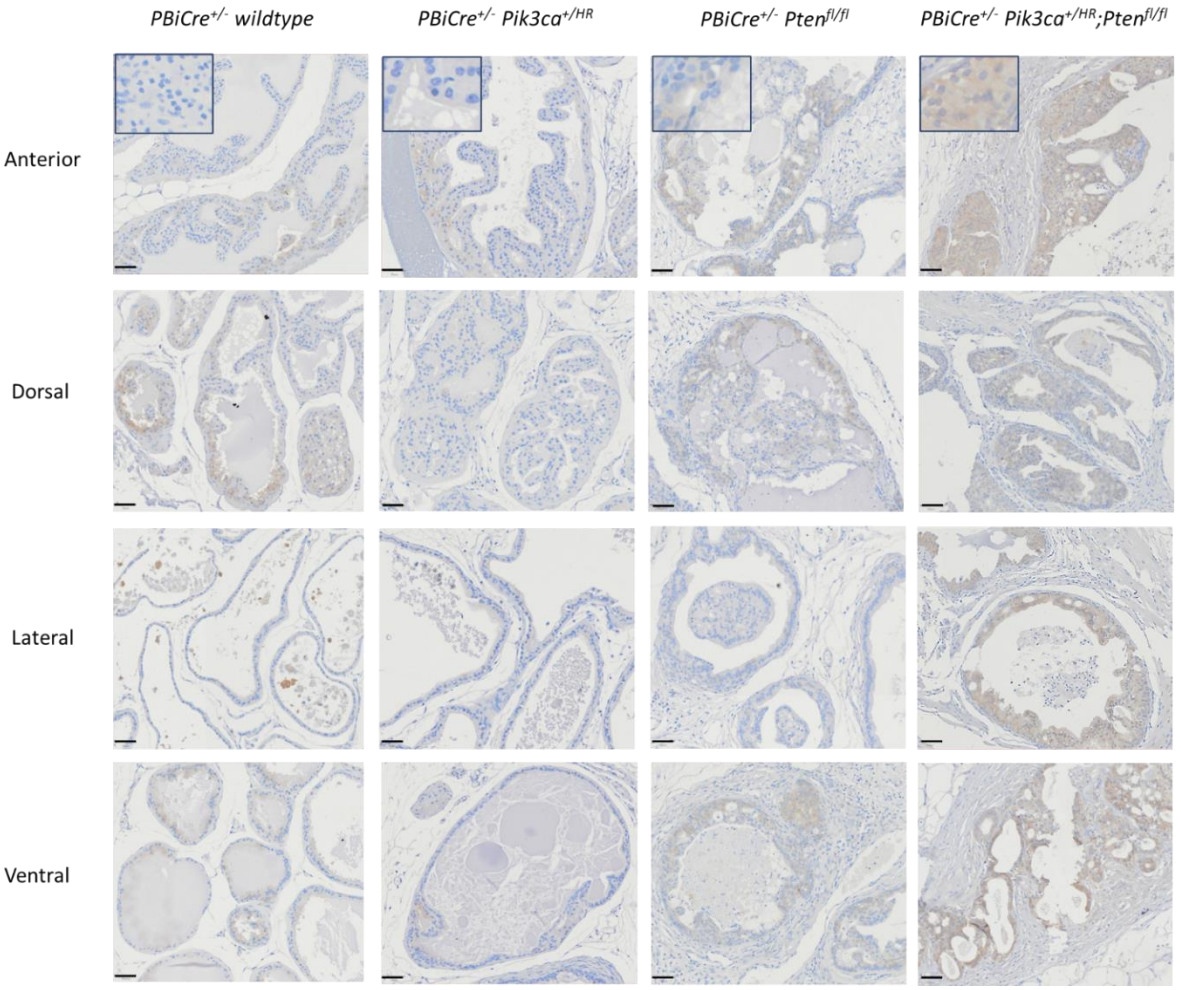

Figure 3.20: Cytoplasmic p50 is detected in both *Pten*-deficient prostate cancer and *Pik3ca*-mutant prostate cancer. Representative images of p50 IHC in all mouse prostate lobes from *PBiCre*$^{+/-}$ wildtype prostate tissue and stage-matched *Pik3c*a-hyperactivated, *Pten*-null and double mutant tumours (10x magnification, scale bar = 50 µm).

Although RNA-Seq fold change expression data for *Nfkb1* was not significant, staining showed higher levels of p50 within the models harbouring *Pten* loss, therefore it may be beneficial to perform western blotting to fully confirm the accuracy of p105/p50 expression. Despite this, the IHC data indicates the transcriptional outputs identified by RNA-Sequencing, also provide a comparative insight into levels of NF-κB protein expression within the tumours.

In support of the IHC data, mRNA expression of *RelA* (*p65*) and *Nfkb1* (*p50*), showed to be insignificantly deregulated when comparing *Pten*-deficient and *Pik3ca*-mutant prostate tumour RNA-Seq data (Log_2 fold change 0.6835, adj. P value = 0.0002, and Log_2 fold change value -0.0892, adj. P value = 0.49177 respectively). Taken together, these findings strongly indicate that p65-mediated activation of the canonical NF-κB pathway does not facilitate *Pik3ca*-mutant nor *Pten*-deficient prostate cancer growth. Although many mRNA targets of the canonical pathway were shown to be upregulated in *Pten*-null tumours relative to *Pik3ca*-mutant tumours (Table 3.2), this IHC data suggests additional upstream regulators may be involved in mediating increased expression of canonical NF-κB pathway target genes.

3.3.6. *Pten*-deficient and *Pik3ca*-hyperactived GEMM prostate carcinomas display altered immune profiles

Given the stark transcriptional upregulation of genes involved in inflammation including cytokines and pattern-recognition receptors and the observed activation/nuclear localisation of the NF-κB non-canonical subunit RelB within the *PBiCre$^{+/-}$; Pten $^{fl/fl}$* model in contrast to *Pik3ca*-mutant prostate cancer, it is likely that there is also a tumour immune-microenvironment difference between the two models that could influence tumour progression.

Given the time constraints, to gain an initial insight into which immune cells could be contributing to the phenotypes observed, complete RNA-Seq matrix read data was inputted into TIMER2.0 software (Dana Farber Cancer Institute – http://timer.cistrome.org/ (Li et al. 2020), for an estimation of immune filtration within each tumour type using several independent immune deconvolution models. Deconvolution is a computational approach that utilises bulk transcriptome profiling data to estimate the relative abundance of immune cell subtypes from a mixture of cells based on expression data (Chiu et al. 2019).

To identify immune infiltrate differences between *PBiCre$^{+/-}$; Pik3ca $^{+/H1047R}$* and *PBiCre$^{+/-}$; Pten $^{fl/fl}$* prostate tumours, RNA-Seq outputs from both models were inputted into TIMER2.0 for evaluation

against TCGA prostate adenocarcinoma datasets. Results from each deconvolution model were plotted for a side-by side comparison (Figure 3.21).

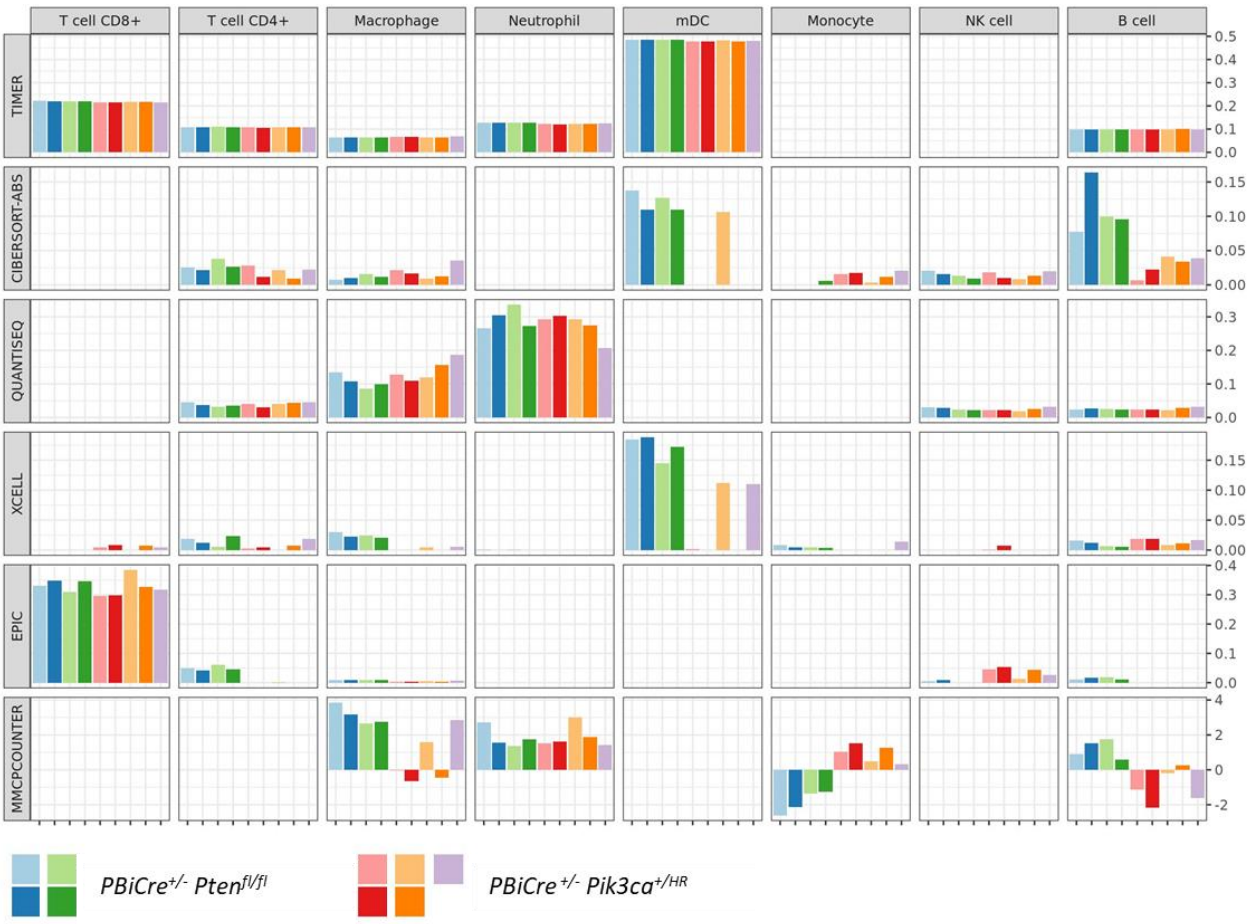

Figure 3.21: Estimates of immune cell infiltration levels within *Pten*-deficient prostate cancer and *Pik3ca*-mutant prostate cancer. Graphs show immune cell estimates from TIMER2.0. analysis of *PBiCre*$^{+/-}$ *Pten*$^{fl/fl}$ and *PBiCre*$^{+/-}$ *Pik3ca*$^{+/H1047R}$ GEMM RNA-Seq data (n = 4 / 5, 200 and 300 d old, ventral prostate carcinoma respectively). Significance of this data was not determined.

Interestingly there was limited cohesion between the different deconvolution models, thus the data is difficult to interpret without direct quantitation of the immune populations, probably attributable to the fact that many of the deconvolution models used were not mouse-specific with the exemption of mMCP-counter. Although TIMER2.0 documentation states that mouse gene IDs are converted to orthologous human gene IDs, cautious interpretation is still due to potential discrepancies between human and mouse tumour immune properties (Li et al. 2020). For example, most of the models indicated little to no presence of CD8+ T cells in *Pik3ca*-hyperactivated and *Pten*-deleted prostate cancer whereas the TIMER and EPIC models displayed a relatively high incidence of CD8+ T cells within both tumour types; despite evidence suggesting that *PTEN* loss and genomic gain of *PIK3CA* is

associated with a reduction in CD8+ T cells within a range of different cancer types, as established by xCell based cell type enrichment analysis on TCGA RNA-seq data (Lin et al. 2021b).

Nevertheless, several deconvolution models indicated a high level of macrophages present within the *PBiCre$^{+/-}$; Pten $^{fl/fl}$* model (xCell, EPIC and mMCP-counter), which was relatively comparable to the *PBiCre$^{+/-}$; Pik3ca $^{+/H1047R}$* tumours, possibly indicating macrophages play a role during both Pik3ca-mutant and Pten-deficient prostate tumour growth. However, due to the large-scale variance in results, the data generated appears unreliable and further work is needed to determine the true status of the immune populations in these models, and to determine the accuracy of these deconvolution models.

To better determine any immune cell population differences between *Pten*-deficient and *Pik3ca*-mutant prostate tumours, mast cells were detected by toluidine blue staining of FFPE sections from *PBiCre$^{+/-}$; Pik3ca $^{+/H1047R}$* and *PBiCre$^{+/-}$; Pten $^{fl/fl}$* prostate tumours. Visual analysis of toluidine blue staining indicated an increased abundance of mast cells present within the *PBiCre$^{+/-}$; Pten $^{fl/fl}$* tumours relative to the *PBiCre$^{+/-}$; Pik3ca $^{+/H1047R}$* and wildtype prostate tissue, with even higher expression prominent within the compound mutant (Figure 3.22).

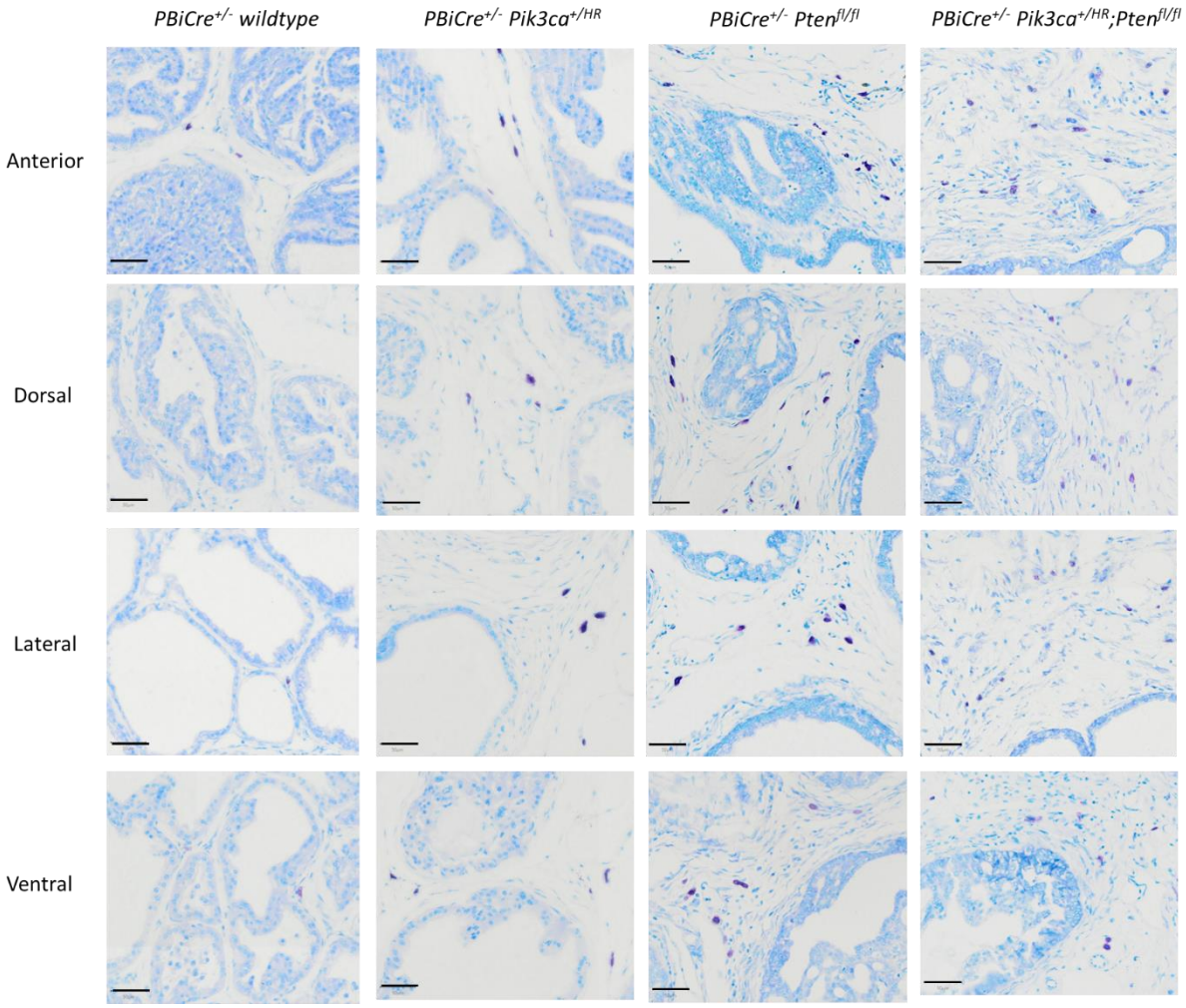

Figure 3.21: Mast cell presence is augmented in *Pten*-deficient prostate cancer relative to *Pik3ca*-mutant prostate cancer. Representative images of toluidine blue staining of mast cells (shown in purple) in each mouse prostate lobe within wildtype, *Pten*-null, *Pik3c*a-hyperactivated and double mutant tumours. Images displayed show 10x magnification images, scale bar = 50 µm.

It is interesting that mast cells, which secrete various peptidases, proteases and proinflammatory cytokines that contribute to activation of processes such as angiogenesis and pathogen elimination, have also been recently associated with promoting biliary and cholangial senescence (Kundu et al. 2020). In addition, it has also been noted that an increased accumulation of mast cells correlates with a worsened prognosis, increased metastasis and reduced survival in cancers such as squamous cell carcinoma, melanoma and even prostate cancer (Maciel et al. 2015), further supporting an extensive role for the immune and inflammatory responses in tumour progression.

3.3.7. NF-κB signalling is upregulated in patients with *PTEN*-deficient prostate cancer

To determine whether the RNA-Seq data indicating that *Pten*-deficient prostate cancer displays elevated NF-κB signalling relative to *Pik3ca*-mutant prostate cancer tumours in mice is clinically relevant, four large-scale human prostate adenocarcinoma transcriptomic studies covering the various stages of prostate cancer were selected from the cBioPortal database (Table 3.5) (Cerami et al., 2012) (Gao et al., 2013) for assessment. Enriched NF-κB related mouse genes identified within the intact *PBiCre*$^{+/-}$*; Pten* $^{fl/fl}$ model relative to the *PBiCre*$^{+/-}$*; Pik3ca* $^{+/H1047R}$ model (Figure 3.8) were inputted into the query by gene function for assessment of increased mRNA expression, increased copy number and gene co-occurrence with *PTEN* homozygous deletion in human prostate cancer.

Table 3.5: Human prostate transcriptomic study data used for establishing human relevancy of mouse data.

Human prostate adenocarcinoma study	Cohort size and sample type
Memorial Sloan-Kettering Cancer Centre (MSKCC) (Taylor et al. 2010)	218 samples (181 primaries, 37 metastases) and 14 prostate cancer cell lines and xenografts)
The Cancer Genome Atlas (TCGA), Firehose Legacy (2015)	499 samples (primary, prostate adenocarcinoma)
Michigan Center for Translational Pathology (MCTP) (Grasso et al. 2012)	61 samples (50 metastatic CRPCs and 11 high-grade localised prostate cancers)
Stand Up 2 Cancer/ Prostate Cancer Foundation (SU2C/PCF Dream Team) (Abida et al. 2019)	444 CRPC samples compared to matched normal tissue

Analysis revealed various high percentage alterations within the queried set of genes, particularly when looking at copy number amplification or gain within the metastatic MTCP and SU2C/PCF datasets, indicating these genetic alterations correlate with disease progression (Table 3.6). Interestingly, *TNFSF10* (highlighted in Table 3.6) was identified to be commonly, and highly altered amongst all human datasets, with respect to copy number alteration, but not mRNA expression. *TNFSF10* encodes the tumour necrosis factor (TNF)–related apoptosis-inducing ligand, also known as

TRAIL, that facilitates apoptosis through initiation of death inducing signalling complexes. TRAIL-induced NF-κB pathway signalling, can drive evasion of TRAIL-mediated apoptosis, with resistance evidenced in cancers such as leukaemia and myeloma (Whang et al. 2004), suggesting TRAIL may be involved in anti-apoptotic mechanisms, possibly driven through NF-κB, that enables further growth and proliferation of cells within the *Pten*-deficient prostate tumour model. This finding warrants further work exploring the effect of NF-κB mediated TRAIL signalling in PTEN-null prostate cancer and whether the alterations observed in TRAIL expression are driven by PI3K dependent or independent events.

Table 3.6: Comparative table of alteration frequencies in NF-κB related genes within clinical localised and metastatic prostate cancer datasets. Increased mRNA expression indicates expression greater than two standard deviations above the mean.

Gene	Copy number alteration: amplification frequency (%)				Copy number alteration: gain frequency (%)				Increased mRNA expression frequency (%)			
	MSKCC	TCGA	MCTP	SU2C	MSKCC	TCGA	MCTP	SU2C	MSKCC	TCGA	MCTP	SU2C
TAP1	0	0.2	0	2.7	3.33	3.46	8.2	20.0	11.67	4.07	N/A	1.58%
CD44	0.56	0	0	0.9	2.78	4.88	0	13.51	5	2.85	N/A	1.13
ICAM1	0	0	0	1.8	1.11	1.83	8.2	10.14	12.22	4.07	N/A	2.7
TNC	0	1.22	0	4.28	5.56	9.35	16.39	25	2.22	4.07	N/A	2.25
VCAM1	0	0.41	0	0.45	0.56	1.22	1.61	10.59	7.78	3.66	N/A	1.8
CCL4	1.67	0	0	2.03	2.78	2.64	6.56	14.41	15	5.89	N/A	1.35
CCL20	0.56	0.2	0	1.58	2.22	1.42	1.64	11.26	1.11	3.05	N/A	0.45
CCL22	0	0	0	1.13	0.56	1.42	3.28	6.31	5	3.05	N/A	2.03
CXCL1	0.56	0.2	4.92	5.18	2.22	3.66	6.56	15.54	1.67	3.66	N/A	0.68
CXCL11	0	0.2	4.92	2.48	1.67	2.85	9.84	14.64	13.33	4.27	N/A	1.13
CXCL3	0.56	0.41	4.92	4.5	2.22	3.86	6.56	15.54	1.67	2.03	N/A	1.58
CXCL5	0.56	0.41	4.92	4.73	2.22	3.66	6.56	15.54	1.67	2.64	N/A	0.45
IL1A	0	0	0	1.8	2.78	1.63	1.64	8.58	3.33	1.42	N/A	0.23
IL1B	0	0	0	1.8	3.33	1.63	1.64	8.33	0.56	2.85	N/A	0.23
IL1RN	0	0	0	1.8	2.78	1.42	3.28	8.11	3.89	2.44	N/A	0.45
CXCL8	0.56	0.41	6.56	4.73	2.22	3.46	6.56	16.22	0	3.05	N/A	0.23
TNF	0	0	1.64	2.7	3.33	3.05	9.84	20.27	1.11	3.25	N/A	2.03
TNFSF10	0	2.03	6.56	8.33	5.56	11.38	22.95	32.21	2.22	2.85	N/A	1.13
CCR7	0	0	0	2.93	1.67	1.42	6.56	15.77	6.11	2.85	N/A	1.35
CD83	0.56	0	0	2.93	2.22	3.66	4.92	14.86	2.22	4.07	N/A	1.35
TLR2	0	0.2	1.64	2.7	2.22	2.64	8.2	11.94	2.22	3.25	N/A	1.35
TNFRSF9	0	0.41	0	0.45	1.11	0.81	1.64	9.91	12.22	2.44	N/A	1.58
MMP3	0	0.2	1.64	1.35	2.78	6.5	6.56	15.32	0.56	0.41	N/A	0.9
NOS2	0.56	0.4	0	2.7	2.22	2.03	11.48	13.74	2.22	2.03	N/A	1.35
BCL3	0	0.2	0	2.25	1.67	1.63	9.84	11.04	5	5.49	N/A	1.58
IRF7	0	0	0	1.8	4.44	4.88	1.64	10.81	5.56	4.27	N/A	1.58
NFKBIE	0	0	0	2.98	2.78	3.46	18.03	18.24	5.56	5.69	N/A	2.03
RELB	0	0.2	0	1.58	1.67	1.63	4.92	12.16	3.89	5.08	N/A	3.38
TNFAIP3	0	0	0	2.25	1.67	1.22	3.28	14.64	2.78	3.86	N/A	2.25

For all genes identified to be significantly upregulated following loss of *Pten* within the GEMM, frequency of NF-κB related gene co-occurrence with *PTEN* homozygous deletion in human prostate cancer was also assessed for clinical relevance using the same datasets listed in Table 3.5. Through functions present on cBioPortal, this was explored, with data revealing presence of clinical co-occurrence between *PTEN* homozygous deletion and 8 NF-κB related genes *(*Table 3.7). Whilst none of the results were identified to be significant, this could be attributed to the relatively low sample size assessed. Regardless, associations were made for *CXCL8* and *NOS2* in human PTEN-deficient prostate cancer, suggesting an importance of these two genes, which could also function as effective therapeutic targets.

Table 3.7: Co-occurrence tendency between *PTEN* homozygous deletion and the presence of NF-κB related gene expression within prostate cancer patients. Using the cBioPortal platform, clinical data from 1244 patient samples (Table 3.5) were screened for co-occurrence data. P values were derived using the one-sided Fisher exact test and q values using the Benjamini-Hochberg FDR correction test.

Gene alteration	Secondary gene	Log_2 odds ratio	p value	q value
PTEN: HOMDEL	*CCL22*	0.605	0.174	0.306
PTEN: HOMDEL	*NOS2*	0.649	0.188	0.323
PTEN: HOMDEL	*TNFSF10*	0.324	0.267	0.396
PTEN: HOMDEL	*CCL4*	0.58	0.314	0.428
PTEN: HOMDEL	*CXCL8*	0.126	0.486	0.563
PTEN: HOMDEL	*IL1A*	0.125	0.522	0.592
PTEN: HOMDEL	*IL1B*	0.125	0.522	0.592
PTEN: HOMDEL	*CCL22*	0.605	0.174	0.306

Taken together with our RNA-Seq and eGSEA data, these findings have identified a clinically relevant panel of putative PI3K-independent therapeutic targets for PTEN-deficient prostate cancer that may assist in improving patient responses to currently available treatments, including existing PI3K pathway therapies. Furthermore, the panel could also be used as biomarkers and warrant further high-throughput analysis.

3.4. Discussion

PTEN-deficient prostate cancer is prevalent in the clinic, correlating with worsened outcomes due to the lack of response to current therapies; highlighting a clear clinical need for novel treatments. To combat this lethal form of prostate cancer driven by PTEN loss, we aimed to identify targetable PI3K-independent functions of PTEN via transcriptomic comparison of the well-established *PBiCre*$^{+/-}$ *Pten*$^{fl/fl}$ prostate tumour model with the novel PIK3CA-hyperactivated transgenic model (Pearson et al. 2018).

Through the analysis of RNA-Sequencing data and eGSEA outputs comparing *Pik3ca*-mutant and *Pten*-deficient prostate cancer, novel mechanistic insight into how these two genetic drivers of the PI3K cascade promote prostate tumorigeneses has been identified. This chapter reveals for the first time that elevated NF-κB signalling is augmented in *Pten*-deficient prostate cancer and not *Pik3ca*-mutant prostate cancer and may therefore provide a new PI3K-independent therapeutic target for PTEN-deficient prostate cancer and contributing molecular mechanism for the accelerated rate of prostate tumour onset and progression observed in the *PBiCre*$^{+/-}$*; Pten*$^{fl/fl}$ model relative to the *PBiCre*$^{+/-}$*; Pik3ca* $^{+/H1047R}$ model (Pearson et al., 2018).

In support, activated focal adhesion kinase (FAK) signalling and consequent NF-κB activation following PTEN loss is reported to be a PI3K-independent compensatory survival mechanism in *PTEN*-null T-cell acute lymphoblastic leukaemia (ALL) *in vitro* (You et al. 2015). Despite evidence indicating that FAK can also be activated by AKT through phosphorylation events (Alfieri et al. 2017), You et al additionally demonstrated a direct relationship between PTEN and FAK, whereby PTEN could bind to FAK in a phosphatase independent manner both in JURKAT and ALL cells (You et al. 2015). Within the *PBiCre*$^{+/-}$*; Pten*$^{fl/fl}$ model, *Pten* loss does not appear to increase *Ptk2* (gene encoding FAK) expression when compared to the *PBiCre*$^{+/-}$*; Pik3ca*$^{+/H1047R}$ model (Log_2 fold change; 0.056, adj. P value 0.464), however results from the reverse phase protein array (RPPA) analysis previously performed show an increase in FAK protein following *Pten* loss relative to *Pik3ca*-hyperactivation (Pearson et al. 2018). FAK may therefore be involved in the PI3K-independent activation of NF-κB within the *Pten*-null prostate tumours, but further investigation would be required to determine if this is the mechanism in play.

The RNA-Seq findings imply that both the canonical and non-canonical NF-κB signalling axes are being deregulated following *Pten* loss, however due to the significant upregulation of RelB mRNA and protein, our data suggests that *Pten*-deletion can mediate upregulation of non-canonical NF-κB signalling. This type of event has not been explicitly documented in prostate cancer; although studies have suggested that multiple myeloma has a particular dependence on non-canonical NF-κB activation, and estrogen receptor (ER) negative breast cancer can also be reliant on upregulated non-

canonical NF-κB signalling, driving self-renewal of tumour cells and epithelial to mesenchymal transition (EMT) (Tegowski and Baldwin 2018).

It is understood that both NF-κB signalling axes do not function in isolation, with cross talk occurring between the two pathways, therefore the significant upregulation of *RelB* seen within the *PBiCre$^{+/-}$; Pten $^{fl/fl}$* tumours could have been a consequence of canonical NF-κB (RelA dependent) activation, which has been shown to initiate transcription of *RelB* (Tegowski and Baldwin 2018), yet neither the gene expression data or immunohistochemical staining of the prostate tumours support this. Although many of the canonical NF-κB target genes are significantly upregulated (Table 3.3), transcriptional and translational levels of p65 and p50 are considerably low, suggesting that expression of the canonical-specific target genes may be regulated via other mechanisms and that activation and signalling through the non-canonical NF-κB pathway alone may be an essential driver of *Pten*-deficient prostate cancer.

With such a strong NF-κB signature identified through eGSEA, it can be hypothesised that loss of *Pten* within the mouse prostate drives chronic inflammation and the development of a pro-tumorigenic environment, substantially increasing NF-κB signalling events to further drive malignant prostate growth. Additional studies investigating the immune landscapes and the metabolome of the intact *PBiCre$^{+/-}$; Pik3ca $^{+/H1047R}$* and *PBiCre$^{+/-}$; Pten $^{fl/fl}$* tumour models and their contribution to the phenotypes observed would be very insightful, such as performing the Nanostring GeoMx protein assay for immune-oncology.

PTEN loss has also been shown to contribute to cell senescence due to stress driven by excessive cell proliferation (Parisotto et al. 2019), therefore there may also be a senescence associated secretory phenotype (SASP) within the *PBiCre$^{+/-}$; Pten $^{fl/fl}$* tumour model due to the upregulation of various extracellular modulators and signalling via NF-κB (Lopes-Paciencia et al. 2019). For an initial insight, fold change data calculated using RNA-Sequencing process, for genes encoding p21 and p16 were assessed. *Cdkn1a* appeared to be downregulated (Log_2 fold change; -1.05 / adj. P value 0.003) whereas *Cdkn2a* was significantly upregulated (Log_2 fold change value; 3.03, adj. P value 5.36E-06) following *Pten* deletion, relative to Pik3ca-hyperactivation.

There was an expectation that if senescence was occurring within the cells of the *Pten*-null tumour, p53 would cause overexpression of p21 (Lleonart et al. 2011), however the transcriptomic data did not show this. To address this in the future, senescence-associated β-galactosidase (SA-β-gal) staining could be performed for indication of DNA damage-induced senescence, or senescence-associated

heterochromatin foci (SAHF) staining could be performed for indication of oncogene-induced senescence (Noren Hooten and Evans 2017).

The key results obtained by the RNA-Seq and bioinformatic analyses performed however, suggest oncogenic activation of NF-κB within the prostate is a direct consequence of *Pten* loss alone, that could consequently be defined as a PI3K-independent mechanism. It is of both high scientific and clinical importance to further explore this finding, in which use of PI3K and NF-κB inhibitors will be requisite in doing so. Not only will this ascertain whether NF-κB signalling still occurs in a PTEN deficient setting when a PI3K pathway inhibitor is administered but will also determine if there is a therapeutic benefit in combining use of both pathway inhibitors for patients with PTEN-null prostate cancer.

With our RNA-Seq and eGSEA data suggesting a clear role of NF-κB signalling within PTEN-deleted prostate cancer, it seems firstly imperative that a general NF-κB inhibitor should be trialled as a proof-of-concept experiment. A frequently used NF-κB pathway inhibitor such as BAY 11-7082, that has also been shown to inhibit TNF-α-induced surface expression of ICAM-1 and VCAM-1 (Pierce et al. 1997), would be ideal, given how genes encoding those proteins were significantly upregulated within the *Pten*-deficient prostate tumours (Figure 3.8) and frequently altered in human prostate cancer (Table 3.4). Since *Cxcl1*/*2/3/8* were upregulated in a large number of pathways identified by eGSEA (Figure 3.6), targeting the CXCR1 and CXCR2 receptors required for their signalling, may also be of great therapeutic interest.

PBiCre$^{+/-}$ *Pten*$^{fl/fl}$ tumours also displayed a significant upregulation of *Tlr2*, *Il1a* and *Nos2* mRNA relative to *Pik3ca*-mutant tumours, suggesting heightened activation and increased signalling of the toll-like receptor 2 - myeloid differentiation primary response gene 88 (TLR2-MyD88) signalling pathway, which has been shown to drive production of proinflammatory cytokines through induction of NF-κB subunit nuclear translocation (Zheng et al. 2019). Therefore, targeting the TLR2 pathway in *PTEN*-deficient prostate cancer could also provide huge insight, which is supported by the correlation within clinical specimens (Table 3.6).

In addition to finding novel targets for invasive carcinoma, it is also hugely important that new drivers of *de novo* CRPC are established to contribute towards development of therapeutics that may be more effective on current non-responders within the clinic.

To do so we utilised the approach of RNA-Seq, however when comparing the castrated *PBiCre*$^{+/-}$*; Pik3ca*$^{+/H1047R}$*; Pten*$^{fl/fl}$ prostate tumour model with the castrated *PBiCre*$^{+/-}$*; Pten*$^{fl/fl}$ model, there were surprisingly few genes deregulated. Even though clear phenotypic differences were observed between the models, very few CRPC transition effects could be determined at the transcriptional level, suggesting post-translational or epigenetic changes may strongly influence or facilitate innate resistance mechanisms.

Despite this, various collagen genes were identified to be significantly upregulated, while eGSEA identified many proteosome and degradation pathways to be downregulated in the castrated compound model relative to the castrated *Pten*-deficient model. To fully understand how these pathways may promote *de novo* castration resistance is yet to be determined however warrants further investigation. With a very limited number of enriched genes recognised and very few also identified as significant under the set criteria, it may be more beneficial to run spatial transcriptomics and proteomics studies to better comprehend signalling mediated directly from the epithelial cells in addition to the contributions of the tumour microenvironment.

Chapter 4

4. Understanding how NF-κB signalling contributes to *Pten*-deficient prostate cancer

4.1. Introduction

As discussed in Chapter 3, RNA-sequencing of *PBiCre*$^{+/-}$ *Pten*$^{fl/fl}$ and *PBiCre*$^{+/-}$ *Pik3ca*$^{+/H1407R}$ prostate tumours provided new insight into key tumorigenic process driven by the loss of PTEN that are not mediated by PI3K. We identified the NF-κB signalling pathway to be significantly upregulated within tumours deficient in *Pten* when compared with tumours driven by hyperactive p110α, the catalytic subunit of Class IA PI3K, and therefore reason that pharmacologically targeting the NF-κB pathway may benefit patients with PTEN-depleted prostate cancer.

Due to the high complexity of the NF-κB signalling cascade, owing to several diverse stimuli, multiple points of activation and a range of downstream targets, it is important to explore NF-κB pathway blockade at different levels of the cascade to delineate how the NF-κB pathway contributes to cancer progression following the loss of PTEN, and to establish which NF-κB pathway inhibitor is the most efficacious.

A number of inhibitors targeting the NF-κB pathway have been developed and are currently being explored as anti-cancer agents. The range of inhibitors available includes those targeting both upstream, and downstream components of the NF-κB pathway (summarised in Figure 4.1 & Table 4.1).

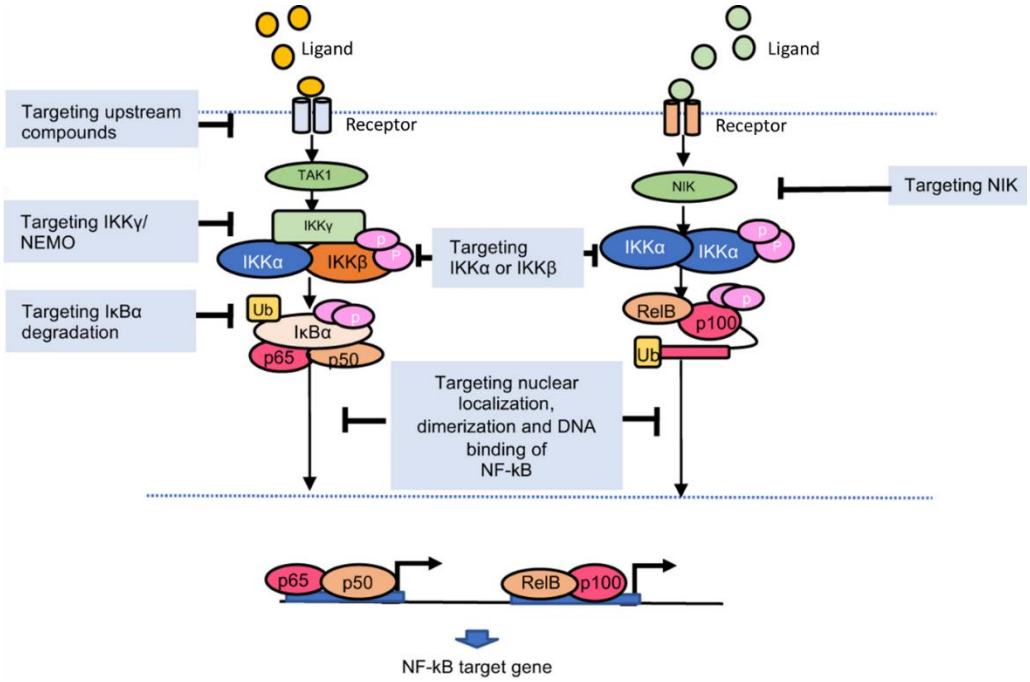

Figure 4.1: Therapeutically targetable arms within the NF-κB signalling pathway. Image adapted from (Khongthong et al. 2019).

Table 4.1: Current treatments for targeting the NF-κB pathway in disease.

NF-κB pathway target	FDA approved / in trial inhibitors
Upstream compounds e.g. TNFα	Infliximab, Adalimumab and Golimumab (Yu et al. 2020)
IKKγ / NEMO	Currently none, due to drug delivery issues (Ramadass et al. 2020)
NIK	TRC694 (Cheng et al. 2021)
IKKα / IKKβ	Sulfasalazine (Ramadass et al. 2020)
IκBα degradation	Aspirin and sodium salicylate (Yu et al. 2020)
Nuclear export	Selinexor (Ramadass et al. 2020)
Subunit binding to DNA	Currently none have been developed (Ramadass et al. 2020)

One generic NF-κB inhibitor, BAY11-7082, that suppresses IκBα phosphorylation whilst increasing its stabilisation to protect against degradation (Dai et al. 2004; Rauert-Wunderlich et al. 2013), has been shown to potently prevent p65 (RelA) mediated NF-κB signalling and inhibit a plethora of biological processes including ERK/AP-1, IRF-3, and JAK/STAT signalling via the suppression of nitric oxide (NO), prostaglandin E_2 and TNF-α release (Lee et al. 2012).

The efficacy of BAY11-7082 has previously been investigated within androgen independent prostate cancer cell lines *in vitro* (Kong et al. 2019), however the impact of PTEN loss has not yet been assessed. Whilst BAY11-7082 has not been used in a clinical setting, owing to observed high toxicity it is widely used to target the canonical NF-κB pathway preclinically (Wang et al. 2018c).

A novel patented small-molecule inhibitor CB1 that targets B cell leukaemia/lymphoma 3 (BCL3), a well characterised oncoprotein and member of the IκB family has recently been developed by Cardiff University in conjunction with Tiziana (Yang 2018). CB1 attaches to the hydrophobic binding pocket within the ankyrin repeat domain of BCL3 to prevent subsequent NF-kB subunit binding (Soukupová et al. 2021).

CB1 treatment of triple negative breast cancer (TNBC) cells recapitulates *Bcl3* siRNA-mediated knockdown, resulting in reduced cell viability *in vitro* and reduced metastatic burden *in vivo* (Yang 2018). In addition to being able to directly upregulate proliferative and anti-apoptotic genes, BCL3 primarily forms stable complexes with NF-κB family members, with preference for p50 and p52 homodimers (Wang et al. 2017). BCL3 possesses a nuclear localization sequence (NLS), that depending on its phosphorylation status, can prevent NF-κB transcriptional activity. This can occur via cytoplasmic sequestration of p52 and p50 homodimers, or by forming tertiary structures with either p50 or p52 and DNA to mediate transcriptional activation of target genes (little to no phosphorylation and

moderate phosphorylation respectively)(Wang et al. 2017). Importantly *Bcl3* mRNA was shown to be significantly upregulated in *Pten*-deficient prostate cancer relative to *Pik3ca*-mutant prostate cancer (Figure 3.8), indicating BCL3 may be a valuable therapeutic target for PTEN-null prostate cancer.

Toll-like receptor 2 (TLR2) inhibitors have also been shown to reduce NF-κB signalling, such as AP177 (Chang et al. 2009), OPN-305 (Reilly et al. 2013) and C29 (Mistry et al. 2015). Upon activation of TLR2, IκK becomes activated; leading to phosphorylation of IκBα and its subsequent degradation, which releases p50 and p65 NF-κB subunits from cytoplasmic inhibition (Hou et al. 2017).

C29 prevents the interaction of TLR2 with MyD88, through binding of the BB loop (a highly conserved sequence), present within the cytoplasmic intracellular Toll/IL-1 receptor resistance (TIR) domain of the TLR2 receptor that is essential for activation of TLR2-MyD88 signalling pathway (Mistry et al. 2015). Although C29 has not been widely tested, alternative TLR2 inhibitors including the synthetic lipopeptide CBLB612 and the monoclonal antibody OPN-305, have been explored in clinical trials for breast cancer (NCT02778763) and inflammatory disease (NCT02363491) respectively (Anwar et al. 2019).

A series of CXCR1/2 inhibitors have also been developed, such as Ladarixin, AstraZeneca compound AZD5069 and Reparixin (also known as Repertaxin). Reparixin is an allosteric, non-competitive, CXCR1-CXCR2 dual inhibitor that selectively inhibits biological processes mediated by CXCL8 (IL8) ligand binding, without affecting signalling induced by other chemotactic factors, by means of binding to the hydrophobic channel present in the transmembrane domain of receptor (Bertini et al. 2004; Zarbock et al. 2008; Liotti et al. 2017).

Furthermore, this CXCR1/2 inhibitor has already entered clinical trials for metastatic TNBC (NCT02370238; (Schott et al. 2017)), HER2-negative breast cancer (NCT01861054; (Goldstein et al. 2020)), and more recently is being explored as a treatment for severe COVID-19 pneumonia (NCT04794803). In support of CXCR1/2 inhibition for cancer patients, the small molecular inhibitor AZ13381758, a compound closely linked to AZD5069, showed to reduce metastases, and prolong survival of mice with pancreatic ductal adenocarcinoma *in vivo* (Steele et al. 2016).

As the RNA-Seq analysis revealed that *Cxcl8* mRNA (encoding IL-8) was significantly increased in *Pten*-deficient prostate tumours compared to *Pik3ca*-mutant tumours (Figure 3.8), and given that IL-8 can activate CXCR1/2 signalling through induction of numerous proteins including cAMP response element

binding protein (CREB), activating protein (AP-1) and NF-κB (Jundi and Greene 2015), inhibition of CXCR1 and CXCR2, may also be therapeutically beneficial for PTEN-deficient prostate cancer.
Although a range of different inhibitors have been developed to target the NF-κB signalling pathway in disease, it yet remains undetermined whether they are effective against prostate cancer, especially PTEN-null prostate cancer. Some studies have begun to explore this concept, where inhibition of mTOR kinase activity via rapamycin has been shown to reduce AKT mediated NF-κB signalling in PC3 prostate cancer cells due to suppressed activation of IKK by mTORC1 (Dan et al., 2008), however more work is needed to establish whether NF-κB inhibitors can be efficacious in PTEN-deficient prostate cancer that does not signal through the PI3K pathway.

4.2. Aims

With many PI3K pathway specific inhibitors displaying lack of efficacy in the clinic due to compensatory signalling mechanisms (Pearson et al. 2018) and in some cases toxicity (Greenwell et al. 2017), it is hugely important that new PI3K pathway directed therapeutic approaches are discovered, evaluated and implemented to improve patient outcome.

Associations between oncogenic PI3K signalling and NF-κB pathway activation have been established within different types of cancer including primary effusion lymphoma (PEL) (Hussain et al. 2012), breast cancer (Khongthong et al. 2019), and more recently investigated within prostate cancer (Torrealba et al. 2020). Despite elevated NF-κB signalling being a common characteristic of prostate cancer, very few prostate cancer clinical trials have been launched to examine the effects of using NF-κB inhibitors in patients (Labbozzetta et al. 2020), thus highlighting a clear need for further pre-clinical exploration.

Since the RNA-Seq data in Chapter 3 indicates NF-κB signalling contributes to *Pten*-deleted prostate cancer, we hypothesised that targeting the NF-κB pathway in *PTEN*-deficient prostate cancer would be an effective treatment and may overcome AKT-inhibitor resistance.

This chapter therefore aimed to:

1) Explore the efficacy of treating PTEN-deficient vs. PTEN proficient prostate cancer models with upstream and downstream NF-κB inhibitors *in vitro* and *ex vivo*
2) Investigate the efficacy in combining NF-κB inhibition with AKT inhibition *in vitro*
3) Discover new insights into the molecular mechanisms that drive NF-κB activation in the context of *PTEN* deletion

4.3. Results

4.3.1. *In vitro* targeting of the NF-κB pathway

4.3.1.1. Cell viability is altered when NF-κB is inhibited in human prostate cancer cell lines

To determine whether targeting the NF-κB pathway could be of therapeutic potential in *PTEN*-null human prostate cancer, as well as prostate cancer possessing either one or two functional alleles; a panel of well-studied, immortalised human cell lines (Table 2.8), were treated with a range of NF-κB inhibitors to establish half maximal inhibitory concentration values (IC_{50} values) and to assess the effect on cell viability.

Cell viability assays were performed on DU145, LNCAP, PC3 and 22RV1 prostate cancer cells 48 hours following treatment with (i) a canonical NF-κB inhibitor (BAY11-7082. Abcam, #ab141228), (ii) a BCL3 inhibitor (CB1, produced in-house by the Cardiff University School of Pharmacy), (iii) a CXCR1/2 inhibitor (Reparixin; Sigma Aldrich, #SML2655-5MG), or (iv) a TLR2 inhibitor (C29; Cambridge Bioscience, #HY-100461-5mg) (Figures 4.2 – 5) relative to the vehicle control (0.1% DMSO). Importantly, these inhibitors were selected based on the observation that *Bcl3*, *Cxcl8* and *Tlr2* mRNA expression is significantly increased in *Pten*-deficient prostate cancer relative to *Pik3ca*-mutant prostate cancer (Figure 3.8).

This experiment was designed to assess cell intrinsic responses to blockade of NF-κB signalling upstream at the level of the receptors (CXCR1/2i and TLR2i), as well as downstream signalling events (canonical NF-κBi), including at the level of transcription (BCL3i), whereby findings may help determine the best approach for targeting NF-κB signalling in PTEN-null prostate cancer.

Published work has established the IC_{50} value for the canonical NF-κB inhibitor (BAY11-7082) to be 10 μM within human umbilical vein endothelial cells (HUVEC), whilst IC_{50} values ranging between 30 – 50 μM have been observed within human pancreatic cancer cells for the CXCR1/2 inhibitor (Reparixin) (Fu et al. 2018b), and 19 – 37 μM for the TLR2 inhibitor (C29) in human embryonic kidney cells *in vitro* (Mistry et al. 2015). A published IC_{50} value for the BCL3 inhibitor (CB1) could not be found.

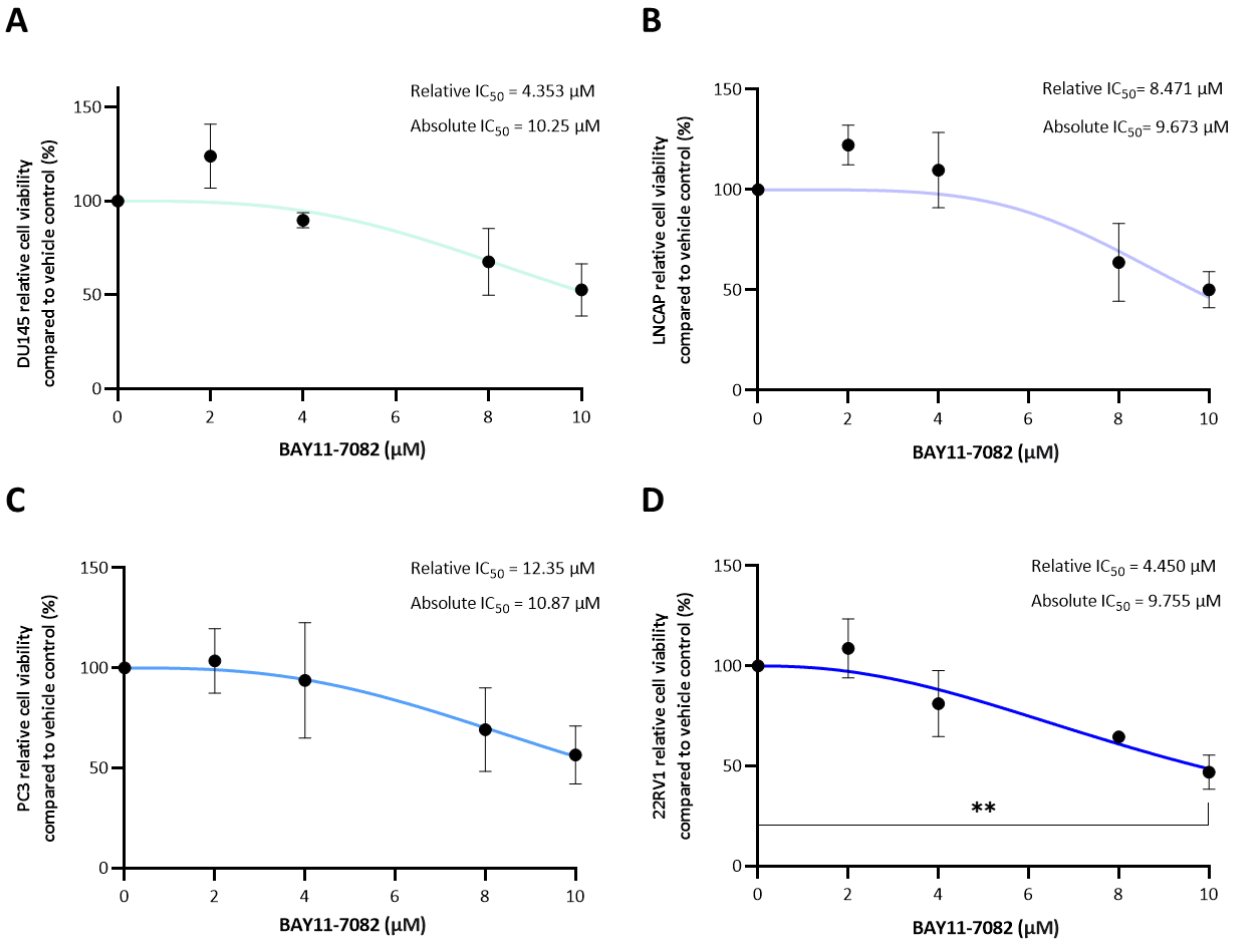

Figure 4.2: Cell viability responses to the NF-κB pathway inhibitor BAY11—7082. Graphs show mean percentage cell viability following 48 h treatment of BAY11-7082 to inhibit canonical NF-κB signalling in A) DU145, B) LNCAP, C) PC3 and D) 22RV1 prostate cancer cells. Data shows n = 3 biological repeats (3 independent repeats validated findings). A One-way ANOVA with a Tukey's multiple comparison test was performed to determine statistical significance relative to the vehicle control containing 0.1% DMSO. Error bars = SEM.

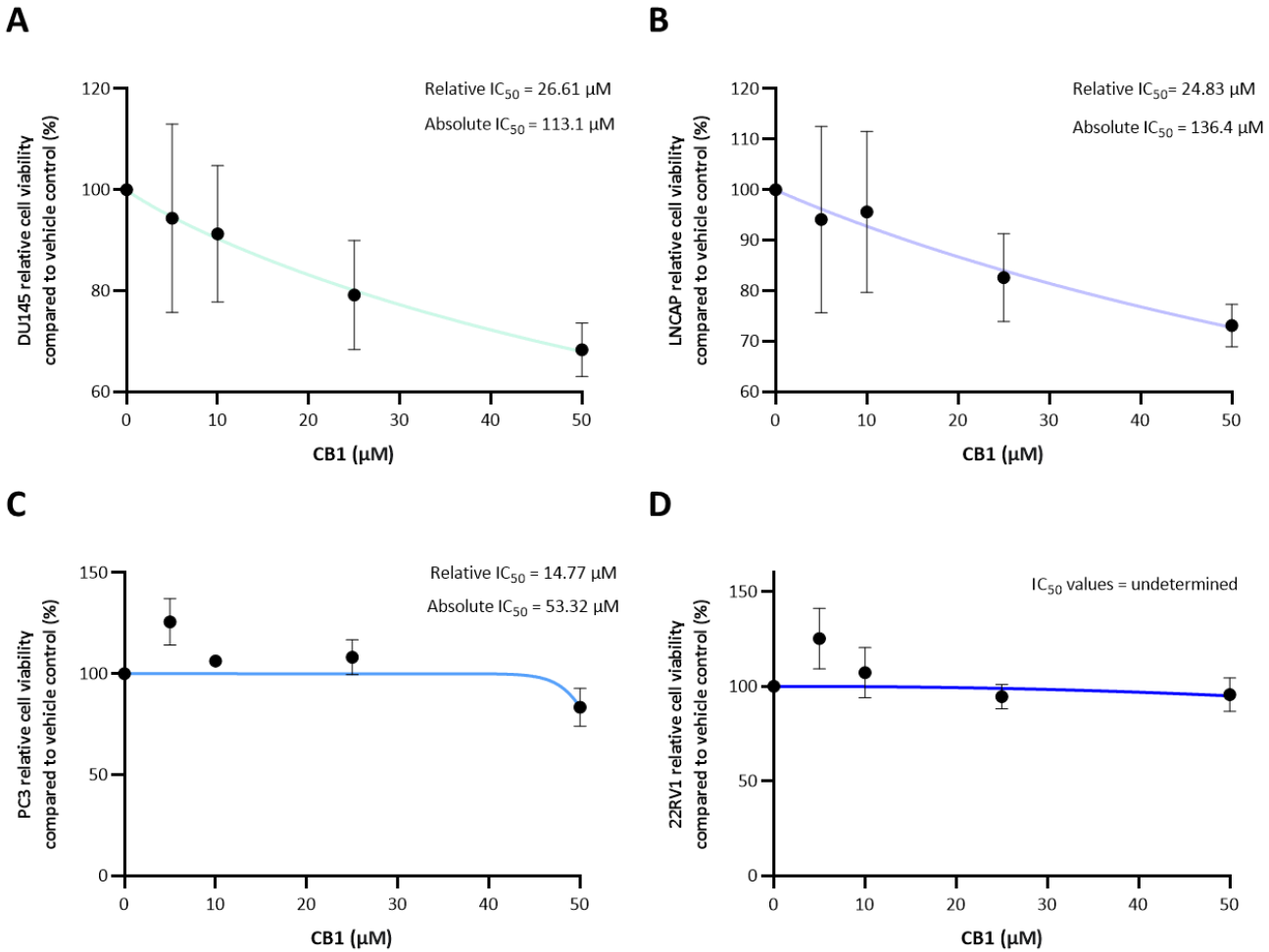

Figure 4.3: Cell viability responses to BCL3 inhibition. Graphs show mean percentage cell viability following 48 h treatment of CB1 to inhibit BCL3 in A) DU145, B) LNCAP, C) PC3 and D) 22RV1 prostate cancer cells. Data shows n = 3 biological repeats (3 independent repeats validated findings). A One-way ANOVA with a Tukey's multiple comparison test was performed to determine statistical significance relative to the vehicle control containing 0.1% DMSO. Error bars = SEM.

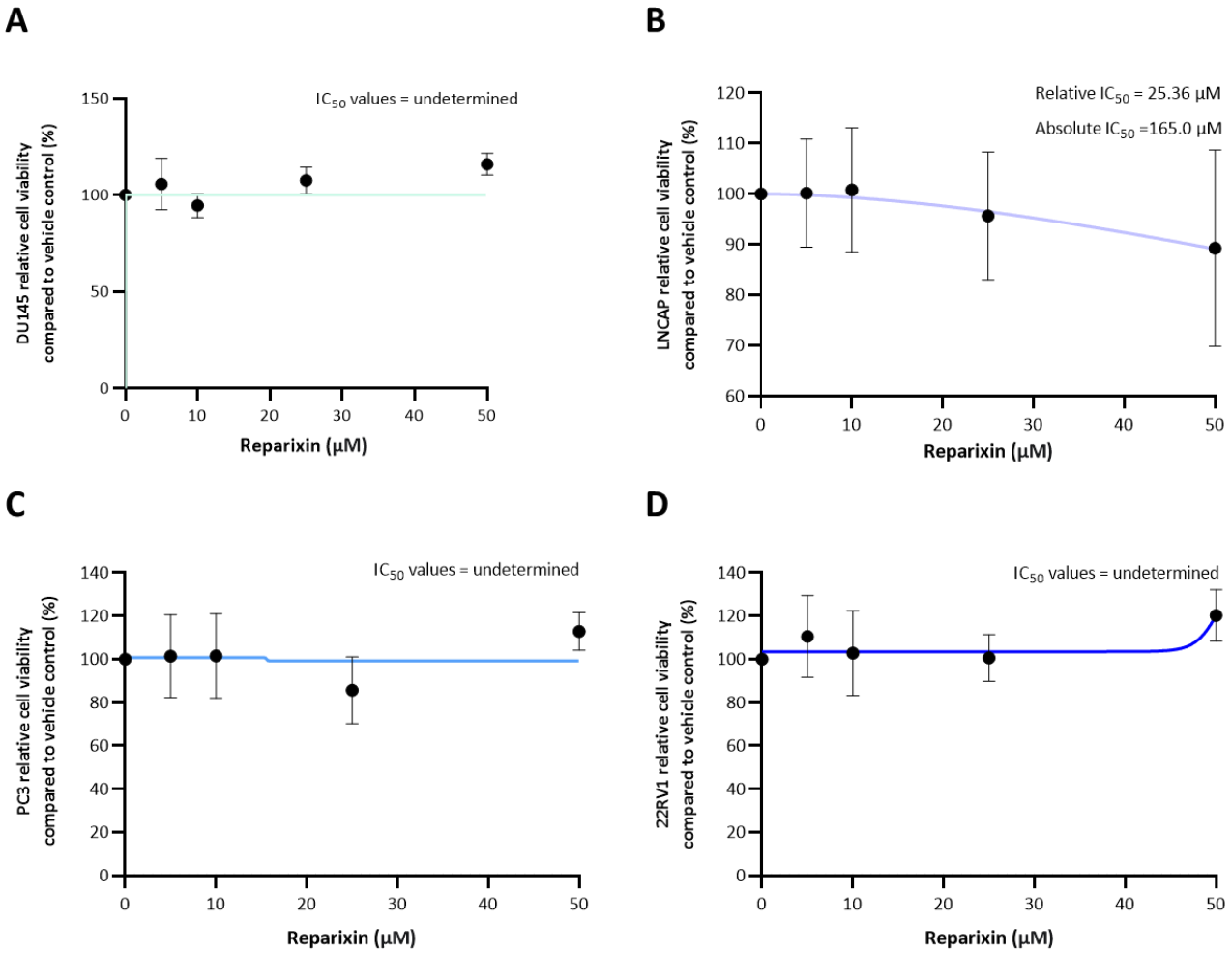

Figure 4.4: Cell viability responses to CXCR1/2 inhibition. Graphs show mean percentage cell viability following 48 h treatment of Reparixin to inhibit CXCR1/2 in A) DU145, B) LNCAP, C) PC3 and D) 22RV1 prostate cancer cells. Data shows n = 3 biological repeats (3 independent repeats validated findings). A One-way ANOVA with a Tukey's multiple comparison test was performed to determine statistical significance relative to the vehicle control containing 0.1% DMSO. Error bars = SEM.

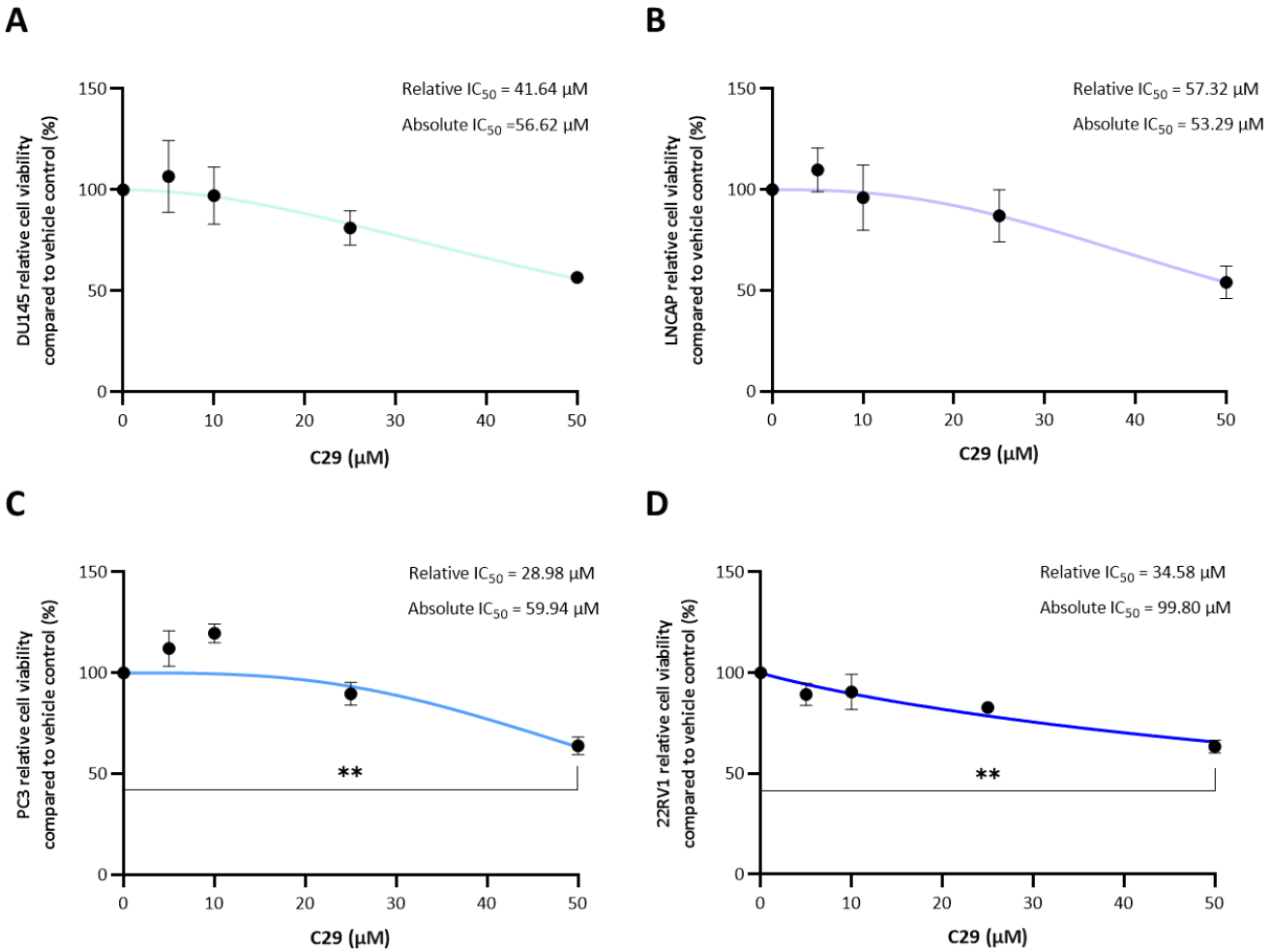

Figure 4.5: Cell viability responses to TLR2 inhibition. Graphs show mean percentage cell viability following 48 h treatment of C29 to inhibit TLR2 in A) DU145, B) LNCAP, C) PC3 and D) 22RV1 prostate cancer cells. Data shows n = 3 biological repeats (3 independent repeats validated findings). A One-way ANOVA with a Tukey's multiple comparison test was performed to determine statistical significance relative to the vehicle control containing 0.1% DMSO. Error bars = SEM.

All inhibitors were initially trialled at 5, 10, 25 and 50 μM doses, however use of the canonical NF-κB inhibitor BAY11-7082 at 25 and 50 μM doses to test the effect of canonical NF-κB inhibition was highly toxic, resulting in no detectable living cells after 48-hours of treatment (data not shown). The dose range for this inhibitor was therefore lowered to 2, 4, 8 and 10 μM, which resulted in a marked reduction in cell viability relative to the vehicle control for all the cell lines explored, however statistical significance was only achieved in 22RV1 cells with 10 μM BAY11-7082 (48h, n = 3) (Figure 4.2).

Absolute IC_{50} values for the canonical NF-κB inhibitor BAY11-7082 were very similar amongst the cell line panel (range: 9.75 – 2.75 μM), thus matching published data for this drug. However, the relative IC_{50} values calculated were much lower for both PTEN-proficient lines (4.4 μM in DU145 and 4.5 μM in 22RV1 cells) compared to the PTEN-deficient cell lines (LNCAP and PC3 cells, 8.5 μM and 12.4 μM respectively). These findings suggest that supressing IκBα degradation in prostate cancer can be effective in supressing growth and viability *in vitro*. The higher relative IC_{50} values in the PTEN-deficient cell lines supports our previous findings that *PTEN*-depleted prostate cancer is not highly reliant on canonical signalling (Section 3.3.3.4 and 3.3.5), suggesting inhibition of the canonical NF-κB signalling axis may be more efficacious in PTEN-proficient prostate cancer.

To determine the response of our prostate cancer cell line panel to NF-κB inhibition at the transcription factor level, cell viability in response to the BCL3 inhibitor CB1 was assessed (Figure 4.3). As this BCL3 inhibitor is only in its early experimental stages of development, very few studies have been performed on a range of cancer types. However, from the published data available, CB1 treatment has been shown to significantly reduce cell viability in a panel of triple negative breast cancer (TNBC) cell lines by approximately 20% at a 100 μM dose (Yang 2018). Interestingly, when treating the prostate cancer cells at 50 μM (a dose that lies between the relative and absolute Ic50 values for each cell line), we observed a 33% and 28% reduction in cell viability within the DU145 and LNCAP cell lines respectively, relative to vehicle controls (Figure 4.3). Although these results were not statistically significant, the data suggests that lower doses of the BCL3 inhibitor given to different cancer types such as prostate cancer may be just as effective as the higher doses tested in TNBC.

Furthermore, the DU145 and LNCAP cells appeared to be more sensitive to BCL3 inhibition in comparison to the PC3 cell lines, despite lower absolute and relative IC_{50} values calculated within this cell line. The 22RV1 cells appeared to be insensitive to CB1 treatment and no IC_{50} values could be determined. Whilst the initial results obtained show that BCL3 inhibition in prostate cancer can

influence cell growth, further work is needed to address whether BCL3 inhibitors alone are efficacious in prostate cancer and whether PTEN status truly influences drug response.

To determine the response of PTEN-deficient and proficient prostate cancer cells to inhibition of the NF-κB pathway by targeting the CXCR1/2 receptors (upstream blockade), our panel of prostate cancer cells were treated with the CXCR1/2 inhibitor Reparixin. The cell viability plots showed no reduction in growth post-CXCR1/2i treatment, suggesting all lines regardless of PTEN status were insensitive to Reparixin (Figure 4.4). To further verify this finding, we additionally tested another CXCR1/2 inhibitor, AZD5069 (Universal Biologicals, #S6645-5mg), that is currently being explored at clinical trials alongside enzalutamide (NCT03177187). 5, 10, 25 and 50 μM doses were given to the panel of lines, and we obtained near identical results to Reparixin (Figure 4.6), confirming the effect of CXCR1/2 inhibition alone within our prostate cancer cell lines.

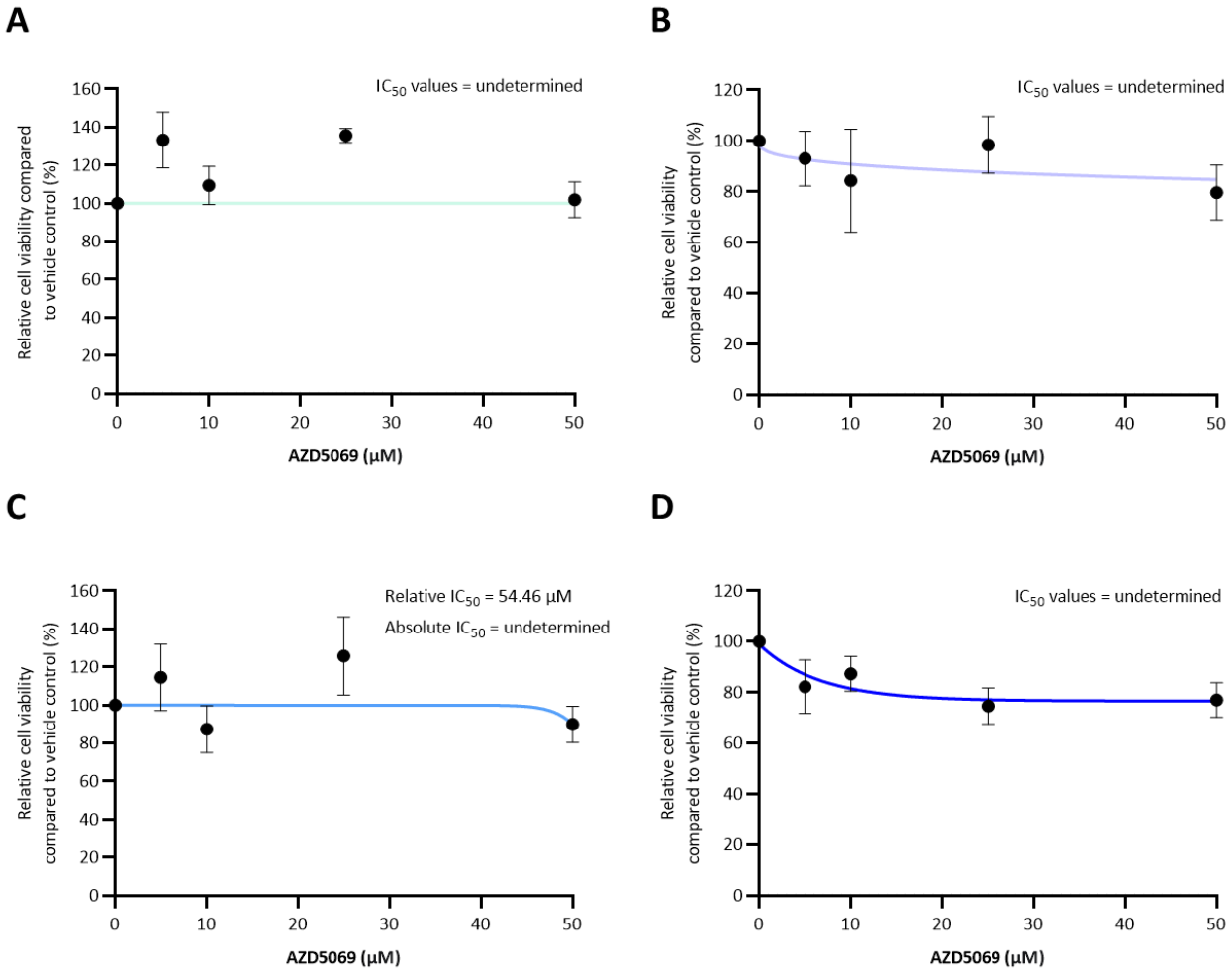

Figure 4.6: Additional cell viability responses to CXCR1/2 inhibition. Graphs show mean percentage cell viability following 48 h treatment of AZD5069 to inhibit CXCR1/2 in A) DU145, B) LNCAP, C) PC3 and D) 22RV1 prostate cancer cells. Data shows n = 3 biological repeats (3 independent repeats validated findings). A One-way ANOVA with a Tukey's multiple comparison test was performed to determine statistical significance relative to the vehicle control containing 0.1% DMSO. Error bars = SEM.

Whilst it was puzzling that 48-hour treatment of Reparixin at high doses (50 μM) resulted in heightened cell viability (Figure 4.4), an increase in cell viability was interestingly also reported when Reparixin was dosed in non-malignant human epithelial thyroid cells *in vitro* (Liotti et al. 2017); these results obtained may be attributed to the lack of ECM or TME factors required to stimulate the CXCR1/2-NF-κB pathway. Moreover, IC_{50} values could not be calculated, suggesting resistance. Thus, a repeated experiment in the presence of ligands / stimuli may help determine effectiveness of the inhibitor in 2D *in vitro* culture.

To test another form of upstream NF-κB pathway blockade, cell viability assays were performed on the panel of prostate cancer cell lines to assess the effect of 48-hour TLR2 inhibition through use of the small molecule inhibitor, C29 (Figure 4.5). Calculated absolute IC_{50} values were very similar within the DU145, LNCAP and PC3 cell lines, and all cell lines displayed partial sensitivity to C29 indicating there is no correlation between PTEN status and treatment response. A significant reduction in cell viability only occurred with 50 μM TLR2i in the PC3 and 22RV1 lines compared to the vehicle control and none of the cell lines reached less than 60% viability following treatment (Figure 4.5).

Taken together, these findings indicate that in the *in vitro* setting, targeting receptors upstream of NF-κB subunits in prostate cancer are not effective regardless of PTEN setting, possibly owing to the lack of receptor ligands that would be normally present within the ECM / stroma. Repressing activation of the subunits (e.g., via BAY11-7082), can reduce growth of PTEN-proficient and deficient prostate cancer cells, however doses at higher concentrations result in toxicity-associated death. Collectively the *in vitro* data indicates that *ex vivo* and *in vivo* testing of the inhibitors are required to make a conclusion on their potential efficacy in patients.

4.3.1.2. Cell viability is altered following AKT inhibition in human prostate cancer cells

A wide spectrum of AKT inhibitors have been developed, and recent work has revealed AKT inhibition to be a promising approach for targeting prostate cancer, especially for patients who harbour *PTEN* loss (de Bono et al. 2019; Shorning et al. 2020).

One particular drug, Capivasertib (also known as AZD5363), has been shown to potently inhibit all isoforms of AKT, in addition to possessing good pharmacokinetic and metabolic properties (Nitulescu et al. 2016). AZD5363 is a pan-isoform, ATP-pocket competitive inhibitor, that upon enzyme binding, stabilises AKT phosphorylation at sites Thr308 and Ser473; contributing to its degradation (Xu et al. 2021).

There are several active/recruiting metastatic CRPC clinical trials studying the effects of AKT inhibition via Capivasertib, which also include combining pre-existing therapies such as chemotherapy (NCT02121639) or Enzalutamide (NCT02525068). The CAPItello-281 study (assessment of Capivasertib and Abiraterone in patients with *de novo* metastatic hormone-sensitive prostate cancer with PTEN deficiency: NCT04493853) is also now recruiting for phase III of the trial.

Although early reports from these trials have revealed good responses for the combination therapies relative to monotherapy, there are a number of non-responders, indicating mechanisms of resistance. Since PI3K and NF-κB cross talk has previously been shown to mediate resistance to PI3K-directed therapies (Yang et al. 2019a), experiments were designed to test if NF-κB and AKT co-inhibition is more efficacious than monotherapy in DU145, LNCAP, PC3 and 22RV1 cells.

Firstly, the panel of PTEN-deficient (LNCAP / PC3) and PTEN-proficient (DU145 / 22RV1) human metastatic prostate cancer cell lines were employed to determine AKTi sensitivity by performing a cell viability assay after 48 h treatment with Capivasertib (0 - 25 μM range, n = 3 biological repeats, 3 independent repeats).

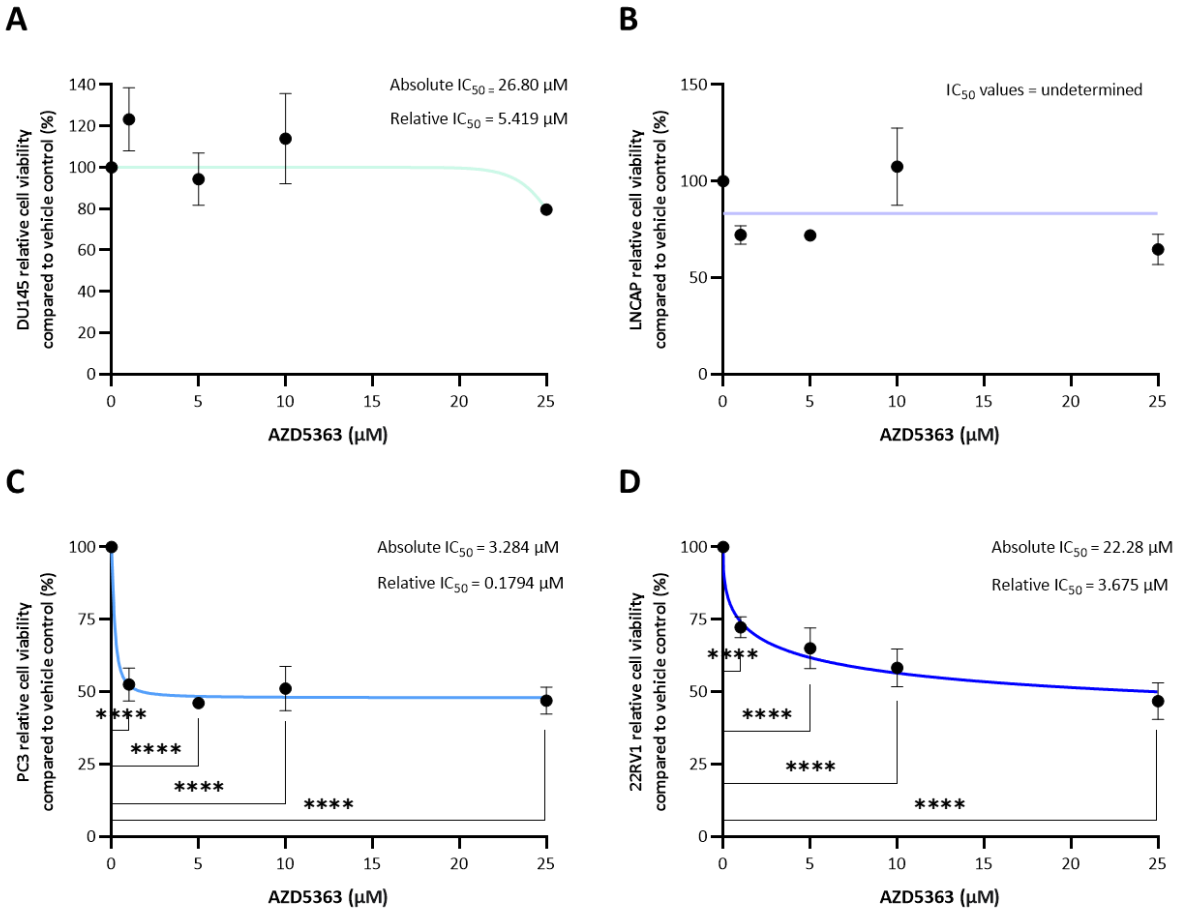

Figure 4.7: Cell viability responses to AKT inhibition. Graphs show mean percentage cell viability following 48 h treatment of AZD5363 to inhibit AKT in A) DU145, B) LNCAP, C) PC3 and D) 22RV1 prostate cancer cells. Data shows n = 3 biological repeats (3 independent repeats validated findings). A One-way ANOVA with a Tukey's multiple comparison test was performed to determine statistical significance relative to the vehicle control containing 0.1% DMSO. Error bars = SEM

The PrestoBlue cell viability assay revealed that PTEN-deficient PC3 CRPC cells were the most sensitive to pan-AKT inhibition, closely followed by the PTEN-proficient 22RV1 cell line, where in both models each dose generated a highly significant reduction in viability compared to the vehicle control (Figure 4.7C & D). Interestingly the LNCAP cell line appears to be resistant to AKT inhibition (Figure 4.7B), and the PTEN-proficient DU145 cell line was partially sensitive to Capivasertib (Relative IC_{50}= 5.4 µM, Figure 4.7A).

A previous study investigating the effects of Capivasertib treatment in DU145 and PC3 prostate cancer cell lines claimed both lines were insensitive to the AKT inhibitor due to induction of autophagy that drove cell survival and not apoptosis (Lamoureux et al. 2013). Our data supports limited AKT inhibitor sensitivity within the DU145 line, although a moderate response was observed in the PC3 cell line, possibly reflecting differences in culture conditions, drug preparation and the type of cell viability assay performed within this project. Of note, all cell lines studied in this project were STR-authenticated (Eurofins).

Our findings suggest that all the cell lines (both PTEN-deficient and PTEN-proficient) assessed are partially sensitive to the AKT inhibitor Capivasertib, except for the *PTEN* heterozygous LNCAP line that was showed to be resistant. As the treatment responses do not correlate with PTEN status, other mutations or signalling pathways are likely to promote the treatment insensitivity observed in the LNCAP line and perhaps also the partial sensitivity in the DU145 cell line, reiterating the need to explore combination therapies that target both PI3K-AKT signalling and compensatory/feedback signalling.

4.3.1.3. Cell viability is further reduced when a NF-κB inhibitor is added to AKT inhibition in human prostate cancer cells

To assess the efficacy of co-treating the cell lines with AKT and NF-κB inhibitors, the panel of metastatic prostate cancer cell lines were each treated with Capivasertib and an NF-κB pathway inhibitor in combination (BAY11-7082, CB1, Reparixin or C29) for 48 h, across a range of increasing concentrations to determine if a synergistic relationship exists between the combinations assessed (Figures 4.8, 4.10, 4.12 and 4.14).

To determine if the treatment responses observed were antagonistic, additive or synergistic, the different combination therapies assessed were analysed using SynergyFinder 2.0 software (Finnish

Institute for Molecular Medicine), an online platform that enables interactive analysis and visualisation of drug combination data (Ianevski et al. 2020). The tool enabled creation of dose-response matrices (i.e., cell viability data in heatmap format: Appendix 9), in addition to testing the data for synergism and creation of 2D contour plots (Figures 4.9, 4.11, 4.13 and 4.15, summarised in Table 4.4). The average excess response generated by the drug interaction can be inferred from these scores, such that a score greater than 10 is deemed synergistic (represented in red), a score between -10 and 10 regarded as additive, and a score less than -10 antagonistic (represented in green).

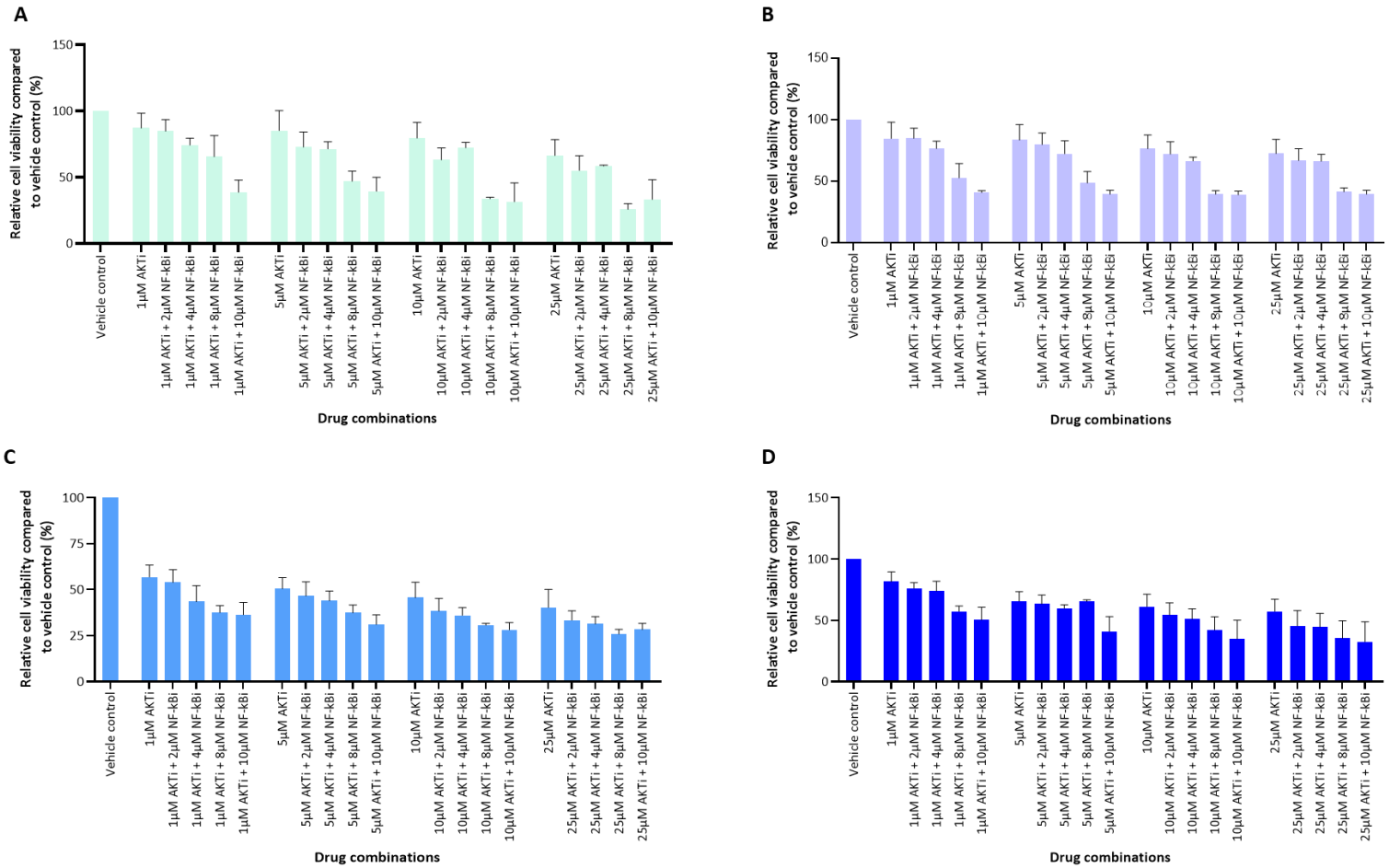

Figure 4.8: Co-inhibition of the canonical NF-κB pathway and AKT signalling further reduces cellular viability. Graphs show results obtained by treating A) DU145, B) LNCAP, C) PC3 and D) 22RV1 cells with BAY11-7082 and Capivasertib for 48 hours. Data shows the mean of n = 3 biological repeats. Error bars = SEM. A One-way ANOVA with a Tukey's multiple comparison test was performed to determine statistical significance relative to each respective AKT inhibitor dose alone; however, no statistical significance was observed.

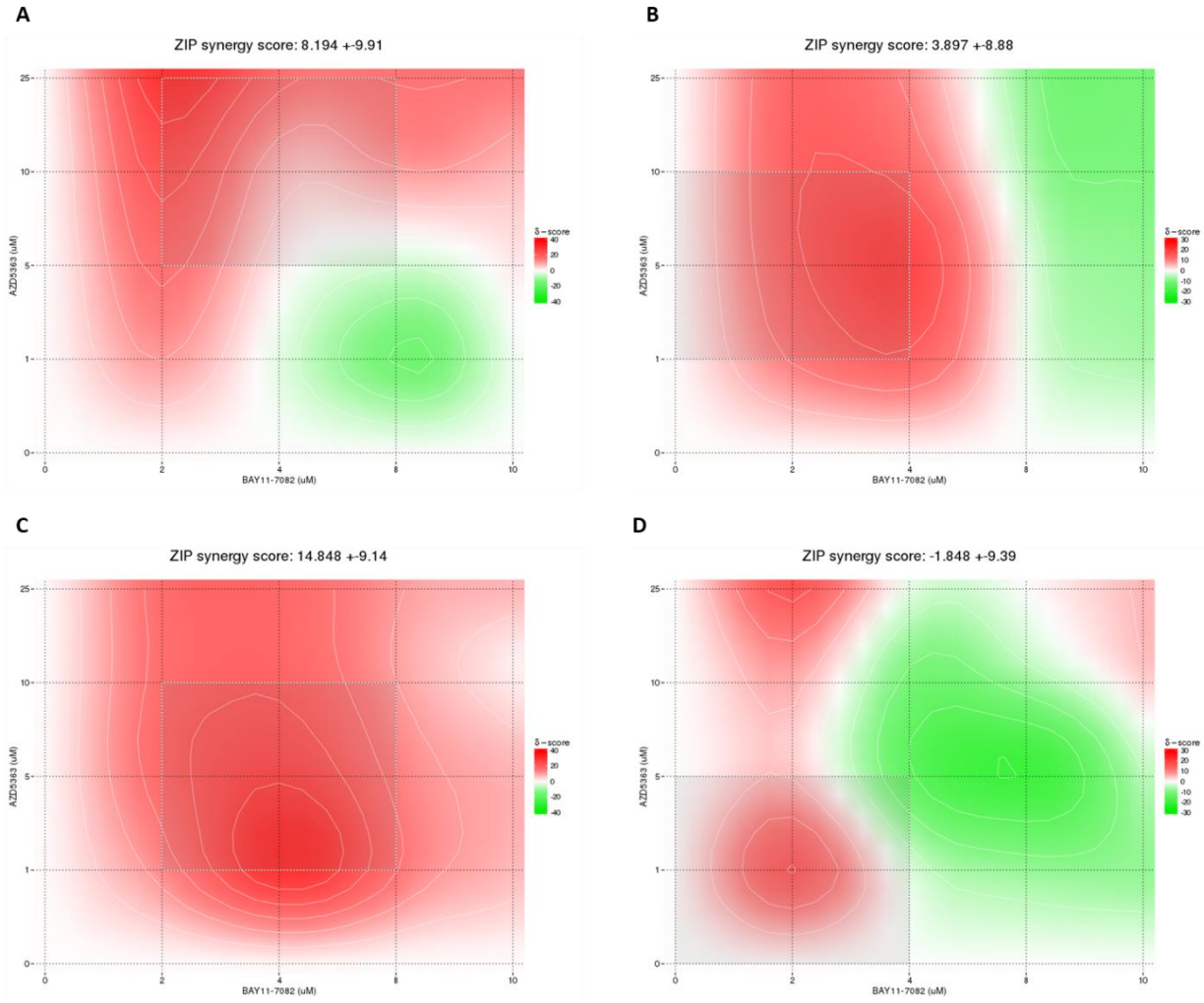

Figure 4.9: BAY11-7082 and AZD5363 display an antagonistic relationship at higher doses in prostate cancer cell lines. Plots show SynergyFinder results obtained by treating A) DU145, B) LNCAP, C) PC3 and D) 22RV1 prostate cancer cells with canonical NF-κB inhibitor BAY11-7082 (x-axis) and AKT AZD5363 (Capivasertib) (y-axis). Data shows n = 3 biological repeats, with ZIP synergy score and 95% confidence interval represented.

In our panel of prostate cancer cell lines, combining the canonical NF-κB inhibitor BAY11-7082 at increasing concentrations (2, 4, 8 and 10 μM) with the AKT inhibitor Capivasertib resulted in reduced viability compared to AKTi monotherapy at 1, 5, 10 and 25 μM doses (Figure 4.8). This finding was not significant within any of the lines, however the most prominent effects were seen in the DU145 and LNCAP lines at both higher doses of NF-KB and AKT inhibitor, whereas in the PC3 and 22RV1 lines, reduced cell viability was observed in a stepwise manner as concentrations for both drugs increased.

Surprisingly, combining high doses of BAY11-7082 and Capivasertib was antagonistic in LNCAP cells (Figure 4.9B), despite these high doses showing the strongest reduction in cell viability within this line (Figure 4.8B), possibly indicating toxicity. At mid-range doses, the canonical NF-κB inhibitor and AKT inhibitor appeared to be synergistic within the LNCAP and PC3 lines, the two PTEN-deficient lines. Large variability was noticed across the panel of cell lines, suggesting the combination of the two drugs at can yield either antagonistic, additive or synergistic effects in different cell types, thus it is unlikely this combination treatment will prove to be effective for the majority of patients, and further work is needed to determine which patients may respond.

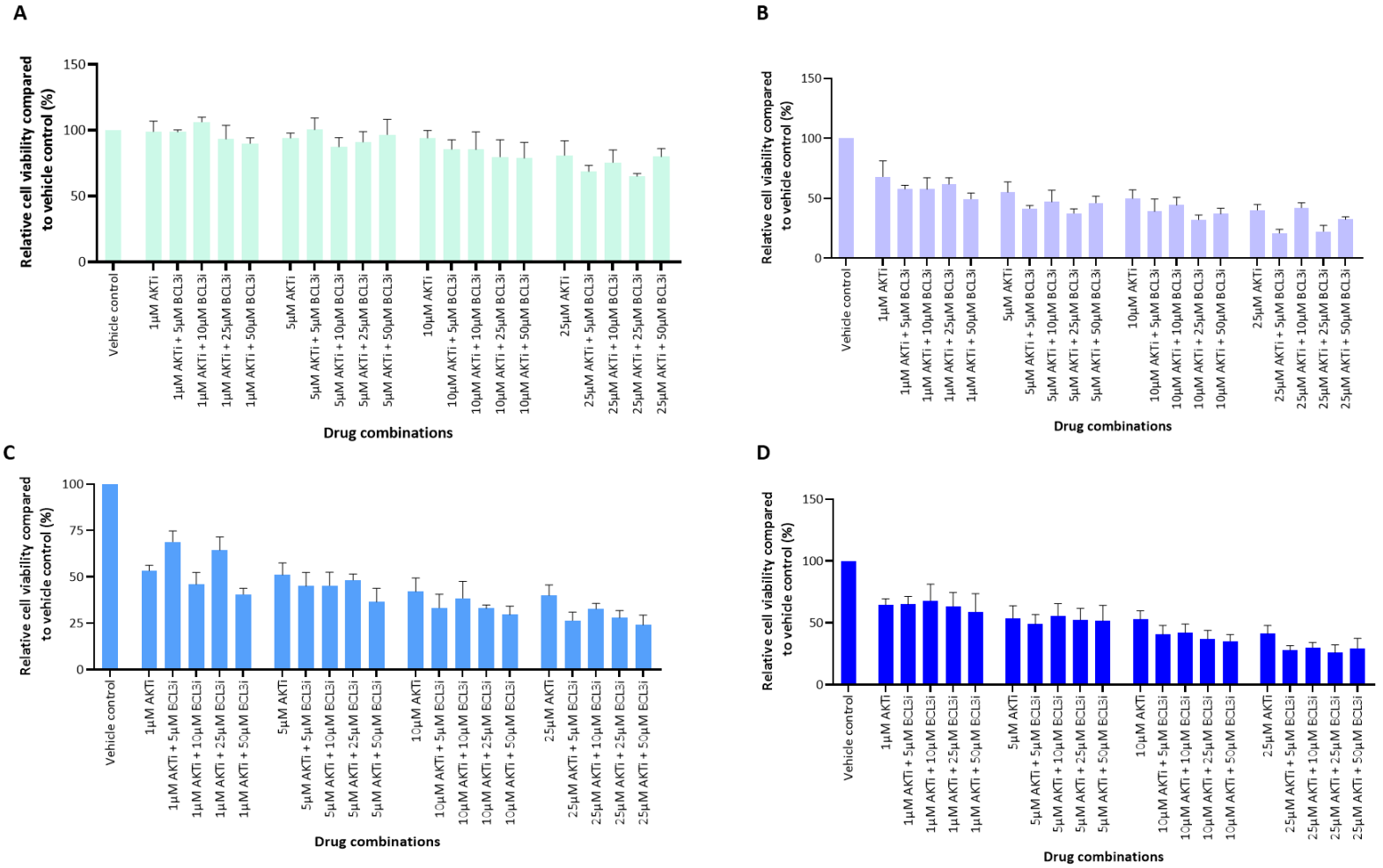

Figure 4.10: Co-inhibition of BCL3 and AKT signalling does not further reduce cellular viability. Graphs show results obtained by treating A) DU145, B) LNCAP, C) PC3 and D) 22RV1 cells with CB1 and Capivasertib for 48 hours. Data shows the mean of n = 3 biological repeats. Error bars = SEM. A One-way ANOVA with a Tukey's multiple comparison test was performed to determine statistical significance relative to each respective AKT inhibitor dose alone; however, no statistical significance was observed.

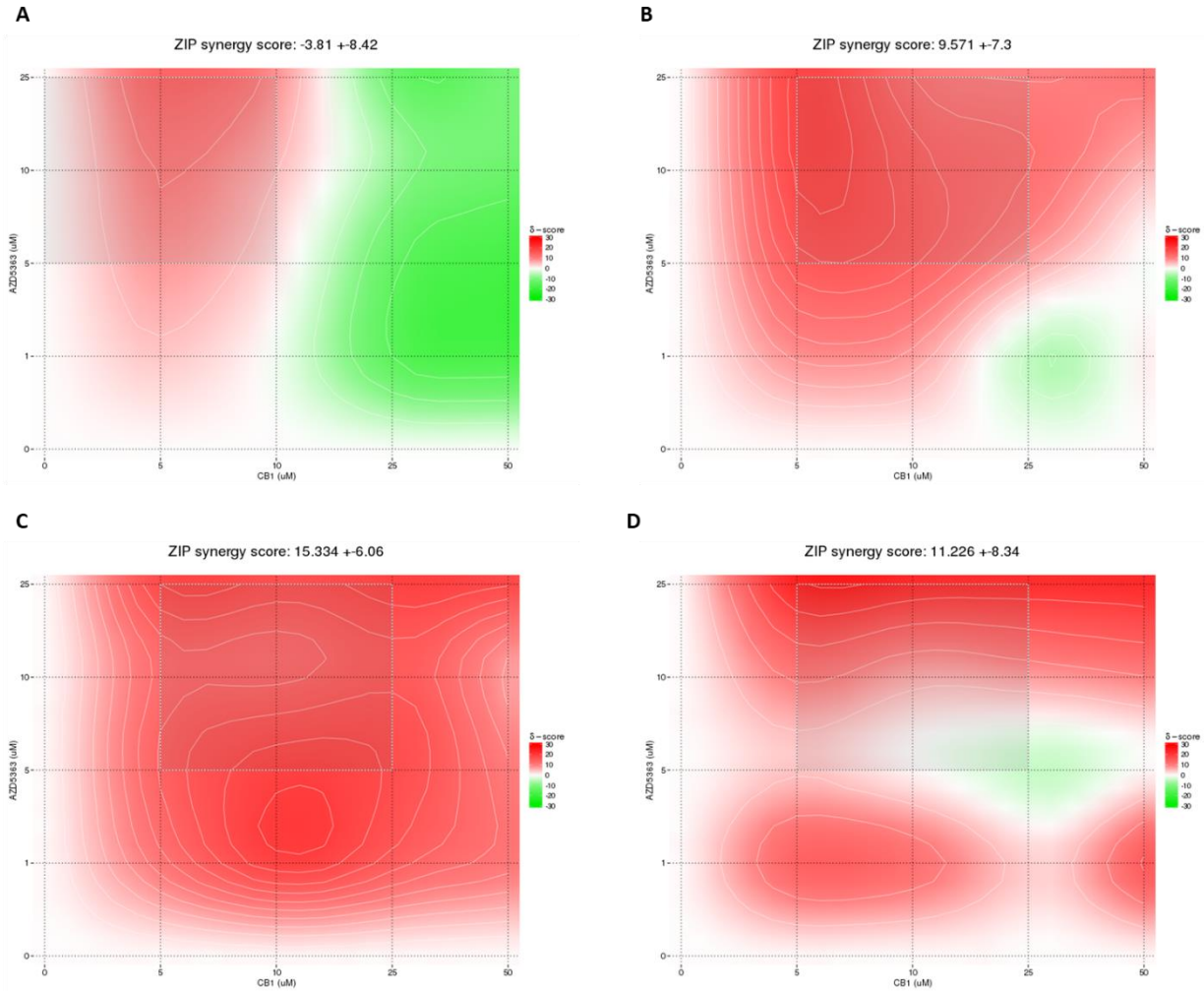

Figure 4.11: CB1 and AZD5363 display an additive relationship in prostate cancer cell lines. Plots show SynergyFinder results obtained by treating A) DU145, B) LNCAP, C) PC3 and D) 22RV1 prostate cancer cells with BCL3 inhibitor CB1 (x-axis) and AKT inhibitor AZD5363 (Capivasertib) (y-axis). Data shows n = 3 biological repeats, with ZIP synergy score and 95% confidence interval represented.

Combined treatment of BCL3 inhibitor CB1 and the AKT inhibitor Capivasertib, had limited effect on cell viability relative to AKT inhibition alone in DU145 cells (Figure 4.10A). This finding indicates that these PTEN-proficient cells are insensitive to AKT inhibition and that the addition of BCL3 inhibitor is unable to overcome AKTi-resistance in this setting.

Interestingly, co-treatment of 1 µM AKT inhibitor plus 5 or 25 µM BCL3 inhibitor, drove an increase in PC3 cell viability relative to 1 µM AKT inhibition alone (Figure 4.10C). The 5- and 25 µM concentrations of BCL3 inhibitor as monotherapy increased PC3 cell viability relative to the vehicle control (Figure 4.3), indicating that CB1 can induce PC3 cell growth both in the presence and absence of an AKT inhibitor treatment. Therefore, this data suggests BCL3 signalling may not be a compensatory mechanism for the PI3K pathway or that NF-κB and AKT co-inhibition may activate a feed forward loop to further stimulate AKT and/or NF-κB signalling.

When assessing the relationship between the two inhibitors, a largely antagonistic / mildly additive effect was reported for the AKT inhibitor and BCL3 inhibitor within the DU145 cell line (Figure 4.11A). Synergy was detected in the PC3 cells, but once again a varied range of results were obtained within the other LNCAP and 22RV1 lines, suggesting the combination of CB1 and Capivasertib may not be the most effective for targeting prostate cancer.

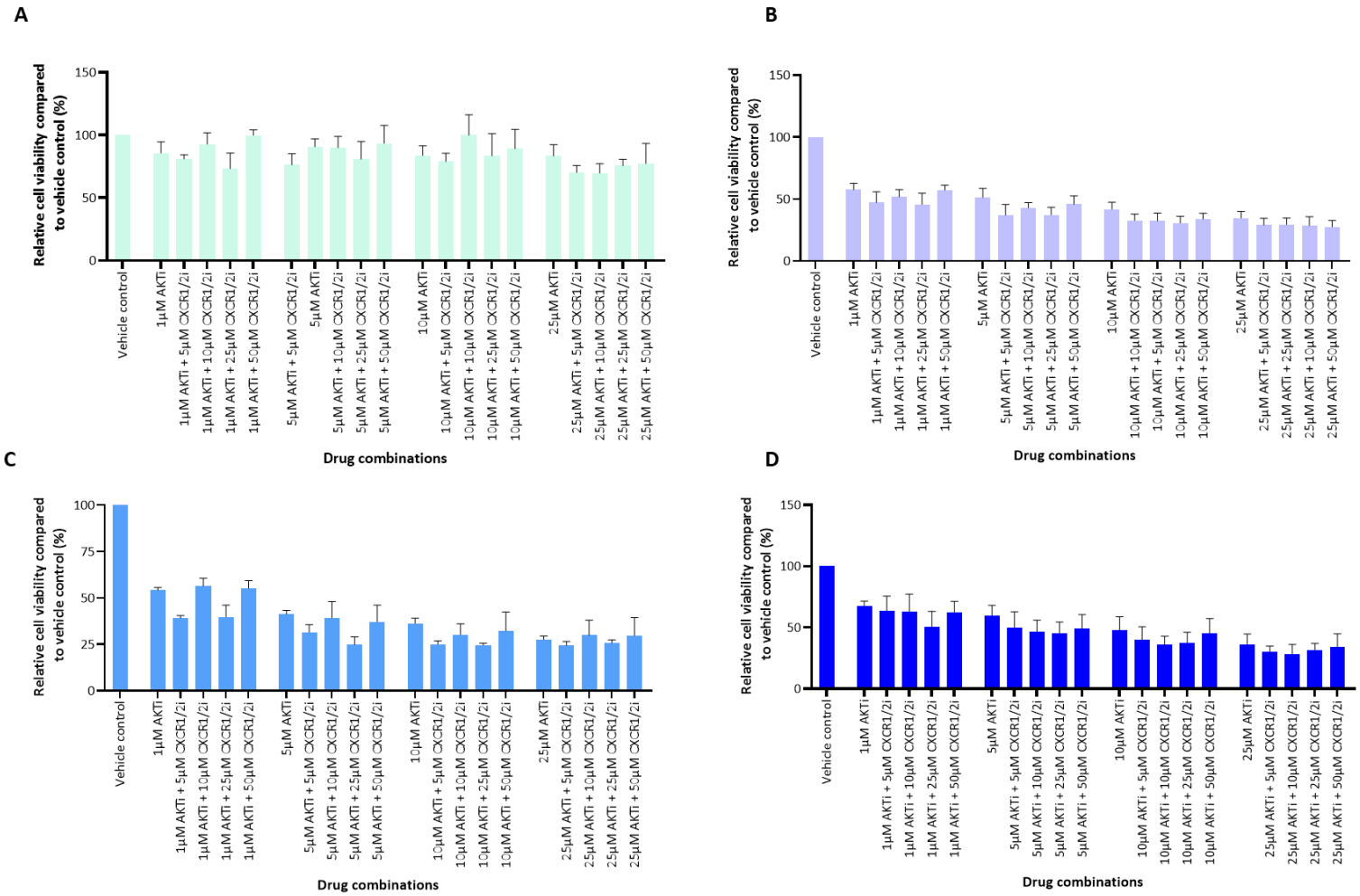

Figure 4.12: Co-inhibition of CXCR1/2 and AKT signalling further reduces cellular viability. Graphs show results obtained by treating A) DU145, B) LNCAP, C) PC3 and D) 22RV1 cells with Reparixin and Capivasertib for 48 hours. Data shows the mean of n = 3 biological repeats. Error bars = SEM. A One-way ANOVA with a Tukey's multiple comparison test was performed to determine statistical significance relative to each respective AKT inhibitor dose alone; however, no statistical significance was observed.

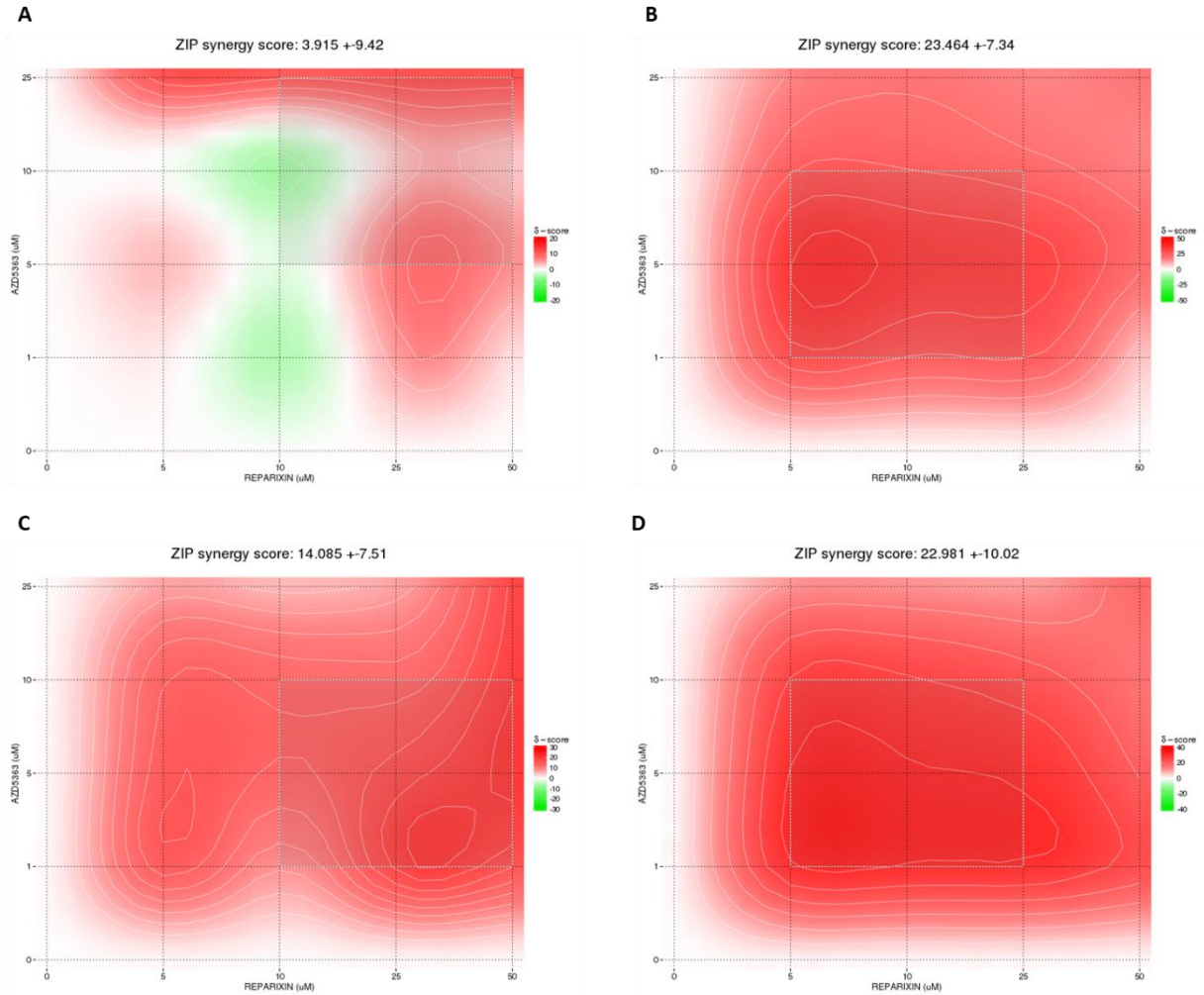

Figure 4.13: Reparixin and AZD5363 display a synergistic relationship in prostate cancer cell lines. Plots show SynergyFinder results obtained by treating A) DU145, B) LNCAP, C) PC3 and D) 22RV1 prostate cancer cells with CXCR1/2 inhibitor Reparixin (x-axis) and AKT inhibitor AZD5363 (Capivasertib) (y-axis). Data shows n = 3 biological repeats, with ZIP synergy score and 95% confidence interval represented.

Whilst CXCR1/2 inhibition via treatment with Reparixin alone had no impact on reducing DU145, LNCAP, PC3 and 22RV1 prostate cancer cell growth (Figure 4.4), combining AKT inhibition with CXCR1/2 inhibition further reduced cell viability in LNCAP, PC3 and 22RV1 cells compared to AKT inhibition alone, however these findings were not statistically significant (Figure 4.12). This effect was not observed in the DU145 PTEN-proficient line, indicating these cells are insensitive to this combination treatment (Figure 4.12A), similar to BCL3 and AKT combined inhibition.

Once again, an improved response was not just mediated in PTEN-deficient cells as indicated by the 22RV1 cell line data (Figure 4.12D), therefore suggesting combined AKT and CXCR1/2 inhibition could be used in PTEN proficient and deficient disease. Moreover, the ZIP model identified the action of Reparixin and Capivasertib to be highly synergistic within the LNCAP and 22RV1 cell lines and additive/synergistic for the PC3 cell line (Figure 4.13), indicating AKT and CXCR1/2 combined therapy as a potentially effective therapeutic for prostate cancer regardless of PTEN status.

Together, these findings indicate that while combining canonical NF-κB or BCL3 inhibitors with AKT blockade is not likely to be efficacious in the clinic, synergy was observed with co-inhibition of AKT and CXCR1/2 inhibitors. Since PTEN-proficient and PTEN-deficient cells responded to this treatment, more work is needed to better understand PTEN-NF-κB signalling interactions to identify novel treatment approaches that benefit patients. Of note, although this *in vitro* approach enabled rapid assessment of various drug combinations, it excludes external stimulation from the TME, therefore future work exploring co-cultures and *in vivo* preclinical assessment is needed to determine if co-targeting AKT and CXCR1/2 is efficacious for prostate cancer patients (with and without PTEN loss).

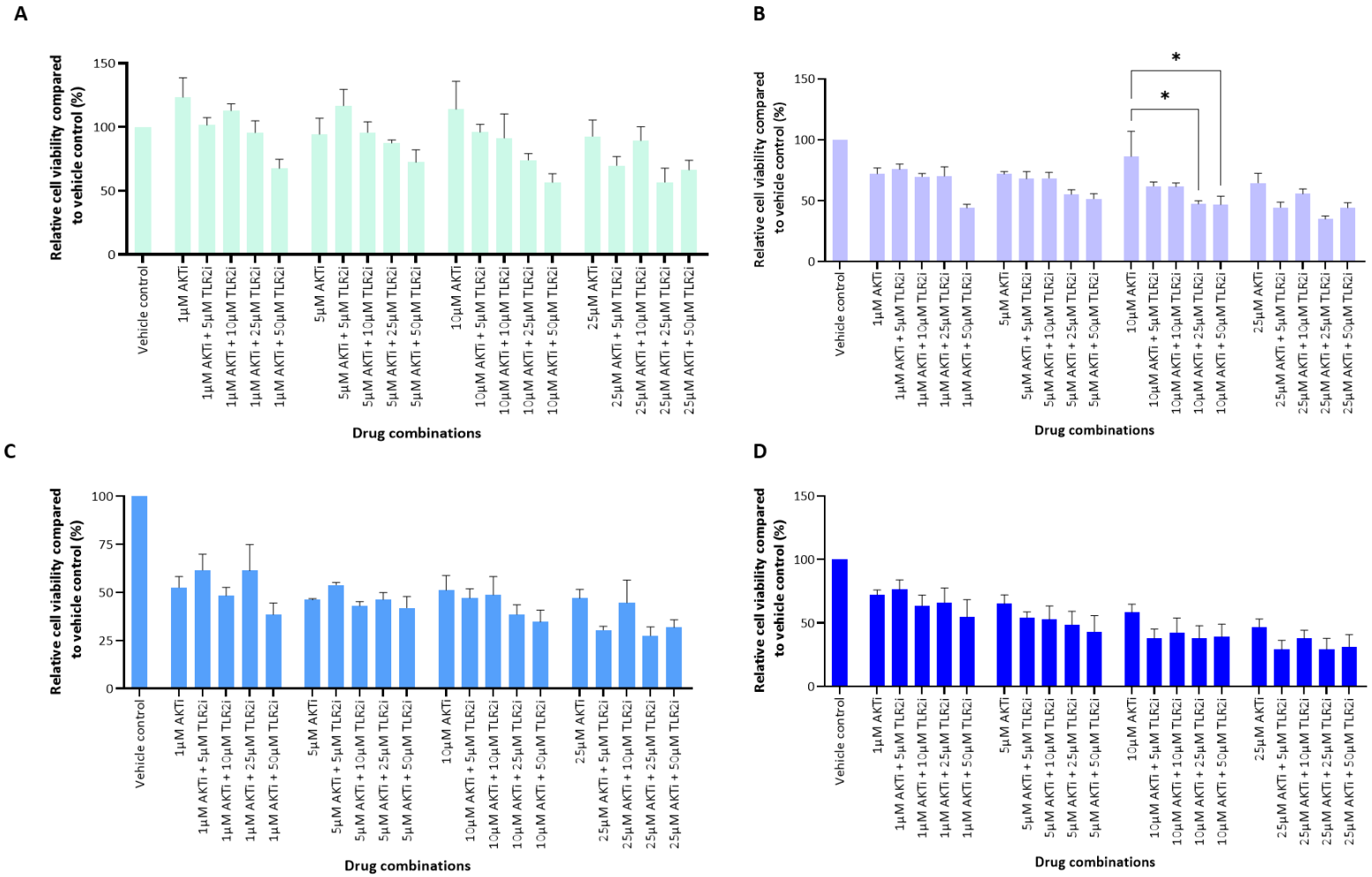

Figure 4.14: Co-inhibition of TLR2 and AKT signalling further reduces cellular viability. Graphs show results obtained by treating A) DU145, B) LNCAP, C) PC3 and D) 22RV1 cells with C29 and Capivasertib for 48 hours. Data shows the mean of n = 3 biological repeats. Error bars = SEM. A One-way ANOVA with a Tukey's multiple comparison test was performed to determine statistical significance relative to each respective AKT inhibitor dose alone.

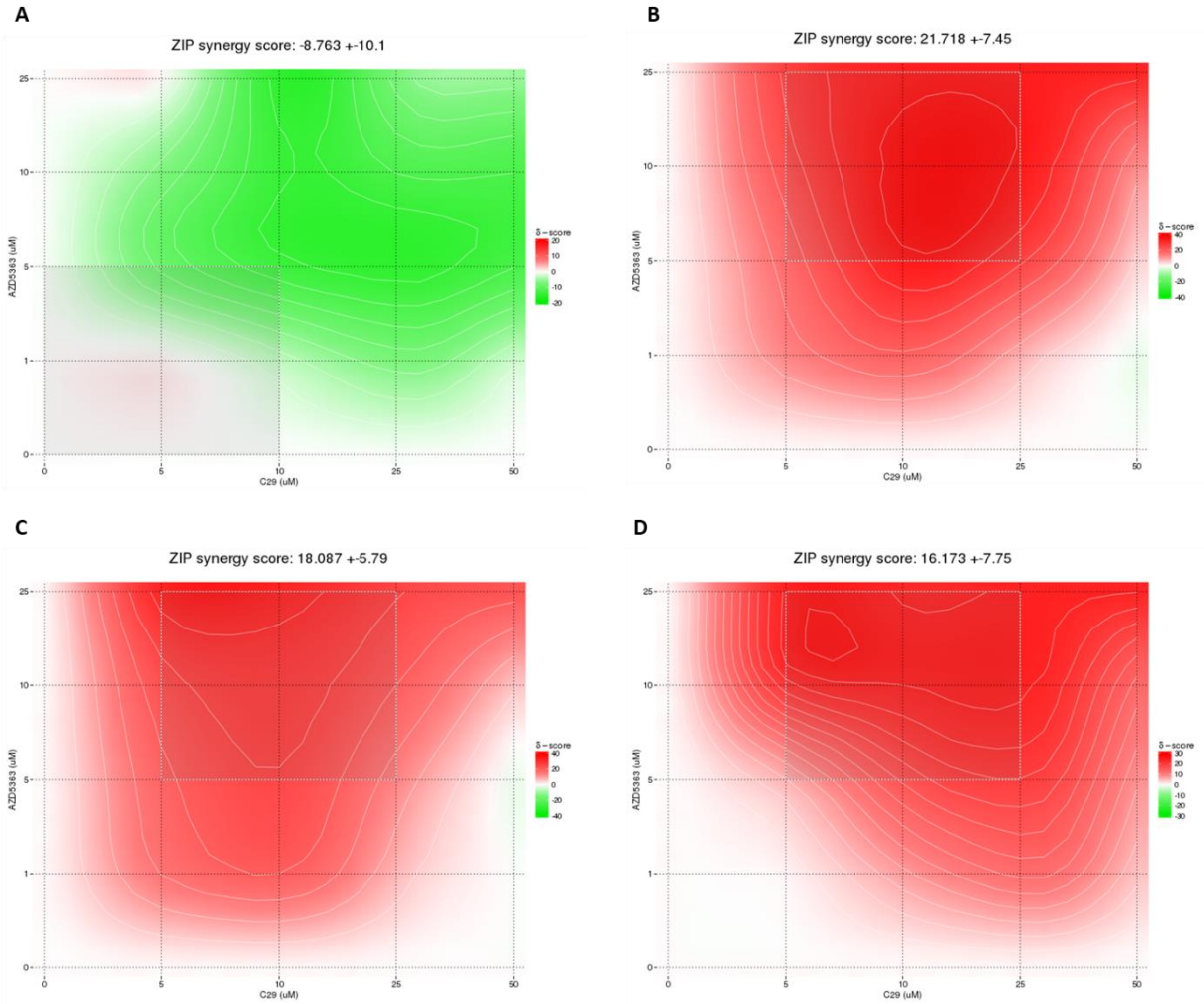

Figure 4.15: C29 and AZD5363 display a synergistic relationship in prostate cancer cell lines. Plots show SynergyFinder results obtained by treating A) DU145, B) LNCAP, C) PC3 and D) 22RV1 prostate cancer cells with TLR2 inhibitor C29 (x-axis) and AKT inhibitor AZD5363 (Capivasertib) (y-axis). Data shows n = 3 biological repeats, with ZIP synergy score and 95% confidence interval represented.

Within all of the prostate cancer cell lines tested, the combination of TLR2 and AKT inhibitor yielded reduced cell viability in comparison AKT inhibition alone. It was surprising to see reduced viability within the DU145 cells following co-treatment (Figure 4.14A), given the lack of sensitivity to other co-therapies tested in this project, however this result was not deemed significant by the One-way ANOVA and Tukey multiple comparison test performed.

Interestingly a significant result was obtained following 10 µM AKTi treatment combined with 25- or 50 µM TLR2i treatment in comparison to 10 µM AKTi treatment alone in LNCAPs (Figure 4.14B), yet no significance was established following combination therapy in the PC3 and 22RV1 lines (Figures 4.14 C and D respectively). However, 10 µM Capivasertib is generally considered to induce off-target effects, and so results should be treated with caution.

Analysis of synergism revealed the combination of C29 and Capivasertib to be highly synergistic in the LNCAP and PC3 PTEN-deficient prostate cancer cell lines and additive / synergistic within the PTEN-proficient 22RV1 line (Figure 4.15). Interestingly, combined treatment within the DU145 was deemed highly antagonistic and partly additive (Figure 4.15A), a finding that was somewhat conflicting given the improved results in Figure 4.14A. Irrespective of the DU145 cell line data, the overall findings suggest that TLR2 inhibition can improve the effects of AKT inhibition, thus combining the two could be largely beneficial for prostate cancer patients.

The SynergyFinder platform enables application of four frequently used reference models to determine synergism, which include the highest single agent (HSA), Bliss, Loewe, and Zero interaction potency (ZIP) models. The initial SynergyFinder analysis was undertaken using the ZIP model that assumes that the two drugs are non-interacting, and thus incur minimal changes in their dose–response curves by combining aspects of both the Bliss independence model and the Loewe additivity model that generates a response upon the assumption the two drugs function the same (Ianevski et al. 2020).

To further validate the ZIP model SynergyFinder data, analysis was repeated using the Bliss model that assumes the two drugs tested produce their effects independently. Findings revealed minimal differences in the summary synergy scores determined by both models (Table 4.2).

Table 4.2: Synergy scores for each NF-κB pathway inhibitor and Capivasertib as determined by the ZIP and Bliss reference models.

Drug combination	Cell line	ZIP synergy score	Bliss synergy score	Result
NF-κB i + AKTi	DU145	8.194 ±9.91	8.759 ±9.91	Additive & synergistic
	LNCAP	3.897 ±8.88	3.956 ±8.88	Additive & synergistic
	PC3	14.848 ±9.14	14.637 ±9.14	Additive & synergistic
	22RV1	-1.848 ±9.39	-2.733 ±9.39	Antagonistic & additive
BCL3i + AKTi	DU145	-3.81 ±8.41	-4.232 ±8.42	Antagonistic & additive
	LNCAP	9.571 ±7.3	9.371 ±7.3	Additive & synergistic
	PC3	15.334 ±6.06	15.144 ±6.06	Additive & synergistic
	22RV1	11.226 ±8.24	11.409 ±8.34	Additive & synergistic
CXCR1/2i + AKTi	DU145	3.915 ±9.42	3.296 ±9.42	Additive & synergistic
	LNCAP	23.464 ±7.34	23.302 ±7.34	Synergistic
	PC3	14.085 ±7.51	13.977 ±7.51	Additive & synergistic
	22RV1	22.981 ±10.02	22.987 ±10.02	Synergistic
TLR2i + AKTi	DU145	-8.763 ±10.1	-9.428 ±10.1	Antagonistic & additive
	LNCAP	21.718 ±7.45	21.785 ±7.45	Synergistic
	PC3	14.085 ±7.51	13.977 ±7.51	Additive & synergistic
	22RV1	16.173 ±7.75	15.876 ±7.75	Additive & synergistic

To summarise, when considering the 95% confidence interval generated to encompass results from each of the biological repeats, the combination of AKT inhibitor with CXCR1/2 inhibitor generated scores that indicated interactions were highly additive and highly synergistic across all cell lines tested (excluding the PTEN-positive DU145 line) (Figure 4.13), and that the combination of AKT inhibitor with TLR2 inhibitor tested also generated scores that were highly additive and highly synergistic within the prostate cancer cell line panel with the exception of the DU145 line (Figure 4.15). Interestingly, AKTi in combination with canonical NF-κB inhibitor BAY11-7082 or the BCL3 inhibitor CB1, displayed non-correlative yet reproducible cell type-specific responses, that were not reflective of PTEN status. For instance, the PTEN positive cell line 22RV1, responded to combined AKT and NF-κB pathway inhibition in a manner similar to the PC3 cells (Figures 4.8 and 4.10).

4.3.1.4. AKT inhibition in combination with CXCR1/2i or TLR2i suppresses prostate cancer cell proliferation *in vitro*

To further corroborate findings indicating combining either CXCR1/2i or TLR2i with AKT inhibition is more efficacious than monotherapies for the treatment of prostate cancer cells over time, the

Sartorius IncuCyte live-cell image analysis system was employed to analyse cell proliferation in response to treatment in real-time for 96 h.

DU145, LNCAP, PC3 and 22RV1 human prostate cancer cells were plated in 96 well plates as described in Section 4.3.1.1, and subsequently given CXCR1/2 and TLR2 inhibitors (± AKT inhibitor) at a synergistic dose, pre-determined using SynergyFinder analysis following 48 h of treatment. Immediately after dosing (0-hours), plates were placed into an incubator connected to the IncuCyte system, and confluency phase contrast images collected and analysed every 6 hours for a total period of 96 hours. After completion of the experiment, data was normalised to phase contrast images taken at 0 hr, then plotted using GraphPad (Figure 4.16 and 4.17).

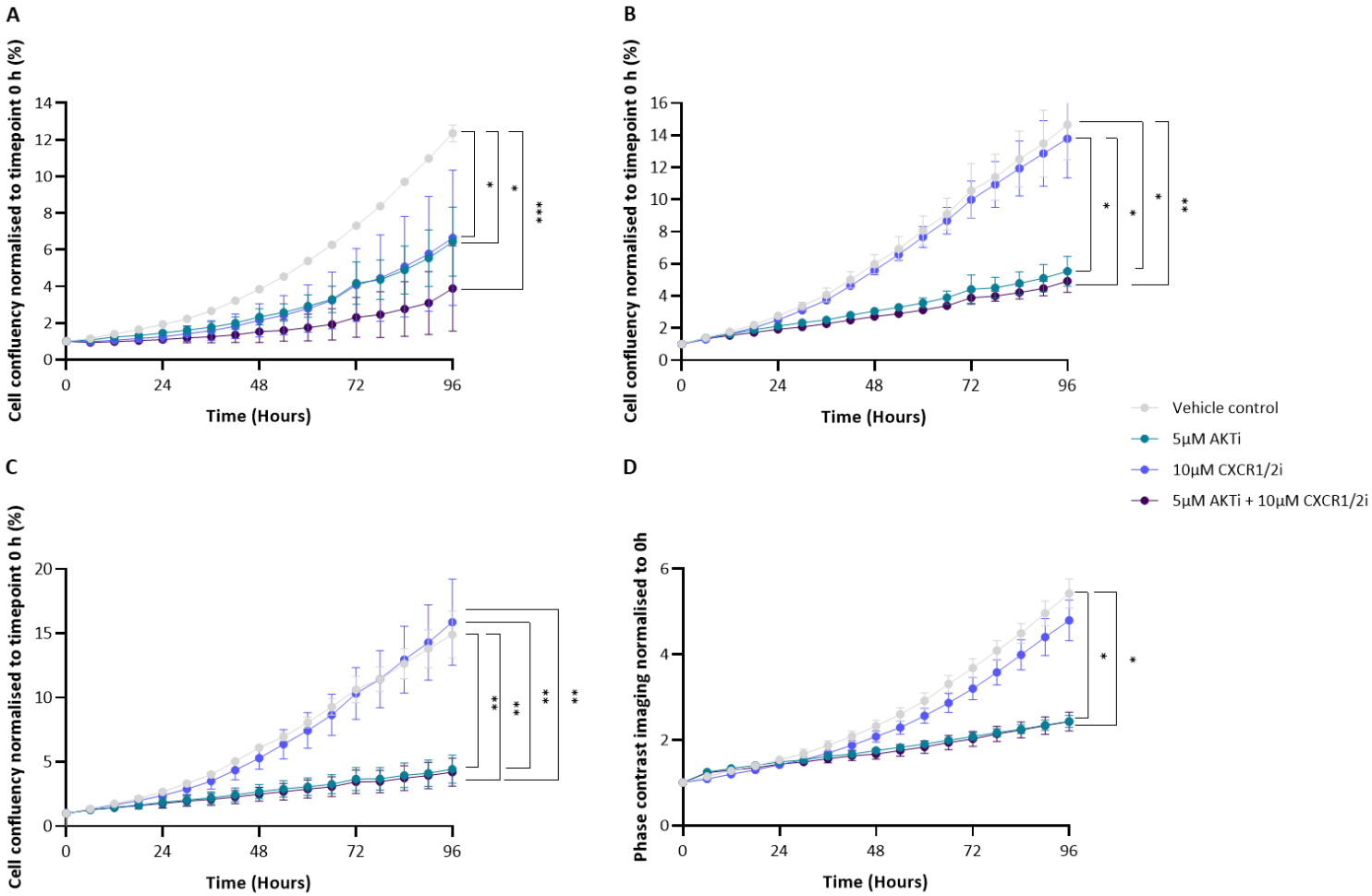

Figure 4.16: Co-inhibition of CXCR1/2 and AKT signalling does not reduce prostate cancer cell proliferation relative to AKTi alone. Graphs show results obtained by treating A) DU145, B) LNCAP, C) PC3 and D) 22RV1 cells with Capivasertib and Reparixin at synergistic doses (n = 3 biological repeats). A One-way ANOVA with a Tukey's multiple comparison test was performed to determine statistical significance of the trend line between each treatment group. Error bars = SEM.

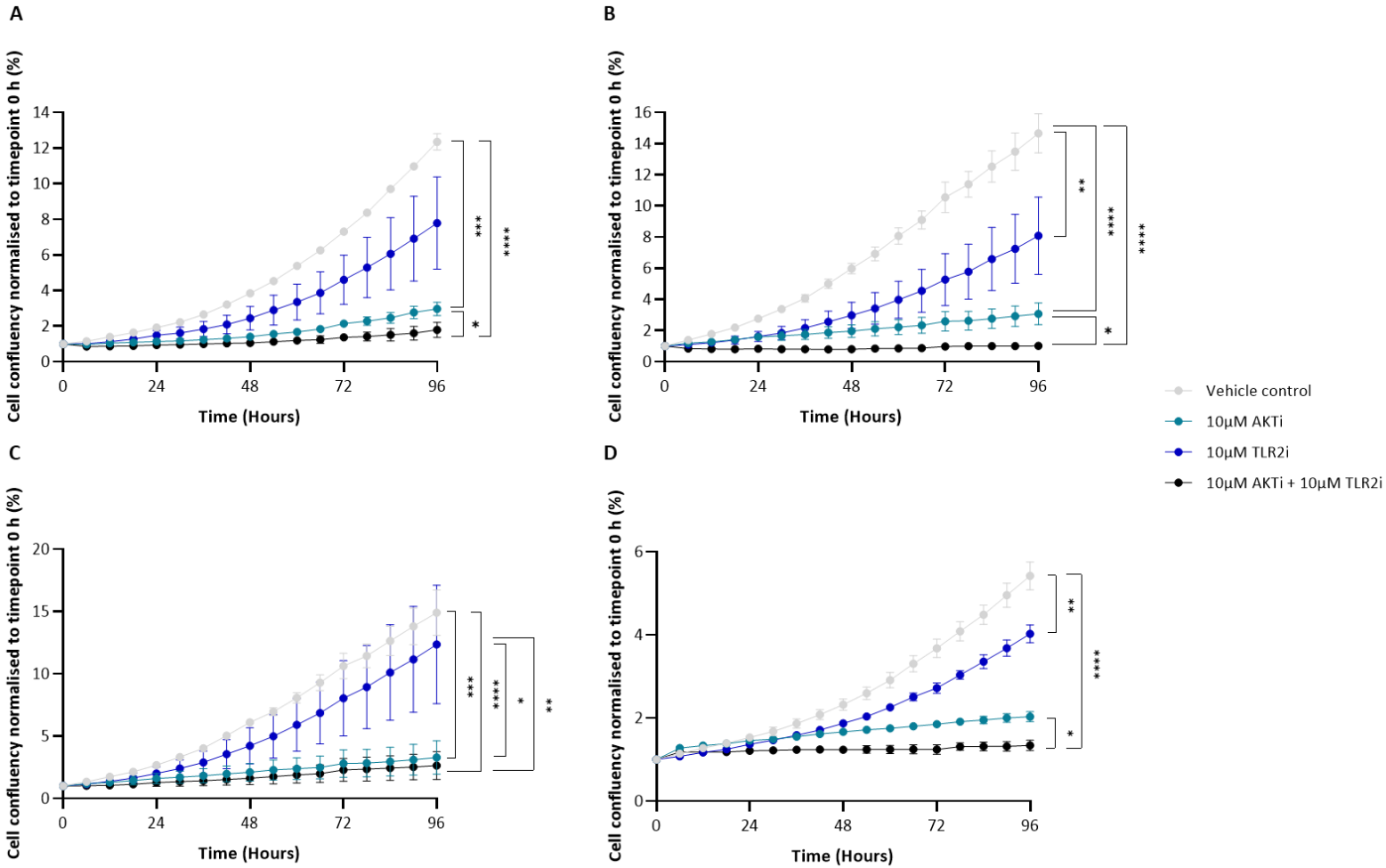

Figure 4.17: Co-inhibition of TLR2 and AKT signalling reduces prostate cancer cell proliferation relative to monotherapies. Graphs show results obtained by treating A) DU145, B) LNCAP, C) PC3 and D) 22RV1 cells with Capivasertib and C29 at synergistic doses (n = 3 biological repeats). A One-way ANOVA with a Tukey's multiple comparison test was performed to determine statistical significance of the trend line between each treatment group. Error bars = SEM.

Cell proliferation in response to Reparixin treatment alone was largely comparable to the vehicle control, except for the DU145 cells that displayed a reduction in proliferation upon Reparixin treatment relative to vehicle. All cell lines displayed sensitivity to the AKTi, which was not further increased when compared to cells co-treated with CXCR1/2 inhibitor and AKT inhibitor (Figure 4.16). However, a significant difference was obtained in the LNCAP and PC3 PTEN-deficient lines, when comparing co-treatment to CXCR1/2 treatment alone at 96-hours (Figure 4.16B and C). These findings indicate that CXCR1/2i and AKTi do not synergise, contrasting the cell viability data, and highlight the importance of running several different functional assays to assess treatment response. While the IncuCyte assay analyses the confluency of cells on the surface of the tissue culture dish, the cell viability assay measures metabolic activity, which may be re-wired in response to AKTi treatment.

When comparing the confluency of prostate cancer cells in response to vehicle, TLR2i, AKTi or TLR2i plus AKTi; DU145, 22RV1 and LNCAP cells (PTEN-proficient and PTEN-deficient) displayed a significant reduction in the number of cells co-treated with the TLR2i and AKTi compared to vehicle or monotherapies, while PC3 cells showed a similar trend (Figure 4.17). These findings indicate that TLR2 and AKT co-inhibition is synergistic, supporting the 48-h cell viability assay data (Figure 4.14). TLR2 inhibition also reduced cell proliferation relative to the vehicle control, however there was a large degree of variability between biological repeats resulting in large error bars.

Whilst the SynergyFinder plots indicated 10 µM AKT inhibitor was the most optimal synergistic dose with the TLR2 inhibitor in the LNCAP, PC3 and 22RV1 cell lines (as shown by the shaded boxes in Figure 4.15), in hindsight this dose may have been too high, especially given that the relative IC_{50} values calculated were considerably lower (Figure 4.7), therefore this high dose could lead to off-target effects and suggests these experiments should be repeated using a lower AKTi dose. Overall, when considering all the cell lines, this experiment highlighted that combined TLR2i and AKTi therapy is indeed more effective in inducing a response relative to monotherapies at 96 h.

While the proliferation assay data supported the cell viability data and provided additional information on the effects mediated within a longer treatment period, looking at the apoptotic status of the treated cells would also be beneficial in understanding whether the NF-κB pathway inhibitors drive cell death or simply impede their replicative capabilities, which could be investigated through use of an annexin V cell death time course assay.

It is also important to note that within all the cell lines analysed, a spike in proliferation appeared at 72-hours in response to the AKT inhibitor either alone or in combination with CXCR1/2 or TLR2 inhibitor, suggesting the possible necessity for re-dosing of the AKT inhibitor at this time point to keep proliferation repressed and that perhaps the cell cycle is indeed influenced.

Considering the cell viability and confluency data, and the synergy scores established though combined inhibition of CXCR1/2 or TLR2 signalling with AKT signalling, the combined therapies appear to show promise against prostate cancer. Thus, the remainder of this chapter focuses on determining the efficacy of these combination therapies using Reparixin, C29 and Capivasertib, within a variety of *ex vivo* functional assays (discussed in section 4.3.3).

4.3.2. Western blot (WB) validation of AKT, CXCR1/2 and TLR2 inhibitors

To investigate if AKTi on-target effects were achieved, protein lysates from DU145 and PC3 human prostate cancer cells treated with either vehicle, CXCR1/2i Reparixin, TLR2i C29, AKTi Capivasertib and CXCR1/2i or TLR2i +/- AKTi for 48 h (at their pre-determined synergistic doses) were analysed by WB to establish p-AKT and total AKT protein expression levels (n = 3, Figures 4.18 – 21).

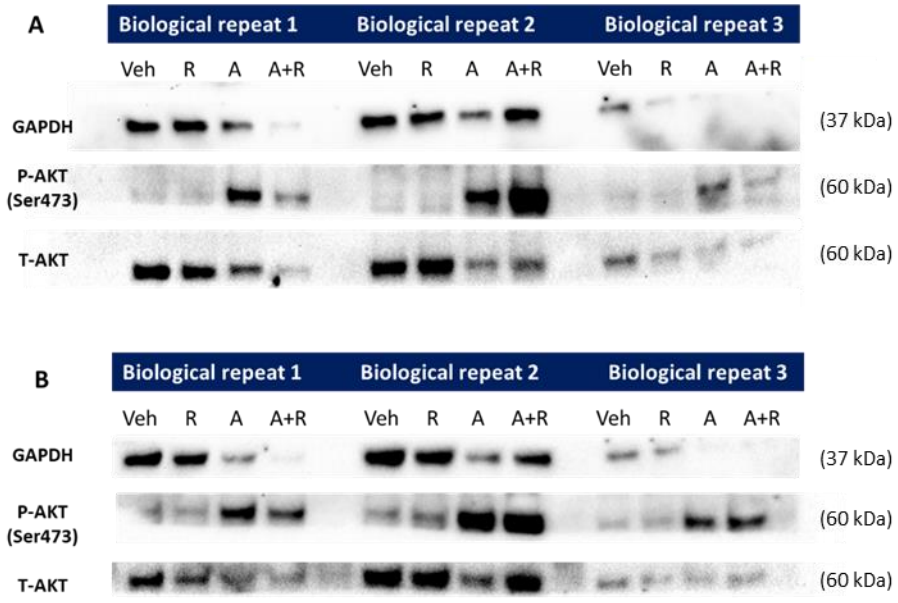

Figure 4.18: Phosphorylated AKT and total AKT WB images of protein lysates from DU145 and PC3 cell lines treated with CXCR1/2 inhibitor Reparixin and AKT inhibitor Capivasertib. Images show GAPDH, phosphorylated AKT and total AKT stained protein blots of A) DU145 cells and B) PC3 cells treated with vehicle control (0.1% DMSO), 5 µM Reparixin (CXCR1/2i), 5 µM Capivasertib (AKTi) and both inhibitors in combination for 48 h (n = 3 / biological repeats). All biological repeats were assessed on a single gel. Bands present in empty lanes reflect non-specific background staining. Veh; vehicle control, R; Reparixin, A; AZD5363, A+R; AZD5363 and Reparixin.

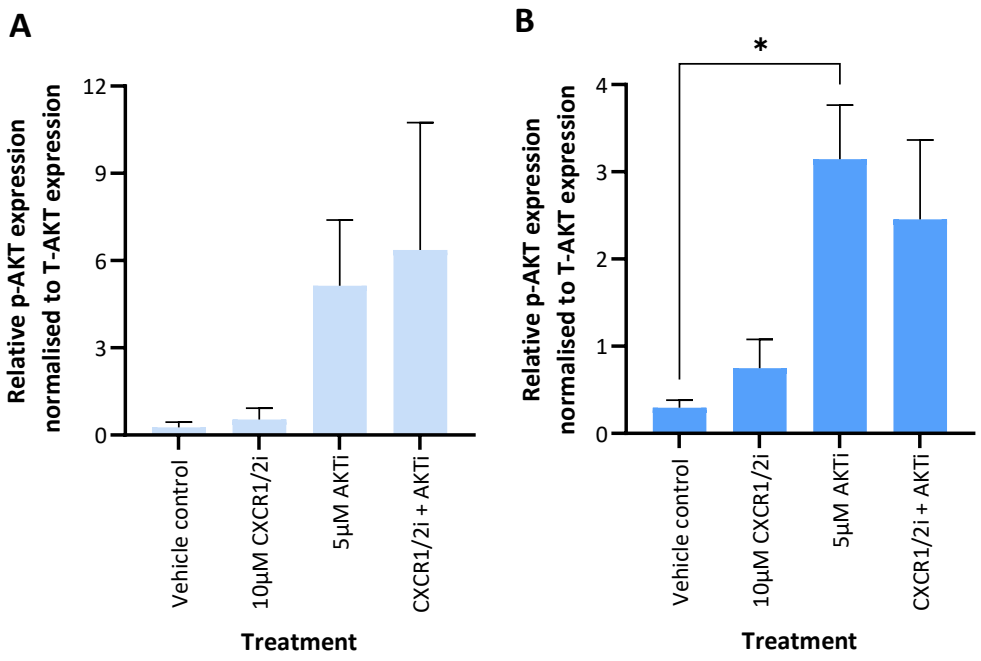

Figure 4.19: p-AKT protein expression is elevated in prostate cancer cells following AKTi. Graphs show protein expression quantitation of p-AKT (at site Ser473) within A) DU145 cells and B) PC3 cells treated for 48 hours with vehicle, Reparixin (CXCR1/2i), Capivasertib (AKTi) and combined Reparixin and Capivasertib treatment at pre-determined synergistic doses indicated. Data was both normalised to the housekeeping protein (GAPDH), then to total AKT. n = 3 biological repeats. A One-way ANOVA with a Tukey's multiple comparison test was performed to determine statistical significance between each treatment group. Error bars = SEM.

WB analysis revealed 48-hour treatment with the AKTi induces p-AKT expression in both DU145 and PC3 cells relative to the vehicle or Reparixin treatment alone, where expression remained high when Capivasertib was combined with Reparixin (Figure 4.18)

Densitometry analysis confirmed p-AKT protein expression normalised to total-AKT, was significantly overexpressed following treatment with AKT inhibitor alone in comparison to the vehicle control within the PC3 cell line (Figure 4.16B). Although high p-AKT expression was also observed in the DU145 cells, there was more variability in the biological repeats, thus this response was not statistically significant (Figure 4.19).

Similarly, p-AKT was also augmented in PC3 and DU145 cells upon AKTi or AKTi plus TLR2i treatment relative to the vehicle or TLR2i alone (Figure 4.20).

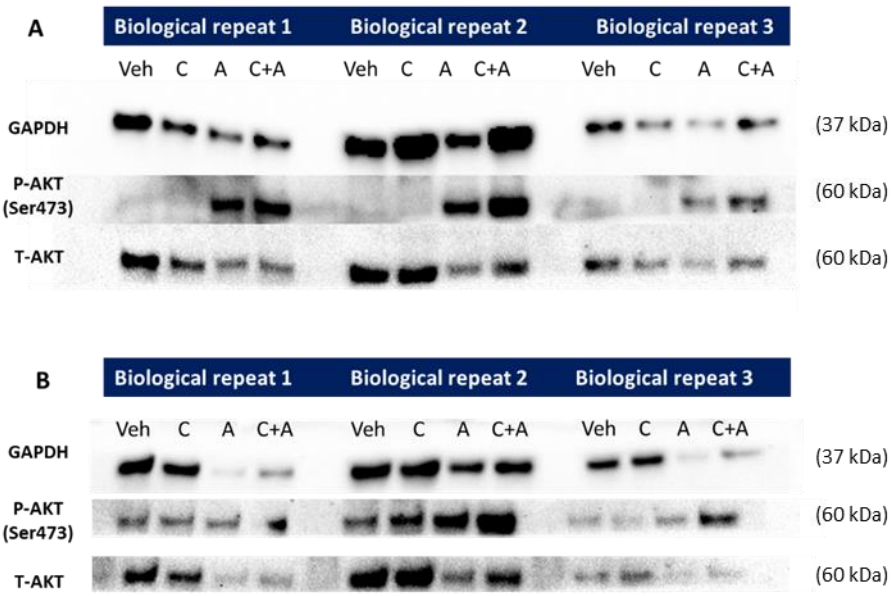

Figure 4.20: Phosphorylated AKT and total AKT western blot images of protein lysates from DU145 and PC3 cell lines treated with TLR2 inhibitor C29 and AKT inhibitor Capivasertib. Images show GAPDH, phosphorylated AKT and total AKT stained protein blots of A) DU145 cells and B) PC3 cells treated with vehicle control (0.1% DMSO), 10 µM C29 (TLR2i), 10 µM Capivasertib (AKTi) and both inhibitors in combination for 48 h (n = 3 / biological repeats). All biological repeats were assessed on a single gel. Bands present in empty lanes reflect non-specific background staining. Veh; vehicle control, C; C29, A; AZD5363, C+A; C29 and AZD5363.

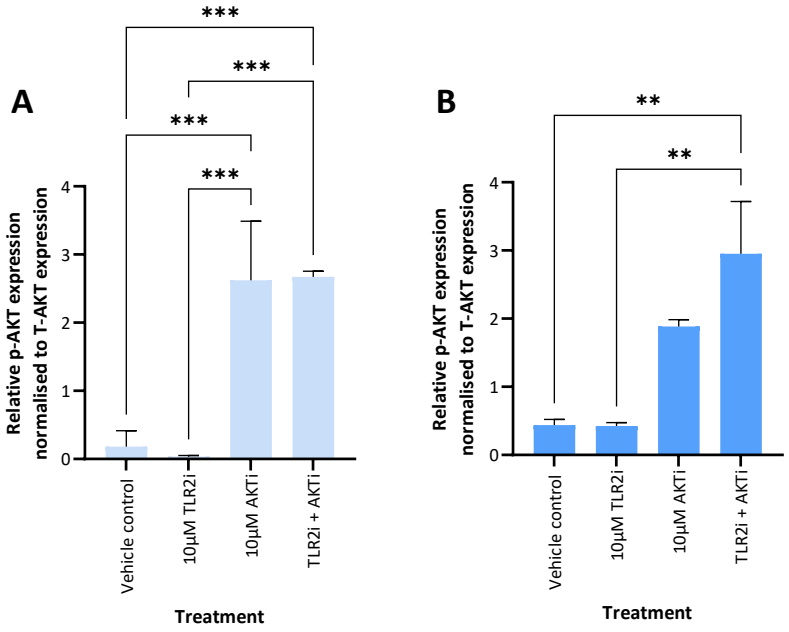

Figure 4.21: p-AKT protein expression is elevated in prostate cancer cells following TLR2 and AKT co-inhibition. Graphs show protein expression quantitation of p-AKT (at site Ser473) within A) DU145 cells and B) PC3 cells treated for 48 hours with vehicle, C29 (TLR2i), Capivasertib (AKTi) and combined C29 and Capivasertib treatment at pre-determined synergistic doses. Data was both normalised to the housekeeping protein (GAPDH), then to

total AKT. n = 3 biological repeats. A One-way ANOVA with a Tukey's multiple comparison test was performed to determine statistical significance between each treatment group. Error bars = SEM.

Interestingly, total AKT expression levels in PC3 cells were not consistent across the treatment groups, with biological repeats 1 and 3 indicating less total AKT expression following AKT treatment alone or in combination with TLR2 inhibition (Figure 4.20B). Densitometry analysis in DU145 cells revealed an increase in p-AKT expression following AKTi, where combined AKT and TLR2i treatment was statistically significant relative to cells treated with vehicle or the TLR2 inhibitor alone (Figure 4.21A).

Furthermore, significant differences were only observed following combined therapy in PC3 cells relative to the vehicle and TLR2 inhibitor alone (Figure 4.21B). Notably, these findings correspond with previous work showing Capivasertib treatment leads to the accumulation of AKT phosphorylation (Zhang et al. 2016b).

To better determine whether AKT signalling is suppressed in response to the AKTi, WB to detect the AKT/mTORC1 downstream target, phosphorylated eukaryotic translation initiation factor 4E-binding protein 1 (p-4EBP1), was performed on protein lysates isolated from PC3 cells treated with either vehicle, TLR2i, AKTi or TLR2i+AKTi for 48 h (Figure 4.22).

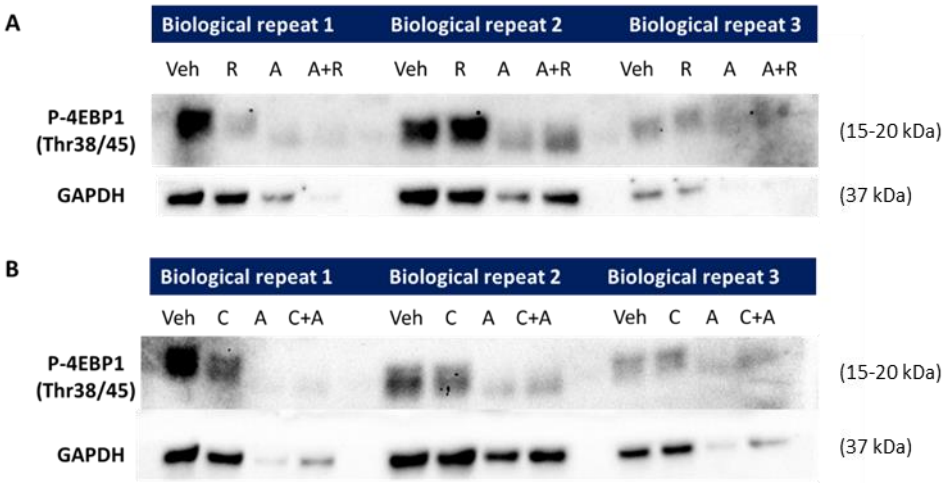

Figure 4.22: Phosphorylated 4EBP1 expression is reduced in response to AKTi in PC3 cells. Images show p-4EBP1 and GAPDH stained protein blots of PC3 cells treated with A) vehicle control (0.1% DMSO), 5 µM Reparixin (CXCR1/2i), 5 µM Capivasertib (AKTi) and both inhibitors in combination, and B) vehicle control (0.1% DMSO), 10 µM C29 (TLR2i), 10 µM Capivasertib (AKTi) and both inhibitors in combination for 48 h (n = 3 / biological repeats. All biological repeats were assessed on a single gel. Bands present in empty lanes reflect non-specific

background staining. Veh; vehicle control, R; Reparixin, A; AZD5363, A+R; AZD5363 and Reparixin, C; C29, C+A; C29 and AZD5363.

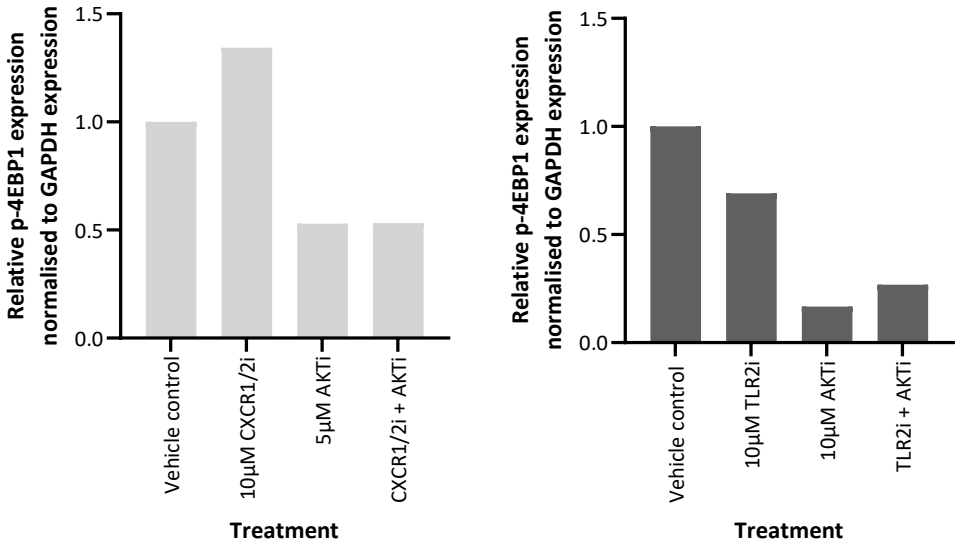

Figure 4.23: p-4EBP1 protein expression is reduced following AKT inhibition (± NF-κB pathway inhibition). Graphs show protein expression quantitation of p-4EBP1 (at sites Thr38 and Th45) within a representative biological repeat of PC3 cells treated for 48 hours with Reparixin (CXCR1/2i), C29 (TLR2i), Capivasertib (AKTi) and combination therapies at pre-determined synergistic doses. Data was both normalised to the housekeeping protein (GAPDH) and the vehicle control (0.1% DMSO).

Due to some very faint bands generated within the GAPDH blots despite the same amount of protein being loaded per treatment, densitometry analysis of p-4EBP1 expression relative to GAPDH expression within all biological repeats was not possible owing to variations in the housekeeping protein between samples. It was not possible to determine if the same amount of protein had been loaded per well, therefore biological repeat 2 alone was quantitated to enable partial assessment of the dataset (Figure 4.23).

WB analysis revealed that p-4EBP1 expression was considerably lower in cells treated with AKT inhibitor or AKT inhibitor in combination with CXCR1/2 inhibitor or TLR2 inhibitor, relative to vehicle control or single NF-κB inhibitors, indicating AKT function to be indeed repressed following treatment including Capivasertib.

Whilst every effort was made to ensure even loading of protein, housekeeping proteins such as GAPDH can also be influenced and thus reduced in response to treatment. Use of the alterative house-keeping protein, β-actin, was trialled however appeared to be worse (data not shown), therefore a repeat of

this experiment alongside a different housekeeping protein may be beneficial. Normalisation to total 4EBP1 levels in the future would also enable a better interpretation of these findings.

As part of the studies into the C29 (TLR2i) mechanism of action, Mistry et al, probed for p-ERK via western blot following 50 µM C29 treatment of murine peritoneal macrophages in the presence of stimulated TLR2/1 and TLR2/6 signalling pathways. They demonstrated that after 30 minutes, phosphorylation of ERK1/2, P38 and JNK1/2 protein all decreased following C29 treatment relative to no treatment (Mistry et al. 2015). Toll-like receptor signalling has been shown to activate mitogen-activated protein kinase (MAPK) pathways (Li et al. 2014); accordingly immunoblotting for p-ERK was performed to determine if C29 reduces MAPK signalling in prostate cancer cells (Figures 4.25 and 4.25).

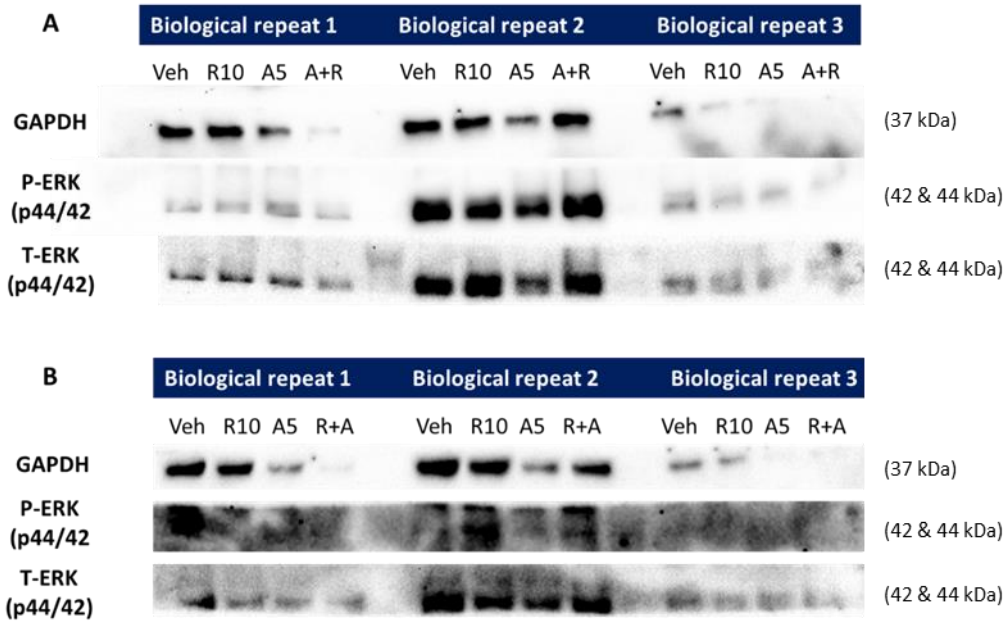

Figure 4.24: Phosphorylated ERK and total ERK western blot images of protein lysates from DU145 and PC3 cell lines treated with CXCR1/2 inhibitor Reparixin and AKT inhibitor Capivasertib. Images show GAPDH, phosphorylated ERK and total ERK stained protein blots of A) DU145 cells and B) PC3 cells treated with vehicle control (0.1% DMSO), 5 µM Reparixin (CXCR1/2i), 5 µM Capivasertib (AKTi) and both inhibitors in combination for 48 h (n = 3 / biological repeats). All biological repeats were assessed on a single gel. Bands present in empty lanes reflect non-specific background staining. Veh; vehicle control, R; Reparixin, A; AZD5363, A+R; AZD5363 and Reparixin.

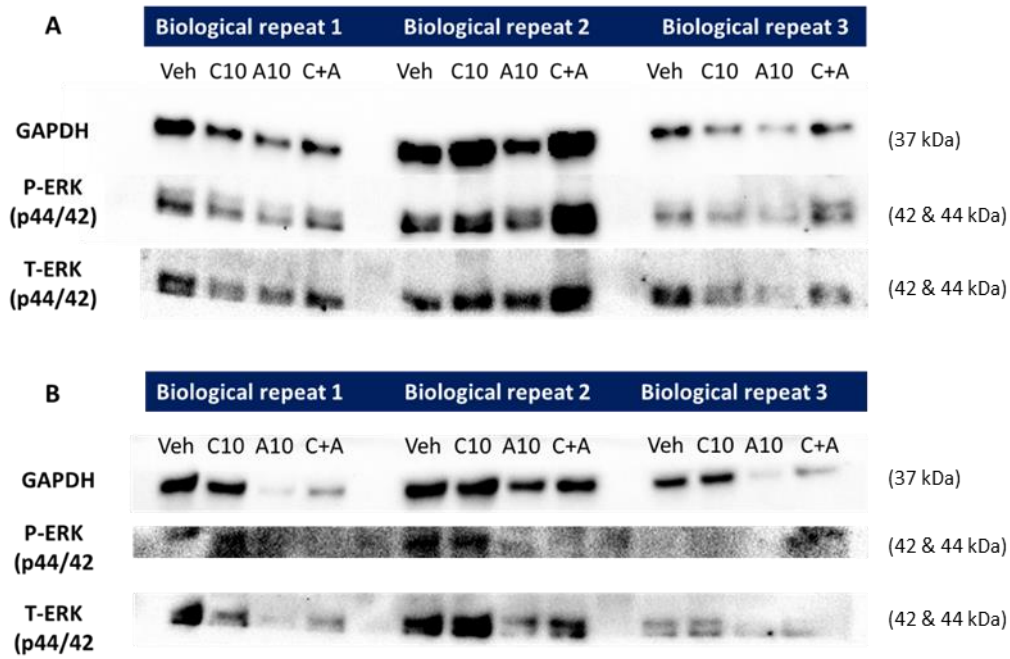

Figure 4.25: Phosphorylated ERK and total ERK western blot images of protein lysates from DU145 and PC3 cell lines treated with TLR2 inhibitor C29 and AKT inhibitor Capivasertib. Images show GAPDH, phosphorylated ERK and total ERK stained protein blots of A) DU145 cells and B) PC3 cells treated with vehicle control (0.1% DMSO), 10 µM C29 (TLR2i), 10 µM Capivasertib (AKTi) and both inhibitors in combination for 48 h (n = 3 / biological repeats). All biological repeats were assessed on a single gel. Bands present in empty lanes reflect non-specific background staining. Veh; vehicle control, C; C29, A; AZD5363, C+A; C29 and AZD5363.

Quantitation of treated DU145 cell protein blots suggested that inhibition of CXCR1/2, AKT or both, does not alter total ERK or phosphorylated ERK protein expression relative to the vehicle control (Figure 4.24A). The response in PC3 cells following treatment with these inhibitors largely varied between biological repeats, indicating a repeat of this experiment may be required (Figure 4.24B). Similarly, when assessing the effect of TLR2 inhibition, AKT inhibition and combined therapy on p-ERK expression within DU145 cells, no differences were observed between treatment groups relative to the vehicle control (Figure 4.25). These findings were confirmed by densitometry analysis (Figure 2.26).

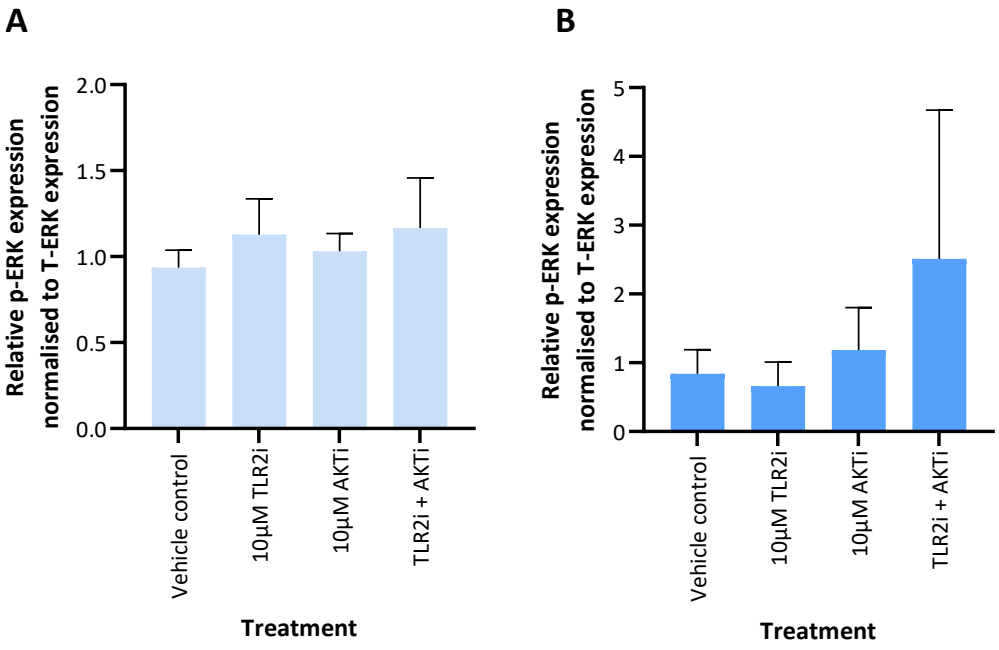

Figure 4.26: Phosphorylated ERK expression remains unaltered following TLR2 and AKT inhibition in DU145 and PC3 cells. Graphs show protein expression quantitation of p-ERK within A) DU145 cells and B) PC3 cells treated for 48 hours with vehicle, C29 (TLR2i), Capivasertib (AKTi) and combined C29 and Capivasertib treatment at pre-determined synergistic doses. Data was both normalised to the housekeeping protein (GAPDH), then to total ERK. n = 3 biological repeats. A One-way ANOVA with a Tukey's multiple comparison test was performed to determine statistical significance between each treatment group. Error bars = SEM.

In summary, we have confirmed that Capivasertib does mediate blockade of AKT signalling, as identified by a reduction in p-4EBP1 expression in DU145 and PC3 cells, and the characteristic AKTi-induced increase in p-AKT. We were not able to replicate the Mistry group's finding that p-ERK expression is reduced following inhibition of the TLR2 pathway by C29, however it is important to both note that our *in vitro* approach did not include external TME/ECM stimulation of the toll-like receptor pathways and that this response could be tissue dependent. It is evident that further work is essential in determining how these inhibitors impact signalling pathways in the prostate cancer cell lines and whether the treatment responses are influenced by PTEN status.

Whilst the western blotting experiments provided insight, it is important to note that due to loading control issues and variability in target protein staining, firm conclusions cannot be made on the set of results obtained and will need repeating.

4.3.3. *Ex vivo* inhibition of the NF-κB pathway and AKT in prostate cancer organoids

Despite the good reproducibility and high-throughput performance of 2D cell lines, they do not replicate the natural 3D composition of *in vivo* tissue. In 3D cell culture, cell-cell and cell-extracellular environment interactions are better maintained, thus allowing more accurate phenotype diversity and preservation of morphology (Kapałczyńska et al. 2018).

Cellular responses to drugs can be strongly influenced by proteins, cytokines, and sequestered growth factors secreted/present within the extracellular matrix (ECM), which can both promote drug resistance within cells or modify the drugs mechanism of action, by modulating drug availability, altering cell intrinsic molecular mechanisms, in addition to limiting the expression of drug targets (Langhans 2018).

To assess whether our NF-κB pathway inhibitors instigated a cell intrinsic (innate) or extrinsic response, organoid cultures were established in growth factor reduced Matrigel, an organic hydrogel that mimics some characteristics of the ECM (Langhans 2018).Whilst this type of *ex vivo* model does not take into consideration immune influence on cellular responses to drugs, it does enable us to explore short-term drug responses in a 3D architectural structure surrounded by an ECM to better mimic a patient tumour.

4.3.3.1. *Pten*-deleted prostate tumour organoid viability is unaltered following CXCR1/2 and TLR2 inhibition (± AKT inhibition)

To test if Reparixin or C29 can synergise with Capivasertib to increase therapeutic efficacy in *ex vivo* culture, experiments were performed using primary organoids derived from *PBiCre*$^{+/-}$ *Pten*$^{fl/fl}$ and *PBiCre*$^{+/-}$ *Pik3ca*$^{+H1407R}$ GEMM prostate tumours (n = 3 / cohort, prepared by Dr Daniel Turnham, as detailed in Section 2.14.4).

Five days post-seeding, *PBiCre*$^{+/-}$ *Pten*$^{fl/fl}$ organoids had established and were treated with either the vehicle, AKTi or CXCR1/2i or TLR2i ± AKTi (using pre-determined synergistic doses established in the human prostate cancer cell lines). After 48-hours, cell viability was assessed using the Cell Titre Glo assay (detailed in Section 2.14.6), that provides a relative light unit (RLU) readout that is proportional to cell viability. 10 minutes prior to the Cell Titre Glo assay, images of the *Pten*-null and *Pik3ca*-mutant organoids were also taken at 2x magnification using a standard light microscope (Figures 4.27 and 4.28 respectively).

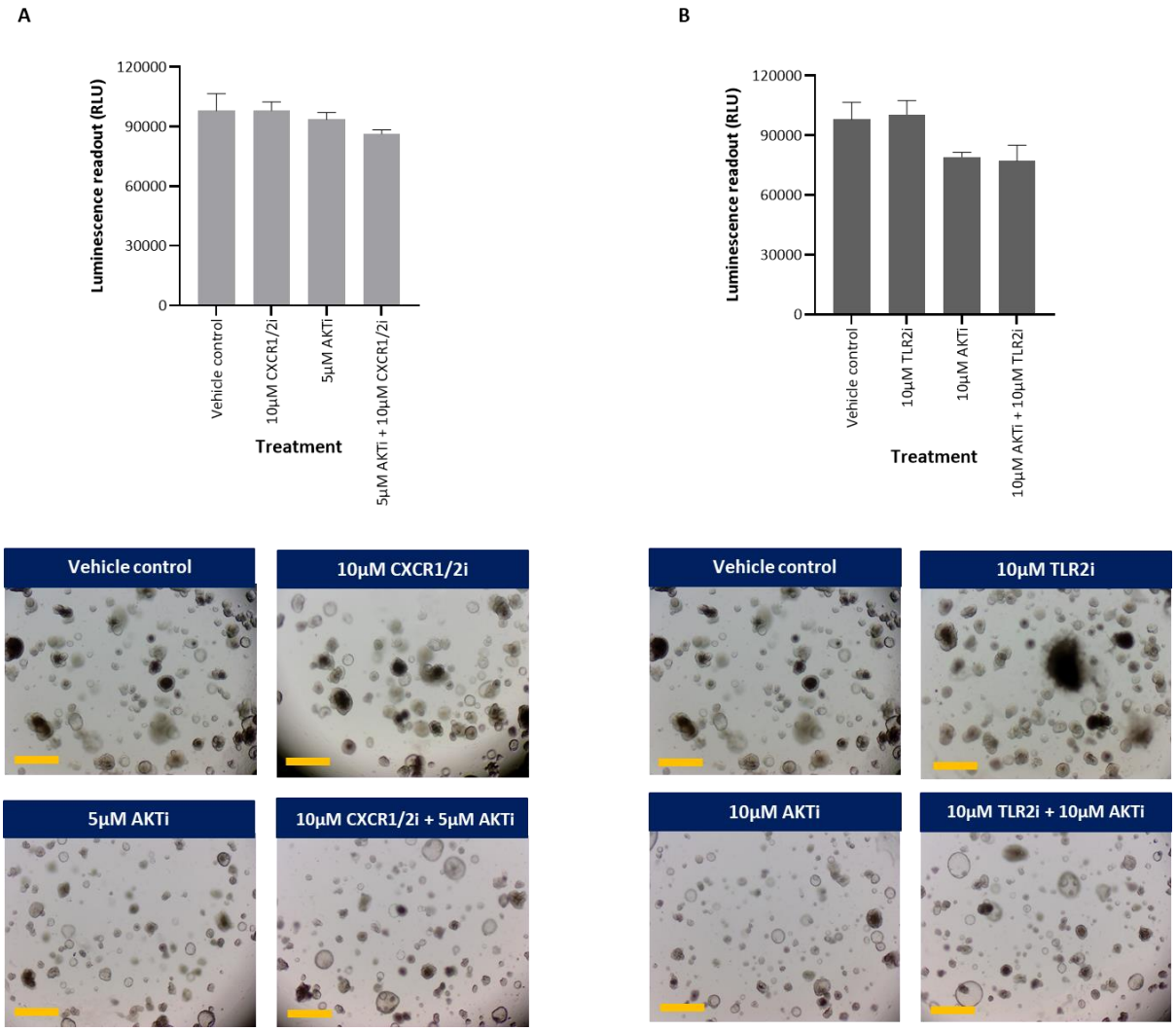

Figure 4.27: *Pten*-deficient murine prostate cancer organoid viability is not affected by AKT or NF-κB pathway directed therapies alone or in combination. Graphs show results obtained by treating *PBiCre*$^{+/-}$ *Pten* $^{fl/fl}$ prostate cancer primary organoids (pre-propagated for 5 days) with either (A) vehicle, Reparixin (CXCR1/2i), Capivasertib (AKTi), and Reparixin + Capivasertib and B) vehicle, C29 (TLR2i), Capivasertib, and C29 + Capivasertib for 48 hours. Data shows mean viability, n = 3 biological repeats. Error bars = SEM. A one-way ANOVA with a Tukey's multiple comparison test was performed to determine statistical significance between each treatment group, and no statistical differences were observed. Images represent organoid culture 48 hr post inhibitor treatment, taken using a basic light microscope at 2x magnification. Vehicle control images shown in A and B are identical as they depict the same condition (assays investigating CXR1/2i and TLR2i were performed in parallel). Scale bar = 500 µm.

Cell-titre Glo assay outputs revealed that treatment with 5 µM AKT inhibitor slightly reduced PTEN-null organoid viability relative to the vehicle control (0.1% DMSO), with the 10 µM AKT inhibitor generating an even greater response, however neither trend reached statistical significance (One-way ANOVA, p value = 0.9291 and 0.2915 respectively, Figure 4.27A and 4.27B respectively). Combined CXCR1/2 and AKT inhibition seemingly further reduced viability relative to the 5 µM AKT inhibition alone, however this result was not significant.

Furthermore, treatment of PTEN-null organoids with combined TLR2 and AKT inhibition appeared to show a marked reduction in viability relative to the vehicle control and TLR2i alone, however once again statistical significance was not reached for either treatment group using the one-way ANOVA test. Importantly, a Kruskal Wallis test revealed the organoid viability data generated was normally distributed as expected, thus confirming the One-way ANOVA statistical analysis undertaken was appropriate.

Due our previous finding that *Pten*-null prostate cancer and *Pik3ca*-mutant prostate tumours can mediate distinct signalling events and thus may respond differently to therapeutics, we also sought to determine whether *Pik3ca*-mutant mouse tumours respond to AKTi and/or NF-κB pathway directed therapies alone or in combination. *PBiCre$^{+/-}$; Pik3ca$^{+/HR1047}$* organoids (established by Dr Daniel Turnham, Pearson Lab) were grown for 5 days, then assessed for cell viability and morphology responses to vehicle, AKT inhibition, NF-κB-inhibition (via CXCR1/2 and TLR2) and combined AKT and NF-κB inhibition after 48 hours. Once again, pre-determined synergistic doses that were established in 2D culture were used, however, the Capivasertib (AKTi) dose was reduced from 10 µM to 5 µM for our TLR2i co-therapy assessment to minimise the quantity of organoids required for the experiment as *Pik3ca*-mutant organoids were limited in number.

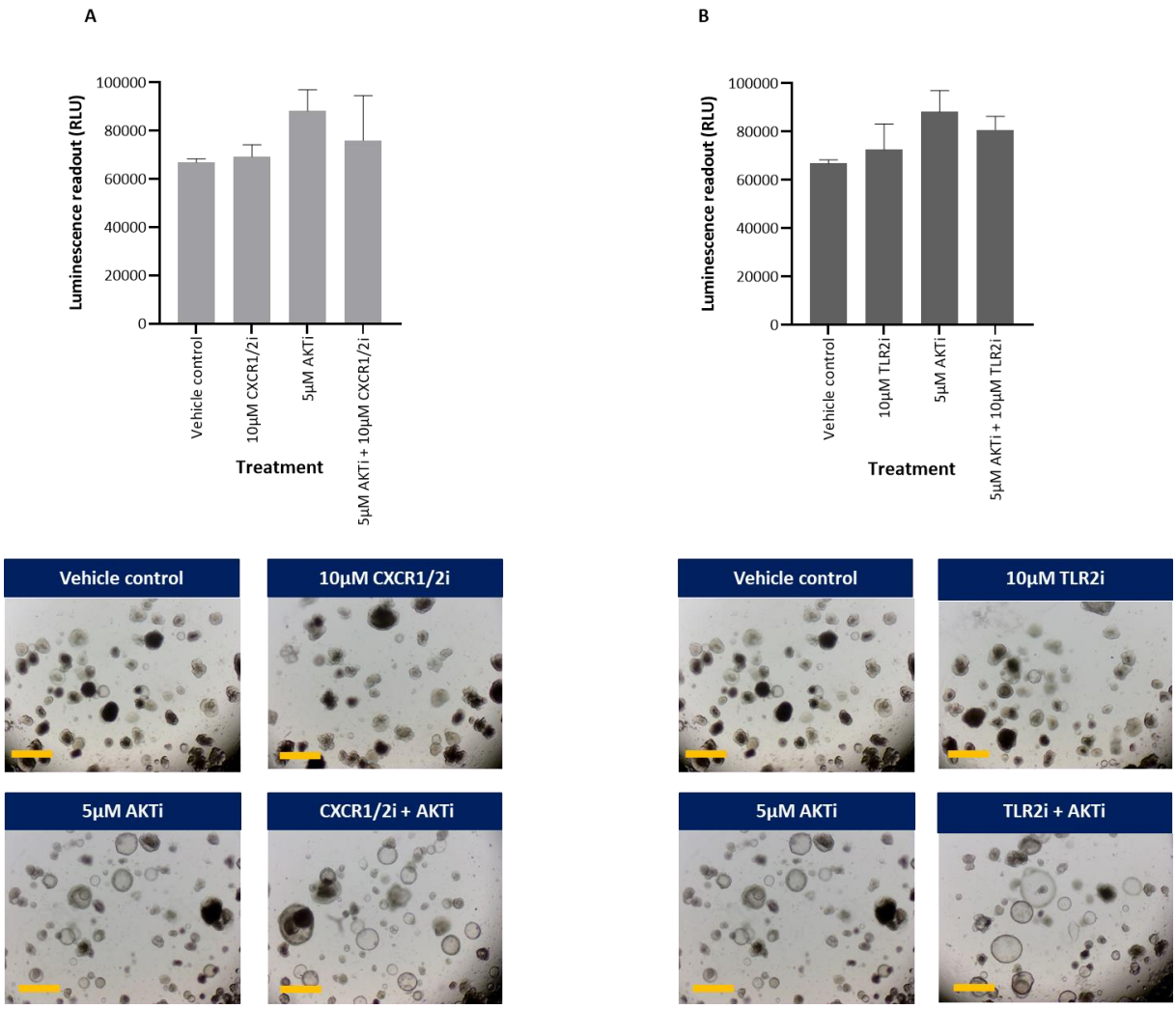

Figure 4.28: *Pik3ca*-mutant murine prostate cancer organoid viability is not affected by AKT or NF-κB pathway directed therapies alone or in combination. Graphs show results obtained by treating *PBiCre*$^{+/-}$ *Pik3ca* $^{+/HR}$ prostate cancer primary organoids (pre-propagated for 5 days) with either (A) vehicle, Reparixin (CXCR1/2i), Capivasertib (AKTi), and Reparixin + Capivasertib and B) vehicle, C29 (TLR2i), Capivasertib, and C29 + Capivasertib for 48 hours. Data shows mean viability, n = 3 biological repeats. Error bars = SEM. A one-way ANOVA with a Tukey's multiple comparison test was performed to determine statistical significance between each treatment group, and no statistical differences were observed. Images represent organoid culture 48 hr post inhibitor treatment, taken using a basic light microscope at 2x magnification. Vehicle control images shown in A and B are identical as they depict the same condition (assays investigating CXR1/2i and TLR2i were performed in parallel). Scale bar = 500 μm.

The data indicated *Pik3ca*-mutant prostate cancer organoid cell viability is not altered in response to either CXCR1/2 or TLR2 inhibition, relative to the vehicle (0.1% DMSO) (Figure 4.28). Each NF-κB inhibitor in combination with AKT inhibitor additionally showed to have no effect on organoid cell viability.

Although a slight trend for increased organoid viability was observed in response to 5 µM AKT inhibitor treatment, this finding was not statistically significant (normal distribution of the data was confirmed via a Kruskal Wallis test). Together, the data from the *Pten*-deficient and *Pik3ca*-mutant prostate cancer organoid experiments did not show any significant differences in response to AKTi or NF-κB pathway directed therapies, alone or in combination, suggesting that perhaps in an organoid setting we see no effect of the inhibitor due to a lack of receptor stimulation from cytokines and growth factors that would normally be present within a TME to promote activation of the NF-κB pathway.

Collectively, these findings show no statistically significant reduction in organoid viability following treatment either NF-κB inhibitor, AKT inhibitor or combination therapy in primary organoids and that perhaps an alternative viability assay such as IncuCyte analysis may be required help correlate the 3D data to the 2D results.

Moreover, the organoids due to their mutational status may have been facilitating reduced drug uptake. To address this potential issue, organoid permeability and efflux could be assessed, in addition to quantifying the activity of the drug metabolising enzymes, to determine efficiency of uptake and processing of the inhibitors by the organoids (Onozato et al. 2018).

In 2D cell culture, prominent changes were observed following NF-κB pathway and AKT signalling inhibition, thus suggesting that a cell intrinsic response is mediated; however, it is important to remember that the drug doses used in organoid culture were established from the 2D culture findings and may have not been optimal for 3D culture. If time had permitted, calculation of organoid culture IC_{50} values or establishing drug dose curves may have helped to identify whether inhibitor synergy exists in *ex vivo* organoid culture.

Furthermore, supplements that were added to the complete organoid culture media but not 2D cell culture media, may have also contributed to the different responses observed in organoid culture relative to 2D culture. For example, EGF was added to organoid media and is well known to activate the RAS-RAF-MEK-ERK MAPK and PI3K-AKT-mTOR signalling cascades, stimulating cancer cell proliferation and survival ((Wee and Wang 2017), (Lin et al. 2021a)). Using such additives for optimal organoid growth may have also activated pathways to counteract the effects of NF-κB pathway inhibition and thus diminish the impact of the inhibitors previously observed in 2D cell culture.

4.3.3.2. Organoid morphology differs following CXCR1/2, TLR2 and AKT inhibition

Careful observation of the organoids treated with TLR2 inhibitor, CXCR1/2 inhibitor and AKT inhibitor revealed that morphological changes occurred in response to treatment compared to the vehicle control (0.1% DMSO only). Three distinct phenotypes were detected, including organoids that were cystic (a spherical layer of cells surrounding a large lumen), solid (a spherical structure filled with numerous cells), and multi-lobular (glandular-like structures with several lumina) (Servant et al. 2021) (Figure 4.26). To quantify this, 2x magnification images of 48 h vehicle and drug treated organoids were assessed for the different organoid morphologies present (n = 3 biological repeats) (Figure 4.29).

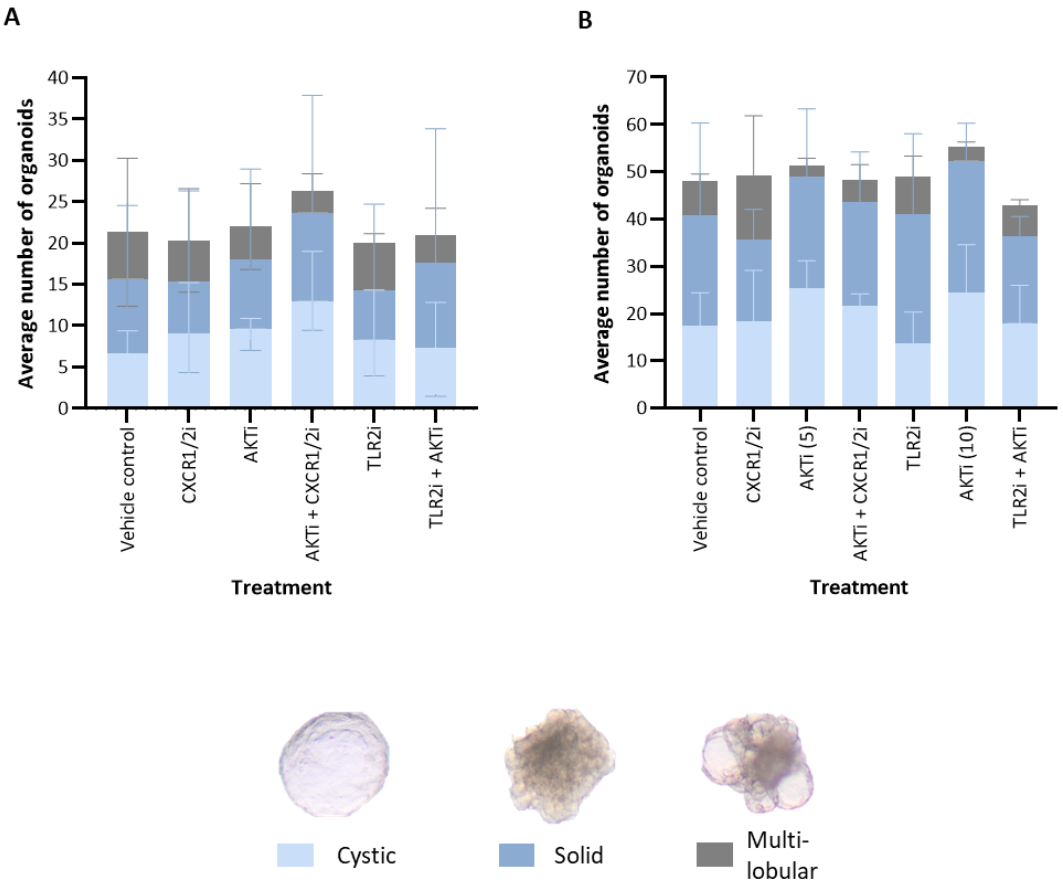

Figure 4.29: NF-κB pathway and AKT inhibition drives morphological differences in prostate tumour organoid culture. Stacked bar graphs show the average number of organoids observed with varying phenotypes within the A) *PBiCre*$^{+/-}$ *Pik3ca*$^{+/H1407R}$ and B) *PBiCre*$^{+/-}$ *Pten*$^{fl/fl}$ prostate tumour derived organoids treated with Reparixin (CXCR1/2i), C29 (TLR2i) and Capivasertib (AKTi) at pre-determined synergistic doses. Data depicts mean values, n = 3 biological repeats. Average number of organoids assessed per plane of view: A) Vehicle control; n = 21, 10 µM Reparixin; n = 20, 5 µM Capivasertib; n = 22, Reparixin + Capivasertib; n = 26, 10 µM C29; n = 20, C29 + Capivasertib; n = 21, and B) Vehicle control; n = 48, 10 µM Reparixin; n = 49, 5 µM Capivasertib; n = 51, Reparixin + Capivasertib; n = 48, 10 µM C29; n = 49, 5 µM Capivasertib; n = 55 , C29 + Capivasertib; n = 43.Error bars = SEM.

Within the *Pik3ca*-mutant organoids (Figure 4.29A), treatment with CXCR1/2 or AKT inhibitor alone showed similar proportions of each organoid phenotype, however in combination, the number of organoids displaying a cystic phenotype was increased and the number of multi-lobular organoids reduced, relative to the vehicle control and both monotherapies. A different trend was observed following treatment with TLR2 inhibitor, where the number of solid organoids appeared to be reduced, however in the presence of both combined AKTi and TLR2i treatment, this phenotype was recovered, and the proportion of solid organoids detected following this co-therapy was much higher than any other treatment or the vehicle control (49%).

The histogram plotted in Figure 4.29B shows that treatment with the AKT inhibitor alone was associated with an increase in the number of organoids displaying a cystic phenotype within the *Pten*-deficient organoids relative to the vehicle control (49% and 44% incidence of phenotype at 5 µM and 10 µM respectively compared to 36% incidence in the vehicle control), whereas the number of multi-lobular organoids was reduced in response to AKTi compared to vehicle (5% respectively compared to 15% incidence in the vehicle control). CXCR1/2i monotherapy showed an increase in the number of multi-lobular organoids relative to the vehicle control, however in combination with AKT inhibition, the number of multi-lobular type organoids were reduced to 10% incidence, therefore less than the vehicle control. Interestingly, TLR2i treatment alone appeared to increase the number of solid organoids relative to the vehicle control, contrasting the reduction of solid organoids observed within the *Pik3ca*-mutant organoids following TLR2i monotherapy.

A recent study assessing CK5 and CK8 expression levels within these three prostate organoid phenotypes showed CK8 expression to be higher in the cystic organoids, CK5 and CK8 expression to be equal within the dense organoids, and CK5 expression to be abundant within the multi-lobular organoids (Servant et al. 2021). Together with our data, this suggests that within *Pten*-deficient organoids, AKT inhibition results in push towards the luminal lineage, whereas CXCR1/2 inhibition and TLR2 inhibition promotes growth of basal type cells.

Thus, future work to determine the status of CK5/CK8 expression within the organoids by IHC pre- and post- treatment is warranted, to better understand the mode of action of the TLR2 and CXCR1/2 inhibitors. For instance, investigation into whether NF-κB pathway inhibitors selectively promote basal growth or instead instigate a switch from luminal-to-basal phenotype switch would be highly informative.

4.3.4. *Ex vivo* targeting of the NF-κB pathway – explants

It is well appreciated that 2D cell culture and 3D organoid culture can be highly informative when it comes to investigational drug studies, however both models cannot evaluate the contribution of a tumour microenvironment (TME), a factor hugely important for the outcome of drug responses.
The TME which can be divided into further specialised microenvironments such as hypoxic, innervated and acidic niches, plus immune and metabolic microenvironments, can all impact therapeutic efficacy (Jin and Jin 2020). To address this, explant cultures were employed to determine drug efficacy in the presence of the TME.

4.3.4.1. Optimisation of explant culture methods

Whilst protocols for establishing explant culture have been published as operational and high throughput for various wildtype, diseased and tumour tissue types (Nagaraj et al. 2018; Martin et al. 2019; Kokkinos et al. 2021), prostate tumours are often highly heterogenous, and generating representative tumour tissue slices from whole tumour specimens often difficult, owing to the vibratome blade encountering fluid filled cystic regions or areas with high adipose content.

To improve tumour slice sectioning using the Leica V1200 vibratome, an additional step of agarose embedding prior to the attachment of tissue onto the vibratome plate. Generating a larger contact surface area for the blade, enhanced tissue rigidity; thus preventing the blade from distorting any soft tissue, which enabled improved sectioning. Agarose with low-melt properties (setting within the range of 24 - 28°C) was selected to protect the prostate tissue from degradation, and various percentages trialled to identify optimal conditions for the sectioning process. Percentages lower than 4% often broke down however >5% gels displayed good stability (data not shown) and therefore were chosen for use within subsequent experiments.

To establish if air-interface explant cultures are viable for 48 hours using the gelatin-based sponge approach (Powley et al. 2020), for 48-hours, prostate tumour tissue was analysed at 0 h, 24 h and 48 h, with the number of apoptotic cells analysed by IHC to detect cleaved caspase-3 (CC3) on formalin-fixed paraffin-embedded (FFPE) sections (Figure 4.30). IHC analysis revealed a minimal increase in the number of CC3-positive apoptotic cells at 24-hours and 48-hours of culture, indicating 48-hour timepoint inhibitor experiments would be feasible.

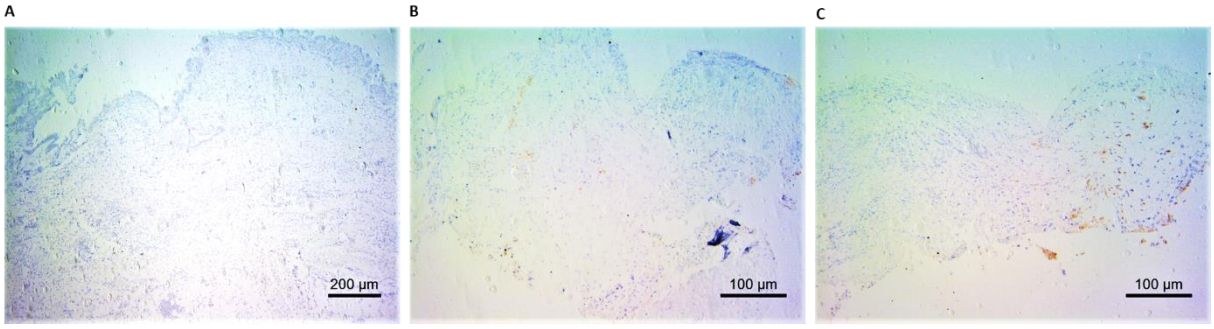

Figure 4.30: Apoptosis is infrequent after 48 hours of explant culture growth. Representative images of CC3 stained FFPE sections of p53-mutant (*PBiCre*$^{+/-}$*; p53*$^{fl/fl}$ *Pten*$^{fl/fl}$) prostate tumour explant culture at A) 0 hours, B) 24 hours and C) 48 hours of culture on gelatin sponges under standard growth conditions.

4.3.4.2. Epithelial cell proliferation and apoptosis is altered following NF-κB pathway inhibition (± AKT inhibition) in explants derived from *Pten*$^{fl/fl}$ GEMM prostate tumours

To determine the effect of NF-κB inhibition with and without additional AKT inhibition in a model possessing both an ECM and TME, explant cultures were established from prostate tumours harvested from 160 – 200 day old *PBiCre*$^{+/-}$ *Pten*$^{fl/fl}$ mice as detailed in Section 2.14. NF-κB inhibitors Reparixin (CXCR1/2i) and C29 (TLR2i) were administered along with the AKT inhibitor Capivasertib, then explants formalin fixed for paraffin embedding after 48-hours post dosage.

Unfortunately given the time restraints, it was not possible to determine explant culture IC_{50} for investigation. Instead, explant culture experiments were performed with drug doses determined by a literature search and drug datasheets from commercial suppliers.

IHC staining and quantitation for the apoptotic marker CC3 and the proliferation marker, proliferating cell nuclear antigen (PCNA) was performed to assess the effects of the different drug treatments on apoptosis and proliferation respectively (Figures 4.31 – 34).

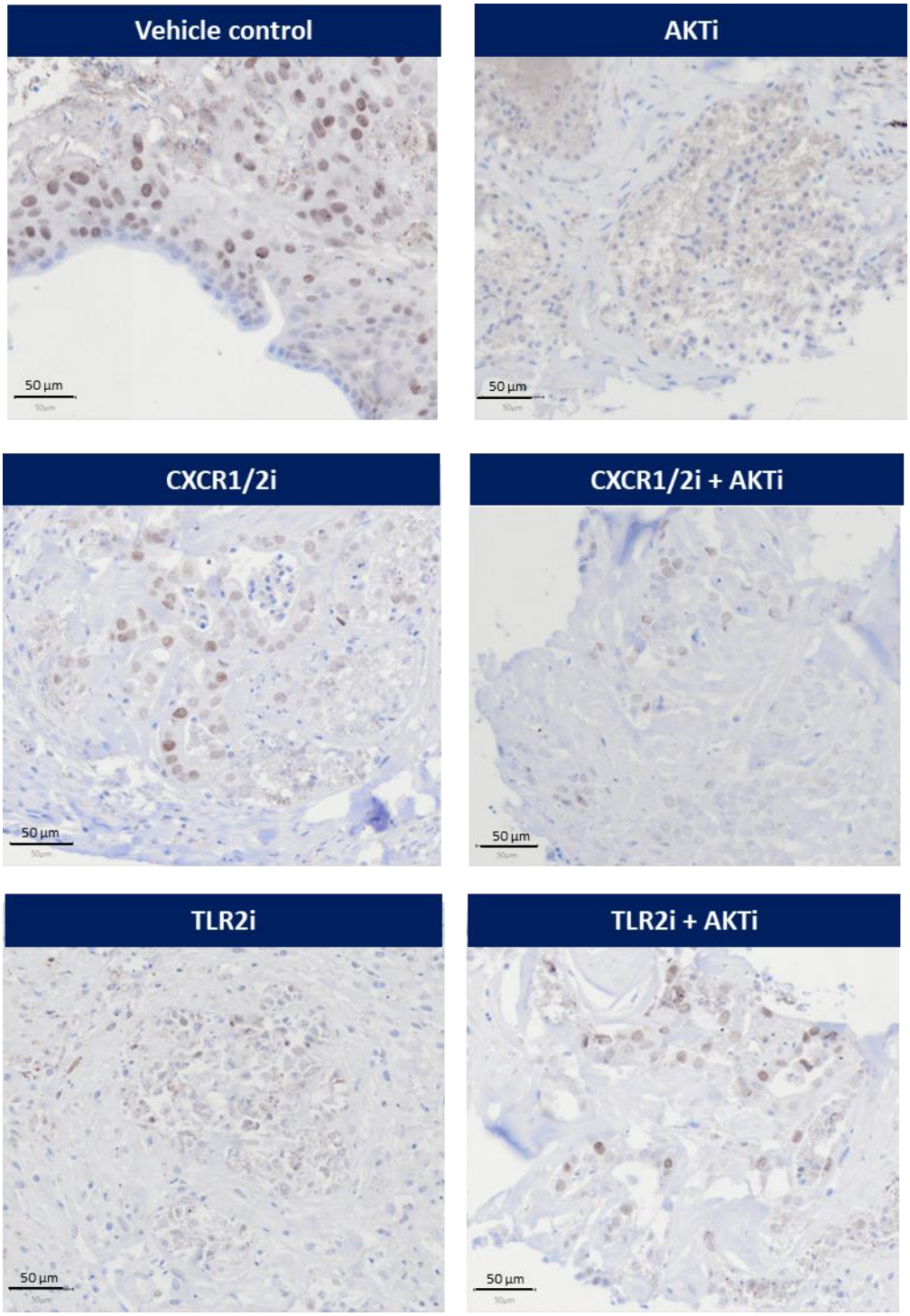

Figure 4.31: Combined NF-κB pathway and AKT inhibition appears to reduce the number of PCNA positive epithelial tumour cells in *Pten*-null GEMM explant culture. Representative 10x magnification images of *PBiCre*$^{+/-}$ *Pten*$^{fl/fl}$ explants stained for PCNA (shown in brown), following 48-hour treatment with the vehicle control (0.1% DMSO), 50 µM Reparixin, 30 µM C29 ± 1 µM Capivasertib. Scale bar = 50 µm.

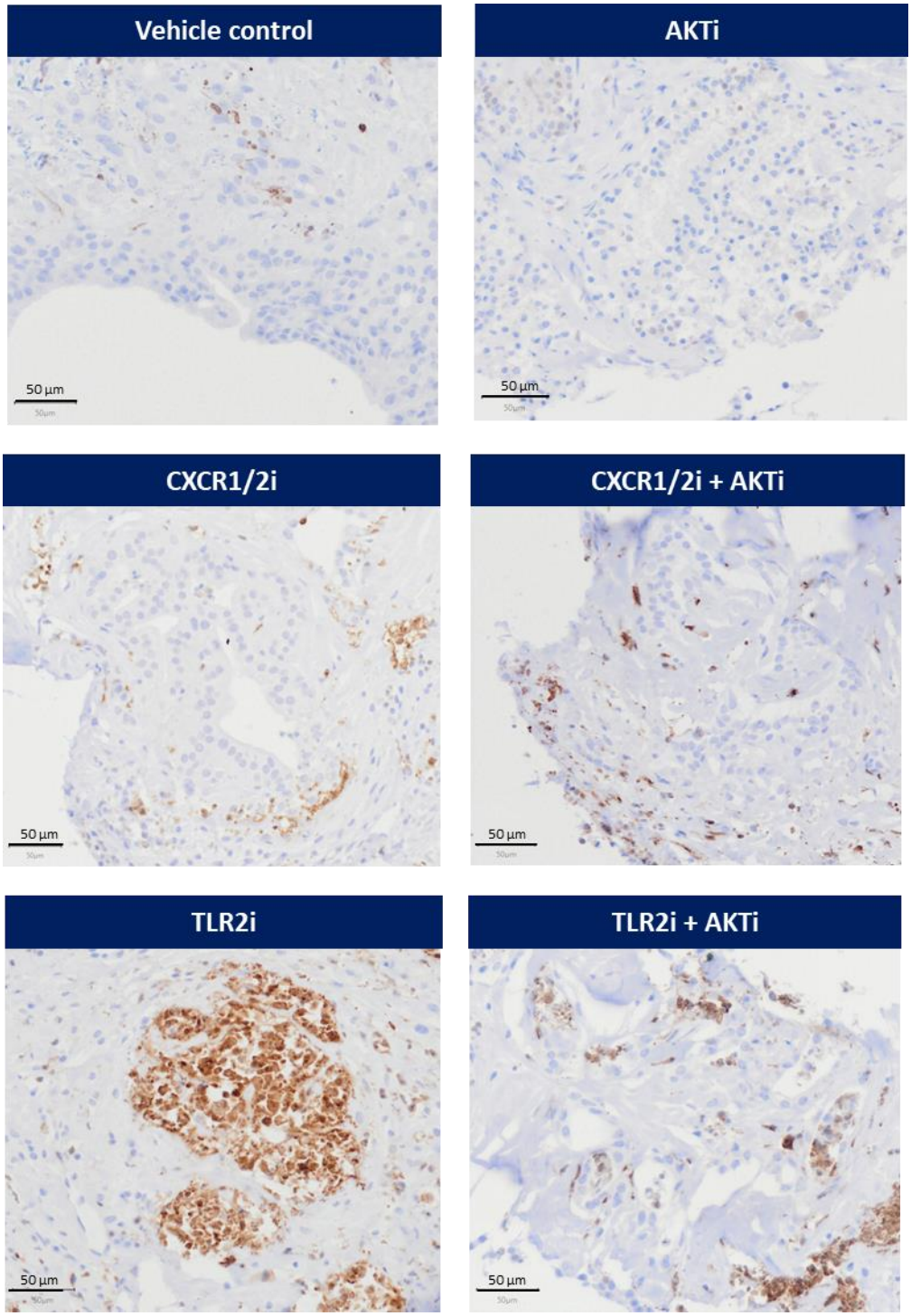

Figure 4.32: NF-κB pathway inhibition appears to increase the number of CC3 positive epithelial tumour cells in *Pten*-null GEMM explant culture. Representative 10x magnification images of *PBiCre*$^{+/-}$ *Pten*$^{fl/fl}$ explants stained for CC3 (shown in brown), following 48-hour treatment with the vehicle control (0.1% DMSO), 50 µM Reparixin, 30 µM C29 ± 1 µM Capivasertib. Scale bar = 50 µm.

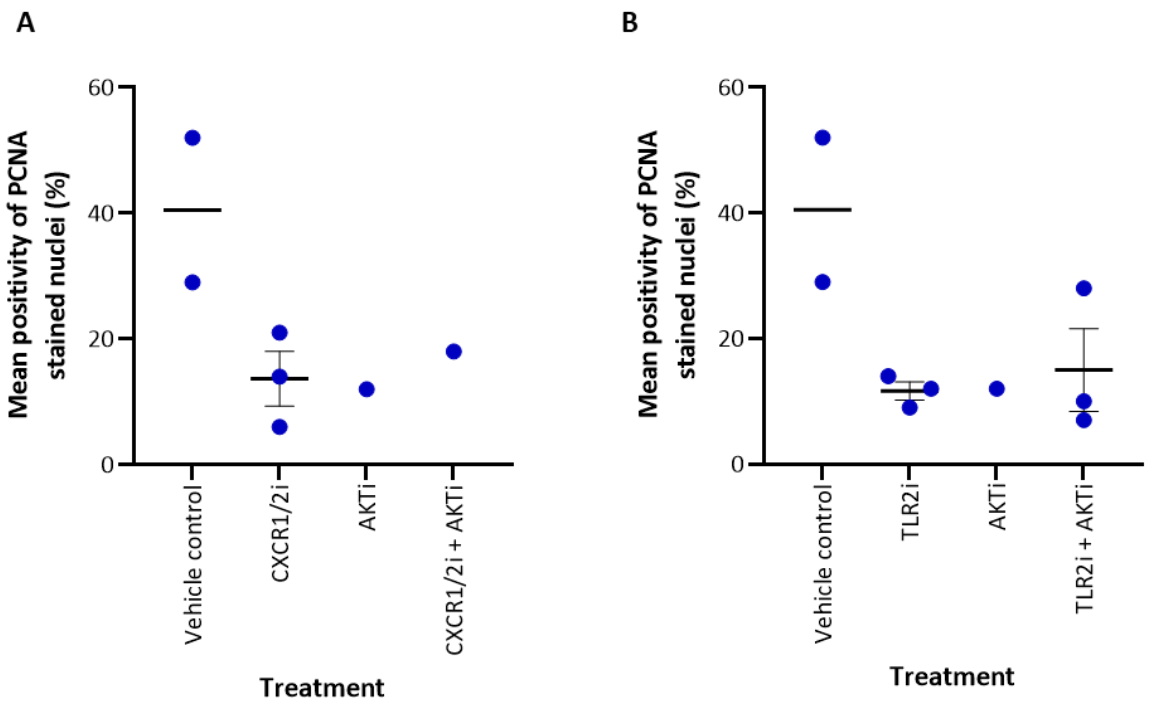

Figure 4.33: NF-κB pathway and AKT inhibition reduces the number of proliferating epithelial tumour cells in *Pten*-null GEMM explant culture. Plots show quantitation of PCNA staining in *PBiCre*$^{+/-}$ *Pten*$^{fl/fl}$ explant culture treated for 48 hours with A) vehicle control, 50 µM Reparixin (CXCR1/2i), 1 µM Capivasertib (AKTi), and in combination, and B) vehicle control, 30 µM C29 (TLR2i), 1 µM Capivasertib and in combination. No statistical test could be performed as n = 3 biological repeats for each treatment group were not available. Where possible, data shows biological repeats, with the mean and SEM represented.

A difficulty faced with explant culture, is the uncertainty that every tissue section will contain epithelial tumour cells. Occasionally, the sections we had treated were simply adipose or connective tissue and therefore not possible to quantitate n = 3 biological repeats, at times rendering the data incomplete for statistical analysis.

Despite this, trends could still be seen such as reduced proliferation within the *Pten*-deficient epithelial tumour cells following NF-κBi and AKTi monotherapies, however the combination of AKTi with either CXCR1/2i or TLR2i does not appear to further exacerbate the phenotype. These findings indicate that AKTi or inhibition of NF-κB upstream receptors are not likely to synergise by reducing cell proliferation, although further work is needed.

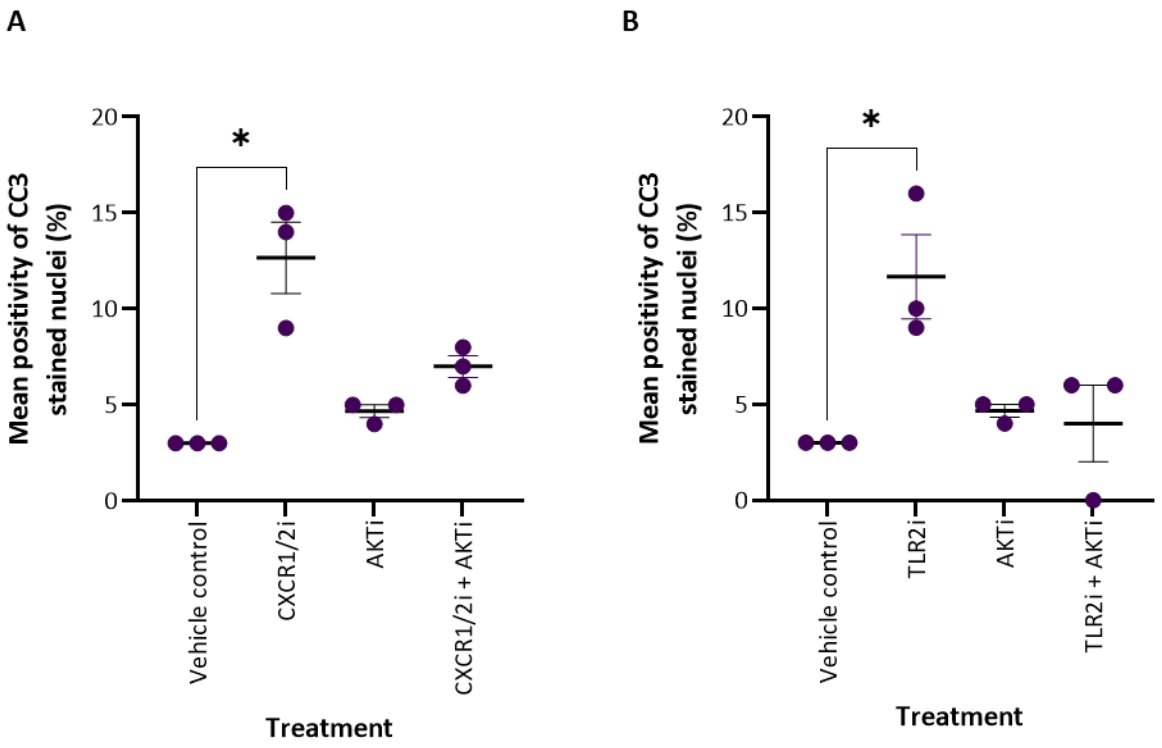

Figure 4.34: NF-κB pathway inhibition increases the number of apoptotic epithelial tumour cells in *Pten*-null GEMM explant culture. Plots show quantitation of CC3 staining in *PBiCre*$^{+/-}$ *Pten*$^{fl/fl}$ explant culture treated for 48 hours with A) vehicle control, 50 µM Reparixin (CXCR1/2i), 1 µM Capivasertib (AKTi), and in combination, and B) vehicle control, 30 µM C29 (TLR2i), 1 µM Capivasertib and in combination. n = 3 biological repeats. A One-way ANOVA with a Tukey's multiple comparison test was performed to determine statistical significance between each treatment group. Error bars = SEM.

When assessing the CC3 staining in the *Pten*-null explants, the presence of apoptotic tumour cells was significantly higher in the CXCR1/2 inhibitor and TLR2 inhibitor treated sections, relative to the vehicle control (0.1% DMSO) (Figure 3.34). The AKT inhibitor did not yield a large apoptotic response, despite a 1 µM dose being effective at reducing viability within the PC3 (PTEN-null) cell line, which could be attributed to the fact it is a cytostatic agent. Combined CXCR1/2i and AKTi treatment increased the number of cells undergoing apoptosis relative to both the vehicle control and AKT monotherapy however neither was deemed a significant result.

Evaluation of apoptotic cells in tissue sections given combined TLR2i and AKTi treatment showed no difference to explant treated with vehicle control or AKT treatment, however more variability was observed between the biological repeats following combination therapy. Together these findings indicate the NF-κB monotherapy increases apoptosis of tumour cells however combining this with AKT inhibition, does not yield the same result, therefore in combination the inhibitors may function via another mechanism to reduce tumour cell viability.

4.3.4.3. Expression of RelB and p-4EBP1 protein is affected following NF-κB pathway inhibition (± AKT inhibition) in explants derived from *Pten*$^{fl/fl}$ GEMM prostate tumours

Given the observation that drug treatments appear to reduce proliferation and increase apoptosis, experiments to confirm on-target drug targets for AKT, CXCR1/2 and TLR2 inhibition were performed by IHC staining to detect RELB (non-canonical NF-κB pathway transcription factor) and phosphorylated eukaryotic translation initiation factor 4E-binding protein 1 (p-4EBP1), that is phosphorylated when AKT-mTORC1 signalling is activated (Figures 4.35 - 36).

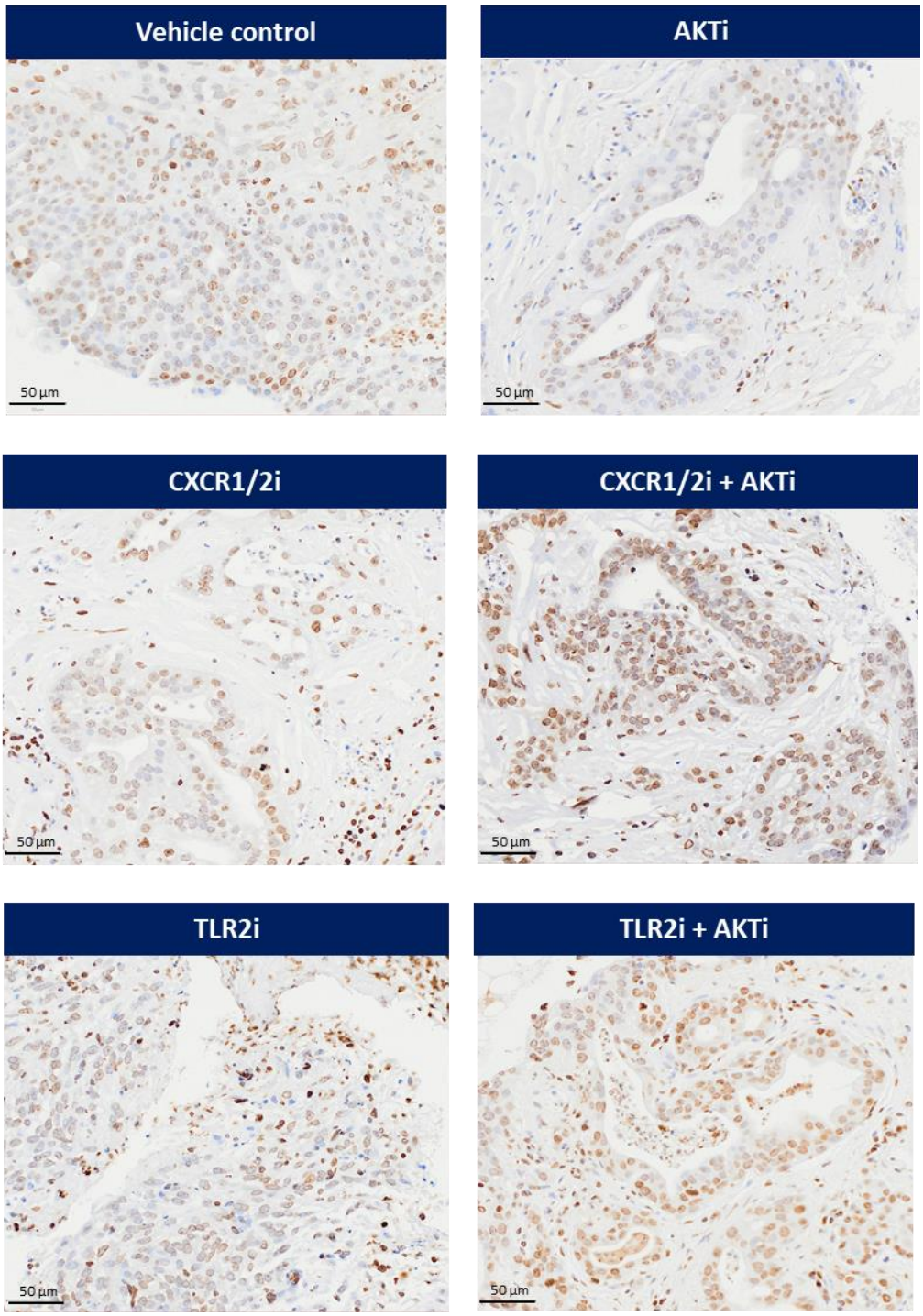

Figure 4.35: Combined NF-κB pathway and AKT inhibition appears to increase the number of RELB positive epithelial tumour cells in *Pten*-null GEMM explant culture. Representative 10x magnification images of *PBiCre*$^{+/-}$ *Pten*$^{fl/fl}$ explants stained for RELB (shown in brown), following 48-hour treatment with the vehicle control (0.1% DMSO), 50 µM Reparixin, 30 µM C29 ± 1 µM Capivasertib. n = 3 / treatment group. Scale bar = 50 µm.

Observational analysis of RELB staining within PTEN-null explants revealed that monotherapy of AKT, CXCR1/2 or TLR2 inhibition did not appear to alter the number of RELB positive prostate cancer cells relative to vehicle control (Figure 4.35). RELB nuclear expression within the epithelial tumour cells was similarly heterogenous between the monotherapies and vehicle control, indicating a mixture of transcriptionally active and inactive protein, although no cytoplasmic staining was detected. Furthermore, when CXCR1/2 or TLR2 inhibitors were combined with AKT inhibition, RELB positive nuclear staining within the tumour cells appeared to increase.

These findings could indicate that within this tumorigenic setting, AKT signalling does not occur upstream of NF-κB to initiate activation, but instead, the two pathways act in isolation as suggested by the absence of decreased RELB nuclear expression when inhibition of both pathways occurs, thus supporting our previous finding (Section 3.3.5) that increased activation of the non-canonical NF-κB pathway is indeed PI3K-independent when PTEN is lost.

However, these findings do not assist in understanding why proliferation is reduced and apoptosis is in monotherapies relative to the vehicle control (Figure 4.33 and 4.34). Given that we observed no visual difference in RELB positivity following treatment with either NF-κB inhibitor or AKT inhibitor alone, this suggests pathways other than non-canonical NF-κB signalling may be contributing to the PCNA and CC3 results obtained.

Interestingly tumour cells of the vehicle control treated explants stained for RELB, did not yield similar results as the RELB stain of the *PBiCre*$^{+/-}$ *Pten*$^{fl/fl}$ tumours performed in Section 3.3.4, therefore it could be speculated that the manipulation involved in generating explant culture may have caused stress to the tissue, generating changes in protein expression accordingly. Further quantitation and statistical analysis of this RELB explant staining would be required for a more accurate comparison.

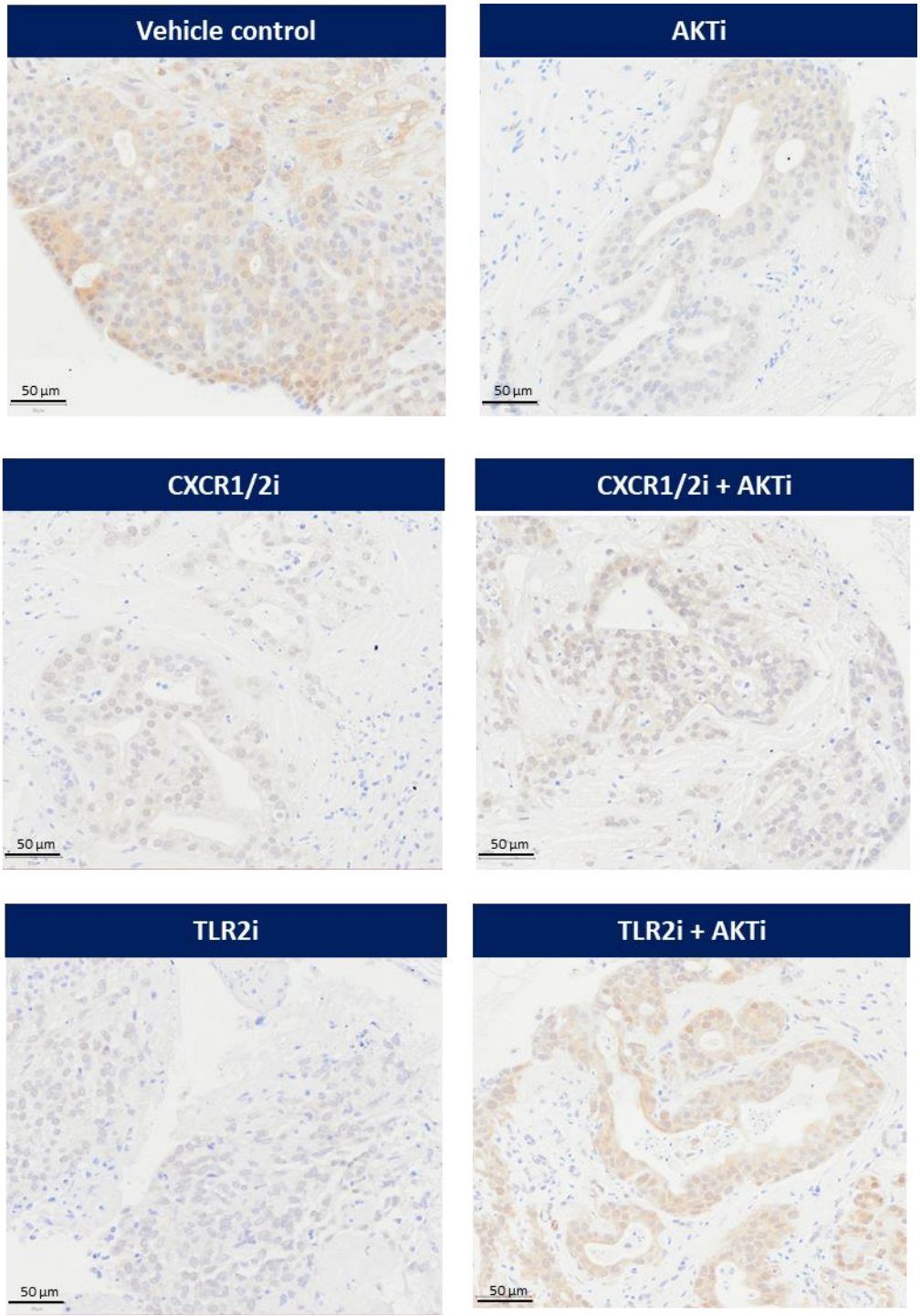

Figure 4.36: Combinations of NF-κB pathway and AKT inhibition appear to decrease the number of phosphorylated-4EBP1 positive epithelial tumour cells in *Pten*-null GEMM explant culture. Representative 10x magnification images of *PBiCre*$^{+/-}$ *Pten*$^{fl/fl}$ explants stained for p-4EBP1 (shown in brown), following 48-hour treatment with the vehicle control (0.1% DMSO), 50 µM Reparixin, 30 µM C29, all ± 1 µM Capivasertib. n = 3 / treatment group. Scale bar = 50 µm.

Explant stained cells revealed a reduction in p-4EBP1 positivity in response to AKT inhibition relative to the vehicle control as expected, indicating suppression of AKT-mTORC1 signalling (Figure 4.36). p-4EBP1 staining following CXCR1/2i or TLR2i treatment alone also appeared to be reduced compared to the vehicle, especially within the TLR2i treated tissue, suggesting inhibition of upstream NF-κB pathway receptors can block AKT-mTORC1 signalling, indicating both these receptors may function upstream of AKT. Interestingly, combined TLR2 inhibition and AKT inhibition, increased p-4EBP1 positivity relative to the TLR2i and AKTi monotherapy treated sections, a result that was not observed in CXCR1/2 and AKT inhibitor co-treated sections.

Whilst it has been commonly acknowledged that phosphorylation of 4EBP1 occurs through an AKT-mTORC dependent mechanism, other mTOR-independent kinases have now also been associated with 4EBP1 phosphorylation, including GSK3β, ERK, ATM and CDC2/CDK1 (Qin et al. 2016); it could thus also be speculated that inhibition of both TLR2 and AKT signalling, initiates activation of another cell signalling pathway that stimulates 4EBP1 phosphorylation independently of the AKT-mTORC1 signalling axis via one of these supplementary kinases. For example, a recent renal cell carcinoma study had established that GSK-3β could directly phosphorylate 4EBP1, additionally providing means of establishing acquired clinical chemoresistance to mTORC1 inhibitors (Ito et al. 2016).

Therefore, it may be necessary to perform further staining or western blotting on protein lysates extracted from the treated tissues to evaluate the expression of mTORC1 proteins and additional mTOR-independent kinases that could be contributing to the results observed, especially following combined TLR2 inhibition and AKT inhibition.

Taken together the increased p-4EBP1 protein expression following co-inhibition of TLR2 and AKT in the context of *Pten*-deficient prostate cancer indicates that this TLR2i + AKTi combination therapy is not likely to be efficacious in the clinic for prostate cancer patients with PTEN loss, however both therapies appear to be effective as monotherapies in reducing AKT-mTORC1 signalling, particularly TLR2i. Further work linking both this data and the RELB data to the proliferation and apoptosis findings is required to better determined inhibitor mechanisms of action.

4.3.4.4. Epithelial cell proliferation and apoptosis is altered following NF-κB pathway inhibition (± AKT inhibition) in explants derived from a novel neuroendocrine prostate cancer (NEPC) PDX tumour

To determine if similar responses can be observed in human prostate cancer following inhibition of CXCR1/2 or TLR2, with and without AKT inhibition, PDX model explant cultures were assessed. To this end, the LN-NEPC PDX model derived from a lymph node needle biopsy donated by a patient with metastatic neuroendocrine prostate was employed, which was recently established by the Pearson lab in collaboration with the Wales Prostate Cancer Multidisciplinary Group and the Wales Cancer Bank (Turnham et al., publication in preparation). Importantly this model represents a rare, hard-to-treat cohort of patients with AR-negative, PTEN-negative, treatment-induced mNEPC, for which alternative treatment approaches are in high demand.

LN-NEPC PDX tumours implanted subcutaneously into the flank of NOD scid gamma (NSG) mice were harvested when tumour burden approached ethical limits (performed by Dr Turnham), and tissue slices prepared for explant culture (as per Section 2.2).

To assess proliferation and apoptosis within these explants, human mitochondrial IHC staining was performed to identify human prostate cancer cells for assessment and serial sections overlaid for IHC PCNA and CC3 staining, to ensure only human tumour cells were quantitated (data not shown). Unfortunately, statistical analysis of PCNA staining within 3 biological repeats for each treatment arm was not possible owing to sectioning complications, however stains were still quantitated (Figures 4.37 – 8).

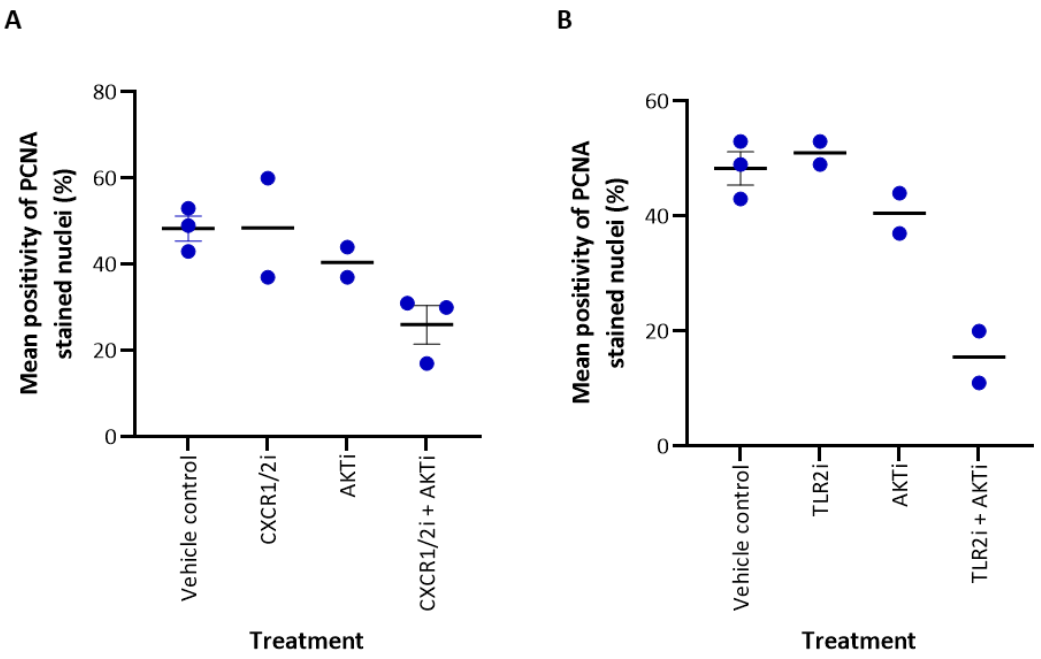

Figure 4.37: Combined NF-κB pathway and AKT inhibition shows a trend of reduction in the number of proliferating epithelial tumour cells in *Pten*-null NEPC PDX explant culture. Plots show quantitation of PCNA staining in mNEPC PTEN-negative explant culture treated for 48 hours with A) vehicle control, 50 µM Reparixin (CXCR1/2i), 1 µM Capivasertib (AKTi), and in combination, and B) vehicle control, 30 µM C29 (TLR2i), 1 µM Capivasertib and in combination. No statistical test could be performed as n = 3 biological repeats for each treatment group were not available. Where possible, data shows biological repeats with the mean and SEM represented.

When comparing the number of PCNA-positive proliferative human prostate cancer epithelial cells, the AKT inhibitor and all combination treatments appeared to reduce the number of PCNA positive cells (Figure 4.37). Both CXCR1/2 and TLR2 inhibitors alone did not change the number of proliferating cells relative to the vehicle control, suggesting they are not effective as monotherapies in PTEN-deficient metastatic NEPC.

The combination of CXCR1/2i with AKTi however, looks to drive a significant reduction in proliferation relative to the vehicle control however statistical analysis is required (Figure 4.37A). Quantitation of 3 biological repeats for the AKTi + TLR2i combination treatment also appears likely to reach statistical significance when comparing the combined therapy with the vehicle control or AKTi monotherapy (Figure 4.36B). These findings, albeit incomplete, suggest that combining CXCR1/2 or TLR2 inhibition with AKT inhibition may be an effective treatment for mNEPC, and support previous GEMM study findings that these inhibitors in combination can reduce proliferation in PTEN-null prostate cancer.

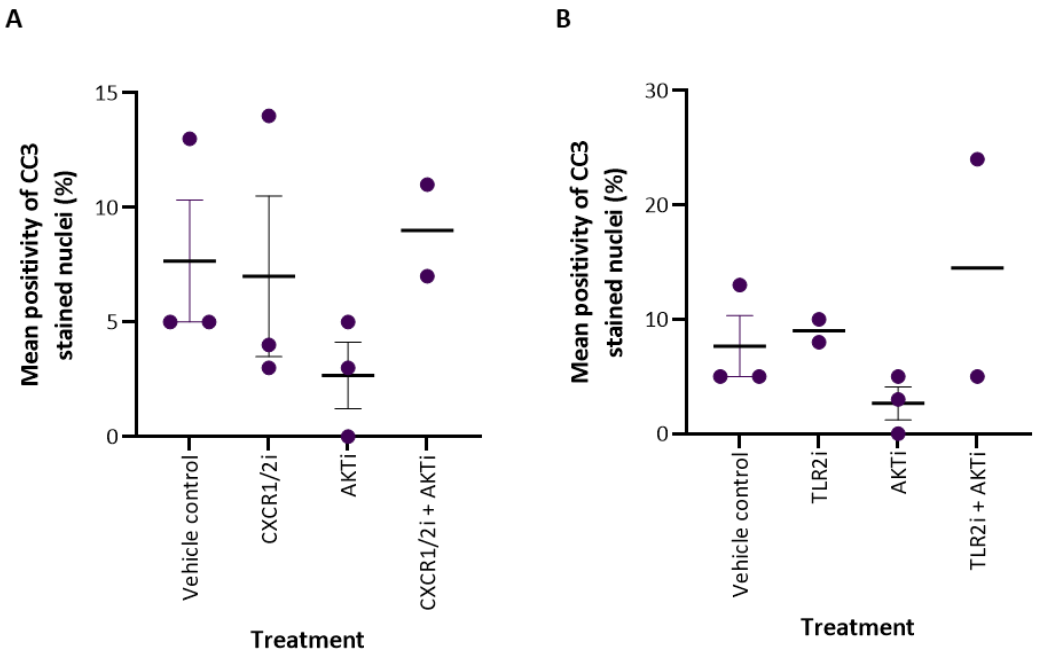

Figure 4.38: AKT inhibition shows to reduce the number of apoptotic epithelial tumour cells in *Pten*-null NEPC PDX explant culture. Plots show quantitation of CC3 staining in mNEPC PTEN-negative explant culture treated for 48 hours with A) vehicle control, 50 µM Reparixin (CXCR1/2i), 1 µM Capivasertib (AKTi), and in combination, and B) vehicle control, 30 µM C29 (TLR2i), 1 µM Capivasertib and in combination. No statistical test could be performed as n = 3 biological repeats for each treatment group were not available. Where possible data shows biological repeats, with the mean and SEM represented.

When comparing the number of CC3-positive human prostate cancer epithelial cells, no difference was observed in CXCR1/2 or TLR2 inhibitor treated explants relative to the vehicle control (Figure 4.38). Once again, treatment with AKT inhibitor resulted in low apoptotic cell detection, relative to all other therapies. CC3-positive cell numbers following CXCR1/2 and AKT combined therapy showed to be very similar to CXCR1/2 monotherapy and the vehicle control (Figure 4.38A), however combined TLR2 and AKT inhibition in one biological repeat showed to greatly increase apoptosis of tumour cells within the mNEPC explant culture (Figure 4.38B). For each treatment, the percentage of positivity within biological replicates were highly variable, thus leading to overlap between treatment groups and no apparent visual significant differences, given that statistical analyses could not be performed.

The large diversity in error bars could be attributed to the air interface experienced by the culture despite every effort to examine the tissue at the same depth. Furthermore, the explant culture tissue may have curled up during FFPE processing, which may have led to sectioning of tissue in different

planes and thus would have result in PLL slides containing tissue that has potentially experienced different doses of treatment.

While the NEPC PDX has been validated by IHC to be PTEN negative (Turnham et al, publication in preparation), it did not respond to monotherapy of CXCR1/2, TLR2 and even AKT inhibition in a way similar to the *Pten*-null GEMM explant culture. This data is interesting, given that *PBiCre*$^{+/-}$ *Pten*$^{fl/fl}$ GEMM explant sections retained their natural TME during treatment, whilst the PDX explants possessed its host TME which may have significantly influenced its responses to therapy. Together these explant findings warrant further investigation of both NF-κB monotherapies and co-therapy with AKT inhibitor *in vivo*, to fully comprehend how these treatments function in a model possessing natural immune responses and a TME.

4.4. Discussion

There is still a lot yet to be understood and established with regards to possible PI3K-independent signalling pathways activated within the prostate following loss of *PTEN*, however the analysis of our RNA-Seq data comparing tumours developed within the *PBiCre*$^{+/-}$ *Pten*$^{fl/fl}$ and *PBiCre*$^{+/-}$ *Pi3kca*$^{+/H1047R}$ genetically engineered mouse models in Chapter 3 identified that NF-κB signalling plays a role in *Pten*-null prostate cancer progression.

By targeting multiple components of the NF-κB pathway *in vitro* and *ex vivo*, we were able to determine the effects of NF-κB inhibition on key tumour biological process such as cell viability, cell proliferation and apoptosis. In the panel of established prostate cancer cell lines, we saw effective and significant reductions of cell viability mediated by the TLR2 inhibitor, C29, and when combining our chosen range of NF-κB therapeutics with AKT inhibition (mediated by Capivasertib), we saw further reductions in cell viability relative to the AKT inhibitor alone, suggesting combination treatment to be a substantially effective way of targeting prostate cancer driven by allelic deletion or functional loss of *PTEN*.

Whilst it currently remains elusive whether the improved response generated from combined treatment is due to inhibition of the same signalling axes (i.e., AKT upstream of NF-κB activation) or inhibition of two separate pathways (i.e., NF-κB signalling mediated via PI3K-independent and PTEN-dependant mechanisms), as both inhibition of the NF-κB pathway and AKT were tested at the same timepoint i.e., 48 hours, it would be interesting to whether dosing the inhibitors sequentially, may provide more information into the relationship of these interconnected pathways. This type of

experiment may also provide data on whether NF-κB inhibition can prime the tumour cells for improved AKT inhibition and vice versa.

Progressing on these findings, we were also able to determine whether the combinations were synergistic, additive or antagonistic. From our 4 initial candidates, this enquiry highlighted the combinations of C29 plus Capivasertib, and CXCR1/2 inhibitor Reparixin along with Capivasertib, to be highly synergistic and worth further exploration within other 3D models deemed customary for drug studies.

Explant culture and organoid culture were used to help determine the mechanisms in which *Pten*-deletion drives elevated NF-κB signalling. The organoid culture treated at synergistic doses revealed the inhibitors yielded innate responses, whereas the explant culture revealed C29 and Reparixin could drive apoptosis regardless of a TME and ECM, which has notoriously been known to impact drug delivery and uptake by tumour cells. In hindsight, co-cultures of cancer organoids in the presence of fibroblasts or immune cells along with ligands, may have been a better approach to test the effect of the NF-κB inhibitors.

As combined treatments act upon both the NF-κB and PI3K pathways, it would be imperative to also assess the effect of these inhibitors on both *Pik3ca*-mutant and *Pten*-null prostate tumours. Despite having access to the *PBiCre*$^{+/-}$ *Pik3ca*$^{+/H1407R}$; *Pten*$^{fl/fl}$ GEMM developed by Pearson et al, unfortunately time did not allow for the *ex vivo* experiment.

PBiCre$^{+/-}$ *Pik3ca*$^{+/H1407R}$ explants were additionally generated and subjected to NF-κB pathway inhibition, however due to issues following formalin fixation, many of the technical and biological repeats were lost to degradation during paraffin embedding. Nonetheless, it would be informative to repeat this experiment to both validate the results seen within the *Pik3ca*-mutant treated organoids but also to assess whether the tumour-microenvironment surrounding *Pik3ca*-hyperactive tumour cells impacts drug efficacy differently to one that surrounds *Pten*-null tumour cells.

Performing western blots on protein isolated from CXCR1/2, TLR2 and AKT inhibitor treated prostate cancer cells provided further information as to why targeting these NF-κB associated receptors could be of therapeutic benefit. Although only a few proteins were assessed, we were able to partly determine that the inhibitors of interest were acting upon their intended targets.

Recently, a study investigating TLR signalling in human astrocytomas and glioblastoma multiform (GBM) proposed a direct mechanism of PTEN regulation upon TLR signalling; suggesting that PTEN may inhibit TIRAP, the key protein involved in bridging MyD88 to the ligand-TLR2 complex to enable subsequent signalling (Verstak et al. 2009), such that when PTEN is inactive, downstream TLR signalling such as NF-κB is increased, leading to increased tumour cell proliferation (Moretti et al. 2018).

Thus, performing co-immunoprecipitation or pull-down experiments may also be worthwhile, especially for the interactions that have been hypothesised such as PTEN with TIRAP (using the DU145 cell line, wildtype prostate or Pik3ca-mutant prostate tumours), as well as to evaluate possible PTEN and FAK interactions.

When assessing all the data generated within this chapter, it appears that inhibition of TLR2 signalling along with AKT, was the most effective at suppressing essential tumorigenic processes within all the 2D and 3D prostate cancer models explored, and most prominently within models harbouring loss of *Pten*.

Testing the TLR2 inhibitor C29 (or others that have excelled through cancer oriented clinical trials), with and without Capivasertib *in vivo*, will enable us to truly decided whether TLR2 inhibition holds a place within the clinic for *Pten*-deficient prostate cancer and whether it can improve efficacy of current treatments such as Capivasertib, that have already shown promise when given as combined therapy ((de Bono et al. 2019). Human *PTEN*-null prostate cancer cells could be bilaterally implanted into immunocompromised mice, then treated with the inhibitors at their synergistically determined doses to reveal if the drug is truly effective within a model encompassing nearly all factors a human prostate tumour would be exposed to.

Through the process of sequencing two genetically dissimilar prostate tumours involving the PI3K pathway, we believe to have found a potential therapeutic target for *PTEN*-deficient prostate cancer, as well as a possible PI3K-independent function of PTEN.

Chapter 5

5. Characterisation of a GEMM harbouring fibroblastic *Pten* loss in the prostate

5.1 Introduction

The role of the tumour microenvironment (TME) during prostate cancer formation, progression and drug resistance is not fully characterised, and presents an area of active research that is gaining significant interest in the field, especially around the topic of epithelial and stroma cell crosstalk (Bahmad et al. 2021; Stultz and Fong 2021; Thienger and Rubin 2021). Many TME biomarkers have also been identified for use within the clinic; including aldehyde dehydrogenase 1 family members A1 and 3 (ALDH1A1 / ALDH1A3) as markers of castration resistance, MUC1-C protein indicating stimulated angiogenesis, and overexpression of IL-8 as a marker of metastasis (Bahmad et al. 2021). Developing our understanding of prostate tumour-stroma interactions will be vital in finding new therapeutics and providing better informed prognoses, especially given that decreased stromal AR expression has been linked to worse outcome in prostate cancer patients, and increased myofibroblasts associated with biochemical recurrence (determined by high PSA levels despite treatment) (Valkenburg et al. 2018).

As outlined in Chapter 1, fibroblasts constitute a large proportion of the stroma and have been widely implicated in a variety of cancers including breast, pancreatic and prostate cancer (Tripathi et al. 2012). In addition to their primary function of secreting collagens into the ECM to maintain tissue structure, fibroblasts also produce structural proteins that assist basal and myo-epithelial cells in the development of the basement membrane, such as collagen VI, laminin and entactin (Bhowmick et al. 2004). Furthermore, fibroblasts facilitate ECM reabsorption, angiogenesis, inflammation, wound healing and ultimately cancer progression through paracrine and autocrine signalling (Kendall and Feghali-Bostwick 2014).

Fibroblasts are a form of mesenchymal cells derived from the embryonic mesoderm that display distinct morphologies depending on their tissue location and activity status (Baum and Duffy 2011; Kendall and Feghali-Bostwick 2014). Since fibroblasts are not terminally differentiated, they can be transformed. For instance, transforming growth factor beta (TGF-β) activates fibroblasts, inducing their transformation into contractile myofibroblasts to drive the development of fibrotic tissue (D'Urso and Kurniawan 2020). This process is termed fibroblast-to-myofibroblast transition (FMT) and can also mediate changes in ECM architecture and deposition to assist in the development of pathological states, including tumorigenesis (D'Urso and Kurniawan 2020). Remarkably, cells derived from a mesenchymal origin such as adipocytes and pericytes have also been shown to de-differentiate into fibroblasts, and endothelial and epithelial cells have additionally been identified to transform into cells with fibroblast-like phenotypes (Tracy et al. 2016).

The TME contains heterogenous cancer-associated fibroblasts (CAFs), that in addition to the functions detailed above, also secrete paracrine growth factors, proteolytic enzymes and ECM components that can promote tumorigenesis (Tripathi et al. 2012). Originally believed to be a cancer activated form of the normal resident fibroblast, the origin of CAFs now includes mesenchymal stem cells where differentiation is driven by the JAK/STAT3 pathway, epithelial cells that are differentiated through the process of epithelial-to-mesenchymal transition (EMT) and pericytes, where differentiation is stimulated by the PI3K and MAPK pathways (Ping et al. 2021). Exosome-mediated transformation of CAFs has also been observed, whereby bladder cancer cells have been shown to induce differentiation of normal fibroblasts via exosomal-mediated TGFβ transmission and stimulation of the SMAD signalling pathway, as well as differentiation of endothelial cells promoted by melanoma-derived exosomes through activation of endothelial–to-mesenchymal transition (EndMT) (Ping et al. 2021). Taken together these findings highlight the complex nature of fibroblast transformation and their diverse functions that can facilitate tumour formation, progression and drug resistance.

Previous work has shown that co-inoculation of normal or activated fibroblasts with prostate cancer LNCAP cells in athymic mice, increases tumour burden compared to LNCAP cells alone, and that CAFs can increase collagen and growth factor secretion to promote tumour growth when cultured with pre-cancerous neoplastic prostate epithelial cells *in vitro* (Tripathi et al. 2012). These findings suggest signalling mediated by fibroblasts can contribute to prostate cancer progression. In breast cancer, *Pten* deletion in mouse mammary stromal fibroblasts accelerated initiation, progression and malignant transformation of mammary epithelial tumours in mice (Trimboli et al. 2009). Using the *Fsp-cre;Pten$^{loxP/loxP}$ GEMM,* Trimboli and colleagues highlighted a tumour suppressive role of PTEN in fibroblasts, dependent on the transcription factor Ets2 in the *MMTV-ErbB2/neu* mammary tumour mouse model (Trimboli et al. 2009). *Ets2* deletion suppressed mammary epithelial tumours growth owing to reduced infiltration of inflammatory cells, ECM remodelling and angiogenesis (Trimboli et al. 2009).

In support of a tumour suppressive function of PTEN in fibroblasts, Pearson and colleagues also identified that the *PBiCre$^{+/-}$ Pik3ca$^{+/H1704R}$ Pten$^{fl/fl}$* prostate tumour model displayed a faster rate of progression compared to the *PBiCre$^{+/-}$ Pik3ca$^{+/H1704R}$* and *PBiCre$^{+/-}$ Pten$^{fl/fl}$* single mutant models and could be associated with fewer PTEN-positive fibroblasts within its reactive stroma as indicated by PTEN IHC staining of whole tumour sections (Pearson et al. 2018) (as exemplified in Figure 5.1); further implicating loss of stromal PTEN with the development of adenocarcinoma.

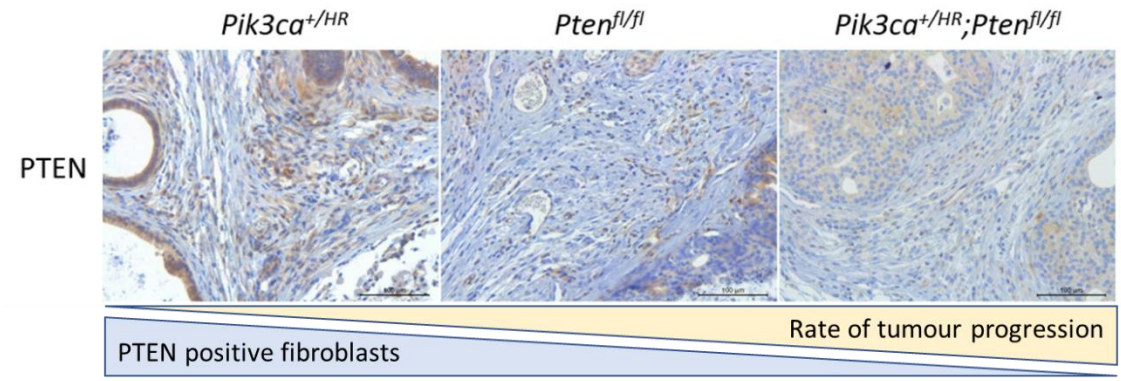

Figure 5.1: PTEN-positive fibroblasts are reduced in *Pten*-deleted prostate cancer compared to *Pik3ca*-mutant prostate cancer in mice. Images show staining to detect PTEN (shown in brown), where PTEN expression in stromal fibroblasts is markedly reduced in stage matched tumours from *PBiCre*$^{+/-}$ mice expressing *Pten*$^{fl/fl}$ *(Pten*$^{fl/fl}$*)* (300 d) and *Pik3ca*$^{+/HR}$*; Pten*$^{fl/fl}$ (100 d) relative to *PBiCre*$^{+/-}$ *Pik3ca*$^{+/HR}$ prostate tumours (400 d). Scale bar = 100 µm. Figure source: Dr Helen Pearson, Cardiff University (unpublished data).

Moreover, intestinal tumorigenesis has been observed following the loss of PTEN in a stromal fibroblast population mediated by the inducible *Col1a2CreER(T2)* transgene in mice (Dr Valerie Meniel and Dr Karen Reed, Cardiff University, unpublished data). *Pten* loss in FSP1-positive fibroblasts has additionally been shown to mediate lung fibrosis in mice, owing to excessive collagen deposition and AKT activation in the lung stroma (Parapuram et al. 2015). Collectively, these findings imply PTEN loss in fibroblasts can promote tumour progression, possibly by altering stromal composition. Currently, there is very little published data exploring the consequences of stromal *Pten* loss on prostate tumorigenesis (Turnham et al. 2020), thus experiments to determine if PTEN plays a tumour suppressive function in prostate fibroblasts are of significant interest to the field.

5.2 Aims

Given that previous work strongly indicates that PTEN plays a tumour suppressive role in fibroblasts, we hypothesised that PTEN in fibroblasts is required for normal prostate tissue homeostasis. Delineating epithelial-stroma interactions in the prostate may help identify new treatment avenues and gain new insights into new mechanisms of resistance to standard treatments such as chemo-, radio- and hormone therapy to aid patient care.

To this extent, this chapter aimed to:

1. Characterise the phenotype of the prostate in response to PTEN loss in fibroblasts during normal adult tissue homeostasis in mice.
2. Establish that *Col1a2CreER(T2)*-mediated recombination induces fibroblast-specific recombination in the mouse prostate.
3. Explore if fibroblast populations are altered in response to *PTEN* loss mediated by the *Col1a2Cre-ERT2* transgene.

5.3. Results

5.3.1. *Col1a2CreER(T2)* mediated *Pten* deletion causes prostate epithelial hyperplasia and ductal atrophy in mice

To determine if PTEN exerts a tumour suppressive function in fibroblasts to maintain normal prostate tissue homeostasis, the *Col1a2CreER(T2)* transgenic line (Zheng et al. 2002), was crossed to the *Pten*-floxed mouse (Suzuki et al. 2001), to develop cohorts of tamoxifen inducible *Col1a2CreER(T2)* positive mice harbouring either wildtype, heterozygous or homozygous *Pten* floxed alleles (n = 5 – 9 per genotype). To induce *Pten* loss in fibroblasts, experimental mice were dosed with 80 mg/kg tamoxifen at 8 weeks old (when adult prostates are fully developed) to induce Cre-mediated recombination. Cohorts were aged to either 100- or 300-days post- induction to assess the short-term and long-term response to *Pten* depletion in *Col1a2*-expressing fibroblasts.

At experimental end points, prostate tissue was dissected, weighed, formalin-fixed, and paraffin-embedded for subsequent histopathological and IHC analysis. Corn oil was administered to a cohort of *Col1a2CreER(T2)*$^{+/-}$ (*Cre*-positive) *Pten*$^{fl/fl}$ (n = 5, 300 d) and tamoxifen administered to a cohort of *Col1a2CreERT2*$^{-/-}$ (*Cre*-negative) *Pten*$^{fl/fl}$ mice (n = 8, 300 d) to control for any phenotypic differences owing to the presence of the *Col1a2Cre-ERT2* transgene and the hypomorphic *Pten* floxed allele (Trotman et al. 2003).

Taking into consideration the local differences in stromal composition and function within individual ducts of the mouse prostate (Hägglöf and Bergh 2012), we assessed histopathology by examining H&E sections for each prostate lobe independently (Figures 5.2 – 3).

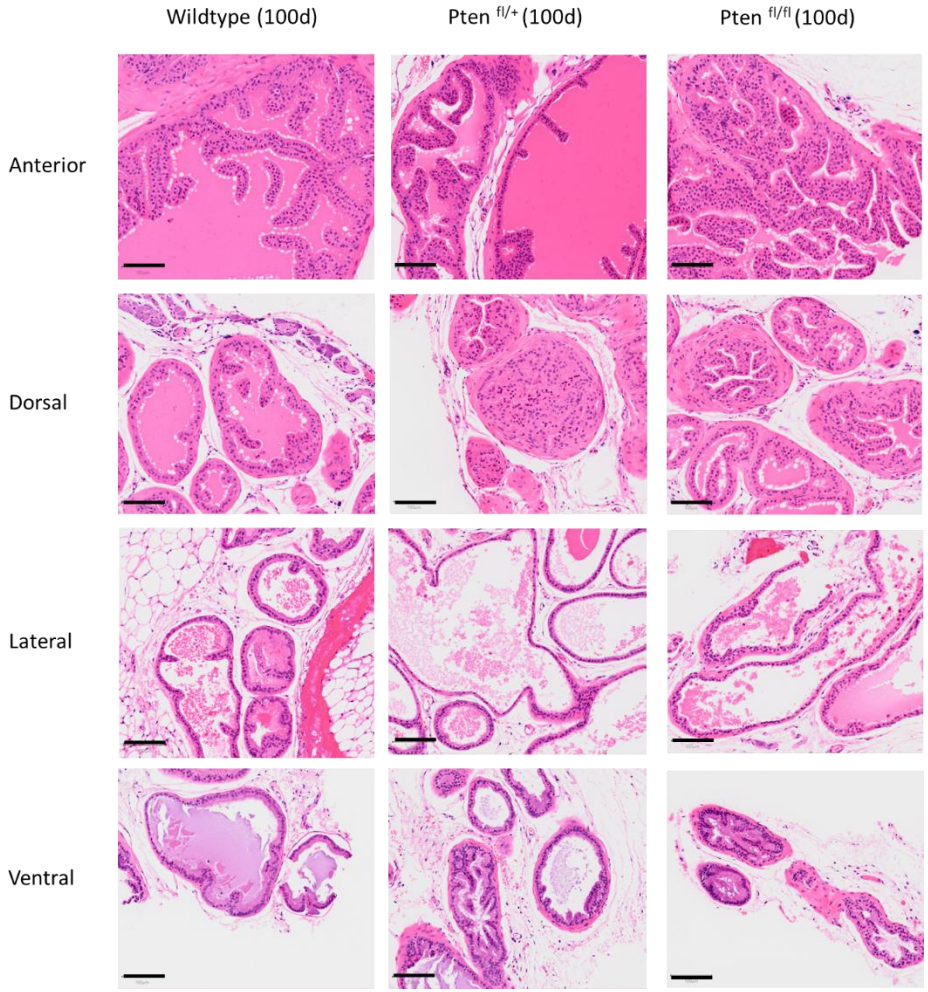

Figure 5.2: Stromal cell *Pten* deletion alters prostate morphology in 100 d *Col1a2CreER(T2)* mouse prostates. Representative H&E images of tamoxifen induced *Col1a2CreER(T2)$^{+/-}$ Pten$^{+/+}$* (wildtype), *Col1a2CreER(T2)$^{+/-}$ Pten$^{+/fl}$* and *Col1a2CreER(T2)$^{+/-}$ Pten$^{fl/fl}$* mouse prostates, harvested 100 days post tamoxifen-induction. Scale bar = 100 µm.

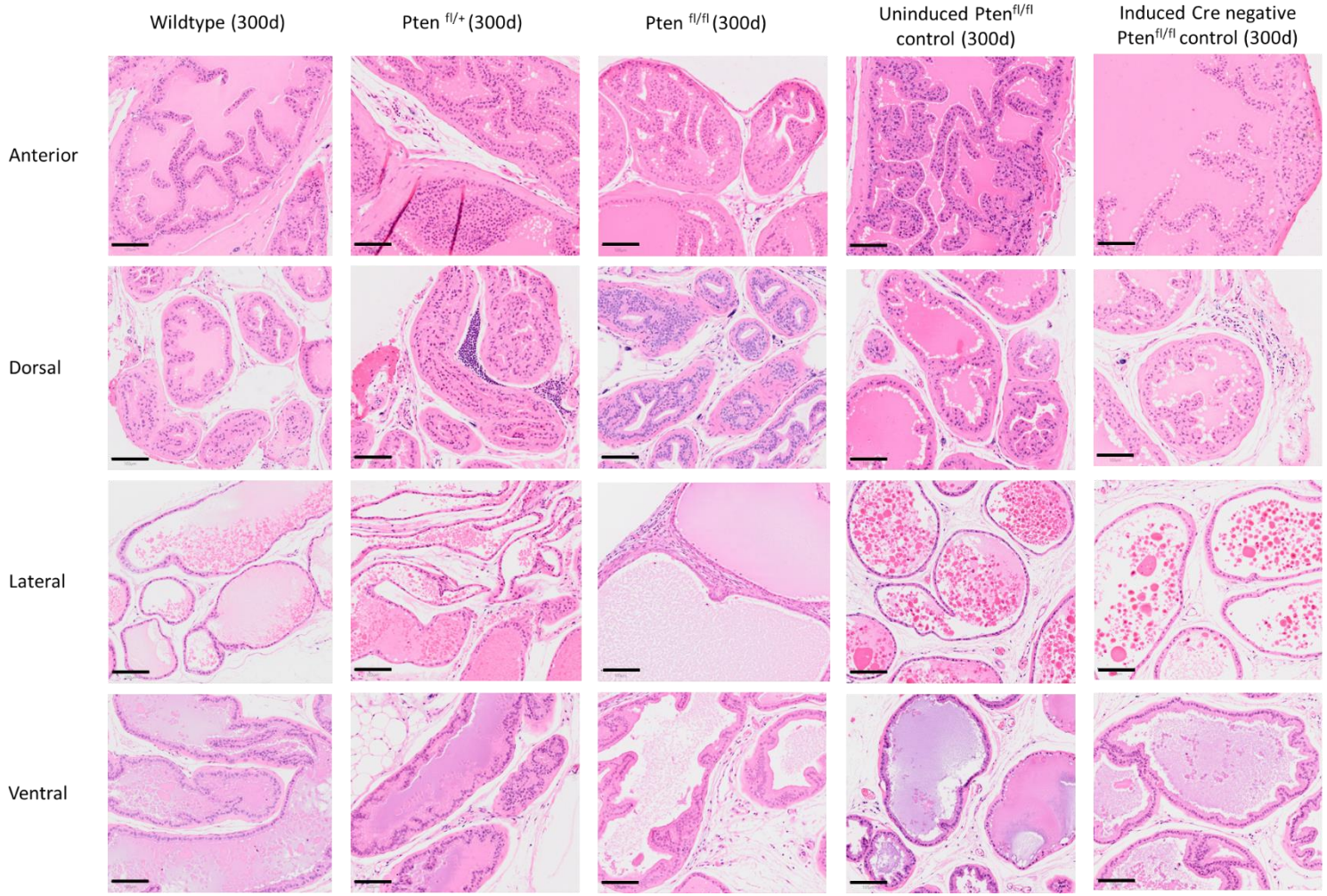

Figure 5.3: Stromal cell *Pten* deletion alters prostate morphology in 300 d *Col1a2CreER(T2)* mouse prostates. Representative H&E images of tamoxifen induced *Col1a2CreER(T2)$^{+/-}$ Pten$^{+/+}$* (wildtype), *Col1a2CreER(T2)$^{+/-}$ Pten$^{+/fl}$* and *Col1a2CreER(T2)$^{+/-}$ Pten$^{fl/fl}$*, uninduced (corn oil only) *Col1a2CreER(T2)$^{+/-}$ Pten$^{fl/fl}$* and tamoxifen induced *Col1a2CreER(T2)$^{-/-}$ Pten$^{fl/fl}$* mouse prostates, harvested 300 days post induction. Scale bar = 100 µm.

Histopathological analysis revealed that the anterior prostate showed normal epithelial prostate histology, with tall columnar cells showing central nuclei along evenly spaced branches infolding into the lumen of the prostate duct in the *Col1a2CreER(T2)$^{+/-}$; Pten$^{+/+}$* (wildtype) mice at 100 d and 300 d time points (Figures 5.2 – 3). 300 d controls also displayed normal prostate epithelial histology, however flat focal hyperplastic lesions were detected within *Col1a2CreER(T2)$^{+/-}$; Pten$^{+/fl}$* and *Col1a2CreER(T2)$^{+/-}$; Pten$^{fl/fl}$* cohorts.

Histopathological analysis of the wildtype and control dorsal prostates showed normal epithelial prostate histology i.e., simple columnar epithelium with centrally located nuclei, both at 100 d and 300 d time points (Figures 5.2 - 3). Wildtype lateral prostates in 100 d and 300 d cohorts additionally displayed normal histology, with cuboidal epithelium and basally located nuclei.

Interestingly, in addition to hyperplasia, unusually dilated lobes with a thinner, more flattened epithelial lining were observed in the lateral and ventral lobes of *Pten$^{fl/fl}$* mice aged 300 d post-induction, indicating these lobes were displaying glandular atrophy (Shappell et al. 2004).

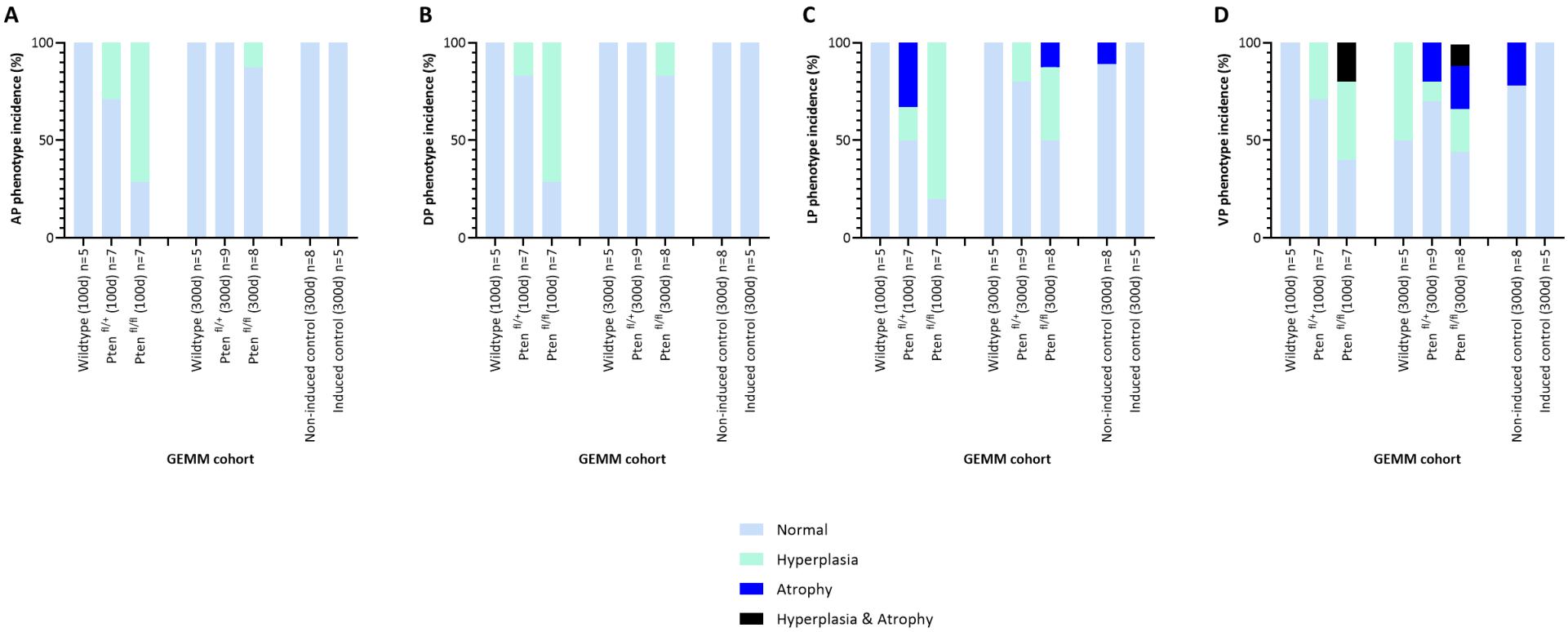

Figure 5.4: *Col1a2CreER(T2)*-mediated PTEN loss causes prostate hyperplasia in all four mouse prostate lobes. Graphs show histopathological analysis of tamoxifen induced *Col1a2CreER(T2)*$^{+/-}$ *Pten*$^{+/+}$ (wildtype), *Col1a2CreER(T2)*$^{+/-}$ *Pten*$^{+/fl}$ (*Pten*$^{+/fl}$) and *Col1a2CreER(T2)*$^{+/-}$ *Pten*$^{fl/fl}$ (*Pten*$^{fl/fl}$) mouse A) anterior, B) dorsal, C) lateral and D) ventral prostate lobes harvested 100 and 300 days post-induction, alongside control tissue consisting of non-induced (corn oil only) *Col1a2CreER(T2)*$^{+/-}$ *Pten*$^{fl/fl}$ and tamoxifen induced *Col1a2CreER(T2)*$^{-/-}$ *Pten*$^{fl/fl}$ mouse anterior prostate lobes (300 d). The number of lobes assessed for each cohort are detailed in the x-axis.

Remarkably, prostate hyperplasia in the anterior lobe was evident in 29% and 71% of *Col1a2CreER(T2)$^{+/-}$ Pten$^{+/fl}$* and *Col1a2CreT2$^{+/-}$ Pten$^{fl/fl}$* induced mice respectively at 100 days post-tamoxifen induction (Figure 5.4A), indicating that *Pten* loss in *Col1a2CreER(T2)*-expressing cells is sufficient to cause prostate epithelial hyperplasia. Likewise, the dorsal lobe also displayed epithelial hyperplasia in the *Pten$^{+/fl}$* and *Pten$^{fl/fl}$* mice (17% and 71% respectively at 100 d), which was absent in wild-type and control cohorts (Fig 5.4B).

Interestingly, the hyperplastic phenotype in anterior and dorsal prostate lobes in *Pten*-deficient mice did not increase with age, instead a slight reduction in phenotype incidence was observed at the 300 d time point (Figure 5.4A and B). Within the 100-day post induction cohorts, lateral and ventral lobes also displayed hyperplasia in 17% and 29% of *Col1a2CreER(T2)$^{+/-}$ Pten$^{+/fl}$* mice, in addition to 80% and 40% of *Col1a2CreER(T2)$^{+/-}$ Pten$^{fl/fl}$* mice respectively. In contrast to the dorsal and anterior lobes, this phenotype was maintained at a similar prevalence at 300 d post-tamoxifen induction (Figure 5.4C and D).

Prostate ductal atrophy was not observed in *Col1a2CreER(T2)$^{+/-}$* wildtype mouse prostate, supporting findings from the Bar Harbour Mouse prostate pathology report that indicate prostate atrophy is rare in wild-type mice (Shappell et al., 2004), however lateral and ventral lobe atrophy was detected in both *Col1a2CreER(T2)$^{+/-}$ Pten$^{+/fl}$* and *Pten$^{fl/fl}$* cohorts at both 100 d and 300 d timepoints. Moreover, both atrophy and hyperplasia were additionally observed as distinct focal events within ventral prostate lobes of 100- and 300-day post induction in *Col1a2CreER(T2)$^{+/-}$ Pten$^{fl/fl}$* mice (20% and 11% respectively, Figure 5.4D).

Surprisingly, hyperplasia was observed within the ventral lobes of 300-day wildtype mice, where non-induced *Col1a2CreER(T2)$^{+/-}$ Pten$^{fl/fl}$* control lateral and ventral lobes also displayed a low incidence of atrophy at 300 d. Epithelial hyperplasia has previously been observed in aged wildtype mice (Kindblom et al. 2003), but can also be strain dependent (Coleman and Hummel 1973). Moreover, BPH is a common in event in older men, with an approximated 80% prevalence in men aged 70 – 80 (Cannarella et al. 2021). Additionally, this finding could indicate leaky Cre-recombination associated with the ER(T2) construct, especially given that no hyperplasia was observed in the tamoxifen induced *Col1a2CreER(T2)$^{-/-}$ Pten$^{fl/fl}$* control.

Interestingly, hyperplasia was not observed within anterior lobes in *Col1a2CreER(T2)$^{+/-}$ Pten$^{+/fl}$* mice aged to 300 d post-induction and was reduced from 72% to 13% in *Col1a2CreER(T2)$^{+/-}$* Pten$^{fl/fl}$ mice

(100 d and 300 d cohorts respectively). It could therefore be speculated that as the anterior lobes of the prostate age, stromal signalling mediating the growth of the epithelial cells diminishes, and/or other stromal-epithelial regulatory signalling events can rescue the phenotype over-time. For instance, androgen receptor signalling in the prostate has been shown to reduce with age (Izumi et al. 2013), and it is possible the hyperplastic phenotype observed upon PTEN loss may require androgen signalling as the PI3K and AR cascades are known to interact and regulate one another (Carver et al. 2011). Future work assessing AR signalling and serum testosterone levels within the *Col1a2CreER(T2)* model would help determine if there are significant differences within each lobe with age, that may be contributing to the hyperplastic/atrophic phenotype.

The difference in phenotypic incidence between the prostate lobes may also reflect the difference in thickness of the fibromuscular sheath surrounding each lobe, given that both the mouse lateral and ventral lobes possess a thinner fibromuscular stroma in comparison to the anterior and dorsal lobes, where a strong phenotypic incidence was not observed. Taken together, our findings indicate that PTEN function in fibroblasts is required to maintain normal adult prostate tissue homeostasis in all 4 lobes of the mouse prostate.

5.3.2. *Col1a2CreER(T2)* mediated homozygous deletion of *Pten* reduces prostate weight at 300 d

During the experimental tissue harvests, smaller sized prostates were visually observed in *Col1a2CreER(T2)*$^{+/-}$ *Pten*$^{fl/fl}$ mice compared to all other genotypes assessed. Indeed, total prostate weight as a percentage of body mass, was significantly reduced in *Col1a2CreER(T2)*$^{+/-}$ *Pten*$^{fl/fl}$ mice (0.24 g ± SEM) relative to *Col1a2CreER(T2)*$^{+/-}$ *Pten*$^{+/+}$ mice at 300 d (0.34 g ± SEM) (Figure 5.5A).

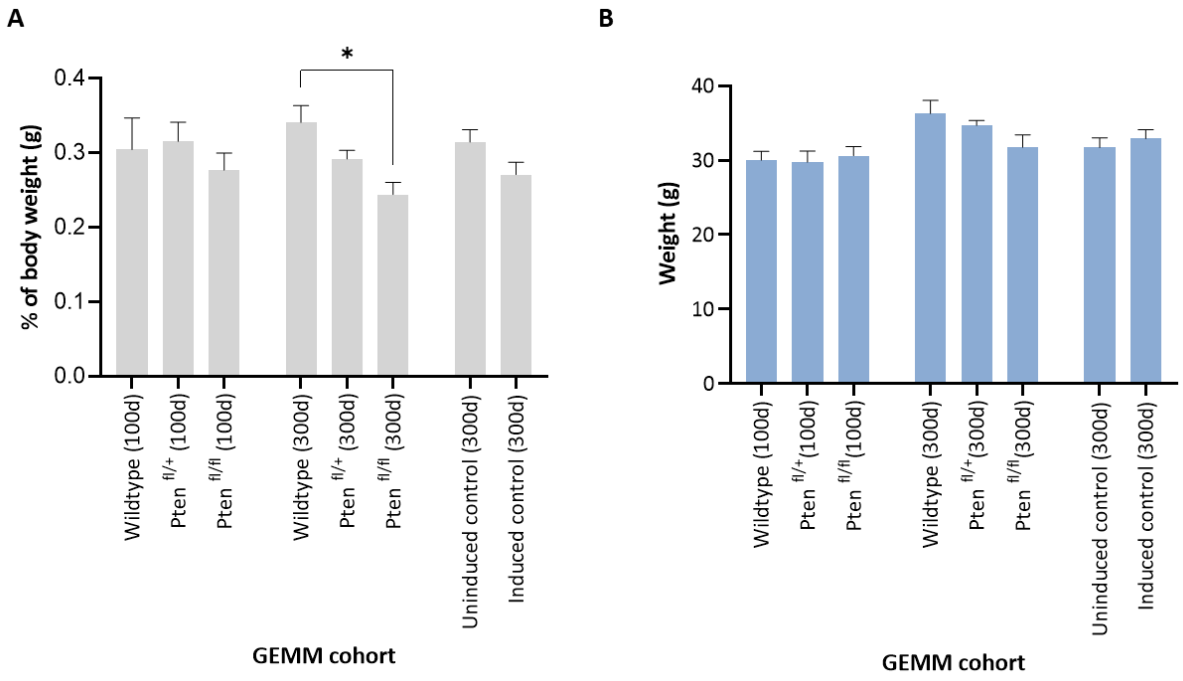

Figure 5.5: *Col1a2CreER(T2)* mediated homozygous *Pten* deletion reduces prostate weight relative to body mass. Graphs display A) mean total prostate weight data (as a percentage of body weight) and B) average body weight of tamoxifen induced *Col1a2CreER(T2)*$^{+/-}$ *Pten*$^{+/+}$ (wildtype), *Col1a2CreER(T2)*$^{+/-}$ *Pten*$^{+/fl}$ and *Col1a2CreER(T2)*$^{+/-}$ *Pten*$^{fl/fl}$ mice harvested 100 and 300 days post induction, alongside control prostates consisting of non-induced (corn oil only) *Col1a2CreER(T2)*$^{+/-}$ *Pten*$^{fl/fl}$ and tamoxifen induced *Col1a2CreER(T2)*$^{-/-}$ *Pten*$^{fl/fl}$ mice (300 d). A One-way ANOVA was performed with a Tukey's multiple comparison test. Error bars = SEM.

At the 100 d timepoint, mice with homozygous *Pten* loss also appeared to display lighter prostates relative to body weight compared to *Col1a2CreER(T2)*$^{+/-}$ *Pten*$^{+/+}$ and *Pten*$^{+/fl}$ prostates (Figure 5.5A), however this result was not statistically significant. Due to the hyperplasia observed within the 100- and 300-day post induction models with bi-allelic *Pten* loss, we postulated GEMM prostates may have been heavier owing to the increased number of cells present within the ducts. Instead, shrinkage was observed, which is probably attributable to the presence of atrophic glands (Figure 5.4). Total body weights were comparable between the genotypes where no significant differences were identified (Figure 5.5B), however as expected, body mass was increased at the later 300 d time point compared to the 100-d time point.

5.3.3. *Col1a2CreER(T2)* mediated stromal cell *Pten* loss reduces life expectancy of mutant mice

To address if *Col1a2CreER(T2)*-mediated *Pten* deletion affects overall survival, a Kaplan-Meier survival plot was generated (Figure 5.6).

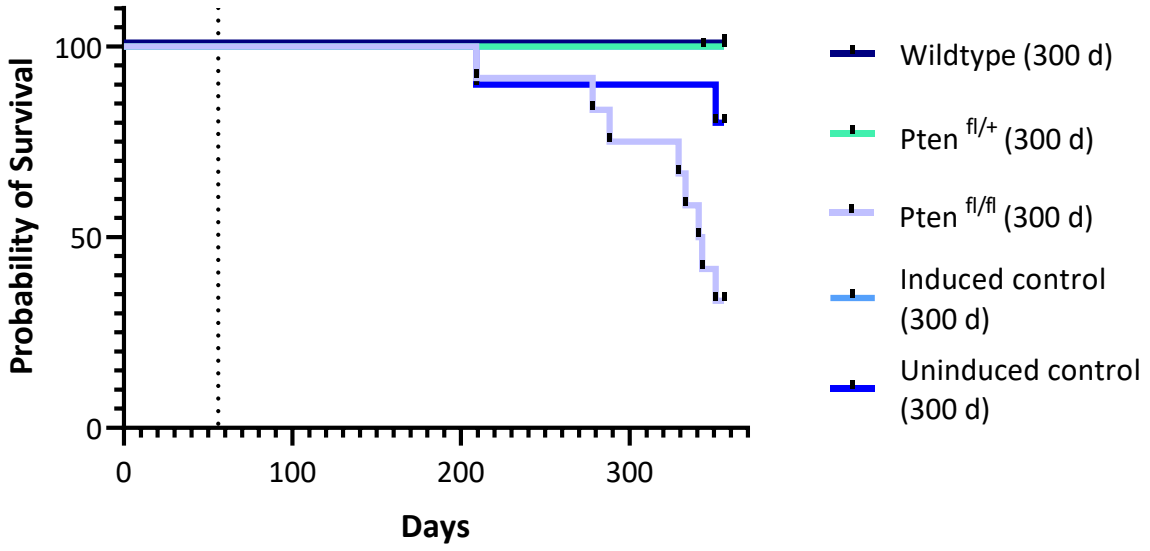

Figure 5.6: *Col1a2CreER(T2)*-mediated *Pten*-deletion reduces survival. Kaplan-Meier plot of tamoxifen-induced *Col1a2CreER(T2)*$^{+/-}$ *Pten*$^{+/+}$ (wildtype) (n = 9), *Col1a2CreER(T2)*$^{+/-}$ *Pten*$^{+/fl}$ (n = 12), *Col1a2CreER(T2)*$^{+/-}$ *Pten*$^{fl/fl}$ (n = 12) experimental cohorts (300 d), and induced *Col1a2CreER(T2)* $^{-/-}$ *Pten*$^{fl/fl}$ mice (induced control) (n = 10) and uninduced (corn oil only) *Col1a2CreER(T2)*$^{+/-}$ *Pten*$^{fl/fl}$ (uninduced control)(n = 10) mice (300 d). The log-rank (Mantel-Cox) test performed indicated the survival curves were significantly different (Chi squared value = 29.8, p value = <0.0001). The median survival for induced *Col1a2CreER(T2)*$^{+/-}$ *Pten*$^{+/+}$, *Col1a2CreER(T2)*$^{+/-}$ *Pten*$^{fl/+}$ and *Col1a2CreER(T2)*$^{-/-}$ *Pten*$^{fl/fl}$ mice was 356 d, whilst for *Col1a2CreER(T2)*$^{+/-}$ *Pten*$^{fl/fl}$ 342 days. Dotted line indicates time of tamoxifen-induction.

Remarkably, 66% of mice with induced homozygous *Pten* deletion displayed signs of illness leading to their early sacrifice. Notably, the *Col1a2* promoter is ubiquitously expressed, thus *Col1a2CreER(T2)* mediated deletion of *Pten* occurs systemically and is not specific to prostate fibroblasts. Consequently, reduced survival in *Col1a2CreER(T2)*$^{+/-}$ *Pten* $^{fl/fl}$ mice reflected the formation of intestinal tumours associated with anaemia (pale feet), anal prolapse, hunching and pilo-erect fur (Table 5.1). The formation of intestinal tumours in this model is the focus of additional researchers at the European Cancer Stem Cell Research Institute (Dr Valerie Meniel and Dr Karen Reed, unpublished findings).

Table 5.1: Incidence of sickness traits within 300 d *Col1a2CreER(T2)* experimental and control mice. Mice displaying multiple sickness traits are included in each type of illness presented.

Cohort	Experimental timepoint	Illness presented	Proportion of cohort displaying signs
Induced *Col1a2CreER(T2)$^{+/-}$ Pten$^{+/+}$*	300 d	None	N/A
Induced *Col1a2CreER(T2)$^{+/-}$ Pten$^{+/fl}$*	300 d	Hunching of body	8 %
Induced *Col1a2CreER(T2)$^{+/-}$ Pten$^{fl/fl}$*	300 d	Anaemia Anal prolapse Hunching of body Pilo-erect fur Reduced body temperature Slow movement	42 % 8.3 % 42 % 16.6% 16.6 % 8.3 %
Induced *Col1a2CreER(T2) $^{-/-}$ Pten$^{fl/fl}$*	300 d	Anaemia Reduced body temperature	
Uninduced *Col1a2CreER(T2)$^{+/-}$ Pten$^{fl/fl}$*	300 d	Anal prolapse	10%

Interestingly one of the uninduced Cre-positive control cohort mice (*Col1a2CreER(T2)$^{+/-}$ Pten $^{fl/fl}$* administered with corn oil) required sacrifice prior to their 300-day post induction experimental timepoint due to health issues (Table 5.1). Together with the histopathology data (Figures 5.1 – 3), these findings suggest that although *Pten* has not been excised, this mouse developed illness that is unrelated to *Pten* and may have been simply an anomaly. Furthermore, given this GEMM was on mixed background that was briefly back crossed with C57BL/6 mice, this particular control mouse may have possessed differences in genetic background compared to its cohort litter mates.

No mice within the tamoxifen induced *Col1a2CreER(T2)$^{+/-}$ Pten$^{+/+}$, Col1a2CreER(T2)$^{+/-}$ Pten$^{+/fl}$* and *Col1a2CreER(T2)$^{-/-}$ Pten$^{fl/fl}$* (Cre-negative control) cohorts required early sacrifice before their 300-day post induction experimental endpoint, despite partial phenotypes observed in mice harbouring heterozygous and homozygous *Pten* loss in *Col1a2*-expressing cells. Additionally, all 100-day post-induction GEMM cohorts reached their experimental end point (data not shown). Taken together, these findings indicate that systemic homozygous loss of PTEN in *Col1a2*-expressing fibroblasts reduces survival owing to non-prostate related illnesses, primarily intestinal tumours that lead to intestinal blockages.

5.3.4. Proliferative and apoptotic characterisation of mouse prostates following *Col1a2CreER(T2)* mediated depletion of PTEN

To gain a better understanding of how *Pten* depletion in *Col1a2*-expressing fibroblasts causes prostate epithelial hyperplasia/atrophy, IHC staining and quantitation for the proliferation marker, proliferating cell nuclear antigen (PCNA) and the apoptotic marker cleaved caspase 3 (CC3) was performed on FFPE sections of prostates taken from experimental *Col1a2CreER(T2)*$^{+/-}$ *Pten*$^{+/+}$, *Pten*$^{+/fl}$ *and Pten* $^{fl/fl}$ cohorts aged to either 100 or 300 days post tamoxifen induction, with uninduced *Col1a2CreER(T2)*$^{+/-}$ *Pten*$^{fl/fl}$ mice included as controls (n = 3 / cohort).

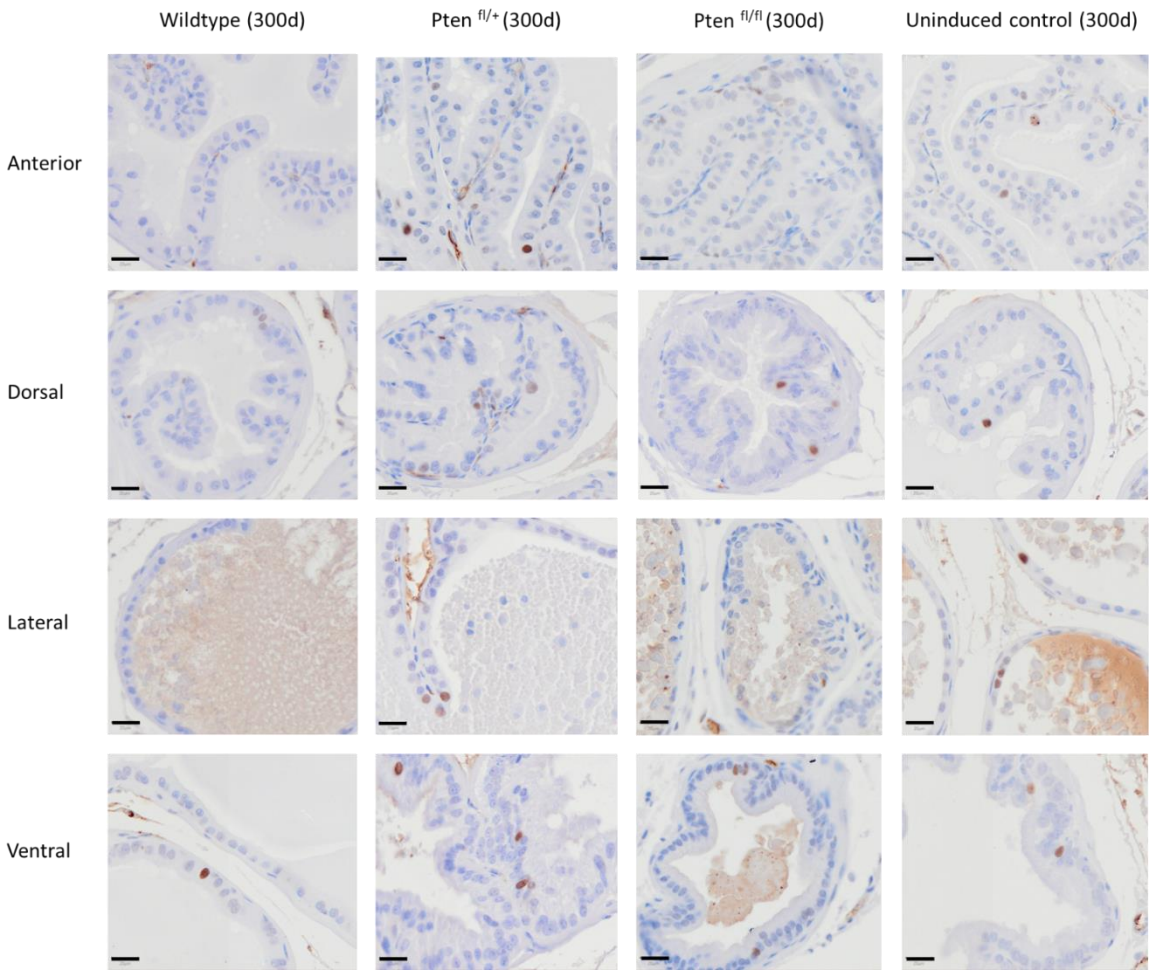

Figure 5.7: Fibroblast *Pten* deletion appears to increase the number of PCNA positive epithelial cells in *Col1a2CreER(T2)* mouse prostates. Representative 20x magnification images of post tamoxifen induction *Col1a2CreER(T2)$^{+/-}$ Pten$^{+/+}$* (wildtype), *Col1a2CreER(T2)$^{+/-}$ Pten$^{+/fl}$* (*Pten$^{+/fl}$*), *Col1a2CreER(T2)$^{+/-}$ Pten$^{fl/fl}$* (*Pten$^{fl/fl}$*) and non-induced Cre-positive (corn oil only) *Col1a2CreER(T2)$^{+/-}$ Pten$^{fl/fl}$* (uninduced control) mouse prostates stained for PCNA (shown in brown) via IHC. Only 300 d cohorts shown. Scale bar = 20 µm.

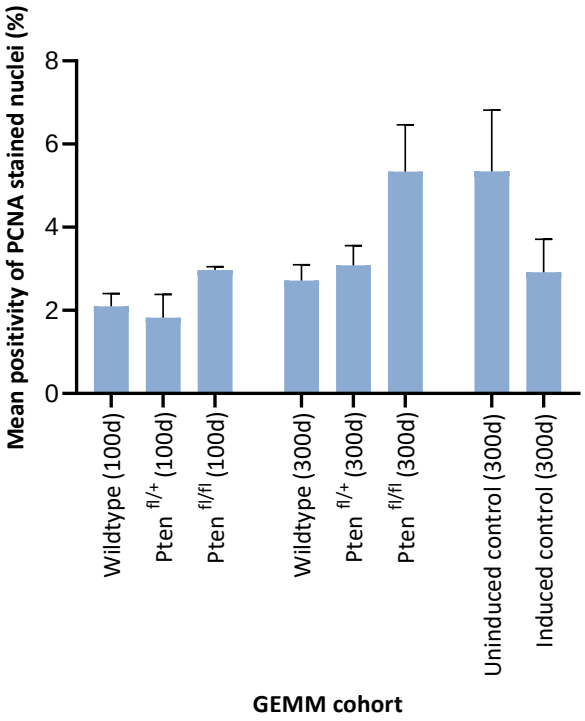

Figure 5.8: *Col1a2CreER(T2)* mediated depletion of *Pten in vivo* shows a trend for increased prostate epithelial cell proliferation. Plots show quantitation of PCNA IHC staining in *Col1a2CreER(T2)*$^{+/-}$ *Pten*$^{+/+}$ (wildtype), *Col1a2CreER(T2)*$^{+/-}$ *Pten*$^{+/fl}$ (*Pten*$^{+/fl}$), *Col1a2CreER(T2)*$^{+/-}$ *Pten*$^{fl/fl}$ (*Pten*$^{fl/fl}$) total mouse prostates harvested 100 and 300 days post tamoxifen induction. Controls include uninduced (corn oil only) *Col1a2CreER(T2)*$^{+/-}$ *Pten*$^{fl/fl}$ (uninduced controls) and tamoxifen induced *Col1a2CreER(T2)* $^{-/-}$ *Pten*$^{fl/fl}$ (induced control) mice. Data represents the mean, n = 3 biological repeats. Error bars = SEM. A one-way ANOVA with a Tukey's multiple comparison test was performed to determine statistical significance between each treatment group; results were non-significant (P value > 0.05).

When assessing proliferation at the induced 100- day time point, wildtype and *Pten*$^{+/fl}$ prostate lobes had similar levels of epithelial PCNA positive staining, whereas the *Pten*$^{fl/fl}$ model displayed an increase in the number of PCNA-positive cells, however quantification revealed this finding was not statistically significant (Figure 5.8). A similar trend was also observed in the 300 d time point (Figure 5.7). Notably, the *Pten*$^{+/+}$ and *Pten*$^{+/fl}$ 300 d induced cohorts showed similar levels of proliferation to the 100-day *Pten*-deficient prostate, with the 300 day post induction *Pten*$^{fl/fl}$ model once again showing to have the highest amount of positivity within the later experimental timepoint cohort, however this was also deemed non-significant by the One-way ANOVA and Tukey's multiple comparison test performed.
The higher levels of proliferation observed following homozygous *Pten* deletion within the 100- and 300- post induction cohorts support the findings of increased hyperplasia within the prostate lobes.

Thus, these data indicate that *Col1a2CreER(T2)* mediated PTEN depletion could increase prostate epithelial cell proliferation to promote hyperplastic growth in the prostate. Nevertheless, further analysis of this data is required, where future experiments looking at each lobe on an individual basis, plus scoring hyperplastic foci rather than the whole gland will provide better insight into the signalling mechanisms activated in areas of hyperplasia.

Interestingly, the uninduced *Col1a2CreER(T2)*$^{+/-}$ *Pten*$^{fl/fl}$ control model displayed highly elevated levels of PCNA positivity relative to the induced *Col1a2CreER(T2)*$^{-/-}$ *Pten*$^{fl/fl}$ model which highlights further possibility of the uninduced control model a displaying hypomorphic phenotype, as proliferation has been shown to increase with a reduction in *Pten* dosage (Alimonti et al. 2010), additionally this may once again be reflective of leaky Cre-recombination.

PTEN loss is commonly associated with a reduction in apoptosis (Weng et al. 2001), therefore to identify whether *Col1a2CreER(T2)*-mediated *Pten* deletion reduces apoptosis in the prostate epithelium to promote hyperplastic growth, total prostate sections from *Col1a2CreER(T2)*$^{+/-}$ wildtype, *Pten*$^{+/fl}$ and *Pten*$^{fl/fl}$ *cohort mice* 100- and 300- day post induction GEMM were stained for the apoptotic marker CC3 and the number of positive cells quantitated (Figure 5.9) (n = 3/cohort).

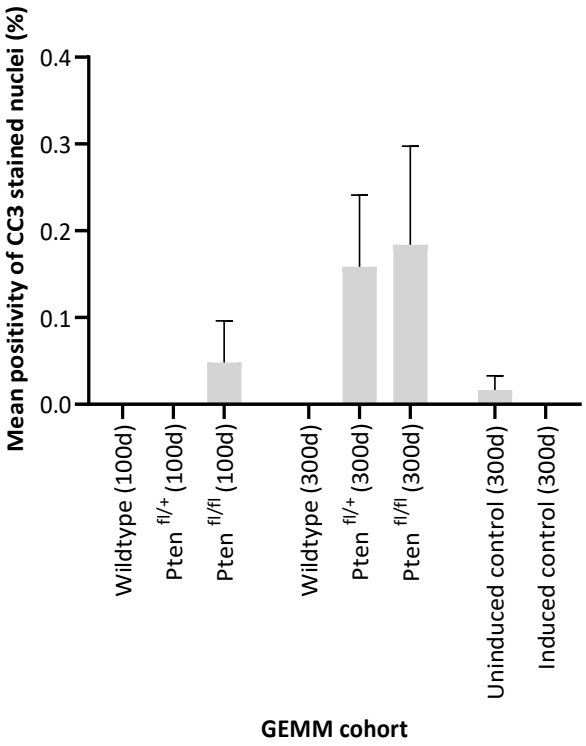

Figure 5.9: *Col1a2CreER(T2)* mediated depletion of *Pten in vivo* shows a trend for increased prostate epithelial cell apoptosis. Plots show quantitation of CC3 IHC staining in *Col1a2CreER(T2)$^{+/-}$ Pten$^{+/+}$* (wildtype), *Col1a2CreER(T2)$^{+/-}$ Pten$^{+/fl}$* , *Col1a2CreER(T2)$^{+/-}$ Pten$^{fl/fl}$* total mouse prostates harvested 100 and 300 days post tamoxifen induction. Controls include uninduced (corn oil only) *Col1a2CreER(T2)$^{+/-}$ Pten$^{fl/fl}$* and tamoxifen induced *Col1a2CreER(T2) $^{-/-}$ Pten$^{fl/fl}$* mice. Data represents the mean, n = 3 biological repeats, where additional PLL sections were stained if lobes were missing). Error bars = SEM. A one-way ANOVA with a Tukey's multiple comparison test was performed to determine statistical significance between each treatment group; results were non-significant (p value > 0.05).

CC3 staining in the 100 d wildtype and *Pten$^{+/fl}$* prostate sections showed on average no cells undergoing apoptosis. In contrast, the number of CC3-positive cells was dramatically increased in the *Pten$^{fl/fl}$* setting, though not statistically significant given the large variability observed within the lobes (Figure 5.9). Similar to the 100 d wildtype prostates, CC3-positive staining in the 300 d mice was negligible, however the number of CC3 positive cells was augmented in *Pten$^{+/fl}$* and *Pten$^{fl/fl}$* prostates, albeit statistically insignificant, possibly owing to the large error bars.

Although regarded non-significant by the One-way ANOVA and Tukey's multiple comparison tests performed, more apoptotic epithelial cells were detected in the 300-day post induction homozygous and heterozygous stromal *Pten*-deleted prostates in comparison to their 100-day post-induction counterparts (Figure 5.9).

With no detectable CC3-positivity in the 300-day wildtype cohort and 300-day induced control cohort (n = 3); it could be speculated that that the small increase in apoptotic cells within the 300-day post induction mutant cohorts are not due to age but are linked specifically somehow to the loss of *Pten,* which could also be facilitating the atrophy observed within the models. However, it has been recognised that depending on the cell population that has been targeted for *Pten* loss, both increased and decreased apoptosis can occur within a tissue (Fraser et al. 2004).

Furthermore, slight differences were also observed within the longer timepoint cohorts, with the number of apoptotic cells increasing with increased *Pten* allele loss, however these results were not significant. Error bars for this analysis were also relatively large, owing to the heterogeneity and negligible levels of staining present within the cohorts.

Taken together, these findings indicate that *Col1a2CreER(T2)* mediated *Pten* loss increases apoptosis, potentially in an attempt to overcome the hyperplastic phenotype and maintain normal prostate epithelial tissue homeostasis.

5.3.5. ECM remodelling may occur following *Col1a2CreER(T2)* mediated depletion of PTEN

As *Pten* loss in FSP1-positive fibroblasts has been previously linked to excessive collagen deposition in the lung stroma (Parapuram et al. 2015), it was hypothesised that changes in collagen expression or ECM remodelling may also occur within the prostate following loss of fibroblast PTEN. To assess this, Masson's trichrome staining to identify collagens, was performed by the Cardiff University Histology Department on prostate sections from previous 50 d post-tamoxifen induced cohorts generated by Dr Valerie Meniel.

Increased collagen staining around ducts was observed within mouse prostates harbouring loss of fibroblastic *Pten* relative to an uninduced Cre-negative control (Figure 5.10), suggesting potential ECM remodelling or activation events also occur within the prostate. This staining was attempted in the 100 d and 300 d cohort tissues but yielded poor colour contrasts and thus unsuccessful. CD45 staining was also performed however this additionally did not work either; further investigation into the effects mediated upon the ECM following *Pten* loss is therefore required.

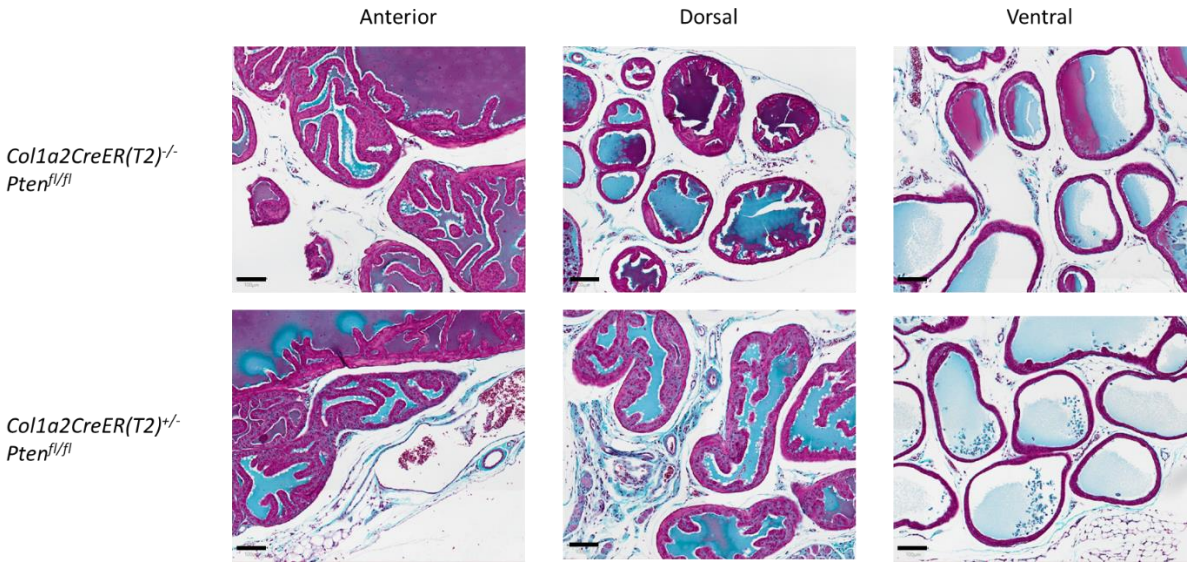

Figure 5.10: Masson's trichrome staining suggests collagen expression increases following *Col1a2CreER(T2)*-mediated loss of *Pten* in the prostate. Representative 4x magnification images of 50 d post-tamoxifen induction *Col1a2CreER(T2)*$^{-/-}$ *Pten*$^{fl/fl}$ and *Col1a2CreER(T2)*$^{+/-}$ *Pten*$^{fl/fl}$ (*Pten*$^{fl/fl}$) mouse prostates stained with Masson's Trichrome stain (collagen surrounding ducts shown in blue). Scale bar = 100 µm.

5.3.6. Identification of *Pten*-deleted stromal cells

5.3.6.1. Addition of an RFP reporter gene enables identification of cells that have undergone recombination events

To validate previous work that simply states the inducible *Col1a2CreER(T2)* transgenic line drives Cre-LoxP mediated recombination specifically within fibroblasts (Denton et al. 2009; Swonger et al. 2016), experiments were performed to confirm if fibroblasts are recombined upon tamoxifen induction and to gain new insight into which fibroblasts are targeted. To this end, a mouse carrying a Cre-LoxP inducible RFP reporter was crossed to *Col1a2CreER(T2) Pten* mice, to generate offspring that upon Cre-mediated recombination, recombined cells will express RFP (Li et al. 2018). Subsequently cohorts of *Col1a2CreER(T2)* $^{+/-}$ *Pten* $^{+/+}$*; Rfp* $^{+/-}$, *Col1a2CreER(T2)* $^{+/-}$ *Pten* $^{fl/+}$*; Rfp* $^{+/-}$ and *Col1a2CreER(T2)* $^{+/-}$ *Pten* $^{fl/fl}$*; Rfp* $^{+/-}$ GEMM were generated, dosed with tamoxifen at 8 weeks of age and prostate tissue harvested at 100 days post-induction.

5.3.6.1.1. RFP expression is observed in the stroma and FMS

FFPE sections from harvested RFP-positive mouse prostates underwent IHC to detect RFP and thus identify recombined cells. Analysis of IHC images revealed RFP staining was detected in a discrete stromal cell population in all genotypes, however the presence of RFP-positive cells was significantly increased upon *Pten* loss (Figure 5.11).

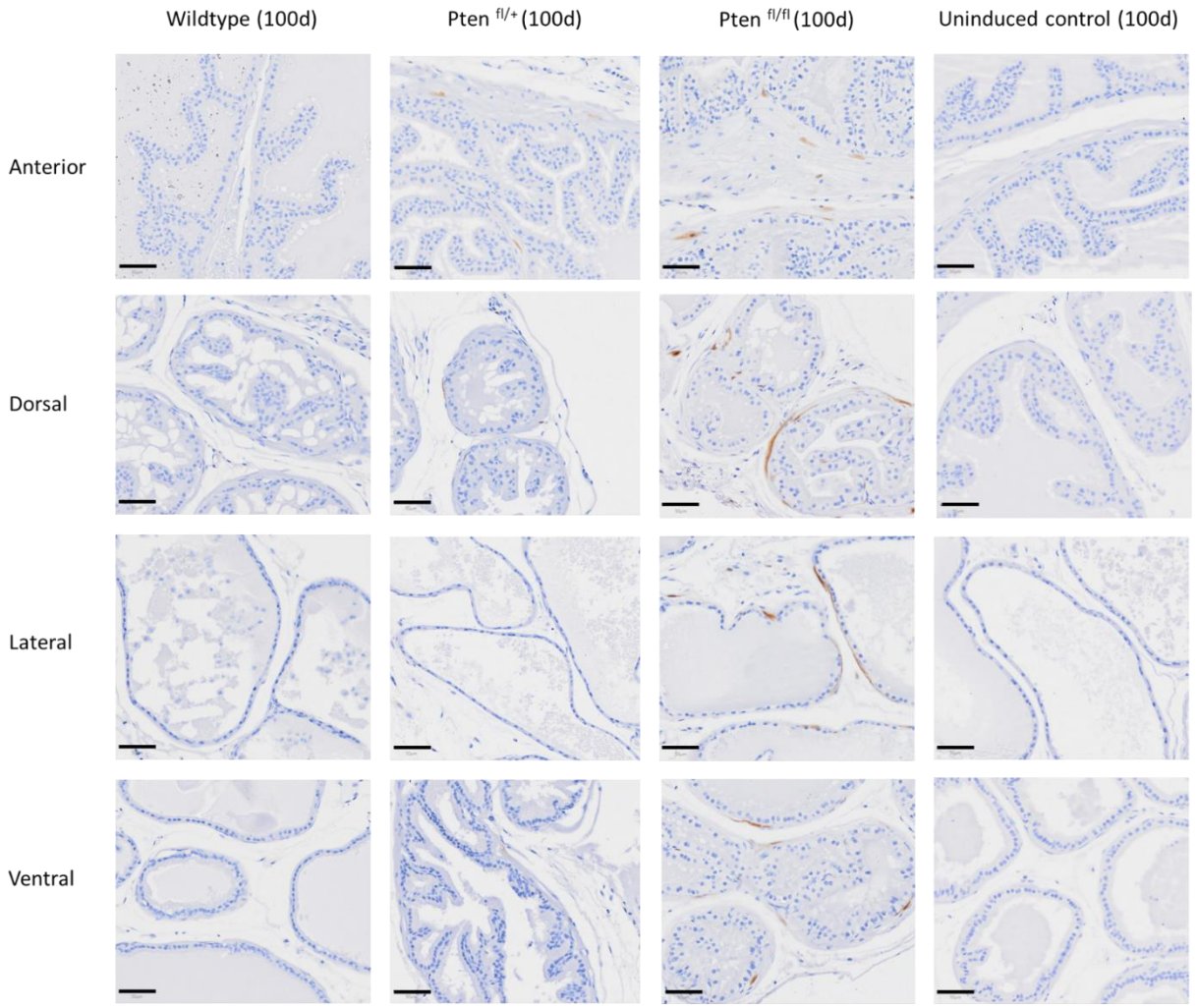

Figure 5.11: *Col1a2CreER(T2)* mediated recombination occurs in a population of stromal cells surrounding each prostate lobe. Representative 10x magnification images of 100 day old post tamoxifen induced *Col1a2CreER(T2)$^{+/-}$ Pten$^{+/+}$ Rfp$^{+/-}$* (wildtype), *Col1a2CreER(T2)$^{+/-}$ Pten+/fl Rfp$^{+/-}$*, *Col1a2CreER(T2)$^{+/-}$ Pten$^{fl/fl}$ Rfp$^{+/-}$* and non-induced (corn oil only) *Col1a2CreER(T2)$^{+/-}$ Pten$^{+/+}$ Rfp$^{+/-}$* mouse prostates stained for RFP (shown in brown) via IHC. Scale bar = 50 µm.

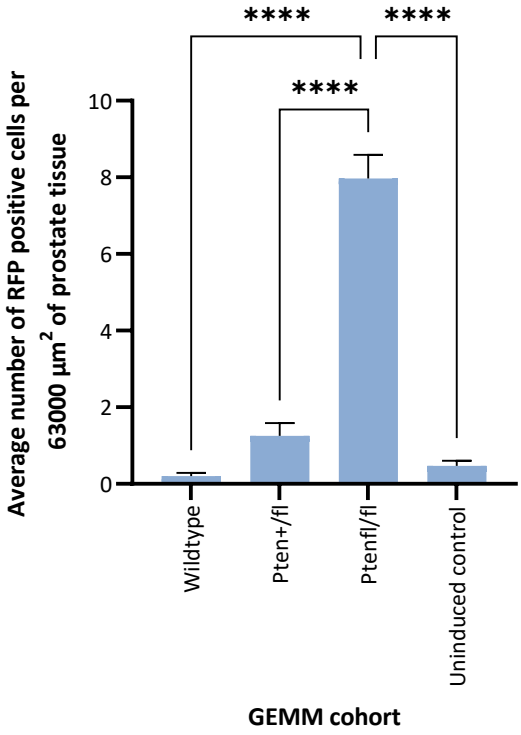

Figure 5.12: The number of RFP-positive cells that have undergone *Col1a2CreER(T2)*-mediated recombination is significantly increased in *Col1a2CreER(T2)$^{+/-}$ Pten$^{fl/fl}$ Rfp$^{+/-}$* prostate stroma, relative to *Col1a2CreER(T2)$^{+/-}$ Rfp$^{+/-}$ wild-type* and *Pten$^{+/fl}$* cohorts. Plots show quantitation of RFP positivity in 100 day old post tamoxifen induced *Col1a2CreER(T2)$^{+/-}$ Pten$^{+/+}$ Rfp$^{+/-}$* (wildtype), *Col1a2CreER(T2)$^{+/-}$ Pten$^{+/fl}$ Rfp$^{+/-}$* (Pten+/fl), *Col1a2CreER(T2)$^{+/-}$ Pten$^{fl/fl}$ Rfp$^{+/-}$* (Ptenfl/fl) and non-induced (corn oil only) *Col1a2CreER(T2)$^{+/-}$ Pten$^{+/+}$ Rfp$^{+/-}$* (uninduced) GEMM (n = 3). Error bars = SEM. A one-way ANOVA with a Tukey's multiple comparison test was performed to determine statistical significance between each treatment group; significant results indicate a p value <0.0001.

Quantitation of RFP positive staining revealed a significant increase in the number of RFP positive cells in induced *Col1a2CreER(T2)$^{+/-}$ Pten$^{fl/fl}$* prostate tissue (7.9%, ± SEM) relative to *Col1a2CreER(T2)$^{+/-}$ Pten$^{+/fl}$* (1.25% ± SEM), *Col1a2CreER(T2)$^{+/-}$ wildtype* (0.2%, ± SEM) and *Col1a2CreER(T2)$^{+/-}$ Pten$^{fl/fl}$* uninduced controls (0.4%, ± SEM) ($P < 0.0001$, Figure 5.12). These findings indicate that tamoxifen induced *Col1a2CreER(T2)* mediates recombination in a small stromal cell population in the prostate, and that this population is augmented in response to PTEN loss.

The trend for increased RFP positivity was common to all lobes, however owing to issues with FFPE processing leaving n = 2 for some lobes, statistical analysis could not be performed (Figure 5.13). Interestingly, RFP positive cells were also detected in wildtype and control prostate tissue, suggesting the *Col1a2CreER(T2*) construct has a very low level of leakiness in the absence of tamoxifen induction.

Of note, CreER leakiness has been previously identified via fluorescent reporter and conditional knock-out studies, thus leakiness of the tamoxifen inducible CreER system has been acknowledged as a limitation to this model (Stifter and Greter 2020), and emphasises the importance of including Cre-positive uninduced controls.

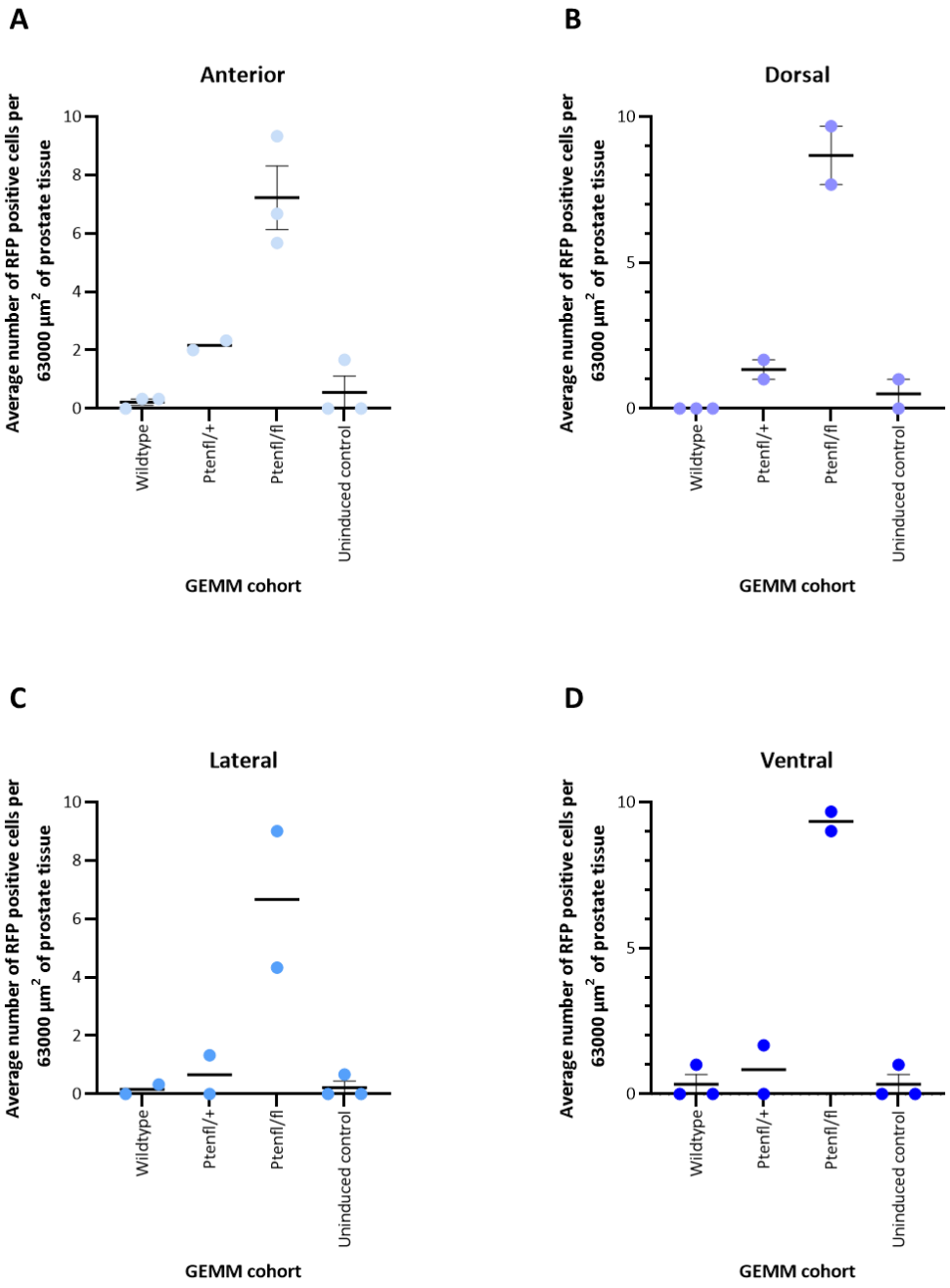

Figure 5.13: Stromal cell recombination events occur in all lobes of the *Col1a2CreER(T2)$^{+/-}$ Pten$^{fl/fl}$ Rfp$^{+/-}$* mouse prostate. Plots show quantitation of RFP positivity in 100 day old post tamoxifen induced *Col1a2CreER(T2)$^{+/-}$ Pten$^{+/+}$ Rfp$^{+/-}$* (wildtype), *Col1a2CreER(T2)$^{+/-}$ Pten$^{+/fl}$ Rfp$^{+/-}$* (Pten+/fl), *Col1a2CreER(T2)$^{+/-}$ Pten$^{fl/fl}$ Rfp$^{+/-}$* (Ptenfl/fl), and non-induced (corn oil only) *Col1a2CreER(T2)$^{+/-}$ Pten$^{+/+}$ Rfp$^{+/-}$* (uninduced control) GEMM A) anterior, B) dorsal, C) lateral and D) ventral prostate lobes as determined by IHC (n = 2 - 3, thus statistical analyses was not possible).

Interestingly RFP positive cells were detected in the fibromuscular sheath (FMS) surrounding the prostate lobes, in addition to those present within the stroma. Analysis of RFP positive cell distribution indicated there were significantly more RFP positive cells in the FSM in *Pten*$^{fl/fl}$ mice compared to wildtype mice (Figure 4.14). Thus, indicating that the direct or close cell-to-cell contact between *Pten*-depleted fibroblasts that accumulate in the FSM and epithelial cells of the prostatic ducts could help promote the hyperplastic phenotype observed upon *Col1a2CreER(T2)*-mediated Pten loss, possibly enabling better interactions and cellular communication.

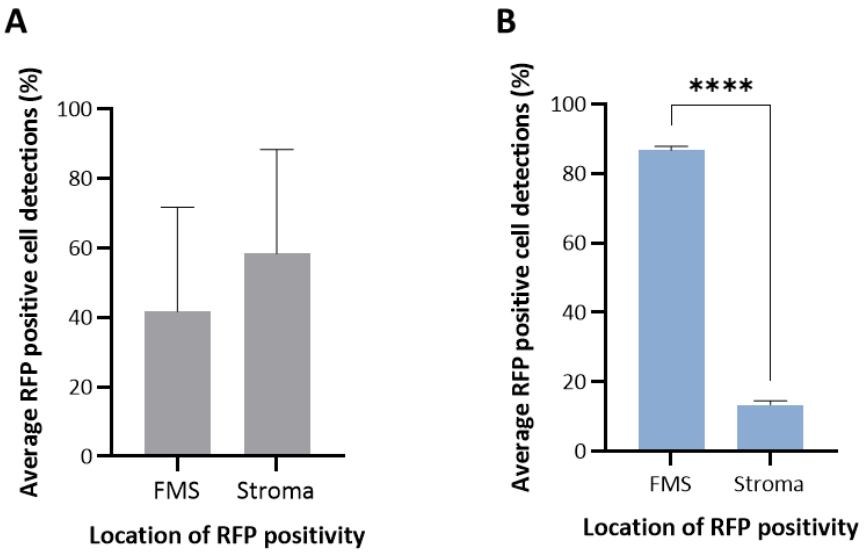

Figure 4.14: RFP positive cells are abundant within the FMS of *Col1a2CreER(T2)*$^{+/-}$ *Pten*$^{fl/fl}$ *Rfp*$^{+/-}$ mouse prostates. Graphs show the percentage of RFP positive cells identified within the fibromuscular sheath and stroma of tamoxifen-induced A) *Col1a2CreER(T2)*$^{+/-}$ *Pten*$^{+/+}$ *Rfp*$^{+/-}$ and B) *Col1a2CreER(T2)*$^{+/-}$ *Pten*$^{fl/fl}$ *Rfp*$^{+/-}$ mouse prostates (100 d). n = 3 / cohort, error bars = SEM. An unpaired two-tailed t-test was performed to determine statistical significance between each treatment group; significant result indicates a p value <0.0001.

5.3.6.1.2. *Col1a2CreER(T2)* mediates recombination in FSP1-positive fibroblasts

To identify whether fibroblasts are undergoing *Col1a2CreER(T2)*-mediated recombination, co-IF staining was performed to detect the fibroblast marker fibroblast specific protein 1 (FSP1, also known as S100A4) and RFP in tamoxifen-induced *Col1a2CreER(T2)* $^{+/-}$ *Pten* $^{+/+}$*; Rfp* $^{+/-}$, *Col1a2CreER(T2)* $^{+/-}$ *Pten* $^{fl/+}$*; Rfp* $^{+/-}$ and *Col1a2CreER(T2)* $^{+/-}$ *Pten* $^{fl/fl}$*; Rfp* $^{+/-}$ mice (n = 3 / cohort) (Figure 5.15).

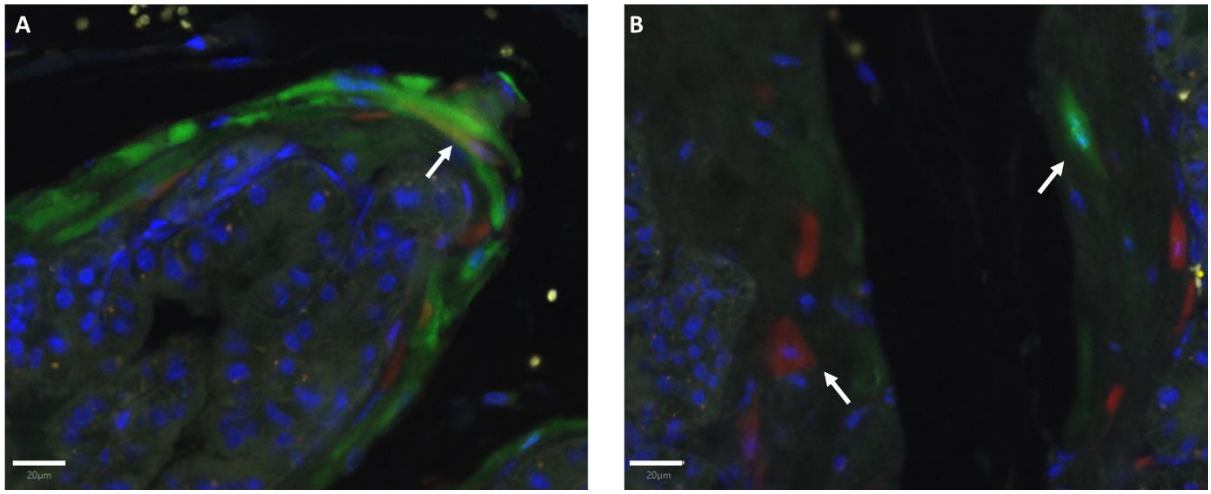

Figure 5.15: Fluorescent staining identifies FSP1 and RFP positive cell populations in *Col1a2CreER(T2)*$^{+/-}$ *Pten*$^{fl/fl}$ *Rfp*$^{+/-}$ mice. Representative 20x magnification images of 100 day old post tamoxifen induced *Col1a2CreER(T2)*$^{+/-}$ *Pten*$^{fl/fl}$ *Rfp*$^{+/-}$ anterior prostate stained for RFP (shown in red), FSP1 (shown in green) and nuclei (shown in blue). White arrows pinpoint three distinct type of cell population: A) FSP1 and RFP positive cells = recombined FSP1-positive fibroblasts, B) cells expressing RFP only = additional recombined cell type, and cells expressing FSP1 only = FSP1 fibroblasts with poor recombination efficiency or derived from non-recombined cells after recombination events. Scale bar = 20 µm.

Analysis of co-IF staining revealed FSP1 positive fibroblasts undergo *Col1a2CreER(T2)*-mediated recombination in the prostate, corroborating with previous validation of the model indicating recombination events within FSP1 positive fibroblasts (Parapuram et al. 2015).

To better assess the proportion of FSP1 positive fibroblasts, co-IF stained prostate sections were quantitated on an individual lobe basis using tissue obtained from tamoxifen-induced *Col1a2CreER(T2)*$^{+/-}$ *Pten*$^{fl/fl}$ *Rfp*$^{+/-}$ biological repeats (Figure 5.16).

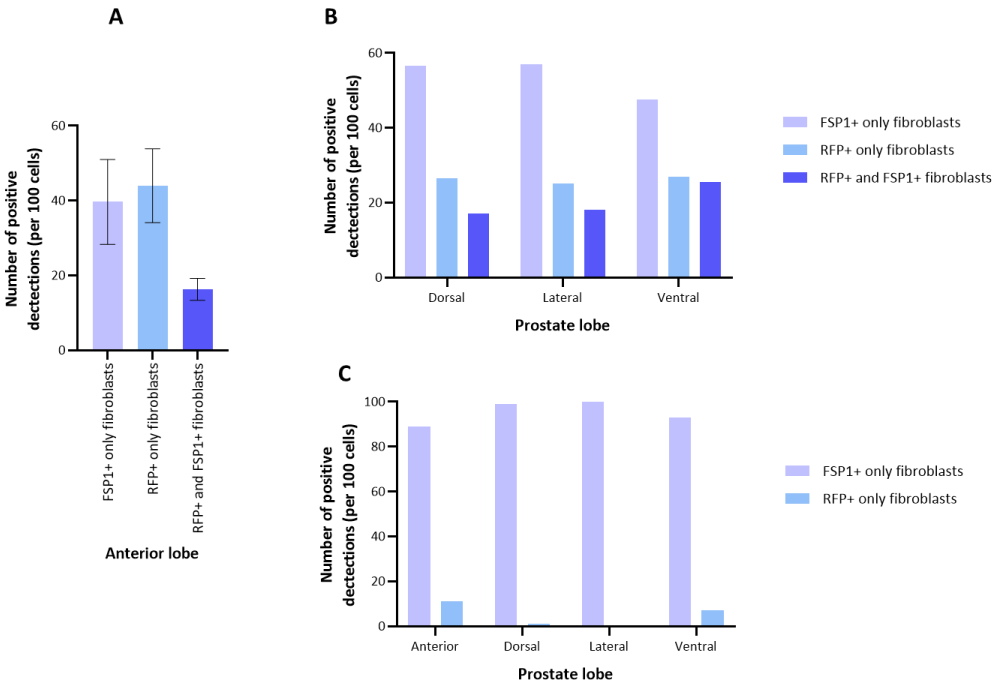

Figure 5.16: *Col1a2CreER(T2)*-mediated recombination occurs in FSP1 positive and negative fibroblasts in the *Col1a2CreER(T2)$^{+/-}$ Pten$^{fl/fl}$ Rfp$^{+/-}$* mouse prostate. Plots show quantitation of FSP1, RFP and co-stain positivity in 100 day old post tamoxifen induced *Col1a2CreER(T2)$^{+/-}$ Pten$^{fl/fl}$ Rfp$^{+/-}$* A) anterior and B) dorsal, lateral and ventral prostate lobes and C) *Col1a2CreER(T2)$^{+/-}$ Pten$^{+/+}$ Rfp$^{+/-}$* (wildtype) prostate as determined by IF staining. Bars represent the mean number of detections. A One-Way ANOVA and Tukey's multiple comparison test was performed on the anterior lobe data (n = 3 biological repeats); however, results were not statistically significant. Error bars in Graph A depict standard error of the mean. Statistical analyses were not performed on data in Graph B and C (as only n = 2 and n = 1 biological repeat were available respectively).

A similar number of FSP1-positive and RFP-positive expressing cells were detected within the anterior lobes of mice with *Col1a2CreER(T2)*-mediated bi-allelic deletion of *Pten* (5.16A), however the number of cells expressing both markers was considerably lower, with a mean number of detections averaging at 16% across all *Col1a2CreER(T2)$^{+/-}$ Pten$^{fl/fl}$ Rfp$^{+/-}$* biological repeats.

This trend was not observed within the other prostate lobes (Figure 5.16B), where the number of FSP1-positive/RFP-negative cells was markedly higher than FSP1/RFP co-expressing cells or RFP-positive/FSP1-negative cells. For instance, within the ventral lobes of the *Col1a2CreER(T2)$^{+/-}$ Pten$^{fl/fl}$ Rfp$^{+/-}$* prostate, the number of co-stained cells and RFP only expressing cells were very similar, suggesting that almost half of the cells that underwent *Col1a2Cre-ERT2* mediated recombination in the context of PTEN loss were FSP1 positive fibroblasts, yet the other half of the recombined cells remains an unknown cell type. The proportion of FSP1-negative RFP-positive cells in the dorsal, lateral

and even anterior prostate lobes were higher than those also positive for FSP1, indicating that recombination within these lobes to mainly occur within an FSP1 negative stromal cell.

Although FSP1 is a frequently used marker of fibroblasts within a range of different organs, recent work has also established activated M2 macrophages as a secretor of FSP1 (Zhang et al., 2018), therefore it could also be speculated that the IF staining may have also identified other cell populations. To overcome this, further RFP co-staining with other established fibroblast markers such as cell surface receptor CD34 and platelet-derived growth factor receptor alpha (PDGFRα) (Muhl et al. 2020), could be performed on serial tissue sections and cross-compared to the FSP1 stain to confirm validity of *Pten* loss in fibroblasts only. However, based on the location and shape of the cells identified by IF staining, there is some confidence that the FSP1 positive cells are highly likely to be fibroblasts. Furthermore, if the FSP1 positive cells detected are fibroblasts, this data may indicate that *Col1a2CreER(T2)*-mediated recombination occurs within a subset of fibroblasts that are involved in host surveillance, promotion of angiogenesis and regenerative wound healing (Zhang et al. 2013; Saraswati et al. 2019).

The RFP positive cells also displayed a fibroblastic morphology, suggesting that recombination events do occur in fibroblasts, however performing additional stains for alternative cell types to see whether they co-stain, or performing single cell RNA-Seq will help determine their identify.

Given that not all FSP1-positive cells express RFP, an alternative explanation could be that not all FSP1 cells are recombined upon tamoxifen-induction of the *Col1a2CreERT2* transgene. In an attempt to determine the recombination efficiency within the *Col1a2CreER(T2) Pten*-floxed model, co-IF stained prostate sections were used to calculate the percentage of cells co-stained for both FSP1 and RFP, relative to the total number of FSP1-positive cells (Table 5.2).

Table 5.2: *Col1a2CreER(T2)* model recombination efficiency in FSP1 positive prostate fibroblasts.

Prostate lobe	Average recombination efficiency in FSP1+ cells	95% confidence interval
Anterior (n = 3)	31%	0.15
Dorsal (n = 2)	23%	0.03
Lateral (n = 2)	24%	0.08
Ventral (n = 2)	35%	0.06
All lobes combined	28%	0.09

On average, 28% of the FSP1-positive fibroblast population within the prostate is recombined (i.e. RFP-positive) upon tamoxifen induction in *Col1a2CreER(T2)$^{+/-}$ Pten$^{fl/fl}$ Rfp$^{+/-}$* prostate tissue. When assessing prostate lobes individually, the number of FSP1/RFP co-expressing cells was higher in the anterior and ventral lobes (31% and 35% respectively) was markedly higher than the dorsal and lateral lobes (23% and 24% respectively), indicating recombination efficiency might not be as high in the dorsal and lateral lobes. In *Col1a2CreER(T2)$^{+/-}$ Pten$^{+/+}$ Rfp$^{+/-}$* (wildtype) prostate tissue, no recombined (FSP1 and RFP positive cells) were detected within any of the lobes (n = 1), therefore indicating a repeat of the experiment is required in order to correctly interpret these findings.

It is important to note that the exact recombination efficiency of this GEMM cannot be deduced from these results as they only consider fibroblasts expressing FSP1, therefore other fibroblast markers could be used to determine a more accurate recombination efficiency within fibroblasts. Furthermore, this analysis also does not take into account the presence of any unrecombined FSP1-positive fibroblasts which may have been derived from an alternative cell type in response to the loss of PTEN in the originally recombined FSP1 positive fibroblast cell population, thus lineage tracing may be required to better determine the impact of PTEN deletion on cells such as FSP1 positive fibroblasts.

5.3.7. Identification of the fibroblast cell population targeted by the *Col1a2CreER(T2)* construct in mouse prostate

In lung fibroblasts, loss of PTEN has been shown to drive activation of fibroblasts which exhibit cancer cell type features including increased proliferation and migration (Geng et al. 2014), therefore it could also be speculated that loss of *Pten* in fibroblasts mediated by tamoxifen induction of the *Col1a2CreER(T2)* promoter could generate associated fibroblasts. As activated fibroblasts can arise from a wide variety of origins, recent studies have concluded that use of a single fibroblast marker is not sufficient to identify activated fibroblasts as they do not recapitulate their heterogeneous composition (Sandberg et al. 2019). Recent investigation into fibroblast populations in pancreatic ductal adenocarcinoma (PDAC) using single-cell RNA-Seq, identified three distinct subtypes termed myofibroblastic CAFs (myCAF, expressing podoplanin (PDPN) only) that were primarily found adjacent to the PDAC cancer cells, inflammatory CAFs (iCAF, expressing PDPN and lymphocyte antigen 6 complex (LY6C)) which were located amongst fibrotic and highly dense areas of connective tissue, and antigen-presenting CAFs (apCAF, expressing PDPN and major histocompatibility complex class II (MHCII)) (Elyada et al. 2019).

To determine if PTEN loss can disrupt the fibroblast subpopulations in the prostate, flow cytometry was used to identify multiple fibroblast populations simultaneously within tamoxifen-induced *Col1a2CreER(T2)$^{+/-}$ Pten$^{fl/fl}$ Rfp$^{+/-}$* and uninduced *Col1a2CreER(T2)$^{+/-}$ Pten$^{+/fl}$ Rfp$^{+/-}$* mouse prostates.

5.3.7.1. Inflammatory fibroblasts appear to be the cell type undergoing recombination

As the previously identified myofibroblast, inflammatory and antigen-presenting fibroblast populations were identified to express COL1A2 (Elyada et al., 2019), live cells dissociated from tamoxifen induced *Col1a2CreER(T2)$^{+/-}$ Pten$^{fl/fl}$ Rfp$^{+/-}$* mouse prostates aged 300 days post-induction underwent flow cytometry analysis (n = 3) to identify the distinct fibroblasts populations using antibodies detailed in Table 5.3, and the gating strategy detailed in Figure 5.17.

Table 5.3: Cell staining rationale for flow cytometry experiment.

Antibody/stain	Purpose
DAPI +	Elimination of dead cells
CD45 + and CD24 +	Elimination of hematopoietic cells and epithelial cells respectively
PDPN +	Pan-activated fibroblast marker
LY6C +	Marker of inflammatory fibroblasts
MHCII +	Marker of antigen-presenting fibroblasts

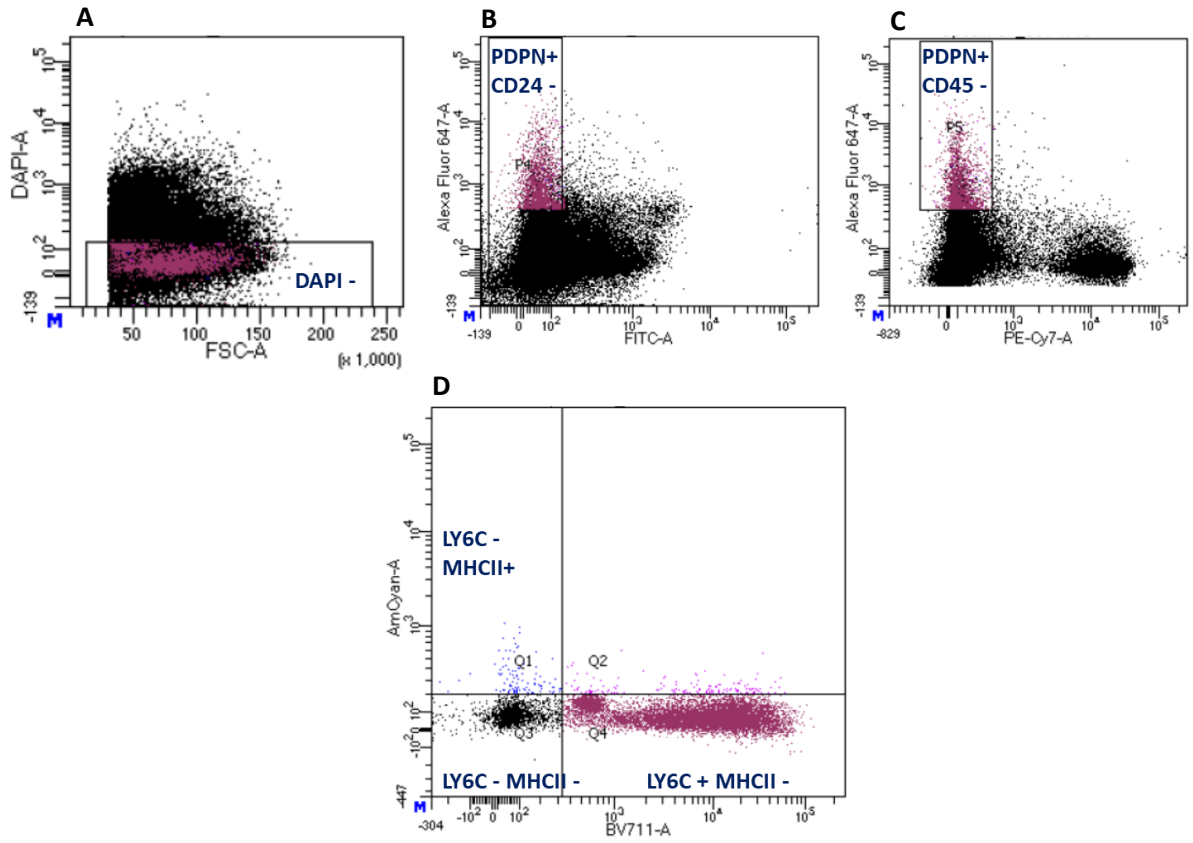

Figure 5.17: Gating strategy for fibroblast population analysis. Flow cytometry plots displaying the gating strategy for isolation of antigen-presenting, myofibroblast and inflammatory fibroblast cell populations. Plots represent A) DAPI negative gating for removal of dead cells, B) PDPN positive gating of CD24 negative cells for selection of fibroblasts and removal of hematopoietic cells, C) PDPN positive gating of CD45 negative cells for selection of fibroblasts and removal of epithelial cells and D) gating of each activated fibroblast cell population. Q1 indicates selection of antigen-presenting fibroblasts, Q3 indicates myofibroblasts and Q4, inflammatory fibroblasts.

Col1a2CreER(T2)$^{+/-}$ induced mice harbouring bi-allelic *Pten* deletion (n = 3, 300 d post induction) and uninduced *Col1a2CreER(T2)*$^{+/-}$ *Pten*$^{fl/fl}$ controls (n = 3, 120 – 200 d old) underwent flow cytometry to determine the number and subtype of fibroblasts present within the total prostate (Figure 5.18). It is important to note, that the uninduced control tissue was not taken at the same timepoint as the experimental *Pten*$^{fl/fl}$ prostates due to GEMM availability.

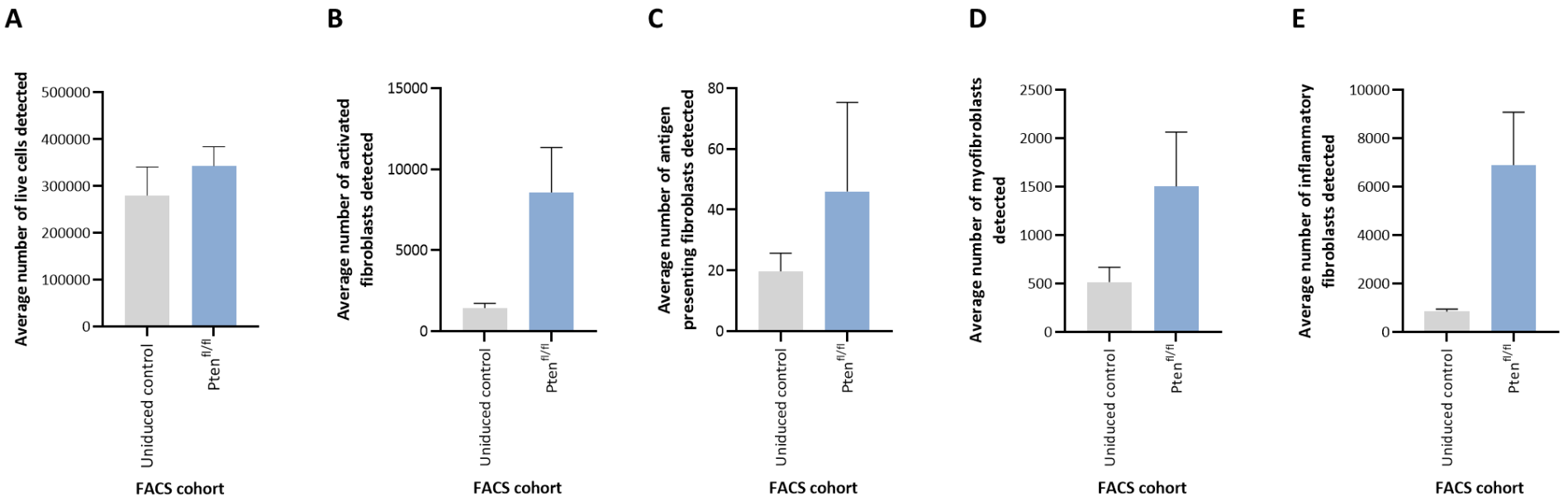

Figure 5.18: Inflammatory fibroblasts are the most abundant type of activated fibroblast population present within tamoxifen induced *Col1a2CreER(T2)$^{+/-}$ Pten$^{fl/fl}$ Rfp$^{+/-}$* mouse prostates tissue. Graphs show the mean number of total PDPN positive fibroblasts, alongside the average number of antigen-presenting, myofibroblastic and inflammatory fibroblast detections, determined by flow cytometry in tamoxifen-induced *Col1a2CreER(T2)$^{+/-}$ Pten$^{fl/fl}$ Rfp$^{+/-}$* (300 d) and uninduced mature *Col1a2CreER(T2)$^{+/-}$ Pten$^{+/fl}$ Rfp$^{+/-}$* mouse prostates (n = 3 / cohort). Error bars = SEM. An unpaired two-tailed t-test was performed to determine statistical significance between each treatment group; however non-significant results were obtained.

An equal amount of experimental and control prostate cells were sorted by flow cytometry (Figure 5.18A), however a considerably larger number of activated fibroblasts were detected in the *Pten*$^{fl/fl}$ model relative to the control (5.18B). Visually the difference appeared to be significant however was deemed insignificant by the statistical test performed (P value = 0.0630).

Within the *Pten*$^{fl/fl}$ mouse prostates processed through flow cytometry, approximately 2.5% of live cells were fibroblasts (PDPN positive, CD45 negative and CD24 negative). When analysing the fibroblast populations, around 0.4% were determined to be antigen-presenting fibroblasts, 16% were myofibroblastic, and the most predominant population comprising 80% of the fibroblasts present were identified to be inflammatory fibroblasts. Taken together, these findings indicate that the presence of activated fibroblast populations are increased following loss of fibroblast PTEN in the *Col1a2CreER(T2)*$^{+/-}$ *Pten*$^{fl/fl}$ *Rfp*$^{+/-}$ mouse model relative to the uninduced control. Whilst the comparison of the inflammatory fibroblast population appeared to be significantly increased in the *Pten*-null setting, the p value obtained was just on the cusp of significance (P value = 0.0507). Therefore, a repeat of this experiment with bigger cohort sizes may be beneficial for determining if this increase in inflammatory fibroblast population is significantly altered following *Col1a2CreER(T2)*-mediated loss of fibroblast *Pten.*

Despite having successfully isolated 3 fibroblast populations, the flow cytometry data could not distinguish which of these cells were RFP positive due to overlap of laser channel excitation ranges, which would significantly skew the detection of other markers. Therefore, to determined which cells had undergone recombination, 100 cells from the myofibroblast and inflammatory fibroblast populations from each of the biological repeats were directly sorted onto poly-L-lysine coated microscope slides for IF staining to detect RFP (Figure 5.19). Cells from the antigen-presenting fibroblast population could not be assessed due to the limited number of cells detected.

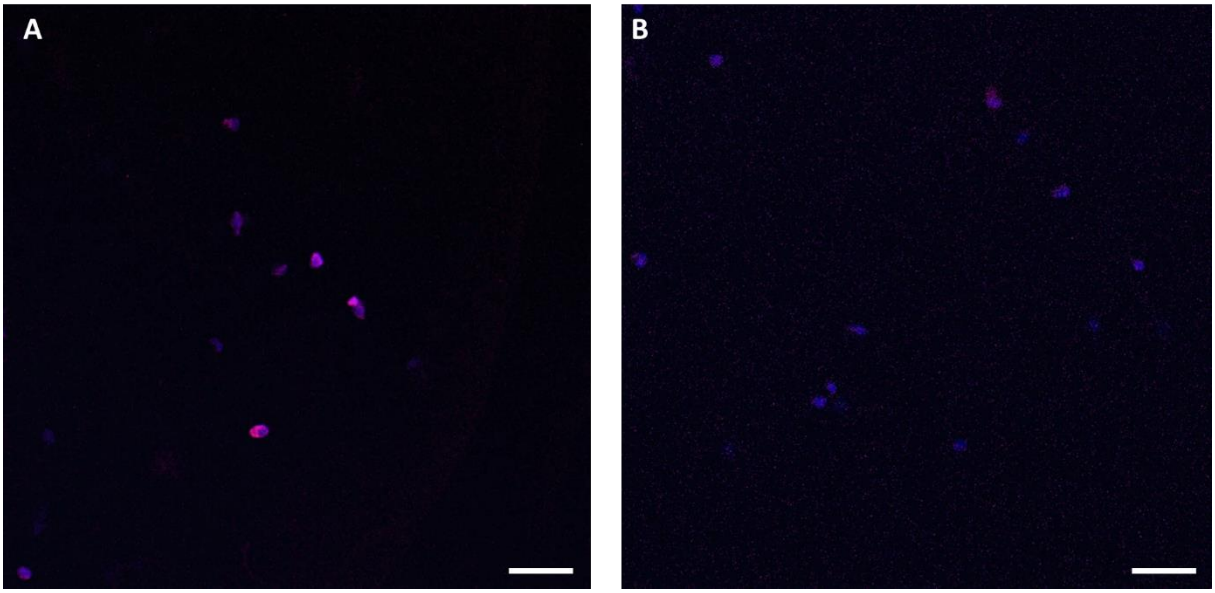

Figure 5.19: RFP IF staining is present in the inflammatory fibroblast population, but not the myofibroblast population isolated from *Col1a2CreER(T2)$^{+/-}$ Pten$^{fl/fl}$ Rfp$^{+/-}$* mice. Representative 20x magnification images of 300 day post tamoxifen induced *Col1a2CreER(T2)$^{+/-}$ Pten$^{fl/fl}$ Rfp$^{+/-}$* A) inflammatory fibroblasts and B) myofibroblasts stained for RFP (shown in red) and nuclei (shown in blue). Scale bar = 20 µm.

A high proportion of the inflammatory fibroblasts were RFP positive (visual assessment only), indicating inflammatory fibroblasts have undergone *Col1a2CreER(T2)* mediated recombination. The myofibroblast population was predominantly negative for RFP indicating that *Col1a2CreER(T2)* induction does not result in the recombination of myofibroblasts. The rare RFP-positive staining present in the myofibroblast population is likely to reflect inflammatory fibroblast contamination, as the inflammatory fibroblasts were the first to encounter the sorting nozzle used to expel the cells onto the microscope slides.

To fully confirm whether recombination did or did not occur within each of the sorted fibroblast populations, and the efficiency of the recombination events, assessment of *Pten* expression via qRT-PCR could be performed, however a considerably larger cohort size would be required to yield enough mRNA to analyse each subpopulation. Furthermore, control tissue taken from tamoxifen induced *Col1a2CreER(T2)$^{+/-}$ Pten$^{+/+}$ Rfp$^{+/-}$* mouse prostate aged 300 days post induction, was not included within this experiment therefore assumptions cannot be fully made as to whether *Pten* loss alters these fibroblast populations to contribute to the hyperplastic phenotype. If more time were available, a repeat of the flow cytometry and IF study on *Col1a2CreER(T2)$^{+/-}$ Pten$^{+/+}$ Rfp$^{+/-}$* prostate tissue would have been performed.

In summary, we found the loss of fibroblastic *Pten* alone in the prostate is sufficient to activate or drive focal hyperplasia in all lobes of the Col1a2CreER(T2) mouse prostate, whereby the frequency of the phenotype increases as *Pten* loss increases, relative to wildtype mice and controls. This indicates a tumour suppressive role of fibroblast *Pten*, supporting previous published findings, and warrants further characterisation to help determine its clinical relevancy.

5.4. Discussion

PTEN has been shown to play a major tumour suppressive role in prostate epithelial cells, where genetic alteration of PTEN is a common occurrence in the clinic. This PhD project has identified that PTEN also plays a role in FSP1 positive fibroblasts to maintain normal tissue homeostasis in mice. Although the mouse prostate does not possess a homologue for the human transition zone where BPH lesions are most commonly found in patients (Oliveira et al. 2016), this data is still informative on how events such as loss of a tumour suppressor in the prostatic stroma are highly influential on the epithelial compartment, including how loss of PTEN can contribute to disease progression.

To address if PTEN loss driven by *Col1a2CreER(T2)* can influence PTEN status in the prostate epithelium, IHC staining to detect PTEN was attempted on prostate tissue from induced 100- and 300-day GEMM cohorts, however, was unsuccessful. A repeat of this experiment in the future would help to determine whether PTEN loss in the stroma can mediate signalling events which are received by epithelial cells to trigger *PTEN* alterations. Further work to characterise the hyperplastic phenotype is needed, and it would be interesting to determine if AKT signalling is activated both in the epithelium and stroma following both heterozygous and homozygous *Pten* loss, as the current data suggests substantial changes can occur regardless of *Pten* dosage. Furthermore, alterations within the AR signalling pathway subsequent to *Pten* deletion in this model would also be worth investigating, considering the extensive role played by AR in epithelial-stromal cell communication.

Alongside hyperplasia we also observed atrophy, which is deemed a common event within the human prostate epithelium (Ittmann 2018). As atrophy has been associated with the reduction of hormone signalling (Qian et al. 2001; Frisbie et al. 2006), it may be beneficial to assess androgen levels and AR status within the fibroblast PTEN-depleted GEMM prostates to help determine whether a reduction in AR signalling could be contributing to the atrophy observed.

By trying to pinpoint the exact cell type undergoing recombination using the RFP reporter, we also identified a few caveats with the *Col1a2CreER(T2) Pten*$^{fl/fl}$ GEMM, including potential leakiness of the Cre. Within more recent years, newer mouse models that enable manipulation of fibroblasts have

been generated (Swonger et al., 2016), which may also be worth evaluating. To better understand which cells are recombined upon induction of the *Col1a2CreER(T2)* transgene, it will be important to perform experiments that can directly isolate these cells such as laser capture micro-dissection to enable subsequent analysis such as qRT-PCR or for a more in-depth analysis, single cell RNA-Seq (Civita et al. 2019).

Through co-IF experiments, we also established that a large proportion of RFP positive cells did not also express FSP1, which suggests other fibroblast cell types to be also under the influence of the *Col1a2CreER(T2)* promoter. Spatial transcriptomic profiling would additionally provide information to determine exactly which types of fibroblasts or cell may be recombining within this GEMM.

Stromal fibroblasts aid in the production of the collagen and laminin networks that contribute to the structure of the basement membrane (BM), however CAFs have additionally been shown to breach the BM to aid with cancer cell invasion (Glentis et al. 2017). Although in support of potential FMS residing fibroblasts, this data may also be indicative of possible recombination events within the epithelial cell population, as certain epithelial cells including those present in gastric cancer have been shown to express *Col1a2* mRNA (Li et al. 2016). Due to time constraints this could not be confirmed, however CK5 (basal-cell marker) and CK8 (luminal-cell marker) staining could be performed in conjunction with RFP staining to establish if any COL1A2-positive epithelial cells also recombine and consequently lose *Pten*.

Our flow cytometry data indicated that inflammatory fibroblasts are the predominant fibroblast population to be recombined in the *Col1a2CreER(T2)* model, although a deeper analysis is required in a wildtype setting.

Together these findings indicate that *Pten* loss in fibroblasts may trigger the active transformation of fibroblasts. However, the necessary controls were not available, thus future work is needed to determine if inflammatory fibroblasts are augmented in the absence of PTEN, and to establish if this population represents the fraction of FSP1-positive cells that express RFP. Since FSP1 positivity is observed in resident fibroblasts with inflammatory functions during normal tissue homeostasis (Strutz et al. 1995), our data collectively implies fibroblasts with inflammatory functions may be capable of mediating stromal centred signalling events that promote hyperplastic epithelial growth via an unknown mechanism.

If the *Col1a2CreER(T2)* model did not ubiquitously target all organs, it would have been fascinating to see whether continued aging of the prostate could have resulted in the development of PIN or if combining *Col1a2Cre* driven *Pten* loss in combination with the well characterised *PBiCre*$^{+/-}$ *Pten*$^{fl/fl}$ model of prostate cancer can influence the rate of progression.

Interestingly CAFs isolated from human prostate carcinoma have been previously shown to initiate tumorigenesis of hyperplastic human prostate epithelial cells *in vitro*, however they did not facilitate increased growth of normal prostate epithelial cells, suggesting that CAFs cannot induce tumour initiation, but can promote the progression of pre-existing aberrant cells (Alkasalias et al. 2018). Therefore, it would be also informative to assess the stromal landscape for mediators that could be driving transformation of the *Pten*-deleted fibroblasts to CAFs, such as TGF-β signalling. Attempts were made to initiate characterisation of the TME in the 300-day post induction *Col1a2CreER(T2)* cohorts however were relatively unsuccessful, including assessment of collagen deposition via Masson's Trichrome staining given that loss of *Pten* within mammary fibroblasts have also been associated with increased collagen remodelling (Jones et al. 2019). If time had permitted, this type of histological stain could have been better optimised to assist in this enquiry of the aged cohort mice.

Together our data shows that stromal PTEN, more specifically fibroblast PTEN, has a role in maintaining normal prostate homeostasis, although further investigation is required to better understand its clinical relevance. Future work could additionally utilise tissue microarrays to assess stromal PTEN expression both in tumour and surrounding non-tumour tissue. This type of analysis would also enable correlation of PTEN status to overall survival and biochemical recurrence of patients, in addition to correlating resistance to therapeutics such as AKT inhibition.

Despite the partial characterisation of the *Col1a2CreER(T2) Pten*$^{fl/fl}$ model prostate, a considerable start has been made with regards to establishing the effect of fibroblast *PTEN* loss on the prostate epithelium, a topic that has not been extensively discussed or investigated within published literature and therefore the impact on patient lives unknown. It is essential that studies such as these continue to occur as the effects mediated by *Pten* loss in the prostate stroma, may also be applicable to other tissues that regularly succumb to oncogenic transformation.

Chapter 6

6. Final Discussion

6.1. Summary of findings and achievements

Despite new treatments being developed and entering clinical trials, advanced prostate cancer patients continue to have a poor outcome, as resistance and bypass mechanisms overcome treatment. Increasing clinical data has emphasised the benefit of combination therapies to overcome monotherapy resistance (Li et al. 2021; Qu et al. 2021), therefore it is important that we fully understand how signalling pathways interact to identify resistance mechanisms so that novel treatments that benefit patients can be developed.

The fundamental discovery that *Pik3ca*-mutant and *Pten*-deleted murine prostate cancer models do not phenocopy one another, despite a shared ability to activate the PI3K/AKT signalling cascade (Pearson et al. 2018), led this project in search of identifying key transcriptional differences between these two clinically relevant genetic drivers, with the aim of finding novel, targetable PI3K-independent roles of PTEN in prostate cancer.

The comparative and non-biased gene set enrichment analysis of RNA-Seq data from *Pik3ca*-mutant and *Pten*-deleted prostate, revealed a significant upregulation of NF-κB pathway components and mediators within the *Pte*n-null tumours relative to the *Pik3ca*-mutant tumours. Whilst published literature has proposed that NF-κB activation can be triggered by AKT signalling, it appears that activation of the NF-κB pathway occurs through PI3K-independent mechanisms when PTEN is lost, highlighting the NF-κB signalling pathway as an actionable target for PTEN-deficient prostate cancer. Since limited research has explored targeting the NF-κB cascade in prostate cancer, it was necessary to establish which component of the pathway would be the most optimal to target.

Further analysis of the RNA-Seq data provided several key candidates, for which small molecule inhibitors were available. To determine their effectiveness against PTEN-deficient and PTEN proficient prostate cancer models, we selected a range of upstream and downstream NF-κB inhibitors, and further investigated how the NF-κB and AKT signalling cascades interact, in addition to exploring a new potential treatment strategy that combines NF-κB blockade with AKT inhibition.

Through initial screening of NF-κB pathway inhibitors on a range of *in vitro* and *ex vivo* prostate cancer models, we identified TLR2 inhibition could significantly hinder *PTEN*-deficient prostate cancer cell line growth, which could be further impeded by the addition of AKT inhibition. These data reveal that NF-κB and AKT inhibitors can synergise to reduce prostate cancer growth, thus identifying a potentially beneficial therapeutic route for patients. Despite our experiments exploring NF-κB inhibition in *ex vivo*

prostate cancer models yielding varied results, it was clear that a TME is vital for drug studies and that testing the TLR2 inhibitor (with and without AKT inhibition) *in vivo* will provide valuable preclinical data needed to guide clinical translation.

Whilst *PTEN* deletion in the prostate epithelium is a well-characterised driver of prostate tumorigenesis, little has been published with regards to the impact of *PTEN* deletion in the prostatic stroma, and genetic alterations in the prostate TME have been largely understudied; however, it is likely this will be an emerging topic with digital spatial profiling technology becoming more widely available.

Through use of the *Col1a2CreER(T2)* GEMM model, the final arm of this PhD project aimed to address if PTEN in fibroblasts is required to maintain normal prostate tissue homeostasis, in addition to establishing in which fibroblast population(s) *Col1aa2CreER(T2)* drives recombination and the overall efficiency of recombination within the prostate.

Epithelial cell hyperplasia was observed in all prostate lobes of 100-day and 300-day aged *Col1a2CreER(T2)*$^{+/-}$ tamoxifen-induced mice with bi-allelic *Pten* loss relative to age matched wild-type controls, alluding to a protective role for PTEN in fibroblasts on prostate epithelial cell homeostasis. We determined through the addition of a fluorescent reporter, that recombination events partially occurred within FSP1-positive fibroblasts, and potentially within cells expressing PDPN and LY6C, markers of inflammatory activated fibroblasts (Elyada et al. 2019). These findings further implicate PTEN as a mediator of immune / inflammatory responses and highlight the importance of epithelial-stromal interactions for tissue homeostasis, however it is imperative that this experiment is repeated with the correct wildtype controls to confirm the findings thus far. Although attempted, further work is necessary to establish the true status of PTEN in fibroblasts targeted by *Col1a2Cre* and in exactly which fibroblast population(s) recombination is mediated.

6.2. Implications within the clinic

Previous studies have determined that loss of PTEN in prostate patients is significantly associated with a reduced overall median survival in comparison to patients with normal PTEN expression (Ferraldeschi et al. 2015), emphasising the urgent need for clinically relevant therapies for patients with *PTEN* genetic alterations.

Whilst PI3K isoform–specific monotherapies have been deemed ineffective against PTEN-null prostate cancer owing to feedback and resistance mechanisms, pan-PI3K or AKT inhibition are emerging as more effective treatments (Triscott and Rubin 2018; Mao et al. 2021). The combination of PI3K inhibition (or AKT inhibition) with either AR, Axl, GTPase, PKC, or SGK inhibition have also all shown promise for overcoming resistance to PI3K/AKT pathway inhibition in several malignancies (Turnham et al. 2020), indicating co-therapies may be more effective than PI3K targeted monotherapy in cancer. Authors within a recent review covering small molecule NF-κB pathway inhibitors currently within the clinic, have drawn attention to how PI3K inhibitors can also contribute to reduced activation and transcription of NF-κB targets (Ramadass et al. 2020). Furthermore, macrophages activated by NF-κB within the breast tumour microenvironment have been implicated in driving resistance to PI3K inhibitors (Yang et al. 2019a). Together with our data, this suggests a clinical need for further investigation of NF-κB and PI3K pathway co-inhibition in cancer.

Whilst limited literature could be found exploring NF-κB and PI3K combination therapy in disease, a recent publication by Liu et al, has linked activation of the PI3K/AKT/NF-κB axis to promotion of multidrug resistance in pancreatic cancer, and that inhibition of this PI3K/AKT/NF-κB oncogenic signalling pathway in nasopharyngeal carcinoma (NPC) could reverse any multidrug resistance previously observed; facilitated through p53 and Bax protein mediated inhibition of cyclin D1 overexpression driven by NF-κB (Liu et al. 2020), further supporting the need for PI3K/AKT/NF-κB studies, especially given the potential of the pathway to stimulate therapeutic resistance and facilitate relapse.

Whilst the prostate tumour microenvironment is a current hot topic in the field, much of the current literature focuses on the chronic inflammatory and immunosuppressive environment that can facilitate tumour growth. Consequently, current TME studies are predominantly tailored towards immune check point inhibitors and other immunotherapies (Kwon et al. 2021). Current methods within clinical pathology labs to detect PTEN loss include genomic sequencing, fluorescence in situ hybridization (FISH) and IHC (Lotan et al. 2016), whereby published studies investigating PTEN loss in Gleason grade 7 prostate tumours, state clinically trained pathologists exclude regions enriched with stromal cells during their digital analyses of IHC stained tumour microarray (TMA) core biopsies (Picanço-Albuquerque et al. 2019).

Furthermore, PTEN positive stained benign glands and stromal cells are used as internal controls and when the sections lacked these internal positive controls (i.e., loss of stromal cell PTEN observed), the

cores are classified as inconclusive and subsequently removed from further analyses (Picanço-Albuquerque et al. 2019). This approach towards detection of PTEN loss in human specimens has also been detailed in various other studies and review articles (Lotan et al. 2017; Jamaspishvili et al. 2018), highlighting a gap in our knowledge of whether PTEN genetic alterations in the stroma are functionally important in prostate cancer progression.

As we and others have identified that loss of PTEN in stromal cells can mediate epithelial cell changes, the current approach of disregarding PTEN loss within the stroma may need to be reconsidered, with future work needed to determine if PTEN loss in the stroma can be predictive of disease progression. One study has delved deeper into the cancer-associated stroma of the prostate to identify small somatic copy number aberrations (SCNAs) using 400K microarrays on laser captured cells from frozen human prostate adenocarcinomas and adjacent benign tissue (Bianchi-Frias et al. 2016).

They observed hetero- and homozygous *PTEN* copy number loss in 45% of epithelial samples and loss of *PTEN* within the cancer-associated stroma of one patient. Upon closer inspection they deemed this result to be cross-contamination of tumour epithelial cells within the stroma sample during the microdissection process of a tangentially cut section of tumour tissue. They also concluded that cells within prostate cancer-associated stroma lack recurrent clonal somatic genomic aberrations (Bianchi-Frias et al. 2016), however on a cohort size of n = 20, Gleason grade 7+ tumours, very little can be deduced on PTEN stromal expression in the majority of patients.

In addition, Shah et al assessed 260 prostate tumour core needle biopsies for PTEN loss via immunohistochemical methods and found that a subset of stromogenic prostate cancer (grade 3 reactive tumour stroma with an epithelial to stroma ratio of greater than 50% reactive stroma), 23% of cases presented with PTEN loss in the stroma. Furthermore, the authors reasoned that these findings support the inclusion of stromal analysis during routine histopathological prognostication of prostate cancer patient specimens (Shah et al. 2019). Whilst in the clinic, loss of *PTEN* in stromal cells may not be a common event, improved methods of detection may also be required given that mRNA levels do not always correlate with protein levels.

6.3. Future avenues of research

Whilst this project primarily focused on the implications of PTEN loss in prostate cancer, significant amounts *Pik3ca*$^{+/HR}$ mutant mouse transcriptional data was generated but not investigated in detail. In prostate tumours possessing *PIK3CA* activating mutations but wild-type *PTEN,* selective inhibition

of p110α has been found to be therapeutically superior to AKT inhibition (Mao et al. 2021), owing to p110α-dependent selective pressures that were also identified by Pearson and colleagues (Pearson et al. 2018).

Given the immediate availability of these datasets; comparing uncastrated *PBiCre$^{+/-}$Pik3ca$^{+/HR}$* prostate tumour RNA-Seq outputs to uncastrated *PBiCre$^{+/-}$Pik3ca$^{+/+}$* (wildtype) mouse prostate transcriptional data, other key targets that are contributing to the *Pik3ca* mutant phenotype may be discovered. The additional uncastrated comparison of *PBiCre$^{+/-}$Pik3ca$^{+/HR}$Pten$^{fl/fl}$* tumour data with the *PBiCre$^{+/-}$Pten$^{fl/fl}$* model may also provide insight into how *PIK3CA*-activating mutations synergise with PTEN loss to accelerate prostate adenocarcinoma progression. Furthermore, this deep dive into finding *Pik3ca* specific functions within the compound model, may also help identify novel treatment options for prostate tumours, which is particularly important since *PIK3CA* activating mutations in mCRPC have been relatively uncharacterised (Herberts et al. 2020).

Furthermore, future work comparing fold change and eGSEA outputs of the castrated *PBiCre$^{+/-}$Pik3ca$^{+/HR}$Pten$^{fl/fl}$* model with outputs from the uncastrated *PBiCre$^{+/-}$Pik3ca$^{+/HR}$Pten$^{fl/fl}$* model, will also improve our understanding of mechanisms that initiate the transition to castrate resistant disease.

Although considerable amounts of significant and highly informative data were generated through use of GEMMs utilising the *PBiCre* and *Col1a2CreER(T2)* promoters, both models presented their own limitations. Whilst the effects of epithelial cell genetic alterations *Pik3ca^{H1047R}* and *Pten* deletion specifically within the prostate could be evaluated, additional non-prostate lesions also developed due to leakage of the Probasin Cre construct, therefore it was not possible to age compound mutants beyond 3.5 months of age, thus limiting our ability to determine if the two genetic drivers can cooperate to promote metastasis in a castrated setting (Pearson et al. 2018).

Future work to determine whether *Pik3ca*-hyperactivation and *Pten*-loss (± castration) can cause prostate cancer metastasis, could be achieved by using an alternative GEMM such the tamoxifen-inducible, prostate specific *PSACre-ERT2* model (Ratnacaram et al. 2008). Although recombination within this model is constrained to luminal cells, recombinase activity is prominent within all lobes of the mouse prostate whereas the *PBiCre* model shows preference for the ventral lobe over all others (Parisotto and Metzger 2013). As the murine ventral lobe does not possess a human homologue, the *PSACre-ERT2* model may additionally be more clinically relevant for primary tumour characterisation.

To further explore the rate and magnitude of metastasis within the compound *PBiCre*$^{+/-}$ *Pik3ca*$^{+/HR}$*Pten*$^{fl/fl}$ tumour model, cells isolated from the GEMM prostate tumours could be injected into mice of the same genetic background, to assess whether PIK3CA-mutant and PTEN-deficient tumour cells within the bloodstream have the potential to colonise and form tumours at secondary sites.

A major setback with the *Col1a2CreER(T2) Pten*$^{fl/fl}$ model involved ubiquitous recombination events that caused intestinal tumours, resulting in early sacrifice of the cohorts and limited aging of the prostates. Although no fibroblast specific GEMMs that act explicitly on the prostate have been developed, recent studies have utilised patient-derived fibroblast primary cultures in orthotopic xenografts models to assess primary tumour growth and metastasis, facilitated by the addition of CAFs (Linxweiler et al. 2020).

If normal resident fibroblasts isolated from wildtype murine prostates could be genetically manipulated to remove *Pten* via siRNA or CRISPR, then added to xenografts composed of non-tumorigenic or benign prostate cancer cells (such as PNT2 or BPH-1 cells respectively), or allografts composed of normal wildtype mouse prostate cells in GEMMs, the effect of *Pten*-null fibroblasts on normal epithelial cells or already hyperplastic cells in a setting containing a functioning microenvironment and immune system could be assessed. This experiment would enable direct assessment of prostate cells and not suffer implications driven by other tumorigenic events, whereby a varied range of fibroblast cell types could be evaluated by single-cell RNA-Seq rather and would not be limited to populations expressing *Col1a2* only.

Whilst we have established that fibroblast PTEN loss causes pre-malignant prostate epithelial phenotypes, the signalling mechanisms behind this crosstalk are still unknown. There are 3 main ways communication between the *Pten*-deficient fibroblasts and the epithelial cells of the prostate ducts may occur. There could be secretion of ligands from the fibroblasts that bind to cognate receptors on the ductal cells (autocrine signalling), diffusion of secreted signalling molecules into extracellular space (paracrine signalling) or cell-to-cell contact-dependent molecule signalling through structures such as gap junctions or membrane nanotubes (Armingol et al. 2021).

Epithelial-mesenchymal communication (EMC) mediated by soluble factors such as hepatocyte and connective tissue growth factors, can trigger activation of intracellular signalling pathways that can also lead to increased transcription of target genes (Tan et al. 2016), such that TGF-β and Wnt ligands

have been identified to play important regulatory roles in stromal-epithelial interaction within the prostate (Tyekucheva et al. 2017).

In addition, exosomes can also be secreted from stromal cells including fibroblasts and CAFs to mediate both local and systemic cell communication (Yang et al. 2019b), and have been identified to induce an EMT phenotype in ovarian cancer through the release of TGFβ1 filled exosomes from CAFs triggering oncogenic SMAD signalling in the epithelial compartment (Li et al. 2017). Despite their considerably small size (30 – 150 nm), exosomes and other extracellular vesicles are becoming more extensively studied and methods for their detection improved (Ko et al. 2016; Patel et al. 2019). Thus, it would be highly informative to identify the direct method of communication between the *Pten*-null fibroblasts and ducts of the prostates to help us better understand the mechanisms in which hyperplasia were driven. Likewise, single cell RNA-Seq or spatial transcriptomic profiling may provide further insight into the key signalling pathways that have become altered both in the stroma and/or epithelium, which could further lead to investigation of how PTEN-deficient fibroblasts may respond to PI3K pathway directed therapies and how communication mediated from these fibroblasts impact epithelial cell responses to treatment.

Moreover, if the Masson's Trichrome immunohistochemical stain could be better optimised, this would enable validation of the RNA-Seq and eGSEA results obtained from the comparison of the castrated *PBiCre*$^{+/-}$ *Pik3ca*$^{+/HR}$ *Pten*$^{fl/fl}$ vs castrated *PBiCre*$^{+/-}$ *Pten*$^{fl/fl}$ prostate tumours that revealed an upregulation of collagen related pathways in the double mutant model, as well as confirming whether loss of *Pten* in fibroblasts within the *Col1a2CreER(T2)* model, drives increased collagen remodelling in the 100- and 300-day post induction prostates.

6.4. Conclusion

In conclusion, this project has identified key functions of PTEN that are independent of PI3K, in addition to functions of PTEN within prostate stromal cells. Through use of genetically engineered mouse models, we have shown that loss of PTEN in FSP1-positive fibroblasts causes prostate epithelial cell hyperplasia, whilst loss of PTEN in the basal and luminal epithelial cells can activate the NF-κB pathway to facilitate prostate tumour progression in a PI3K-independent manner. Collectively, these data provide insight into the roles played by PTEN in both the epithelium and stroma of the prostate and have opened up avenues for further exploration to target PTEN-deficient prostate cancer.

Although the clinical significance of *Pten*-deleted fibroblasts within the prostate remains yet to be determined, our data supports the notion that genetical alterations within the stroma should also be taken into consideration when establishing cause or prognosis of prostate disease. Furthermore, we have identified the NF-κB pathway as a potential target for PTEN-deficient prostate cancer, whereby inhibition of TLR2 and CXCR1/2 proteins appears to be effective in *Pten*-null *in vitro* and *ex vivo* models of prostate cancer. Once corroborated *in vivo*, this finding may provide a new effective treatment avenue for patients with *PTEN*-deficient prostate cancer, which may also be applicable to other PTEN-negative cancer.

References

Alimonti, A. et al. 2010. Subtle variations in Pten dose determine cancer susceptibility. *Nat Genet* 42(5), pp. 454-458. doi: 10.1038/ng.556

Alkasalias, T., Moyano-Galceran, L., Arsenian-Henriksson, M. and Lehti, K. 2018. Fibroblasts in the Tumor Microenvironment: Shield or Spear? *Int J Mol Sci* 19(5), doi: 10.3390/ijms19051532

Armingol, E., Officer, A., Harismendy, O. and Lewis, N. E. 2021. Deciphering cell-cell interactions and communication from gene expression. *Nat Rev Genet* 22(2), pp. 71-88. doi: 10.1038/s41576-020-00292-x

Bahmad, H. F. et al. 2021. Tumor Microenvironment in Prostate Cancer: Toward Identification of Novel Molecular Biomarkers for Diagnosis, Prognosis, and Therapy Development. *Front Genet* 12, p. 652747. doi: 10.3389/fgene.2021.652747

Baum, J. and Duffy, H. S. 2011. Fibroblasts and myofibroblasts: what are we talking about? *J Cardiovasc Pharmacol* 57(4), pp. 376-379. doi: 10.1097/FJC.0b013e3182116e39

Bhowmick, N. A., Neilson, E. G. and Moses, H. L. 2004. Stromal fibroblasts in cancer initiation and progression. *Nature* 432(7015), pp. 332-337. doi: 10.1038/nature03096

Bianchi-Frias, D. et al. 2016. Cells Comprising the Prostate Cancer Microenvironment Lack Recurrent Clonal Somatic Genomic Aberrations. *Mol Cancer Res* 14(4), pp. 374-384. doi: 10.1158/1541-7786.Mcr-15-0330

Cannarella, R., Condorelli, R. A., Barbagallo, F., La Vignera, S. and Calogero, A. E. 2021. Endocrinology of the Aging Prostate: Current Concepts. *Front Endocrinol (Lausanne)* 12, p. 554078. doi: 10.3389/fendo.2021.554078

Carver, B. S. et al. 2011. Reciprocal feedback regulation of PI3K and androgen receptor signaling in PTEN-deficient prostate cancer. *Cancer Cell* 19(5), pp. 575-586. doi: 10.1016/j.ccr.2011.04.008

Civita, P. et al. 2019. Laser Capture Microdissection and RNA-Seq Analysis: High Sensitivity Approaches to Explain Histopathological Heterogeneity in Human Glioblastoma FFPE Archived Tissues. *Front Oncol* 9, p. 482. doi: 10.3389/fonc.2019.00482

Coleman, D. L. and Hummel, K. P. 1973. The influence of genetic background on the expression of the obese (ob) gene in the mouse. *Diabetologia* 9(4), pp. 287-293. doi: 10.1007/BF01221856

D'Urso, M. and Kurniawan, N. A. 2020. Mechanical and Physical Regulation of Fibroblast-Myofibroblast Transition: From Cellular Mechanoresponse to Tissue Pathology. *Front Bioeng Biotechnol* 8, p. 609653. doi: 10.3389/fbioe.2020.609653

Denton, C. P. et al. 2009. Inducible lineage-specific deletion of TbetaRII in fibroblasts defines a pivotal regulatory role during adult skin wound healing. *J Invest Dermatol* 129(1), pp. 194-204. doi: 10.1038/jid.2008.171

Elyada, E. et al. 2019. Cross-Species Single-Cell Analysis of Pancreatic Ductal Adenocarcinoma Reveals Antigen-Presenting Cancer-Associated Fibroblasts. *Cancer Discov* 9(8), pp. 1102-1123. doi: 10.1158/2159-8290.Cd-19-0094

Ferraldeschi, R. et al. 2015. PTEN protein loss and clinical outcome from castration-resistant prostate cancer treated with abiraterone acetate. *Eur Urol* 67(4), pp. 795-802. doi: 10.1016/j.eururo.2014.10.027

Fraser, M. M., Zhu, X., Kwon, C. H., Uhlmann, E. J., Gutmann, D. H. and Baker, S. J. 2004. Pten loss causes hypertrophy and increased proliferation of astrocytes in vivo. *Cancer Res* 64(21), pp. 7773-7779. doi: 10.1158/0008-5472.Can-04-2487

Frisbie, J. H., Kumar, S., Aguilera, E. J. and Yalla, S. 2006. Prostate atrophy and spinal cord lesions. *Spinal Cord* 44(1), pp. 24-27. doi: 10.1038/sj.sc.3101804

Geng, J., Huang, X. and Dai, H. 2014. Loss of PTEN induced lung fibroblasts exhibiting similar pathogenic features to cancer cells in idiopathic pulmonary fibrosis. *European Respiratory Journal* 44(Suppl 58), p. P754.

Glentis, A. et al. 2017. Cancer-associated fibroblasts induce metalloprotease-independent cancer cell invasion of the basement membrane. *Nat Commun* 8(1), p. 924. doi: 10.1038/s41467-017-00985-8

Hägglöf, C. and Bergh, A. 2012. The stroma-a key regulator in prostate function and malignancy. *Cancers (Basel)* 4(2), pp. 531-548. doi: 10.3390/cancers4020531

Herberts, C. et al. 2020. Activating AKT1 and PIK3CA Mutations in Metastatic Castration-Resistant Prostate Cancer. *Eur Urol* 78(6), pp. 834-844. doi: 10.1016/j.eururo.2020.04.058

Ittmann, M. 2018. Anatomy and Histology of the Human and Murine Prostate. *Cold Spring Harb Perspect Med* 8(5), doi: 10.1101/cshperspect.a030346

Izumi, K., Mizokami, A., Lin, W. J., Lai, K. P. and Chang, C. 2013. Androgen receptor roles in the development of benign prostate hyperplasia. *Am J Pathol* 182(6), pp. 1942-1949. doi: 10.1016/j.ajpath.2013.02.028

Jamaspishvili, T., Berman, D. M., Ross, A. E., Scher, H. I., De Marzo, A. M., Squire, J. A. and Lotan, T. L. 2018. Clinical implications of PTEN loss in prostate cancer. *Nat Rev Urol* 15(4), pp. 222-234. doi: 10.1038/nrurol.2018.9

Jones, C. E. et al. 2019. Stromal PTEN Regulates Extracellular Matrix Organization in the Mammary Gland. *Neoplasia* 21(1), pp. 132-145. doi: 10.1016/j.neo.2018.10.010

Kendall, R. T. and Feghali-Bostwick, C. A. 2014. Fibroblasts in fibrosis: novel roles and mediators. *Front Pharmacol* 5, p. 123. doi: 10.3389/fphar.2014.00123

Kindblom, J., Dillner, K., Sahlin, L., Robertson, F., Ormandy, C., Törnell, J. and Wennbo, H. 2003. Prostate hyperplasia in a transgenic mouse with prostate-specific expression of prolactin. *Endocrinology* 144(6), pp. 2269-2278. doi: 10.1210/en.2002-0187

Ko, J., Carpenter, E. and Issadore, D. 2016. Detection and isolation of circulating exosomes and microvesicles for cancer monitoring and diagnostics using micro-/nano-based devices. *Analyst* 141(2), pp. 450-460. doi: 10.1039/c5an01610j

Kwon, J. T. W., Bryant, R. J. and Parkes, E. E. 2021. The tumor microenvironment and immune responses in prostate cancer patients. *Endocr Relat Cancer* 28(8), pp. T95-t107. doi: 10.1530/erc-21-0149

Li, J., Ding, Y. and Li, A. 2016. Identification of COL1A1 and COL1A2 as candidate prognostic factors in gastric cancer. *World J Surg Oncol* 14(1), p. 297. doi: 10.1186/s12957-016-1056-5

Li, S. et al. 2018. Overview of the reporter genes and reporter mouse models. *Animal Model Exp Med* 1(1), pp. 29-35. doi: 10.1002/ame2.12008

Li, S., Zhang, F., Xiao, X., Guo, Y., Wen, Z., Li, M. and Pu, X. 2021. Prediction of Synergistic Drug Combinations for Prostate Cancer by Transcriptomic and Network Characteristics. *Front Pharmacol* 12, p. 634097. doi: 10.3389/fphar.2021.634097

Li, W. et al. 2017. TGFβ1 in fibroblasts-derived exosomes promotes epithelial-mesenchymal transition of ovarian cancer cells. *Oncotarget* 8(56), pp. 96035-96047. doi: 10.18632/oncotarget.21635

Linxweiler, J. et al. 2020. Cancer-associated fibroblasts stimulate primary tumor growth and metastatic spread in an orthotopic prostate cancer xenograft model. *Sci Rep* 10(1), p. 12575. doi: 10.1038/s41598-020-69424-x

Liu, R. et al. 2020. PI3K/AKT pathway as a key link modulates the multidrug resistance of cancers. *Cell Death Dis* 11(9), p. 797. doi: 10.1038/s41419-020-02998-6

Lotan, T. L. et al. 2017. PTEN loss detection in prostate cancer: comparison of PTEN immunohistochemistry and PTEN FISH in a large retrospective prostatectomy cohort. *Oncotarget* 8(39), pp. 65566-65576. doi: 10.18632/oncotarget.19217

Lotan, T. L. et al. 2016. Analytic validation of a clinical-grade PTEN immunohistochemistry assay in prostate cancer by comparison with PTEN FISH. *Mod Pathol* 29(8), pp. 904-914. doi: 10.1038/modpathol.2016.88

Mao, N. et al. 2021. Defining the therapeutic selective dependencies for distinct subtypes of PI3K pathway-altered prostate cancers. *Nat Commun* 12(1), p. 5053. doi: 10.1038/s41467-021-25341-9

Muhl, L. et al. 2020. Single-cell analysis uncovers fibroblast heterogeneity and criteria for fibroblast and mural cell identification and discrimination. *Nat Commun* 11(1), p. 3953. doi: 10.1038/s41467-020-17740-1

Oliveira, D. S., Dzinic, S., Bonfil, A. I., Saliganan, A. D., Sheng, S. and Bonfil, R. D. 2016. The mouse prostate: a basic anatomical and histological guideline. *Bosn J Basic Med Sci* 16(1), pp. 8-13. doi: 10.17305/bjbms.2016.917

Parapuram, S. K., Thompson, K., Tsang, M., Hutchenreuther, J., Bekking, C., Liu, S. and Leask, A. 2015. Loss of PTEN expression by mouse fibroblasts results in lung fibrosis through a CCN2-dependent mechanism. *Matrix Biol* 43, pp. 35-41. doi: 10.1016/j.matbio.2015.01.017

Parisotto, M. and Metzger, D. 2013. Genetically engineered mouse models of prostate cancer. *Mol Oncol* 7(2), pp. 190-205. doi: 10.1016/j.molonc.2013.02.005

Patel, G. K., Khan, M. A., Zubair, H., Srivastava, S. K., Khushman, M., Singh, S. and Singh, A. P. 2019. Comparative analysis of exosome isolation methods using culture supernatant for optimum yield, purity and downstream applications. *Sci Rep* 9(1), p. 5335. doi: 10.1038/s41598-019-41800-2

Pearson, H. B. et al. 2018. Identification of Pik3ca Mutation as a Genetic Driver of Prostate Cancer That Cooperates with Pten Loss to Accelerate Progression and Castration-Resistant Growth. *Cancer Discov* 8(6), pp. 764-779. doi: 10.1158/2159-8290.Cd-17-0867

Picanço-Albuquerque, C. G. et al. 2019. PTEN loss in Gleason grade 7 prostate tumors exhibits intratumoral heterogeneity and is associated with unfavorable pathological features. *Applied Cancer Research* 39(1), p. 1. doi: 10.1186/s41241-018-0071-y

Ping, Q. et al. 2021. Cancer-associated fibroblasts: overview, progress, challenges, and directions. *Cancer Gene Ther* 28(9), pp. 984-999. doi: 10.1038/s41417-021-00318-4

Qian, L. H., Wang, X. L. and Tu, Z. H. 2001. Atrophy and apoptosis in ventral prostate of rats induced by 5alpha-reductase inhibitor, epristeride. *Acta Pharmacol Sin* 22(5), pp. 399-404.

Qu, Z., Ren, Y., Shen, H., Wang, H., Shi, L. and Tong, D. 2021. Combination Therapy of Metastatic Castration-Recurrent Prostate Cancer: Hyaluronic Acid Decorated, Cabazitaxel-Prodrug and Orlistat Co-Loaded Nano-System. *Drug Des Devel Ther* 15, pp. 3605-3616. doi: 10.2147/dddt.S306684

Ramadass, V., Vaiyapuri, T. and Tergaonkar, V. 2020. Small Molecule NF-κB Pathway Inhibitors in Clinic. *Int J Mol Sci* 21(14), doi: 10.3390/ijms21145164

Ratnacaram, C. K., Teletin, M., Jiang, M., Meng, X., Chambon, P. and Metzger, D. 2008. Temporally controlled ablation of PTEN in adult mouse prostate epithelium generates a model of invasive prostatic adenocarcinoma. *Proc Natl Acad Sci U S A* 105(7), pp. 2521-2526. doi: 10.1073/pnas.0712021105

Sandberg, T. P., Stuart, M., Oosting, J., Tollenaar, R., Sier, C. F. M. and Mesker, W. E. 2019. Increased expression of cancer-associated fibroblast markers at the invasive front and its association with tumor-stroma ratio in colorectal cancer. *BMC Cancer* 19(1), p. 284. doi: 10.1186/s12885-019-5462-2

Saraswati, S., Marrow, S. M. W., Watch, L. A. and Young, P. P. 2019. Identification of a pro-angiogenic functional role for FSP1-positive fibroblast subtype in wound healing. *Nat Commun* 10(1), p. 3027. doi: 10.1038/s41467-019-10965-9

Shah, R. B., Shore, K. T., Yoon, J., Mendrinos, S., McKenney, J. K. and Tian, W. 2019. PTEN loss in prostatic adenocarcinoma correlates with specific adverse histologic features (intraductal carcinoma, cribriform Gleason pattern 4 and stromogenic carcinoma). *Prostate* 79(11), pp. 1267-1273. doi: 10.1002/pros.23831

Stifter, S. A. and Greter, M. 2020. STOP floxing around: Specificity and leakiness of inducible Cre/loxP systems. *Eur J Immunol* 50(3), pp. 338-341. doi: 10.1002/eji.202048546

Strutz, F., Okada, H., Lo, C. W., Danoff, T., Carone, R. L., Tomaszewski, J. E. and Neilson, E. G. 1995. Identification and characterization of a fibroblast marker: FSP1. *J Cell Biol* 130(2), pp. 393-405. doi: 10.1083/jcb.130.2.393

Stultz, J. and Fong, L. 2021. How to turn up the heat on the cold immune microenvironment of metastatic prostate cancer. *Prostate Cancer Prostatic Dis* 24(3), pp. 697-717. doi: 10.1038/s41391-021-00340-5

Suzuki, A. et al. 2001. T cell-specific loss of Pten leads to defects in central and peripheral tolerance. *Immunity* 14(5), pp. 523-534. doi: 10.1016/s1074-7613(01)00134-0

Swonger, J. M., Liu, J. S., Ivey, M. J. and Tallquist, M. D. 2016. Genetic tools for identifying and manipulating fibroblasts in the mouse. *Differentiation* 92(3), pp. 66-83. doi: 10.1016/j.diff.2016.05.009

Tan, R. J., Zhou, D. and Liu, Y. 2016. Signaling Crosstalk between Tubular Epithelial Cells and Interstitial Fibroblasts after Kidney Injury. *Kidney Dis (Basel)* 2(3), pp. 136-144. doi: 10.1159/000446336

Thienger, P. and Rubin, M. A. 2021. Prostate cancer hijacks the microenvironment. *Nat Cell Biol* 23(1), pp. 3-5. doi: 10.1038/s41556-020-00616-3

Tracy, L. E., Minasian, R. A. and Caterson, E. J. 2016. Extracellular Matrix and Dermal Fibroblast Function in the Healing Wound. *Adv Wound Care (New Rochelle)* 5(3), pp. 119-136. doi: 10.1089/wound.2014.0561

Trimboli, A. J. et al. 2009. Pten in stromal fibroblasts suppresses mammary epithelial tumours. *Nature* 461(7267), pp. 1084-1091. doi: 10.1038/nature08486

Tripathi, M., Billet, S. and Bhowmick, N. A. 2012. Understanding the role of stromal fibroblasts in cancer progression. *Cell Adh Migr* 6(3), pp. 231-235. doi: 10.4161/cam.20419

Triscott, J. and Rubin, M. A. 2018. Prostate Power Play: Does Pik3ca Accelerate Pten-Deficient Cancer Progression? *Cancer Discov* 8(6), pp. 682-685. doi: 10.1158/2159-8290.Cd-18-0369

Trotman, L. C. et al. 2003. Pten dose dictates cancer progression in the prostate. *PLoS Biol* 1(3), p. E59. doi: 10.1371/journal.pbio.0000059

Turnham, D. J., Bullock, N., Dass, M. S., Staffurth, J. N. and Pearson, H. B. 2020. The PTEN Conundrum: How to Target PTEN-Deficient Prostate Cancer. *Cells* 9(11), doi: 10.3390/cells9112342

Tyekucheva, S. et al. 2017. Stromal and epithelial transcriptional map of initiation progression and metastatic potential of human prostate cancer. *Nature Communications* 8(1), p. 420. doi: 10.1038/s41467-017-00460-4

Valkenburg, K. C., de Groot, A. E. and Pienta, K. J. 2018. Targeting the tumour stroma to improve cancer therapy. *Nat Rev Clin Oncol* 15(6), pp. 366-381. doi: 10.1038/s41571-018-0007-1

Weng, L., Brown, J. and Eng, C. 2001. PTEN induces apoptosis and cell cycle arrest through phosphoinositol-3-kinase/Akt-dependent and -independent pathways. *Hum Mol Genet* 10(3), pp. 237-242. doi: 10.1093/hmg/10.3.237

Yang, J., Nie, J., Ma, X., Wei, Y., Peng, Y. and Wei, X. 2019a. Targeting PI3K in cancer: mechanisms and advances in clinical trials. *Mol Cancer* 18(1), p. 26. doi: 10.1186/s12943-019-0954-x

Yang, X., Li, Y., Zou, L. and Zhu, Z. 2019b. Role of Exosomes in Crosstalk Between Cancer-Associated Fibroblasts and Cancer Cells. *Front Oncol* 9, p. 356. doi: 10.3389/fonc.2019.00356

Zhang, J., Chen, L., Liu, X., Kammertoens, T., Blankenstein, T. and Qin, Z. 2013. Fibroblast-specific protein 1/S100A4-positive cells prevent carcinoma through collagen production and encapsulation of carcinogens. *Cancer Res* 73(9), pp. 2770-2781. doi: 10.1158/0008-5472.Can-12-3022

Zheng, B., Zhang, Z., Black, C. M., de Crombrugghe, B. and Denton, C. P. 2002. Ligand-dependent genetic recombination in fibroblasts : a potentially powerful technique for investigating gene function in fibrosis. *Am J Pathol* 160(5), pp. 1609-1617. doi: 10.1016/s0002-9440(10)61108-x

2015. The Molecular Taxonomy of Primary Prostate Cancer. *Cell* 163(4), pp. 1011-1025. doi: 10.1016/j.cell.2015.10.025

Abida, W. et al. 2019. Genomic correlates of clinical outcome in advanced prostate cancer. *Proc Natl Acad Sci U S A* 116(23), pp. 11428-11436. doi: 10.1073/pnas.1902651116

Acevedo, V. D. et al. 2007. Inducible FGFR-1 activation leads to irreversible prostate adenocarcinoma and an epithelial-to-mesenchymal transition. *Cancer Cell* 12(6), pp. 559-571. doi: 10.1016/j.ccr.2007.11.004

Albensi, B. C. 2019. What Is Nuclear Factor Kappa B (NF-κB) Doing in and to the Mitochondrion? *Front Cell Dev Biol* 7, p. 154. doi: 10.3389/fcell.2019.00154

Alfieri, R., Giovannetti, E., Bonelli, M. and Cavazzoni, A. 2017. New Treatment Opportunities in Phosphatase and Tensin Homolog (PTEN)-Deficient Tumors: Focus on PTEN/Focal Adhesion Kinase Pathway. *Front Oncol* 7, p. 170. doi: 10.3389/fonc.2017.00170

Alhamdoosh, M., Law, C. W., Tian, L., Sheridan, J. M., Ng, M. and Ritchie, M. E. 2017. Easy and efficient ensemble gene set testing with EGSEA. *F1000Res* 6, p. 2010. doi: 10.12688/f1000research.12544.1

Anwar, M. A., Shah, M., Kim, J. and Choi, S. 2019. Recent clinical trends in Toll-like receptor targeting therapeutics. *Med Res Rev* 39(3), pp. 1053-1090. doi: 10.1002/med.21553

Araki, S. et al. 2007. Interleukin-8 is a molecular determinant of androgen independence and progression in prostate cancer. *Cancer Res* 67(14), pp. 6854-6862. doi: 10.1158/0008-5472.Can-07-1162

Ardura, J. A., Álvarez-Carrión, L., Gutiérrez-Rojas, I. and Alonso, V. 2020. Role of Calcium Signaling in Prostate Cancer Progression: Effects on Cancer Hallmarks and Bone Metastatic Mechanisms. *Cancers (Basel)* 12(5), doi: 10.3390/cancers12051071

Banno, A. et al. 2016. Downregulation of 26S proteasome catalytic activity promotes epithelial-mesenchymal transition. *Oncotarget* 7(16), pp. 21527-21541. doi: 10.18632/oncotarget.7596

Benakanakere, M. R., Finoti, L. S., Tanaka, U., Grant, G. R., Scarel-Caminaga, R. M. and Kinane, D. F. 2016. Investigation of the functional role of human Interleukin-8 gene haplotypes by CRISPR/Cas9 mediated genome editing. *Sci Rep* 6, p. 31180. doi: 10.1038/srep31180

Cahill, K. E., Morshed, R. A. and Yamini, B. 2016. Nuclear factor-κB in glioblastoma: insights into regulators and targeted therapy. *Neuro Oncol* 18(3), pp. 329-339. doi: 10.1093/neuonc/nov265

Carlson, E. C. et al. 2005. Keratocan, a cornea-specific keratan sulfate proteoglycan, is regulated by lumican. *J Biol Chem* 280(27), pp. 25541-25547. doi: 10.1074/jbc.M500249200

Carver, B. S. et al. 2011. Reciprocal feedback regulation of PI3K and androgen receptor signaling in PTEN-deficient prostate cancer. *Cancer Cell* 19(5), pp. 575-586. doi: 10.1016/j.ccr.2011.04.008

Chang, Y. C., Kao, W. C., Wang, W. Y., Wang, W. Y., Yang, R. B. and Peck, K. 2009. Identification and characterization of oligonucleotides that inhibit Toll-like receptor 2-associated immune responses. *Faseb j* 23(9), pp. 3078-3088. doi: 10.1096/fj.09-129312

Cheng, J., Feng, X., Li, Z., Zhou, F., Yang, J. M. and Zhao, Y. 2021. Pharmacological inhibition of NF-κB-inducing kinase (NIK) with small molecules for the treatment of human diseases. *RSC Med Chem* 12(4), pp. 552-565. doi: 10.1039/d0md00361a

Chiu, Y. J., Hsieh, Y. H. and Huang, Y. H. 2019. Improved cell composition deconvolution method of bulk gene expression profiles to quantify subsets of immune cells. *BMC Med Genomics* 12(Suppl 8), p. 169. doi: 10.1186/s12920-019-0613-5

de Bono, J. S. et al. 2019. Randomized Phase II Study Evaluating Akt Blockade with Ipatasertib, in Combination with Abiraterone, in Patients with Metastatic Prostate Cancer with and without PTEN Loss. *Clin Cancer Res* 25(3), pp. 928-936. doi: 10.1158/1078-0432.Ccr-18-0981

de Bono, J. S. et al. 2020. Prostate carcinogenesis: inflammatory storms. *Nature Reviews Cancer* 20(8), pp. 455-469. doi: 10.1038/s41568-020-0267-9

Dhatchinamoorthy, K., Colbert, J. D. and Rock, K. L. 2021. Cancer Immune Evasion Through Loss of MHC Class I Antigen Presentation. *Front Immunol* 12, p. 636568. doi: 10.3389/fimmu.2021.636568

Dowling, C. M. et al. 2017. Expression of protein kinase C gamma promotes cell migration in colon cancer. *Oncotarget* 8(42), pp. 72096-72107. doi: 10.18632/oncotarget.18916

Frankland-Searby, S. and Bhaumik, S. R. 2012. The 26S proteasome complex: an attractive target for cancer therapy. *Biochim Biophys Acta* 1825(1), pp. 64-76. doi: 10.1016/j.bbcan.2011.10.003

Fu, J. et al. 2018a. A novel, homozygous nonsense variant of the CDHR1 gene in a Chinese family causes autosomal recessive retinal dystrophy by NGS-based genetic diagnosis. *J Cell Mol Med* 22(11), pp. 5662-5669. doi: 10.1111/jcmm.13841

Fu, S., Chen, X., Lin, H. J. and Lin, J. 2018b. Inhibition of interleukin 8/C-X-C chemokine receptor 1,/2 signaling reduces malignant features in human pancreatic cancer cells. *Int J Oncol* 53(1), pp. 349-357. doi: 10.3892/ijo.2018.4389

Gabriele, F., Martinelli, C. and Comincini, S. 2018. Prostate cancer cells at a therapeutic gunpoint of the autophagy process. *Journal of Cancer Metastasis and Treatment* 4, p. 17. doi: 10.20517/2394-4722.2018.06

Goldstein, L. J. et al. 2020. A window-of-opportunity trial of the CXCR1/2 inhibitor reparixin in operable HER-2-negative breast cancer. *Breast Cancer Res* 22(1), p. 4. doi: 10.1186/s13058-019-1243-8

Gong, L. et al. 2021. Comprehensive single-cell sequencing reveals the stromal dynamics and tumor-specific characteristics in the microenvironment of nasopharyngeal carcinoma. *Nat Commun* 12(1), p. 1540. doi: 10.1038/s41467-021-21795-z

Grasso, C. S. et al. 2012. The mutational landscape of lethal castration-resistant prostate cancer. *Nature* 487(7406), pp. 239-243. doi: 10.1038/nature11125

Greenwell, I. B., Ip, A. and Cohen, J. B. 2017. PI3K Inhibitors: Understanding Toxicity Mechanisms and Management. *Oncology (Williston Park)* 31(11), pp. 821-828.

Gui, S. L. et al. 2016. Overexpression of CXCL3 can enhance the oncogenic potential of prostate cancer. *Int Urol Nephrol* 48(5), pp. 701-709. doi: 10.1007/s11255-016-1222-2

Hinata, K., Gervin, A. M., Jennifer Zhang, Y. and Khavari, P. A. 2003. Divergent gene regulation and growth effects by NF-kappa B in epithelial and mesenchymal cells of human skin. *Oncogene* 22(13), pp. 1955-1964. doi: 10.1038/sj.onc.1206198

Hol, J., Wilhelmsen, L. and Haraldsen, G. 2010. The murine IL-8 homologues KC, MIP-2, and LIX are found in endothelial cytoplasmic granules but not in Weibel-Palade bodies. *J Leukoc Biol* 87(3), pp. 501-508. doi: 10.1189/jlb.0809532

Hou, A., Tin, M. Q. and Tong, L. 2017. Toll-like receptor 2-mediated NF-kappa B pathway activation in ocular surface epithelial cells. *Eye Vis (Lond)* 4, p. 17. doi: 10.1186/s40662-017-0082-x

Huper, G. and Marks, J. R. 2007. Isogenic normal basal and luminal mammary epithelial isolated by a novel method show a differential response to ionizing radiation. *Cancer Res* 67(7), pp. 2990-3001. doi: 10.1158/0008-5472.Can-06-4065

Hussain, A. R. et al. 2012. Cross-talk between NFkB and the PI3-kinase/AKT pathway can be targeted in primary effusion lymphoma (PEL) cell lines for efficient apoptosis. *PLoS One* 7(6), p. e39945. doi: 10.1371/journal.pone.0039945

Ianevski, A., Giri, A. K. and Aittokallio, T. 2020. SynergyFinder 2.0: visual analytics of multi-drug combination synergies. *Nucleic Acids Res* 48(W1), pp. W488-w493. doi: 10.1093/nar/gkaa216

Ito, H. et al. 2016. GSK-3 directly regulates phospho-4EBP1 in renal cell carcinoma cell-line: an intrinsic subcellular mechanism for resistance to mTORC1 inhibition. *BMC Cancer* 16, p. 393. doi: 10.1186/s12885-016-2418-7

Jang, H. H. 2018. Regulation of Protein Degradation by Proteasomes in Cancer. *J Cancer Prev* 23(4), pp. 153-161. doi: 10.15430/jcp.2018.23.4.153

Jiang, R., Gu, L., Findley, H. and Zhou, M. 2004. Loss of PTEN expression induces NF-κB via PI3K/Akt pathway involving resistance to chemotherapy in acute lymphoblastic leukemia cell lines. *Cancer Research* 64(7 Supplement), pp. 1277-1277.

Jin, C., McKeehan, K. and Wang, F. 2003. Transgenic mouse with high Cre recombinase activity in all prostate lobes, seminal vesicle, and ductus deferens. *Prostate* 57(2), pp. 160-164. doi: 10.1002/pros.10283

Jin, M. Z. and Jin, W. L. 2020. The updated landscape of tumor microenvironment and drug repurposing. *Signal Transduct Target Ther* 5(1), p. 166. doi: 10.1038/s41392-020-00280-x

Jundi, K. and Greene, C. M. 2015. Transcription of Interleukin-8: How Altered Regulation Can Affect Cystic Fibrosis Lung Disease. *Biomolecules* 5(3), pp. 1386-1398. doi: 10.3390/biom5031386

Kapałczyńska, M. et al. 2018. 2D and 3D cell cultures - a comparison of different types of cancer cell cultures. *Arch Med Sci* 14(4), pp. 910-919. doi: 10.5114/aoms.2016.63743

Khongthong, P., Roseweir, A. K. and Edwards, J. 2019. The NF-KB pathway and endocrine therapy resistance in breast cancer. *Endocr Relat Cancer* 26(6), pp. R369-r380. doi: 10.1530/erc-19-0087

Kogan-Sakin, I. et al. 2009. Prostate stromal cells produce CXCL-1, CXCL-2, CXCL-3 and IL-8 in response to epithelia-secreted IL-1. *Carcinogenesis* 30(4), pp. 698-705. doi: 10.1093/carcin/bgp043

Kokkinos, J. et al. 2021. Ex vivo culture of intact human patient derived pancreatic tumour tissue. *Sci Rep* 11(1), p. 1944. doi: 10.1038/s41598-021-81299-0

Kong, C. et al. 2019. NF-κB inhibition promotes apoptosis in androgen-independent prostate cancer cells by the photothermal effect via the IκBα/AR signaling pathway. *Biomater Sci* 7(6), pp. 2559-2570. doi: 10.1039/c8bm01007b

Kukurba, K. R. and Montgomery, S. B. 2015. RNA Sequencing and Analysis. *Cold Spring Harb Protoc* 2015(11), pp. 951-969. doi: 10.1101/pdb.top084970

Kundu, D., Kennedy, L., Meadows, V., Baiocchi, L., Alpini, G. and Francis, H. 2020. The Dynamic Interplay Between Mast Cells, Aging/Cellular Senescence, and Liver Disease. *Gene Expr* 20(2), pp. 77-88. doi: 10.3727/105221620x15960509906371

Labbozzetta, M., Notarbartolo, M. and Poma, P. 2020. Can NF-κB Be Considered a Valid Drug Target in Neoplastic Diseases? Our Point of View. *Int J Mol Sci* 21(9), doi: 10.3390/ijms21093070

Lamoureux, F. et al. 2013. Blocked autophagy using lysosomotropic agents sensitizes resistant prostate tumor cells to the novel Akt inhibitor AZD5363. *Clin Cancer Res* 19(4), pp. 833-844. doi: 10.1158/1078-0432.Ccr-12-3114

Langhans, S. A. 2018. Three-Dimensional in Vitro Cell Culture Models in Drug Discovery and Drug Repositioning. *Front Pharmacol* 9, p. 6. doi: 10.3389/fphar.2018.00006

Lee, J., Rhee, M. H., Kim, E. and Cho, J. Y. 2012. BAY 11-7082 is a broad-spectrum inhibitor with anti-inflammatory activity against multiple targets. *Mediators Inflamm* 2012, p. 416036. doi: 10.1155/2012/416036

Lesche, R. et al. 2002. Cre/loxP-mediated inactivation of the murine Pten tumor suppressor gene. *Genesis* 32(2), pp. 148-149. doi: 10.1002/gene.10036

Li, J. Y., Liu, Y., Gao, X. X., Gao, X. and Cai, H. 2014. TLR2 and TLR4 signaling pathways are required for recombinant Brucella abortus BCSP31-induced cytokine production, functional upregulation of mouse macrophages, and the Th1 immune response in vivo and in vitro. *Cell Mol Immunol* 11(5), pp. 477-494. doi: 10.1038/cmi.2014.28

Li, T. et al. 2020. TIMER2.0 for analysis of tumor-infiltrating immune cells. *Nucleic Acids Res* 48(W1), pp. W509-w514. doi: 10.1093/nar/gkaa407

Lin, H. K., Hu, Y. C., Lee, D. K. and Chang, C. 2004. Regulation of androgen receptor signaling by PTEN (phosphatase and tensin homolog deleted on chromosome 10) tumor suppressor through distinct mechanisms in prostate cancer cells. *Mol Endocrinol* 18(10), pp. 2409-2423. doi: 10.1210/me.2004-0117

Lin, Z., Huang, L., Li, S. L., Gu, J., Cui, X. and Zhou, Y. 2021. PTEN loss correlates with T cell exclusion across human cancers. *BMC Cancer* 21(1), p. 429. doi: 10.1186/s12885-021-08114-x

Liotti, F., De Pizzol, M., Allegretti, M., Prevete, N. and Melillo, R. M. 2017. Multiple anti-tumor effects of Reparixin on thyroid cancer. *Oncotarget* 8(22), pp. 35946-35961. doi: 10.18632/oncotarget.16412

Lleonart, M. E., Carnero, A., Paciucci, R., Wang, Z. Q. and Shomron, N. 2011. Cancer, senescence, and aging: translation from basic research to clinics. *J Aging Res* 2011, p. 692301. doi: 10.4061/2011/692301

Lopes-Paciencia, S., Saint-Germain, E., Rowell, M. C., Ruiz, A. F., Kalegari, P. and Ferbeyre, G. 2019. The senescence-associated secretory phenotype and its regulation. *Cytokine* 117, pp. 15-22. doi: 10.1016/j.cyto.2019.01.013

Maciel, T. T., Moura, I. C. and Hermine, O. 2015. The role of mast cells in cancers. *F1000Prime Rep* 7, p. 09. doi: 10.12703/p7-09

Man, X., Piao, C., Lin, X., Kong, C., Cui, X. and Jiang, Y. 2019. USP13 functions as a tumor suppressor by blocking the NF-κB -mediated PTEN downregulation in human bladder cancer. *J Exp Clin Cancer Res* 38(1), p. 259. doi: 10.1186/s13046-019-1262-4

March, B., Faulkner, S., Jobling, P., Steigler, A., Blatt, A., Denham, J. and Hondermarck, H. 2020. Tumour innervation and neurosignalling in prostate cancer. *Nat Rev Urol* 17(2), pp. 119-130. doi: 10.1038/s41585-019-0274-3

Margaria, J. P., Ratto, E., Gozzelino, L., Li, H. and Hirsch, E. 2019. Class II PI3Ks at the Intersection between Signal Transduction and Membrane Trafficking. *Biomolecules* 9(3), doi: 10.3390/biom9030104

Martin, S. Z., Wagner, D. C., Hörner, N., Horst, D., Lang, H., Tagscherer, K. E. and Roth, W. 2019. Ex vivo tissue slice culture system to measure drug-response rates of hepatic metastatic colorectal cancer. *BMC Cancer* 19(1), p. 1030. doi: 10.1186/s12885-019-6270-4

Maxwell, P. J., Neisen, J., Messenger, J. and Waugh, D. J. 2014. Tumor-derived CXCL8 signaling augments stroma-derived CCL2-promoted proliferation and CXCL12-mediated invasion of PTEN-deficient prostate cancer cells. *Oncotarget* 5(13), pp. 4895-4908. doi: 10.18632/oncotarget.2052

Maynard, J. P., Ertunc, O., Kulac, I., Baena-Del Valle, J. A., De Marzo, A. M. and Sfanos, K. S. 2020. IL8 Expression Is Associated with Prostate Cancer Aggressiveness and Androgen Receptor Loss in Primary and Metastatic Prostate Cancer. *Mol Cancer Res* 18(1), pp. 153-165. doi: 10.1158/1541-7786.Mcr-19-0595

Mistry, P. et al. 2015. Inhibition of TLR2 signaling by small molecule inhibitors targeting a pocket within the TLR2 TIR domain. *Proc Natl Acad Sci U S A* 112(17), pp. 5455-5460. doi: 10.1073/pnas.1422576112

Mitchell, S., Vargas, J. and Hoffmann, A. 2016. Signaling via the NFκB system. *Wiley Interdiscip Rev Syst Biol Med* 8(3), pp. 227-241. doi: 10.1002/wsbm.1331

Moretti, I. F., Franco, D. G., de Almeida Galatro, T. F., Oba-Shinjo, S. M. and Marie, S. K. N. 2018. Plasmatic membrane toll-like receptor expressions in human astrocytomas. *PLoS One* 13(6), p. e0199211. doi: 10.1371/journal.pone.0199211

Munezane, H. et al. 2019. Roles of Collagen XXV and Its Putative Receptors PTPσ/δ in Intramuscular Motor Innervation and Congenital Cranial Dysinnervation Disorder. *Cell Rep* 29(13), pp. 4362-4376.e4366. doi: 10.1016/j.celrep.2019.11.112

Nagaraj, A. S., Bao, J., Hemmes, A., Machado, M., Närhi, K. and Verschuren, E. W. 2018. Establishment and Analysis of Tumor Slice Explants As a Prerequisite for Diagnostic Testing. *J Vis Exp* (141), doi: 10.3791/58569

Nguyen, Y. T., Rodriguez-Nieves, J. A., Yang, Q. and VanderWeele, D. 2018. Abstract 5420: Nuclear PTEN directly regulates androgen receptor activity in prostate cancer. *Cancer Research* 78(13 Supplement), pp. 5420-5420. doi: 10.1158/1538-7445.Am2018-5420

Nissen, N. I., Karsdal, M. and Willumsen, N. 2019. Collagens and Cancer associated fibroblasts in the reactive stroma and its relation to Cancer biology. *J Exp Clin Cancer Res* 38(1), p. 115. doi: 10.1186/s13046-019-1110-6

Nitulescu, G. M. et al. 2016. Akt inhibitors in cancer treatment: The long journey from drug discovery to clinical use (Review). *Int J Oncol* 48(3), pp. 869-885. doi: 10.3892/ijo.2015.3306

Noren Hooten, N. and Evans, M. K. 2017. Techniques to Induce and Quantify Cellular Senescence. *J Vis Exp* (123), doi: 10.3791/55533

Ohmuraya, M., Sugano, A., Hirota, M., Takaoka, Y. and Yamamura, K. 2012. Role of Intrapancreatic SPINK1/Spink3 Expression in the Development of Pancreatitis. *Front Physiol* 3, p. 126. doi: 10.3389/fphys.2012.00126

Onozato, D. et al. 2018. Generation of Intestinal Organoids Suitable for Pharmacokinetic Studies from Human Induced Pluripotent Stem Cells. *Drug Metab Dispos* 46(11), pp. 1572-1580. doi: 10.1124/dmd.118.080374

Parisotto, M., Grelet, E., El Bizri, R. and Metzger, D. 2019. Senescence controls prostatic neoplasia driven by Pten loss. *Mol Cell Oncol* 6(1), p. 1511205. doi: 10.1080/23723556.2018.1511205

Pearson, H. B. et al. 2018. Identification of Pik3ca Mutation as a Genetic Driver of Prostate Cancer That Cooperates with Pten Loss to Accelerate Progression and Castration-Resistant Growth. *Cancer Discov* 8(6), pp. 764-779. doi: 10.1158/2159-8290.Cd-17-0867

Pellicciotta, I., Cortez-Gonzalez, X., Sasik, R., Reiter, Y., Hardiman, G., Langlade-Demoyen, P. and Zanetti, M. 2008. Presentation of telomerase reverse transcriptase, a self-tumor antigen, is down-regulated by histone deacetylase inhibition. *Cancer Res* 68(19), pp. 8085-8093. doi: 10.1158/0008-5472.Can-08-1014

Pierce, J. W., Schoenleber, R., Jesmok, G., Best, J., Moore, S. A., Collins, T. and Gerritsen, M. E. 1997. Novel inhibitors of cytokine-induced IkappaBalpha phosphorylation and endothelial cell adhesion molecule expression show anti-inflammatory effects in vivo. *J Biol Chem* 272(34), pp. 21096-21103. doi: 10.1074/jbc.272.34.21096

Powley, I. R. et al. 2020. Patient-derived explants (PDEs) as a powerful preclinical platform for anti-cancer drug and biomarker discovery. *Br J Cancer* 122(6), pp. 735-744. doi: 10.1038/s41416-019-0672-6

Prescott, J. L., Blok, L. and Tindall, D. J. 1998. Isolation and androgen regulation of the human homeobox cDNA, NKX3.1. *Prostate* 35(1), pp. 71-80. doi: 10.1002/(sici)1097-0045(19980401)35:1<71::aid-pros10>3.0.co;2-h

Qin, X., Jiang, B. and Zhang, Y. 2016. 4E-BP1, a multifactor regulated multifunctional protein. *Cell Cycle* 15(6), pp. 781-786. doi: 10.1080/15384101.2016.1151581

Ramadass, V., Vaiyapuri, T. and Tergaonkar, V. 2020. Small Molecule NF-κB Pathway Inhibitors in Clinic. *Int J Mol Sci* 21(14), doi: 10.3390/ijms21145164

Rauert-Wunderlich, H., Siegmund, D., Maier, E., Giner, T., Bargou, R. C., Wajant, H. and Stühmer, T. 2013. The IKK inhibitor Bay 11-7082 induces cell death independent from inhibition of activation of NFκB transcription factors. *PLoS One* 8(3), p. e59292. doi: 10.1371/journal.pone.0059292

Reilly, M. et al. 2013. Randomized, double-blind, placebo-controlled, dose-escalating phase I, healthy subjects study of intravenous OPN-305, a humanized anti-TLR2 antibody. *Clin Pharmacol Ther* 94(5), pp. 593-600. doi: 10.1038/clpt.2013.150

Roeckel, N. et al. 2009. High frequency of LMAN1 abnormalities in colorectal tumors with microsatellite instability. *Cancer Res* 69(1), pp. 292-299. doi: 10.1158/0008-5472.Can-08-3314

Romac, J. M. et al. 2010. Transgenic expression of pancreatic secretory trypsin inhibitor-1 rescues SPINK3-deficient mice and restores a normal pancreatic phenotype. *Am J Physiol Gastrointest Liver Physiol* 298(4), pp. G518-524. doi: 10.1152/ajpgi.00431.2009

Sana, T. R., Janatpour, M. J., Sathe, M., McEvoy, L. M. and McClanahan, T. K. 2005. Microarray analysis of primary endothelial cells challenged with different inflammatory and immune cytokines. *Cytokine* 29(6), pp. 256-269. doi: 10.1016/j.cyto.2004.11.003

Schott, A. F. et al. 2017. Phase Ib Pilot Study to Evaluate Reparixin in Combination with Weekly Paclitaxel in Patients with HER-2-Negative Metastatic Breast Cancer. *Clin Cancer Res* 23(18), pp. 5358-5365. doi: 10.1158/1078-0432.Ccr-16-2748

Scott, E. and Munkley, J. 2019. Glycans as Biomarkers in Prostate Cancer. *Int J Mol Sci* 20(6), doi: 10.3390/ijms20061389

Servant, R. et al. 2021. Prostate cancer patient-derived organoids: detailed outcome from a prospective cohort of 81 clinical specimens. *J Pathol* 254(5), pp. 543-555. doi: 10.1002/path.5698

Shen, C., Zhang, J., Qi, M., WYChang, Y. and Han, B. 2014. Roles of Serine Protease Inhibitor Kazal type 1 (SPINK1) in Prostate Cancer. *Medicinal Chemistry* 4,

Shih, V. F., Tsui, R., Caldwell, A. and Hoffmann, A. 2011. A single NFκB system for both canonical and non-canonical signaling. *Cell Res* 21(1), pp. 86-102. doi: 10.1038/cr.2010.161

Shorning, B. Y., Dass, M. S., Smalley, M. J. and Pearson, H. B. 2020. The PI3K-AKT-mTOR Pathway and Prostate Cancer: At the Crossroads of AR, MAPK, and WNT Signaling. *Int J Mol Sci* 21(12), doi: 10.3390/ijms21124507

Steele, C. W. et al. 2016. CXCR2 Inhibition Profoundly Suppresses Metastases and Augments Immunotherapy in Pancreatic Ductal Adenocarcinoma. *Cancer Cell* 29(6), pp. 832-845. doi: 10.1016/j.ccell.2016.04.014

Stewart, T. A., Yapa, K. T. and Monteith, G. R. 2015. Altered calcium signaling in cancer cells. *Biochim Biophys Acta* 1848(10 Pt B), pp. 2502-2511. doi: 10.1016/j.bbamem.2014.08.016

Subramanian, A. et al. 2005. Gene set enrichment analysis: a knowledge-based approach for interpreting genome-wide expression profiles. *Proc Natl Acad Sci U S A* 102(43), pp. 15545-15550. doi: 10.1073/pnas.0506580102

Taylor, B. S. et al. 2010. Integrative Genomic Profiling of Human Prostate Cancer. *Cancer Cell* 18(1), pp. 11-22. doi: https://doi.org/10.1016/j.ccr.2010.05.026

Tegowski, M. and Baldwin, A. 2018. Noncanonical NF-κB in Cancer. *Biomedicines* 6(2), doi: 10.3390/biomedicines6020066

Tiwari, R. et al. 2020. Androgen deprivation upregulates SPINK1 expression and potentiates cellular plasticity in prostate cancer. *Nat Commun* 11(1), p. 384. doi: 10.1038/s41467-019-14184-0

Torrealba, N., Vera, R., Fraile, B., Martínez-Onsurbe, P., Paniagua, R. and Royuela, M. 2020. TGF-β/PI3K/AKT/mTOR/NF-κB pathway. Clinicopathological features in prostate cancer. *Aging Male* 23(5), pp. 801-811. doi: 10.1080/13685538.2019.1597840

Triscott, J. and Rubin, M. A. 2018. Prostate Power Play: Does Pik3ca Accelerate Pten-Deficient Cancer Progression? *Cancer Discov* 8(6), pp. 682-685. doi: 10.1158/2159-8290.Cd-18-0369

Turnham, D. J., Bullock, N., Dass, M. S., Staffurth, J. N. and Pearson, H. B. 2020. The PTEN Conundrum: How to Target PTEN-Deficient Prostate Cancer. *Cells* 9(11), doi: 10.3390/cells9112342

Valkenburg, K. C., de Groot, A. E. and Pienta, K. J. 2018. Targeting the tumour stroma to improve cancer therapy. *Nat Rev Clin Oncol* 15(6), pp. 366-381. doi: 10.1038/s41571-018-0007-1

Verstak, B., Nagpal, K., Bottomley, S. P., Golenbock, D. T., Hertzog, P. J. and Mansell, A. 2009. MyD88 adapter-like (Mal)/TIRAP interaction with TRAF6 is critical for TLR2- and TLR4-mediated NF-kappaB proinflammatory responses. *J Biol Chem* 284(36), pp. 24192-24203. doi: 10.1074/jbc.M109.023044

Waldeck, K. et al. 2016. Long term, continuous exposure to panobinostat induces terminal differentiation and long term survival in the TH-MYCN neuroblastoma mouse model. *Int J Cancer* 139(1), pp. 194-204. doi: 10.1002/ijc.30056

Wang, N. et al. 2018a. CXCL1 derived from tumor-associated macrophages promotes breast cancer metastasis via activating NF-κB/SOX4 signaling. *Cell Death Dis* 9(9), p. 880. doi: 10.1038/s41419-018-0876-3

Wang, S., Garcia, A. J., Wu, M., Lawson, D. A., Witte, O. N. and Wu, H. 2006. Pten deletion leads to the expansion of a prostatic stem/progenitor cell subpopulation and tumor initiation. *Proc Natl Acad Sci U S A* 103(5), pp. 1480-1485. doi: 10.1073/pnas.0510652103

Wang, V. Y., Li, Y., Kim, D., Zhong, X., Du, Q., Ghassemian, M. and Ghosh, G. 2017. Bcl3 Phosphorylation by Akt, Erk2, and IKK Is Required for Its Transcriptional Activity. *Mol Cell* 67(3), pp. 484-497.e485. doi: 10.1016/j.molcel.2017.06.011

Wang, Y. et al. 2016. Tumor-suppressor NFκB2 p100 interacts with ERK2 and stabilizes PTEN mRNA via inhibition of miR-494. *Oncogene* 35(31), pp. 4080-4090. doi: 10.1038/onc.2015.470

Wang, Y., Zhang, X. L. and Sun, C. M. 2018b. BAY-11-7082 induces apoptosis of multiple myeloma U266 cells through inhibiting NF-κB pathway. *Eur Rev Med Pharmacol Sci* 22(9), pp. 2564-2571. doi: 10.26355/eurrev_201805_14949

Waugh, D. J. and Wilson, C. 2008. The interleukin-8 pathway in cancer. *Clin Cancer Res* 14(21), pp. 6735-6741. doi: 10.1158/1078-0432.Ccr-07-4843

Whang, Y. E., Yuan, X. J., Liu, Y., Majumder, S. and Lewis, T. D. 2004. Regulation of sensitivity to TRAIL by the PTEN tumor suppressor. *Vitam Horm* 67, pp. 409-426. doi: 10.1016/s0083-6729(04)67021-x

Yang, J., Nie, J., Ma, X., Wei, Y., Peng, Y. and Wei, X. 2019. Targeting PI3K in cancer: mechanisms and advances in clinical trials. *Mol Cancer* 18(1), p. 26. doi: 10.1186/s12943-019-0954-x

You, D. et al. 2015. FAK mediates a compensatory survival signal parallel to PI3K-AKT in PTEN-null T-ALL cells. *Cell Rep* 10(12), pp. 2055-2068. doi: 10.1016/j.celrep.2015.02.056

Yu, H., Lin, L., Zhang, Z., Zhang, H. and Hu, H. 2020. Targeting NF-κB pathway for the therapy of diseases: mechanism and clinical study. *Signal Transduct Target Ther* 5(1), p. 209. doi: 10.1038/s41392-020-00312-6

Yun, C. W. and Lee, S. H. 2018. The Roles of Autophagy in Cancer. *Int J Mol Sci* 19(11), doi: 10.3390/ijms19113466

Zarbock, A., Allegretti, M. and Ley, K. 2008. Therapeutic inhibition of CXCR2 by Reparixin attenuates acute lung injury in mice. *Br J Pharmacol* 155(3), pp. 357-364. doi: 10.1038/bjp.2008.270

Zhang, Y. et al. 2008. IkappaBalpha kinase inhibitor IKI-1 conferred tumor necrosis factor alpha sensitivity to pancreatic cancer cells and a xenograft tumor model. *Cancer Res* 68(22), pp. 9519-9524. doi: 10.1158/0008-5472.Can-08-1549

Zhang, Y. et al. 2016a. Targeting IκB Kinase β/NF-κB Signaling in Human Prostate Cancer by a Novel IκB Kinase β Inhibitor CmpdA. *Mol Cancer Ther* 15(7), pp. 1504-1514. doi: 10.1158/1535-7163.Mct-15-0999

Zhang, Y. et al. 2016b. A novel AKT inhibitor, AZD5363, inhibits phosphorylation of AKT downstream molecules, and activates phosphorylation of mTOR and SMG-1 dependent on the liver cancer cell type. *Oncol Lett* 11(3), pp. 1685-1692. doi: 10.3892/ol.2016.4111

Zheng, C., Chen, J., Chu, F., Zhu, J. and Jin, T. 2019. Inflammatory Role of TLR-MyD88 Signaling in Multiple Sclerosis. *Front Mol Neurosci* 12, p. 314. doi: 10.3389/fnmol.2019.00314

Zhu, Y. P., Wan, F. N., Shen, Y. J., Wang, H. K., Zhang, G. M. and Ye, D. W. 2015. Reactive stroma component COL6A1 is upregulated in castration-resistant prostate cancer and promotes tumor growth. *Oncotarget* 6(16), pp. 14488-14496. doi: 10.18632/oncotarget.3697

2015. The Molecular Taxonomy of Primary Prostate Cancer. *Cell* 163(4), pp. 1011-1025. doi: 10.1016/j.cell.2015.10.025

Abate-Shen, C. and Shen, M. M. 2000. Molecular genetics of prostate cancer. *Genes Dev* 14(19), pp. 2410-2434.

Abida, W. et al. 2019. Genomic correlates of clinical outcome in advanced prostate cancer. *Proc Natl Acad Sci U S A* 116(23), pp. 11428-11436. doi: 10.1073/pnas.1902651116

Acevedo, V. D. et al. 2007. Inducible FGFR-1 activation leads to irreversible prostate adenocarcinoma and an epithelial-to-mesenchymal transition. *Cancer Cell* 12(6), pp. 559-571. doi: 10.1016/j.ccr.2007.11.004

Albensi, B. C. 2019. What Is Nuclear Factor Kappa B (NF-κB) Doing in and to the Mitochondrion? *Front Cell Dev Biol* 7, p. 154. doi: 10.3389/fcell.2019.00154

Alfieri, R., Giovannetti, E., Bonelli, M. and Cavazzoni, A. 2017. New Treatment Opportunities in Phosphatase and Tensin Homolog (PTEN)-Deficient Tumors: Focus on PTEN/Focal Adhesion Kinase Pathway. *Front Oncol* 7, p. 170. doi: 10.3389/fonc.2017.00170

Alhamdoosh, M., Law, C. W., Tian, L., Sheridan, J. M., Ng, M. and Ritchie, M. E. 2017. Easy and efficient ensemble gene set testing with EGSEA. *F1000Res* 6, p. 2010. doi: 10.12688/f1000research.12544.1

Alimonti, A. et al. 2010. Subtle variations in Pten dose determine cancer susceptibility. *Nat Genet* 42(5), pp. 454-458. doi: 10.1038/ng.556

Alkasalias, T., Moyano-Galceran, L., Arsenian-Henriksson, M. and Lehti, K. 2018. Fibroblasts in the Tumor Microenvironment: Shield or Spear? *Int J Mol Sci* 19(5), doi: 10.3390/ijms19051532

Anwar, M. A., Shah, M., Kim, J. and Choi, S. 2019. Recent clinical trends in Toll-like receptor targeting therapeutics. *Med Res Rev* 39(3), pp. 1053-1090. doi: 10.1002/med.21553

Araki, S. et al. 2007. Interleukin-8 is a molecular determinant of androgen independence and progression in prostate cancer. *Cancer Res* 67(14), pp. 6854-6862. doi: 10.1158/0008-5472.Can-07-1162

Ardura, J. A., Álvarez-Carrión, L., Gutiérrez-Rojas, I. and Alonso, V. 2020. Role of Calcium Signaling in Prostate Cancer Progression: Effects on Cancer Hallmarks and Bone Metastatic Mechanisms. *Cancers (Basel)* 12(5), doi: 10.3390/cancers12051071

Armenia, J. et al. 2018. The long tail of oncogenic drivers in prostate cancer. *Nat Genet* 50(5), pp. 645-651. doi: 10.1038/s41588-018-0078-z

Armingol, E., Officer, A., Harismendy, O. and Lewis, N. E. 2021. Deciphering cell-cell interactions and communication from gene expression. *Nat Rev Genet* 22(2), pp. 71-88. doi: 10.1038/s41576-020-00292-x

Armstrong, L. C., Westlake, G., Snow, J. P., Cawthon, B., Armour, E., Bowman, A. B. and Ess, K. C. 2017. Heterozygous loss of TSC2 alters p53 signaling and human stem cell reprogramming. *Hum Mol Genet* 26(23), pp. 4629-4641. doi: 10.1093/hmg/ddx345

Arneth, B. 2019. Tumor Microenvironment. *Medicina (Kaunas)* 56(1), doi: 10.3390/medicina56010015

Bachmann, A. and de la Rosette, J. 2011. *Benign Prostatic Hyperplasia and Lower Urinary Tract Symptoms in Men*. OUP Oxford.

Baghban, R. et al. 2020. Tumor microenvironment complexity and therapeutic implications at a glance. *Cell Commun Signal* 18(1), p. 59. doi: 10.1186/s12964-020-0530-4

Bahmad, H. F. et al. 2021. Tumor Microenvironment in Prostate Cancer: Toward Identification of Novel Molecular Biomarkers for Diagnosis, Prognosis, and Therapy Development. *Front Genet* 12, p. 652747. doi: 10.3389/fgene.2021.652747

Bankhead, P. et al. 2017. QuPath: Open source software for digital pathology image analysis. *Sci Rep* 7(1), p. 16878. doi: 10.1038/s41598-017-17204-5

Banno, A. et al. 2016. Downregulation of 26S proteasome catalytic activity promotes epithelial-mesenchymal transition. *Oncotarget* 7(16), pp. 21527-21541. doi: 10.18632/oncotarget.7596

Baum, J. and Duffy, H. S. 2011. Fibroblasts and myofibroblasts: what are we talking about? *J Cardiovasc Pharmacol* 57(4), pp. 376-379. doi: 10.1097/FJC.0b013e3182116e39

Benakanakere, M. R., Finoti, L. S., Tanaka, U., Grant, G. R., Scarel-Caminaga, R. M. and Kinane, D. F. 2016. Investigation of the functional role of human Interleukin-8 gene haplotypes by CRISPR/Cas9 mediated genome editing. *Sci Rep* 6, p. 31180. doi: 10.1038/srep31180

Bennett, N. C., Gardiner, R. A., Hooper, J. D., Johnson, D. W. and Gobe, G. C. 2010. Molecular cell biology of androgen receptor signalling. *The International Journal of Biochemistry & Cell Biology* 42(6), pp. 813-827. doi: https://doi.org/10.1016/j.biocel.2009.11.013

Bertini, R. et al. 2004. Noncompetitive allosteric inhibitors of the inflammatory chemokine receptors CXCR1 and CXCR2: prevention of reperfusion injury. *Proc Natl Acad Sci U S A* 101(32), pp. 11791-11796. doi: 10.1073/pnas.0402090101

Bhattacharya, K., Maiti, S. and Mandal, C. 2016. PTEN negatively regulates mTORC2 formation and signaling in grade IV glioma via Rictor hyperphosphorylation at Thr1135 and direct the mode of action of an mTORC1/2 inhibitor. *Oncogenesis* 5(5), p. e227. doi: 10.1038/oncsis.2016.34

Bhowmick, N. A., Neilson, E. G. and Moses, H. L. 2004. Stromal fibroblasts in cancer initiation and progression. *Nature* 432(7015), pp. 332-337. doi: 10.1038/nature03096

Bianchi-Frias, D. et al. 2016. Cells Comprising the Prostate Cancer Microenvironment Lack Recurrent Clonal Somatic Genomic Aberrations. *Mol Cancer Res* 14(4), pp. 374-384. doi: 10.1158/1541-7786.Mcr-15-0330

Board, P. D. Q. A. T. E. 2002. Prostate Cancer Treatment (PDQ(R)): Patient Version.*PDQ Cancer Information Summaries*. Bethesda MD.

Bosso, D. et al. 2017. PSA declines and survival in patients with metastatic castration-resistant prostate cancer treated with enzalutamide: A retrospective case-report study. *Medicine (Baltimore)* 96(24), p. e6817. doi: 10.1097/md.0000000000006817

Cahill, K. E., Morshed, R. A. and Yamini, B. 2016. Nuclear factor-κB in glioblastoma: insights into regulators and targeted therapy. *Neuro Oncol* 18(3), pp. 329-339. doi: 10.1093/neuonc/nov265

Cai, T., Santi, R., Tamanini, I., Galli, I. C., Perletti, G., Bjerklund Johansen, T. E. and Nesi, G. 2019. Current Knowledge of the Potential Links between Inflammation and Prostate Cancer. *Int J Mol Sci* 20(15), doi: 10.3390/ijms20153833

Cannarella, R., Condorelli, R. A., Barbagallo, F., La Vignera, S. and Calogero, A. E. 2021. Endocrinology of the Aging Prostate: Current Concepts. *Front Endocrinol (Lausanne)* 12, p. 554078. doi: 10.3389/fendo.2021.554078

Carlson, E. C. et al. 2005. Keratocan, a cornea-specific keratan sulfate proteoglycan, is regulated by lumican. *J Biol Chem* 280(27), pp. 25541-25547. doi: 10.1074/jbc.M500249200

Carnero, A. and Paramio, J. M. 2014. The PTEN/PI3K/AKT Pathway in vivo, Cancer Mouse Models. *Front Oncol* 4, p. 252. doi: 10.3389/fonc.2014.00252

Carver, B. S. et al. 2011. Reciprocal feedback regulation of PI3K and androgen receptor signaling in PTEN-deficient prostate cancer. *Cancer Cell* 19(5), pp. 575-586. doi: 10.1016/j.ccr.2011.04.008

Centenera, M. M., Raj, G. V., Knudsen, K. E., Tilley, W. D. and Butler, L. M. 2013. Ex vivo culture of human prostate tissue and drug development. *Nat Rev Urol* 10(8), pp. 483-487. doi: 10.1038/nrurol.2013.126

Cerami, E. et al. 2012. The cBio cancer genomics portal: an open platform for exploring multidimensional cancer genomics data. *Cancer Discov* 2(5), pp. 401-404. doi: 10.1158/2159-8290.Cd-12-0095

Chagpar, R. B., Links, P. H., Pastor, M. C., Furber, L. A., Hawrysh, A. D., Chamberlain, M. D. and Anderson, D. H. 2010. Direct positive regulation of PTEN by the p85 subunit of phosphatidylinositol 3-kinase. *Proc Natl Acad Sci U S A* 107(12), pp. 5471-5476. doi: 10.1073/pnas.0908899107

Chang, Y. C., Kao, W. C., Wang, W. Y., Wang, W. Y., Yang, R. B. and Peck, K. 2009. Identification and characterization of oligonucleotides that inhibit Toll-like receptor 2-associated immune responses. *Faseb j* 23(9), pp. 3078-3088. doi: 10.1096/fj.09-129312

Chaturvedi, M. M., Sung, B., Yadav, V. R., Kannappan, R. and Aggarwal, B. B. 2011. NF-κB addiction and its role in cancer: 'one size does not fit all'. *Oncogene* 30(14), pp. 1615-1630. doi: 10.1038/onc.2010.566

Chauhan, G., Mehta, A. and Gupta, S. 2020. Stromal-AR influences the growth of epithelial cells in the development of benign prostate hyperplasia. *Mol Cell Biochem* 471(1-2), pp. 129-142. doi: 10.1007/s11010-020-03773-z

Chen, M. L. et al. 2006. The deficiency of Akt1 is sufficient to suppress tumor development in Pten+/- mice. *Genes Dev* 20(12), pp. 1569-1574. doi: 10.1101/gad.1395006

Chen, N. and Zhou, Q. 2016. The evolving Gleason grading system. *Chin J Cancer Res* 28(1), pp. 58-64. doi: 10.3978/j.issn.1000-9604.2016.02.04

Chen, Z. et al. 2005. Crucial role of p53-dependent cellular senescence in suppression of Pten-deficient tumorigenesis. *Nature* 436(7051), pp. 725-730. doi: 10.1038/nature03918

Cheng, J., Feng, X., Li, Z., Zhou, F., Yang, J. M. and Zhao, Y. 2021. Pharmacological inhibition of NF-κB-inducing kinase (NIK) with small molecules for the treatment of human diseases. *RSC Med Chem* 12(4), pp. 552-565. doi: 10.1039/d0md00361a

Cheng, L., Montironi, R., Bostwick, D. G., Lopez-Beltran, A. and Berney, D. M. 2012. Staging of prostate cancer. *Histopathology* 60(1), pp. 87-117. doi: 10.1111/j.1365-2559.2011.04025.x

Chiu, Y. J., Hsieh, Y. H. and Huang, Y. H. 2019. Improved cell composition deconvolution method of bulk gene expression profiles to quantify subsets of immune cells. *BMC Med Genomics* 12(Suppl 8), p. 169. doi: 10.1186/s12920-019-0613-5

Christian, F., Smith, E. L. and Carmody, R. J. 2016. The Regulation of NF-κB Subunits by Phosphorylation. *Cells* 5(1), doi: 10.3390/cells5010012

Civita, P. et al. 2019. Laser Capture Microdissection and RNA-Seq Analysis: High Sensitivity Approaches to Explain Histopathological Heterogeneity in Human Glioblastoma FFPE Archived Tissues. *Front Oncol* 9, p. 482. doi: 10.3389/fonc.2019.00482

Coleman, D. L. and Hummel, K. P. 1973. The influence of genetic background on the expression of the obese (ob) gene in the mouse. *Diabetologia* 9(4), pp. 287-293. doi: 10.1007/BF01221856

Crawford, E. D. et al. 2019. Androgen-targeted therapy in men with prostate cancer: evolving practice and future considerations. *Prostate Cancer Prostatic Dis* 22(1), pp. 24-38. doi: 10.1038/s41391-018-0079-0

Crumbaker, M., Khoja, L. and Joshua, A. M. 2017. AR Signaling and the PI3K Pathway in Prostate Cancer. *Cancers (Basel)* 9(4), doi: 10.3390/cancers9040034

Cunha, G. R. et al. 2018. Development of the human prostate. *Differentiation* 103, pp. 24-45. doi: https://doi.org/10.1016/j.diff.2018.08.005

Cunningham, D. and You, Z. 2015. In vitro and in vivo model systems used in prostate cancer research. *J Biol Methods* 2(1), doi: 10.14440/jbm.2015.63

Cuzick, J. et al. 2014. Prevention and early detection of prostate cancer. *Lancet Oncol* 15(11), pp. e484-492. doi: 10.1016/s1470-2045(14)70211-6

D'Urso, M. and Kurniawan, N. A. 2020. Mechanical and Physical Regulation of Fibroblast-Myofibroblast Transition: From Cellular Mechanoresponse to Tissue Pathology. *Front Bioeng Biotechnol* 8, p. 609653. doi: 10.3389/fbioe.2020.609653

Da Silva, L. R. C. 2018. Zika Virus Trafficking and Interactions in the Human Male Reproductive Tract. *Pathogens* 7(2), p. 51.

Dai, Y., Pei, X. Y., Rahmani, M., Conrad, D. H., Dent, P. and Grant, S. 2004. Interruption of the NF-kappaB pathway by Bay 11-7082 promotes UCN-01-mediated mitochondrial dysfunction and apoptosis in human multiple myeloma cells. *Blood* 103(7), pp. 2761-2770. doi: 10.1182/blood-2003-09-3037

Dan, H. C., Cooper, M. J., Cogswell, P. C., Duncan, J. A., Ting, J. P. and Baldwin, A. S. 2008. Akt-dependent regulation of NF-{kappa}B is controlled by mTOR and Raptor in association with IKK. *Genes Dev* 22(11), pp. 1490-1500. doi: 10.1101/gad.1662308

de Bono, J. S. et al. 2019. Randomized Phase II Study Evaluating Akt Blockade with Ipatasertib, in Combination with Abiraterone, in Patients with Metastatic Prostate Cancer with and without PTEN Loss. *Clin Cancer Res* 25(3), pp. 928-936. doi: 10.1158/1078-0432.Ccr-18-0981

de Bono, J. S. et al. 2020. Prostate carcinogenesis: inflammatory storms. *Nature Reviews Cancer* 20(8), pp. 455-469. doi: 10.1038/s41568-020-0267-9

Denton, C. P. et al. 2009. Inducible lineage-specific deletion of TbetaRII in fibroblasts defines a pivotal regulatory role during adult skin wound healing. *J Invest Dermatol* 129(1), pp. 194-204. doi: 10.1038/jid.2008.171

Dhatchinamoorthy, K., Colbert, J. D. and Rock, K. L. 2021. Cancer Immune Evasion Through Loss of MHC Class I Antigen Presentation. *Front Immunol* 12, p. 636568. doi: 10.3389/fimmu.2021.636568

Donnelly, D. W. et al. 2019. Quality of life among symptomatic compared to PSA-detected prostate cancer survivors - results from a UK wide patient-reported outcomes study. *BMC Cancer* 19(1), p. 947. doi: 10.1186/s12885-019-6164-5

Dorrington, M. G. and Fraser, I. D. C. 2019. NF-κB Signaling in Macrophages: Dynamics, Crosstalk, and Signal Integration. *Front Immunol* 10, p. 705. doi: 10.3389/fimmu.2019.00705

Dowling, C. M. et al. 2017. Expression of protein kinase C gamma promotes cell migration in colon cancer. *Oncotarget* 8(42), pp. 72096-72107. doi: 10.18632/oncotarget.18916

Drobkova, H., Jurecekova, J., Grendar, M., Kliment, J., Jr., Halasova, E. and Kliment, J. 2017. Testosterone as a prospective predictor of pathological Gleason score and pathological stage in prostate cancer. *Gen Physiol Biophys* 36(5), pp. 549-556. doi: 10.4149/gpb_2017044

Drost, J., Karthaus, W. R., Gao, D., Driehuis, E., Sawyers, C. L., Chen, Y. and Clevers, H. 2016. Organoid culture systems for prostate epithelial and cancer tissue. *Nat Protoc* 11(2), pp. 347-358. doi: 10.1038/nprot.2016.006

Duchesne, G. 2011. Localised prostate cancer - current treatment options. *Aust Fam Physician* 40(10), pp. 768-771.

Ebner, M., Sinkovics, B., Szczygiel, M., Ribeiro, D. W. and Yudushkin, I. 2017. Localization of mTORC2 activity inside cells. *J Cell Biol* 216(2), pp. 343-353. doi: 10.1083/jcb.201610060

Edlind, M. P. and Hsieh, A. C. 2014. PI3K-AKT-mTOR signaling in prostate cancer progression and androgen deprivation therapy resistance. *Asian J Androl* 16(3), pp. 378-386. doi: 10.4103/1008-682x.122876

Elyada, E. et al. 2019. Cross-Species Single-Cell Analysis of Pancreatic Ductal Adenocarcinoma Reveals Antigen-Presenting Cancer-Associated Fibroblasts. *Cancer Discov* 9(8), pp. 1102-1123. doi: 10.1158/2159-8290.Cd-19-0094

Faes, S. and Dormond, O. 2015. PI3K and AKT: Unfaithful Partners in Cancer. *Int J Mol Sci* 16(9), pp. 21138-21152. doi: 10.3390/ijms160921138

Fernandez-Marcos, P. J. et al. 2009. Simultaneous inactivation of Par-4 and PTEN in vivo leads to synergistic NF-kappaB activation and invasive prostate carcinoma. *Proc Natl Acad Sci U S A* 106(31), pp. 12962-12967. doi: 10.1073/pnas.0813055106

Ferraldeschi, R. et al. 2015. PTEN protein loss and clinical outcome from castration-resistant prostate cancer treated with abiraterone acetate. *Eur Urol* 67(4), pp. 795-802. doi: 10.1016/j.eururo.2014.10.027

Fontana, F., Raimondi, M., Marzagalli, M., Sommariva, M., Gagliano, N. and Limonta, P. 2020. Three-Dimensional Cell Cultures as an In Vitro Tool for Prostate Cancer Modeling and Drug Discovery. *Int J Mol Sci* 21(18), doi: 10.3390/ijms21186806

Foo, K. T. 2017. Pathophysiology of clinical benign prostatic hyperplasia. *Asian Journal of Urology* 4(3), pp. 152-157. doi: 10.1016/j.ajur.2017.06.003

Frankland-Searby, S. and Bhaumik, S. R. 2012. The 26S proteasome complex: an attractive target for cancer therapy. *Biochim Biophys Acta* 1825(1), pp. 64-76. doi: 10.1016/j.bbcan.2011.10.003

Fraser, M. M., Zhu, X., Kwon, C. H., Uhlmann, E. J., Gutmann, D. H. and Baker, S. J. 2004. Pten loss causes hypertrophy and increased proliferation of astrocytes in vivo. *Cancer Res* 64(21), pp. 7773-7779. doi: 10.1158/0008-5472.Can-04-2487

Frisbie, J. H., Kumar, S., Aguilera, E. J. and Yalla, S. 2006. Prostate atrophy and spinal cord lesions. *Spinal Cord* 44(1), pp. 24-27. doi: 10.1038/sj.sc.3101804

Fu, J. et al. 2018a. A novel, homozygous nonsense variant of the CDHR1 gene in a Chinese family causes autosomal recessive retinal dystrophy by NGS-based genetic diagnosis. *J Cell Mol Med* 22(11), pp. 5662-5669. doi: 10.1111/jcmm.13841

Fu, S., Chen, X., Lin, H. J. and Lin, J. 2018b. Inhibition of interleukin 8/C-X-C chemokine receptor 1,/2 signaling reduces malignant features in human pancreatic cancer cells. *Int J Oncol* 53(1), pp. 349-357. doi: 10.3892/ijo.2018.4389

Gabriele, F., Martinelli, C. and Comincini, S. 2018. Prostate cancer cells at a therapeutic gunpoint of the autophagy process. *Journal of Cancer Metastasis and Treatment* 4, p. 17. doi: 10.20517/2394-4722.2018.06

Gandhi, J. et al. 2017. The molecular biology of prostate cancer: current understanding and clinical implications. *Prostate Cancer Prostatic Dis*, doi: 10.1038/s41391-017-0023-8

Gao, D. et al. 2014. Organoid cultures derived from patients with advanced prostate cancer. *Cell* 159(1), pp. 176-187. doi: 10.1016/j.cell.2014.08.016

Gao, J. et al. 2013. Integrative analysis of complex cancer genomics and clinical profiles using the cBioPortal. *Sci Signal* 6(269), p. pl1. doi: 10.1126/scisignal.2004088

Garg, R., Blando, J. M., Perez, C. J., Abba, M. C., Benavides, F. and Kazanietz, M. G. 2017. Protein Kinase C Epsilon Cooperates with PTEN Loss for Prostate Tumorigenesis through the CXCL13-CXCR5 Pathway. *Cell Rep* 19(2), pp. 375-388. doi: 10.1016/j.celrep.2017.03.042

Geng, J., Huang, X. and Dai, H. 2014. Loss of PTEN induced lung fibroblasts exhibiting similar pathogenic features to cancer cells in idiopathic pulmonary fibrosis. *European Respiratory Journal* 44(Suppl 58), p. P754.

Ghomlaghi, M., Hart, A., Hoang, N., Shin, S. and Nguyen, L. K. 2021. Feedback, Crosstalk and Competition: Ingredients for Emergent Non-Linear Behaviour in the PI3K/mTOR Signalling Network. *Int J Mol Sci* 22(13), doi: 10.3390/ijms22136944

Gillessen, S. et al. 2018. Management of Patients with Advanced Prostate Cancer: The Report of the Advanced Prostate Cancer Consensus Conference APCCC 2017. *Eur Urol* 73(2), pp. 178-211. doi: 10.1016/j.eururo.2017.06.002

Glentis, A. et al. 2017. Cancer-associated fibroblasts induce metalloprotease-independent cancer cell invasion of the basement membrane. *Nat Commun* 8(1), p. 924. doi: 10.1038/s41467-017-00985-8

Godwin, P., Baird, A. M., Heavey, S., Barr, M. P., O'Byrne, K. J. and Gately, K. 2013. Targeting nuclear factor-kappa B to overcome resistance to chemotherapy. *Front Oncol* 3, p. 120. doi: 10.3389/fonc.2013.00120

Goldstein, L. J. et al. 2020. A window-of-opportunity trial of the CXCR1/2 inhibitor reparixin in operable HER-2-negative breast cancer. *Breast Cancer Res* 22(1), p. 4. doi: 10.1186/s13058-019-1243-8

Gong, L. et al. 2021. Comprehensive single-cell sequencing reveals the stromal dynamics and tumor-specific characteristics in the microenvironment of nasopharyngeal carcinoma. *Nat Commun* 12(1), p. 1540. doi: 10.1038/s41467-021-21795-z

Grabowska, M. M., DeGraff, D. J., Yu, X., Jin, R. J., Chen, Z., Borowsky, A. D. and Matusik, R. J. 2014. Mouse models of prostate cancer: picking the best model for the question. *Cancer Metastasis Rev* 33(2-3), pp. 377-397. doi: 10.1007/s10555-013-9487-8

Grasso, C. S. et al. 2012. The mutational landscape of lethal castration-resistant prostate cancer. *Nature* 487(7406), pp. 239-243. doi: 10.1038/nature11125

Greenwell, I. B., Ip, A. and Cohen, J. B. 2017. PI3K Inhibitors: Understanding Toxicity Mechanisms and Management. *Oncology (Williston Park)* 31(11), pp. 821-828.

Gu, L., Zhu, N., Findley, H. W. and Zhou, M. 2004. Loss of PTEN Expression Induces NF-kB Via PI3K/Akt Pathway Involving Resistance to Chemotherapy in Acute Lymphoblastic Leukemia Cell Lines. *Blood* 104(11), pp. 4438-4438. doi: 10.1182/blood.V104.11.4438.4438

Gui, S. L. et al. 2016. Overexpression of CXCL3 can enhance the oncogenic potential of prostate cancer. *Int Urol Nephrol* 48(5), pp. 701-709. doi: 10.1007/s11255-016-1222-2

Hägglöf, C. and Bergh, A. 2012. The stroma-a key regulator in prostate function and malignancy. *Cancers (Basel)* 4(2), pp. 531-548. doi: 10.3390/cancers4020531

Hashemzadeh, K., Jokar, M. H., Sedighi, S. and Moradzadeh, M. 2019. Therapeutic Potency of PI3K Pharmacological Inhibitors of Gastrointestinal Cancer. *Middle East J Dig Dis* 11(1), pp. 5-16. doi: 10.15171/mejdd.2018.122

Hayden, M. S. and Ghosh, S. 2012. NF-κB, the first quarter-century: remarkable progress and outstanding questions. *Genes Dev* 26(3), pp. 203-234. doi: 10.1101/gad.183434.111

Henry, G. H. et al. 2018. A Cellular Anatomy of the Normal Adult Human Prostate and Prostatic Urethra. *Cell Rep* 25(12), pp. 3530-3542.e3535. doi: 10.1016/j.celrep.2018.11.086

Herberts, C. et al. 2020. Activating AKT1 and PIK3CA Mutations in Metastatic Castration-Resistant Prostate Cancer. *Eur Urol* 78(6), pp. 834-844. doi: 10.1016/j.eururo.2020.04.058

Hers, I., Vincent, E. E. and Tavare, J. M. 2011. Akt signalling in health and disease. *Cell Signal* 23(10), pp. 1515-1527. doi: 10.1016/j.cellsig.2011.05.004

Hinata, K., Gervin, A. M., Jennifer Zhang, Y. and Khavari, P. A. 2003. Divergent gene regulation and growth effects by NF-kappa B in epithelial and mesenchymal cells of human skin. *Oncogene* 22(13), pp. 1955-1964. doi: 10.1038/sj.onc.1206198

Hinz, N. and Jücker, M. 2019. Distinct functions of AKT isoforms in breast cancer: a comprehensive review. *Cell Commun Signal* 17(1), p. 154. doi: 10.1186/s12964-019-0450-3

Hoeger, B., Serwas, N. K. and Boztug, K. 2017. Human NF-κB1 Haploinsufficiency and Epstein-Barr Virus-Induced Disease-Molecular Mechanisms and Consequences. *Front Immunol* 8, p. 1978. doi: 10.3389/fimmu.2017.01978

Hoesel, B. and Schmid, J. A. 2013. The complexity of NF-κB signaling in inflammation and cancer. *Mol Cancer* 12, p. 86. doi: 10.1186/1476-4598-12-86

Hol, J., Wilhelmsen, L. and Haraldsen, G. 2010. The murine IL-8 homologues KC, MIP-2, and LIX are found in endothelial cytoplasmic granules but not in Weibel-Palade bodies. *J Leukoc Biol* 87(3), pp. 501-508. doi: 10.1189/jlb.0809532

Hoogeveen-Westerveld, M., van Unen, L., van den Ouweland, A., Halley, D., Hoogeveen, A. and Nellist, M. 2012. The TSC1-TSC2 complex consists of multiple TSC1 and TSC2 subunits. *BMC Biochem* 13, p. 18. doi: 10.1186/1471-2091-13-18

Hou, A., Tin, M. Q. and Tong, L. 2017. Toll-like receptor 2-mediated NF-kappa B pathway activation in ocular surface epithelial cells. *Eye Vis (Lond)* 4, p. 17. doi: 10.1186/s40662-017-0082-x

Hua, H., Kong, Q., Zhang, H., Wang, J., Luo, T. and Jiang, Y. 2019. Targeting mTOR for cancer therapy. *J Hematol Oncol* 12(1), p. 71. doi: 10.1186/s13045-019-0754-1

Huang, J. and Manning, B. D. 2008. The TSC1-TSC2 complex: a molecular switchboard controlling cell growth. *Biochem J* 412(2), pp. 179-190. doi: 10.1042/BJ20080281

Huang, Y., Jiang, X., Liang, X. and Jiang, G. 2018. Molecular and cellular mechanisms of castration resistant prostate cancer. *Oncol Lett* 15(5), pp. 6063-6076. doi: 10.3892/ol.2018.8123

Hunter, S. M. et al. 2015. Molecular profiling of low grade serous ovarian tumours identifies novel candidate driver genes. *Oncotarget* 6(35), pp. 37663-37677. doi: 10.18632/oncotarget.5438

Huper, G. and Marks, J. R. 2007. Isogenic normal basal and luminal mammary epithelial isolated by a novel method show a differential response to ionizing radiation. *Cancer Res* 67(7), pp. 2990-3001. doi: 10.1158/0008-5472.Can-06-4065

Hussain, A. R. et al. 2012. Cross-talk between NFkB and the PI3-kinase/AKT pathway can be targeted in primary effusion lymphoma (PEL) cell lines for efficient apoptosis. *PLoS One* 7(6), p. e39945. doi: 10.1371/journal.pone.0039945

Ianevski, A., Giri, A. K. and Aittokallio, T. 2020. SynergyFinder 2.0: visual analytics of multi-drug combination synergies. *Nucleic Acids Res* 48(W1), pp. W488-w493. doi: 10.1093/nar/gkaa216

Ireland, H., Kemp, R., Houghton, C., Howard, L., Clarke, A. R., Sansom, O. J. and Winton, D. J. 2004. Inducible Cre-mediated control of gene expression in the murine gastrointestinal tract: effect of loss of beta-catenin. *Gastroenterology* 126(5), pp. 1236-1246. doi: 10.1053/j.gastro.2004.03.020

Isikbay, M. et al. 2014. Glucocorticoid receptor activity contributes to resistance to androgen-targeted therapy in prostate cancer. *Horm Cancer* 5(2), pp. 72-89. doi: 10.1007/s12672-014-0173-2

Ito, H. et al. 2016. GSK-3 directly regulates phospho-4EBP1 in renal cell carcinoma cell-line: an intrinsic subcellular mechanism for resistance to mTORC1 inhibition. *BMC Cancer* 16, p. 393. doi: 10.1186/s12885-016-2418-7

Ittmann, M. 2018. Anatomy and Histology of the Human and Murine Prostate. *Cold Spring Harb Perspect Med* 8(5), doi: 10.1101/cshperspect.a030346

Izumi, K., Mizokami, A., Lin, W. J., Lai, K. P. and Chang, C. 2013. Androgen receptor roles in the development of benign prostate hyperplasia. *Am J Pathol* 182(6), pp. 1942-1949. doi: 10.1016/j.ajpath.2013.02.028

Jamaspishvili, T., Berman, D. M., Ross, A. E., Scher, H. I., De Marzo, A. M., Squire, J. A. and Lotan, T. L. 2018. Clinical implications of PTEN loss in prostate cancer. *Nat Rev Urol* 15(4), pp. 222-234. doi: 10.1038/nrurol.2018.9

Jang, H. H. 2018. Regulation of Protein Degradation by Proteasomes in Cancer. *J Cancer Prev* 23(4), pp. 153-161. doi: 10.15430/jcp.2018.23.4.153

Jean, S. and Kiger, A. A. 2014. Classes of phosphoinositide 3-kinases at a glance. *Journal of Cell Science* 127(5), pp. 923-928. doi: 10.1242/jcs.093773

Jefferies, M. T. et al. 2017. PTEN loss and activation of K-RAS and beta-catenin cooperate to accelerate prostate tumourigenesis. *J Pathol* 243(4), pp. 442-456. doi: 10.1002/path.4977

Jiang, R., Gu, L., Findley, H. and Zhou, M. 2004. Loss of PTEN expression induces NF-kB via PI3K/Akt pathway involving resistance to chemotherapy in acute lymphoblastic leukemia cell lines. *Cancer Research* 64(7 Supplement), pp. 1277-1277.

Jimenez, C., Hernandez, C., Pimentel, B. and Carrera, A. C. 2002. The p85 regulatory subunit controls sequential activation of phosphoinositide 3-kinase by Tyr kinases and Ras. *J Biol Chem* 277(44), pp. 41556-41562. doi: 10.1074/jbc.M205893200

Jin, C., McKeehan, K. and Wang, F. 2003. Transgenic mouse with high Cre recombinase activity in all prostate lobes, seminal vesicle, and ductus deferens. *Prostate* 57(2), pp. 160-164. doi: 10.1002/pros.10283

Jin, M. Z. and Jin, W. L. 2020. The updated landscape of tumor microenvironment and drug repurposing. *Signal Transduct Target Ther* 5(1), p. 166. doi: 10.1038/s41392-020-00280-x

Jin, R. et al. 2014. NF-κB gene signature predicts prostate cancer progression. *Cancer Res* 74(10), pp. 2763-2772. doi: 10.1158/0008-5472.Can-13-2543

Jones, C. E. et al. 2019. Stromal PTEN Regulates Extracellular Matrix Organization in the Mammary Gland. *Neoplasia* 21(1), pp. 132-145. doi: 10.1016/j.neo.2018.10.010

Jundi, K. and Greene, C. M. 2015. Transcription of Interleukin-8: How Altered Regulation Can Affect Cystic Fibrosis Lung Disease. *Biomolecules* 5(3), pp. 1386-1398. doi: 10.3390/biom5031386

Jung, J., Seol, H. S. and Chang, S. 2018. The Generation and Application of Patient-Derived Xenograft Model for Cancer Research. *Cancer Res Treat* 50(1), pp. 1-10. doi: 10.4143/crt.2017.307

Jurmeister, S. et al. 2018. Identification of potential therapeutic targets in prostate cancer through a cross-species approach. *EMBO Mol Med* 10(3), doi: 10.15252/emmm.201708274

Kapałczyńska, M. et al. 2018. 2D and 3D cell cultures - a comparison of different types of cancer cell cultures. *Arch Med Sci* 14(4), pp. 910-919. doi: 10.5114/aoms.2016.63743

Karan, D. and Dubey, S. 2016. From Inflammation to Prostate Cancer: The Role of Inflammasomes. *Adv Urol* 2016, p. 3140372. doi: 10.1155/2016/3140372

Kato, M., Sasaki, T. and Inoue, T. 2021. Current experimental human tissue-derived models for prostate cancer research. *Int J Urol* 28(2), pp. 150-162. doi: 10.1111/iju.14441

Kendall, R. T. and Feghali-Bostwick, C. A. 2014. Fibroblasts in fibrosis: novel roles and mediators. *Front Pharmacol* 5, p. 123. doi: 10.3389/fphar.2014.00123

Kersten, K., de Visser, K. E., van Miltenburg, M. H. and Jonkers, J. 2017. Genetically engineered mouse models in oncology research and cancer medicine. *EMBO Mol Med* 9(2), pp. 137-153. doi: 10.15252/emmm.201606857

Khan, K. H., Yap, T. A., Yan, L. and Cunningham, D. 2013. Targeting the PI3K-AKT-mTOR signaling network in cancer. *Chin J Cancer* 32(5), pp. 253-265. doi: 10.5732/cjc.013.10057

Khongthong, P., Roseweir, A. K. and Edwards, J. 2019. The NF-KB pathway and endocrine therapy resistance in breast cancer. *Endocr Relat Cancer* 26(6), pp. R369-r380. doi: 10.1530/erc-19-0087

Kim, H., Kim, M., Im, S. K. and Fang, S. 2018. Mouse Cre-LoxP system: general principles to determine tissue-specific roles of target genes. *Lab Anim Res* 34(4), pp. 147-159. doi: 10.5625/lar.2018.34.4.147

Kim, J., Koo, B. K. and Knoblich, J. A. 2020. Human organoids: model systems for human biology and medicine. *Nat Rev Mol Cell Biol* 21(10), pp. 571-584. doi: 10.1038/s41580-020-0259-3

Kindblom, J., Dillner, K., Sahlin, L., Robertson, F., Ormandy, C., Törnell, J. and Wennbo, H. 2003. Prostate hyperplasia in a transgenic mouse with prostate-specific expression of prolactin. *Endocrinology* 144(6), pp. 2269-2278. doi: 10.1210/en.2002-0187

Kinross, K. M. et al. 2012. An activating Pik3ca mutation coupled with Pten loss is sufficient to initiate ovarian tumorigenesis in mice. *J Clin Invest* 122(2), pp. 553-557. doi: 10.1172/jci59309

Klarenbeek, S., van Miltenburg, M. H. and Jonkers, J. 2013. Genetically engineered mouse models of PI3K signaling in breast cancer. *Mol Oncol* 7(2), pp. 146-164. doi: 10.1016/j.molonc.2013.02.003

Knobbe, C. B., Lapin, V., Suzuki, A. and Mak, T. W. 2008. The roles of PTEN in development, physiology and tumorigenesis in mouse models: a tissue-by-tissue survey. *Oncogene* 27(41), pp. 5398-5415. doi: 10.1038/onc.2008.238

Ko, J., Carpenter, E. and Issadore, D. 2016. Detection and isolation of circulating exosomes and microvesicles for cancer monitoring and diagnostics using micro-/nano-based devices. *Analyst* 141(2), pp. 450-460. doi: 10.1039/c5an01610j

Kogan-Sakin, I. et al. 2009. Prostate stromal cells produce CXCL-1, CXCL-2, CXCL-3 and IL-8 in response to epithelia-secreted IL-1. *Carcinogenesis* 30(4), pp. 698-705. doi: 10.1093/carcin/bgp043

Kokkinos, J. et al. 2021. Ex vivo culture of intact human patient derived pancreatic tumour tissue. *Sci Rep* 11(1), p. 1944. doi: 10.1038/s41598-021-81299-0

Kong, C. et al. 2019. NF-κB inhibition promotes apoptosis in androgen-independent prostate cancer cells by the photothermal effect via the IκBα/AR signaling pathway. *Biomater Sci* 7(6), pp. 2559-2570. doi: 10.1039/c8bm01007b

Kõressaar, T., Lepamets, M., Kaplinski, L., Raime, K., Andreson, R. and Remm, M. 2018. Primer3_masker: integrating masking of template sequence with primer design software. *Bioinformatics* 34(11), pp. 1937-1938. doi: 10.1093/bioinformatics/bty036

Koul, H. K., Pal, M. and Koul, S. 2013. Role of p38 MAP Kinase Signal Transduction in Solid Tumors. *Genes Cancer* 4(9-10), pp. 342-359. doi: 10.1177/1947601913507951

Kukurba, K. R. and Montgomery, S. B. 2015. RNA Sequencing and Analysis. *Cold Spring Harb Protoc* 2015(11), pp. 951-969. doi: 10.1101/pdb.top084970

Kundu, D., Kennedy, L., Meadows, V., Baiocchi, L., Alpini, G. and Francis, H. 2020. The Dynamic Interplay Between Mast Cells, Aging/Cellular Senescence, and Liver Disease. *Gene Expr* 20(2), pp. 77-88. doi: 10.3727/105221620x15960509906371

Kwon, J. T. W., Bryant, R. J. and Parkes, E. E. 2021. The tumor microenvironment and immune responses in prostate cancer patients. *Endocr Relat Cancer* 28(8), pp. T95-t107. doi: 10.1530/erc-21-0149

Labani-Motlagh, A., Ashja-Mahdavi, M. and Loskog, A. 2020. The Tumor Microenvironment: A Milieu Hindering and Obstructing Antitumor Immune Responses. *Front Immunol* 11, p. 940. doi: 10.3389/fimmu.2020.00940

Labbozzetta, M., Notarbartolo, M. and Poma, P. 2020. Can NF-κB Be Considered a Valid Drug Target in Neoplastic Diseases? Our Point of View. *Int J Mol Sci* 21(9), doi: 10.3390/ijms21093070

Lamoureux, F. et al. 2013. Blocked autophagy using lysosomotropic agents sensitizes resistant prostate tumor cells to the novel Akt inhibitor AZD5363. *Clin Cancer Res* 19(4), pp. 833-844. doi: 10.1158/1078-0432.Ccr-12-3114

Langhans, S. A. 2018. Three-Dimensional in Vitro Cell Culture Models in Drug Discovery and Drug Repositioning. *Front Pharmacol* 9, p. 6. doi: 10.3389/fphar.2018.00006

Lawrence, M. G. et al. 2018. Patient-derived Models of Abiraterone- and Enzalutamide-resistant Prostate Cancer Reveal Sensitivity to Ribosome-directed Therapy. *Eur Urol* 74(5), pp. 562-572. doi: 10.1016/j.eururo.2018.06.020

Lawrence, M. G. et al. 2013. A preclinical xenograft model of prostate cancer using human tumors. *Nat Protoc* 8(5), pp. 836-848. doi: 10.1038/nprot.2013.043

Lee, C., Jia, Z., Rahmatpanah, F., Zhang, Q., Zi, X., McClelland, M. and Mercola, D. 2014. Role of the adjacent stroma cells in prostate cancer development and progression: synergy between TGF-β and IGF signaling. *Biomed Res Int* 2014, p. 502093. doi: 10.1155/2014/502093

Lee, J., Rhee, M. H., Kim, E. and Cho, J. Y. 2012. BAY 11-7082 is a broad-spectrum inhibitor with anti-inflammatory activity against multiple targets. *Mediators Inflamm* 2012, p. 416036. doi: 10.1155/2012/416036

Lee, Y. R. and Pandolfi, P. P. 2020. PTEN Mouse Models of Cancer Initiation and Progression. *Cold Spring Harb Perspect Med* 10(2), doi: 10.1101/cshperspect.a037283

Lesche, R. et al. 2002. Cre/loxP-mediated inactivation of the murine Pten tumor suppressor gene. *Genesis* 32(2), pp. 148-149. doi: 10.1002/gene.10036

Leslie, S. W. and Siref, L. E. 2018. Cancer, Prostate.*StatPearls*. Treasure Island (FL).

Levesque, C. and Nelson, P. S. 2017. Cellular Constituents of the Prostate Stroma: Key Contributors to Prostate Cancer Progression and Therapy Resistance. *Cold Spring Harb Perspect Med*, doi: 10.1101/cshperspect.a030510

Li, J., Ding, Y. and Li, A. 2016. Identification of COL1A1 and COL1A2 as candidate prognostic factors in gastric cancer. *World J Surg Oncol* 14(1), p. 297. doi: 10.1186/s12957-016-1056-5

Li, J. Y., Liu, Y., Gao, X. X., Gao, X. and Cai, H. 2014. TLR2 and TLR4 signaling pathways are required for recombinant Brucella abortus BCSP31-induced cytokine production, functional upregulation of mouse macrophages, and the Th1 immune response in vivo and in vitro. *Cell Mol Immunol* 11(5), pp. 477-494. doi: 10.1038/cmi.2014.28

Li, S. et al. 2018. Overview of the reporter genes and reporter mouse models. *Animal Model Exp Med* 1(1), pp. 29-35. doi: 10.1002/ame2.12008

Li, S., Zhang, F., Xiao, X., Guo, Y., Wen, Z., Li, M. and Pu, X. 2021. Prediction of Synergistic Drug Combinations for Prostate Cancer by Transcriptomic and Network Characteristics. *Front Pharmacol* 12, p. 634097. doi: 10.3389/fphar.2021.634097

Li, T. et al. 2020. TIMER2.0 for analysis of tumor-infiltrating immune cells. *Nucleic Acids Res* 48(W1), pp. W509-w514. doi: 10.1093/nar/gkaa407

Li, W. et al. 2017. TGFβ1 in fibroblasts-derived exosomes promotes epithelial-mesenchymal transition of ovarian cancer cells. *Oncotarget* 8(56), pp. 96035-96047. doi: 10.18632/oncotarget.21635

Ligresti, G. et al. 2009. PIK3CA mutations in human solid tumors: role in sensitivity to various therapeutic approaches. *Cell Cycle* 8(9), pp. 1352-1358. doi: 10.4161/cc.8.9.8255

Lim, K. B. 2017. Epidemiology of clinical benign prostatic hyperplasia. *Asian J Urol* 4(3), pp. 148-151. doi: 10.1016/j.ajur.2017.06.004

Lin, H. K., Hu, Y. C., Lee, D. K. and Chang, C. 2004. Regulation of androgen receptor signaling by PTEN (phosphatase and tensin homolog deleted on chromosome 10) tumor suppressor through distinct mechanisms in prostate cancer cells. *Mol Endocrinol* 18(10), pp. 2409-2423. doi: 10.1210/me.2004-0117

Lin, S. R., Yeh, H. L. and Liu, Y. N. 2021a. Interplay of Epidermal Growth Factor Receptor and Signal Transducer and Activator of Transcription 3 in Prostate Cancer: Beyond Androgen Receptor Transactivation. *Cancers (Basel)* 13(14), doi: 10.3390/cancers13143452

Lin, Z., Huang, L., Li, S. L., Gu, J., Cui, X. and Zhou, Y. 2021b. PTEN loss correlates with T cell exclusion across human cancers. *BMC Cancer* 21(1), p. 429. doi: 10.1186/s12885-021-08114-x

Linxweiler, J. et al. 2020. Cancer-associated fibroblasts stimulate primary tumor growth and metastatic spread in an orthotopic prostate cancer xenograft model. *Sci Rep* 10(1), p. 12575. doi: 10.1038/s41598-020-69424-x

Liotti, F., De Pizzol, M., Allegretti, M., Prevete, N. and Melillo, R. M. 2017. Multiple anti-tumor effects of Reparixin on thyroid cancer. *Oncotarget* 8(22), pp. 35946-35961. doi: 10.18632/oncotarget.16412

Liu, R. et al. 2020. PI3K/AKT pathway as a key link modulates the multidrug resistance of cancers. *Cell Death Dis* 11(9), p. 797. doi: 10.1038/s41419-020-02998-6

Liu, T., Zhang, L., Joo, D. and Sun, S. C. 2017. NF-κB signaling in inflammation. *Signal Transduct Target Ther* 2, pp. 17023-. doi: 10.1038/sigtrans.2017.23

Lleonart, M. E., Carnero, A., Paciucci, R., Wang, Z. Q. and Shomron, N. 2011. Cancer, senescence, and aging: translation from basic research to clinics. *J Aging Res* 2011, p. 692301. doi: 10.4061/2011/692301

Lonergan, P. and Tindall, D. 2011. Androgen receptor signaling in prostate cancer development and progression. *Journal of Carcinogenesis* 10(1), pp. 20-20. doi: 10.4103/1477-3163.83937

Lopes-Paciencia, S., Saint-Germain, E., Rowell, M. C., Ruiz, A. F., Kalegari, P. and Ferbeyre, G. 2019. The senescence-associated secretory phenotype and its regulation. *Cytokine* 117, pp. 15-22. doi: 10.1016/j.cyto.2019.01.013

Lotan, T. L. et al. 2011. PTEN protein loss by immunostaining: analytic validation and prognostic indicator for a high risk surgical cohort of prostate cancer patients. *Clin Cancer Res* 17(20), pp. 6563-6573. doi: 10.1158/1078-0432.Ccr-11-1244

Lotan, T. L. et al. 2017. PTEN loss detection in prostate cancer: comparison of PTEN immunohistochemistry and PTEN FISH in a large retrospective prostatectomy cohort. *Oncotarget* 8(39), pp. 65566-65576. doi: 10.18632/oncotarget.19217

Lotan, T. L. et al. 2016. Analytic validation of a clinical-grade PTEN immunohistochemistry assay in prostate cancer by comparison with PTEN FISH. *Mod Pathol* 29(8), pp. 904-914. doi: 10.1038/modpathol.2016.88

Luche, H., Weber, O., Nageswara Rao, T., Blum, C. and Fehling, H. J. 2007. Faithful activation of an extra-bright red fluorescent protein in "knock-in" Cre-reporter mice ideally suited for lineage tracing studies. *Eur J Immunol* 37(1), pp. 43-53. doi: 10.1002/eji.200636745

Luo, J. L., Kamata, H. and Karin, M. 2005. The anti-death machinery in IKK/NF-kappaB signaling. *J Clin Immunol* 25(6), pp. 541-550. doi: 10.1007/s10875-005-8217-6

Ma, L., Li, J., Nie, Q., Zhang, Q., Liu, S., Ge, D. and You, Z. 2017. Organoid culture of human prostate cancer cell lines LNCaP and C4-2B. *Am J Clin Exp Urol* 5(3), pp. 25-33.

Maciel, T. T., Moura, I. C. and Hermine, O. 2015. The role of mast cells in cancers. *F1000Prime Rep* 7, p. 09. doi: 10.12703/p7-09

Maitland, N. J. 2017. Getting closer to prostate cancer in patients - what scientists should want from clinicians. *Journal of Cancer Metastasis and Treatment* 3, pp. 262-270. doi: 10.20517/2394-4722.2017.23

Majumder, B. et al. 2015. Predicting clinical response to anticancer drugs using an ex vivo platform that captures tumour heterogeneity. *Nat Commun* 6, p. 6169. doi: 10.1038/ncomms7169

Majumder, P. K. and Sellers, W. R. 2005. Akt-regulated pathways in prostate cancer. *Oncogene* 24(50), pp. 7465-7474. doi: 10.1038/sj.onc.1209096

Man, X., Piao, C., Lin, X., Kong, C., Cui, X. and Jiang, Y. 2019. USP13 functions as a tumor suppressor by blocking the NF-kB-mediated PTEN downregulation in human bladder cancer. *J Exp Clin Cancer Res* 38(1), p. 259. doi: 10.1186/s13046-019-1262-4

Mao, N. et al. 2021. Defining the therapeutic selective dependencies for distinct subtypes of PI3K pathway-altered prostate cancers. *Nat Commun* 12(1), p. 5053. doi: 10.1038/s41467-021-25341-9

March, B., Faulkner, S., Jobling, P., Steigler, A., Blatt, A., Denham, J. and Hondermarck, H. 2020. Tumour innervation and neurosignalling in prostate cancer. *Nat Rev Urol* 17(2), pp. 119-130. doi: 10.1038/s41585-019-0274-3

Margaria, J. P., Ratto, E., Gozzelino, L., Li, H. and Hirsch, E. 2019. Class II PI3Ks at the Intersection between Signal Transduction and Membrane Trafficking. *Biomolecules* 9(3), doi: 10.3390/biom9030104

Martin, S. Z., Wagner, D. C., Hörner, N., Horst, D., Lang, H., Tagscherer, K. E. and Roth, W. 2019. Ex vivo tissue slice culture system to measure drug-response rates of hepatic metastatic colorectal cancer. *BMC Cancer* 19(1), p. 1030. doi: 10.1186/s12885-019-6270-4

Martorana, F. et al. 2021. AKT Inhibitors: New Weapons in the Fight Against Breast Cancer? *Front Pharmacol* 12, p. 662232. doi: 10.3389/fphar.2021.662232

Mawhinney, M. and Mariotti, A. 2013. Physiology, pathology and pharmacology of the male reproductive system. *Periodontol 2000* 61(1), pp. 232-251. doi: 10.1111/j.1600-0757.2011.00408.x

Maxwell, P. J., Neisen, J., Messenger, J. and Waugh, D. J. 2014. Tumor-derived CXCL8 signaling augments stroma-derived CCL2-promoted proliferation and CXCL12-mediated invasion of PTEN-deficient prostate cancer cells. *Oncotarget* 5(13), pp. 4895-4908. doi: 10.18632/oncotarget.2052

Maynard, J. P., Ertunc, O., Kulac, I., Baena-Del Valle, J. A., De Marzo, A. M. and Sfanos, K. S. 2020. IL8 Expression Is Associated with Prostate Cancer Aggressiveness and Androgen Receptor Loss in Primary and Metastatic Prostate Cancer. *Mol Cancer Res* 18(1), pp. 153-165. doi: 10.1158/1541-7786.Mcr-19-0595

Mayo, M. W., Madrid, L. V., Westerheide, S. D., Jones, D. R., Yuan, X. J., Baldwin, A. S., Jr. and Whang, Y. E. 2002. PTEN blocks tumor necrosis factor-induced NF-kappa B-dependent transcription by inhibiting the transactivation potential of the p65 subunit. *J Biol Chem* 277(13), pp. 11116-11125. doi: 10.1074/jbc.M108670200

McEwan, I. J. 2004. Molecular mechanisms of androgen receptor-mediated gene regulation: structure-function analysis of the AF-1 domain. *Endocr Relat Cancer* 11(2), pp. 281-293.

Milella, M. et al. 2015. PTEN: Multiple Functions in Human Malignant Tumors. *Front Oncol* 5, p. 24. doi: 10.3389/fonc.2015.00024

Mistry, P. et al. 2015. Inhibition of TLR2 signaling by small molecule inhibitors targeting a pocket within the TLR2 TIR domain. *Proc Natl Acad Sci U S A* 112(17), pp. 5455-5460. doi: 10.1073/pnas.1422576112

Mitchell, S., Vargas, J. and Hoffmann, A. 2016. Signaling via the NFκB system. *Wiley Interdiscip Rev Syst Biol Med* 8(3), pp. 227-241. doi: 10.1002/wsbm.1331

Moretti, I. F., Franco, D. G., de Almeida Galatro, T. F., Oba-Shinjo, S. M. and Marie, S. K. N. 2018. Plasmatic membrane toll-like receptor expressions in human astrocytomas. *PLoS One* 13(6), p. e0199211. doi: 10.1371/journal.pone.0199211

Muhl, L. et al. 2020. Single-cell analysis uncovers fibroblast heterogeneity and criteria for fibroblast and mural cell identification and discrimination. *Nat Commun* 11(1), p. 3953. doi: 10.1038/s41467-020-17740-1

Munezane, H. et al. 2019. Roles of Collagen XXV and Its Putative Receptors PTPσ/δ in Intramuscular Motor Innervation and Congenital Cranial Dysinnervation Disorder. *Cell Rep* 29(13), pp. 4362-4376.e4366. doi: 10.1016/j.celrep.2019.11.112

Mussbacher, M. et al. 2019. Cell Type-Specific Roles of NF-κB Linking Inflammation and Thrombosis. *Front Immunol* 10, p. 85. doi: 10.3389/fimmu.2019.00085

Nagaraj, A. S., Bao, J., Hemmes, A., Machado, M., Närhi, K. and Verschuren, E. W. 2018. Establishment and Analysis of Tumor Slice Explants As a Prerequisite for Diagnostic Testing. *J Vis Exp* (141), doi: 10.3791/58569

Nakazawa, M., Paller, C. and Kyprianou, N. 2017. Mechanisms of Therapeutic Resistance in Prostate Cancer. *Curr Oncol Rep* 19(2), p. 13. doi: 10.1007/s11912-017-0568-7

Namekawa, T., Ikeda, K., Horie-Inoue, K. and Inoue, S. 2019. Application of Prostate Cancer Models for Preclinical Study: Advantages and Limitations of Cell Lines, Patient-Derived Xenografts, and Three-Dimensional Culture of Patient-Derived Cells. *Cells* 8(1), doi: 10.3390/cells8010074

Napetschnig, J. and Wu, H. 2013. Molecular basis of NF-κB signaling. *Annu Rev Biophys* 42, pp. 443-468. doi: 10.1146/annurev-biophys-083012-130338

Ng, M. and Baradhi, K. M. 2021. Benign Prostatic Hyperplasia.*StatPearls*. Treasure Island (FL): StatPearls Publishing

Nguyen, Y. T., Rodriguez-Nieves, J. A., Yang, Q. and VanderWeele, D. 2018. Abstract 5420: Nuclear PTEN directly regulates androgen receptor activity in prostate cancer. *Cancer Research* 78(13 Supplement), pp. 5420-5420. doi: 10.1158/1538-7445.Am2018-5420

Ni, Y., Zhou, X., Yang, J., Shi, H., Li, H., Zhao, X. and Ma, X. 2021. The Role of Tumor-Stroma Interactions in Drug Resistance Within Tumor Microenvironment. *Front Cell Dev Biol* 9, p. 637675. doi: 10.3389/fcell.2021.637675

Nisa, L. et al. 2017. PIK3CA hotspot mutations differentially impact responses to MET targeting in MET-driven and non-driven preclinical cancer models. *Mol Cancer* 16(1), p. 93. doi: 10.1186/s12943-017-0660-5

Nissen, N. I., Karsdal, M. and Willumsen, N. 2019. Collagens and Cancer associated fibroblasts in the reactive stroma and its relation to Cancer biology. *J Exp Clin Cancer Res* 38(1), p. 115. doi: 10.1186/s13046-019-1110-6

Nitulescu, G. M. et al. 2016. Akt inhibitors in cancer treatment: The long journey from drug discovery to clinical use (Review). *Int J Oncol* 48(3), pp. 869-885. doi: 10.3892/ijo.2015.3306

Niu, Y. N. and Xia, S. J. 2009. Stroma-epithelium crosstalk in prostate cancer. *Asian J Androl* 11(1), pp. 28-35. doi: 10.1038/aja.2008.39

Noren Hooten, N. and Evans, M. K. 2017. Techniques to Induce and Quantify Cellular Senescence. *J Vis Exp* (123), doi: 10.3791/55533

Oeckinghaus, A., Hayden, M. S. and Ghosh, S. 2011. Crosstalk in NF-κB signaling pathways. *Nat Immunol* 12(8), pp. 695-708. doi: 10.1038/ni.2065

Oh, W. J. and Jacinto, E. 2011. mTOR complex 2 signaling and functions. *Cell Cycle* 10(14), pp. 2305-2316. doi: 10.4161/cc.10.14.16586

Ohmuraya, M., Sugano, A., Hirota, M., Takaoka, Y. and Yamamura, K. 2012. Role of Intrapancreatic SPINK1/Spink3 Expression in the Development of Pancreatitis. *Front Physiol* 3, p. 126. doi: 10.3389/fphys.2012.00126

Oliveira, D. S., Dzinic, S., Bonfil, A. I., Saliganan, A. D., Sheng, S. and Bonfil, R. D. 2016. The mouse prostate: a basic anatomical and histological guideline. *Bosn J Basic Med Sci* 16(1), pp. 8-13. doi: 10.17305/bjbms.2016.917

Olleik, G. et al. 2018. Evaluation of New Tests and Interventions for Prostate Cancer Management: A Systematic Review. *J Natl Compr Canc Netw* 16(11), pp. 1340-1351. doi: 10.6004/jnccn.2018.7055

Onozato, D. et al. 2018. Generation of Intestinal Organoids Suitable for Pharmacokinetic Studies from Human Induced Pluripotent Stem Cells. *Drug Metab Dispos* 46(11), pp. 1572-1580. doi: 10.1124/dmd.118.080374

Parapuram, S. K., Thompson, K., Tsang, M., Hutchenreuther, J., Bekking, C., Liu, S. and Leask, A. 2015. Loss of PTEN expression by mouse fibroblasts results in lung fibrosis through a CCN2-dependent mechanism. *Matrix Biol* 43, pp. 35-41. doi: 10.1016/j.matbio.2015.01.017

Parisotto, M., Grelet, E., El Bizri, R. and Metzger, D. 2019. Senescence controls prostatic neoplasia driven by Pten loss. *Mol Cell Oncol* 6(1), p. 1511205. doi: 10.1080/23723556.2018.1511205

Parisotto, M. and Metzger, D. 2013. Genetically engineered mouse models of prostate cancer. *Mol Oncol* 7(2), pp. 190-205. doi: 10.1016/j.molonc.2013.02.005

Park, J. W., Lee, J. K., Phillips, J. W., Huang, P., Cheng, D., Huang, J. and Witte, O. N. 2016. Prostate epithelial cell of origin determines cancer differentiation state in an organoid transformation assay. *Proc Natl Acad Sci U S A* 113(16), pp. 4482-4487. doi: 10.1073/pnas.1603645113

Park, M. H. and Hong, J. T. 2016. Roles of NF-κB in Cancer and Inflammatory Diseases and Their Therapeutic Approaches. *Cells* 5(2), doi: 10.3390/cells5020015

Park, S., Kim, Y. S., Kim, D. Y., So, I. and Jeon, J. H. 2018. PI3K pathway in prostate cancer: All resistant roads lead to PI3K. *Biochim Biophys Acta Rev Cancer* 1870(2), pp. 198-206. doi: 10.1016/j.bbcan.2018.09.001

Patel, G. K., Khan, M. A., Zubair, H., Srivastava, S. K., Khushman, M., Singh, S. and Singh, A. P. 2019. Comparative analysis of exosome isolation methods using culture supernatant for optimum yield, purity and downstream applications. *Sci Rep* 9(1), p. 5335. doi: 10.1038/s41598-019-41800-2

Pearson, H. B. et al. 2018. Identification of Pik3ca Mutation as a Genetic Driver of Prostate Cancer That Cooperates with Pten Loss to Accelerate Progression and Castration-Resistant Growth. *Cancer Discov* 8(6), pp. 764-779. doi: 10.1158/2159-8290.Cd-17-0867

Peehl, D. M., Wong, S. T., Terris, M. K. and Stamey, T. A. 1991. Culture of prostatic epithelial cells from ultrasound-guided needle biopsies. *Prostate* 19(2), pp. 141-147. doi: 10.1002/pros.2990190207

Pellicciotta, I., Cortez-Gonzalez, X., Sasik, R., Reiter, Y., Hardiman, G., Langlade-Demoyen, P. and Zanetti, M. 2008. Presentation of telomerase reverse transcriptase, a self-tumor antigen, is down-regulated by histone deacetylase inhibition. *Cancer Res* 68(19), pp. 8085-8093. doi: 10.1158/0008-5472.Can-08-1014

Picanço-Albuquerque, C. G. et al. 2019. PTEN loss in Gleason grade 7 prostate tumors exhibits intratumoral heterogeneity and is associated with unfavorable pathological features. *Applied Cancer Research* 39(1), p. 1. doi: 10.1186/s41241-018-0071-y

Pierce, J. W., Schoenleber, R., Jesmok, G., Best, J., Moore, S. A., Collins, T. and Gerritsen, M. E. 1997. Novel inhibitors of cytokine-induced IkappaBalpha phosphorylation and endothelial cell adhesion molecule expression show anti-inflammatory effects in vivo. *J Biol Chem* 272(34), pp. 21096-21103. doi: 10.1074/jbc.272.34.21096

Ping, Q. et al. 2021. Cancer-associated fibroblasts: overview, progress, challenges, and directions. *Cancer Gene Ther* 28(9), pp. 984-999. doi: 10.1038/s41417-021-00318-4

Porzycki, P. and Ciszkowicz, E. 2020. Modern biomarkers in prostate cancer diagnosis. *Cent European J Urol* 73(3), pp. 300-306. doi: 10.5173/ceju.2020.0067R

Powley, I. R. et al. 2020. Patient-derived explants (PDEs) as a powerful preclinical platform for anti-cancer drug and biomarker discovery. *Br J Cancer* 122(6), pp. 735-744. doi: 10.1038/s41416-019-0672-6

Prescott, J. L., Blok, L. and Tindall, D. J. 1998. Isolation and androgen regulation of the human homeobox cDNA, NKX3.1. *Prostate* 35(1), pp. 71-80. doi: 10.1002/(sici)1097-0045(19980401)35:1<71::aid-pros10>3.0.co;2-h

Qian, L. H., Wang, X. L. and Tu, Z. H. 2001. Atrophy and apoptosis in ventral prostate of rats induced by 5alpha-reductase inhibitor, epristeride. *Acta Pharmacol Sin* 22(5), pp. 399-404.

Qin, X., Jiang, B. and Zhang, Y. 2016. 4E-BP1, a multifactor regulated multifunctional protein. *Cell Cycle* 15(6), pp. 781-786. doi: 10.1080/15384101.2016.1151581

Qu, Z., Ren, Y., Shen, H., Wang, H., Shi, L. and Tong, D. 2021. Combination Therapy of Metastatic Castration-Recurrent Prostate Cancer: Hyaluronic Acid Decorated, Cabazitaxel-Prodrug and Orlistat Co-Loaded Nano-System. *Drug Des Devel Ther* 15, pp. 3605-3616. doi: 10.2147/dddt.S306684

Rabanal-Ruiz, Y., Otten, E. G. and Korolchuk, V. I. 2017. mTORC1 as the main gateway to autophagy. *Essays Biochem* 61(6), pp. 565-584. doi: 10.1042/ebc20170027

Ramadass, V., Vaiyapuri, T. and Tergaonkar, V. 2020. Small Molecule NF-κB Pathway Inhibitors in Clinic. *Int J Mol Sci* 21(14), doi: 10.3390/ijms21145164

Ratnacaram, C. K., Teletin, M., Jiang, M., Meng, X., Chambon, P. and Metzger, D. 2008. Temporally controlled ablation of PTEN in adult mouse prostate epithelium generates a model of invasive prostatic adenocarcinoma. *Proc Natl Acad Sci U S A* 105(7), pp. 2521-2526. doi: 10.1073/pnas.0712021105

Rauert-Wunderlich, H., Siegmund, D., Maier, E., Giner, T., Bargou, R. C., Wajant, H. and Stühmer, T. 2013. The IKK inhibitor Bay 11-7082 induces cell death independent from inhibition of activation of NFκB transcription factors. *PLoS One* 8(3), p. e59292. doi: 10.1371/journal.pone.0059292

Rawla, P. 2019. Epidemiology of Prostate Cancer. *World J Oncol* 10(2), pp. 63-89. doi: 10.14740/wjon1191

Reilly, M. et al. 2013. Randomized, double-blind, placebo-controlled, dose-escalating phase I, healthy subjects study of intravenous OPN-305, a humanized anti-TLR2 antibody. *Clin Pharmacol Ther* 94(5), pp. 593-600. doi: 10.1038/clpt.2013.150

Rinne, N. et al. 2021. Targeting the PI3K/AKT/mTOR pathway in epithelial ovarian cancer, therapeutic treatment options for platinum-resistant ovarian cancer. *Cancer Drug Resistance* 4(3), pp. 573-595. doi: 10.20517/cdr.2021.05

Risbridger, G. P., Toivanen, R. and Taylor, R. A. 2018. Preclinical Models of Prostate Cancer: Patient-Derived Xenografts, Organoids, and Other Explant Models. *Cold Spring Harb Perspect Med* 8(8), doi: 10.1101/cshperspect.a030536

Ritch, C. R. and Cookson, M. S. 2016. Advances in the management of castration resistant prostate cancer. *BMJ* 355, p. i4405. doi: 10.1136/bmj.i4405

Roeckel, N. et al. 2009. High frequency of LMAN1 abnormalities in colorectal tumors with microsatellite instability. *Cancer Res* 69(1), pp. 292-299. doi: 10.1158/0008-5472.Can-08-3314

Romac, J. M. et al. 2010. Transgenic expression of pancreatic secretory trypsin inhibitor-1 rescues SPINK3-deficient mice and restores a normal pancreatic phenotype. *Am J Physiol Gastrointest Liver Physiol* 298(4), pp. G518-524. doi: 10.1152/ajpgi.00431.2009

Roudsari, N. M. et al. 2021. Inhibitors of the PI3K/Akt/mTOR Pathway in Prostate Cancer Chemoprevention and Intervention. *Pharmaceutics* 13(8), doi: 10.3390/pharmaceutics13081195

Rubin, M. A. and Demichelis, F. 2018. The Genomics of Prostate Cancer: emerging understanding with technologic advances. *Mod Pathol* 31(S1), pp. S1-11. doi: 10.1038/modpathol.2017.166

Sana, T. R., Janatpour, M. J., Sathe, M., McEvoy, L. M. and McClanahan, T. K. 2005. Microarray analysis of primary endothelial cells challenged with different inflammatory and immune cytokines. *Cytokine* 29(6), pp. 256-269. doi: 10.1016/j.cyto.2004.11.003

Sandberg, T. P., Stuart, M., Oosting, J., Tollenaar, R., Sier, C. F. M. and Mesker, W. E. 2019. Increased expression of cancer-associated fibroblast markers at the invasive front and its association with tumor-stroma ratio in colorectal cancer. *BMC Cancer* 19(1), p. 284. doi: 10.1186/s12885-019-5462-2

Saranyutanon, S., Deshmukh, S. K., Dasgupta, S., Pai, S., Singh, S. and Singh, A. P. 2020. Cellular and Molecular Progression of Prostate Cancer: Models for Basic and Preclinical Research. *Cancers (Basel)* 12(9), doi: 10.3390/cancers12092651

Saraswati, S., Marrow, S. M. W., Watch, L. A. and Young, P. P. 2019. Identification of a pro-angiogenic functional role for FSP1-positive fibroblast subtype in wound healing. *Nat Commun* 10(1), p. 3027. doi: 10.1038/s41467-019-10965-9

Sarker, D., Reid, A. H., Yap, T. A. and de Bono, J. S. 2009. Targeting the PI3K/AKT pathway for the treatment of prostate cancer. *Clin Cancer Res* 15(15), pp. 4799-4805. doi: 10.1158/1078-0432.ccr-08-0125

Sathianathen, N. J., Konety, B. R., Crook, J., Saad, F. and Lawrentschuk, N. 2018. Landmarks in prostate cancer. *Nat Rev Urol* 15(10), pp. 627-642. doi: 10.1038/s41585-018-0060-7

Schott, A. F. et al. 2017. Phase Ib Pilot Study to Evaluate Reparixin in Combination with Weekly Paclitaxel in Patients with HER-2-Negative Metastatic Breast Cancer. *Clin Cancer Res* 23(18), pp. 5358-5365. doi: 10.1158/1078-0432.Ccr-16-2748

Scott, E. and Munkley, J. 2019. Glycans as Biomarkers in Prostate Cancer. *Int J Mol Sci* 20(6), doi: 10.3390/ijms20061389

Servant, R. et al. 2021. Prostate cancer patient-derived organoids: detailed outcome from a prospective cohort of 81 clinical specimens. *J Pathol* 254(5), pp. 543-555. doi: 10.1002/path.5698

Shah, R. B., Shore, K. T., Yoon, J., Mendrinos, S., McKenney, J. K. and Tian, W. 2019. PTEN loss in prostatic adenocarcinoma correlates with specific adverse histologic features (intraductal carcinoma, cribriform Gleason pattern 4 and stromogenic carcinoma). *Prostate* 79(11), pp. 1267-1273. doi: 10.1002/pros.23831

Shappell, S. B. et al. 2004. Prostate pathology of genetically engineered mice: definitions and classification. The consensus report from the Bar Harbor meeting of the Mouse Models of Human Cancer Consortium Prostate Pathology Committee. *Cancer Res* 64(6), pp. 2270-2305.

Shen, C., Zhang, J., Qi, M., WYChang, Y. and Han, B. 2014. Roles of Serine Protease Inhibitor Kazal type 1 (SPINK1) in Prostate Cancer. *Medicinal Chemistry* 4,

Shih, V. F., Tsui, R., Caldwell, A. and Hoffmann, A. 2011. A single NFκB system for both canonical and non-canonical signaling. *Cell Res* 21(1), pp. 86-102. doi: 10.1038/cr.2010.161

Shorning, B. Y., Dass, M. S., Smalley, M. J. and Pearson, H. B. 2020. The PI3K-AKT-mTOR Pathway and Prostate Cancer: At the Crossroads of AR, MAPK, and WNT Signaling. *Int J Mol Sci* 21(12), doi: 10.3390/ijms21124507

Singh, M., Jha, R., Melamed, J., Shapiro, E., Hayward, S. W. and Lee, P. 2014. Stromal androgen receptor in prostate development and cancer. *Am J Pathol* 184(10), pp. 2598-2607. doi: 10.1016/j.ajpath.2014.06.022

Soliman, G. A., Acosta-Jaquez, H. A., Dunlop, E. A., Ekim, B., Maj, N. E., Tee, A. R. and Fingar, D. C. 2010. mTOR Ser-2481 autophosphorylation monitors mTORC-specific catalytic activity and clarifies rapamycin mechanism of action. *J Biol Chem* 285(11), pp. 7866-7879. doi: 10.1074/jbc.M109.096222

Son, B., Lee, S., Youn, H., Kim, E., Kim, W. and Youn, B. 2017. The role of tumor microenvironment in therapeutic resistance. *Oncotarget* 8(3), pp. 3933-3945. doi: 10.18632/oncotarget.13907

Soukupová, J. et al. 2021. The Discovery of a Novel Antimetastatic Bcl3 Inhibitor. *Mol Cancer Ther* 20(5), pp. 775-786. doi: 10.1158/1535-7163.Mct-20-0283

Staal, J. and Beyaert, R. 2018. Inflammation and NF-κB Signaling in Prostate Cancer: Mechanisms and Clinical Implications. *Cells* 7(9), doi: 10.3390/cells7090122

Steele, C. W. et al. 2016. CXCR2 Inhibition Profoundly Suppresses Metastases and Augments Immunotherapy in Pancreatic Ductal Adenocarcinoma. *Cancer Cell* 29(6), pp. 832-845. doi: 10.1016/j.ccell.2016.04.014

Stelzer, G. et al. 2016. The GeneCards Suite: From Gene Data Mining to Disease Genome Sequence Analyses. *Curr Protoc Bioinformatics* 54, pp. 1.30.31-31.30.33. doi: 10.1002/cpbi.5

Stewart, T. A., Yapa, K. T. and Monteith, G. R. 2015. Altered calcium signaling in cancer cells. *Biochim Biophys Acta* 1848(10 Pt B), pp. 2502-2511. doi: 10.1016/j.bbamem.2014.08.016

Stifter, S. A. and Greter, M. 2020. STOP floxing around: Specificity and leakiness of inducible Cre/loxP systems. *Eur J Immunol* 50(3), pp. 338-341. doi: 10.1002/eji.202048546

Strutz, F., Okada, H., Lo, C. W., Danoff, T., Carone, R. L., Tomaszewski, J. E. and Neilson, E. G. 1995. Identification and characterization of a fibroblast marker: FSP1. *J Cell Biol* 130(2), pp. 393-405. doi: 10.1083/jcb.130.2.393

Stultz, J. and Fong, L. 2021. How to turn up the heat on the cold immune microenvironment of metastatic prostate cancer. *Prostate Cancer Prostatic Dis* 24(3), pp. 697-717. doi: 10.1038/s41391-021-00340-5

Subramanian, A. et al. 2005. Gene set enrichment analysis: a knowledge-based approach for interpreting genome-wide expression profiles. *Proc Natl Acad Sci U S A* 102(43), pp. 15545-15550. doi: 10.1073/pnas.0506580102

Sun, J., Li, S., Wang, F., Fan, C. and Wang, J. 2019. Identification of key pathways and genes in PTEN mutation prostate cancer by bioinformatics analysis. *BMC Med Genet* 20(1), p. 191. doi: 10.1186/s12881-019-0923-7

Sun, S. C. 2017. The non-canonical NF-κB pathway in immunity and inflammation. *Nat Rev Immunol* 17(9), pp. 545-558. doi: 10.1038/nri.2017.52

Sun, Y. 2016. Tumor microenvironment and cancer therapy resistance. *Cancer Lett* 380(1), pp. 205-215. doi: 10.1016/j.canlet.2015.07.044

Suzuki, A. et al. 2001. T cell-specific loss of Pten leads to defects in central and peripheral tolerance. *Immunity* 14(5), pp. 523-534. doi: 10.1016/s1074-7613(01)00134-0

Switlyk, M. D., Salberg, U. B., Geier, O. M., Vlatkovic, L., Lilleby, W., Lyng, H. and Seierstad, T. 2019. PTEN Expression in Prostate Cancer: Relationship With Clinicopathologic Features and Multiparametric MRI Findings. *AJR Am J Roentgenol*, pp. 1-9. doi: 10.2214/ajr.18.20743

Swonger, J. M., Liu, J. S., Ivey, M. J. and Tallquist, M. D. 2016. Genetic tools for identifying and manipulating fibroblasts in the mouse. *Differentiation* 92(3), pp. 66-83. doi: 10.1016/j.diff.2016.05.009

Tai, Y. L., Lin, C. J., Li, T. K., Shen, T. L., Hsieh, J. T. and Chen, B. P. C. 2020. The role of extracellular vesicles in prostate cancer with clinical applications. *Endocr Relat Cancer* 27(5), pp. R133-r144. doi: 10.1530/erc-20-0021

Tan, R. J., Zhou, D. and Liu, Y. 2016. Signaling Crosstalk between Tubular Epithelial Cells and Interstitial Fibroblasts after Kidney Injury. *Kidney Dis (Basel)* 2(3), pp. 136-144. doi: 10.1159/000446336

Tanaka, K. et al. 2011. Oncogenic EGFR signaling activates an mTORC2-NF-κB pathway that promotes chemotherapy resistance. *Cancer Discov* 1(6), pp. 524-538. doi: 10.1158/2159-8290.Cd-11-0124

Taniguchi, K. and Karin, M. 2018. NF-κB, inflammation, immunity and cancer: coming of age. *Nat Rev Immunol* 18(5), pp. 309-324. doi: 10.1038/nri.2017.142

Taylor, B. S. et al. 2010. Integrative Genomic Profiling of Human Prostate Cancer. *Cancer Cell* 18(1), pp. 11-22. doi: https://doi.org/10.1016/j.ccr.2010.05.026

Tegowski, M. and Baldwin, A. 2018. Noncanonical NF-κB in Cancer. *Biomedicines* 6(2), doi: 10.3390/biomedicines6020066

Thienger, P. and Rubin, M. A. 2021. Prostate cancer hijacks the microenvironment. *Nat Cell Biol* 23(1), pp. 3-5. doi: 10.1038/s41556-020-00616-3

Thorpe, L. M., Yuzugullu, H. and Zhao, J. J. 2015. PI3K in cancer: divergent roles of isoforms, modes of activation and therapeutic targeting. *Nat Rev Cancer* 15(1), pp. 7-24. doi: 10.1038/nrc3860

Tiwari, R. et al. 2020. Androgen deprivation upregulates SPINK1 expression and potentiates cellular plasticity in prostate cancer. *Nat Commun* 11(1), p. 384. doi: 10.1038/s41467-019-14184-0

Toivanen, R. and Shen, M. M. 2017. Prostate organogenesis: tissue induction, hormonal regulation and cell type specification. *Development* 144(8), pp. 1382-1398. doi: 10.1242/dev.148270

Torrealba, N., Vera, R., Fraile, B., Martínez-Onsurbe, P., Paniagua, R. and Royuela, M. 2020. TGF-β/PI3K/AKT/mTOR/NF-kB pathway. Clinicopathological features in prostate cancer. *Aging Male* 23(5), pp. 801-811. doi: 10.1080/13685538.2019.1597840

Tracy, L. E., Minasian, R. A. and Caterson, E. J. 2016. Extracellular Matrix and Dermal Fibroblast Function in the Healing Wound. *Adv Wound Care (New Rochelle)* 5(3), pp. 119-136. doi: 10.1089/wound.2014.0561

Traish, A. M. and Morgentaler, A. 2009. Epidermal growth factor receptor expression escapes androgen regulation in prostate cancer: a potential molecular switch for tumour growth. *Br J Cancer* 101(12), pp. 1949-1956. doi: 10.1038/sj.bjc.6605376

Trimboli, A. J. et al. 2009. Pten in stromal fibroblasts suppresses mammary epithelial tumours. *Nature* 461(7267), pp. 1084-1091. doi: 10.1038/nature08486

Tripathi, M., Billet, S. and Bhowmick, N. A. 2012. Understanding the role of stromal fibroblasts in cancer progression. *Cell Adh Migr* 6(3), pp. 231-235. doi: 10.4161/cam.20419

Triscott, J. and Rubin, M. A. 2018. Prostate Power Play: Does Pik3ca Accelerate Pten-Deficient Cancer Progression? *Cancer Discov* 8(6), pp. 682-685. doi: 10.1158/2159-8290.Cd-18-0369

Trotman, L. C. et al. 2003. Pten dose dictates cancer progression in the prostate. *PLoS Biol* 1(3), p. E59. doi: 10.1371/journal.pbio.0000059

Turner, B. and Drudge-Coates, L. 2010. Prostate cancer: risk factors, diagnosis and management. *Cancer Nursing Practice* 9, pp. 29-36. doi: 10.7748/cnp2010.12.9.10.29.c8126

Turnham, D. J., Bullock, N., Dass, M. S., Staffurth, J. N. and Pearson, H. B. 2020. The PTEN Conundrum: How to Target PTEN-Deficient Prostate Cancer. *Cells* 9(11), doi: 10.3390/cells9112342

Tyekucheva, S. et al. 2017. Stromal and epithelial transcriptional map of initiation progression and metastatic potential of human prostate cancer. *Nature Communications* 8(1), p. 420. doi: 10.1038/s41467-017-00460-4

Valkenburg, K. C., de Groot, A. E. and Pienta, K. J. 2018. Targeting the tumour stroma to improve cancer therapy. *Nat Rev Clin Oncol* 15(6), pp. 366-381. doi: 10.1038/s41571-018-0007-1

Vargas, H. A. et al. 2012. Normal central zone of the prostate and central zone involvement by prostate cancer: clinical and MR imaging implications. *Radiology* 262(3), pp. 894-902. doi: 10.1148/radiol.11110663

Vasudevan, K. M., Gurumurthy, S. and Rangnekar, V. M. 2004. Suppression of PTEN expression by NF-kappa B prevents apoptosis. *Mol Cell Biol* 24(3), pp. 1007-1021. doi: 10.1128/mcb.24.3.1007-1021.2004

Verstak, B., Nagpal, K., Bottomley, S. P., Golenbock, D. T., Hertzog, P. J. and Mansell, A. 2009. MyD88 adapter-like (Mal)/TIRAP interaction with TRAF6 is critical for TLR2- and TLR4-mediated NF-kappaB proinflammatory responses. *J Biol Chem* 284(36), pp. 24192-24203. doi: 10.1074/jbc.M109.023044

Verzella, D. et al. 2016. Targeting the NF-κB pathway in prostate cancer: a promising therapeutic approach? *Curr Drug Targets* 17(3), pp. 311-320. doi: 10.2174/1389450116666150907100715

Vidotto, T., Melo, C. M., Castelli, E., Koti, M., Dos Reis, R. B. and Squire, J. A. 2020. Emerging role of PTEN loss in evasion of the immune response to tumours. *Br J Cancer* 122(12), pp. 1732-1743. doi: 10.1038/s41416-020-0834-6

Wade, C. A. and Kyprianou, N. 2018. Profiling Prostate Cancer Therapeutic Resistance. *Int J Mol Sci* 19(3), doi: 10.3390/ijms19030904

Waldeck, K. et al. 2016. Long term, continuous exposure to panobinostat induces terminal differentiation and long term survival in the TH-MYCN neuroblastoma mouse model. *Int J Cancer* 139(1), pp. 194-204. doi: 10.1002/ijc.30056

Wang, G., Zhao, D., Spring, D. J. and DePinho, R. A. 2018a. Genetics and biology of prostate cancer. *Genes Dev* 32(17-18), pp. 1105-1140. doi: 10.1101/gad.315739.118

Wang, N. et al. 2018b. CXCL1 derived from tumor-associated macrophages promotes breast cancer metastasis via activating NF-κB/SOX4 signaling. *Cell Death Dis* 9(9), p. 880. doi: 10.1038/s41419-018-0876-3

Wang, S., Garcia, A. J., Wu, M., Lawson, D. A., Witte, O. N. and Wu, H. 2006. Pten deletion leads to the expansion of a prostatic stem/progenitor cell subpopulation and tumor initiation. *Proc Natl Acad Sci U S A* 103(5), pp. 1480-1485. doi: 10.1073/pnas.0510652103

Wang, V. Y., Li, Y., Kim, D., Zhong, X., Du, Q., Ghassemian, M. and Ghosh, G. 2017. Bcl3 Phosphorylation by Akt, Erk2, and IKK Is Required for Its Transcriptional Activity. *Mol Cell* 67(3), pp. 484-497.e485. doi: 10.1016/j.molcel.2017.06.011

Wang, X. et al. 2009. A luminal epithelial stem cell that is a cell of origin for prostate cancer. *Nature* 461(7263), pp. 495-500. doi: 10.1038/nature08361

Wang, Y. et al. 2016. Tumor-suppressor NFκB2 p100 interacts with ERK2 and stabilizes PTEN mRNA via inhibition of miR-494. *Oncogene* 35(31), pp. 4080-4090. doi: 10.1038/onc.2015.470

Wang, Y., Zhang, X. L. and Sun, C. M. 2018c. BAY-11-7082 induces apoptosis of multiple myeloma U266 cells through inhibiting NF-κB pathway. *Eur Rev Med Pharmacol Sci* 22(9), pp. 2564-2571. doi: 10.26355/eurrev_201805_14949

Wang, Z., Zhong, J., Inuzuka, H., Gao, D., Shaik, S., Sarkar, F. H. and Wei, W. 2012. An evolving role for DEPTOR in tumor development and progression. *Neoplasia* 14(5), pp. 368-375. doi: 10.1593/neo.12542

Waugh, D. J. and Wilson, C. 2008. The interleukin-8 pathway in cancer. *Clin Cancer Res* 14(21), pp. 6735-6741. doi: 10.1158/1078-0432.Ccr-07-4843

Wee, P. and Wang, Z. 2017. Epidermal Growth Factor Receptor Cell Proliferation Signaling Pathways. *Cancers (Basel)* 9(5), doi: 10.3390/cancers9050052

Weng, L., Brown, J. and Eng, C. 2001. PTEN induces apoptosis and cell cycle arrest through phosphoinositol-3-kinase/Akt-dependent and -independent pathways. *Hum Mol Genet* 10(3), pp. 237-242. doi: 10.1093/hmg/10.3.237

Whang, Y. E., Yuan, X. J., Liu, Y., Majumder, S. and Lewis, T. D. 2004. Regulation of sensitivity to TRAIL by the PTEN tumor suppressor. *Vitam Horm* 67, pp. 409-426. doi: 10.1016/s0083-6729(04)67021-x

Wright, S. C. E., Vasilevski, N., Serra, V., Rodon, J. and Eichhorn, P. J. A. 2021. Mechanisms of Resistance to PI3K Inhibitors in Cancer: Adaptive Responses, Drug Tolerance and Cellular Plasticity. *Cancers (Basel)* 13(7), doi: 10.3390/cancers13071538

Xu, J. et al. 2021. AKT Degradation Selectively Inhibits the Growth of PI3K/PTEN Pathway-Mutant Cancers with Wild-Type KRAS and BRAF by Destabilizing Aurora Kinase B. *Cancer Discov* 11(12), pp. 3064-3089. doi: 10.1158/2159-8290.Cd-20-0815

Yamamoto, H., Shi, X. and Nuttall, A. L. 2009. The influence of loud sound stress on expression of osmotic stress protein 94 in the murine inner ear. *Neuroscience* 158(4), pp. 1691-1698. doi: 10.1016/j.neuroscience.2008.10.063

Yang, J., Nie, J., Ma, X., Wei, Y., Peng, Y. and Wei, X. 2019a. Targeting PI3K in cancer: mechanisms and advances in clinical trials. *Mol Cancer* 18(1), p. 26. doi: 10.1186/s12943-019-0954-x

Yang, W. 2018. *Understanding the role of Bcl-3 in triple-negative breast cancer.* Cardiff.

Yang, X., Li, Y., Zou, L. and Zhu, Z. 2019b. Role of Exosomes in Crosstalk Between Cancer-Associated Fibroblasts and Cancer Cells. *Front Oncol* 9, p. 356. doi: 10.3389/fonc.2019.00356

Yates, A. D. et al. 2019. Ensembl 2020. *Nucleic Acids Research* 48(D1), pp. D682-D688. doi: 10.1093/nar/gkz966

Ye, J., Coulouris, G., Zaretskaya, I., Cutcutache, I., Rozen, S. and Madden, T. L. 2012. Primer-BLAST: a tool to design target-specific primers for polymerase chain reaction. *BMC Bioinformatics* 13, p. 134. doi: 10.1186/1471-2105-13-134

You, D. et al. 2015. FAK mediates a compensatory survival signal parallel to PI3K-AKT in PTEN-null T-ALL cells. *Cell Rep* 10(12), pp. 2055-2068. doi: 10.1016/j.celrep.2015.02.056

Yu, H., Lin, L., Zhang, Z., Zhang, H. and Hu, H. 2020. Targeting NF-κB pathway for the therapy of diseases: mechanism and clinical study. *Signal Transduct Target Ther* 5(1), p. 209. doi: 10.1038/s41392-020-00312-6

Yun, C. W. and Lee, S. H. 2018. The Roles of Autophagy in Cancer. *Int J Mol Sci* 19(11), doi: 10.3390/ijms19113466

Zaidi, Adeel H. and Manna, Sunil K. 2016. Profilin–PTEN interaction suppresses NF-κB activation via inhibition of IKK phosphorylation. *Biochemical Journal* 473(7), pp. 859-872. doi: 10.1042/bj20150624

Zarbock, A., Allegretti, M. and Ley, K. 2008. Therapeutic inhibition of CXCR2 by Reparixin attenuates acute lung injury in mice. *Br J Pharmacol* 155(3), pp. 357-364. doi: 10.1038/bjp.2008.270

Zarif, J. C. and Miranti, C. K. 2016. The importance of non-nuclear AR signaling in prostate cancer progression and therapeutic resistance. *Cell Signal* 28(5), pp. 348-356. doi: 10.1016/j.cellsig.2016.01.013

Zhang, J., Chen, L., Liu, X., Kammertoens, T., Blankenstein, T. and Qin, Z. 2013. Fibroblast-specific protein 1/S100A4-positive cells prevent carcinoma through collagen production and encapsulation of carcinogens. *Cancer Res* 73(9), pp. 2770-2781. doi: 10.1158/0008-5472.Can-12-3022

Zhang, W. et al. 2019. Ex vivo treatment of prostate tumor tissue recapitulates in vivo therapy response. *Prostate* 79(4), pp. 390-402. doi: 10.1002/pros.23745

Zhang, Y. et al. 2008. IkappaBalpha kinase inhibitor IKI-1 conferred tumor necrosis factor alpha sensitivity to pancreatic cancer cells and a xenograft tumor model. *Cancer Res* 68(22), pp. 9519-9524. doi: 10.1158/0008-5472.Can-08-1549

Zhang, Y. et al. 2016a. Targeting IκB Kinase β/NF-κB Signaling in Human Prostate Cancer by a Novel IκB Kinase β Inhibitor CmpdA. *Mol Cancer Ther* 15(7), pp. 1504-1514. doi: 10.1158/1535-7163.Mct-15-0999

Zhang, Y. et al. 2016b. A novel AKT inhibitor, AZD5363, inhibits phosphorylation of AKT downstream molecules, and activates phosphorylation of mTOR and SMG-1 dependent on the liver cancer cell type. *Oncol Lett* 11(3), pp. 1685-1692. doi: 10.3892/ol.2016.4111

Zhen, J. T. et al. 2018. Genetic testing for hereditary prostate cancer: Current status and limitations. *Cancer* 124(15), pp. 3105-3117. doi: 10.1002/cncr.31316

Zheng, B., Zhang, Z., Black, C. M., de Crombrugghe, B. and Denton, C. P. 2002. Ligand-dependent genetic recombination in fibroblasts : a potentially powerful technique for investigating gene function in fibrosis. *Am J Pathol* 160(5), pp. 1609-1617. doi: 10.1016/s0002-9440(10)61108-x

Zheng, C., Chen, J., Chu, F., Zhu, J. and Jin, T. 2019. Inflammatory Role of TLR-MyD88 Signaling in Multiple Sclerosis. *Front Mol Neurosci* 12, p. 314. doi: 10.3389/fnmol.2019.00314

Zhou, M. 2018. High-grade prostatic intraepithelial neoplasia, PIN-like carcinoma, ductal carcinoma, and intraductal carcinoma of the prostate. *Mod Pathol* 31(S1), pp. S71-79. doi: 10.1038/modpathol.2017.138

Zhu, Y. P., Wan, F. N., Shen, Y. J., Wang, H. K., Zhang, G. M. and Ye, D. W. 2015. Reactive stroma component COL6A1 is upregulated in castration-resistant prostate cancer and promotes tumor growth. *Oncotarget* 6(16), pp. 14488-14496. doi: 10.18632/oncotarget.3697

Zong, Y. and Goldstein, A. S. 2013. Adaptation or selection--mechanisms of castration-resistant prostate cancer. *Nat Rev Urol* 10(2), pp. 90-98. doi: 10.1038/nrurol.2012.237

Appendices

1. **STR cell authentication results.** Data obtained from Eurofins Scientific.

Client Sample Name	PC-3	DU145	LNCaP	22RV1
Sample Code	21_ZE_001090	21_ZE_001091	21_ZE_001092	21_ZE_001093
D8S1179	10,13,14	12,13,14,15	13,13	12,13,14
D21S11	27,29,31.2,32.2	30,31,31.2,32,33,34	29,31.2	29,30,31
D7S820	8,11	7,9,10,11,12	8,11	9,10,11
CSF1PO	11,11	10,11,12	11,11	10,11,12
D3S1358	14,16	15,16	16,16	15,15
TH01	6,7,9,9.3	7,7	6,7	6,9.3
D13S317	11,12	12,13,14,15	11,11	9,12,13
D16S539	11,12,13	11,12,13	11,11	11,12,13
D2S1338	18,20	15,16,17	18,20	17,18
D19S433	13,14	12,13,14	14,14	13,14
vWA	17,18,19	17,18,19	17,17	15,16,20,21,22
TPOX	8,9	11,11	8,9	8,8
D18S51	14,15	12,12	14,15	13,14,15
AMEL	X,X	X,Y	X,X	X,Y
D5S818	10,12,13	10,12,13,14	13,13	11,12,13,14
FGA	24,24	21,22	24,24	20,22,23
Database Name	PC-3*	DU145*	PC-3	22RV1*

2. **Mycoplasma test results.** Agarose gel showing mycoplasma negativity of the DU145, LNCAP, PC3 and 22RV1 cell lines used within this project.

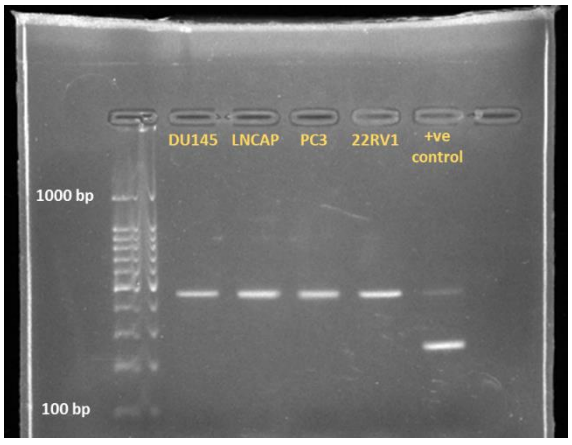

3. **Authentication results of newly used qRT-PCR primers.** Graphs depict A) primer melt curves for i) *Cxcl1* and ii) *RelB* primers tested on *PBiCre*$^{+/-}$ *wildtype* anterior prostate cDNA, ventral prostate cDNA and ddH_2O (n = 3 / technical repeats), B) linear regression trendlines showing average Ct values obtained using 1, 0.1, 0.01 and 0.001 ng of *PBiCre*$^{+/-}$ *wildtype* ventral prostate cDNA (n = 3/technical repeats), and C) image of qRT-PCR products electrophoresed in agarose gel.

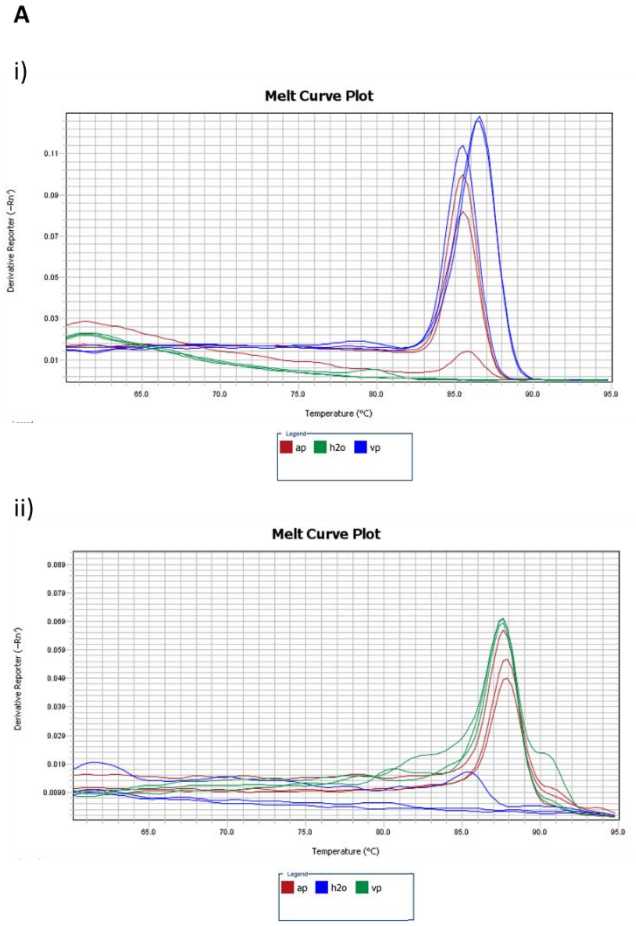

B

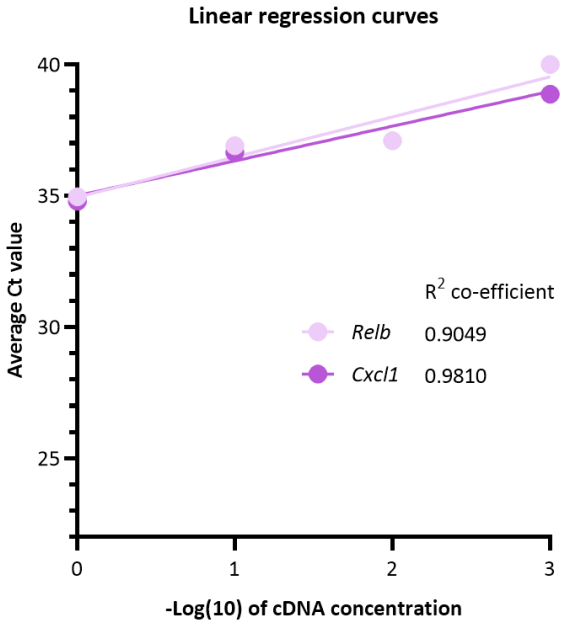
Linear regression curves
40
35
30
25
Average Ct value
0
1
2
3
-Log(10) of cDNA concentration
R2 co-efficient
Relb 0.9049
Cxcl1 0.9810

C

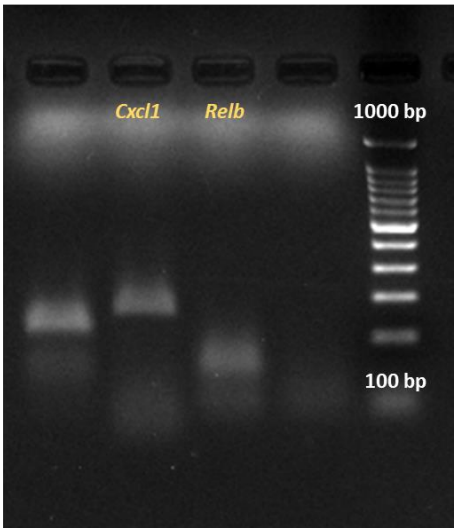
Cxcl1
Relb
1000 bp
100 bp

4. **ΔΔCt methodology used to calculate relative gene expression.** Example shown depicts the calculations performed to establish *Cxcl1* expression relative to *Gapdh*.

Ct values **Gapdh**				
Controls	Technical rep.1	Technical rep.2	Technical rep.3	
H_2O	Undetermined	Undetermined	37.206	
neg RT	Undetermined	Undetermined	34.610	
Experimental samples				**Average Ct**
Wildtype biological rep.1	21.930	21.889	21.682	21.834
Wildtype biological rep.2	22.421	22.419	22.519	22.453
Wildtype biological rep.3	24.420	24.763	24.466	24.550
Intact Pik3ca$^{+/HR}$ biological rep.1	19.676	19.613	19.433	19.574
Intact Pik3ca$^{+/HR}$ biological rep.2	20.630	20.570	19.886	20.362
Intact Pik3ca$^{+/HR}$ biological rep.3	20.236	19.981	19.719	19.979
Cxcl1				
Controls	Technical rep.1	Technical rep.2	Technical rep.3	
H_2O	Undetermined	Undetermined	Undetermined	
neg RT	Undetermined	Undetermined	38.001	
Experimental samples				**Average Ct**
Wildtype biological rep.1	30.928	31.133	31.099	31.054
Wildtype biological rep.2	31.973	31.321	31.593	31.629
Wildtype biological rep.3	33.456	31.661	32.875	32.664
Intact Pik3ca$^{+/HR}$ biological rep.1	26.961	27.038	26.987	26.995
Intact Pik3ca$^{+/HR}$ biological rep.2	27.718	27.968	27.852	27.846
Intact Pik3ca$^{+/HR}$ biological rep.3	28.946	28.918	28.957	28.941
Calculation of fold change				
Experimental samples	Average Ct value for Gapdh	Average Ct value for Cxcl1	Δ Ct (avg2-avg1)	
Wildtype biological rep.1	21.83351072	31.05354436	9.220033646	
Wildtype biological rep.2	22.45308367	31.62898318	9.175899506	
Wildtype biological rep.3	24.55003675	32.66411018	8.114073435	
Intact Pik3ca$^{+/HR}$ biological rep.1	19.57369995	26.99513626	7.42143631	
Intact Pik3ca$^{+/HR}$ biological rep.2	20.36185582	27.8459727	7.484116872	
Intact Pik3ca$^{+/HR}$ biological rep.3	19.97869428	28.94053014	8.961835861	
Average Δ Ct for control	ΔΔ Ct (Δ Ct - control avgΔ Ct)	2^-ΔΔ Ct	Average fold expression per genotype	
8.836668862	0.383364783	0.77		
	0.339230643	0.79	**1.07**	
	-0.722595427	1.65		
	-1.415232552	2.67		
	-1.35255199	2.55	**2.05**	
	0.125166999	0.92		

5. **R script used to perform eGSEA.** The following script was provided by Jason Li, Peter MacCallum Cancer Centre, Victoria, Australia. The necessary packages were downloaded and unpacked using the UK (London) CRAN mirror. This single script was tailored to the individual needs of the analysis, i.e. file paths of the data being evaluated, group names and file paths for the output were altered.

```
#-----------------------------------------------------------------------------------------------------------------------------------------------
>egsea_libpath = "~/junk/rlibs_egsea"
>.libPaths(c(egsea_libpath, .libPaths()))

>library(dplyr)
>library(tibble)

>library(EGSEA)
>library(EGSEAdata)

>library(edgeR)
>library(limma)

### IMPORTANT (1 of 3): modify htseq expression file path
>htseqExpressionMatrixFile = "/researchers/wayne.phillips/Analysis/160715_CAGRF12895/RNA-DEG/Results_v5/HTSEQ/Uncastrated100d2wPtenPik-Castrated100d2wPtenPik_HTSeq_Expression_Matrix.txt"
>toc <- read.table(htseqExpressionMatrixFile, sep="\t", comment="", as.is=T)

#row1: group info: extract group name from htseq matrix (seqliner-dependent?)
>groups <- sapply(toc[1, -1], strsplit, ":")
>for(i in 1:length(groups)) { g <- make.names(groups[[i]][2]); names(groups)[i] <- g; groups[[i]] <- groups[[i]][-2] }

#row2: column header of the data matrix (feature - smpl1 - smpl2 - ... - smplN)
>colNames = make.names(toc[2,])

#get cleaning up feature/gene names?
>featureNames <- gsub(",", ".", toc[-(1:2),1])

>exprMatrix = toc[-(1:2), -1]
>colnames(exprMatrix) = colNames[-1] #exclude the first (feature) column, as is coded as rownames
>rownames(exprMatrix) = featureNames

#casts exprMatrix to numeric
>for(i in colnames(exprMatrix)) exprMatrix[, i] <- as.numeric(exprMatrix[,i])

#calc normalisation factors
>norm_factors <- calcNormFactors(as.matrix(exprMatrix))

#removes feature/genes that are lowly expressed by majority of samples
>isexpr <- rowSums(cpm(exprMatrix)>1) >= 2
>exprMatrix <- exprMatrix[isexpr, ]

#contruct design matrix from group names
>group_fact <- factor(names(groups))
>design <- model.matrix(~ -1 + group_fact)
>colnames(design) <- sub("group_fact", "", colnames(design))

#----------convert featureNames to entrezId
#create symbol to entrezgene lookups
>library("org.Mm.eg.db")

#get canonical gene name first -- note, symbol-entrez mapping still got many-to-many warning..
>globalSym2EntrezTbl = as.data.frame(org.Mm.egALIAS2EG) %>%
        mutate(ENTREZID=gene_id, SYMBOL=alias_symbol) %>%
        dplyr::select(SYMBOL,ENTREZID)
```

```
#need to create SYMBOL column which is a result of alias2SymbolTable() - can't do in one dplyr call
>exprMatrix_genelist = exprMatrix %>%
                rownames_to_column("originalSymbol") %>%
                mutate(SYMBOL=originalSymbol) %>%
                dplyr::select(originalSymbol, SYMBOL)
#leave alias2SymbolTable() NA result as is
>a2s = alias2SymbolTable(exprMatrix_genelist[,"originalSymbol"], species="Mm")
>exprMatrix_genelist[!is.na(a2s),"SYMBOL"] =  a2s[!is.na(a2s)]

#join with globalSym2EntrezTbl to get the EntrezId
>sym2entrez_map = exprMatrix_genelist %>%
                left_join(globalSym2EntrezTbl, by="SYMBOL")

#Note that there could be 1:n mapping happening,
# judgement call: find the 1:n mapping and remove them.
# better to be consistently missing a feature, ie. more predictable outcomes rather than unintended randomisation happening.
>one2ManyMappedGenes =  sym2entrez_map %>%
> group_by(originalSymbol) %>% summarise(n = n()) %>% filter(n > 1) %>%
> dplyr::select(originalSymbol) %>% pull()

>one2ManyMappedGenesEntrez =  sym2entrez_map %>%
 > filter(!is.na(ENTREZID)) %>% group_by(ENTREZID) %>% summarise(n = n()) %>% filter(n > 1) %>%
  >dplyr::select(ENTREZID) %>% pull()

>mappable_exprMatrix_genelist = sym2entrez_map %>%
                        filter(!(originalSymbol %in% one2ManyMappedGenes)) %>%
                        filter(!is.na(ENTREZID)) %>%
                        filter(!(ENTREZID %in% one2ManyMappedGenesEntrez)) %>%
                        column_to_rownames("originalSymbol") %>%
                        dplyr::select("ENTREZID")


#apply mapping on 1:1 genes EntrezID mapping only, and leave the rest as is
>mapped_entrezIds = exprMatrix_genelist  %>%
                mutate(ENTREZID = originalSymbol) %>%
                column_to_rownames("originalSymbol") %>%
                dplyr::select(ENTREZID)
>mappable_genelist = rownames(mappable_exprMatrix_genelist)
>mapped_entrezIds[mappable_genelist,"ENTREZID"] = >mappable_exprMatrix_genelist[mappable_genelist,"ENTREZID"]
#update exprMatrix rownames
>rownames(exprMatrix) = mapped_entrezIds[,"ENTREZID"]

#Entrez to Symbolname, for egsea (heading is "FeatureID" and "Symbols"; for ENTREZID/symbol name)
>symbolsMap = mapped_entrezIds %>%
            rownames_to_column("Symbols") %>%
            mutate(FeatureID=ENTREZID) %>%
            dplyr::select(FeatureID, Symbols)
#create voom object
>y <- voom(exprMatrix, design, plot=F, lib.size=colSums(exprMatrix)*norm_factors)


### IMPORTANT (2 of 3): Define contrast from group
#create contrast matrix (column is contrasts, row is groups)
#contrasts=matrix(c(-1,1), ncol=1, nrow=2)
>contrasts=matrix(c(-1,1), ncol=1, nrow=2)
>rownames(contrasts) = unique(names(groups))
>colnames(contrasts) = c("Castrated100d2wPtenPik_vs_Uncastrated100d2wPtenPik")

#setup and run egsea
### IMPORTANT (3 of 3): configure egsea runs: (a) base methods, (b) geneset to check, (c) report path

>baseMethods = c("camera", "safe", "gage", "padog", "zscore",
```

```
        "gsva", "globaltest", "ora")

#gs.annots = buildKEGGIdx(entrezIDs = rownames(exprMatrix), species = "mouse")
>gs.annots = buildMSigDBIdx(entrezIDs = rownames(exprMatrix), species = "mouse", geneSets = c("c2"))


>reportPath='~/rna-seq/egsea/helenpearson_egsea1b/c2/'
>dir.create(reportPath, showWarnings = TRUE, recursive = T)
>gsa = egsea(voom.results = y, contrasts = contrasts, gs.annots = gs.annots,
        symbolsMap = symbolsMap, baseGSEAs = baseMethods, sort.by = "med.rank",
        num.threads = 8, report = TRUE, report.dir = reportPath, interactive=T)
#-------------------------------------------------------------------------------------------------------------------------------------------------------------
```

6. **RIN values of samples used in RNA-Sequencing.** RIN values were determined by Dr Helen Pearson through use of a Bioanalyzer.

		Dnase treated RNA			Bioanalyser
		ng/ul	260/280	260/230	RIN
PBiCre Pik3ca+/HR	300 d + 10 wk non-castrate	303.73	2.06	1.65	9.4
PBiCre Pik3ca+/HR	300 d + 10 wk non-castrate	212.94	2.06	1.64	9.6
PBiCre Pik3ca+/HR	300 d + 10 wk non-castrate	314.53	2.06	1.69	7.7
PBiCre Pik3ca+/HR	300 d + 10 wk non-castrate	306.37	1.99	2	9
PBiCre Pik3ca+/HR	300 d + 10 wk non-castrate	436.65	2.04	1.89	8.1
PBiCre Pik3ca+/HR	300 d castrate, 10 wk	150.58	1.92	1.51	8.3
PBiCre Pik3ca+/HR	300 d castrate, 10 wk	145.59	2.06	1.51	7.7
PBiCre Pik3ca+/HR	300 d castrate, 10 wk	51.53	1.89	1.45	7.8
PBiCre Pik3ca+/HR	300 d castrate, 10 wk	72.92	1.79	1.6	9
PBiCre Pik3ca+/HR	300 d castrate, 10 wk	127.81	2	1.02	7.3
PBiCre WT	100 d	162.86	2.04	1.67	7.6
PBiCre WT	100 d	74.48	2.01	1.35	7.4
PBiCre WT	100 d	69.06	2.05	1.3	8.4
PBiCre WT	100 d	97.18	2.04	0.95	9.1
PBiCre WT	100 d	88.49	2.03	1.36	8.9
PBiCre Ptenfl/fl	castrated 200 d, 10 wk	123.6	2.08	1.45	9.2
PBiCre Ptenfl/fl	castrated 200 d, 10 wk	112.84	2.06	1.66	8.7
PBiCre Ptenfl/fl	castrated 200 d, 10 wk	142.44	2.08	1.55	8.3
PBiCre Ptenfl/fl	castrated 200 d, 10 wk	395.06	2.1	1.97	7.5
PBiCre Ptenfl/fl	castrated 200 d, 10 wk	175.78	2.09	1.7	8.2
PBiCre Ptenfl/fl	non-castrate 200d, 10 wk	82.68	2.02	1.46	8.8
PBiCre Ptenfl/fl	non-castrate 200d, 10 wk	217.26	2.11	1.7	9.1
PBiCre Ptenfl/fl	non-castrate 200d, 10 wk	189.57	2.11	1.66	8.6
PBiCre Ptenfl/fl	non-castrate 200d, 10 wk	269.59	2.1	1.88	8.9
PBiCre Ptenfl/fl	non-castrate 200d, 10 wk	117.33	2.1	1.48	9.2

7. **Transcription factor binding sites on promoter regions of significantly deregulated genes enriched within *Pten*-deficient prostate cancer relative to *Pik3ca*-mutant prostate cancer.** Data obtained from GeneCards, (Weizmann Institute of Science and LifeMap Sciences).

Gene	Regulatory transcription factor binding sites present
Aldehyde dehydrogenase 3 family member A1 (Aldh3a1)	AML1a
ADP ribosylation factor like GTPase 14 (Arl14)	CHOP-10 AP-4 Evi-1 C/EBPalpha
Asialoglycoprotein receptor 1 (Asgr1)	SREBP-1a Pax-6 HSF1short HSF1 (long) c-Myb ARP-1 ZID ATF
ATPase 13A4 (Atp13a4)	CREB deltaCREB
UDP-GlcNAc:betaGal beta-1,3-N-acetylglucosaminyltransferase 5 (B3gnt5)	Pbx1a AML1a Lmo2 RelA POU3F2 (N-Oct-5a) POU3F2 (N-Oct-5b) POU3F2 RORalpha1 Sox9
Beta-1,4-galactosyltransferase 6 (B4galt6)	AhR POU3F2 (N-Oct-5a) POU3F2 (N-Oct-5b) CUTL1 POU3F2 E47 RORalpha1 POU2F1 POU2F1a HFH-1
Basic leucine zipper ATF-like transcription factor (Batf)	STAT1 AP-1 ATF-2 STAT1beta STAT1alpha STAT2 STAT3 c-Jun
BCL3 transcription coactivator (Bcl3)	STAT5B STAT1 Lmo2 Olf-1 AP-2gamma NF-kappaB C/EBPalpha GATA-2 STAT3 NF-kappaB1
Caspase 1 (Casp1)	C/EBPbeta ISGF-3 AP-1 ATF-2 IRF-1 c-Jun
C-C motif chemokine ligand 20 (Ccl20)	HFH-3 Pax-5 Nkx2-2 NF-kappaB E47 C/EBPalpha FOXI1 Chx10 NF-kappaB1 LyF-1
C-C motif chemokine ligand 22 (Ccl22)	GATA-3 AP-1 ATF-2 IRF-7A c-Jun NF-kappaB1
C-C motif chemokine ligand 4 (Ccl4)	CREB AML1a deltaCREB STAT3
C-C motif chemokine ligand 8 (Ccl8)	Brachyury C/EBPalpha NF-AT YY1 PPAR-gamma1 NF-AT4 NF-AT2 NF-AT3 PPAR-gamma2 NF-AT1
C-C motif chemokine receptor 7 (Ccr7)	Bach2 STAT5A GATA-1 c-Ets-1 Egr-4 MEF-2A STAT3 aMEF-2
C-C motif chemokine receptor like 2 (Ccrl2)	USF1 STAT1 USF-1 STAT5A
CD44 molecule (Cd44)	PPAR-gamma1 PPAR-gamma2
CD83 molecule (Cd83)	FOXF2 AML1a Olf-1 MIF-1 LCR-F1 Evi-1 S8 POU2F1 POU2F1a Cart-1
C-type lectin domain containing 7A (Clec7a)	Nkx3-1 Nkx3-1 v4 AML1a GATA-3 FOXD3 Nkx3-1 v1 GATA-2 GATA-1 Nkx3-1 v2 Nkx3-1 v3

CAP-Gly domain containing linker protein family member 4 (Clip4)	STAT5A Arnt C/EBPalpha HNF-1A GATA-1 AREB6 E2F-1 E2F HNF-1 TGIF
Cytidine/uridine monophosphate kinase 2 (Cmpk2)	NF-1 NF-1/L Pax-5 STAT5A NF-kappaB c-Ets-1 AREB6 HEN1 Sox9 NF-kappaB1
Collagen triple helix repeat containing 1 (Cthrc1)	GR AML1a NRSF form 1 GR-beta FOXD3 AP-4 NRSF form 2 GR-alpha c-Myc ATF6
C-X-C motif chemokine ligand 1 (Cxcl1)	Bach1 C/EBPbeta STAT1 AML1a NF-kappaB2 MyoD STAT1beta NF-kappaB1 Evi-1 STAT1alpha
C-X-C motif chemokine ligand 11 (Cxcl11)	AML1a STAT3
C-X-C motif chemokine ligand 2 (Cxcl2)	TBP PPAR-gamma1 AML1a TFIID PPAR-gamma2 NF-E2 C/EBPalpha
C-X-C motif chemokine ligand 3 (Cxcl3)	Max1 STAT1 STAT4 STAT1beta HNF-3beta STAT1alpha STAT2 ARP-1 STAT3 Ik-1
C-X-C motif chemokine ligand 5 (Cxcl5)	HEN1 AML1a HNF-3beta Meis-1b GATA-1
DExD/H-box helicase 58 (Ddx58)	TBP GR AP-1 GR-beta ATF-2 YY1 GATA-1 STAT3 c-Jun GR-alpha
DExD/H-box helicase 60 (Ddx60)	RORalpha1 NF-AT4 NF-AT2 p300 NF-AT3 AP-4 NF-AT NF-AT1 C/EBPalpha
DNA damage regulated autophagy modulator 1 (Dram1)	-
Dual specificity phosphatase 2 (Dusp2)	HEN1 p53 AP-1 ATF-2 HNF-4alpha2 c-Jun HNF-4alpha1
Epithelial stromal interaction 1 (Epsti1)	GR GR-beta Brachyury POU2F1 POU2F1b HSF2 POU2F1a IRF-7A POU2F1c GR-alpha
Fc fragment of IgM receptor (Faim3)	ER-alpha HNF-1 CUTL1 Nkx2-5 HNF-1A HNF-4alpha1
Guanylate binding protein 2 (Gbp2)	AML1a
Gamma-secretase activating protein (Gsap)	-
Glutathione S-transferase omega 1 (Gsto1)	GCNF Tal-1beta E47 Arnt c-Ets-1 CREB HEN1 GCNF-1 deltaCREB GCNF-2
Histone deacetylase 9 (Hdac9)	MEF-2A aMEF-2
HECT and RLD domain containing E3 ubiquitin protein ligase family member 6 (Herc6)	Nkx3-1 v4 AML1a AP-4 NF-AT Nkx3-1 v2 NF-AT4 NF-AT2 Nkx3-1 v3 NF-AT3 NF-AT1
Homocysteine inducible ER protein with ubiquitin like domain 1 (Herpud1)	CREB deltaCREB
5-hydroxytryptamine receptor 3A (Htr3a)	GR NRSF form 1 GR-alpha NRSF form 2

Intercellular adhesion molecule 1 (Icam1)	CREB AP-2alpha isoform 3 deltaCREB AP-2alpha isoform 4 AP-2alpha isoform 2 AP-2alpha AP-2alphaA
Interferon induced protein 44 (Ifi44)	TBP Bach1 Tal-1 Pbx1a Bach2 STAT5A CUTL1 IRF-1 TFIID
Interferon induced protein with tetratricopeptide repeats 1 (Ifit1)	ISGF-3 AML1a POU3F2 (N-Oct-5a) POU3F2 (N-Oct-5b) POU3F2 Gfi-1 GATA-1 ATF6
Interferon induced protein with tetratricopeptide repeats 3 (Ifit3)	RFX1 STAT1 Nkx6-1 IRF-7A Evi-1 C/EBPalpha
Interferon induced transmembrane protein 1 (Ifitm1)	GR STAT1 Pax-5 STAT3 ZID GR-alpha c-Ets-1
Interferon induced transmembrane protein 3 (Ifitm3)	GR STAT1 GATA-3 Pax-5 Cart-1 STAT3 GR-alpha
Immunoglobulin heavy constant mu (Ighm)	-
Joining chain of multimeric IgA and IgM (Igj)	Oct-B1 oct-B2 AML1a FOXJ2 (long isoform) Lmo2 FOXJ2 XBP-1 STAT5A
Interleukin 1 alpha (Il1a)	c-Fos AP-1 ATF-2 c-Jun
interleukin 1 beta (Il1b)	COUP-TF1 AP-1 ATF-2 COUP HNF-4alpha2 HNF-4alpha1 COUP-TF STAT3 GR-alpha c-Jun
Interleukin 1 receptor antagonist (Il1rn)	FOXI1 HFH-3 POU2F1 POU2F1a STAT3
Interleukin 2 receptor subunit gamma (Il2rg)	GR RP58 GR-beta p300 Nkx2-5 Evi-1 COMP1 HOXA5 IRF-7A GR-alpha
Interleukin 7 receptor (Il7r)	AML1a
Interleukin 8 (Il8)	GR AML1a HNF-4alpha2 NF-E2 p45 HNF-4alpha1 C/EBPalpha GR-alpha NF-E2
Interferon regulatory factor 7 (Irf7)	p300 STAT3 C/EBPalpha
ISG15 ubiquitin like modifier (Isg15)	CREB p53 deltaCREB MyoD STAT3
Integrin subunit beta 6 (Itgb6)	STAT5B STAT1 STAT4 STAT6 STAT1beta STAT5A Nkx2-5 STAT1alpha STAT2 STAT3
IL2 inducible T cell kinase (Itk)	STAT1 AML1a GATA-3 FOXJ2 (long isoform) c-Myb Nkx3-1 v1 FOXJ2 IRF-1
Potassium calcium-activated channel subfamily N member 4 (Kcnn4)	Egr-3 p53 AP-1 ATF-2 NRSF form 1 c-Jun NRSF form 2
Keratin 14 (Krt14)	TBP Sp1 AP-2alpha isoform 3 AP-2alpha isoform 2 C/EBPalpha STAT3 AP-2alpha isoform 4 AP-2alpha AP-2alphaA
Keratin 17 (Krt17)	CRE-BP1 STAT1 p53 RREB-1 Lmo2 STAT3 Gfi-1

Keratin 4 (Krt4)	RFX1 p300 FOXD3 Tal-1beta HNF-4alpha1 YY1 E47 PPAR-alpha Zic1 STAT3
Keratin 5 (Krt5)	AP-1 p53 COMP1 NRSF form 1 ATF-2 c-Jun NRSF form 2
Keratin 6A (Krt6a)	AP-1 AML1a Pax-5 AP-4 STAT5A HNF-4alpha1 GATA-2 AREB6 FOXO4
Keratin 75 (Krt75)	TBP AML1a AP-1 Bach2 C/EBPalpha GATA-2 CHOP-10 JunD FOXC1 SEF-1 (1)
LCK proto-oncogene, Src family tyrosine kinase (Lck)	STAT1 Sp1 AP-1 AML1a STAT3 STAT1alpha
Galectin 3 binding protein (Lgals3bp)	RP58 FOXF2 Pax-5 RelA HNF-3beta NF-kappaB PPAR-gamma2 ZIC2/Zic2 MRF-2 NF-kappaB1
Galectin 9 (Lgals9)	POU2F2 (Oct-2.1) Oct-B1 oct-B3 oct-B2 CUTL1 POU2F2 POU2F2C POU2F1 POU2F1a POU2F2B
LHFPL tetraspan subfamily member 2 (Lhfpl2)	STAT1 NF-1 Pbx1a RelA POU3F2 E47 c-Ets-1 Ik-2 LyF-1 ATF
LIF interleukin 6 family cytokine (Lif)	STAT1 ATF-2 STAT1beta STAT5A Max STAT3 c-Jun c-Myc
Mitogen-activated protein kinase 10 (Mapk10)	CREB deltaCREB
MARCKS like 1 (Marcksl1)	AP-1 ATF-2 AP-2gamma PPAR-gamma1 AP-2beta PPAR-gamma2 c-Jun NF-kappaB1 AP-2alphaA
Matrix metallopeptidase 13 (Mmp13)	CREB STAT1 deltaCREB FOXO3a FOXO3 FOXO3b
Matrix metallopeptidase 16 (Mmp16)	Pax-5 Nkx2-2 ITF-2 Tal-1beta E47 ATF
Matrix metallopeptidase 3 (Mmp3)	SRF Sox5 AP-1 SRF (504 AA) HNF-1A SRY HNF-1 STAT3
Macrophage scavenger receptor 1 (Msr1)	AP-1 ATF-2 c-Jun GATA-1
NLR family apoptosis inhibitory protein (Naip5 *NAIP)	AML1a FOXD1 Pax-2 STAT5A Pax-2a MEF-2A Pax-2b POU2F1 POU2F1a aMEF-2
NFKB inhibitor epsilon (Nfkbie)	ISGF-3 Elk-1 GATA-3 MyoD E47 Egr-4 Egr-2 RORalpha1 IRF-2 c-Myb
Hydroxycarboxylic acid receptor 2 (Niacr1 *HCAR2)	-
Nitric oxide synthase 2 (Nos2)	p300 MyoD IRF-1 HNF-3beta HNF-4alpha1
Out at first homolog (Oaf)	AML1a HNF-3beta Ik-3 RORalpha2 PPAR-alpha AREB6 POU2F1 POU2F1a FOXO1a FOXO1
2'-5'-oligoadenylate synthetase 2 (Oas2)	Elk-1 En-1

2'-5'-oligoadenylate synthetase 3 (Oas3)	HEN1 E47
2'-5'-oligoadenylate synthetase like (Oasl1 *OASL)	Elk-1 RFX1 STAT1beta Olf-1 STAT1alpha PPAR-gamma1 IRF-2 NRF-2 Ik-2 PPAR-gamma2
Poly(ADP-ribose) polymerase family member 14 (Parp14)	CUTL1 IRF-1 LCR-F1 GATA-1 Meis-1b c-Ets-1 GATA-2 c-Myb Meis-1a Meis-1
Phosphatase and actin regulator 1 (Phactr11)	HOXA9 HOXA9B Gfi-1 Meis-1b MEF-2A FOXJ2 (long isoform) FOXJ2 aMEF-2 FOXO1 Meis-1
Plasminogen activator, tissue type (Plat)	CREB deltaCREB
Pleckstrin (Plek)	AML1a
Phospholipid scramblase 2 (Plscr2)	Nkx2-2 GCNF FOXL1 GATA-1 Nkx6-1 POU2F1 GCNF-1 POU2F1a GCNF-2
Plexin C1 (Plxnc1)	E2F-4 E2F-3a E2F-5 Spz1 Pax-5 E2F-2 GATA-2 E2F E2F-1
Protein kinase AMP-activated catalytic subunit alpha 2 (Prkaa2)	Nkx3-1 v2 Nkx3-1 FOXI1 HFH-3 Nkx3-1 v4 HFH-1 Nkx3-1 v3 Nkx3-1 v1
Pyrin and HIN domain family member 1 (Pyhin1)	Nkx2-2 Pax-6 Tal-1beta Meis-1b Evi-1 E47 AREB6 IRF-7A ITF-2
RELB proto-oncogene, NF-kB subunit (Relb)	GR AP-1 GR-beta ATF-2 STAT3 GR-alpha c-Jun
Regulator of G protein signaling 1 (Rgs1)	TBP Nkx2-5 IRF-1 Nkx5-1 E47 TFIID STAT3 Hand1 RSRFC4
Radical S-adenosyl methionine domain containing 2 (Rsad2)	NF-1 NF-1/L STAT5A NF-kappaB GATA-1 c-Ets-1 AREB6 HEN1 Sox9 NF-kappaB1
Receptor transporter protein 4 (Rtp4)	Nkx2-5 STAT5A IRF-1 FOXO3b Max FOXJ2 (long isoform) FOXO3a FOXJ2 ATF6 c-Myc
Sterile alpha motif domain containing 9 like (Samd9l)	MEF-2A IRF-2 FOXO4 MEF-2 IRF-1 aMEF-2
Solute carrier family 15 member 3 (Slc15a3)	AML1a AP-1 ATF-2 c-Jun NF-kappaB NF-kappaB1 Arnt
Solute carrier family 2 member 6 (Slc2a6)	AML1a Lmo2 LCR-F1 GATA-2 c-Ets-1 E2F-1 E2F FOXO1a FOXO1
Solute carrier family 7 member 2 (Slc7a2)	E2F-3a E2F-1 E2F Chx10 Nkx2-5 E2F-2
Small proline rich protein 1A (Sprr1a)	ER-alpha ISGF-3 p300 NCX/Ncx Olf-1 Ik-3 E47 C/EBPalpha SEF-1 (1) En-1
Serglycin (Srgn)	TBP STAT1 HNF-3beta c-Ets-1 FAC1 E2F-1 CP2 E2F TFIID
Signal transducer and activator of transcription 1 (Stat1)	STAT5B Max1 AP-1 IRF-1 S8 COMP1 FOXO1a RSRFC4 c-Myc FOXO1

Signal transducer and activator of transcription 4 (Stat4)	c-Fos Bach1 GR AP-1 GATA-3 IRF-1 POU2F1 POU2F1a GR-alpha c-Jun
Transporter 1, ATP binding cassette subfamily B member (Tap1)	AML1a STAT3
Toll like receptor 2 (Tlr2)	AP-1 ATF-2 CREB PPAR-gamma1 deltaCREB STAT3 IRF-7A PPAR-gamma2 c-Jun
Transmembrane protein 171 (Tmem171)	STAT5B USF1 POU2F1 p53 USF-1 POU2F1a LCR-F1 Meis-1b
Tenascin C (Tnc)	Sp1 AP-1 ATF-2 STAT3 c-Jun NF-kappaB1
Tumour necrosis factor (Tnf)	c-Fos p53 AP-1 ATF-2 c-Jun
TNF alpha induced protein 3 (Tnfaip3)	-
TNF alpha induced protein 8 like 3 (Tnfaip8l3)	TBP HFH-3 FOXD1 NF-AT AREB6 FOXI1 FOXC1 FOXJ2 (long isoform) FOXJ2 ATF6
TNF receptor superfamily member 9 (Tnfrsf9)	Bach2 SREBP-1c SREBP-1b c-Ets-1 FOXL1 Max POU2F1 SREBP-1a POU2F1a c-Myc
TNF superfamily member 10 (Tnfsf10)	GR STAT1 Sp1 HSF1 (long) STAT5A PPAR-gamma1 HSF1short IRF-7A PPAR-gamma2 GR-alpha
Tripartite motif containing 15 (Trim15)	Max1 AML1a MyoD Nkx2-5 c-Ets-1 Arnt MZF-1 E2F-1 E2F
Tripartite motif containing 6 (Trim6)	Sp1 AP-1 MyoD LCR-F1 Meis-1 C/EBPalpha
Tubulin beta 2B class IIb (Tubb2b)	C/EBPbeta MyoD Olf-1 HNF-3beta Arnt Gfi-1 IRF-2 Cart-1 Pax-4a
Ubiquitin D (Ubd)	Nkx3-1 SREBP-1c Egr-1 E47 SREBP-1b Egr-2 Max SREBP-1a Hand1 c-Myc
Ubiquitin conjugating enzyme E2 L6 (Ube2l6)	AREB6 STAT1 CUTL1 Roaz
Ubiquitin specific peptidase 18 (Usp18)	STAT1 HTF Pax-2 STAT1beta Pax-2a STAT1alpha Pax-2b POU2F1 HOXA5 POU2F1a
Vascular cell adhesion molecule 1 (Vcam1)	CREB STAT1 deltaCREB PPAR-gamma2 IRF-1
WAP four-disulfide core domain 2 (Wfdc2)	STAT1 Sp1 Pax-6 Pax-2 STAT1beta Nkx2-5 IRF-1 Pax-2a STAT1alpha COMP1

8. **Transcription factor binding sites on promoter regions of significantly deregulated genes enriched within castrated *Pik3ca*-mutant and *Pten*-deficient prostate cancer relative to castrated *Pten*-null prostate cancer.** Data obtained from GeneCards, (Weizmann Institute of Science and LifeMap Sciences).

Gene	Regulatory transcription factor binding sites present
ATP binding cassette subfamily C member 5 (Abcc5)	SRF NF-1 SRF (504 AA) POU6F1 (c2) CUTL1 Tal-1beta E47 FOXL1 AREB6
ATP binding cassette subfamily C member 8 (Abcc8)	GR Max1 CREB AML1a Sp1 GR-beta GR-alpha Nkx2-5
Caspase recruitment domain-containing protein 11 (Card11)	STAT1 AML1a AP-1 ATF-2 STAT1beta Lmo2 STAT1alpha STAT2 c-Jun NF-kappaB1
Collagen type I alpha 1 chain (Col1a1)	GR USF1 GR-beta HSF1 (long) GATA-1 AREB6 USF-1 c-Myb HSF1short GR-alpha
Collagen type I alpha 2 chain (Col1a2)	c-Fos C/EBPbeta Sp1 AP-1 ATF-2 c-Jun CBF(2)
Collagen type III alpha 1 chain (Col3a1)	Pbx1a Bach2 FOXD1 Nkx2-5 POU3F2 (N-Oct-5a) POU3F2 (N-Oct-5b) POU3F2 NF-kappaB NF-kappaB1 Hlf
Collagen type IIII alpha 5 chain (Col4a5)	Nkx3-1 Nkx3-1 v1 NF-AT NF-AT4 NF-AT2 HOXA5 SEF-1 (1) NF-AT3 Nkx3-1 v3 NF-AT1
Collagen type IIII alpha 6 chain (Col4a6)	NF-AT4 NF-AT2 HOXA5 NF-AT3 NF-AT1 NF-AT
Collagen type V alpha 1 chain (Col5a1)	Max1 AhR AP-2alpha isoform 3 AP-2alpha isoform 2 C/EBPalpha Arnt RORalpha2 AP-2alpha isoform 4 AP-2alphaA
Collagen type V alpha 2 chain (Col5a2)	CUTL1 C/EBPalpha HNF-1A CHOP-10 HNF-1 FOXO1a STAT3 Meis-1 En-1 FOXO1
Collagen type V alpha 3 chain (Col5a3)	Bach1 AML1a Sp1 Bach2 NRSF form 1 NRSF form 2 HEN1 ATF
Collagen type VI alpha 1 chain (Col6a1)	Max1 AML1a AP-1 ATF-2 RelA NF-kappaB c-Jun NF-kappaB1 c-Myc Ik-1
Collagen type VI alpha 2 chain (Col6a2)	TBP Elk-1 AP-1 RREB-1 SREBP-1c Nkx2-5 SREBP-1b SREBP-1a HOXA5
Collagen type VI alpha 3 chain (Col6a3)	LHX3b/Lhx3b AML1a RelA NF-kappaB POU2F1 POU2F1a LHX3a/Lhx3a NF-kappaB1 Pax-4a RSRFC4
Collagen type VII alpha 1 chain (Col7a1)	HEN1 GR Pax-5 AP-1 ATF-2 GR-alpha c-Jun
Collagen type VIII alpha 1 chain (Col8a1)	p53 SREBP-1c FOXD3 Evi-1 E47 SREBP-1b AREB6 SREBP-1a RSRFC4
Collagen type IX alpha 3 chain (Col9a3)	AhR MAZR HNF-4alpha2 Ik-3 HNF-4alpha1 CP2 POU2F1 POU2F1a Pax-4a Zic3

Collagen type X alpha 1 chain (Col10a1)	TBP ISGF-3 AML1a STAT5A NF-kappaB TFIID NF-kappaB2 ARP-1 Sox9 NF-kappaB1
Collagen type XI alpha 2 chain (Col11a2)	Sp1
Collagen type XV alpha 1 chain (Col15a1)	COUP-TF1 LHX3b/Lhx3b Brachyury COUP HNF-4alpha2 CUTL1 HNF-4alpha1 c-Ets-1 COUP-TF LHX3a/Lhx3a
Collagen type XX alpha 1 chain (Col20a1)	STAT5B ATF-2 STAT5A Ik-3 LCR-F1 CREB IRF-7A c-Jun MRF-2 ATF6
Collagen type XXV alpha 1 chain (Col25a1)	C/EBPbeta NF-1/L NF-1 FOXF2 MyoD MIF-1 POU2F1 E2F-1 E2F HFH-1
Collagen type XXVII alpha 1 chain (Col27a1)	RFX1 ISGF-3 NCX/Ncx XBP-1 RelA Nkx2-5 Nkx5-1 Egr-4 PPAR-alpha Hlf
Eukaryotic translation initiation factor 4E-binding protein 1 (Eif4ebp1)	USF1 Pax-5 MyoD AP-2gamma USF-1 Zic1 STAT3 AP-2beta AP-2alpha AP-2alphaA
Homeobox B6 (Hoxb6)	E2F AP-1 AML1a
Integrin subunit alpha 8 (Itga8)	GR RP58 ATF-2 FOXD1 CRE-BP1 MEF-2A AREB6 c-Myb GR-alpha aMEF-2
Plexin B1 (Plxnb1)	HEN1 p53
Protein kinase C gamma (Prkcg)	Egr-3 TBP Sp1 HSF1 (long) GATA-1 CREB deltaCREB HSF1short Pax-4a
Proline and serine rich coiled-coil 1 (Psrc1)	E2F-4 E2F-3a E2F-5 E2F-1 p53 Nkx2-5 E2F-2
SEC61 translocon alpha 2 subunit (Sec61a2)	AML1a Brachyury FOXD1 HSF1 (long) Pax-2 IRF-1 Pax-2a C/EBPalpha FOXL1 HSF1short
Stanniocalcin 2 (Stc2)	MAZR STAT5A HNF-4alpha1 Max S8 E2F POU2F1 POU2F1a ATF6 c-Myc

9. **SynergyFinder generated heatmaps of viability data.** Plots represent viability data following combination treatment with AKTi (Capivasertib) and i) canonical NF-κBi (BAY11-7082), ii) BCL3i (CB1), iii) CXCR1/2i (Reparixin) and iv) TLR2i (C29), in A) DU145, B) LNCAP, C) PC3 and D) 22RV1 prostate cancer cell lines. n = 3 / biological repeats and 95% confidence interval shown.

i)

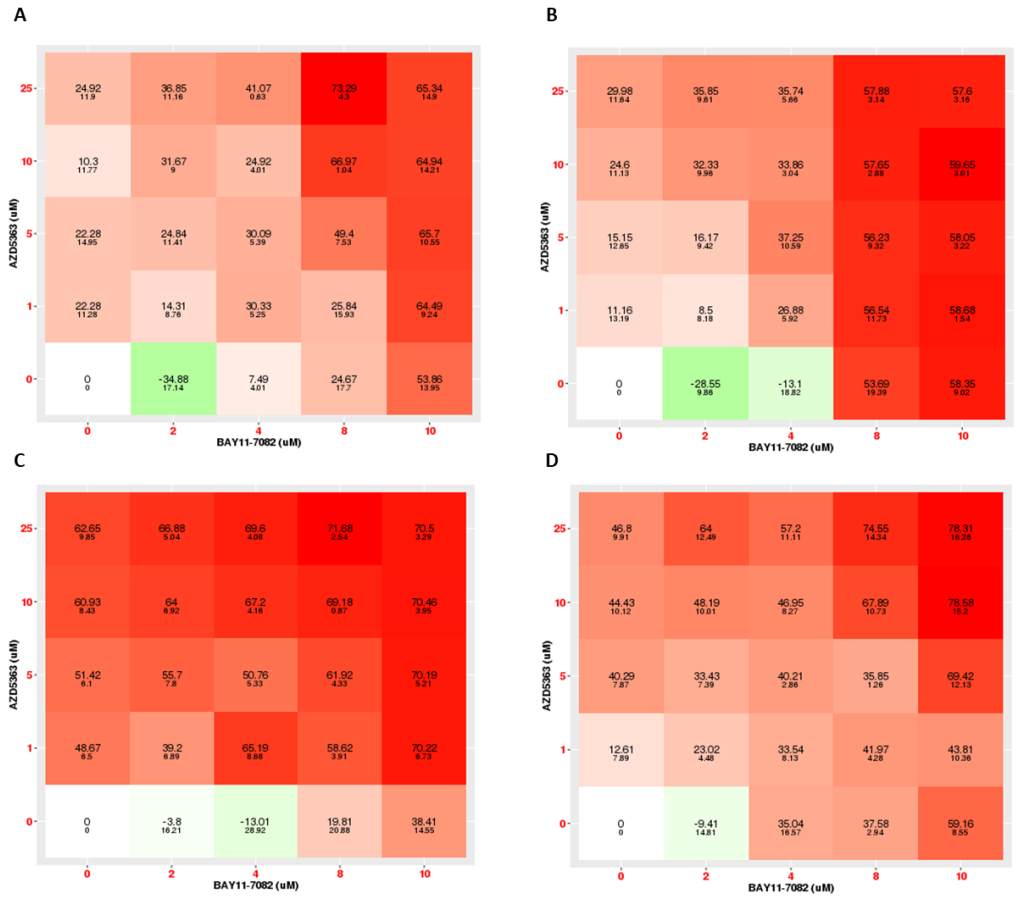
A
B
C
D
AZD5363 (uM)
BAY11-7082 (uM)
25
10
5
1
0
0
2
4
8
10

ii)

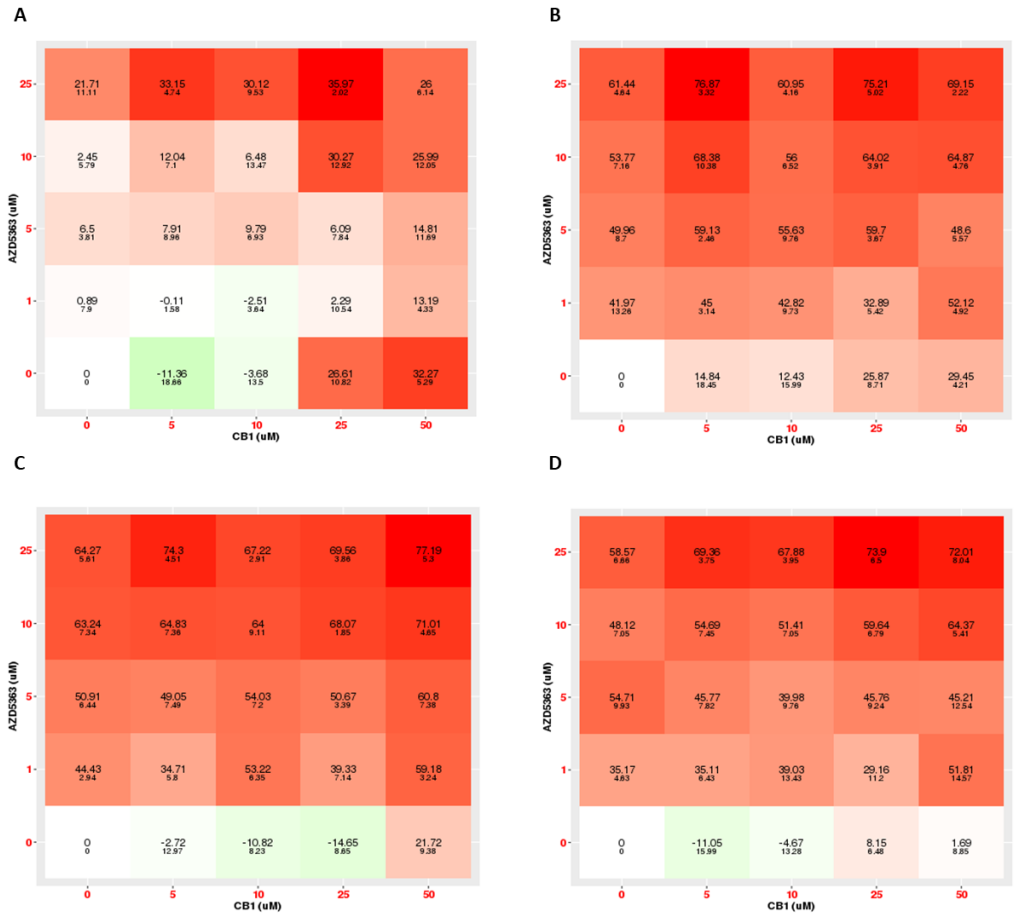
A
B
C
D
AZD5363 (uM)
CB1 (uM)
25
10
5
1
0
0
5
10
25
50

iii)

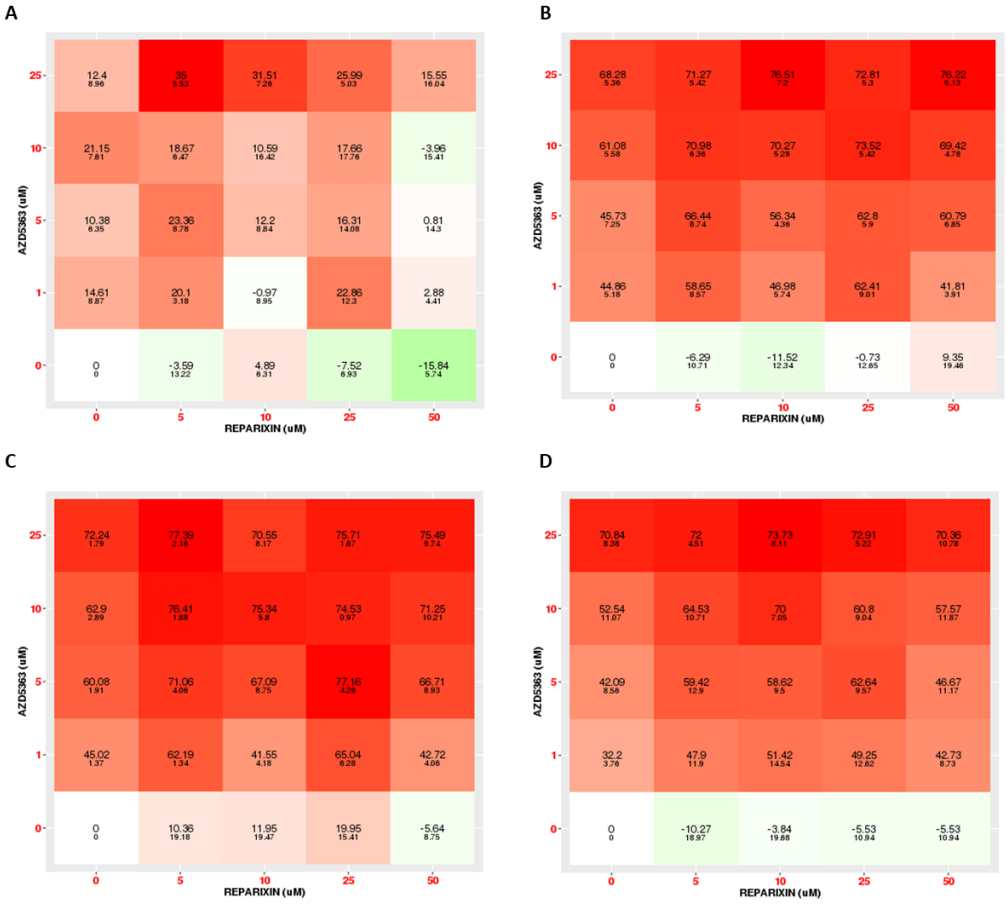
A
B
C
D
AZD5363 (uM)
REPARIXIN (uM)
0
5
10
25
50
12.4 8.96
35 5.53
31.51 7.26
25.99 5.03
15.55 16.04
21.15 7.81
18.67 6.47
10.59 16.42
17.66 17.76
-3.96 15.41
10.38 6.35
23.36 8.78
12.2 8.84
16.31 14.08
0.81 14.3
14.61 8.87
20.1 3.18
-0.97 8.95
22.86 12.3
2.88 4.41
0 0
-3.59 13.22
4.89 6.31
-7.52 6.93
-15.84 5.74
68.28 5.36
71.27 5.42
76.51 7.2
72.81 5.3
76.22 5.13
61.08 5.58
70.98 6.36
70.27 5.28
73.52 5.42
69.42 4.78
45.73 7.25
66.44 8.74
56.34 4.36
62.8 5.9
60.79 6.85
44.86 5.18
58.65 8.57
46.98 5.74
62.41 9.01
41.81 3.91
0 0
-6.29 10.71
-11.52 12.34
-0.73 12.65
9.35 19.48
72.24 1.79
77.39 2.16
70.55 8.17
75.71 1.87
75.49 9.74
62.9 2.89
76.41 1.88
75.34 5.8
74.53 0.97
71.25 10.21
60.08 1.91
71.06 4.06
67.09 8.75
77.16 4.26
66.71 8.93
45.02 1.37
62.19 1.34
41.55 4.18
65.04 6.28
42.72 4.06
0 0
10.36 19.18
11.95 19.47
19.95 15.41
-5.64 8.75
70.84 8.36
72 4.51
73.73 8.11
72.91 5.22
70.36 10.78
52.54 11.07
64.53 10.71
70 7.05
60.8 9.04
57.57 11.87
42.09 8.56
59.42 12.9
58.62 9.5
62.64 9.57
46.67 11.17
32.2 3.76
47.9 11.9
51.42 14.54
49.25 12.82
42.73 8.73
0 0
-10.27 18.97
-3.84 19.88
-5.53 10.94
-5.53 10.94

iv)

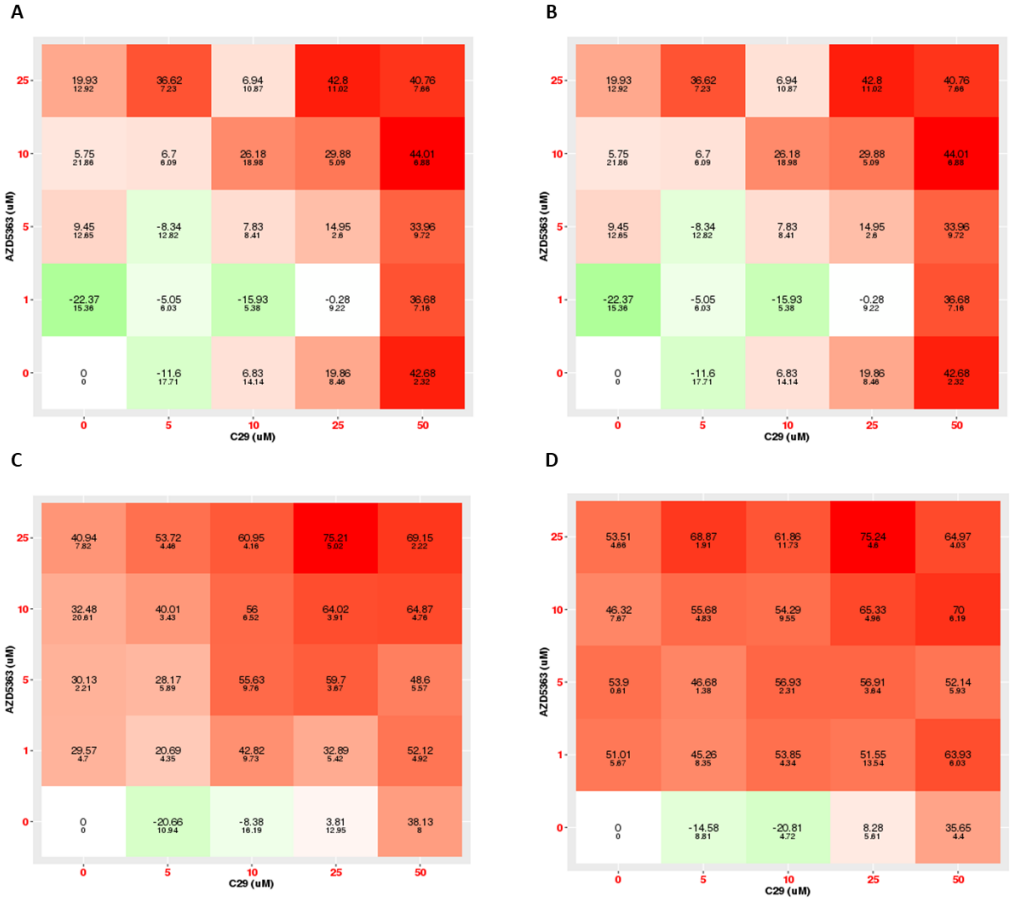
A
B
C
D
AZD5363 (uM)
C29 (uM)
0
5
10
25
50
19.93 12.92
36.62 7.23
6.94 10.87
42.8 11.02
40.76 7.86
5.75 21.86
6.7 6.09
26.18 18.98
29.88 5.09
44.01 6.88
9.45 12.65
-8.34 12.82
7.83 8.41
14.95 2.8
33.96 9.72
-22.37 15.36
-5.05 6.03
-15.93 5.38
-0.28 9.22
36.68 7.16
0 0
-11.6 17.71
6.83 14.14
19.86 8.46
42.68 2.32
40.94 7.82
53.72 4.46
60.95 4.16
75.21 5.02
69.15 2.22
32.48 20.81
40.01 3.43
56 6.52
64.02 3.91
64.87 4.76
30.13 2.21
28.17 5.89
55.63 9.76
59.7 3.87
48.6 5.57
29.57 4.7
20.69 4.35
42.82 9.73
32.89 5.42
52.12 4.92
0 0
-20.66 10.94
-8.38 16.19
3.81 12.95
38.13 8
53.51 4.66
68.87 1.91
61.86 11.73
75.24 4.6
64.97 4.03
46.32 7.87
55.68 4.83
54.29 9.55
65.33 4.96
70 6.19
53.9 0.61
46.68 1.38
56.93 2.31
56.91 3.84
52.14 5.93
51.01 5.87
45.26 8.35
53.85 4.34
51.55 13.54
63.93 6.03
0 0
-14.58 8.81
-20.81 4.72
8.28 5.81
35.65 4.4